Nutritional Assessment and Proximate Analysis of Selected Vegetables Grown in Larkana, Sindh, Pakistan

Niaz Ali Malghani[1] iD **, Sarfaraz Ahmed Mahesar[1]** iD **, Jameel Ahmed Baig[1]** iD **,**
Farah Naz Talpur[1] iD **, Syed Tufail Hussain Sherazi[1]** iD **, and Mirza Junaid[2]** iD

[1]National Centre of Excellence in Analytical Chemistry, University of Sindh, Jamshoro-76060, Pakistan
[2]Department of Paediatric, Peoples University of Medical and Health Sciences for Women, Shaheed Banazirabad, Nawabshah, Pakistan

Abstract: Food security and protection are the most crucial concerns worldwide. However, vegetables may significantly contribute to the macro and micro-nutrients for good health compared to dietary supplements. Eight vegetables of the Larkanadivision, namely spinach (*Spinacia oleracea*), brinjal (*Solanum melongina* L.), sponge gourd (*Luffa acutangula*), lotus root *(Lelumbo nucifera)*, okra (*Abelmoschus esculentus*), coriander leave *(Coriandrum sativum)*, fenugreek leave (*Trigonella foenum graecum*), and cauliflower (*Brassica oleracea*) were studied for their proximate, macro and micro-mineral contents to estimate their importance in human nutrition. The results showed that almost all vegetables contain appreciable amounts of essential nutrients. All the vegetables showed moisture contents of >70.00%. Lotus and sponge gourd have a maximum level of carbohydrates (>10.00%). Fiber was found in the range of 2.70 – 5.10%, with the highest in the okra. Protein and fat were found at < 4.00%, with maximum protein in spinach and fat in fenugreek leaves. The studied vegetables showed maximum levels of K and Ca, followed by Na, Mg, Fe, Zn, and Cu while Cr and Mn were observed to be < 5.00 μg/g. The macro and micro-minerals in the studied vegetables were within the maximum permissible limits recommended by WHO. Moreover, the eight studied vegetables of the Larkana division can also provide up to 1.00% of the required dietary daily intake of macro and micro-nutrients as recommended by the Food and Nutrition Board.

INTRODUCTION

Compared to other food products, vegetables are low-cost sources of energy. Vegetables are rich in essential nutrients comprising carbohydrates, protein, vitamins, calcium (Ca), iron (Fe), ascorbic acid, trace minerals, and phytochemicals (1). These vegetables provide energy and nutrients to human beings (2). Quality control and management are important aspects of food selection. Therefore, the national and international agencies, especially Food and Agricultural Organization (FAO) and the World Health Organization (WHO) have set the recommended levels for this nutrition in the food commodities for human beings (3). There are two types of essential nutrients that are required for a healthy life. The first one is the macronutrients, including water (moisture content), carbohydrates, fibers, fats, and proteins while the second is the micro-nutrients, including minerals (macro and micro minerals), vitamins, and phytochemicals (4). These macronutrients (carbohydrate, lipid, and protein) are instant and general sources of energy for humans and all other living organisms. However, ash and water only play a part in mass (5).

Furthermore, the vegetables contain macro minerals such as Ca, potassium (K), sodium (Na), and magnesium (Mg), as well as micro minerals such as Fe, copper (Cu), manganese (Mn), chromium (Cr), and zinc (Zn). Minerals are important because they significantly contribute to the several metabolic functions in living cells (6, 7).

Minerals can be conjugated proteins or bonded to other micromolecules, such as phosphates and polyphenols (8). These minerals can participate in several metabolic processes in living cells because they are constituents of several enzymes (9). Deficiencies in micro-nutrients have become a major health issue globally. These deficiency disorders lead to poor quality of life. The deficiencies may raise when people lack access to micronutrient-rich foods such as animal products, vegetables, fruits, and fortified foods, typically due to low dietary quality or a lack of dietary variety from several food groups (10, 11). The weakest groups usually suffering from micronutrient deficiencies are pregnant women, young children, and lactating women because of relatively higher micronutrient requirements, which are more susceptible to the harmful consequences of micronutrient deficiencies (12, 13). Macro-minerals (Na, K, Ca, and Mg) and chloride ions must be required to balance extracellular fluid for muscular irritability (4). Ca has a significant effect on growth. However, it has a negative impact on health and increases the risk of osteoporosis (14, 15). Fe and vitamin A deficiencies are the most prevalent forms of micro-nutrient malnutrition apart from Zn deficiency (16, 17). It has been reported that over 25% of the global population suffers from Fe deficiency, particularly in young women and children. Anemia is caused by insufficient consumption of Fe, leading to a decrease in red blood cells (RBCs) or hemoglobin. This may cause tiredness and fatigue, weakness, shortness of breath, and reduced exercise tolerance (18, 19). Similarly, Zn acts as a cofactor of various enzymes involved in gene expression, nucleic acid and amino acid metabolism, and cell replication (20). Moreover, the metabolism and bioavailability of essential vitamins (A and E) may also depend on the status of Zn (21). Cu is another important micro-mineral and assists Fe in being used in an early stage of hemopoiesis as well as essential for the neurologic and haematologic systems. Its deficiency may increase the content of Fe in the liver and vice versa (21, 22). Metabolism and reproductive function are only a few of the metabolic roles of Mn. It plays a role similar to an antioxidant, which protects cells from damage due to free radicals (23). Mn also plays an essential role in the regulation of cellular energy, bone and connective tissue growth, and blood clotting (24). Compared to dietary supplements, vegetables may contain large amounts of these macro and micro nutrients, which are necessary for optimal health (25). Based on the aforementioned facts, it is important to establish food composition data of macro and micro-nutrients in common vegetables in the Larkana region, which is required for nutritional planning and epidemiological studies.

The objective of this study is to establish the levels of macro-nutrients (moisture, ash, carbohydrates, fats, proteins, fiber), macro-minerals (Na, K, Ca, and Mg) and micro-minerals (Cr, Cu, Fe, Mn, and Zn) in local vegetables of Larkana division, Pakistan. The analytical characteristics such as precision and accuracy of methods for each element were studied in detail. Meanwhile, the obtained estimated daily dietary intake of each vegetable was compared with the recommended daily mineral requirements for adults. The contents of macro and micro-nutrients in vegetables were compared to literature reported values.

MATERIAL AND METHOD

Description of the study area
Larkana is located in the northwest part of Sindh (upper Sindh) on the right bank of the River Indus. Larkana district is split into four sub-divisions and 48 union councils for administrative purposes. The climate of Larkana is subtropical, with hot summers and freezing winters. It has an average temperature of 2 to 48 °C. The annual rainfall in the study area is more significant than 127 mm. The total population of this district is about 1.4 million, and 28.7% of the total population lives in urban areas. The coordinates of the research area 27°33′30″ N and 68°12′40″E are north of the Indus River and lie between North (6.41 km) and East (3.43 km), covering an area of 18.08 km^2. Larkana is famous due to the thousands of tons of quality production of Guava fruit. The weather permits the growth of various cereals and vegetable crops, including rice, wheat, tomato, cabbages, brinjal, okra, spinach, sponge gourd, coriander, fenugreek, lotus, onion and chilly, etc. grow in different villages of Larkana on the right bank of River Indus such as Gulab Bhutto, Goth Dodo, Shadan JatoiMahotta, Naudero, Chooharpur, Agani, Metla, Izzat Ji Wandh, Phulpota, and other villages.

Sampling of vegetables
During 2020–2021, fifty-seven samples of eight vegetables were collected randomly from Gulab Bhutto, Goth Dodo, Chooharpur, and ShadanJatoi villages of Larkana, Sindh, Pakistan. Vegetable samples include eight spinach (*Spinacia oleracea),* seven brinjals (*Solanum melongina. L*), eight sponge gourd (*Luffa acutangula*), ten lotus root *(Lelumbo nucifera)*, eight okra (*Abelmoschus esculentus*), six coriander leaves (*Coriandrum sativum*), six fenugreek leaves (*Trigonella foenum graecum*), and four cauliflower (*Brassica oleracea*) were collected as shown in Table 1.

Table 1: List of studied vegetables with their English & local names family, scientific name, and edible parts.

English Names	Local name	Family	Botanical Names	Part used
Spinach	Palak	Amaranthacea	*Spinacia oleracea*	Leaves
Brinjal	Wagan	Solanaceae	*Solanum melongina* L.	Fruits
Spongiguord	Tore	Cucurbitae	*Luffa acutangula*	Fruits
Lotus root	Bahi	Nelumbonaceae	*Lelumbo nucifera*	Roots
Okra	Bhandi	Malvaceae	*Abelmoschus esculentus*	Fruits (pods)
Coriander leaves	Dhana	Apiaceae	*Coriandrum sativum*	Leaves
Fenugreek leaves	Hurbo	Fabaceae	*Trigonella foenum graecum*	Leaves
Cauliflower	Gobe	Brassicaceae	*Brassica oleracea*	Fruits

As reported by Kazi et al. (27), all-vegetable samples were returned to the lab, they were placed through a three-step washing procedure that included agitating and rinsing with distilled water. A freeze drier was used to dry the vegetables, as Khan et al. (26) briefly reported. The dried vegetable samples were pulverized in an agate mortar and sieved through a nylon sieve with a mesh size of 75 mm. Before standard procedure analysis, the final samples were maintained in a labeled polypropylene container at room temperature.

Reagents and glassware
During the experiment, high-purity water (conductivity 0.05 S/cm) was acquired from a Milli-Q purification system (Bedford, MA, USA). The concentrated reagents of Merck (Darmstadt, Germany) such as sulphuric acid (H_2SO_4), nitric acid (HNO_3), hydrochloric acid (HCl), hydrogen peroxide (H_2O_2), boric acid (H_3BO_3), copper sulphate ($CuSO_4$), and other analytical reagents, while acetone (C_3H_6O) and sodium hydroxide (NaOH) was purchased from Sigma Aldrich (St. Louis, MO, USA). The essential metals' typical working solutions (Ca, Cr, Cu, Fe, Mn, Mg, K, Na, and Zn) were freshly prepared by diluting recognized standard solutions of the respective element in a series of steps (1,000 mg/L) purchased from Fluka Kamica (Buchs, Switzerland) in 0.2 mol.L^{-1} HNO_3. The acid digestion method for metals in vegetables was validated using BCR-189 (wholemeal flour) and BCR-100 (beech leaves). Table 2 indicated that the method is quantitative for metals analysis by the AAS method, as reported earlier (28).

Apparatus
The analysis of Na, K, Ca, Mg, Cu, Fe, and Zn were determined by flame atomic absorption spectrometer (FAAS) of Hitachi (Tokyo, Japan) assembled with a hollow cathode lamp flame atomizer (air-acetylene). In contrast, Cr and Mn were measured using pyrocoated graphite tubes by graphite furnace atomic absorption spectrometer (GF-AAS). The instrumental conditions for measurement by both techniques were set according to the vendor's manual, as reported elsewhere (27). For digestion of vegetable samples, a hotplate (Heidolph MR Hei-Standard, Germany) was used. The hollow cathode lamps of Cr and Mn were used, working at 7.5 mA current, passing through a 1.3 and 0.4 nm spectral bandwidth for 357.9 and 279.5 nm, respectively. The heating program for Cr and Mn by GF was adjusted according to the manual for drying, ashing, atomization, and cleaning steps as temperature range °C/time (s) [(80-120/15), (300-700/15), (2600-2700/5), and (2700-2900/2)] and [(80-120/15), (400-500/15), (2400-2500/5), (2500-2800/5)], respectively. The acid digested and chemical modifier solutions (10 + 10 µL) were introduced directly into the GF. A deuterium lamp was used for background correction. Argon gas was used as a carrier gas with 200 mL.min^{-1} for each analysis.

The wavelengths, lamp currents, and spectral bandwidths for Na, K, Ca, Mg, Cr, Cu, Fe, Mn, and Zn were used as 589 nm, 10 mA, and 0.4 nm; 767 nm,10 mA, and 2.6nm, 423 nm,7.5 mA, and 2.6 nm; 285 nm,7.5 mA, and 2.6 nm; 357.9 nm, 7.5 mA, and 1.3 nm; 325 nm, 8.0 mA, and 1.3 nm; 248 nm,10 mA, and 0.2 nm; 279.5 nm, 7.5 mA, and 0.4 nm; and 214 nm, 7.55 mA, and 1.3 nm, respectively. The flame air pressure were set at 1.60 kg.cm^{-2} for all studied elements whilst the pressures of acetylene and height of burner for analysis of Na, K, Ca, Mg, Cu, Fe, and Zn are set as 0.20 kg.cm^{-2}, and 7.5 mm; 0.30 kg.cm^{-2}, and 7.5 mm; 0.40 kg.cm^{-2}, and 12.5 mm; 0.30 kg.cm^{-2}, and 7.5 mm; 0.20 kg.cm^{-2}, and 7.5 mm; 0.30 kg.cm^{-2}, and 7.5 mm; and 0.25 kg.cm^{-2}, and 7.5 mm, respectively.

Table 2: Analytical characteristics of conventional acid digestion method for essential metals by certified reference materials.

a. Certified reference material Wholemeal Flour BCR-189			
Metals	Certified / Estimated value	Obtained Values	Recovery(%)[a]
Cu	6.40±0.20	6.32±0.08	98.70
Mn	63.30±1.60	62.90±0.07	99.40
b. Certified reference material Beech leaves BCR-100			
Metals	Certified / Estimated value	Obtained Values	Recovery(%)[a]
Na	240.00	247±2.40	103.00
K	9940.00	9935±180.00	100.00
Ca	5300.00	5288±42.00	99.80
Mg	878.00	880±15.00	100.00
Cr	8.00	7.95±0.08	99.40
Fe	550.00	547±5.00	99.50
Zn	69.00	73.0±1.85	99.50

[a]Recovery % = Obtained / Certified/estimated × 100.

Procedures for Proximate Analysis

The term "proximate analysis of vegetables" refers to examining the entire content of a dietary component (29). The dried vegetables were analyzed for proximate composition, including moisture content, ash content, fats, protein, fiber, and carbohydrates. The proximate analysis of vegetables was performed at the laboratories of NCEAC, University of Sindh, Jamshoro. For the moisture, ash, protein, fat, fiber, and carbohydrate content of the vegetables, the Association of Official Analytical Chemists (30) procedures were used. Moisture content was determined using an AOAC method No. 930.15 reported by Iheanacho et al. (28). The standard methods No. 942.05, No. 984.13, No. 920.39, and No. 978-10 were used to estimate ash, protein, fat, and fiber content in vegetable samples, and total carbohydrates were determined by the difference method (100 - (proteins + fats + moisture + ash) as reported by Hussain et al. (31).

Conventional Wet Acid Digestion Methods

For minerals analyses, 0.5 g of vegetable samples in triplicate and 0.2 g of BCR-100 samples in separate conical flasks were treated with the concentrated 5 mL mixture of H_2O_2 and HNO_3 (1:2, v/v), initially for 30 min at ordinary temperature and then at 80 °C on an electric hotplate until the transparent semi-dried materials left. The digested vegetable samples were cooled at ordinary temperature and added 10 mL 0.2 N solution of HNO_3. The mixture solutions were filtered using filter paper (Whatman No. 42). Likewise, the same method was used for the preparation of blank samples.

Analytical Figure of Merit and Method Validation

The equations for the detection limit of the normal calibration curves of essential elements are given in Table 3.

Statistical Analysis

The calibration analyses and compilation of experimental data were performed by "*Excel*" 2010 (Microsoft Office ®). The significance of each statistical test was measured at $p< 0.05$. The assessment of the significant variation of elemental experimental data was tested by the student *t-test*.

Estimation of Daily Intake

The daily intake of macro and micronutrients in vegetables was calculated using adults' average vegetable consumption rate (g/day), followed by the formula given below as reported elsewhere (32).

$$DI = C_{\text{macro and micronutrients in vegetables}} \times AC$$

Where DI stands for daily intake of macronutrients (fiber, fat, protein, and carbohydrate) and micronutrients (Na, K, Ca, Mg, Cr, Cu, Fe, Mn, and Zn) in $g.day^{-1}$ or $mg.day^{-1}$ or $\mu g.day^{-1}$ from vegetables, C is the concentration of macronutrients in g/kg, micronutrients (macro-minerals Na, K, Ca, and Mg) in mg/kg and micro-minerals (Cr, Cu, Fe, Mn, and Zn) in $\mu g.kg^{-1)}$ in each vegetable, and AC is the average consumption of vegetable g/day. The AC of spinach, brinjal, sponge gourd, lotus root, okra, and cauliflower was estimated at 25 g/day based on their consumption of 1.0 kg for a family of four people in a week. In contrast, AC of coriander and fenugreek leaves was $5.00\ g.day^{-1}$ based on their 20.00 g application per day to prepare daily meals for a family of four-people.

Table 3: Slope and intercepts with linear regression lines of concentration versus absorption data of standard solutions of different elements.

Element	Dynamic Range ($\mu g.L^{-1}$)	Regression equation	R^2	LOD/LOQ ($\mu g.L^{-1}$)
Na	100-5000	$y = 0.363x - 2.9 \times 10^{-3}$	0.991	5.52/18.40
K	100-5000	$y = 0.143x - 5.0 \times 10^{-4}$	0.996	14.00/46.80
Ca	750-2000	$Y = 1.44 \times 10^{-2}x + 4.0 \times 10^{-4}$	0.999	164.00/547.00
Mg	100- 5000	$Y = 9.0 \times 10^{-4}x + 1.0 \times 10^{-3}$	0.998	2.46/8.21
Cu	100-1000	$y = 0.128x + 6.0 \times 10^{-5}$	0.997	17.30/57.70
Cr	50-500	$y = 5.0 \times 10^{-4}x + 2.3 \times 10^{-3}$	0.998	4.70/15.80
Fe	500 – 2000	$y = 3.2 \times 10^{-2}x - 4.0 \times 10^{-4}$	0.992	69.20/231.00
Mn	100-2000	$y = 0.138x + 2.0 \times 10^{-3}$	0.995	17.70/59.10
Zn	100-2000	$y = 0.199x + 4.0 \times 10^{-4}$	0.990	10.00/33.50

RESULTS AND DISCUSSION

The proximate analysis of all the vegetables depends on the source of water and soil used for their growth as reported by Naz et al. (33). The proximate analyses like moisture, ash, protein, fat, fiber, and carbohydrate contents in vegetable samples were measured and found to be significantly different from each other ($p < 0.05$), as listed in Table 4. Moisture content in vegetables is a good source of water and is necessary as it is considered that around 20% of the total water consumption must come from food moisture (34). The average moisture content holding capacities depended on the vegetables' nature and the environment (34). Moisture contents in spinach, brinjal, sponge gourd, lotus root, okra, coriander leaves, fenugreek leaves, and cauliflower were found in the range of 73.30 ± 0.10 – 87.50 ± 0.20% (Table 4). The highest moisture content was observed in brinjal (87.50 ± 0.20%), whereas the lowest was in lotus root (73.30 ± 0.10%). The high moisture content in vegetables (>73.00%) might be due to their water holding capacity, which may vary based on the available pose in leaves/fruit/stem as well as the size and length of xylem in each case. These moisture values in spinach, sponge gourd, coriander leaves, fenugreek leaves, and cauliflower aligned with FAO recommendations (60.00 – 90.00%) for the examined vegetables (29). The comparatively high moisture levels (>73.00%) in the examined vegetables indicated that the vegetables require special attention for proper preservation since they are prone to degradation (35). Similarly, the high moisture content may enhance the activity of water-soluble enzymes and co-enzymes participating in the metabolic processes (29). Similarly, ash content is also an essential biochemical parameter for all the nutritional ingredients, especially minerals, both micro and macronutrients, which are important for the body's normal physiological functions (36). Ash content in spinach, brinjal, sponge gourd, lotus root, okra, coriander leaves, fenugreek leaves, and cauliflower was found to be (3.07 ± 0.40, 4.37 ± 0.20,3.24 ± 0.30,1.66 ± 0.20,3.38 ± 0.10,4.12 ± 0.10,3.60 ± 0.20 and 2.10 ± 0.10%), respectively (Table 4). The lowest amount of ash content was observed in lotus root, whilst higher amount of ash was found in brinjal as compared to all the vegetables. These results suggest that these vegetables may be regarded as a good source of minerals when compared to grains and tubers (2 to 10%) as reported by Baloch et al. (37).

Table 4: Proximate analysis of vegetables collected from Larkana division.

Samples		Moisture (%)	Ash (%)	Fiber (%)	Total Fat (%)	Protein (%)	Carbohydrate (%)
Spinach	Mean ± SD	85.00± 0.34	3.07 ± 0.40	3.50± 0.10	0.85 ± 0.10	3.50± 0.40	8.03± 0.20
Brinjal	Mean ± SD	87.50 ± 0.20	4.37 ± 0.20	2.83 ±0.20	0.55 ± 0.10	1.55 ± 0.10	6.03 ±0.20
Spongi gourd	Mean ± SD	79.40± 0.10	3.24 ± 0.30	2.65±0.90	1.00 ± 0.20	0.82 ± 0.20	15.54 ± 0.40
Lotus root	Mean ± SD	73.30± 0.1	1.66 ± 0.20	5.50± 0.40	0.55 ± 0.40	1.74 ± 0.20	22.75± 0.55
Okra	Mean ± SD	79.40± 0.25	3.38 ± 0.10	5.60 ±0.70	1.50± 0.30	2.54 ± 0.50	13.63 ± 0.23
Coriander leaves	Mean ± SD	85.80± 0.10	4.12 ± 0.10	2.77± 0.20	1.25 ± 0.30	2.80± 0.40	5.98± 0.20
Fenugreek leaves	Mean ± SD	79.70± 0.18	3.60± 0.20	5.50±0.50	2.52 ± 0.40	1.94 ± 0.80	12.21 ± 0.20
Cauliflower	Mean ± SD	87.00± 0.11	2.10± 0.10	2.80± 0.10	0.80 ± 0.20	2.20± 0.10	15.24 ± 0.21

The crude fiber in spinach, brinjal, sponge gourd, lotus root, okra, coriander leaves, fenugreek leaves, and cauliflower were found to be 3.50 ± 0.10, 2.80 ± 0.20, 2.65 ± 0.95, 5.50 ± 0.40,5.60 ± 0.70, 2.77 ± 0.20, 5.50 ± 0.50, and 2.80 ± 0.10 %, respectively (Table 4). The resultant data shows that okra is the richest source of fiber as compared to other vegetables ($p < 0.05$), followed by lotus root (5.10–5.90%), whereas the least was observed in coriander leaves (2.75–2.80%). Furthermore, the high amount of crude fiber (9.00–26.00%) in these vegetables would be favorable for their active participation in controlling intestinal transportation and improving dietary bulk due to their capacity to absorb water (37). Fibers have the capability to lower cholesterol levels as well as smoothen intestinal functions (38). Fat content is very important from the nutritional point of view because 1 g of the lipid gives 9 kcal of energy. The fate contents in spinach, brinjal, sponge gourd, lotus root, okra, and coriander leaves, fenugreek leaves, and cauliflower were found to be 0.85 ± 0.10, 0.55 ± 0.10, 1.00 ± 0.20, 0.55 ± 0.40, 1.50 ± 0.30, 1.25 ± 0.30, 2.52 ± 0.40, and 0.80 ± 0.20 %, respectively. It was observed that fenugreek leaves have high fat contents (Table 4). The values obtained (0.51– 2.56 %) for fat in these vegetables endorsed the results of many authors, which showed that leafy and green vegetables are poor sources of fat, as reported by Nawab et al. (39). Moreover, it is significant to remember that a diet containing 1 – 2% of total caloric energy as fat is believed to be sufficient for humans. In contrast, excess fat consumption leads to cardiovascular diseases such as atherosclerosis, aging, and cancer (39). Thus, these green vegetables with low fat levels may benefit those suffering from obesity and other related disorders. Protein contents in spinach, brinjal, sponge gourd, lotus root, okra, coriander leaves, fenugreek leaves, and cauliflower are listed in Table 4. The current results indicated that spinach has high levels of protein (3.50 ± 0.40%) followed by coriander leaves (2.80 ± 0.40%) and okra (2.54 ± 0.50%). Thus, these three vegetables

are a good source of protein to produce. At the same time, the lowest contents of protein were present in sponge gourd (0.82 ± 0.20%) followed by brinjal (1.55 ± 0.10%) and lotus root (1.74 ± 0.20%). These findings were in good agreement with those studies reported in the literature that indicated that leafy and green vegetables are poor protein sources (39). Thus, these vegetables may be helpful for those suffering from weight-related disorders due to the consumption of high energy foodstuffs. Carbohydrates are the primary source of energy in the body. The highest content of carbohydrates was obtained in lotus root (22.75 ± 0.55 %). Lotus root is one of the very famous vegetables in the traditional food of Sindhi culture as fried pakora (fritter) and lotus salad are delicious and yummy local food dishes. Whereas sponge gourd and okra were also rich sources of carbohydrates, containing > 7.00% in Table 4.

Daily Intake of Macronutrients
The daily intake (DI) of fiber, fat, protein, and carbohydrates from the studied vegetables by the local adult population are listed in Table 5. The higher DI of fiber was consumed from spinach (8.31 g.day^{-1}). In contrast, lower fiber consumption was observed from the fenugreek leaves (1.37 g.day^{-1}). The DI of carbohydrates was found to be higher from sponge gourd (9.38 g/day) whereas lower from cauliflower (1.04 g.day^{-1}). The studied vegetables contributed < 1.00% for the dietary DI of carbohydrates compared to the Food Nutritional Board value as reported by Shan et al. (40). Fiber is important because it reduces the risk of chronic disease; it also has gastrointestinal benefits for health. It has been observed that the local population acquires carbohydrates and fiber from each vegetable. The highest DI values of fat were observed from cauliflower (8.80 g.day^{-1}) and protein from okra (9.74 g.day^{-1}), while lower fat and protein were obtained from spinach (1.44 g.day^{-1}), (1.02 g.day^{-1}), respectively. Generally, the studied vegetables could contribute to a small portion of the dietary DI of fat and protein.

Table 5: Daily intake of macronutrients (g.day^{-1}) in vegetables of Larkana division.

Samples	Consumption	Fiber	Total Fat	Protein	Carbohydrate
Spinach	20	8.31	1.44	1.02	1.11
Brinjal	28	3.13	6.63	7.23	3.14
Spongi gourd	36	3.62	8.20	4.92	9.38
Lotus root	25	6.09	6.65	7.25	2.29
Okra	23	1.59	1.70	9.74	3.61
Coriander leaves	6	2.74	5.94	2.85	2.70
Fenugreek leaves	11	1.37	1.49	3.56	2.79
Cauliflower	18	4.11	8.80	6.60	1.04
RDA* (g.day^{-1})			56	18	38

Mineral Content
Essential minerals like Ca, K, Na, and Mg may serve as structural components of tissues. These may have an active function in many cellular and basal metabolism as well as the control of water levels based on the acid-base balance (41). The concentrations of Na, K, Ca, and Mg in common vegetables are reported in Table 6. The levels of Na

in the eight studied vegetables were observed in the range of (3.80 ± 0.40 – 10.90 ± 0.92) mg.kg^{-1}. The highest contents of Na were found in cauliflower (10.90 ± 0.92 mg.kg^{-1}) followed by sponge gourd (8.75 ± 0.46 mg.kg^{-1}), lotus root (8.44 ± 0.20 mg.kg^{-1}), and brinjal (7.00 ± 0.12 mg.kg^{-1}). Thus, these vegetables may play an important role in fulfilling the daily dietary requirements of Na.

The reported content of Na in brinjal and okra was lower than in the reported study (31). However, the contents of Na in sponge guard, coriander (32) and okra (42) were significantly higher than the contents of Na in these vegetables. Potassium (K) is a major intracellular ion that generates electrical potentials in nervous tissues (43). The levels of K were observed in the studied vegetables in the range of (38.40 ± 0.40– 57.30 ± 0.10mg.kg^{-1}**)** Table.6 The highest contents of K were found in coriander leaves (57.30 ± 0.10 mg.kg^{-1}) and cauliflower (57.10 ± 0.10 mg.kg^{-1}), whereas the lowest contents of K were observed in spinach (30.20 ± 0.45 mg.kg^{-1}) and fenugreek leaves

(33.60 ± 0.50 mg.kg^{-1}). Generally, the low level of K in humans may cause severe neurological dysfunctions (43). However, all studied vegetables have K levels greater than 30.20 ± 0.45 mg.kg^{-1}, indicating that the studied vegetables are enriched with K, which may lead to providing a sufficient amount of K to humans for their consumption. The levels of K in all studied vegetables were higher than the reported values of K in the literature (37, 44, 45). The Ca levels were observed in the studied vegetables (10.30 ± 0.40, 41.80± 0.50 mg.kg^{-1} (Table 6). The highest contents of Ca were observed in spinach (41.8 ± 0.5 mg.kg^{-1}), whereas the lowest was in okra (10.30 ± 0.40 mg.kg^{-1}).

Table 6: Macro minerals (mg.kg^{-1}) in vegetables of Larkana division.

Samples		Na	K	Ca	Mg
Spinach	Mean±SD	4.76±0.39	30.20±0.45	41.80±0.50	5.42±0.20
Brinjal	Mean±SD	7.00 ±0.12	39.00±0.50	29.90±0.40	8.63±0.10
Spongi gourd	Mean±SD	8.75 ±0.460	50.40±0.40	30.40±0.20	10.60±0.10
Lotus root	Mean±SD	8.44 ± 0.20	38.40±0.40	22.90±0.50	7.30±0.20
Okra	Mean±SD	6.60±0.11	42.30±0.10	10.30±0.40	9.89±0.30
Coriander leaves	Mean±SD	4.60 ±0.35	57.30± 0.10	23.50±0.30	16.94±0.80
Fenugreek leaves	Mean±SD	3.80 ±0.40	33.60±0.50	22.50±0.10	12.16±0.70
Cauliflower	Mean±SD	10.90±0.92	57.10±0.10	27.00±0.40	10.44±0.60

The current study revealed that the levels of Ca were higher in brinjal and okra as compared to the reported study (46). Similarly, the current study shows higher Ca in sponge gourd and coriander leaves (47). In contrast, lower Ca was observed in okra compared to the reported study (47), whereas (37) reported lower Ca in cauliflower compared to the current study. Similarly, the Ca levels in okra and coriander leaves were reported lower (35) than in the current study (Table 7).

The concentration of Mg was found in the range of (5.42 ± 0.20 – 16.94 ± 0.80 mg.kg^{-1}) in all the studied vegetables (Table 6). The highest contents of Mg were obtained in the coriander leaves (16.94 ± 0.80mg.kg^{-1}), and the lowest was found in the spinach (5.42 ± 0.20 mg.kg^{-1}). Mg plays a vital role in stabilizing the entire cellular polyphosphate compounds, primarily in the synthesis of DNA and RNA (45). However, the levels of Mg in brinjal, okra, coriander leaves, and cauliflower of the study area were higher than the reported levels of Mg in these vegetables (35, 37, 39) as listed in Table 7.

Daily Intake of Macronutrients
The DI of Na, K, Ca, and Mg from the studied vegetables by the local adult population are listed in Table 8. The higher DI of Na and K was consumed from fenugreek leaves at 6.97 and 6.16 (mg/kg bw/day), respectively. The maximum DI of Ca was estimated in the lotus root (9.54 mg.kg^{-1} bw.day^{-1}), and the highest DI of Mg was found in the sponge gourd (6.36 mg/kg bw/day). The lowest DI of Na, K, Ca, and Mg was observed (1.59, 1.01, 1.39, and 1.81 mg.kg^{-1} bw.day^{-1}), respectively, by consuming fenugreek leaves. The studied vegetables contributed < 1.00% to the daily dietary

intake of Ca and Mg as compared to the food nutritional board (39).

Micro Minerals in Vegetables
Micro minerals are essential nutrients for the sustenance of human beings with a range of functions. They are incorporated into the structures of proteins, enzymes, and carbohydrates to participate in biochemical reactions. Cr complexes play a key role in the metabolism of carbohydrates and lipids, so the use of vegetables in our diet is a good source of Cr (43). The concentration of Cr was found in the range of 0.82–6.00 µg.kg^{-1} (Table 9). The highest content of Cr (5.60–6.00 µg.kg^{-1}) was observed in the sponge gourd, whereas the lowest concentration was observed in the cauliflower (0.82 –1.20 µg.kg^{-1}). The content of Cr in vegetables was compared with the reported values in the literature (Table 10a). The contents of Cr in spinach for study areas were higher than reported in the literature (33, 48). The Cr content reported by Islam et al.(36) in brinjal was slightly lower than in the current study. While the current study has lower Cr content in brinjal as compared to those reported by Ashraf et al. (38). Okra and coriander leaves showed higher contents of Cr than the reported studies (33, 38, 39, 43, 44, 48). Cauliflower collected from the study areas has higher contents of Cr, as reported by Hameed et al. (33). In contrast, it was comparable with those reported by Mahmood et al. (48) and lower than those reported by Perveen et al. (44). The contents of Cr in all studied vegetables were found to be within the WHO maximum permissible limit (30 µg.kg^{-1}) in vegetables. Cu is an essential component of many enzymes, therefore, it plays a significant role in different physiological processes like iron utilization, free radicals

elimination, bone and connective tissue development, melanin production, and many others (4). The range of Cu in studied vegetables was (1.72-9.30 µg.kg⁻¹ (Table 9). The highest concentration of Cu was found in the cauliflower samples (7.50 – 9.30 µg.kg⁻¹), whereas the lowest was found in okra (1.72 – 2.30 µg.kg⁻¹). The Cu contents in spinach and brinjal were higher reported by ur Rehman et al. (49) than studied spinach and brinjal whereas lower was in cauliflower reported by (48). The current study has a higher concentration of Cu in spinach than in the reported literature (26, 33, 48, 41, 50). In brinjal and okra, Cu content reported in the literature (33, 36, 38, 41, 49) was higher than in the current study. Coriander leaves reported by (38) have a lower concentration than coriander leaves in the current study (Table 10a). It has been observed that the contents of Cu in all studied vegetables were within the WHO maximum permissible limit (50.00 µg.kg⁻¹). The Fe concentrations in the studied vegetables of Larkana division were between 2.70 and 11.30 µg.kg⁻¹ (Table 9). The highest contents of Fe were found in okra (11.10 µg.kg⁻¹) followed by spinach (7.45 µg.kg⁻¹), lotus root (6.99 µg.kg⁻¹), and sponge gourd (4.17 µg.kg⁻¹),whereas the lowest was found in coriander leaves (2.76 µg.kg⁻¹). Thus, these vegetables may be considered a good alternative to the supplementary source of Fe (46). The concentrations of Fe in spinach, brinjal, okra, and cauliflower were reported in the literature (26, 33, 38, 47, 49, 51) to be higher than the Fe contents in these studied vegetables. The contents of Fe were found in all the vegetables within the WHO maximum permissible limit (300.00 µg.kg⁻¹). However, the deficiency of Fe is very common in all types of physiological disorders (46). The concentration of Mn in studied vegetables was found in the range of 1.21–4.76 µg.kg⁻¹ (Table 9). The highest content of Mn was found in the fenugreek leaves (4.73 µg.kg⁻¹) and the lowest was found in the lotus root (1.23 µg.kg⁻¹). The resulting data showed that Mn contents in the studied vegetables were within the WHO maximum permissible limit (100.00 µg.kg⁻¹). The contents of Mn in spinach, cauliflower, brinjal, and okra in the literature (38, 47, 49, 50, 51) were higher than the current study in these vegetables of Larkana (Table 10b). Zn is an essential element and plays an important role in hormonal growth. The concentration of Zn in the vegetables of the Larkana was found in the range of (1.95 – 4.83) µg.kg⁻¹ (Table 9). In the present study, the highest content of Zn were observed in spinach (4.68 µg.kg⁻¹), whereas the lowest was found in the lotus root (2.07 µg.kg⁻¹). Studied vegetables have Zn levels within the permissible limit recommended by WHO (100.00 µg.kg⁻¹). The levels of Zn in spinach and cauliflower reported in the literature (26, 45, 59) were lower as compared to currently studied vegetables reported by Akhtar et al. (45). There were lower Zn values in fenugreek leaves than those from Larkana (Table 10b).

Similarly, the concentrations of Zn in spinach were reported to be higher (39, 41, 50, 51) than in the currently studied spinach. In the studied vegetables, brinjal has a lower concentration of Zn as compared to the reported literature (36, 38). On the other hand, okra (38, 39, 41) and cauliflower (41, 47) were higher in the same studied vegetables of Larkana divisions listed in Table 10b. However, the variations in levels of micro minerals might be due to the uptake of these elements from the soil, irrigation water, geochemical, or geographical/climatic changes in native countries.

Table 8: Daily intake of macro minerals from the studied vegetables by the local adult population.

Samples	Consumption (g . day⁻¹)	mg.kg⁻¹bw.day⁻¹			
		Na	K	Ca	Mg
Spinach	20	1.59	1.01	1.39	1.81
Brinjal	28	3.27	1.82	1.40	4.03
Spongi gourd	36	5.25	3.02	1.82	6.36
Lotus root	25	3.52	1.60	9.54	3.04
Okra	23	2.53	1.62	3.95	3.79
Coriander leaves	6	4.60	5.73	2.35	1.69
Fenugreek leaves	11	6.97	6.16	4.13	2.23
Cauliflower	18	3.27	1.71	8.10	3.13
RDA (mg.day⁻¹)		1300 – 1500	1000 – 1200	300 – 3500	

Daily Intake of Macro and Micro Minerals
The DI of Cr, Cu, Fe, Mn, and Zn from the studied vegetables of Larkana division by the local adult population are listed in Table 11. The highest DI of Cr and Cu were observed at 9.33 and 8.56 µg.kg⁻¹ bw.day⁻¹, respectively, by the consumption of spinach and fenugreek leaves, while the highest DI of Fe, Mn, and Zn were observed (8.37, 8.67, and 1.69 µg.kg⁻¹ bw.day⁻¹) by the consumption of fenugreek and okra, respectively. Fenugreek leaves showed the lowest DI of Cr, and Cu, while coriander leaves have the lowest DI of Fe, Mn, and Zn, as listed in Table 11. However, these eight vegetables of the Larkana division can also provide up to 1% of the required dietary daily intake of micro minerals recommended by FNB (FNB 2002).

Table 9: Micro minerals (µg.kg^{-1}) in vegetables of Larkana division.

Samples		Cr	Cu	Fe	Mn	Zn
Spinach	Mean±SD	2.80±0.20	4.66±0.40	7.45±0.80	2.49±0.14	4.68±0.20
Brinjal	Mean±SD	1.30±0.40	2.70±0.20	3.43±0.40	3.07±0.11	3.23±0.10
Spongi gourd	Mean±SD	5.80±0.20	3.70±0.30	4.17±0.60	3.36±0.30	2.74±0.20
Lotus root	Mean±SD	1.30±0.30	7.20±0.40	6.99±0.90	1.23±0.20	2.07±0.12
Okra	Mean±SD	3.44±0.20	2.00±0.30	11.1±0.20	1.81±0.80	4.41±0.16
Coriander leaves	Mean±SD	2.67±0.70	5.62±0.60	2.76 ±0.15	3.27±0.21	2.10±0.90
Fenugreek leaves	Mean±SD	1.61±0.21	4.67±0.40	3.77±0.30	4.73±0.30	3.52±0.20
Cauliflower	Mean±SD	1.00±0.20	8.41±0.90	2.79±0.90	1.37±0.40	2.54±0.90
WHO permissible levels		30.00	50.00	300.00	100.00	100 .00

Table 10a: Comparison of Cu (µg.kg^{-1}) in common vegetables with literature.

Vegetables	Current study	26	33	38	41	50	36	49	48
Spinach	4.66	0.02	0.19	0.44	0.03	0.17	-	8.48	-
Brinjal	2.70	-	-	-	10.23	-	17.04	3.18	-
Spongi gourd	3.70	-	-	-	-	-	-	-	-
Lotus root	7.20	-	-	-	-	-	-	-	-
Okra	2.04	-	5.34	3.91	13.65	-	-	-	-
Coriander leaves	5.62	-	-	1.65	-	-	-	-	-
Fenugreek leaves	4.67	-	-	-	-	-	-	-	-
Cauliflower	8.41	-	-	-	-	-	-	4.58	1.19

Table 10b: Comparison of Cr (µg.kg^{-1}) in common vegetables with literature.

Vegetables	Current study	33	48	36	39	44	38	43
Spinach	2.80	0.56	0.91	-	-	-	-	-
Brinjal	1.03	-	-	1.02	-	-	2.36	-
Spongi gourd	5.37	-	-	-	-	-	-	-
Lotus root	1.19	-	-	-	-	-	-	-
Okra	3.44	0.71	-	-	2.37	-	1.56	2.23
Coriander leaves	2.67	-	1.40	-	-	1.52	-	-
Fenugreek leaves	1.61	-	-	-	-	-	-	-
Cauliflower	1.00	0.61	0.99	-	-	1.24	-	-

Table 7: Comparison of macro minerals (mg.kg^{-1}) in common vegetables with literature.

Vegetables	Na				K				Ca					Mg			
	Curr. study	(31)	(32)	(42)	Curr. study	(37)	(44)	(45)	Curr. study	(46)	(47)	(35)	(37)	Curr. study	(35)	(37)	(39)
Spinach	4.76	-	-	-	30.2	-	-	-	41.8	-	-	-	-	5.42	-	-	-
Brinjal	7.00	0.2	-	-	39.0	-	-	2.4	29.9	0.14	-	-	-	8.63	0.14	-	-
Spongi gourd	8.75	-	55.5	-	50.4	-	-	-	30.4	-	10.5	-	-	10.6	-	-	-
Lotus root	8.44	-	-	-	38.4	-	-	-	22.9	-	-	-	-	7.30	-	-	-
Okra	6.60	0.63	-	42	42.3	-	1.7	2.52	10.3	0.75	11.9	6.4	-	9.89	7.51	3.0	-
Coriander leaves	4.60	-	39.5	-	57.3	-	1.62	-	23.5	-	12.7	6.6	-	16.94	-	5.2	-
Fenugreek leaves	3.80	-	-	-	33.6	-	-	-	22.5	-	-	-	-	12.16	-	-	-
Cauliflower	10.9	-	-	-	57.1	73.9	-	-	27	-	-	-	3.8	10.44	-	-	1.13

Table 10c: Comparison of Fe (μg.kg^{-1}) in common vegetables with literature.

Vegetables	Current study	26	33	38	51	47	49
Spinach	7.45	71	179	58.1	60	-	69.7
Brinjal	3.43	-	-	-	98.3	-	-
Spongi gourd	4.17	-	-	-	-	-	-
Lotus root	6.99	-	-	-	-	-	-
Okra	11.1	-	123	-	94.3	13.4	-
Coriander leaves	2.79	-	-	-	-	-	-
Fenugreek leaves	3.77	-	-	-	-	-	-
Cauliflower	2.79	48	117	-	-	52.4	-

CONCLUSION

This research illustrated the significance of plant species, especially vegetables used in the daily diet. The studies on these vegetables indicated that all of them could provide essential nutrients to human beings. Coriander leaves, lotus roots were envisaged as good sources of fibers and carbohydrates. These vegetable species were also significantly helpful in terms of elemental resources, mainly Na, K, Ca, Mg, Cr, Cu, Fe, Mn, and Zn levels. Hence, elemental toxicity in the vegetables, which is lethal, is well below WHO standards. Moreover, the macro and micro minerals in studied vegetables were comparable with the literature reported on the same vegetables in different areas of Pakistan and other countries. This study indicated that the vegetables of Larkana have an excellent profile of studied macro and micro-nutrients and equally contribute to providing these nutrients to the local population.

REFERENCES

1. Jimoh F, Oladiji A. Preliminary Studies on Piliostigma thonningii seeds: Proximate analysis, mineral composition and phytochemical screening. AfrJBiotechnol [Internet]. 2005;4(12):1439–42. Available from: <URL>.

2. Akwaowo EU, Ndon BA, Etuk EU. Minerals and antinutrients in fluted pumpkin (Telfairia occidentalis Hook f.). Food Chemistry [Internet]. 2000 Aug [cited 2022 Aug 4];70(2):235–40. Available from: <URL>.

3. Taiga A, Suleiman M, Aina D, Sule W, Alege G. Proximate analysis of some dry season vegetables in Anyigba, Kogi State, Nigeria. Afr J Biotechnol [Internet]. 2008;7(10):1588–90. Available from: <URL>.

4. Bhatti S, Baig JA, Kazi TG, Afridi HI, Pathan AA. Macro and micro mineral composition of Pakistani common spices: a case study. Food Measure [Internet]. 2019 Dec [cited 2022 Aug 4];13(4):2529–41. Available from: <URL>.

5. Hussain J, Rehman NU, Khan AL, Hamayun M, Hussain SM, Shinwari ZK. Proximate and essential nutrients evaluation of selected vegetables species from Kohat region, Pakistan. Pak J bot. 2010;42(4):2847–55.

6. Akhter P, Akram M, Orfi S, Ahmad N. Assessment of dietary zinc ingestion in Pakistan. Nutrition [Internet]. 2002 Mar [cited 2022 Aug 4];18(3):274–8. Available from: <URL>.

7. Özcan MM, Akbulut M. Estimation of minerals, nitrate and nitrite contents of medicinal and aromatic plants used as spices, condiments and herbal tea. Food Chemistry [Internet]. 2008 Jan [cited 2022 Aug 4];106(2):852–8. Available from: <URL>.

8. Tulchinsky TH. Micronutrient Deficiency Conditions: Global Health Issues. Public Health Rev [Internet]. 2010 Jun [cited 2022 Aug 4];32(1):243–55. Available from: <URL>.

9. Muller O. Malnutrition and health in developing countries. Canadian Medical Association Journal [Internet]. 2005 Aug 2 [cited 2022 Aug 4];173(3):279–86. Available from: <URL>.

10. Burchi F, Fanzo J, Frison E. The Role of Food and Nutrition System Approaches in Tackling Hidden Hunger. IJERPH [Internet]. 2011 Jan 31 [cited 2022 Aug 4];8(2):358–73. Available from: <URL>.

11. Miller BDD, Welch RM. Food system strategies for preventing micronutrient malnutrition. Food Policy [Internet]. 2013 Oct [cited 2022 Aug 4];42:115–28. Available from: <URL>.

12. Benton D, ILSI Europe a.i.s.b.l. Micronutrient status, cognition and behavioral problems in childhood. Eur J Nutr [Internet]. 2008 Aug [cited 2022 Aug 4];47(S3):38–50. Available from: <URL>.

13. Fanzo J. Ethical issues for human nutrition in the context of global food security and sustainable development. Global Food Security [Internet]. 2015 Dec [cited 2022 Aug 4];7:15–23. Available from: <URL>.

14. Kin CFW, Shan WSY, Shun LJC, Chung LP, Jean W. Experience of famine and bone health in post-menopausal women. International Journal of Epidemiology [Internet]. 2007 Oct 1 [cited 2022 Aug 4];36(5):1143–50. Available from: <URL>.

15. Morris J, Hawthorne KM, Hotze T, Abrams SA, Hirschi KD. Nutritional impact of elevated calcium transport activity in carrots. Proc Natl Acad Sci USA [Internet]. 2008 Feb 5 [cited 2022 Aug 4];105(5):1431–5. Available from: <URL>.

16. Akeredolu IA, Oguntona BE, Okafor C, Osisanya OJ. Iron, Zinc, and Copper Malnutrition among Primary School Children in Lagos, Niagara. FNS [Internet]. 2011 [cited 2022 Aug 4];02(10):1063–70. Available from: <URL>.

17. Bhandari S, Banjara MR. Micronutrients Deficiency, a Hidden Hunger in Nepal: Prevalence, Causes, Consequences, and Solutions. International Scholarly

Research Notices [Internet]. 2015 Jan 15 [cited 2022 Aug 4];2015:1–9. Available from: <URL>.

18. Camaschella C. Iron-Deficiency Anemia. Longo DL, editor. N Engl J Med [Internet]. 2015 May 7 [cited 2022 Aug 4];372(19):1832–43. Available from: <URL>.

19. Burden RJ, Morton K, Richards T, Whyte GP, Pedlar CR. Is iron treatment beneficial in, iron-deficient but non-anaemic (IDNA) endurance athletes? A systematic review and meta-analysis. Br J Sports Med [Internet]. 2015 Nov [cited 2022 Aug 4];49(21):1389–97. Available from: <URL>.

20. Arinola OG. Essential Trace Elements and Metal Binding Proteins in Nigerian Consumers of Alcoholic Beverages. Pakistan J of Nutrition [Internet]. 2008 Oct 15 [cited 2022 Aug 4];7(6):763–5. Available from: <URL>.

21. KO S, CO O, O EO. The importance of mineral elements for humans, domestic animals and plants-A review. African journal of food science. 2010;4(5):200–22.

22. Tan JC, Burns DL, Jones HR. Severe Ataxia, Myelopathy, and Peripheral Neuropathy Due to Acquired Copper Deficiency in a Patient With History of Gastrectomy. JPEN J Parenter Enteral Nutr [Internet]. 2006 Sep [cited 2022 Aug 4];30(5):446–50. Available from: <URL>.

23. Santamaria AB. Manganese exposure, essentiality & toxicity. Indian J Med Res. 2008 Oct;128(4):484–500.

24. Erikson KM, Aschner M. Manganese neurotoxicity and glutamate-GABA interaction. Neurochemistry International [Internet]. 2003 Sep [cited 2022 Aug 4];43(4–5):475–80. Available from: <URL>.

25. Pandey M, Abidi AB, Singh S, Singh RP. Nutritional Evaluation of Leafy Vegetable Paratha. Journal of Human Ecology [Internet]. 2006 Feb [cited 2022 Aug 4];19(2):155–6. Available from: <URL>.

26. Khan S, Rehman S, Zeb Khan A, Amjad Khan M, Tahir Shah M. Soil and vegetables enrichment with heavy metals from geological sources in Gilgit, northern Pakistan. Ecotoxicology and Environmental Safety [Internet]. 2010 Oct [cited 2022 Aug 4];73(7):1820–7. Available from:<URL>.

27. Kazi TG, Wadhwa SK, Afridi HI, Talpur FN, Tuzen M, Baig JA. Comparison of essential and toxic elements in esophagus, lung, mouth and urinary bladder male cancer patients with related to controls. Environ Sci Pollut Res [Internet]. 2015 May [cited 2022 Aug 4];22(10):7705–15. Available from: <URL>.

28. Iheanacho K, Udebuani A. Nutritional Composition of Some Leafy Vegetables Consumed in Imo State, Nigeria. J Appl Sci Environ Manag [Internet]. 2009;13(3):35–8. Available from: <URL>.

29. Patricia O, Zoue L, Megnanou RM, Doue R, Niamke S. Proximate composition and nutritive value of leafy vegetables consumed in Northern Cote d'Ivoire. European Scientific Journal. 2014;10(6).

30. AOAC BAM. Official Methods of Analysis. 17th edition. Gaithersburg, MD, USA.: The Association of Official Analytical Chemists; 2000.

31. Hussain J, Rehman N, Khan AL, Hussain H, Al-Harrasi A, Ali L, et al. Determination of macro and micronutrients and nutritional prospects of six vegetable species of Mardan, Pakistan. Pak J Bot. 2011;43(6):2829–33.

32. Hussain J, Latif Khan A, ur Rehman N, . Z, Khan F, Tasleem Hu S, et al. Proximate and Nutrient Investigations of Selected Medicinal Plants Species of Pakistan. Pakistan J of Nutrition [Internet]. 2009 Apr 15 [cited 2022 Aug 4];8(5):620–4. Available from: <URL>.

33. Naz S, Anjum MA, Akhtar S, Naqvi SAH, Zulfiqar MA. Effect of Different Irrigation Sources on Proximate Composition and Heavy Metals Uptake in Some Selected Vegetables. PJAR [Internet]. 2018 Nov [cited 2022 Aug 4];31(4). Available from: <URL>.

34. Akindahunsi A, Salawu S. Phytochemical screening and nutrient-antinutrient composition of selected tropical green leafy vegetables. African Journal of Biotechnology [Internet]. 2005;4(6):497–501. Available from: <URL>.

35. Kwenin W, Wolli M, Dzomeku B. Assessing the nutritional value of some African indigenous green leafy vegetables in Ghana. 2011;

36. Islam MS, Hoque M. Concentrations of heavy metals in vegetables around the industrial area of Dhaka city, Bangladesh and health risk assessment. International Food Research Journal. 2014;21(6).

37. Bux Baloch A, Xia X, Ahmed Sheikh S. Proximate and Mineral Compositions of Dried Cauliflower (Brassica Oleracea L.) Grown In Sindh, Pakistan. JFNR [Internet]. 2015 Mar 27 [cited 2022 Aug 4];3(3):213–9. Available from: <URL>.

38. Ashraf I, Ahmad F, Sharif A, Altaf AR, Teng H. Heavy metals assessment in water, soil, vegetables and their associated health risks via consumption of vegetables, District Kasur, Pakistan. SN Appl Sci [Internet]. 2021 May [cited 2022 Aug 4];3(5):552. Available from: <URL>.

39. Nawab J, Farooqi S, Xiaoping W, Khan S, Khan A. Levels, dietary intake, and health risk of potentially toxic metals in vegetables, fruits, and cereal crops in Pakistan. Environ Sci Pollut Res [Internet]. 2018 Feb [cited 2022 Aug 4];25(6):5558–71. Available from: <URL>.

40. Shan Z, Rehm CD, Rogers G, Ruan M, Wang DD, Hu FB, et al. Trends in Dietary Carbohydrate, Protein, and Fat Intake and Diet Quality Among US Adults, 1999-2016. JAMA [Internet]. 2019 Sep 24 [cited 2022 Aug 4];322(12):1178. Available from: <URL>.

41. Ahmad N, Akhtar MS, Ahmed R, Zafar R, Hussain S, Ishaqe M, et al. Assessment of heavy metals in vegetables, sewage and soil grown near Babu Sabu Toll Plaza of Lahore, Pakistan. Pakistan Journal of Analytical & Environmental Chemistry. 2019;20(1):82–7.

42. Hameed O, Shafi F. Studies on nutritional composition of coriander leaves by using sun and cabinet drying methods. 2017 [cited 2022 Aug 4]; Available from: <URL>.

43. Choudhury R, Garg A. Variation in essential, trace and toxic elemental contents in Murraya koenigii – A spice and medicinal herb from different Indian states. Food Chemistry [Internet]. 2007 [cited 2022 Aug 4];104(4):1454–63. Available from: <URL>.

44. Perveen S, Samad A, Nazif W, Shah S. Impact of sewage water on vegetables quality with respect to heavy metals in Peshawar, Pakistan. Pakistan Journal of Botany. 2012;44(6):1923–31.

45. Akhtar MS, Ahmed M, HAQ Q. Heavy metals in vegetables grown in Korangi Area, Karachi, Pakistan. FUUAST Journal of Biology. 2013;3(1 june):71–4.

46. Bhagure GR, Mirgane SR. Heavy metal concentrations in groundwaters and soils of Thane Region of Maharashtra, India. Environ Monit Assess [Internet]. 2011 Feb [cited 2022 Aug 4];173(1–4):643–52. Available from: <URL>.

47. Wadood SA, Sharif MK, Ashraf MN, Ejaz R, Kosar G, Azeem M, et al. Estimation of Heavy Metals and Associated Health Risk in Selected Vegetables Grown in Peri-Urban Areas of Multan and Rawalpindi, Pakistan. Pakistan Journal of Scientific & Industrial Research [Internet]. 2021 Mar 3 [cited 2022 Aug 4];64(1):55–63. Available from: <URL>.

48. Mahmood A, Malik RN. Human health risk assessment of heavy metals via consumption of contaminated vegetables collected from different irrigation sources in Lahore, Pakistan. Arabian Journal of Chemistry [Internet]. 2014 Jan [cited 2022 Aug 4];7(1):91–9. Available from: <URL>.

49. ur Rehman K, Bukhari SM, Andleeb S, Mahmood A, Erinle KO, Naeem MM, et al. Ecological risk assessment of heavy metals in vegetables irrigated with groundwater and wastewater: The particular case of Sahiwal district in Pakistan. Agricultural Water Management [Internet]. 2019 Dec [cited 2022 Aug 4];226:105816. Available from: <URL>.

50. Raphael I, Nalawade S, Eagar TN, Forsthuber TG. T cell subsets and their signature cytokines in autoimmune and inflammatory diseases. Cytokine [Internet]. 2015 Jul [cited 2022 Aug 4];74(1):5–17. Available from: <URL>.

51. Rc T, A R. Heavy Metals Contamination in Vegetables and its Growing Soil. J Environ Anal Chem [Internet]. 2015 [cited 2022 Aug 4];02(03). Available from: <URL>.

Chemical Composition and Biological Active Substances from Hazelnut Green Leafy Covers

Farhad Azizov[1*], Vefa Atayeva[1], Zarbali Khalilov[1], Nurmammad Mustafayev[2], Hilal Imanlı[3]

[1]Azerbaijan National Academy of Sciences, Sheki Regional Scientific Center, Sheki, AZ5500, Azerbaijan
[2]Azerbaijan National Academy of Sciences, Institute of Molecular Biology and Biotechnologies, Baku, AZ1073, Azerbaijan
[3]Azerbaijan National Academy of Sciences, Institute of Botany, Baku, AZ1004, Azerbaijan

Abstract: This investigation aims to study the perspectives for obtaining natural remedies and food additives from raw plant materials that can be used in food, pharmaceutical, and other industries. The selection of hazelnut green leafy cover as an item is based on the fact that it is a natural organic resource that is now being discarded as waste. In the article, the results are presented about the determination of mineral elements and bioactive compounds in the bio-extracts of 70% ethyl alcohol (BE-III) and distillation water (BE-IV) obtained from the green leafy cover of the plant (Corylus avellane L.) where grow in the north-western region of Azerbaijan. According to our study, BE-III has 25 chemical elements, excluding Rb, for a total of 12.797%, while BE-IV contains 26 chemical elements for a total of 21.347%. Amounts of macroelements are 10.4%, and microelements are 2.69% in the content of BE-III, while amounts of macroelements are 17.82%, and amounts of microelements are 3.53% in the content of BE-IV. Amounts of organic compounds are 87.2% in the content of BE-III, while their amounts are 78.65% in the content of BE-IV. The amount of Zn, which has antioxidant activity, is 0.009%, and the amount of Se is 0.002% in the content of BE-IV. These values vary in the content of BE-III, the amount of Zn is 0.01%, but the amount of Se is 0.001%. 15 bioactive substances were identified in the content of BE-III bio-extract; however, 5 bioactive substances were identified in the content of BE-IV bio-extract. According to our research results, the bio-extract obtained from hazelnut green leafy cover is abundant with antioxidants and bioactive substances with antibacterial activity. For this reason, these bio-extracts can be used as both a food supplement and a means of treatment.

INTRODUCTION

Researchers studying the common hazelnut plant (*Corylus avellana* L.) growing in different world countries have found that, along with other organs, the green leafy covers also are rich in bioactive compounds (1). However, despite the information that the kernel, shell, leaves, twigs, and other parts of the hazelnut plant are rich in mineral elements (2), no literature data has been found on the presence of mineral elements in hazelnut green leafy covers grown in Azerbaijan. While studying green leafy covers of the hazelnut plant, Turkish researchers S.B.Oguzkhan et al., 2016 found that the bio-extract contained bioactive compounds with high antioxidant and antibacterial properties. They obtained hazelnut green leafy covers extract with methanol at room temperature for 72 h and studied it by diffusion method using 8 different bacterial strains and determined that they had high antirad-

ical activity and antibacterial effect (3). Other researchers A.Hoffman and F.Witness in 2009 found that the extracts obtained from its leaves, brown and green leafy covers with 80% ethyl alcohol in a ratio of 1:10 during 12 h at 40ºC contain 10-deacetylbaccatin III, cephalomannine, and paclitaxel, but green contained only baccatin III (4). The studies of S.S.Siriwardhana and F.Shahidi in 2002 showed that the bio-extract obtained from the hazelnut green leafy covers had a hydrogen peroxide radical scavenger activity of 66% at 100 ppm and 91% at 200 ppm concentrations, which removes organic free radicals effectively (5). F.Shahidi et al.,2007 evaluated the total antioxidant activity (TAA) and free radical scavenger activity of ethanol-derived bio-extract from hazelnut green leafy covers using activity tests such as hydrogen peroxide, superoxide, and DPPH (diphenyl-l-picrylhydrazyl), and have confirmed its high antioxidant activity (6). Extracts obtained from the hazelnut green leafy covers with 80% ethyl alcohol and 80% acetone contain 5 phenolic acids - gallic acid, caffeic acid, p-coumaric acid, ferulic acid, and sinapinic acid, having a high antioxidant activity and free radical scavenger capacity (7). Therefore, it is recommended to consider hazelnut green leafy covers as a potential source of antioxidants. Hexadecanoic acid methyl ester ($C_{17}H_{34}O_2$) determined in green leafy covers had been tested for activity against fungi and proven its a high antifungal effect. It is recommended to use this substance to prepare antifungal drugs (8). The results of our research on the mineral elements and bioactive compounds found in the extracts of the hard shell of this plant have been presented in the articles by F. Azizov et al.,2021 (9, 19). This article presents the results of the determination and identification of minerals and bioactive compounds in bio-extracts obtained by extraction of green leafy covers of common hazelnut plants grown in the north-western region of Azerbaijan with aqueous extract and ethanol, as well as information on the results of quantitative and qualitative changes of the bioactive compounds depends on the extragents used and their comparative analysis.

MATERIAL AND METHODS

Plant material. The research object is the green leafy covers of the common hazelnut plant in Azerbaijan's Sheki region. Firstly, the green leafy covers were washed with ordinary water, then with distilled water, dried, and grounded, and the extracts were obtained using distilled water and 70% ethyl alcohol. The yield extractive substances and extraction regimes were studied separately for each.

Preparation of extracts. Samples of hazelnut green leafy covers dried at room temperature were grounded. 50 g grounded sample was added into a 500 mL flask. And then, 300 mL of distilled water was added to the grounded sample. The mixture was extracted in the water bath at 75-80 °C

temperature for 30 minutes, and obtained extract solution was filtered. Then 100 mL of distilled water was added to the residual grounded sample and extracted for 15 minutes. The obtained extract was filtered and added to the first extract. Again 100 ml distilled water was added to the residual in the flask and extracted for 15 minutes. The obtained extract was filtered and added to the first extract.
Extraction in alcohol was carried out in the same way. Both extracts were powdered in an SPT-200 Vacuum-Drier device (10).

Determination of mineral elements. 0.2 g of powder of both samples was dissolved in 5.2 ml of acid solution (HNO_3: $HClO_4$ in the ratio of 5:0.5). It was heated until it turned white. Solutions were diluted with 40 mL of distilled water and filtered. Mineral elements were determined using the AA220FS atomic absorption spectrometer at the Center for Nuclear Research of the Azerbaijan Republic (11).

Determination of organic compounds. Biologically active substances in the extracts were determined using the gas-chromato-mass-spectroscopy method. For this purpose, Agilent Technologies 6890 N Network CG System, a chromatograph with 5975 inert Mass Selective Detector mass spectrometer, and as a detector Split/Splitless, injection-Split, Inlet pressure 60,608 kpa, Split-100, Low Mass-40, High Mass-400, Threshold 150 were used.

In experiments, a 30-meter quartz capillary column "HP-5MS 5% Methyl Siloxane" (internal diameter 0.25 mm, stationary phase thickness 0.25 μ) was used. Analyzes were performed in temperature programming mode at 50 °C to 280 °C at 15 °C/min.

Temperature regime of the column: starting temperature of the column 50 °C - constant for 2 minutes;
- temperature rise from 15 °C to 200 °C - 2 minutes constant;
- temperature rise from 15 °C to 280 °C - constant for 10 minutes;
- vacuum HiVac - 3.38e-005.

Diluted with a mixture of methanol - chloroform (1:2 ratio).

The flow rate of the gas (He) is 1 mL/min. The standard mass spectroscopic NIST library was used to identify the substances. The analysis lasted 33 minutes (12).

Comparative analysis of the number of minerals in the hazelnut green leafy covers extracts, as well as the identification of bioactive compounds, their synonyms, and therapeutic properties, were performed based on the available literature, Internet data, and the results of researchers from different countries.

RESULTS AND DISCUSSION

In the research work, mineral elements and bioactive compounds were determined separately in hazelnut green leafy covers BE-III and BE-IV extracts. The amounts of mineral elements determined in the content of BE-III and BE-IV extracts have been shown in Table 1.

Table 1: Amounts of mineral elements in the aqueous and ethanol bio-extracts.

Mineral elements	Amount, %	
	BE-III	**BE-IV**
K	4.380	9.133
Na	2.804	3.124
Mg	1.150	1.759
Ca	1.447	3.466
Ti	0.079	0.042
V	0.004	0.002
Cr	0.013	0.008
Mn	0.017	0.021
Fe	0.071	0.078
Ni	0.034	0.017
Cu	0.038	0.020
Zn	0.010	0.009
Ga	0.002	0.001
Zr	0.013	0.009
Sn	0.001	0.001
Sr	0.009	0.012
Y	0.004	0.002
Se	0.001	0.002
Al	1.718	2.476
Si	0.631	0.717
P	0.254	0.270
S	0.043	0.045
Ba	0.057	0.027
Pb	0.003	0.002
Nb	0.014	0.008
Rb	0	0.005
Total	**12.80**	**21.35**

As can be seen from the table, the composition of both BE-III and BE-IV is qualitatively similar except for Rb in BE-III extract, consisting mainly of 26 mineral elements K, Na, Mg, Ca, Ti, V, Cr, Mn, Fe, Ni, Cu, Zn, Ga, Zr, Sn, Sr, Y, Se, Al, Si, P, S, Ba, Pb, Nb, Rb. However, the amounts of mineral elements in BE-IV are noticeably higher (21.35%) than in BE-III (12.80%).

In the composition of BE-III, the amount of macroelements K, Na, Mg, Ca, Fe, and P is 10.11%, other microelements 2.69%, but in the composition of BE-IV, the amount of macroelements K, Na, Mg, Ca, Fe, P is 17.82%, other microelements 3.53%. As can be seen, the total amount of mineral elements and macro and microelements in the bio-extract BE-IV is about twice as high relatively in the bio-extract BE-III. In other words, the aqueous extract contains 21.35% inorganic and 78.65% organic substances, and the ethanol extract contains 12.80% inorganic and 87.20% organic substances. Antioxidant properties and vital elements such as Zn is 0.01% in BE-III, 0.009% in BE-IV, and Se is 0.001% in BE-III, 0.002% in BE-IV (13-16).

The results of the study of bioactive compounds of the bio-extracts have been given in Table 2. The bioactive compound listed in the table were selected sequentially according to the differences in their peaks on the chromatogram. The substances having peaks with lower height indicators have not been included in the table due to their lack of pharmacological properties and economic importance.

Table 2: Biologically active substances in BE-III and BE-IV extracts obtained from hazelnut green leafy covers.

No	Identified components	
	Ethanol extract (BE-III)	**Aqueous extract (BE-IV)**
1	Benzene-1,2-diol ($C_6H_6O_2$)	Benzene-1,2-diol ($C_6H_6O_2$)
2	2,3-dihydro-1-benzofuran (C_8H_8O)	5-(hydroxymethyl) furan-2-carbaldehyde ($C_6H_6O_3$)
3	5-(hydroxymethyl) furan-2-carbaldehyde ($C_6H_6O_3$)	3,5-dihydroxy-6-(hydroxymethyl)oxan-2-one $C_6H_{10}O_5$
4	3,5-dihydroxy-6-methyl-2,3-dihydropyran-4-one ($C_6H_8O_4$)	Methyl hexadecanoate ($C_{17}H_{34}O_2$)
5	4-ethenyl-2-methoxyphenol ($C_9H_{10}O_2$)	Methyl octadecenoate ($C_{19}H_{38}O_2$)
6	Methyl 3-hydroxybenzoate ($C_8H_8O_3$)	
7	2,6-dimethoxyphenol ($C_8H_{10}O_3$)	
8	3,5-dihydroxy-6-(hydroxymethyl)oxan-2-one ($C_6H_{10}O_5$)	
9	1-methylsulfanyl-4-propan-2-ylbenzene ($C_{10}H_{14}S$)	
10	4-((1E)-3-Hydroxy-1-propenyl)-2-methoxyphenol ($C_{10}H_{12}O_3$)	
11	Methyl hexadecanoate ($C_{17}H_{34}O_2$)	
12	Dibutyl benzene-1,2-dicarboxylate ($C_{16}H_{22}O_4$)	
13	Methyl octadecenoate ($C_{19}H_{38}O_2$)	
14	Ethyl icosanoate ($C_{22}H_{44}O_2$)	
15	Gamma-sitosterol ($C_{29}H_{50}O$)	

As can be seen in Table 2, the extracts obtained by these methods differ from the composition of the main bioactive compound. Thus, 15 main bioactive compounds have been identified in BE-III and 5 in BE-IV. Each identified substance was studied separately according to its synonyms; information on their therapeutic properties and applications were obtained based on available literature data. The chromatograms obtained for determining the main bioactive compounds in BE-III and BE-IV are given below (Fig. 1-10).
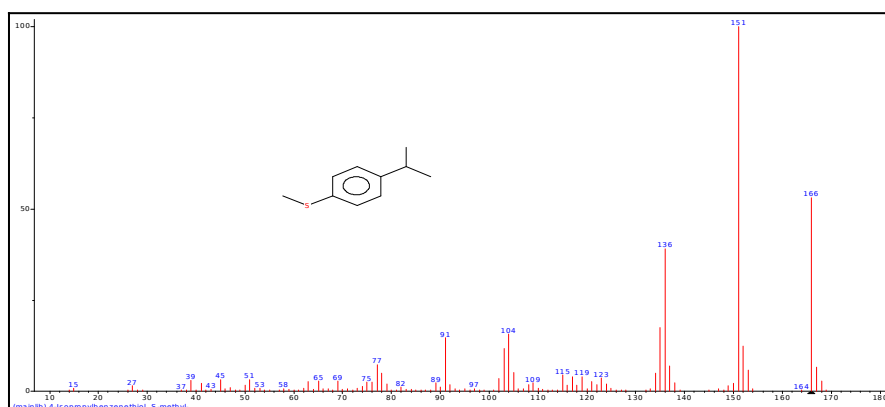
Figure 1: 1-Methylsulfanyl-4-propan-2-ylbenzene; $C_{10}H_{14}S$; MW=166.
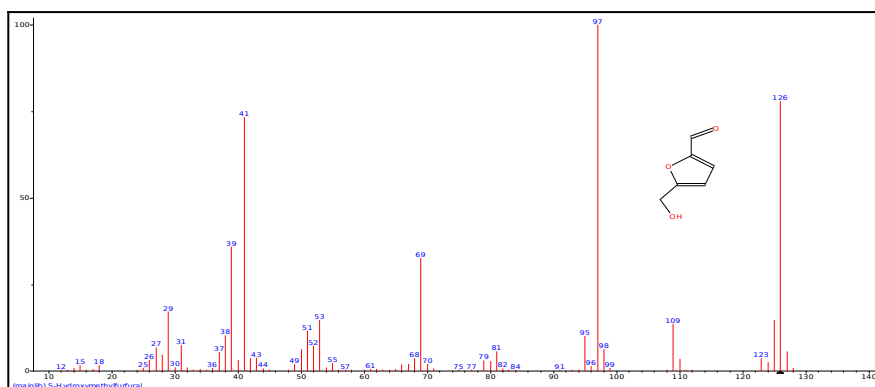
Figure 2: 5-(Hydroxymethyl)furan-2-carbaldehyde; $C_6H_6O_3$; MW=126.
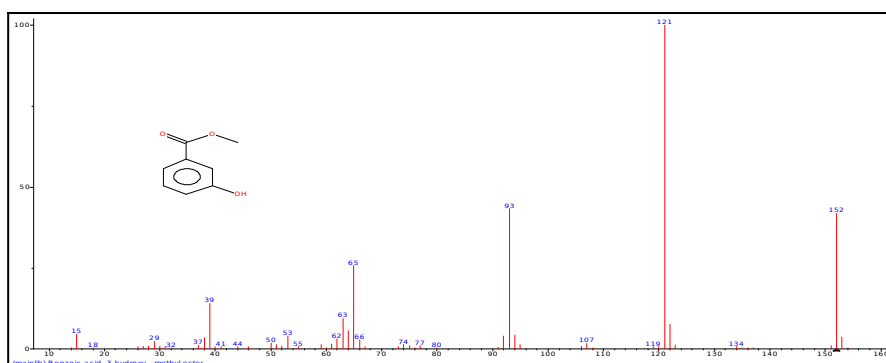
Figure 3: Methyl 3-hydroxybenzoate; $C_8H_8O_3$; MW=152.

Figure 4: Ethyl icosanoate; $C_{22}H_{44}O_2$; MW=340.
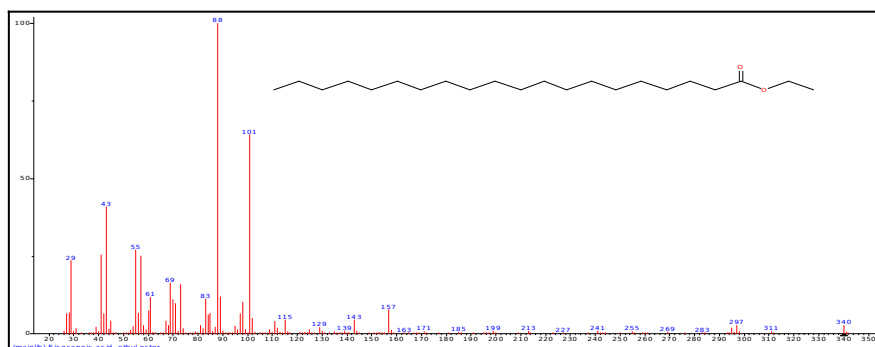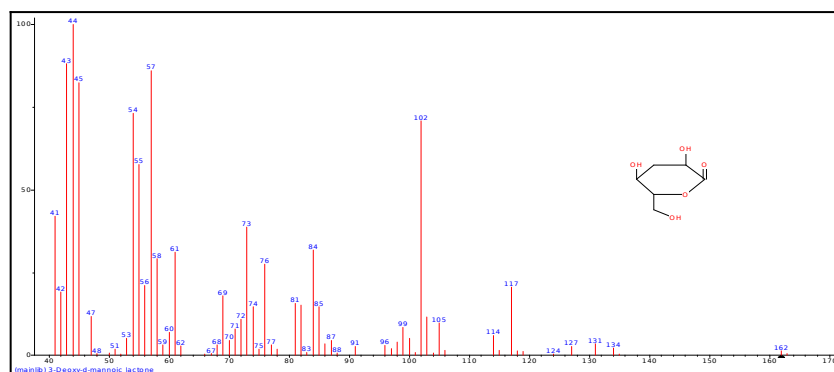
Figure 5: 3,5-Dihydroxy-6-(hydroxymethyl)oxan-2-one; $C_6H_{10}O_5$; MW=162.
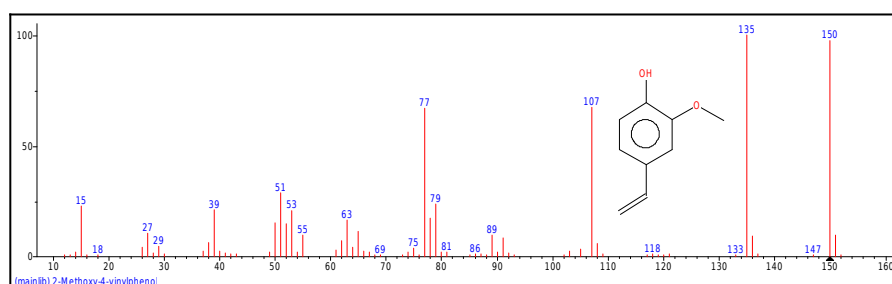
Figure 6: 2-Methoxy-4-vinylphenol; $C_9H_{10}O_2$; MW=150.
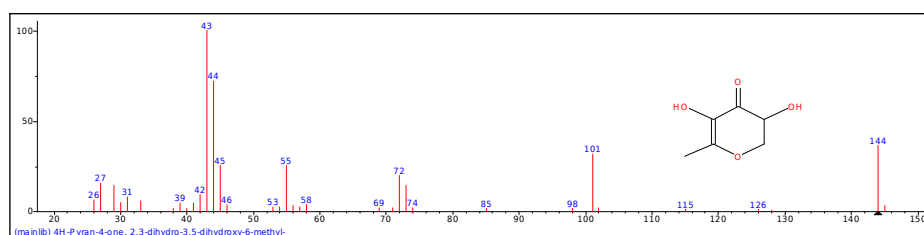
Figure 7: 4H-Pyran-4-one, 2,3-dihydro-3,5-; $C_6H_8O_4$; MW=144.
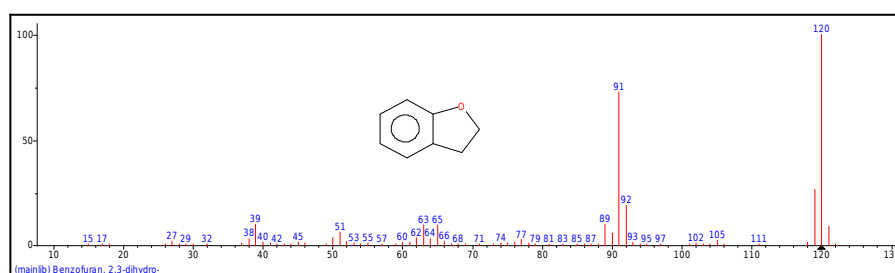
Figure 8: 2,3-Dihydrobenzofuran; C_8H_8O; MW=120.
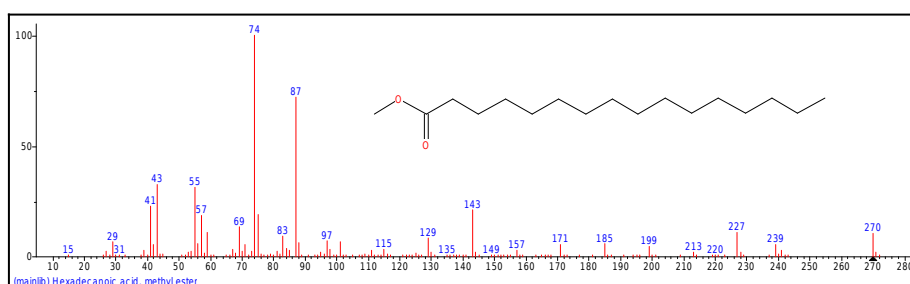
Figure 9: Methyl hexadecanoate; $C_{17}H_{34}O_2$; MW=270.

1004
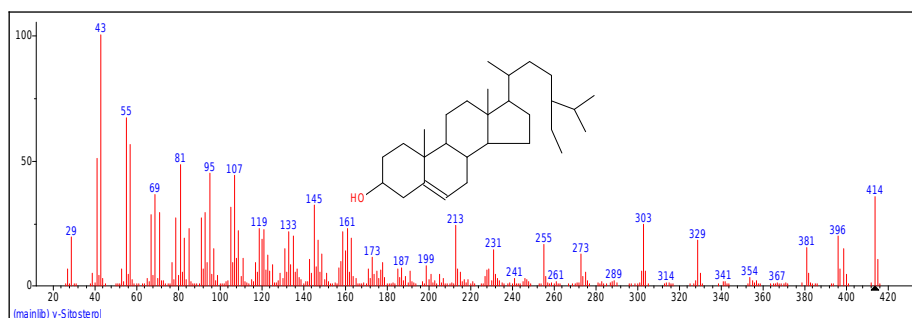
Figure 10: γ-Sitosterol; $C_{29}H_{50}O$; MW=414.

Analysis of the results of the study indicates that bioactive compounds of BE-III hazelnut green leafy covers are rich in organic compounds, such as antioxidant, antibacterial and antifungal properties. Particularly important among them are methyl hexadecanoate ($C_{17}H_{34}O_2$), dibutyl benzene-1,2-dicarboxylate ($C_{16}H_{22}O_4$), methyl octadecanoate ($C_{19}H_{38}O_2$), ethyl icosanoate ($C_{22}H_{44}O_2$), especially gamma-sitosterol ($C_{29}H_{50}O$), which has antimicrobial activity ten times more than beta-sitosterol (17,18). Our previous researches have revealed that the bio-extract obtained from the hard shell of hazelnuts has a wider spectrum range and higher amounts of bioactive compounds (19). However, in the composition of bio-extracts obtained from green leafy covers, these bioactive compounds are in short supply, both in quantity and quality. Besides, in the hazelnut green leafy covers extracts (BE-III and BE-IV) obtained by both methods 5 new organic compounds have been identified: benzene-1,2-diol ($C_6H_6O_2$), 5-(hydroxymethyl)furan-2-carbaldehyde ($C_6H_6O_3$), methyl hexadecanoate ($C_{17}H_{34}O_2$), methyl octadecanoate ($C_{19}H_{38}O_2$), 3,5-dihydroxy-6-(hydroxymethyl)oxan-2-one ($C_6H_{10}O_5$) (Figure 1-5). The presence of 5-(hydroxymethyl) furan-2-carbaldehyde ($C_6H_6O_3$), which has pharmacological properties, especially antioxidant and anti-inflammatory properties, increases the possibility of its use in the treatment of skin diseases (20,21). Other substances in the extracts are also very important and play an important role in the development of the body, the regulation of metabolism, and the strengthening of the immune system (22). The comparative results show that the bio-extracts contain 5 new organic substances such as 1-methylsulfanyl-4-propan-2-ylbenzene ($C_{10}H_{14}S$), 5-(hydroxymethyl)furan-2-carbaldehyde ($C_6H_6O_3$), methyl 3-hydroxybenzoate ($C_8H_8O_3$), ethyl icosanoate ($C_{22}H_{44}O_2$), 3,5-dihydroxy-6-methyl-2,3-dihydropyran-4-one ($C_6H_8O_4$) unlike the bio-extracts obtained from the hazelnut shell in previous studies by F. Azizov et al.,2021 (9, 19).

CONCLUSION

1. In BE-III and BE-IV extracts obtained from hazelnut green leafy covers, there are 26 mineral elements such as K, Na, Mg, Ca, Ti, V, Cr, Mn, Fe, Co, Ni, Cu, Zn, Ga, Zr, Sn, Sr, Y, Se, Al, Si, P, S, Ba, Pb, Nb, Ge, Rb. Their total amount in BE-III is 12.80%, and in BE-IV is 21.35%. In BE-III, macroelements (K, Na, Mg, Ca, Fe, P) is 10.11%, and microelements are 2.69%; in BE-IV macroelements are 17.82%, microelements are 3.53%.

2. The content of organic compounds in BE-III is 87.5%, and in BE-IV is 78.5%. In contrast to the hazelnut hard shell extract, the green leafy covers extracts contain 5 new organic compounds: 1-methylsulfanyl-4-propan-2-ylbenzene ($C_{10}H_{14}S$), 5-(hydroxymethyl)furan-2-carbaldehyde ($C_6H_6O_3$), methyl 3-hydroxybenzoate ($C_8H_8O_3$), ethyl icosanoate ($C_{22}H_{44}O_2$), 3,5-dihydroxy-6-methyl-2,3-dihydropyran-4-one ($C_6H_8O_4$). It provides a basis for obtaining a bio-extract rich in bioactive compounds.

3. It provides a basis for obtaining a bio-extract rich in bioactive compounds with antioxidant, antibacterial, and antifungal properties, as well as vital macro and microelements for the human organism, which has the potential to be used in the treatment and prevention of many diseases.

4. Based on the results, a two-stage extraction regimen is recommended: (I) keep dried and ground hazelnut green leafy covers in 70% ethyl alcohol solution in a 1:3 ratio of solid-liquid phases at 20-22 °C for 3 hours; (II) after evaporation of ethyl alcohol the extraction should be continued with distilled water at 70-80 °C for 3 hours.

5. Bio-extracts obtained from hazelnuts with distilled water BE-IV and BE-III with 70% ethyl alcohol contain 12.797% 25 elements, except for Rb in BE-III, and 26 elements in BE-IV 21.347%. In BE-IV, macronutrients K, Na, Mg, Ca, Fe, and P are 17.82%, microelements are 3.53%, and in BE-III, macroelements are 10.11%, and microelements are 2.69%. Elements with antioxidant activity are Zn-0.01%, Se-0.01%, Mn-0.017% in Be-III, and Zn-0.009%, Se-0.001%, Mn-0.021% in BE-IV.

REFERENCES

1. Cerulli A, Lauro G, Masullo M, Cantone V, Olas B, Kontek B, et al. Cyclic Diarylheptanoids from Corylus avellana Green Leafy Covers: Determination of Their Absolute Configurations and Evaluation of Their Antioxidant and Antimicrobial Activities. J Nat Prod [Internet]. 2017 Jun 23 [cited 2022 Aug 8];80(6):1703–13. Available from: <URL>.

2. Simsek A, Aykut O. Evaluation of the microelement profile of Turkish hazelnut (Corylus avellana L.) varieties for human nutrition and health. International Journal of Food Sciences and Nutrition [Internet]. 2007 Jan [cited 2022 Aug 8];58(8):677–88. Available from: <URL>.

3. Özaslan M, Oğuzkan SB, Uğraş S, Can M, Uzun A, Ülger S, et al. Fındık (Corylus avellana L.) Yeşil Kabuk ve Yaprak Ekstraklarında Biyolojik Aktivite Tayini. Journal Of Agriculture and Nature [Internet]. 2016;19(4):373–8. Available from: <URL>.

4. Hoffman A, Shahidi F. Paclitaxel and other taxanes in hazelnut. Journal of Functional Foods [Internet]. 2009 Jan [cited 2022 Aug 8];1(1):33–7. Available from: <URL>.

5. Siriwardhana SSKW, Shahidi F. Antiradical activity of extracts of almond and its by-products. J Amer Oil Chem Soc [Internet]. 2002 Sep [cited 2022 Aug 8];79(9):903–8. Available from: <URL>.

6. Shahidi F, Alasalvar C, Liyana-Pathirana CM. Antioxidant Phytochemicals in Hazelnut Kernel (Corylus avellana L.) and Hazelnut Byproducts. J Agric Food Chem [Internet]. 2007 Feb 1 [cited 2022 Aug 8];55(4):1212–20. Available from: <URL>.

7. Alasalvar C, Karamać M, Amarowicz R, Shahidi F. Antioxidant and Antiradical Activities in Extracts of Hazelnut Kernel (Corylus avellana L.) and Hazelnut Green Leafy Cover. J Agric Food Chem [Internet]. 2006 Jun 1 [cited 2022 Aug 8];54(13):4826–32. Available from: <URL>.

8. Abubacker M, Deepalakshmi T. In vitro antifungal potential of bioactive compound methyl ester of hexadecanoic acid isolated from Annona muricata linn (annonaceae) leaves. Bioscience Biotechnology Research Asia. 2013;10(2):879–84.

9. Azizov F, Shukurlu Y, Khalilov Z. Bio-extract from hazelnut shell. Patent number I 2020 0015.

10. Ermakov A, Arasimovich V, Iarosh N, Peruanskii I, Lukovnikova G, Ikonnikova M. Metody biokhimicheskogo issledovaniia rastenii. 1987. 430 p.

11. Khan Y. Element content analysis of plants of genus Ficus using atomic absorption spectrometer. Afr J Pharm Pharmacol [Internet]. 2011 Mar 31 [cited 2022 Aug 8];5(3):317–21. Available from: <URL>.

12. Mielniczuk Z, Mielniczuk E, Larsson L. Gas chromatography-mass spectrometry methods for analysis of 2- and 3-hydroxylated fatty acids: Application for endotoxin measurement. Journal of Microbiological Methods [Internet]. 1993 Mar [cited 2022 Aug 8];17(2):91–102. Available from: <URL>.

13. Fernández-Lázaro D, Fernandez-Lazaro CI, Mielgo-Ayuso J, Navascués LJ, Córdova Martínez A, Seco-Calvo J. The Role of Selenium Mineral Trace Element in Exercise: Antioxidant Defense System, Muscle Performance, Hormone Response, and Athletic Performance. A Systematic Review. Nutrients [Internet]. 2020 Jun 16 [cited 2022 Aug 8];12(6):1790. Available from: <URL>.

14. Tinggi U. Selenium: its role as antioxidant in human health. Environ Health Prev Med [Internet]. 2008 Mar [cited 2022 Aug 8];13(2):102–8. Available from: <URL>.

15. Fallah A, Mohammad-Hasani A, Colagar AH. Zinc is an Essential Element for Male Fertility: A Review of Zn Roles in Men's Health, Germination, Sperm Quality, and Fertilization. J Reprod Infertil. 2018 Jun;19(2):69–81.

16. Blasco B, Graham NS, Broadley MartinR. Antioxidant response and carboxylate metabolism in Brassica rapa exposed to different external Zn, Ca, and Mg supply. Journal of Plant Physiology [Internet]. 2015 Mar [cited 2022 Aug 8];176:16–24. Available from: <URL>.

17. Chelliah R, Ramakrishnan S, Antony U. Nutritional quality of Moringa oleifera for its bioactivity and antibacterial properties. International Food Research Journal. 2017;24(2):825.

18. Ramalhosa E, Delgado T, Estevinho L, Pereira JA. Hazelnut (Corylus avellana L.) Cultivars and Antimicrobial Activity. In: Nuts and Seeds in Health and Disease Prevention [Internet]. Elsevier; 2011 [cited 2022 Aug 8]. p. 627–36. Available from: <URL>.

19. AziZov F, Shukurlu Y, Khalilov Z, Atayeva V, Mustafayev N. Chemical composition and biological active substances of bioextracts from hazelnut shell. Eskişehir Teknik Üniversitesi Bilim ve Teknoloji Dergisi - C Yaşam Bilimleri Ve Biyoteknoloji [Internet]. 2021 Jul 30 [cited 2022 Aug 8]; Available from: <URL>.

20. Alasalvar C, Shahidi F. Tree Nuts: Composition, Phytochemicals, and Health Effects: An Overview. In: Alasalvar C, Shahidi F, editors. Tree Nuts [Internet]. 1st edition. CRC Press; 2008. Available from: <URL>.

21. Niu X, Wang Z, Zhang L, Quan Y, Wei K. Experimental study of the protective effect of mesosilica-supported 5-hydroxymethylfurfural on UV-induced aging of human dermal fibroblasts. RSC Adv [Internet]. 2018 [cited 2022 Aug 8];8(44):25021–30. Available from: <URL>.

22. Sookwong P, Yodpitak S, Doungkaew J, Jurithayo J, Boonyawan D, Mahatheeranont S. Application of oxygen-argon plasma as a potential approach of improving the nutrition value of pre-germinated brown rice. Journal of Food and Nutrition Research. 2014;2(12):946–51.

RESEARCH ARTICLE

Optimization and Characterization of Acid-Catalyzed Castor Biodiesel and its Blends

Syed Ubaid Hussain[1], Sajida Noureen[1], Irum Razzaq[1], Saleem Akhter[1],
Fahad Mehmood[1], Zahra Razzaq[1], Mussarat Jabeen*[2]

[1]Department of Chemistry, The Islamia University of Bahawalpur, Punjab, Pakistan
[2]Department of Chemistry, Government Sadiq College Women University Bahawalpur, Punjab, Pakistan

Abstract: In terms of energy security, biodiesel has become an alternative, safe, and biodegradable fuel. Here, to produce biodiesel from castor oil, a transesterification process was carried out using an acid-catalyzed catalyst. Three blends (B_{10}, B_{20} and B_{30}) were prepared by using different proportions of castor biodiesel and petro-diesel. Biodiesel optimum yield of 80% was obtained from 5 mL of castor oil with the influence of different parameters such as 1.75 mL of methanol and 0.08 mL of conc. H_2SO_4, at 65 ℃, for 3 hours with 600 revolutions per minute stirring speed for 5 mL of castor oil. Physiochemical properties of all samples such as moisture contents, iodine value, free fatty acid value, saponification value, ester value, acid value, peroxide value, viscosity (at 40 ℃), specific gravity, refractive index, density, boiling point, average molecular weight, and higher heating value were determined. Castor biodiesel characterization was resulted as 0.112 (percentage), 86 mg KOH/g, 1.0878 mg KOH/g, 0.439 mg KOH/g, 84.9122 mg KOH/g, 86.32 gI_2/100 g, 20.66 Meq/100 g, 0.8850 g, 17.21 cSt, 1.4667 nD, 0.8910 g, 290 ℃, 1982.05 g, and 44.479 MJ/Kg min, respectively. The functional groups were investigated by using FTIR. In the present study, it was demonstrated that biodiesel can be produced using a method of acid-catalyzed transesterification by using castor oil.

INTRODUCTION

As the population grows and energy consumption increases in the industry, agriculture, domestic and public sectors, the energy crisis has become a major problem for the world. (1). At present, energy security has become a central issue because energy demands per capita are also increasing day by day (2). Government of Pakistan taking multiple steps to overcome the energy crisis and has been creating friendly relations with fuel-rich Muslim countries such as Saudi Arabia, UAE, Qatar, Iran etc. Excessive investment has been done in the country's oil refineries. Searching for new and renewable energy such as biodiesel is one of the alternative ideas to put back fossil fuels in the present situation (3). The blending of fossil fuels with biodiesel controls exhaust emission,

moreover it is a green, cheaper, eco-friendly, and easily producible energy source (4). Pakistan is an energy-deficient country and facing an energy crisis because of limited fossil fuels (5). On the other hand, public demands for energy consumption are increasing due to rapid transportation, industrialization, agriculture, and household usage. At present, China has the highest demand in the continent of Asia (6). As world oil prices are continuously rising, developing countries like Pakistan need a cheaper source of energy (7). There is a continuous increase in the cost of energy in Pakistan, which is expected to peak after 2050. A minimum share of 5% of total diesel consumption must be achieved by blending biodiesel with petroleum diesel under current energy sector policies (8). Today, like Pakistan

whole world is facing energy crisis, petrol, electricity, and gas prices increasing more rapidly. In Spain, electricity price raised up to 200% in 2022 while in India price increased 110% more than the last year.

Biodiesel is known as oxygenated fuel having similar properties to diesel and normally can be produced from waste cooking oil, animal fats, and vegetable oils by conversion of triglycerides to esters via transesterification ([9]). It is a non-toxic, clean, bio-degradable, cheaper, technologically feasible, and renewable fuel ([10]). It can also use directly in the diesel engine but using directly is not suitable for the efficiency of the engine due to high viscosity, poor combustion, and non-volatility ([11]). Therefore, some modifications are necessary to oil like high viscosity of oil can be reduced by preheating, transesterification, blending, and thermal cracking. Most commonly, reducing the viscosity of oil transesterification is preferred ([12]). According to literature, 10% of biodiesel is transesterified ([13]). The process is done by the reaction of triglycerides with short-chain alcohol usually methanol or ethanol by using a catalyst resulting alkyl esters (biodiesel) and glycerin ([14],[15]).

As oil is a triglyceride of fatty acid and glycerol and the most widely used feedstock is vegetable oils for the production of biodiesel. Due to the shortfall of edible oil it would not be executable to develop biodiesel from edible oil. Moreover, edible oil is also used for cooking purposes ([16]). So it is necessary to produce biodiesel from non-edible oil resources such as castor oil, atrophy oil, neem oil, Karana etc., ([17-19]). Castor biodiesel is a non-edible, versatile and renewable energy source that replaces the petroleum-derived diesel fuel and can act as lubricant ([20],[21]). Castor-oil is extracted from castor beans and contain 40-55% oil while other commonly used crop seeds contain a low concentration of oil like soybean 15–20%, palm 30-50%, sunflower 25–35% and rapeseed 38–46% ([22]). Castor oil contains hydroxylated fatty acid 80-90% mainly ricinoleic acid and non-hydroxylated fatty acids approximately 10% mainly 4-5% linoleic acid, 2-4% oleic acid, 1% stearic acid and 1% palmitic acid ([23]). In comparison with other vegetable oils, castor oil has a higher cetane number since it does not contain sulfur, indicating it contains more oxygen and is more flammable ([24]). Castor oil, due to the presence of ricinoleic acid, is approximately 7 times more viscous than other vegetable oils which increases the lubricity of biodiesel ([25]). Due to its low pour point -45℃ and cloud point, castor biodiesel is the best fuel for cold weather because it has a low pour point and cloud point ([26]).

For transesterification of castor oil several methods have been reported by using homogeneous catalysts and heterogeneous catalysts. Panwar *et al* by using an alkaline catalyst produced 96% biodiesel from castor oil via transesterification ([27]). Jeong & Park and Thirugnanasambandham *et al* synthesize biodiesel using KOH as a catalyst with a yield up to 92% and 86.9% ([28],[29]). Nurdin *et al* studied the transesterification by using a heterogeneous catalyst (calcined mussel shell) yielding 91.17% ([30]). Amalia *et al* used heterogeneous KOH/zeolite catalyst for the production of castor biodiesel through the transesterification process ([31]). Ferdous *et al* used acid catalyst (sulfuric acid) for the production of biodiesel with a yield of more than 70% ([32]).

In this study, transesterification of castor oil was performed by using acidic catalyst sulfuric acid with an optimum yield of 80%. The physiochemical properties like saponification value, moisture contents, acid value, ester value, iodine value, peroxide value, free fatty acid value, specific gravity, viscosity (at 40 ℃), refractive index, density, boiling point, average molecular weight and higher heating value were studied. Furthermore, the functional groups were investigated by FTIR.

MATERIALS AND METHODS

Collection of feedstock
Castor seeds were purchased from the local market of Bahawalpur, Pakistan, washed to remove dirt, dried for 4 days in sunlight and finally in the oven for 5 hours at 100℃ to remove water. Castor oil was extracted by a conventional extractor and filtered through Whatman filter paper to remove suspended particles.

Transesterification experiments
As free fatty acid (FFA) value of castor oil is very high and can cause a major problem in the preparation of biodiesel. To overcome this problem, acid-catalyzed transesterification can be done.

40 mL of castor oil was heated for 5 min with vigorously stirring. A mixture of 14 mL of methanol and 0.64 mL of conc. H_2SO_4 was added to hot castor oil. The temperature was adjusted to 65 ℃, the mixture was properly covered to control the loss of methanol and stirred with a magnetic stirrer continuously for 3 hours. After the completion of the reaction, the mixture was allowed to settle for 24 hours in 250 mL of separator funnel. After 24 hours two layers were formed, the upper layer was methyl ester (biodiesel) and lower the layer was glycerol & gums. The lower layer was separated safely, without the loss of the upper layer. The biodiesel layer was washed with hot water several times. After washing the biodiesel layer in the separator funnel, 15-20 mL of boiled distilled water was added into the separator funnel and allowed to stand for another 6 hours which resulted in the remaining traces of glycerin setting down into the

water. After 6 hours, water was removed and separated the biodiesel layer into a beaker. Biodiesel was heated above 100℃ to remove the moisture contents. Finally, the biodiesel was

prepared and stored for further usage. The biodiesel percentage yield was measured by using the formula:

$$Biodiesel\ \%age\ yield = \frac{volume\ of\ biodiesel\ obtained\ (mL)}{volume\ of\ raw\ castor\ oil\ (mL)} \times 100 \qquad \text{(Eq. 1)}$$

RESULTS AND DISCUSSION

In transesterification reaction, triglyceride which is a mixture of fatty acids react with alcohol in the

presence of a catalyst (acid or base). In this reaction alkyl ester (biodiesel) is produced and glycerol is obtained as a by-product (Figure 1).
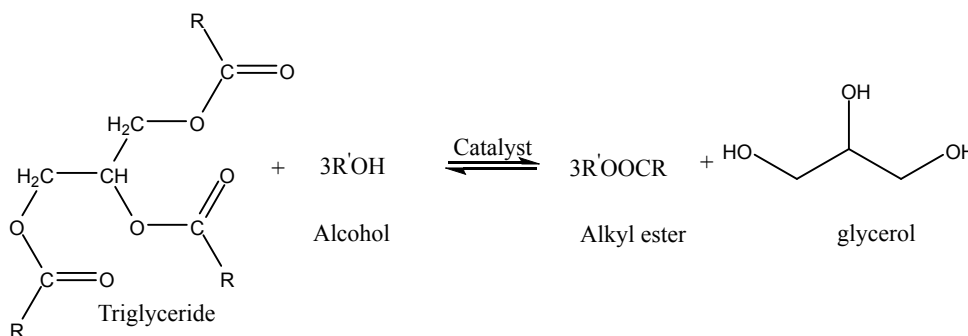
Figure 1: Transesterification reaction of triglyceride.

For high free fatty acids and moisture content feed-stocks, the use of acid catalyst is favorable as compared to alkali catalysis. By acid catalyst, free fatty acid is reduced and oil can convert into biodiesel. Sulfuric acid, orthophosphoric acid, and hydrochloric acid are among mostly used acid catalysts. The reaction of free fatty acid for the

extraction of biodiesel involves the absorption of FFA on catalyst acidic position which forms carbocation. An intermediate is produced by the reaction of methanol with carbocation. By elimination of water from intermediate biodiesel is produced as an end product (Figure 2).
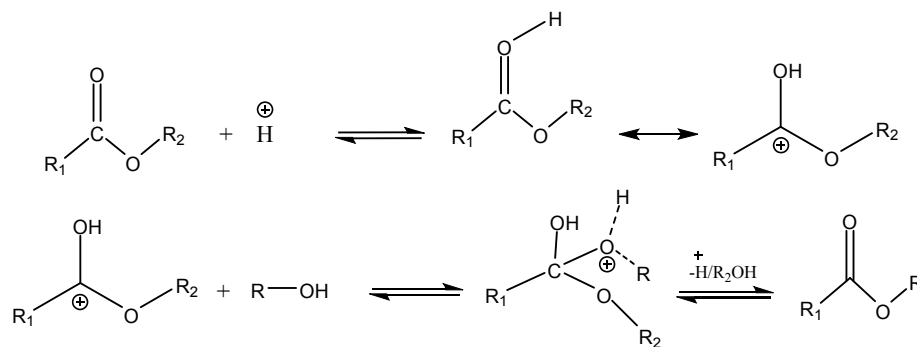
Figure 2: Acid-catalyzed transesterification mechanism.

Effect of variable parameters
The effect of methanol concentration, conc. H_2SO_4 catalyst concentration, reaction temperature,

reaction time and the stirring speed was investigated. The data is summarized in Table 1.

Table 1: Optimization Summary of castor biodiesel

Castor oil	Methanol	H$_2$SO$_4$ catalyst	Reaction temperature	Reaction time	Stirring speed	Biodiesel percentage
Effect of methanol concentration						
20 mL	5 mL	0.32 mL	65℃	3 hours	600 rpm	67.5%
20 mL	7 mL	0.32 mL	65℃	3 hours	600 rpm	77.5%
20 mL	10 mL	0.32 mL	65℃	3 hours	600 rpm	64%
20 mL	12 mL	0.32 mL	65℃	3 hours	600 rpm	56%
Effect of catalyst concentration						
10 mL	3.5 mL	0.16 mL	65℃	3 hours	600 rpm	67%
10 mL	3.5 mL	0.25 mL	65℃	3 hours	600 rpm	60%
10 mL	3.5 mL	0.32 mL	65℃	3 hours	600 rpm	50%
10 mL	3.5 mL	0.50 mL	65℃	3 hours	600 rpm	39%
Effect of reaction temperature						
5 mL	1.75 mL	0.08 mL	45℃	3 hours	600 rpm	48%
5 mL	1.75 mL	0.08 mL	65℃	3 hours	600 rpm	66%
5 mL	1.75 mL	0.08 mL	85℃	3 hours	600 rpm	58%
5 mL	1.75 mL	0.08 mL	105℃	3 hours	600 rpm	0%
Effect of reaction time						
5 mL	1.75 mL	0.08 mL	65℃	1 hour	600 rpm	0%
5 mL	1.75 mL	0.08 mL	65℃	2 hours	600 rpm	28%
5 mL	1.75 mL	0.08 mL	65℃	3 hours	600 rpm	42%
5 mL	1.75 mL	0.08 mL	65℃	4 hours	600 rpm	0%
Effect of stirring speed						
5 mL	1.75 mL	0.08 mL	65℃	3 hours	300 rpm	0%
5 mL	1.75 mL	0.08 mL	65℃	3 hours	400 rpm	28%
5 mL	1.75 mL	0.08 mL	65℃	3 hours	500 rpm	42%
5 mL	1.75 mL	0.08 mL	65℃	3 hours	600 rpm	0%
Optimum conditions for all parameters						
5 mL	1.75 mL	0.08 mL	65℃	3 hours	600 rpm	80%

Effect of methanol concentration

Four transesterification reactions were performed by using 20 mL of castor oil and variable concentration of methanol such as 5 mL, 7 mL, 10 mL & 12 mL, catalyst (0.32 mL of conc. H$_2$SO$_4$), reaction temperature (65 ℃), reaction time (3 hours) and stirring speed (600 rpm). Obtained biodiesel percentage yield were 67.5%, 77.5%, 64% and 56% respectively. Phase separation was also done for all given concentrations of methanol. Below 5 mL of methanol concentration, the reaction was not proceeding and phase separation was not observed due to the low concentration of methanol not equilibrating with castor oil. Hence transesterification did not proceed.

It was noticed that a maximum of 77.5% of biodiesel yield was obtained by using 7 mL of methanol. For acid-catalyzed transesterification, biodiesel percentage yield was decreased as the methanol concentration was increased. These changes resulted that excess methanol lowered the biodiesel yield because of increasing the miscibility of castor oil into excess methanol at a given reaction conditions. A high concentration of methanol increased the solubility of castor oil into methanol. –OH group present in ricinoleic acid makes the castor oil polar. On the other hand, a solvent such as methanol is also polar due to the presence of the -OH group. So, according to the principle "like dissolves like" methanol shows the miscibility into castor oil. That's why biodiesel yield was decreased. Finally, 7 mL of methanol concentration were considered as the optimal value of methanol for 20 mL of castor oil. Keera *et al* (2018) reported the similar results to our findings, increasing the methanol to oil ratio led to decreased biodiesel yield as a result of methanol accumulation and viscous fluids. Figure 3 represents the biodiesel yield at different methanol concentrations.
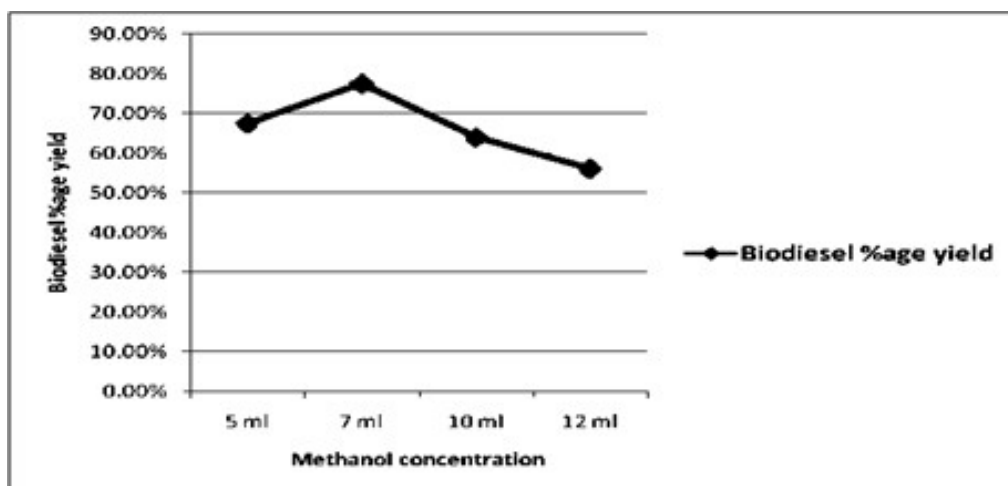
Figure 3: Effect of methanol concentration on biodiesel percentage yield.

Effect of conc. H_2SO_4 catalyst concentration

The acidic catalyst was used for transesterification because the basic catalyst caused emulsion and saponification. Four transesterification reactions were performed by using 10 mL of castor oil and a variable concentration of conc. H_2SO_4 catalyst such as 0.16 mL, 0.25 mL, 0.32 mL, and 0.5 mL; methanol concentration, reaction temperature, reaction time, and stirring speed was 7 mL 65 ℃, 3 hours, and 600 rpm, respectively. Obtained biodiesel percentage yields were 67%, 60%, 50%, and 39%. Below 0.16 mL of conc. H_2SO_4 catalyst, transesterification reaction did not proceed and phase separation was not achieved.

It was observed that maximum of 67% of biodiesel yield were obtained by using 0.16 mL of conc. H_2SO_4 catalyst. Chand *et al* (2013) was also reported a 68% yield by using a 0.5% KOH catalyst ([33]). But when using KOH catalyst, chances of saponification is higher than the use of

conc. H_2SO_4 catalyst. That is why we used conc.H_2SO_4 catalyst to overcome saponification. Biodiesel percentage yield decreased as the conc. H_2SO_4 catalyst increased. These changes resulted in a high volume of acidic catalyst that lowered the biodiesel yield. All this is because of high free fatty acid (FFA) value of castor oil tends to resist biodiesel production. Conc. H_2SO_4 catalyst converted the free fatty acid into biodiesel but over volume of conc. H_2SO_4 catalyst decreased the biodiesel yield because the catalyst start mixing with glycerol and spoil the biodiesel during transesterification. So, an adequate volume of conc. H_2SO_4 catalyst is efficient to produce the biodiesel. Finally, 0.16 mL of conc. H_2SO_4 catalyst were considered as the optimal value of acidic catalyst for 10 mL of castor oil. Carmaker *et al* (2018) agrees with our findings ([34]). Figure 4 represents the biodiesel yield at different conc. H_2SO_4 catalyst concentrations.
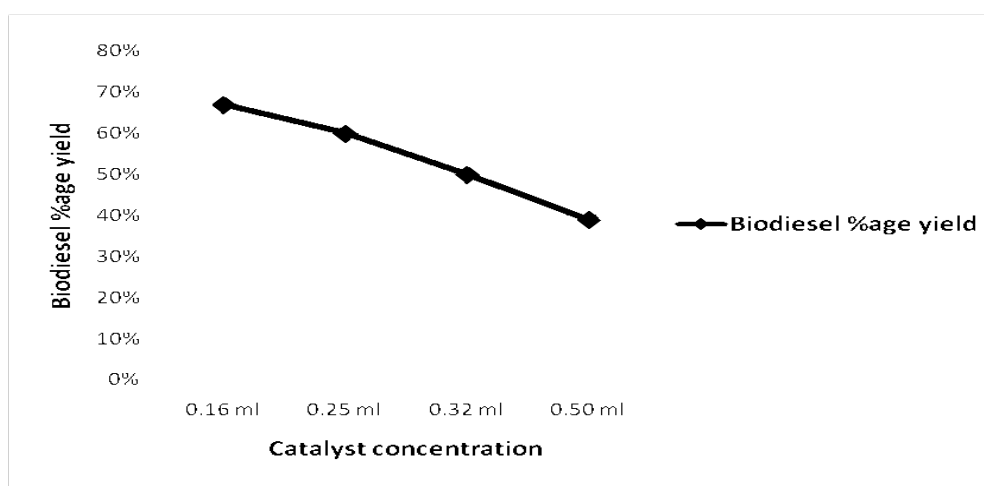
Figure 4: Effect of conc. H_2SO_4 catalyst concentration on biodiesel percentage yield.

Effect of reaction temperature

Four transesterification reactions were performed by using 5 mL of castor oil and variable reaction temperatures such as 45 ℃, 65 ℃, 85 ℃, and 105

℃. The methanol concentration, conc. H_2SO_4 catalyst concentration, reaction time, and stirring speed were 1.75 mL, 0.08 mL, 3 hours & 600 rpm, respectively. The percentage yield of obtained

biodiesel was 48%, 66%, 58% and 0% respectively. Phase separation was performed at 45 ℃, 65 ℃, and 85 ℃ of temperature but not done at 105 ℃.

It was observed that a maximum of 66% of biodiesel yield was obtained at 65 ℃. But minimum biodiesel yield was obtained at 45 ℃. These changes resulted, at 105℃ of high-temperature castor oil contents being dissolved into methanol. That is why no phase separation took place at 105 ℃. At 45 ℃ of temperature phase separation was done but the yield was low because of incomplete transesterification. Finally, 65 ℃ of reaction temperature was considered the optimal value for transesterification. Maryam *et al* (2018) reported

that increased in temperature from 60 ℃, biodiesel yield decreased (10). Similar results were reported by Silting *et al* (2016) that above 65 ℃ biodiesel yield decreased due to the presence of glycerol before transesterification was completed. Carmaker *et al* (2018) reported that acid esterification was unfavorable at high temperature (70 ℃) due to loss of methanol, reaction equilibrium also shifts away from product formation (34). Chand *et al* (2013) reported that temperature above the boiling point of alcohol was avoided because above 65 ℃ methanol evaporated. Hence biodiesel yield is lowered at high temperature (33). Figure 5 represents the biodiesel yield at different reaction temperatures.
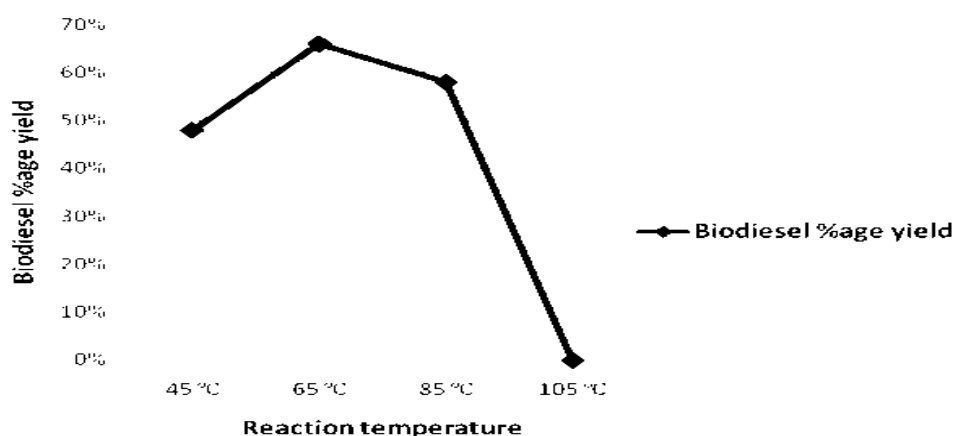
Figure 5: Effect of reaction temperature on biodiesel percentage yield.

Effect of reaction time
Four transesterification reactions were performed by using 5 mL of castor oil and variable reaction times such as 1 hour, 2 hours, 3 hours, and 4 hours. Methanol concentration, conc. H_2SO_4 catalyst concentration, reaction temperature, and stirring speed were 1.75 mL, 0.08 mL, 65 ℃ and 600 rpm, respectively. Obtained biodiesel yields were 0%, 28%, 42% and 0%. Phase separation was done when reaction times were 2 hours and 3 hours. But phase separation was not done at 1 hour and 4 hours of reaction time.

It was noticed that a maximum of 42% biodiesel yield was obtained at 3 hours of reaction time. But at the first hour of reaction time, we did not proceed with the transesterification process, because in this time it was below the limit of

transesterification That is why phase separation was not done and the percentage yield was 0%. Phase separation was also not done at 4 hours because reaction time was over the limit for transesterification. Above 4 hours of reaction time, obtained biodiesel and obtained glycerol reversely start mixing with each other and spoil the biodiesel. That is why at 4 hours of reaction time biodiesel percentage yield was also 0% Finally, 3 hours of reaction time were considered as the optimal value for complete transesterification. Carmaker *et al* (2018) reported similar results that mass transfer between oil and alcohol is enhanced by adequate reaction time provided for reactants to interact (23). Silting *et al* (2016) and Seem *et al* (2015) are in agreement with our findings (35,36). Figure 6 represents the biodiesel yield at different reaction times.
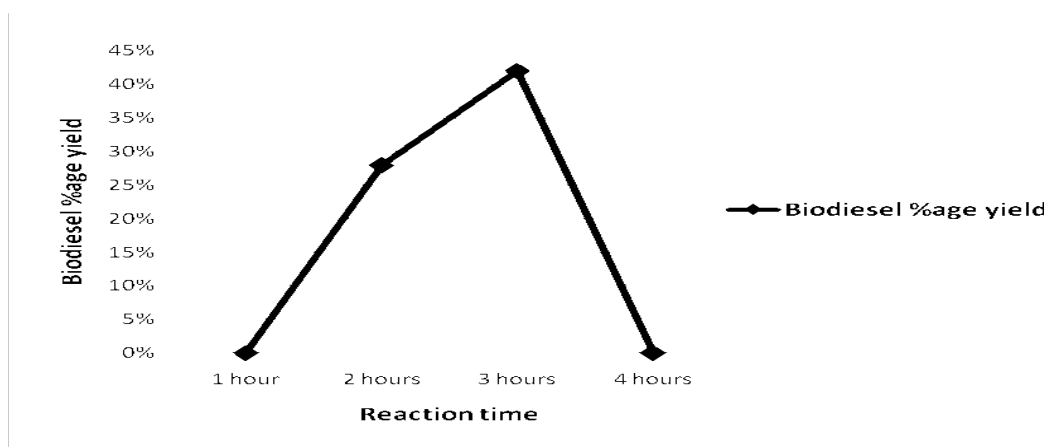
Figure 6: Effect of reaction time on biodiesel percentage yield.

Effect of stirring speed
Four transesterification reactions were performed by using 5 mL of castor oil and variable stirring speeds such as 300 rpm, 400 rpm, 500 rpm and 600 rpm, respectively. Methanol concentration, conc. H_2SO_4 catalyst concentration, reaction temperature and reaction time were 1.75 mL, 0.08 mL, 65 °C and 3 hours, respectively. Obtained biodiesel yields were 22%, 38%, 42%, and 44%. Phase separation was also achieved for all transesterification reactions.

It was noticed that a maximum 44% biodiesel yield was obtained at 600 rpm of stirring speed due to proper mixing of oil and alcohol. But above 600 rpm yield was lowered because of improper mixing of oil and alcohol and chances of mixing up biodiesel and glycerol. So these changes resulted, that high stirring (600 rpm) being needed for the excitation of castor molecules for complete transesterification. Finally, 600 rpm was considered the optimal value for complete transesterification. Chand *et al* (2013) reported similar results that the highest yield was obtained at 600 rpm of stirring speed. Carmaker *et al* (2018), and Dhanani *et al* (2015) are in agreement with our findings ([33],[34]). Figure 7 represents the biodiesel yield at different stirring speeds.
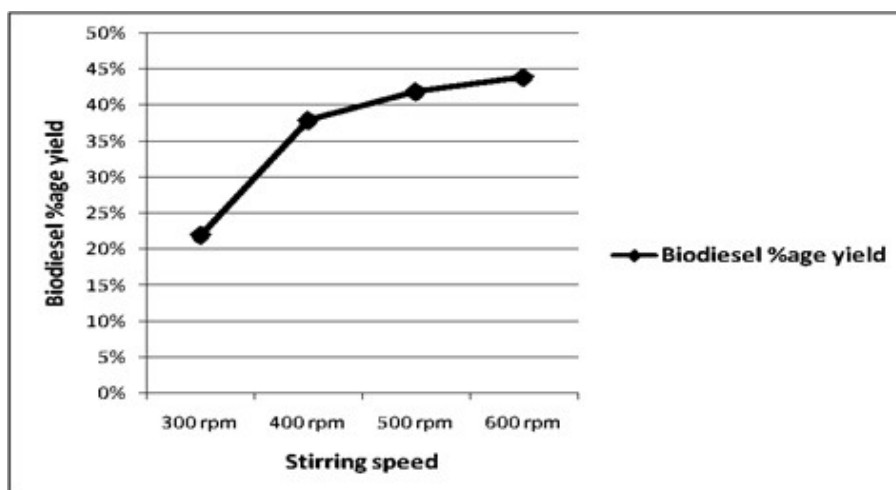
Figure 7: Effect of stirring speed on castor biodiesel percentage yield.

Physicochemical properties of castor oil, castor biodiesel and blends
Physicochemical properties of castor oil, castor biodiesel and blends B_{10}, B_{20} & B_{30} were measured. Blends were prepared on a volume-based ratio of biodiesel: diesel mixtures [B_{10}(1:9), B_{20}(2:8), B_{30}(3:7)]. Moreover, all measured values were also compared with standard tests. The data are given in Table 2.

Table 2: Characterization Summary of castor biodiesel.

Properties	Units	Castor oil	Castor biodiesel	B_{10}	B_{20}	B_{30}	Test method	Test limit
Moisture contents	percentage w/w	0.171	0.112	1.441	1.4424	1.4397	ASTM D2709	0.50 max
Saponification value	mg KOH/g	186.35	86	1.43	2.36	4.32	AOCS Cd3-25	175-187
Acid value	mg KOH/g	2.3002	1.0878	0.514	0.9635	0.9889	ASTM D664	0.8 max
FFA value	mg KOH/g	1.1501	0.439	0.757	0.9817	1.0939	AOCSCa5 a40	3-38
Ester value	mg KOH/g	184.0498	84.9122	0.915	1.3965	3.3321	EN14111	96.5 min
Iodine value	$gI_2/100$ g	86.32	86.32	49.55	54.23	56.86	AOCS Cd1-25	84-112
Peroxide value	Me/100 g	15.4	20.66	16.01	17.74	18.44	-	-
Specific gravity	Gram	0.959	0.8850	0.688	0.693	0.701	ASTM D6751	0.87-0.90
Viscosity at 40 ℃	cSt	239	17.21	3.87	4.53	4.99	ASTM D445	1.9-6
Refractive index	nD	1.4782	1.4667	1.441	1.4424	1.4397	ASTM D960	1.32
Density	Gram	0.9481	0.8910	0.920	0.928	0.932	ASTM D1298	0.83-0.89
Boiling point	℃	316	290	-	-	-	-	-
Molecular weight	Gram	914.42	1982.05	-	-	-	-	-
Higher heating value	MJ/Kg	40.494	44.479	48.628	48.519	48.399	ASTM D240	-

Moisture contents

High moisture contents were present in castor oil (0.171%). Moisture contents of castor biodiesel were also high (0.112%). Khalil *et al* (2017) reported the moisture contents of castor oil as 4.4% ([23]). Keera *et al* (2018) reported the moisture contents of biodiesel as 0.02% ([37]). ASTM D2709 test limit of moisture content is 0.5 (max). Moisture contents percentage must be low in biodiesel because it promotes microbial growth in the biodiesel.

Saponification value

Saponification is the major problem of castor oil for biodiesel production. It is also affected on biodiesel yield. A basic catalyst like KOH and NaOH enhanced the saponification during transesterification. To overcome this problem acid catalyst was used for transesterification.

The saponification value of castor oil and its biodiesel were 186.35 mg KOH/g and 86.0 mg KOH/g. It decreased after transesterification. Saponification values of blends B_{10}, B_{20} & B_{30} were 1.43 mg KOH/g, 2.36 mg KOH/g, and 4.32 mg KOH/g, respectively. The saponification value of blends from B_{10} to B_{30} increased as the biodiesel contents in blends increased. Seem *et al* (2015) reported the saponification value of castor oil as 226.54 mg KOH/g ([36]). Bursary *et al* (2017) reported the saponification value of castor biodiesel as 241.55 mg KOH/g for base-catalyzed transesterification ([38]). AOCS Cd 3-15 test limit of saponification value for oil is 175-187 mg KOH/g. saponification value of castor oil is closed to AOCS Cd 3-15 test limit. Maximum reduction of saponification value from 186.35 mg KOH/g to 86.0 mg KOH/g took place for biodiesel which

resulted that better efficiency of biodiesel due to less specific matter. All blends showed a very low saponification value which means that they have better efficiency as a diesel substitute.

Acid value

The acid value is the number of a milligram of KOH required to neutralize the free fatty acids in 1 g of fats. A low acid value is favorable for biodiesel production**.** The acid value of castor oil was 2.3002 mg of KOH/g and after transesterification, it was decreased to 1.0878 mg of OH/g. Acid value of blends such as B_{10}, B_{20} & B_{30} were 0.5147 mg of KOH/g, 0.9635 mg of KOH/g, and 0.9870 mg of KOH/g, respectively. The acid value of blends from B10 to B30 increased as the biodiesel contents in blends increased. ASTM D664 test limit of acid value is 0.8 mg of KOH/g (max). Chand *et al* (2013) reported the acid value of biodiesel as 0.8 mg KOH/g ([33]). Amite *et al* (2014) reported the acid value of castor oil as 2.629 mg KOH/g but they did not measure the acid value of castor biodiesel ([15]). But our measured acid value of castor biodiesel was 1.0878 mg KOH/g. All above reported values are close to our findings. All blends showed acid values within the range of the ASTM D664 test limit which means that blends can be used as diesel substitutes.

Free fatty acid (FFA) value

The high free fatty acid (FFA) value of castor oil tends to resist biodiesel production during transesterification. >2% free fatty acid value is an acceptable range for biodiesel production reported by Maher *et al* (2004) (19). Free fatty acid percentage of castor oil and its biodiesel were 1.1501 mg of KOH/g and 0.439 mg of KOH/g, respectively. FFA value of blends such as B_{10}, B_{20} & B_{30} were 0.7573 mg of KOH/g, 0.9817 mg of KOH/g, and 1.0939 mg of KOH/g respectively. It was observed that the FFA value of blends from B_{10} to B_{30} increased as the biodiesel contents in blends increased. The standard the value of AOCS Ca5a-40 test limit for oil is 3.38-38.2 mg OH/g. Amite *et al* (2014) reported the FFA value of castor oil as 1.345 mg of KOH/g ([15]). All blends showed the minimum FFA value which means that blends can be used as diesel substitutes.

Ester value

Ester value is the number of mg of KOH required to specify the esters in 1 g of substance. The ester values of castor oil and its biodiesel were 184 mg of KOH/g and 84.2 mg of KOH/g, respectively. It decreased after transesterification. Ester value of blends such as B_{10}, B_{20} & B_{30} were 0.9153 mg of KOH/g, 1.3965 mg of KOH/g, and 3.3321 mg of OH/g, respectively. It was observed that the ester value of blends from B_{10} to B_{30} increased as the biodiesel contents in blends increased. Seem *et al* (2015) reputed the ester value of castor oil as 218.47 mg of KOH/g ([36]). Stagey *et al* (2014) reported the ester value of castor biodiesel as 84.9122 which is similar to our findings (20). It

was clear that a large number of ester contents may specify in castor oil than biodiesel. Whereas, all blends gave positive results of ester values.

Iodine value

The iodine values indicate the level of unsaturation in the oil. The fatty acid (ricinoleic acid, linoleic acid, oleic acid) present in castor oil makes the castor oil unsaturated. Unsaturation makes the fatty acid reactive, unstable and combustible with oxygen in the engine. The iodine test indicates the estimation of unsaturated compounds. More iodine consumption during tests means that high degree of unsaturation. The iodine value of castor oil and its biodiesel were 86.32 g of I_2/100 g oil. The iodine value of blends such as B_{10}, B_{20} & B_{30} were 49.55 g of I_2/100 g oil, 54.23 g of I_2/100 g oil & 56.86 g of I_2/100 g oil respectively. Seem *et al* (2015) reported the iodine value of castor oil as 87 g of I_2/100 g oil ([36]). AOCD Cd1-25 test limit of iodine value is in the range of 84.2-112 g of I_2/100 g oil. It was clear that castor oil and its biodiesel have a high degree of unsaturation but blending the biodiesel with petro-diesel decreased the unsaturation.

Peroxide value

Peroxide value is used to determine the oil's oxidative rancidity. The peroxide value of castor oil and its biodiesel were 15.4 Meq/100 g and 20.66 Meq/100 g. it was increased after transesterification. Epoxide values of blends such as B_{10}, B_{20} & B_{30} were 16.01 Meq/100 g, 17.74 Meq/100 g & 18.44 Meq/100 g respectively. It was observed that the peroxide value of blends from B_{10} to B_{30} was increased as biodiesel contents in blends increased. Stagey *et al* (2014) reported the peroxide value of castor and its biodiesel as 20 mg of KOH/g and 28 mg of KOH/g ([39]). It was clear that castor oil and its biodiesel have high oxidative rancidity due to high peroxide value, but blending positively lowers the peroxide value.

Specific gravity

The specific gravity of castor oil and its biodiesel were 0.959 g and 0.885 g, respectively. It decreased after transesterification. Specific gravity value of blends such as B_{10}, B_{20} & B_{30} were 0.668 g, 0.693 g, and 0.701 g respectively. Specific gravity values of blends from B_{10} to B_{30} were increased as the biodiesel contents in blends increased. ASTM6751-02 test limit of specific gravity is 0.87-0.90 g. Maryam *et al* (2018) reported the specific gravity value of castor oil and castor biodiesel as 0.9 g and 0.5 g, respectively ([10]). Chand *et al* (2013) reported the specific gravity value of castor biodiesel as 0.961 g ([33]). Stagey *et al* (2014) reported the specific gravity value of B_{10}, B_{20} and B_{30} as 0.856 g, 0.860 g and 0.873 g respectively which are similar to our findings ([39]).

Viscosity
Viscosity is the measure of internal fluid resistance of oil to flow. High viscosity is not efficient for diesel. The observed viscosity value of castor oil was 239 cSt at 40℃. It was a high value. Transesterification was performed to minimize the viscosity value as 17.21 cSt at 40 ℃. Transesterification make the viscosity value in a favorable range. When biodiesel contents were blended with petro diesel then it was observed that the viscosity value was further decreased. Observed viscosity of blends such as B_{10}, B_{20} & B_{30} were 3.87 cSt, 4.53 cSt & 4.99 cSt respectively. ASTM D445 test limit of viscosity of biodiesel is 1.9-6.0 cSt. Stagey *et al* (2014) reported the viscosity value (at 40 ℃) of B_{10}, B_{20} and B_{30} as 3.78 cSt, 4.54 cSt, and 4.8 cSt ([39]). Deep *et al* (2017) reported the viscosity value (at 40 ℃) of castor oil and castor biodiesel as 240 cSt and 14.3 cSt, respectively ([40]). Maximum reduction of viscosity was observed when biodiesel is blended with petrodiesel. This resulted in that blends can be used as diesel substitutes.

Refractive index
The Refractive index value of castor oil and its biodiesel were 1.4782 nD and 1.4667 nD, respectively. Refractive index value of blends such as B10, B20 & B_{30} were 1.4418 nD, 1.4424 nD, and 1.4397 nD, respectively. ASTM D960-79 test limit of refractive index is 1.32 (max). Maryam *et al* (2018) and Amite *et al* (2014) agree with our findings ([10],[15]).

Density
The density of castor oil and its biodiesel were 0.9481 g/cm³ and 0.8910 g/cm³ respectively. Density value of blends such as B_{10}, B_{20} and B_{30} were 0.920 g/cm³, 0.928 g/cm³ and 0.932 g/cm³ respectively. ASTM D1298 test limit of biodiesel is 0.830-0.890. Tonoi et al (2016) reported the density value of castor biodiesel as 0.880 g/cm³ ([21]). Stagey *et al* (2014) reported the density value of B_{10}, B_{20} and B_{30} as 0.856 g/cm³, 0.860 g/cm³ and 0.873 g/cm³, respectively ([39]). All these values are close to our findings.

Boiling point
The boiling points of castor oil and its biodiesel were 316 ℃ and 290 ℃. All blend samples were evaporated at high temperatures.

Average molecular weight (MW)
The average molecular weight of castor oil and its biodiesel was 914.42 g and 1982.05 g, respectively. Rahman *et al* (2016) reported the average molecular weight of castor oil as 928 g ([41]).

Higher heating value (HHV)
A higher heating value is the amount of heating energy released by the combustion of a unit value of a fuel. The greater the higher heating value, the lower the fuel consumption. The higher heating value of castor oil and its biodiesel was observed as 40.4949 MJ/kg and 44.4792 MJ/kg respectively. The higher heating value of B_{10}, B_{20} and B_{30} were 48.6288 MJ/kg, 48.5198 MJ/kg and 48.3999 MJ/kg respectively. Silliman *et al* (2014) reported the higher heating value of castor biodiesel, B10, B20 and B30 were 38.576 MJ/kg, 41.626 MJ/kg, and 41.235 MJ/Kg and 40.810 MJ/Kg respectively ([42]). Murat *et al* (2013) reported the higher heating value of castor biodiesel as 42.20 MJ/Kg which is close to our findings ([43]).

Instrumental characterization
Functional groups of castor oil, castor biodiesel, and B_{10}, B_{20} and B_{30} were determined by using an FTIR spectrometer (see Figures 8a-8e).

Castor oil, castor biodiesel and blends such as B_{20} and B_{30} showed a broad band in the range of (3500 cm⁻¹- 3000 cm⁻¹) which indicated the (-OH) stretching vibration of alcohol, phenol, and carboxylic acid. B_{10} did not show any band in the range of (3500 cm⁻¹ - 3000 cm⁻¹) which indicated the absence of the −OH group. The absorption of high intensity peaks of castor oil (2924.13 cm⁻¹, 2853.99 cm⁻¹), castor biodiesel (2924.60 cm⁻¹, 2854.31 cm⁻¹), B_{20} (2924.83 cm⁻¹, 2854.43 cm⁻¹) and B_{30} (2925.08 cm⁻¹, 2855.33 cm⁻¹) indicated the stretching vibration of −CH₃ group. All those samples having a frequency in the range of (3000 cm⁻¹ – 3500 cm⁻¹) show the presence of the −CH₃ group. B_{10} was also indicated in the −CH₃ group but peak frequency was low. The strongest vibrations of castor oil (1742.60 cm⁻¹), castor biodiesel (1742.59 cm⁻¹), B_{20} (1739.21 cm⁻¹) and B_{30} (1740.81 cm⁻¹) were detected which indicated the C=O in carboxylic, ketone or aldehyde groups, suggested the presence of ester in all above samples. B_{10} did not show any peak in this range which indicated the absence of the ester group. Another vibrations of castor oil (1458.65 cm⁻¹), castor biodiesel (1458.07 cm⁻¹), B_{10} (1457.13 cm⁻¹). B_{20} (1458.10 cm⁻¹) and B_{30} (1458.92 cm⁻¹) indicated that the stretching vibration of -C-H (alkane) in mono, di and triglycerides glycerol in all samples. The peaks of all samples except B_{10} in the range of (1245 cm⁻¹ – 1033 cm⁻¹) indicated the vibrations of (C-O) and (C-O-C) group, while an additional peak was observed at (1031.87 cm⁻¹) indicated the O-CH₃ stretching presence in the biodiesel spectrum ([44]). B_{10} just showed the indication of the −CH₃ group and −C-H group. All this is because of a high volume of petro diesel hydrocarbons, the biodiesel character disappeared.
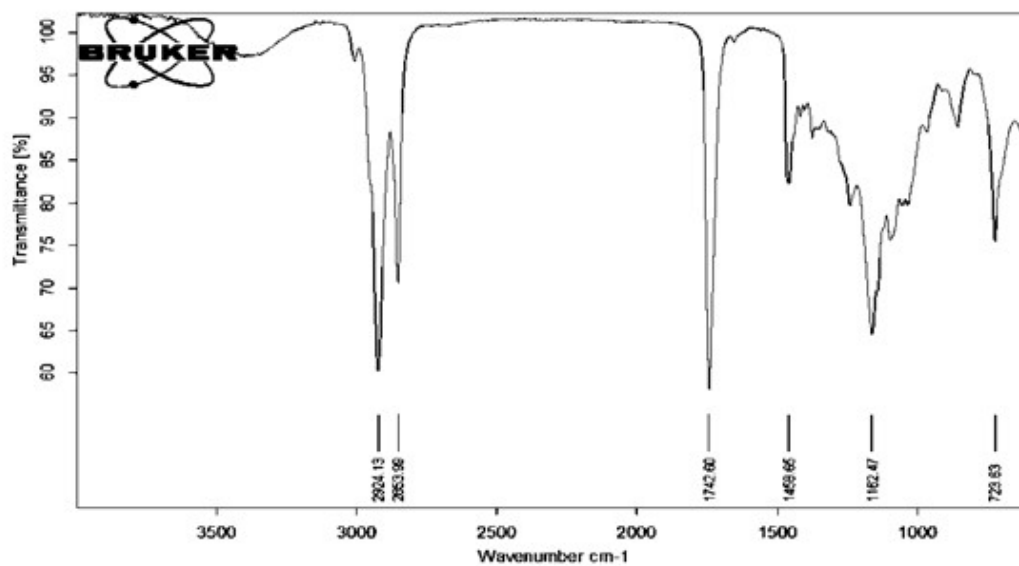
Figure 8a: FTIR spectrum of castor oil.
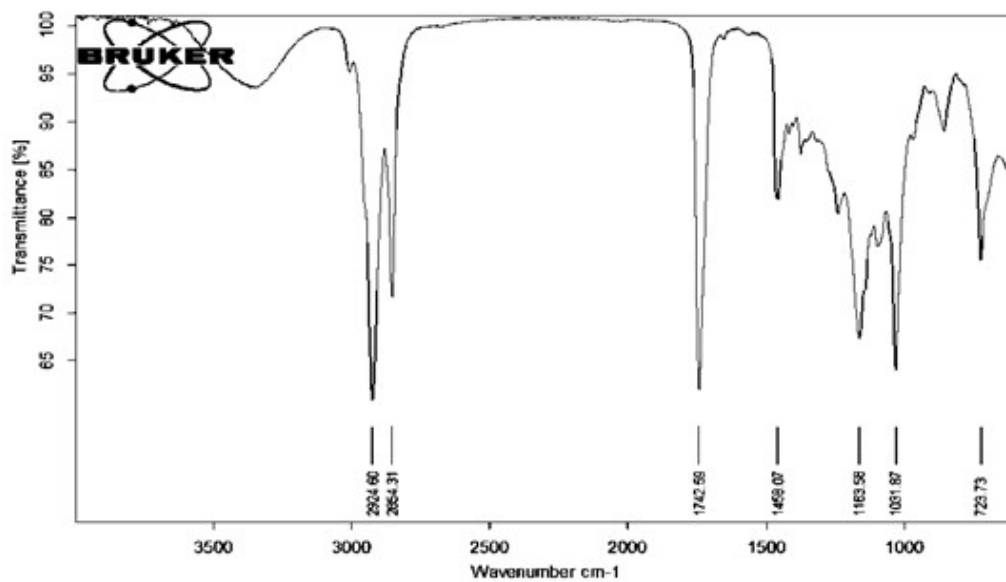
Figure 8b: FTIR spectrum of castor biodiesel.
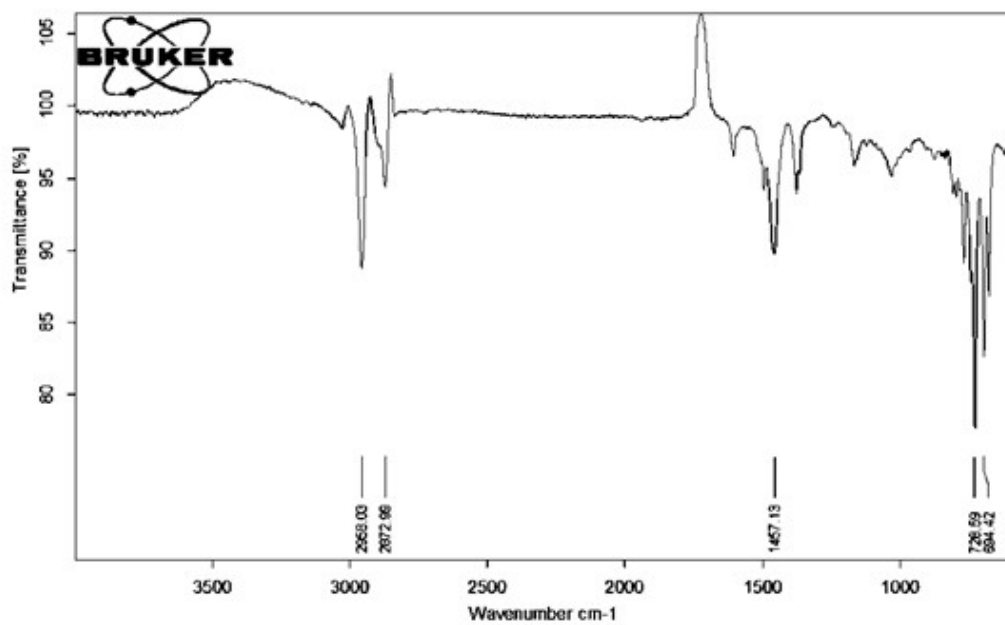
Figure 8c: FTIR spectrum of B_{10}.
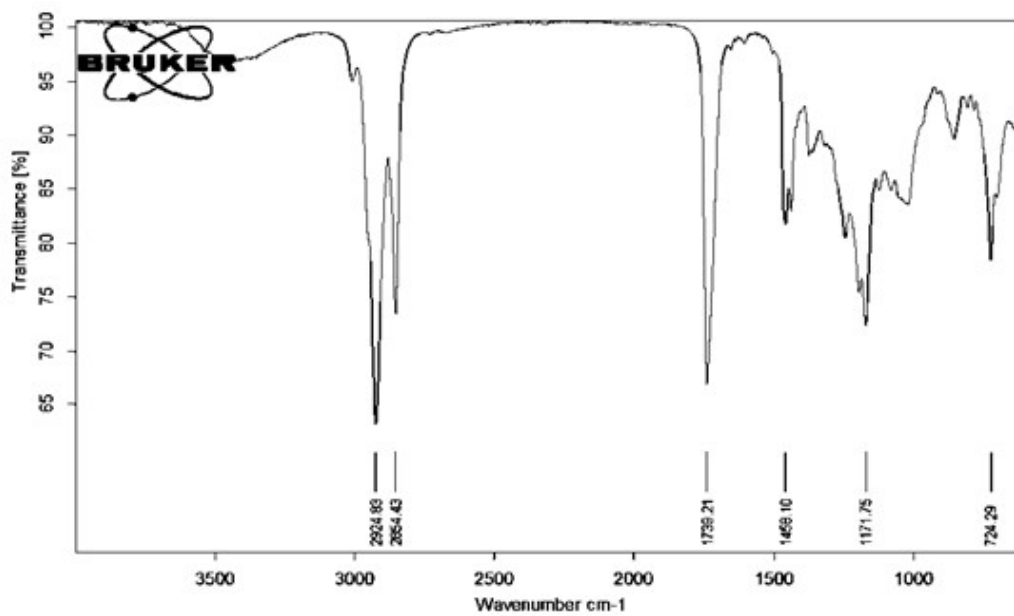
Figure 8d: FTIR spectrum of B_{20}.

Hussain SU et al. JOTCSA. 2022; 9(4): 1007-1022.

RESEARCH ARTICLE
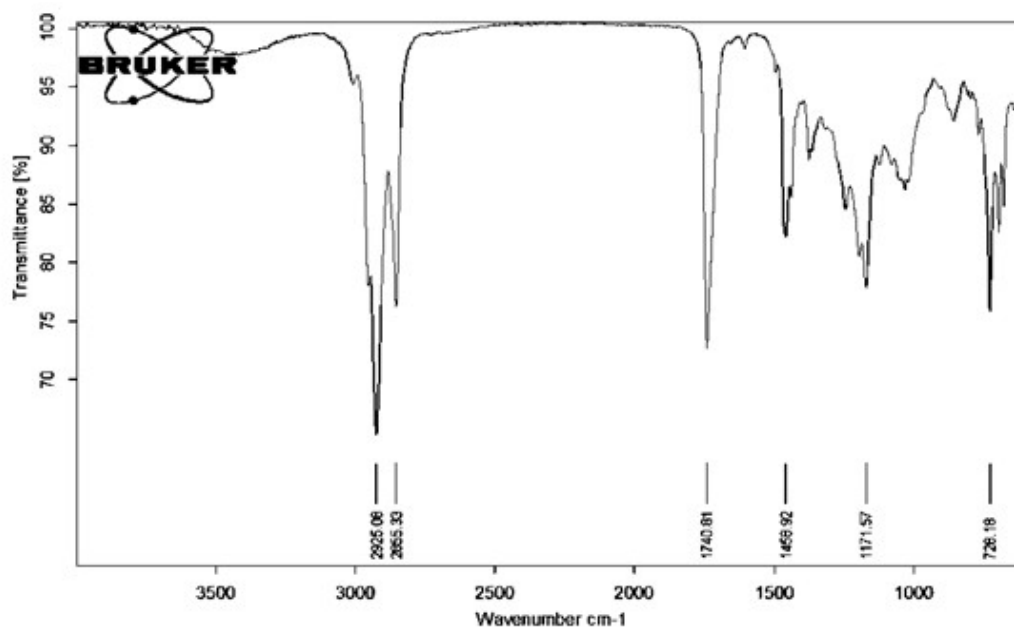
Figure 8e: FTIR spectrum of B_{30}.

CONCLUSION

The overall research work based on the biodiesel production from castor oil, optimization of castor oil for obtaining a maximum yield of castor biodiesel, physico-chemical and instrumental characterization of castor oil and its blends were carried out. The maximum yield of castor biodiesel was 80% by using 20 mL of castor oil, 7 mL of methanol, 0.32 mL of conc. H_2SO_4 catalyst, 65 ℃ of reaction temperature, 3 hours of reaction time and 600 rpm of stirring speed. Moisture content (0.171 w/w to 0.112 w/w), saponification value (186.35 mg of KOH/g to 86 mg of KOH/g), acid value (2.3002 mg of KOH/g to 1.0878 mg of KOH/g), free fatty acid value (1.1501 mg of KOH/g to 0.439 mg of KOH/g), ester value (184.0498 mg of KOH/g), specific gravity (0.959 g to 0.8850 g), viscosity (239 cSt to 17.21 cSt), refractive index (1.4782 nD to 1.4667 nD), density (0.9481 g to 0.8910 g) and boiling point (316 °C to 290 °C) decreased after transesterification. The iodine value of castor oil and its biodiesel remains the same (86.32 g of I_2/100 g). Peroxide value (15.4 meq/100 g to 20.66 meq/100 g), molecular weight (914.42 g to 1982.05 g) and higher heating value (40.494 MJ/kg to 44.479 MJ/kg) increased after esterification. From FTIR spectra, it is investigated that all samples contain an ester group except B_{10}. Actually, the high volume of petro-diesel in the blend B_{10}, Ester group disappeared but petro diesel properties enhanced. Finally blend samples B_{20} and B_{30} were recommended as diesel substitutes because the physicochemical properties of these samples were in favorable ranges. B_{10} showed a similar character to petro diesel due to the high volume of petro diesel the biodiesel character disappeared.

DISCLOSURE STATEMENT

No potential conflict of interest was reported by the authors.

REFERENCES

1. Faheem JB. Energy Crisis in Pakistan. IRA-JTE [Internet]. 2016 Apr 20 [cited 2022 Aug 4];3(1). Available from: <URL>.

2. Oyedepo SO. Energy and sustainable development in Nigeria: the way forward. Energ Sustain Soc [Internet]. 2012 Dec [cited 2022 Aug 4];2(1):15. Available from: <URL>.

3. Valasai GD, Uqaili MA, Memon HR, Samoo SR, Mirjat NH, Harijan K. Overcoming electricity crisis in Pakistan: A review of sustainable electricity options. Renewable and Sustainable Energy Reviews [Internet]. 2017 May [cited 2022 Aug 4];72:734–45. Available from: <URL>.

4. Javed MS, Raza R, Hassan I, Saeed R, Shaheen N, Iqbal J, et al. The energy crisis in Pakistan: A possible solution via biomass-based waste. Journal of Renewable and Sustainable Energy [Internet]. 2016 Jul [cited 2022 Aug 4];8(4):043102. Available from: <URL>.

5. Aftab S. Pakistan's energy crisis: causes, consequences and possible remedies. Expert Analysis, Norway. 2014;1–6.

6. Shrirame HY, Panwar NL, Bamniya BR. Bio Diesel from Castor Oil – A Green Energy Option. LCE [Internet]. 2011 [cited 2022 Aug 4];02(01):1–6. Available from: <URL>.

Hussain SU et al. JOTCSA. 2022; 9(4): 1007-1022.

RESEARCH ARTICLE

7. Khan MR, Gardezi SMAH. Production of Biodiesel in Pakistan. IJISME. 2014;1(10):819–48.

8. Ali T, Huang J, Yang J. An overview of status and policies on biofuels in Pakistan. International Journal of Economics and Research. 2012;3(1):69–76.

9. Demirbas A, Karslioglu S. Biodiesel Production Facilities from Vegetable Oils and Animal Fats. Energy Sources, Part A: Recovery, Utilization, and Environmental Effects [Internet]. 2007 Feb [cited 2022 Aug 4];29(2):133–41. Available from: <URL>.

10. Ijaz M, Bahtti KH, Anwar Z, Dogar UF, Irshad M. Production, optimization and quality assessment of biodiesel from Ricinus communis L. oil. Journal of Radiation Research and Applied Sciences [Internet]. 2016 Apr [cited 2022 Aug 4];9(2):180–4. Available from: <URL>.

11. Ingle S, Nandedkar V, Nagarhalli M. Prediction of Performance and Emission of Palm oil Biodiesel in diesel Engine. IOSR Journal of Mechanical and Civil Engineering (IOSR-JMCE). 2013;16:20.

12. Ganesan D, Rajendran A, Thangavelu V. An overview on the recent advances in the transesterification of vegetable oils for biodiesel production using chemical and biocatalysts. Rev Environ Sci Biotechnol [Internet]. 2009 Dec [cited 2022 Aug 4];8(4):367–94. Available from: <URL>.

13. Anjel H abdul, Abdulrahman RK. The Production of Green sustainable Fuel From Castor Oil. IJETT [Internet]. 2017 Mar 25 [cited 2022 Aug 4];45(7):322–4. Available from: <URL>.

14. Meher L, Vidyasagar D, Naik S. Technical aspects of biodiesel production by transesterification—a review. Renewable and Sustainable Energy Reviews [Internet]. 2006 Jun [cited 2022 Aug 4];10(3):248–68. Available from: <URL>.

15. Nakarmi A, Joshi S. A Study on Castor Oil and Its Conversion into Biodiesel by Transesterification Method. Nepal Journal of Science and Technology [Internet]. 2015 Feb 1 [cited 2022 Aug 4];15(1):45–52. Available from: <URL>.

16. Balat M. Potential alternatives to edible oils for biodiesel production – A review of current work. Energy Conversion and Management [Internet]. 2011 Feb [cited 2022 Aug 4];52(2):1479–92. Available from: <URL>.

17. Ferdous MK, Uddin MR, Uddin MR, Khan MR, Islam M. Optimization of Biodiesel Production From Bakul Oil. Journal of Chemical Engineering. 2017;29(1):14–8.

18. Fatah MA, Farag H, Ossman M. Production of biodiesel from non-edible oil and effect of blending with diesel on fuel properties. Engineering Science and Technology, an International Journal. 2012;2(4):583–91.

19. Demirbas A. Potential Resources of Non-edible Oils for Biodiesel. Energy Sources, Part B: Economics, Planning, and Policy [Internet]. 2009 Oct 30 [cited 2022 Aug 4];4(3):310–4. Available from: <URL>.

20. Keera ST, El Sabagh SM, Taman AR. Castor oil biodiesel production and optimization. Egyptian Journal of Petroleum [Internet]. 2018 Dec [cited 2022 Aug 4];27(4):979–84. Available from: <URL>.

21. Asmare M. Synthesis and Characterization of Biodiesel from Castor Bean as Alternative Fuel for Diesel Engine. AJEE [Internet]. 2014 [cited 2022 Aug 4];2(1):1. Available from: <URL>.

22. Atabani AE, Silitonga AS, Badruddin IA, Mahlia TMI, Masjuki HH, Mekhilef S. A comprehensive review on biodiesel as an alternative energy resource and its characteristics. Renewable and Sustainable Energy Reviews [Internet]. 2012 May [cited 2022 Aug 4];16(4):2070–93. Available from: <URL>.

23. Khaliq IH, Naeem B, Abbas Q, Khalid S. Chemical Composition and Oil Characterization of Some Accessions of Ricinus communis Seeds. J Bus Fin Aff [Internet]. 2017 [cited 2022 Aug 4];06(01). Available from: <URL>.

24. Conceição MM, Candeia RA, Silva FC, Bezerra AF, Fernandes VJ, Souza AG. Thermoanalytical characterization of castor oil biodiesel. Renewable and Sustainable Energy Reviews [Internet]. 2007 Jun [cited 2022 Aug 4];11(5):964–75. Available from: <URL>.

25. Banković-Ilić IB, Stamenković OS, Veljković VB. Biodiesel production from non-edible plant oils. Renewable and Sustainable Energy Reviews [Internet]. 2012 Aug [cited 2022 Aug 4];16(6):3621–47. Available from: <URL>.

26. Ramezani K, Rowshanzamir S, Eikani MH. Castor oil transesterification reaction: A kinetic study and optimization of parameters. Energy [Internet]. 2010 Oct [cited 2022 Aug 4];35(10):4142–8. Available from: <URL>.

27. Panwar NL, Shrirame HY, Bamniya BR. CO2 mitigation potential from biodiesel of castor seed oil in Indian context. Clean Techn Environ Policy [Internet]. 2010 Nov [cited 2022 Aug 4];12(5):579–82. Available from: <URL>.

28. Jeong GT, Park DH. Optimization of Biodiesel Production from Castor Oil Using Response Surface Methodology. Appl Biochem Biotechnol [Internet]. 2009 May [cited 2022 Aug 4];156(1–3):1–11. Available from: <URL>.

29. Thirugnanasambandham K, Shine K, Agatheeshwaren A, Sivakumar V. Biodiesel production from castor oil using potassium hydroxide as a catalyst: Simulation and validation. Energy Sources, Part A: Recovery, Utilization, and Environmental Effects [Internet]. 2016 Oct 1 [cited 2022 Aug 4];38(19):2898–905. Available from: <URL>.

30. Nurdin S, Rosnan NA, Ghazali NS, Gimbun J, Nour AH, Haron SF. Economical Biodiesel Fuel Synthesis from Castor Oil Using Mussel Shell-Base Catalyst (MS-BC). Energy Procedia [Internet]. 2015 Nov [cited 2022 Aug 4];79:576–83. Available from: <URL>.

31. Amalia S, Khalifah SN, Baroroh H, Muiz A, Rahmatullah A, Aini N, et al. Biodiesel production from castor oil using heterogeneous catalyst KOH/zeolite of natural zeolite Bandung Indonesia. In Malang, Indonesia; 2019 [cited 2022 Aug 4]. p. 080016. Available from: <URL>.

32. Ferdous K, Uddin MR, Mondal SK, Khan MR. Preparation of Biodiesel Using Sulfuric Acid as a Catalyst. In 2013.

33. Madankar CS, Pradhan S, Naik SN. Parametric study of reactive extraction of castor seed (Ricinus communis

L.) for methyl ester production and its potential use as bio lubricant. Industrial Crops and Products [Internet]. 2013 May [cited 2022 Aug 4];43:283–90. Available from: <URL>.

34. Karmakar B, Dhawane SH, Halder G. Optimization of biodiesel production from castor oil by Taguchi design. Journal of Environmental Chemical Engineering [Internet]. 2018 Apr [cited 2022 Aug 4];6(2):2684–95. Available from: <URL>.

35. Silitonga AS, Masjuki HH, Ong HC, Yusaf T, Kusumo F, Mahlia TMI. Synthesis and optimization of Hevea brasiliensis and Ricinus communis as feedstock for biodiesel production: A comparative study. Industrial Crops and Products [Internet]. 2016 Jul [cited 2022 Aug 4];85:274–86. Available from: <URL>.

36. Halder S, Dhawane SH, Kumar T, Halder G. Acid-catalyzed esterification of castor (Ricinus communis) oil: optimization through a central composite design approach. Biofuels [Internet]. 2015 Jul 4 [cited 2022 Aug 4];6(3–4):191–201. Available from: <URL>.

37. Keera ST, El Sabagh SM, Taman AR. Castor oil biodiesel production and optimization. Egyptian Journal of Petroleum [Internet]. 2018 Dec [cited 2022 Aug 4];27(4):979–84. Available from: <URL>.

38. Garba A, Abarshi MM, Shuaib MB, Sulaiman R. Optimization of biodiesel production from castor oil by response surface methodology. Nig J Biotechnol

[Internet]. 2017 Oct 30 [cited 2022 Aug 4];33(1):66. Available from: <URL>.

39. Hiwot T. Investigation of the Chemical Composition, Characterization and Determination of Energy Content for Renewable Energy Source (Biodiesel) Produced from Non-Edible Ethiopian Seeds' Particularly Castor Seed (Ricinus communis) Using Homogeneous Catalysis. ILCPA [Internet]. 2014 Aug [cited 2022 Aug 4];37:63–74. Available from: <URL>.

40. Deep A, Sandhu S, Chander S. Optimization of reaction parameters of Transesterification for Castor oil. Journal of Scientific & Industrial Research. 2017;76:115–8.

41. Rahman MS, Hossain MS, Moral MNA. Production of Biodiesel Fuels from Castor Oil Using H2SO4 as Catalyst. In Khulna, BANGLADESH: ICMIEE; 2016. p. 1–6.

42. Narwal SK, Saun NK, Dogra P, Chauhan G, Gupta R. Production and Characterization of Biodiesel Using Nonedible Castor Oil by Immobilized Lipase from Bacillus aerius. BioMed Research International [Internet]. 2015 [cited 2022 Aug 4];2015:1–6. Available from: <URL>.

43. Kılıç M, Uzun BB, Pütün E, Pütün AE. Optimization of biodiesel production from castor oil using factorial design. Fuel Processing Technology [Internet]. 2013 Jul [cited 2022 Aug 4];111:105–10. Available from: <URL>.

44. Elango RK, Sathiasivan K, Muthukumaran C, Thangavelu V, Rajesh M, Tamilarasan K. Transesterification of castor oil for biodiesel production: Process optimization and characterization. Microchemical Journal [Internet]. 2019 Mar [cited 2022 Aug 4];145:1162–8. Available from: <URL>.

Facile Preparation of Carbon Nanopillar Array

Nevin Taşaltın[1,2,3,4*], Selcan Karakuş[5*] Barbaros Akkurt[6*]

[1]Maltepe University, Dept. of Electrical and Electronics Eng., Istanbul, Turkey.
[2]Maltepe University, Dept. of Basic Sciences, Istanbul, Turkey.
[3]CONSENS Inc., Maltepe University Research Center, Technopark Istanbul, Turkey
[4]Maltepe University, Dept. of Renewable Energy Tech. and Management, Istanbul, Turkey.
[5]Istanbul University-Cerrahpasa, Department of Chemistry, Istanbul, Turkey.
[6]Istanbul Technical University, Department of Chemistry, Istanbul, Turkey.

Abstract: Carbon-based nanostructures have attracted extensive interest in obtaining advanced sensing electronic devices in environmental and biological monitoring applications as an alternative to conventional materials. Herein, the facile preparation, control of the growth, and artificial intelligence–based morphological information of the carbon nanopillar array in the Anodized Aluminum Oxide (AAO) template were investigated. A facile approach for controlling the growth of the nanostructure was proposed as a two-step anodization technique for AAO and Plasma Enhanced Chemical Vapor Deposition (PECVD) for carbon nanopillar array. It involved the competitive carbon deposition between the carbon nanopillars electrodeposited on the AAO template and at the bottom of the pores of AAO under vacuum conditions. The morphology and structure of the prepared carbon nanopillars were reported in detail. Hexagonally straight AAO nanotubes were approximately 65 nm in diameter and 360 nm in length, with 90 nm interpore distances. The AAO nanotube density is approximately 1.75×10^{14} cm^{-2}. Carbon nanopillars with a width of ~60 nm were used to create a low-dimensional nanostructure. This controllable preparation leads to the facile and impressive preparation of a free-standing carbon nanopillar array, especially for various chemical sensor applications.

INTRODUCTION

As nanomaterials offer unique mechanical, electrical, optical, and magnetic properties, they are drawing a tremendous amount of attention for many potential applications in nanodevices such as energy storage devices (batteries, supercapacitors, etc.), chemical sensors, and biological sensors (1–4). Nanomaterials are expected to play a key role in the devices by providing surface effects, small-size effects, and even quantum effects. Recent developments and current published research findings in the controlled growth of metal oxide nanowires have raised the need for the fabrication process of emerging high-performance and high-density nanoelectronic devices. A considerable amount of literature has been published on the fabrication of nanomaterials using different physical and chemical methods. More recently, the template-assisted method has been proposed to obtain next-generation functional nanomaterials with directional alignment and uniform size. In this sense, carbon nanostructures (nanotubes, nanopillars, nanofibers, etc.) attract attention as they have versatile redox-dependent properties and wide applications in catalysis, photochromism, electrochromism, energy storage, and chemical/bio detection (5–9).

There are several methods available for the preparation of carbon nanostructures (10–14) but up to date, only a few reports have been encountered describing the preparation of carbon nanopillars. Plasma processing techniques were used in the preparation of carbon nanomaterials. Wang *et al.*(15) prepared diamond nanocones by direct current plasma etching onto the diamond substrate in a methane/hydrogen atmosphere.

Kunuku *et al.* (16) developed carbon nanocones and nanopillars using the reactive ion etching technique to modify the diamond surface. Zou *et al.* (17) fabricated carbon nanopillar arrays by modifying the nanocrystalline diamond film surface with the same technique. Ren *et al.* (18) prepared carbon nanostructures by controlling ion flux and energy in an inductively coupled plasma enhanced chemical vapor deposition (PECVD) system. On the other hand, it has been suggested to use the Anodic Aluminum Oxide (AAO) template assisted technique as a more useful technique in the preparation of carbon nanopillars (19–24). In 2017, Liu *et al*. prepared a novel template-based catalyst (Ni/anodic anodic AAO) to control the growth of carbon nanotubes with a uniform particle size distribution (25).

Recently, researchers have shown an increased interest in the fabrication of carbon nanopillar arrays. In previous studies, carbon nanopillar arrays were prepared by ion beam irradiation into AAO template. Despite its fabrication leading to success, the preparation of carbon nanopillars has a number of problems, such as high production costs and a complex mass production process in use. Taking into account the previous studies, this study investigated the preparation of carbon nanopillars using a dual-role of physical vapor deposition (PVD) technique and an AAO template assisted technique for a simple and low-cost preparation without coating with plasma or ion beam radiation. In this study, the proposed design method with a two-step anodization approach was used and optimized experimental conditions (temperature, time, and pressure) for the preparation of the novel nano-sized carbon nanopillar array. The motivation of this study is to develop a novel carbon nanopillar array in the AAO template to overcome the limitations of the conventional process with low temperature and vacuum. Furthermore, the Al–aided SEM imaging–based characterization of the carbon nanopillar array in the AAO template was investigated to determine the morphology.

EXPERIMENTAL SECTION

In previous methods, there have been some serious disadvantages, such as high-temperature annealing (150 °C–900 °C), high deposition pressure (10^{-5}-10^{-4} Torr), time-consuming nature (2–12 h), and the use of expensive instrumentation and chemicals (8,24,26). However, in this study, we have used a simple two-step anodization technique to obtain the carbon nanopillar array (temperature (60 °C), deposition pressure (10^{-6} Torr), and time (2 h). This study discussed the fabrication of the carbon nanopillar array. Furthermore, the novelty of this study was the fabrication and AI-assisted characterization of the structure of the carbon nanopillar array.

In this study, experimental stages consisted of four steps. In the first step, high purity titanium and then high purity aluminum (≥ 99.999%) were

evaporated in a high vacuum environment on the Si wafer. In the second step, the Al film is anodized in a 0.3 M oxalic acid ($H_2C_2O_4$) solution at a constant applied voltage of 40 V in an environment of constant temperature of 5.0 °C for 10 min. Grown nanoporous AAO film was carried out to obtain AAO nanotubes by the wet etching process in a mixture of 6% (w/w) orthophosphoric acid (H_3PO_4) and 2% (w/w) dichromic acid ($H_2Cr_2O_7$) solution at 60 °C for 5 min. In the third step, prepared AAO films were anodized to obtain the AAO template under the same experimental conditions for 2 h and chemically etched away for 5 min in the second anodization. Finally, the carbon nanopillar array was prepared via PECVD of carbon on the AAO template under vacuum. The morphology of the prepared AAO template and carbon nanopillars were studied by Scanning Electron Microscopy (SEM) and Electron Diffraction Spectroscopy (EDS) (SEM, FEI QUANTA 450 model).

RESULTS AND DISCUSSION

The morphologies of the prepared AAO template and carbon coated AAO template were studied by SEM. Moreover, the chemical composition of the AAO template was studied by EDS. As shown in Figure 1, hexagonally straight AAO nanotubes prepared were approximately 65 nm in diameter and 360 nm in length, with 90 nm interpore distances. The AAO nanotube density was approximately 1.75×10^{14} cm^{-2}. The experimental results showed that it could be based on the electrodeposition on the AAO nanoporous template with controlled pore size and to integrate the nano-sized components due to the electrochemical system under vacuum conditions (27).

The morphologies of the prepared AAO template and carbon coated AAO template were studied by SEM. Moreover, the chemical composition of the AAO template was studied by EDS. As shown in Figure 1, hexagonally straight AAO nanotubes prepared were approximately 65 nm in diameter and 360 nm in length, with 90 nm interpore distances. The AAO nanotube density was approximately 1.75×10^{14} cm^{-2}. The experimental results showed that it could be based on the electrodeposition on the AAO nanoporous template with controlled pore size and to integrate the nano-sized components due to the electrochemical system under vacuum conditions (27).
The prepared carbon-coated alumina template was characterized to determine the surface property of the nanostructure by the SEM technique, which is one of the most used techniques (28) to determine surface topography and three-dimensional (3D) surface topography of nanostructures. Figure 2 shows the SEM images, Artificial Intelligence (AI) analysis, and EDS analysis of the carbon coated AAO template. As shown in Figure 2a-b, prepared vertically free-standing carbon nanopillars are roughly parallel to each other and vertically aligned to form an array with a high surface area as aimed. This can be explained by the higher packing density of nanostructures fabricated by AAO

template-assisted preparation. Furthermore, the AI approach was used to obtain high-quality SEM micrographs of structures. The SEM image (8-bit/mpl-viridis mode) of the prepared carbon nanopillars was improved using the ImageJ software. In Figure 2c-e, AI-assisted SEM image (8-bit), SEM image (8-bit/mpl-viridis), 3D surface topography, and color histogram of the prepared carbon nanopillars were provided. The AI-assisted SEM image (8-bit/mpl-viridis) of the prepared carbon nanopillars was able to improve the SEM image quality of structures and to eliminate background noise in noisy low-contrast SEM images. Furthermore, the 3D topography of the prepared carbon nanopillars was able to enhance the surface characteristics of SEM images. The color histogram of the prepared carbon nanopillars was a representation of the distribution of colors in the SEM image (8-bit/mpl-viridis) of the prepared nanostructure. The AI-assisted method was used to offer not only low feature dimension but also detectable the surface property of the nanostructure, implying that it could detect the distribution in the structure in an effective manner. For the digital SEM image of the nanostructure, the color histogram was used to determine the basic red- blue- green channel (RGB) algorithm of the SEM image. The mean color value of the image was calculated using the distance values according to the minimum and maximum distance values. We compared the color histogram-based mean color values of the AI-assisted SEM image (8-bit/mpl-viridis) of the carbon coated AAO surface and prepared carbon nanopillars. Consequently, the obtained samples were highly uniform, nano-sized, and wire-shaped. Carbon nanopillars were obtained at approximately 60 nm (width). According to the EDS spectra from the nanopillar surface, the strong characteristic absorption peak of C was observed (Figure 2f). These EDS values were consistent with previous studies for carbon nanostructures (28,29).
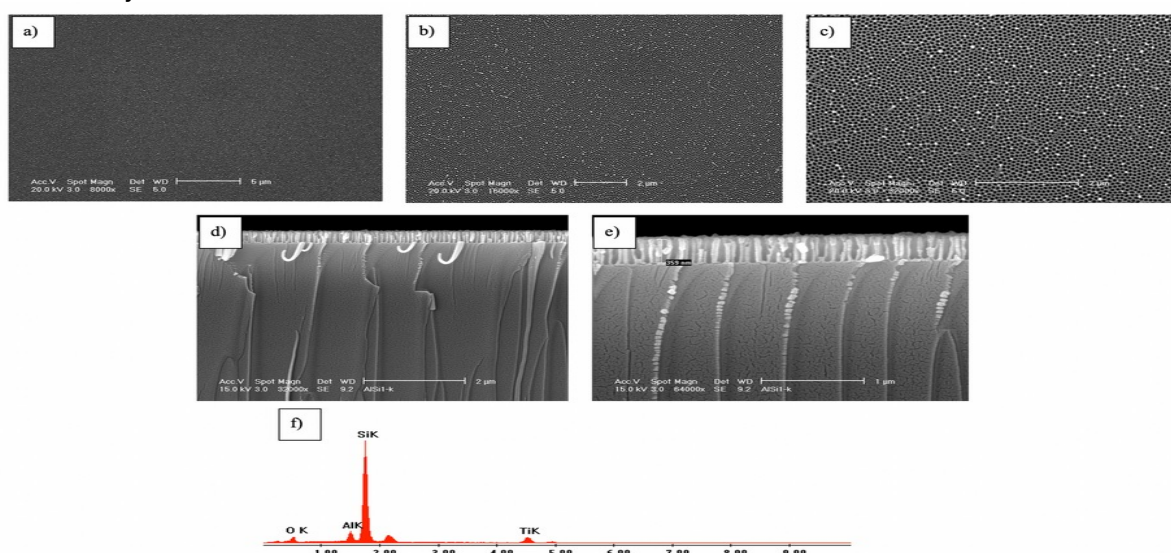
Figure 1: (a-b-c) SEM images from the surface (with different magnifications), **(d-e)** SEM images from the cross-section (with different magnifications), **(f)** EDS analysis of the prepared AAO template on Si.
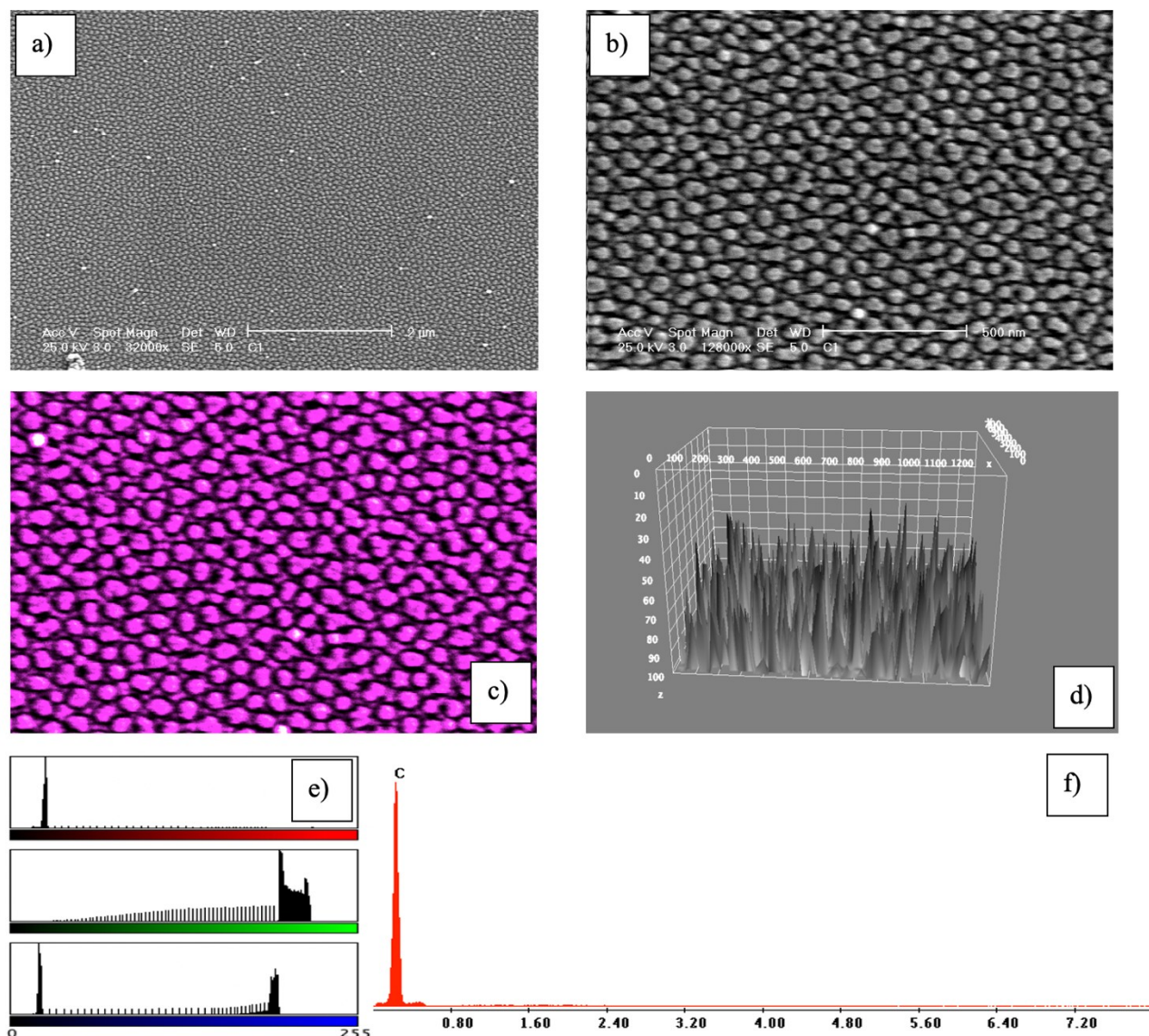
Figure 2: (a) SEM images at 32.,000x, **(b)** SEM images at 128,000x, **(c)** SEM image (8-bit/magenta), **(d)** 3D surface topography, **(e)** color histogram, and **(f)** EDS analysis of the carbon nanopillars.

In this study, AAO template-assisted preparation of carbon nanopillars provided some remarkable advantages over the other methods. The carbon nanopillar array was prepared under mild conditions rather than requiring high temperatures, high vacuum, or expensive instrumentation. The carbon nanopillar array was prepared with controllable morphology due to the shape of the nanopores of the AAO template. The width of the carbon nanopillar can be tuned via the nanopore size of the AAO template in future studies. The results reveal that AAO template assisted preparation of carbon nanopillar array is one of the most prominent method.

CONCLUSION

The carbon nanopillar array was prepared by the AAO template-assisted technique. Hexagonally straight AAO nanotubes were approximately 65 nm in diameter and 360 nm in length, with 90 nm interpore distances. The AAO nanotube density is approximately 1.75×10^{14} cm^{-2}. Carbon nanopillars were obtained at approximately 60 nm (width). This controllable preparation leads to the facile and impressive preparation of free standing carbon nanopillar array, especially for various chemical sensor applications.

CONFLICT OF INTEREST

The authors declare that they have no conflict of interest.

Taşaltın N et al. JOTCSA. 2022; 9(4): 1023-1028.

RESEARCH ARTICLE

AVAILABILITY OF DATA

The authors confirm that the data supporting the findings of this study are available within the article. Raw data that support the findings of this study are available from the corresponding author, upon reasonable request.

REFERENCES

1. Zheng G, Lu W, Jin S, Lieber CM. Synthesis and Fabrication of High-Performance n-Type Silicon Nanowire Transistors. Adv Mater [Internet]. 2004 Nov 4 [cited 2022 Sep 9];16(21):1890–3. Available from: <URL>.

2. Snow ES, Perkins FK, Houser EJ, Badescu SC, Reinecke TL. Chemical Detection with a Single-Walled Carbon Nanotube Capacitor. Science [Internet]. 2005 Mar 25 [cited 2022 Sep 9];307(5717):1942–5. Available from: <URL>.

3. Huo B, Hu Y, Gao Z, Li G. Recent advances on functional nucleic acid-based biosensors for detection of food contaminants. Talanta [Internet]. 2021 Jan [cited 2022 Sep 9];222:121565. Available from: <URL>.

4. Bai W, Kuang T, Chitrakar C, Yang R, Li S, Zhu D, et al. Patchable micro/nanodevices interacting with skin. Biosensors and Bioelectronics [Internet]. 2018 Dec [cited 2022 Sep 9];122:189–204. Available from: <URL>.

5. Wei BQ, Vajtai R, Ajayan PM. Reliability and current carrying capacity of carbon nanotubes. Appl Phys Lett [Internet]. 2001 Aug 20 [cited 2022 Sep 9];79(8):1172–4. Available from: <URL>.

6. Liu J, Wang X, Peng Q, Li Y. Vanadium Pentoxide Nanobelts: Highly Selective and Stable Ethanol Sensor Materials. Adv Mater [Internet]. 2005 Mar 22 [cited 2022 Sep 9];17(6):764–7. Available from: <URL>.

7. Zhang D, Liang R, Yang H, Song Y, Yang L, Zhang C, et al. Formation of helical polyphenyl nanostructures on carbon nanotubes. Inorganic Chemistry Communications [Internet]. 2021 Apr [cited 2022 Sep 9];126:108491. Available from: <URL>.

8. Sai Krishna K, Pavan Kumar BVVS, Eswaramoorthy M. Nanopillar arrays of amorphous carbon nitride. Chemical Physics Letters [Internet]. 2011 Jul [cited 2022 Sep 9];511(1–3):87–90. Available from: <URL>.

9. Tao B, Yang W, Zhou M, Qiu L, Lu S, Wang X, et al. Designing a carbon nanofiber-encapsulated iron carbide anode and nickel-cobalt sulfide-decorated carbon nanofiber cathode for high-performance supercapacitors. Journal of Colloid and Interface Science [Internet]. 2022 Sep [cited 2022 Sep 9];621:139–48. Available from: <URL>.

10. Reddy BR, Ashok I, Vinu R. Preparation of carbon nanostructures from medium and high ash Indian coals via microwave-assisted pyrolysis. Advanced Powder Technology [Internet]. 2020 Mar [cited 2022 Sep 9];31(3):1229–40. Available from: <URL>.

11. Wang D, Zhao B, Jiang Y, Hu P, Gao D, Zhang H. Self-etching preparation of yolk-shell Ag@carbon nanostructures for highly effective reduction of 4-nitrophenol. Catalysis Communications [Internet]. 2017 Dec [cited 2022 Sep 9];102:114–7. Available from: <URL>.

12. Kumar R, Joanni E, Sahoo S, Shim JJ, Tan WK, Matsuda A, et al. An overview of recent progress in nanostructured carbon-based supercapacitor electrodes: From zero to bi-dimensional materials. Carbon [Internet]. 2022 Jun [cited 2022 Sep 9];193:298–338. Available from: <URL>.

13. Li C, Zhang X, Wang K, Su F, Chen CM, Liu F, et al. Recent advances in carbon nanostructures prepared from carbon dioxide for high-performance supercapacitors. Journal of Energy Chemistry [Internet]. 2021 Mar [cited 2022 Sep 9];54:352–67. Available from: <URL>.

14. Wang Q, Tian Z, Li Y, Tian S, Li Y, Ren S, et al. General fabrication of ordered nanocone arrays by one-step selective plasma etching. Nanotechnology [Internet]. 2014 Mar 21 [cited 2022 Sep 9];25(11):115301. Available from: <URL>.

15. Kunuku S, Sankaran KJ, Tsai CY, Chang WH, Tai NH, Leou KC, et al. Investigations on Diamond Nanostructuring of Different Morphologies by the Reactive-Ion Etching Process and Their Potential Applications. ACS Appl Mater Interfaces [Internet]. 2013 Aug 14 [cited 2022 Sep 9];5(15):7439–49. Available from: <URL>.

16. Zou YS, Ma KL, Zhang WJ, Ye Q, Yao ZQ, Chong YM, et al. Fabrication of diamond nanocones and nanowhiskers by bias-assisted plasma etching. Diamond and Related Materials [Internet]. 2007 Apr [cited 2022 Sep 9];16(4–7):1208–12. Available from: <URL>.

17. Ren Y, Xu S, Rider AE, Ostrikov K (Ken). Made-to-order nanocarbons through deterministic plasma nanotechnology. Nanoscale [Internet]. 2011 [cited 2022 Sep 9];3(2):731–40. Available from: <URL>.

18. Chen TM, Pan FM, Hung JY, Chang L, Wu SC, Chen CF. Amorphous Carbon Coated Silicon Nanotips Fabricated by MPCVD Using Anodic Aluminum Oxide as the Template. J Electrochem Soc [Internet]. 2007 [cited 2022 Sep 9];154(4):D215. Available from: <URL>.

19. Rahman S, Yang H. Nanopillar Arrays of Glassy Carbon by Anodic Aluminum Oxide Nanoporous Templates. Nano Lett [Internet]. 2003 Apr 1 [cited 2022 Sep 9];3(4):439–42. Available from: <URL>.

20. Hu Y, Wang X, Zhang M, Wang S, Li S, Chen G. A Hierarchical Anodic Aluminum Oxide Template. Nano Lett [Internet]. 2021 Jan 13 [cited 2022 Sep 9];21(1):250–7. Available from: <URL>.

21. Nakagawa M, Nakaya A, Hoshikawa Y, Ito S, Hiroshiba N, Kyotani T. Size-Dependent Filling Behavior of UV-Curable Di(meth)acrylate Resins into Carbon-Coated Anodic Aluminum Oxide Pores of around 20 nm. ACS Appl Mater Interfaces [Internet]. 2016 Nov 9 [cited 2022 Sep 9];8(44):30628–34. Available from: <URL>.

22. Sohn JI, Kim YS, Nam C, Cho BK, Seong TY, Lee S. Fabrication of high-density arrays of individually isolated nanocapacitors using anodic aluminum oxide templates and carbon nanotubes. Appl Phys Lett [Internet]. 2005 Sep 19 [cited 2022 Sep 9];87(12):123115. Available from: <URL>.

23. Xing H, Zhiyuan L, Kai W, Yi L. Fabrication of three dimensional interconnected porous carbons from branched anodic aluminum oxide template. Electrochemistry Communications [Internet]. 2011 Oct [cited 2022 Sep 9];13(10):1082–5. Available from: <URL>.

24. Liu X, Shen B, Yuan P, Patel D, Wu C. Production of carbon nanotubes (CNTs) from thermochemical conversion of waste plastics using Ni/anodic aluminum oxide (AAO) template catalyst. Energy Procedia [Internet]. 2017 Dec [cited 2022 Sep 9];142:525–30. Available from: <URL>.

25. Zhang PJ, Chen JT, Zhuo RF, Xu L, Lu QH, Ji X, et al. Carbon nanodot arrays grown as replicas of specially widened anodic aluminum oxide pore arrays. Applied Surface Science [Internet]. 2009 Feb [cited 2022 Sep 9];255(8):4456–60. Available from: <URL>.

26. Bertero E, Manzano CV, Bürki G, Philippe L. Stainless steel-like FeCrNi nanostructures via electrodeposition into AAO templates using a mixed-solvent Cr(III)-based electrolyte. Materials & Design [Internet]. 2020 May [cited 2022 Sep 9];190:108559. Available from: <URL>.

27. Vu HT, Lim J. Effects of country and individual factors on public acceptance of artificial intelligence and robotics technologies: a multilevel SEM analysis of 28-country survey data. Behaviour & Information Technology [Internet]. 2022 May 19 [cited 2022 Sep 9];41(7):1515–28. Available from: <URL>.

28. Yeganeh Ghotbi M, Javanmard A, Soleimani H. Layered nanoreactor assisted to produce B-doped and P-doped 3D carbon nanostructures for supercapacitor electrodes. Journal of Energy Storage [Internet]. 2021 Dec [cited 2022 Sep 9];44:103514. Available from: <URL>.

Anti-Inflammatory Effect of Coxibs and their Compositions with Caffeine on the Level of Conjugated Dienes in the Formalin-Induced Edema Model

Ganna Syrova (iD), **Valentina Petiunina** (iD), **Olena Savelieva** (iD), **Tetyana Tishakova** (iD), **and Larysa Lukianova**[*](iD)

Kharkiv National Medical University, Department of Medical and Bioorganic chemistry, Kharkiv, Ukraine

Abstract: The development of novel pharmaceutical compositions, which are effective in the treatment of different inflammatory diseases and have a minimum number of side effects is very relevant. The aim of the present study was biochemical confirmation of anti-inflammatory activity of new pharmaceutical compositions comprising coxibs and caffeine. The level of conjugated dienes as primary products of lipid peroxidation has been evaluated in the plasma of rats at the acute inflammation caused by formalin. The white male rats of WAG line were used. The content of conjugated dienes was determined by spectrophotometric method. It was shown that combinations of caffeine and coxibs showed statistical significant decrease in the content of conjugated dienes in the rats' blood plasma. Caffeine enriched anti-inflammatory action of coxibs effectively.

INTRODUCTION

Continuous development of medical science causes the necessity of search for new medicinal products and carrying out the research for expanding the therapeutic potentialities of already known pharmaceutical preparations.

Nowadays new scientific research has been performing for one of the important groups of medicinal products – non-steroidal anti-inflammatory drugs (NSAIDs). NSAIDs have received great deal of attention compared to traditional analgesics because of their anti-inflammatory, pain-relieving and antipyretic effects. These medications are highly effective for treating musculoskeletal disorders (like osteoarthritis, rheumatoid arthritis) accompanied with pain syndrome. Application of these medicinal products improves quality of life (1-5). However, the usage of NSAIDs results in the development of serious gastrointestinal, liver and cardiovascular side effects (6-8).

That's why, a new perspective for scientists for improving efficiency, reduce toxicity and side effects of NSAIDs is to create combinations of medicinal products. Such investigations have been performed by the scientists of medical and bioorganic chemistry of Kharkiv National Medical University. Researchers of the department have studied antiexudative, analgesic and antipyretic actions of pharmaceutical compositions containing 2,4-dichlorobenzoic acid, caffeine (9), known NSAIDs and non-narcotic analgesics such as paracetamol, diclofenac, ibuprofen, meloxicam with adjuvant caffeine.

The results showed that caffeine potentiates antiexudative and analgesic effect of investigated

Syrova G et al. JOTCSA. 2022; 9(4): 1029-1034.

RESEARCH ARTICLE

NSAIDs (10). Adjuvanticity of caffeine towards NSAIDs and non-narcotic analgesics is explained with its positive influence on bioavailability (11), as well as its structural similarity with adenosine that contributes to neurochemical blocking of "purine" receptors in the brain with caffeine (12).

Today, we have been paying attention on anti-inflammatory, analgesic and antipyretic effects of newer NSAIDs – coxibs (celecoxib and rofecoxib) (8, 9). It is known that these medicinal products belong to highly-selective inhibitor of cyclooxygenase-2 and their pharmacological action is based on the inhibition of the biosynthesis of prostaglandins – moderator of pain and inflammation. As cyclooxygenase-2 is a main trigger mechanism of inflammation and neoangiogenesis, these phenomena accompany a wide range of pathological conditions and diseases. That's why therapeutic properties of celecoxib have been studied in all fields of medicine and it found a wide application (13). Celecoxib is used to treat acute pathologies of musculoskeletal system, during surgery and postrheumatic syndrome (14) or as urgent analgesic (15, 16).

It has been proven that celecoxib is an efficacious and safe at the treatment of psychotic symptoms, particularly in first-episode schizophrenia (17, 18). Cyclooxygenase-2 inhibitors have demonstrated potential therapeutic effects in tumors (19). Celecoxib is one of the few drugs that can be taken for a long time, due to its high tolerability and low risk of gastrointestinal and cardio-vascular adverse effects.

Rofecoxib is widely used in clinical practice in Ukraine (20). It demonstrates pharmacological effect similar to celecoxib (21). This medication is used as analgesic and antipyretic for treating rheumatoid conditions, primary dysmenorrhea (22) and, moreover, rofecoxib exhibits chondroprotective properties.

We selected coxibs as objects of study because there are no data in the literature on the presence of combination medicinal products containing celecoxib and rofecoxib.

Inflammation is a protective reaction of the body against injury or infection. It is a known fact that in the first day's inflammation leads to the changes in blood lipids and to the distress of liver protein synthesis (23, 24). Acute inflammation is marked by the changes in the level of markers of lipid peroxidation in the form of the primary products – conjugated dienes (25, 26).

Conjugated dienes are the primary products of lipid peroxidation and classified as toxic metabolites that impair lipoproteins, enzymes and nucleic acids. Further products of lipid peroxidation are aldehyde and ketones (malondialdehyde and others) that play an important role in the synthesis

of prostaglandins, progesterone and other steroids. Lipid peroxidation can alter vital membrane protein structure and function; it could lead to cellular dysfunction and widespread tissue damage (27).

Therefore, the aim of our investigation was to evaluate the effect of coxibs (celecoxib and rofecoxib) and their composition with caffeine on the process of lipid peroxidation in the form of conjugated dienes by utilizing formalin-induced edema model in experimental animals.

MATERIALS AND METHODS

General
Biochemical investigations of rofecoxib (*4*-(*4'*-methylsulfonylphenyl)-3-phenyl-2-(5H)-furanone), celecoxib (*4-[5-(4-methylphenyl)-3-(*trifluoromethyl*)*-1H-pyrazol-1-yl]benzenesulfonamide) and their compositions with caffeine (1,3,7-trimethylxynthine) were performed to estimate their anti-inflammatory action in comparison to reference drug – sodium diclofenac (28, 29).

Anti-inflammatory action of abovementioned coxibs was studied using the animal experimentation and formalin-induced edema model. The white male rats of WAG line (weighing 180-200 g) were divided into eight equal groups (n = 6). The animals of group 1 received 3% starch mucus (2 mL/200 g body weight of the rat) (Control). Group 2 received subplantar injection of 2% freshly prepared formalin and was treated intragastrically with 3% starch mucus. Groups 3-8 received subplantar injection of 2% formalin and investigated medications, in particular: Group 3: rats were intragastrically injected with (*4*-(*4'*-methylsulfonylphenyl)-3-phenyl-2-(5H)-furanone) (rofecoxib) at a dose of 1.5 mg/kg in 3% starch mucus. Group 4: rats were intragastrically injected with (*4-[5-(4-methylphenyl)-3-(*trifluoromethyl*)*-1H-pyrazol-1-yl]benzenesulfonamide) (celecoxib) at a dose of 5 mg/kg in 3% starch mucus. Group 5: rats were intragastrically injected with caffeine at a dose of 5 mg/kg in 3% starch mucus. Group 6: rats were intragastrically injected with pharmaceutical composition of rofecoxib with caffeine at the same dose. Group 7: rats were intragastrically injected with pharmaceutical composition of celecoxib with caffeine at the same dose. Group 8: rats were intragastrically injected with reference drug – sodium diclofenac at a dose of 8 mg/kg in 3% starch mucus. The formalin-induced edema was produced by subplantar injection of 2% freshly prepared formalin in the right hind paw.

In 4 hours after the injection of formalin acute inflammation was produced in the right hind paw of each rat. Animals of groups 3-8 were treated by investigated medicinal products and their compositions with caffeine at 3 hours after the formalin injection taking into consideration their pharmacokinetics and pharmacodynamics. One

Syrova G et al. JOTCSA. 2022; 9(4): 1029-1034.

RESEARCH ARTICLE

hour after the administration of medicinal products animals were decapitated under ether anesthesia (30). Samples of blood were collected. 1% solution of heparin was used as an anticoagulant. The blood plasma was separated by centrifugation at 1500 rpm/min for 15 minutes and used as biomaterial.

The animals were kept in the vivarium of Kharkiv National Medical University according to the rules of humane treatment of laboratory animals. The studies on animals were performed as per the principles of the "European Convention for the Protection of Vertebrate Animals Used for Experimental and other Scientific Purposes" (31) and the Decree of the First National Congress on Bioethics (32).

Anti-inflammatory action assay
Anti-inflammatory action of investigated substances was studied by the level of conjugated dienes as inflammatory markers. The content of conjugated dienes was determined by spectrophotometric method at 233 nm using the spectrophotometer SF-46. The conjugated diene moiety is a strong chromophore that can be detected spectrophotometrically. When present in fatty acids they show a characteristic absorption in the ultra violet region at around 233 nm (33).

The principle of method. Heptane-isopropanol mixture is used to extract plasma lipids. Because heptane is very non polar, it primarily extracts neutral lipids. Phospholipids have some charges and typically extracted by isopropanol. Because of these differences in charge, extraction of total lipids typically uses mixture of solvents and it becomes possible to estimate level of the lipid peroxidation product in different classes of lipids. Lipid extracts of every phase are analyzed by spectrophotometric method at about 233 nm.

Procedure of determination. 0.5 mL of blood plasma was mixed with 5 mL of heptane-isopropanol mixture at a ratio of 1:1 (v/v), agitated manually for 15 minutes to extract lipids and then centrifuged at 5000 rpm/min for 10 min at 20 °C. The aqueous phase was collected and subjected to two subsequent identical extraction steps. Such procedure is necessary to get optimal values of absorbance in both phases of extract. Then 2 mL of 1 M hydrochloric acid solution was added to lipid extracts to separate and to remove nonlipid impurities. The mixture was then centrifuged at 12000 rpm/min for 15 min at 4 °C. The upper layer (heptane phase) was collected into a dry test tube. Water-alcohol phase was mixed with 1 g of NaCl to separate isopropanol from its mixture with water by a salting out method. After the separation from water isopropyl alcohol was transferred into the dry test tube containing heptane phase. A blank solution was prepared according to the same procedure described above. 0.5 mL of 0.1% Ethylenediaminetetraacetic acid solution in 0.9% sodium chloride solution was used instead of

plasma. Organic phase from a result of extraction was analyzed by spectrophotometer SF-46 at 233 nm. The content of lipid peroxidation products was calculated using the following formula:

$$\text{Conjugated dienes} = \frac{(A_0 - A_x) \times 15}{0.022} \frac{\mu mol}{L} \quad (1)$$

where A_0 is the absorbance of blank solution, and A_x is the absorbance of investigated organic phase; and 0.022 is the extinction coefficient of conjugated dienes, and 15 is the dilution coefficient of plasma in organic extract.

Statistical processing of the obtained data was performed using application packages Microsoft® Excel 2000 (Microsoft®) and STATISTICA® for Windows 6.0 (StatSoft Inc.). Statistical analysis was carried out with one-way analysis of variance, ANOVA. Data at $P < 0.05$ were considered statistically significant.

RESULTS AND DISCUSSION

It is known that exposure to pathogenic factors leads to a disturbance in the pro-oxidant to antioxidant balance, which is accompanied by the increase in intensity of free radical oxidation of membrane phospholipids (18).

The results of biochemical investigations of anti-inflammatory action of coxibs and their compositions with caffeine on the level of conjugated dienes in rats' blood plasma are presented in Figure 1.

Conducted biochemical research demonstrates that level of conjugated dienes in the blood plasma increased 4.5 times in the Group 2 (Formalin-induced edema) compared to the Control (Group 1). Administration of investigated coxibs showed statistically significant decrease in conjugated dienes content in the plasma of rats. It is worth noting, that rofecoxib was more efficacious than celecoxib.

Mono-administration of rofecoxib reduced the conjugated dienes level in rats' blood plasma by 2 times as compared with formalin-induced edema (Group 2). And in return, mono-administration of celecoxib decreased the conjugated dienes content by nearly 1.5 times.

Obtained data statistically significant differ from Control (Group 1) and from the reference drug – sodium diclofenac (Group 8). Administration of caffeine (Group 5) decreased level of conjugated dienes in rats' plasma by 1.8 times compared to formalin-induced edema that is statistically significant different from the second group of animals (formalin-induced edema). This favors efficiency of caffeine for reduction of lipid peroxidation primary products in the plasma of rats

under conditions of formalin-induced edema. Therefore, according the ability to decrease content of conjugated dienes in rats' blood plasma, coxibs and caffeine can be arranged in the following row: rofecoxib ˃ caffeine ˃ celecoxib.
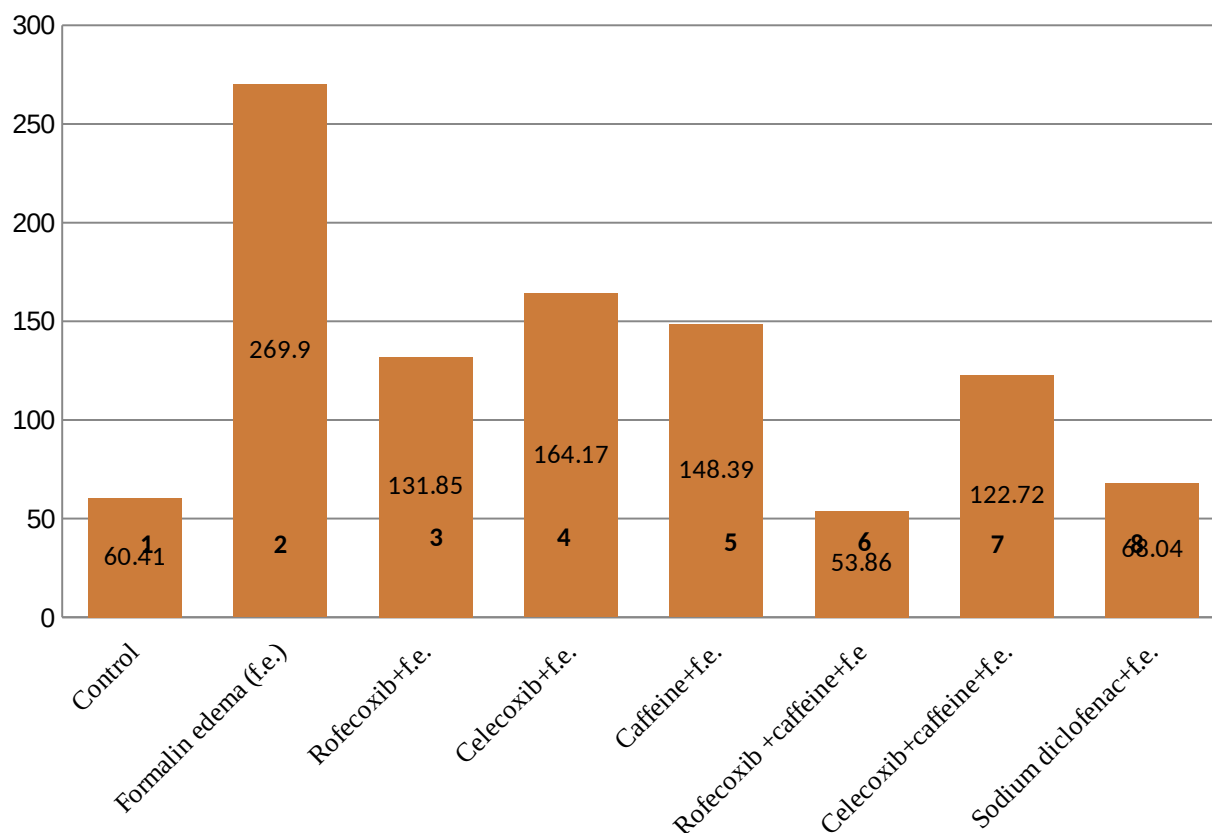
Figure 1: Effect of coxibs and their pharmaceutical composition with caffeine on the level of conjugated dienes in rats' blood plasma under conditions of formalin-induced edema. X axis shows the groups and Y axis shows the concentration of conjugated dienes in µmol/L.

Note 1. (mean ± SEM) * – the difference is significant compared to Control, $p < 0.05$;
Note 2. (mean ± SEM) ** – the difference is significant compared to formalin-induced edema, $p < 0.05$;
Note 3. (mean ± SEM) *** – the difference is significant compared to rofecoxib, $p < 0.05$;
Note 4. (mean ± SEM) **** – the difference is significant compared to celecoxib, $p < 0.05$;
Note 5. (mean ± SEM) ***** – the difference is significant compared to caffeine, $p < 0.05$.
Note 6. (mean ± SEM) ****** – the difference is significant compared to sodium diclofenac, $p < 0.05$.

Combination of adjuvant (caffeine) with coxibs (Groups 6 and 7) promotes the decrease in conjugated dienes level in the plasma of rats that was statistically significant compared to formalin-induced edema as well as compared to the mono-administration of coxibs. Pharmaceutical composition of rofecoxib with caffeine proved to be more efficient than reference drug (Group 8). Statistically significant differences between the results obtained in experimental group (Group 6) and intact control (Group 1) was not observed. It means that caffeine potentiates anti-inflammatory action of rofecoxib effectively.

Combination of caffeine with celecoxib (Group 7) resulted in significantly lower decrease of CD content. Pharmaceutical composition of celecoxib

and caffeine (Group 7) exhibited statistically significant decrease in the level of conjugated dienes in the rats' blood plasma compared to formalin-induced edema (Group 2). However, obtained results were not statistically significant in comparison to the mono-administration of celecoxib (Group 4) but they showed statistically significant difference compared to reference drug (Group 8) and Control. Hence, according the anti-inflammatory activity proposed pharmaceutical compositions can be arranged in the following row: rofecoxib+ caffeine ˃ sodium diclofenac ˃ celecoxib + caffeine.

It is clear that proposed new pharmaceutical composition of caffeine and rofecoxib more effectively suppress the edema produced by

formalin and became the leader of biochemical studies.

CONCLUSION

Based on the results obtained from the study it can be concluded that:
1. Rofecoxib, celecoxib, caffeine and their compositions exhibit anti-inflammatory activity against formalin-induced edema with different efficiency. Composition of rofecoxib and caffeine provided greater overall anti-inflammatory activity than sodium diclofenac but composition of celecoxib and caffeine has effect that is comparable to the reference drug. It was shown that monopreparations and caffeine act worse than the novel proposed compositions.

2. Caffeine potentiates anti-inflammatory action of investigated coxibs in the formalin-induced edema model. The level of conjugated dienes reduced as compared with the value in control group after administration of pharmaceutical composition containing rofecoxib and caffeine. At the same time, composition of celecoxib and caffeine did not significantly affect the formalin-induced edema.

3. The leader in biochemical studies is a two-component composition of rofecoxib and caffeine, which reduces the level of the LOP primary products – conjugated dienes in rats' blood plasma to the level of control group and proved to be better than the reference drug.

CONFLICT OF INTEREST

ACKNOWLEDGMENTS

REFERENCES

1. Omoigui S. The biochemical origin of pain: The origin of all pain is inflammation and the inflammatory response. Part 2 of 3 – Inflammatory profile of pain syndromes. Medical Hypotheses [Internet]. 2007 Jan [cited 2022 Sep 11];69(6):1169–78. Available from: <URL>.

2. Aydede M. Defending the IASP Definition of Pain. The Monist [Internet]. 2017 Oct 1 [cited 2022 Sep 11];100(4):439–64. Available from: <URL>.

3. Jain P, Pandey R, Shukla SS. Inflammation: Natural Resources and Its Applications [Internet]. New Delhi: Springer India; 2015 [cited 2022 Sep 11]. (SpringerBriefs in Immunology). Available from: <URL>.

4. Nasonov E, Lazebnik L, Belenkov Y. The use of non-steroidal anti-inflammatory drugs. Clinical guidelines. Almaz; 2006. 88 p.

5. Meek IL, Van de Laar MAFJ, E. Vonkeman H. Non-Steroidal Anti-Inflammatory Drugs: An Overview of Cardiovascular Risks. Pharmaceuticals [Internet]. 2010 Jul 7 [cited 2022 Sep 11];3(7):2146–62. Available from: <URL>.

6. Bennett JS, Daugherty A, Herrington D, Greenland P, Roberts H, Taubert KA. The Use of Nonsteroidal Anti-Inflammatory Drugs (NSAIDs): A Science Advisory From the American Heart Association. Circulation [Internet]. 2005 Apr 5 [cited 2022 Sep 11];111(13):1713–6. Available from: <URL>.

7. Nikitenko VV, Borisova EG, Polevaya LP, Soldatkina AS, Polevaya AV. Results clinical assessment of the application of nonsteroidal anti-inflammatory drugs for pain symptoms occurring after endodontic dental treatment. Bulletin of the Russian Military Medical Academy [Internet]. 2018 Mar 15 [cited 2022 Sep 11];20(1):91–4. Available from: <URL>.

8. Krasselt M, Baerwald C. Celecoxib for the treatment of musculoskeletal arthritis. Expert Opinion on Pharmacotherapy [Internet]. 2019 Sep 22 [cited 2022 Sep 11];20(14):1689–702. Available from: <URL>.

9. Syrova G. A method of potentiating the analgesic action of potassium salt of 2,4-dichlorobenzoic acid. 51082 UA, 2010.

10. Zhuravleva M, Kukes V, Prokofiev A, Serebryanova SY, Goroditskaya G, Berdnikova N. Rational use of NSAIDs – balance of efficacy and safety (literature review). International Journal of Applied and Basic Research. 2016;6(4):687–96.

11. Mishchenko N. Movalis in clinical practice: the optimal ratio of efficacy and safety. Health of Ukraine. 2011;(1):34–5.

12. Kristian S, Sajeewane S, Paul S. Effectiveness and Safety of Celecoxib for the Treatment of Rheumatoid Arthritis. Am Fam Physician. 2018;97(9):573.

13. Kirane A, Toombs JE, Ostapoff K, Carbon JG, Zaknoen S, Braunfeld J, et al. Apricoxib, a Novel Inhibitor of COX-2, Markedly Improves Standard Therapy Response in Molecularly Defined Models of Pancreatic Cancer. Clinical Cancer Research [Internet]. 2012 Sep 15 [cited 2022 Sep 11];18(18):5031–42. Available from: <URL>.

14. Taranova N, Govorova L. Determination of total lipids in lipid extract obtained from blood plasma. Questions honey chemistry. 1987;2:132–6.

15. Wallgren M, Beranova L, Pham QD, Linh K, Lidman M, Procek J, et al. Impact of oxidized phospholipids on the structural and dynamic organization of phospholipid membranes: a combined DSC and solid state NMR study. Faraday Discuss [Internet]. 2013 [cited 2022 Sep 11];161:499–513. Available from: <URL>.

16. McIntyre TM. Bioactive oxidatively truncated phospholipids in inflammation and apoptosis: Formation, targets, and inactivation. Biochimica et Biophysica Acta (BBA) - Biomembranes [Internet]. 2012 Oct [cited 2022 Sep 11];1818(10):2456–64. Available from: <URL>.

17. Golovach IY. An innovative NSAID with gastroprotective properties in rheumatological practice. Ukrainian Rheumatology Journal. 2016;63(1):9–11.

18. Nasonov E. Analgesic therapy in rheumatology: a journey between Scylla and Charybdis. Klinicheskaya Farmakologiya i Terapiya. 2003;12(1):64–9.

19. Lee YC. Effect and Treatment of Chronic Pain in Inflammatory Arthritis. Curr Rheumatol Rep [Internet]. 2013 Jan [cited 2022 Sep 11];15(1):300. Available from: <URL>.

20. Laine L. Proton pump inhibitor co-therapy with nonsteroidal anti-inflammatory drugs--nice or necessary? Rev Gastroenterol Disord. 2004;4 Suppl 4:S33-41.

21. Belousov YB, Moiseev V. Clinical pharmacology and pharmacotherapy: A guide for physicians. Universum Publishing; 1997. 532 p.

22. Lawrence D, Benitt P. Inflammation and non-steroidal anti-inflammatory drugs. In: Clinical pharmacology: hands per from English. Medicine; 1991. p. 485–523.

23. Matuzov S. Treatment of chronic traumatic osteomyelitis using antioxidants [PhD Thesis]. [Irkutsk]; 1997.

24. Tekin Koruk S, Aksoy N, Hamidanoglu M, Karsen H, Unlu S, Bilinc H. The activity of paraoxonase and arylesterase in patients with osteomyelitis. Scandinavian Journal of Clinical and Laboratory Investigation [Internet]. 2012 Nov [cited 2022 Sep 12];72(7):513–7. Available from: <URL>.

25. Sultonov SR, Azizov A, Saburova A. Dynamics of lipid peroxidation processes and antioxidant defense system in chronic hematogenous osteomyelitis in children. Reports Acad Sciences Resp Tajikistan. 2009;52:723–7.

26. Wallgren M, Beranova L, Pham QD, Linh K, Lidman M, Procek J, et al. Impact of oxidized phospholipids on the structural and dynamic organization of phospholipid membranes: a combined DSC and solid state NMR study. Faraday Discuss [Internet]. 2013 [cited 2022 Sep 12];161:499–513. Available from: <URL>.

27. McIntyre TM. Bioactive oxidatively truncated phospholipids in inflammation and apoptosis: Formation, targets, and inactivation. Biochimica et Biophysica Acta (BBA) - Biomembranes [Internet]. 2012 Oct [cited 2022 Sep 12];1818(10):2456–64. Available from: <URL>.

28. Bachynsky R, Vakulenko N, Boyko E. Experimental study of the effect of caffeine on the analgesic effect of known nonsteroidal anti-inflammatory drugs of different chemical structure. Zaporozhye medical journal. 2011;13(5):60–2.

29. Syrova G, Zvyagintseva T. In Ivano-Frankivsk, Ukraine; 2008. p. 454.

30. Stefanova O. Preclinical studies of drugs: a method. Kyiv: rivers for ed; 2001. 527 p.

31. Anonymous. European convention for the protection of vertebrate animals used for experimental and other scientific purposes. Strasbourg: European Council; 1986 p. 51.

32. Kundiev YI, editor. Modern problems of bioethics. Kyiv: Akademperiodika; 2009. 278 p.

33. Stalnaya I. Method for determination of diene conjugation of unsaturated higher fatty acids. In: Orekhovich V, editor. Modern methods in biochemistry. Medicine; 1972. p. 63–4.

RESEARCH ARTICLE

Mechanical Properties of a Stainless Steel after Annealing in Uranium Carbide

Yüksel Sarıkaya¹ (iD)**, Müşerref Önal¹*** (iD)**, Abdullah Devrim Pekdemir²** (iD)

¹Ankara University, Department of Chemistry, Ankara, Turkey
²Ankara University, Graduate School of Natural and Applied Sciences, Ankara, Turkey

Abstract: The aim of this study was to investigate the interaction of carbide nuclear fuels with steel that is being used as cladding material for nuclear reactors. The specimens prepared from steel EN 1.4988 were consecutively annealed in three uranium carbide (UC) powders, having different carbon contents, at 600 °C for 1000 h. Both Ar and Na were used as bonding elements. The increase in the carbon content of the carburized specimens was determined and evaluated according to the bound and free carbon contents in the UC powders. The migration of free and bound carbon atoms into steel via self-diffusion and over Fe_3C formation is interpreted as carburizing. Microhardness measurements and stress-strain tests were used to determine the mechanical properties of crude and carburized steel specimens. Maximum hardness at the contact surface and depth of the carburized zone were determined from the microhardness profiles and discussed depending on the bonding elements and carbon content in the specimens. These variables have a significant impact on the elongation percent, 0.2% yield stress, and tensile stress.

INTRODUCTION

Austenitic stainless steel, including trace amounts of free carbon atoms, is an alloy with different compositions. A large number of machine components are being made from stainless steel due to their excellent metallurgical, mechanical, and physicochemical properties. Also, they are extensively being used for the construction of nuclear fuel clads. Plutonium-uranium oxide or carbide are used as nuclear fuels (1). The out-of-pile test revealed that the physicochemical effect of oxide fuels on clads is larger than that of carbide ones. Since they have the same chemical properties, nonactive uranium carbide powders are being used instead of real carbide fuels. Carburizing processes are also carried out at elevated temperatures, either by tempering of steels or by reaction among several carbonaceous mediums such as kerosene, methanol, and carbon nanotubes (2–4). Carbon atoms diffused into steel are supplied from a carbonaceous medium (5–7). The depth of the

hardened diffusion layer in steel is determined by the measurement of carbon content or microhardness profiles as well as optical or electron microscopical images (8–10). Carburizing kinetics of various steels are studied using both of these profiles (11–14).

Besides carburizing, other types of corrosion have an effect on the mechanical properties of steels such as hardness, elongation percent, yield stress, ultimate tensile stress, ductility, fracture stress, and wear resistance (15–17). Mechanical properties of hardening steels following carburizing or different thermal and coating treatments are investigated (18–21). The effect of machining induced surface residual stress on the micro crack density of a steel was examined (22). Oxide and carbide films formed on the surface of the steels are characterized (23–25). The effect of annealing temperature and time on steel plasma carburization has previously been studied (26–28). Although such studies exist, the effect of the free and bound carbon content of the

carburizer as well as the bonding types of elements on the mechanical properties of steel is not yet sufficiently examined. Therefore, the aim of this study is to evaluate the change in carbon content, carburized depth, elongation percent, 0.2% yield stress, and tensile stress of a stainless steel depending on the uranium carbide powders that are being proposed as nuclear fuels.

MATERIAL AND METHODS

Materials

EN 1.4988 satinless steel with 1 mm thickness was used in this study as cladding material. The chemical composition of the crude steel is given as mass %: Fe 69.90; Cr 16.10; Ni 13.60; Mo 1.28; Mn 1.10; Ta+Nb 0.87; V 0.70; Si 0.27; C 0.08; Co 0.06; P 0.02; S 0.01 and N trace. Three uranium carbide (UC) powders with different compositions, indicated as UC(1), UC(2), and UC(3) were used as carburizers (Table 1). These powders also contain uranium oxide, uranium nitride, and free carbon as impurities. Due to the pyrophoric property of UC, all carburizing processes were performed under argon atmosphere in a glove box.

Table 1: Chemical composition (mass%) of the uranium carbide powders.

Powders	U	C	C (free)	O	N
UC(1)	95.105	4.820	-	0.037	0.038
UC(2)	94.786	4.960	0.034	0.170	0.050
UC(3)	94.654	5.150	0.053	0.120	0.023

Experimental
All four steel specimens were placed into six steel capsules at equal depths and distances (Figure 1). All the starting UC(1), UC(2), and UC(3) powders were placed into two capsules and vibration was applied to cover the specimens. Then, liquid sodium was added in one of the identical two capsules. After being tightly closed, each capsule was inserted into silica tubes and evacuated to 10^{-4} mmHg, then

sealed off. Silica tube assembly was heated in a muffle furnace for 1000 hours at 600 °C. Working temperature is selected as 600 °C being the maximum working temperature of nuclear reactors. They were removed after the furnace cooled. The crude steel and carburized specimens were marked as S0, S1, S2, and S3, respectively, according to their UC numbers.

Unit (mm)
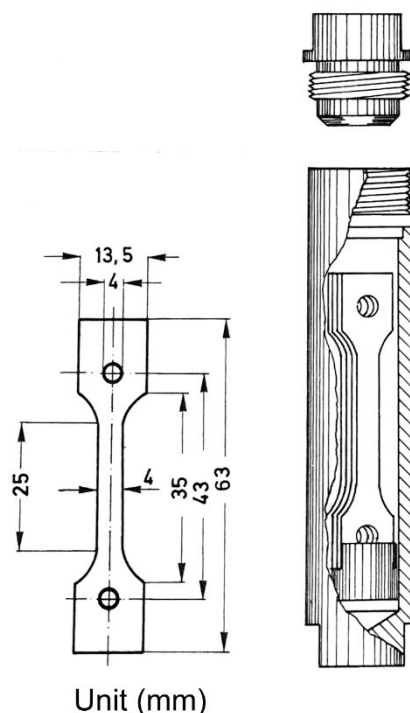
Figure 1: Dimension of steel specimens and their positions in the capsule tree.

Carbon content of the carburized specimens in each capsule was determined by converting it to carbon dioxide at high temperature. Specimens taken from each capsule were cut perpendicular to the contact

surface. The cross section surfaces were respectively polished and etched for microscopic examination and microhardness measurements. The Vickers microhardness gradients were measured

with a Leitz Durimet machine using an intentation load of 100 g. Room temperature elongation percent, 0.2% yield stress, and tensile stress for crude and carburized steel specimens were calculated using stress-strain curves plotted by a commercial testing machine.

RESULTS AND DISCUSSION

Surface Morphology
The microstructure of the cross-section surface of the carburized specimen UC(1) by argon bonding was given in Figure 2. There is a clear distinction between carburized and unaffected regions on the cross-section surfaces. Different metal carbides such as Fe_3C and $Cr_{23}C_6$ (29,30) formed as carburizing precipitates on the grain boundaries in the form of thick lines (Figure 2). Iron carbide (Fe_3C: cementite) is the major component of the heterogeneous solid mixture (31–36). Bonded carbon atoms in UC were migrated into the steel after the formation of Fe_3C, while free carbon impurities in UC powder would be migrated via both Fe_3C formation and self-diffusion.
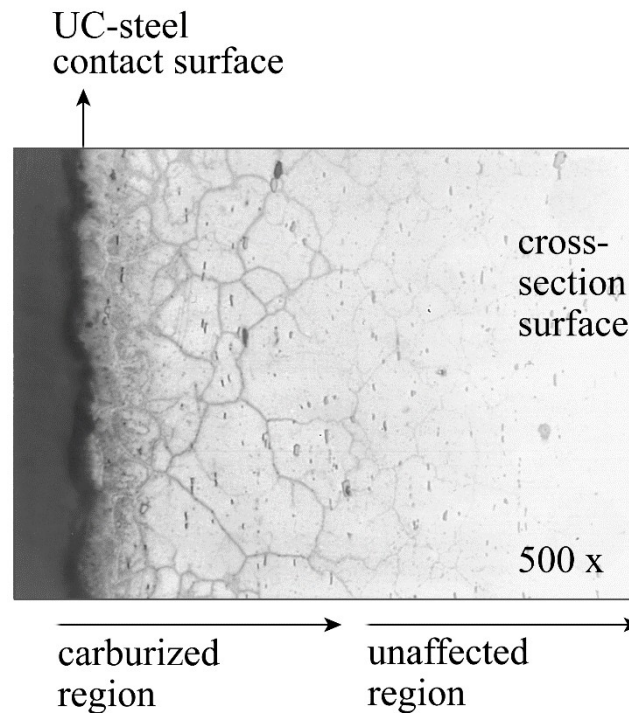
Figure 2: Optical micrographs of the cross-section surface of a specimen carburized in UC(1) by Ar-bonding.

Hard and brittle cementite was formed through the reversible reaction:

$$3Fe + C \rightleftharpoons Fe_3C \qquad \text{(Eq. 1)}$$

Temperature dependence of Gibbs free energy (free enthalpy change) for this reaction is given in SI units as follows

$$\Delta G^0 = \Delta H^0 - T\Delta S^0 = 26694 - 24.769\,T \qquad \text{(Eq. 2)}$$

Where ΔH^0 and ΔS^0 are the change in enthalpy and entropy, respectively (33). Since $\Delta H^0 > 0$, the reaction is endothermic. Based on Le Châtelier's principle, Fe_3C becomes more stable compared to Fe and C with increasing temperature. The carburizing process observed in the interior walls of the steel was explained by this reaction. Since crude or carburized steel is a heterogeneous mixture of Fe, C, and Fe_3C, the ratio among these components has a significant effect on the mechanical properties of steel.

Increasing Carbon Content in the Steel by Carburizing
The effect of carburizing on the physicochemical and mechanical properties of steel changes depending on the chemical composition of steel and carbon content as well as the annealing temperature, heating and cooling rate, and bonding properties. In this study, we have investigated the carbon content and bonding properties. The variation in carbon content of steel through Ar- and Na-bonding along with the carbon content of uranium carbide are given in Table 2 and represented in Figure 3. This variation depends on the total and free carbon content in the uranium carbon powders as well as the bonding materials used. The increase in the carbon content of steel by Na-bonding is greater than that of Ar-bonding. Also, free carbon atoms into the powder diffuse in the steel more effectively. According to the basic laws of thermodynamics, carbon atoms spontaneously move from a high chemical potential state to a low one. The effect of

carbon content on the mechanical properties of the   steel is discussed in the section below.

Table 2: Mechanical properties of the crude and carburized steel samples.

Steels	C %	h_s (VH)	x_{max} (µm)	Elongation (%)	0.2% Yield strength (N/mm^2)	Tensile strength (N/mm^2)
S0	0.08	210	0	54	270	540
S1-Ar	0.19	500	180	24	292	618
S1-Na	0.21	500	180	24	315	585
S2-Ar	0.26	600	220	12	410	635
S2-Na	0.27	600	220	7.5	440	615
S3-Ar	0.30	705	300	10	410	668
S3-Na	0.59	705	300	2	470	685
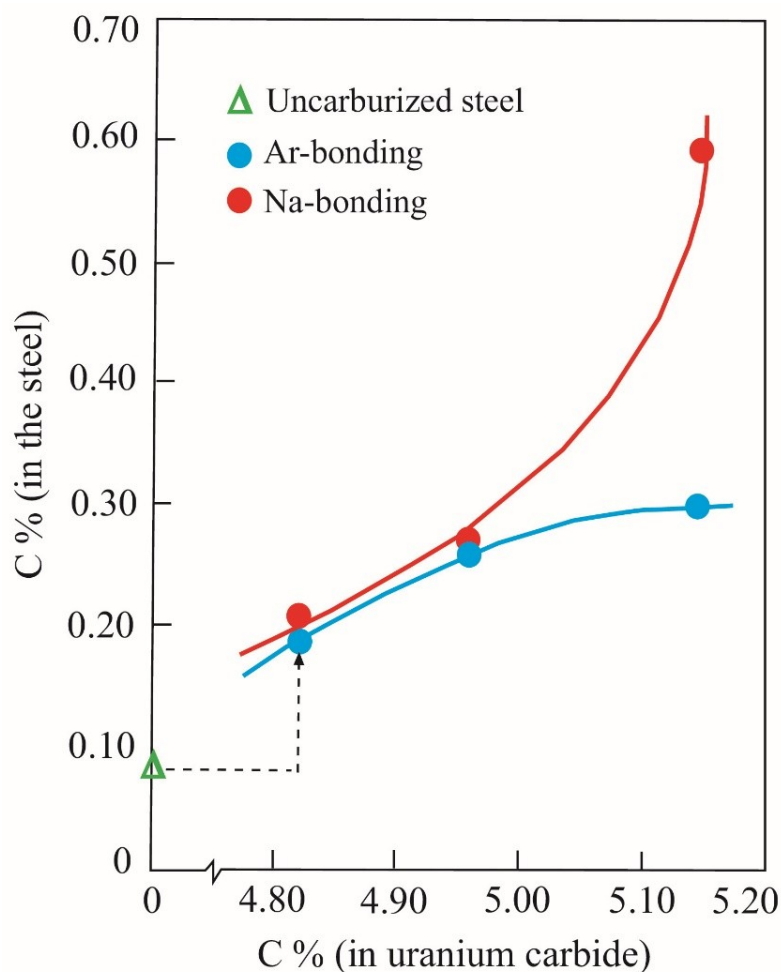
Figure 3: Variation of the carbon content in the steel with the carbon content in the uranium carbide powder.

Microhardness Profiles

Vickers microhardness profiles on the cross-section of the carburized specimens in UC(1), UC(2), and UC(3) by Ar- and Na- bonding are represented in Figure 4, Figure 5, and Figure 6, respectively. Here, h_0 is the microhardness of the uncarburized steel, h_s is the maximum microhardness at the nearest distance to the contact surface, and x_m is the maximum depth of the carburized region. The corresponding microhardness profiles by the Ar- and Na-bonding are overlapped for the specimens carburized in UC(1) and UC(2), while different than those in UC(3). This difference is due to the excess free carbon atoms in the UC(3) carried faster by sodium bonding. Although the results vary considerably depending on the physicochemical

properties of the materials and carburizing conditions (25,26,29,31,35), the outcomes of this study generally agree with the literature data (17,19,36).
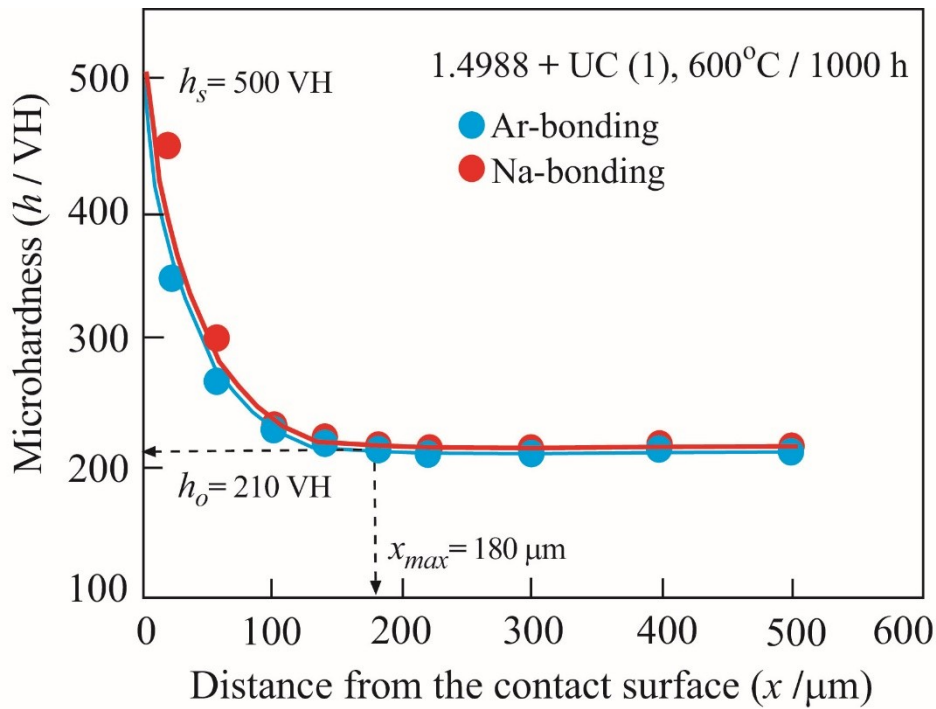
Figure 4: Microhardness profiles for the specimens carburized in UC(1) by the Ar-bonding and Na-bonding.
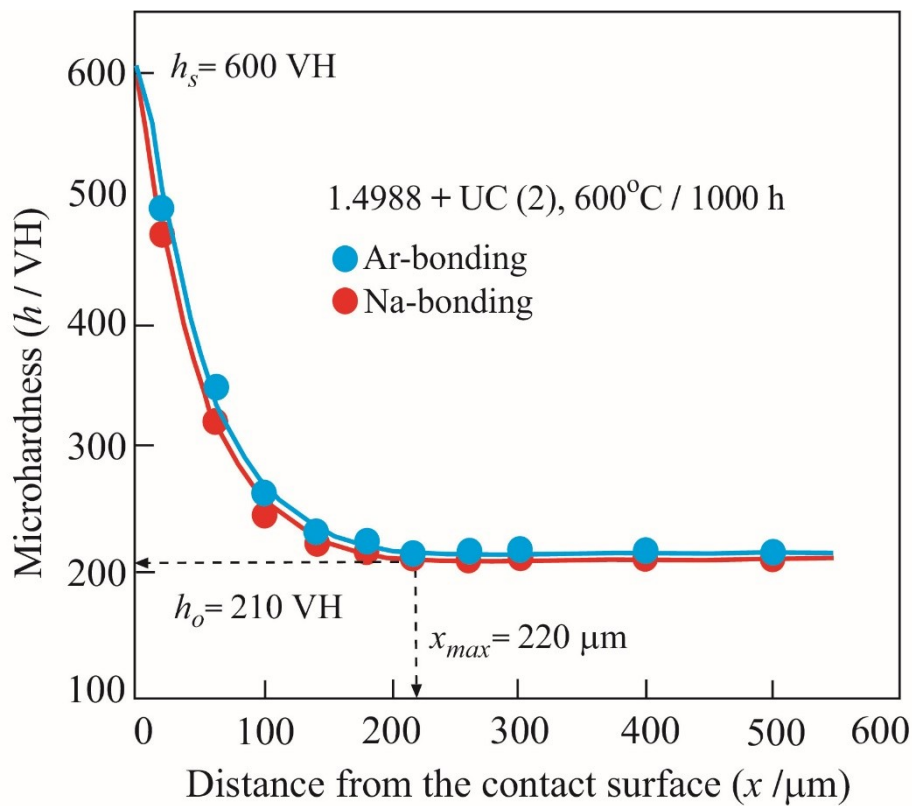
Figure 5: Microhardness profiles for the specimens carburized in UC(2) by the Ar-bonding and Na-bonding.
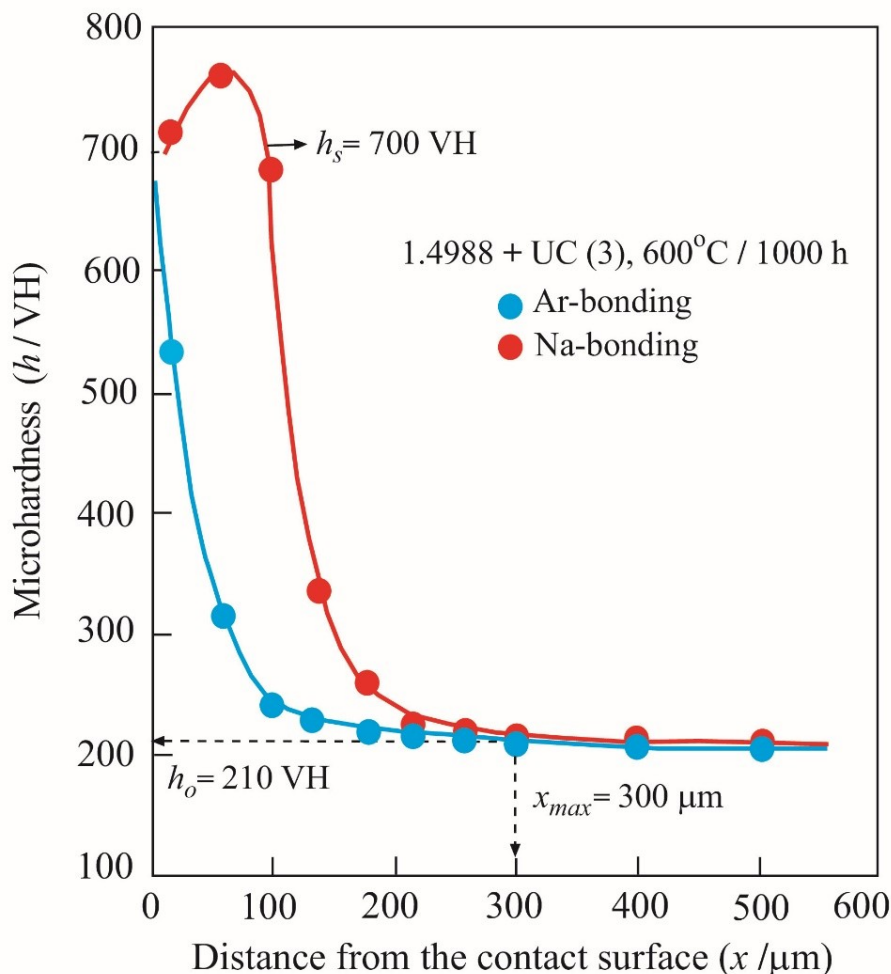
Figure 6: Microhardness profiles for the specimens carburized in UC(3) by Ar-bonding and Na-bonding.

Maximum Hardness and Carburizing Depth

The microhardness profiles revealed that the maximum hardness (h_s) at the contact surface depends on the bonding materials but not the depth (x_{max}) of the carburized zone. The variation of h_s and x_{max} with the mass percent of carbon in the steel was given in Table 2 and represented in Figure 7. The changes in h_s and x_{max} are linear by Ar-bonding, whereas curvilinear by Na-bonding. Consequently, the carbon content in steel has a great effect on the carburizing processes.

Mechanical Properties

The changes in elongation percent, 0.2% yield strength, and tensile strength with increasing carbon content in the uranium carbide powder were given in Table 2 and represented in Figure 8, Figure 9, and Figure 10. The elongation decreases with the carbon content while the 0.2% yield stress and tensile stress increase. These changes are thought to be caused by free carbon atoms in the powders and dissolution of them in Na. The increase in the tensile stress would facilitate the steel cladding process, while a decrease in the elongation percent slows it down. These results are also consistent with the increasing carbon content of steel.
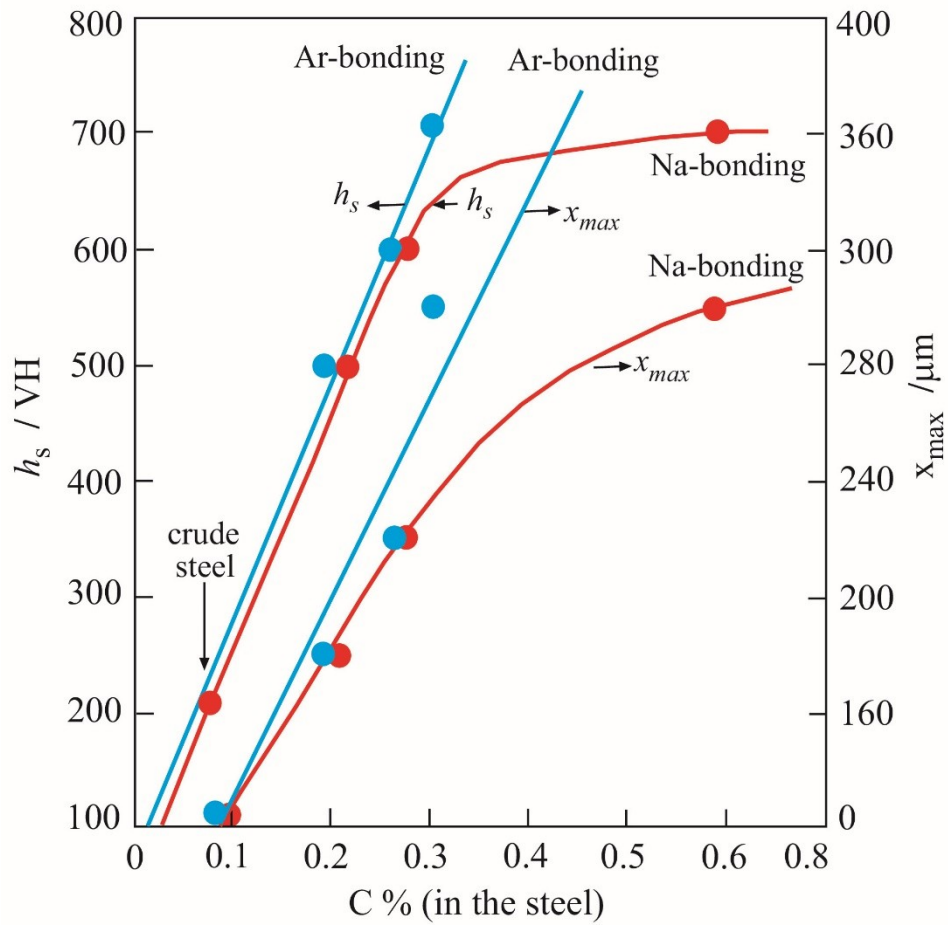
Figure 7: Change in the maximum microhardness (h_s) and maximum depth (x_m) for carburized zone depending on the carbon content in the uranium carbide powder.
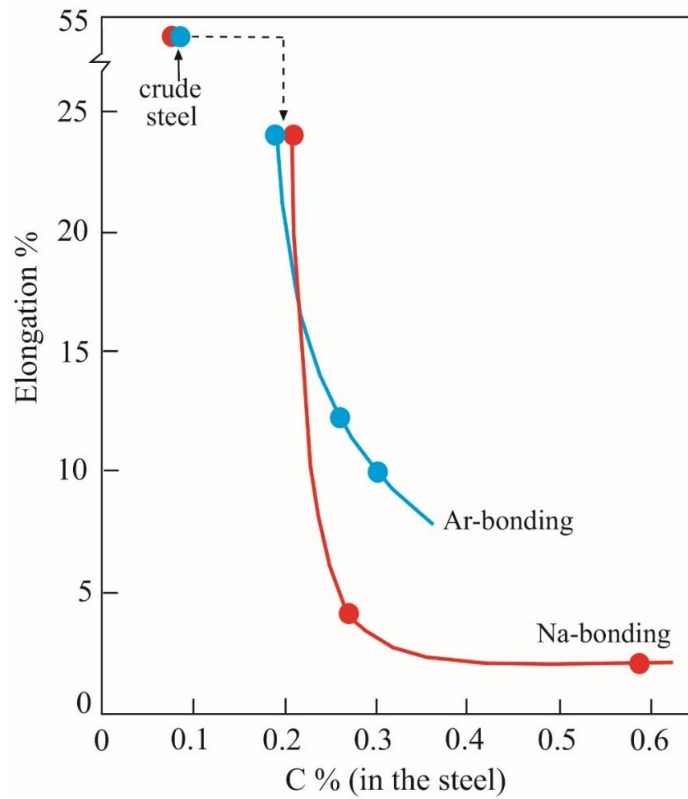
Figure 8: Decreasing of the elongation percent with the carbon content in the steel.
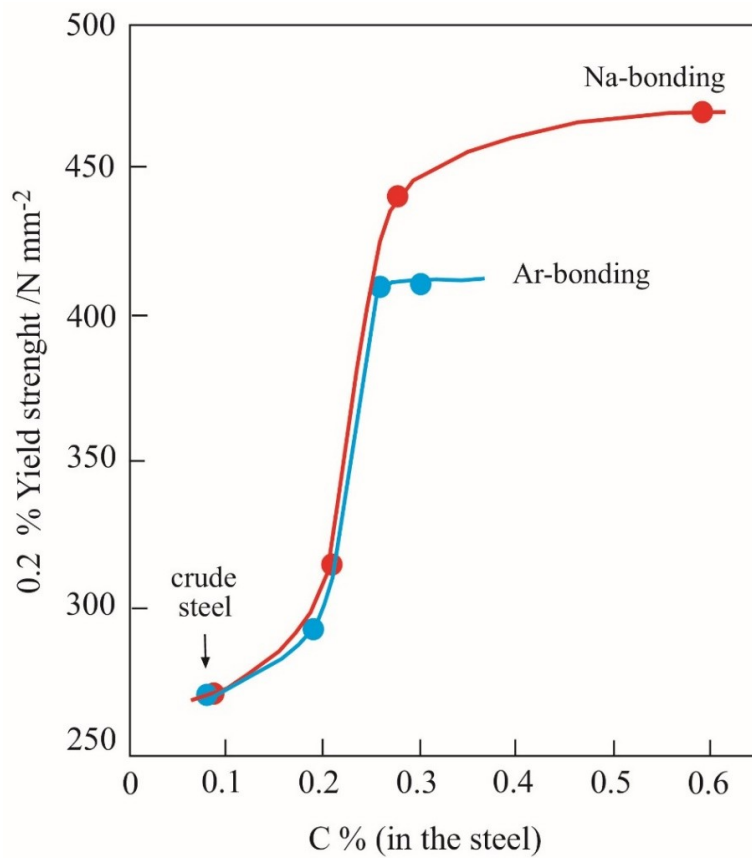
Figure 9: Increasing of the 0.2% yield strength with the carbon content in the steel.
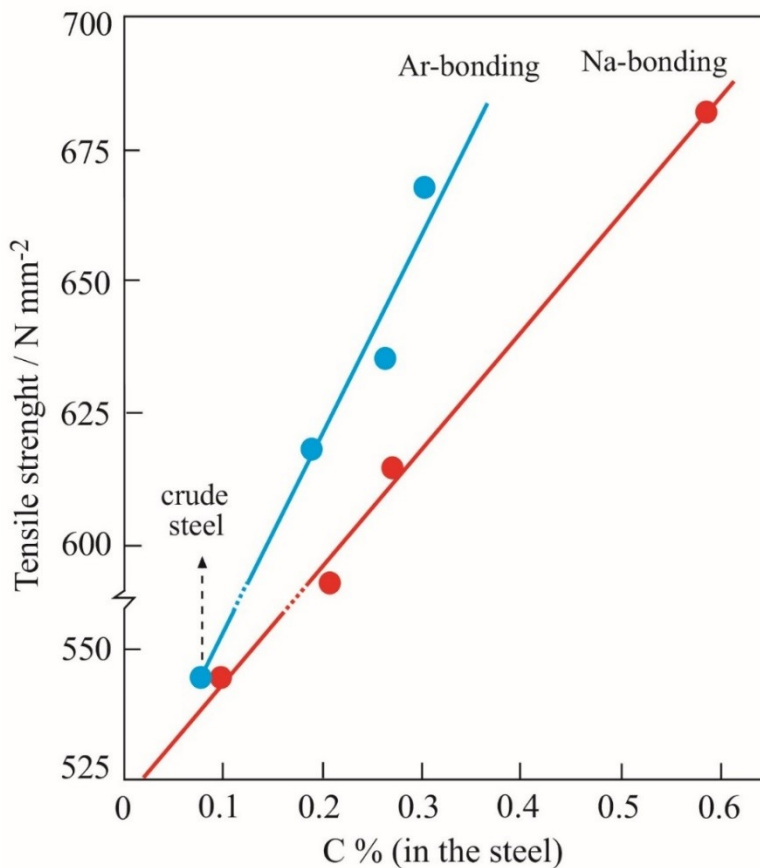
Figure 10: The tensile strength and carbon content in steel.

CONCLUSION

The mechanical properties of steel depend on the physicochemical processes such as the chemical composition of the steel, carburizer, bonding materials, ration of Fe, C, and Fe_3C phases, crystal structure of Fe, heating temperature, and heating and cooling rate. Here, we investigated only the chemical composition of uranium carbide using a carburizer and bonding properties during carburizing of the cladding. Stainless steels was often used as a cladding material for nuclear fuel. The most dangerous nuclear accidents are due to the nuclear fuel and the leakage of the fission products through corroded cladding. Therefore, the corrosion of the cladding materials in contact with nuclear fuels and the fission products at the working temperature of the nuclear reactor should be investigated extensively. Since the chemical properties are similar, non-radioactive materials were used instead of radioactive ones during the experiments. Optimum life of claddings at the high operation temperature of the nuclear reactor was determined according to the effect of corrosion on the mechanical properties such as hardness, elongation, yield stress, and tensile stress. It was determined that bonding characteristics like Ar and Na, in addition to chemical impurities like graphite in uranium carbide, had an impact on the corrosion of the steel.

CONFLICT OF INTEREST

The authors declare that they have no known competing financial interests or personal relationships that could have appeared to influence the work reported in this paper.

REFERENCES

1.   Majumdar S, Sengupta AK, Kamath HS. Fabrication, characterization and property evaluation of mixed carbide fuels for a test Fast Breeder Reactor. J Nucl Mater. 2006;352(1-3):165-73. <DOI>

2.   Yan MF. Study on absorption and transport of carbon in steel during gas carburizing with rare-earth addition. Mater Chem Phys. 2001;70(2):242-4. <URL>

3.   Farfan S. High cycle fatigue, low cycle fatigue and failure modes of a carburized steel. Int J Fatigue. 2004;26(6):673-8.
doi:10.1016/j.ijfatigue.2003.08.022<DOI>

4.   Yao J, Zhang Q, Gao M, Zhang W. Microstructure and wear property of carbon nanotube carburizing carbon steel by laser surface remelting. Appl Surf Sci. 2008;254(21):7092-7. <DOI>

5.   Pertek A, Kulka M. Microstructure and properties of composite (B + C) diffusion layers on low-carbon steel. J Mater Sci. 2003;38:269-73. <URL>

6.   Wang J, Tao Q, Fu L, Lai W, Shen C, Sun Z, vd. Greater diffusion rate of carbon atoms from nonlinear migration in micro-cell and spatially heterogeneous stable states in FCC iron. J Mater Sci. 2018;53(23):15952-68. <DOI>

7.   Pertek A, Kulka M. Characterization of complex (B + C) diffusion layers formed on chromium and nickel-based low-carbon steel. Appl Surf Sci. 2002;202:252-60. <DOI>

8.   Sun Y. Kinetics of low temperature plasma carburizing of austenitic stainless steels. J Mater Process Technol. 2005;168(2):189-94. <DOI>

9.   Balachandran G, Vadiraj A, Sharath BS, Krishnamurthy BR. Studies on induction hardening of gray iron and ductile iron. Trans Indian Inst Met. 2010;63(4):707-13. <DOI>

10. Dong M, Cui X, Jin G, Wang H, Cai Z, Song S. Improved microstructure and properties of 12Cr2Ni4A alloy steel by vacuum carburization and Ti + N co-implantation. Appl Surf Sci. 2018;440:660-8. <DOI>

11. Gençoğlu S, Yazıcı A. Surface Characteristics and distortion analysis of the case-hardened helical gears: a comparison of different case-hardening treatments. Trans Indian Inst Met. 2020;73(1):119-26. <DOI>

12. Kulka M, Pertek A. Characterization of complex (B + C + N) diffusion layers formed on chromium and nickel-based low-carbon steel. Appl Surf Sci. 2003;218(1-4):114-23. <DOI>

13. Scheuer CJ, Cardoso RP, Mafra M, Brunatto SF. AISI 420 martensitic stainless steel low-temperature plasma assisted carburizing kinetics. Surf Coat Technol. 2013;214:30-7. <URL>

14. Sarıkaya Y, Önal M. High temperature carburizing of a stainless steel with uranium carbide. J Alloys Compd. 2012;542:253-6. <DOI>

15. Çavuşlu F, Usta M. Kinetics and mechanical study of plasma electrolytic carburizing for pure iron. Appl Surf Sci. 2011;257(9):4014-20. <DOI>

16. Sarıkaya Y, Önal M, Pekdemir AD. Application of diffusion and transition state theories on the carburizing of steel AISI 316 by annealing in uranium carbide powder. Heliyon. 2019;5(8):e02305. <DOI>

17. Akita M, Tokaji K. Effect of carburizing on notch fatigue behaviour in AISI 316 austenitic stainless steel. Surf Coat Technol. 2006;200(20-21):6073-8. <DOI>

18. Xia X, Idemitsu K, Arima T, Inagaki Y, Ishidera T, Kurosawa S, vd. Corrosion of carbon steel in compacted bentonite and its effect on neptunium diffusion under reducing condition. Appl Clay Sci. 2005;28(1-4):89-100. <DOI>

19. Panda RR, Mohanty DAM, Mohanta DK. Mechanical and wear properties of carburized low carbon steel samples. J Multidiscip Curr Res. 2014; Jan/Feb:109-12.<URL>

20. Savaria V, Monajati H, Bridier F, Bocher P. Measurement and correction of residual stress gradients in aeronautical gears after various induction surface hardening treatments. J Mater Process Technol. 2015;220:113-23. <DOI>

21. Shen S, Song X, Li Q, Li X, Zhu R, Yang G. Effect of CrxCy–NiCr coating on the hydrogen embrittlement of 17-4 PH stainless steel using the smooth bar tensile test. J Mater Sci. 2019;54(9):7356-68. <DOI>

22. Elangeswaran C, Cutolo A, Muralidharan GK, de Formanoir C, Berto F, Vanmeensel K, et al. Effect of post-treatments on the fatigue behaviour of 316L stainless steel manufactured by laser powder bed fusion. Int J Fatigue. 2019;123:31-9. <DOI>

23. Chen Q-Y, Ren J-K, Xie Z-L, Zhang W-N, Chen J, Liu Z-Y. Correlation between reversed austenite and mechanical properties in a low Ni steel treated by ultra-fast cooling, intercritical quenching and tempering. J Mater Sci. 2020;55(4):1840-53. <DOI>

24. Tian Z, Zhao Y, Jiang Y, Ren H, Qin C. Investigation of microstructure and properties of FeCoCrNiAlMox alloy coatings prepared by broadband-beam laser cladding technology. J Mater Sci. 2020;55(10):4478-92. <DOI>

25. Sahu JN, Sasikumar C. Mechanical properties of a Ni–Cr–Mo steel subjected to room temperature carburizing using surface mechano-chemical carburizing treatment (SMCT). Trans Indian Inst Met. Nisan 2018;71(4):915-21. <DOI>

26. Sahu JN, Sasikumar C. Evaluation of microstructure due to addition of carbon in Ni–Cr–Mo steel mechanically through surface mechanochemical case carburizing treatment (SMCT). Trans Indian Inst Met. 2019;72(1):55-63. <DOI>

27. Zhang W, Fang K, Hu Y, Wang S, Wang X. Effect of machining-induced surface residual stress on initiation of stress corrosion cracking in 316 austenitic stainless steel. Corros Sci. 2016;108:173-84. <DOI>

28. Wang S, Hu Y, Fang K, Zhang W, Wang X. Effect of surface machining on the corrosion behaviour of 316 austenitic stainless steel in simulated PWR water. Corros Sci. 2017;126:104-20. <DOI>

29. Yang Y, Yan MF, Zhang YX. Tribological behavior of diamond-like carbon in-situ formed on Fe_3C-containing carburized layer by plasma carburizing. Appl Surf Sci. 2019;479:482-8. <DOI>

30. Sahu JN, Sasikumar C. Room Temperature case carburizing of a Ni–Cr–Mo steel through shot peening/blasting techniques. Trans Indian Inst Met. 2015;68(S2):227-33. <DOI>

31. Yang Y, Yan MF, Zhang SD, Guo JH, Jiang SS, Li DY. Diffusion behavior of carbon and its hardening effect on plasma carburized M50NiL steel: Influences of treatment temperature and duration. Surf Coat Technol. 2018;333:96-103. <DOI>

32. Argade GR, Shukla S, Liu K, Mishra RS. Friction stir lap welding of stainless steel and plain carbon steel to enhance corrosion properties. J Mater Process Technol. 2018;259:259-69. <DOI>

33. Ozturk B, Fearing VL, Ruth JA, Simkovich G. Self-diffusion coefficients of carbon in F_3C at 723 K via the

kinetics of formation of this compound. Metall. Mater. Trans. 1982;13A:1871-73. <U​RL>

34. Ahamad NW, Jauhari I, Azis SAA, Aziz NHA. Kinetics of carburizing of duplex stainless steel (DSS) by superplastic compression at different strain rates. Mater Sci Eng A. 2010;527(16-17):4257-61. <DOI>

35. Yang Y, Yan MF, Zhang YX, Li DY, Zhang CS, Zhu YD, vd. Catalytic growth of diamond-like carbon on Fe_3C-containing carburized layer through a single-step plasma-assisted carburizing process. Carbon. 2017;122:1-8. doi.org/10.1016/j.carbon.2017.06.033 <DOI>

36. Cao Z, Liu T, Yu F, Cao W, Zhang X, Weng Y. Carburization induced extra-long rolling contact fatigue life of high carbon bearing steel. Int J Fatigue. 2020;131:105351. <DOI>

Synthesis, Characterization, and Comparison of Disinfectant Bioactivity Test of Two Triphenyltin(IV) Compounds

Aisyah L. Susangka (iD), **Sutopo Hadi*** (iD), **Noviany Noviany** (iD), **Agung A. Kiswandono** (iD)
Nurhasanah (iD)**, and Kamisah D. Pandiangan** (iD)

Department of Chemistry, Universitas Lampung, Bandar Lampung, Indonesia 35145

Abstract: This paper aims to report the synthesis of two new organotin(IV) carboxylate derivatives, triphenyltin(IV) 4-aminobenzoate (**2**) and triphenyltin(IV) 4-nitrobenzoate (**3**) and to examine their antibacterial activity as a disinfectant. These compounds were prepared by reacting triphenyltin(IV) hydroxide (**1**) with 4-aminobenzoic acid and 4-nitrobenzoic acid, respectively. Compound (**2**) was obtained as a yellow solid with a yield of 84.09% and compound (**3**) in the form of a white solid with a yield of 80.70%. These compounds were well characterized using UV-Vis spectrometry, FT-IR spectrometry and NMR spectroscopy. The bioactivity test as a disinfectant was tested against *Salmonella typhosa* and *Staphylococcus aureus*. The activity test was carried out by measuring the optical density (OD) of the tested compounds with concentration variations of 5×10^{-3}, 1×10^{-3}, and 5×10^{-4} M in methanol and 5% dimethyl sulfoxide (DMSO), commercial Wipol (2.5% pine oil) was used as a positive control with observations monitored at contact times of 0, 5, 10, and 15 minutes. The results showed that of both compounds were active against the two bacteria compared to the positive control with compound **3** found to be more active than compound **2**.

INTRODUCTION

The interest on organotin(IV) compounds is not only because of their interesting structural features (1-5) but mostly because they have been found to show many biological applications since they have strong effect even at very low concentration (5,6). Biological activities of the compounds are primarily dependent on the organic functional groups bound to Sn (4), and on the anion bearing groups attached to the Sn center as a complementary factor (4).

The current results from the study on organotin(IV) compounds have revealed that some organotin(IV) carboxylates show promising activities in many biological tests. For example, they have been widely used in the biological activities as antifungal (3, 7-9), antioxidant activities (10, 11), antimalarial and antiplasmodial agents (12-15), antiviral agents (16, 17), antitumor and anticancer (18-20), corrosion inhibitor (21-23) and antibacterial (24-30). Moreover, these compounds have been found to exhibit strong activity as disinfectant (31). In this context, it is therefore highly valuable to further explore the potential of organotin(IV) carboxylates as disinfectant agent.

It has also been observed that the strength of the activity of organotin(IV) compounds in many biological test is not only influenced by the number of organic groups attached to the central atom of tin (Sn), but the type of organic groups also plays a role as a determinant in their activity (4, 28). The organic group of phenyl that is bound to the central atom of Sn is known to have a stronger antibacterial activity than the butyl group (7) and the higher the

number of phenyl groups, the higher the antibacterial activity observed (6). In addition, the type of anion ligands bound to Sn atom also has an important role as a secondary determinant of reactivity. Therefore, in this paper, we reported the synthesis of two triphenyltin(IV) compounds with ligands of 4-aminobenzoic acid and 4-nitrobenzoic acid and performed activity tests as disinfectant agent against Gram-positive *S. aureus* and Gram-negative *S. typhosa* bacteria.

EXPERIMENTAL SECTION

Materials
The reagents used were triphenyltin(IV) hydroxide ($[(C_6H_5)_3SnOH]$), 4-aminobenzoic acid [(C_6H_4(4-NH_2)COOH] (4-HABz), 4-nitrobenzoic acid [(C_6H_4(4-NO_2)COOH] (4-HNBz), methanol, dimethylsulfoxide (($CH_3)_2SO$, DMSO), nutrient broth, and nutrient agar. They were obtained from Sigma-Aldrich (Burlington, MA, USA) with Pro Analysis (PA) quality and were used as received. The culture of Gram-positive bacteria *S. aureus* and Gram- negative bacteria *S. typhosa* were obtained from Laboratory of Veterinary Centre, Directorate General of Livestock and Animal Health, Ministry of Agriculture, Lampung, Indonesia. A commercial product Wipol (containing 2.5% pine oil) was used as a positive control.

Instrumentantion
Elemental analysis was carried out on an EA Fission 1108 series elemental analyzer, the UV spectra were recorded in the UV region and measured using a UV-Shimadzu UV-245 Spectrophotometer. Measurements were carried in 1 mL quartz cells. The solution was prepared using methanol solvent with a concentration of 1.0×10^{-5} M. The IR spectra were recorded on a Bruker VERTEX 70 FT-IR spectrophotometer with a KBr disc in the range of 4000-400 cm^{-1}. ^1H and ^{13}C NMR spectra were recorded on a Bruker AV 600 MHz NMR (600 MHz for ^1H and 150 MHz for ^{13}C). All experiments were run in DMSO-d_6 at 298 K.

Preparation of Triphenyltin(IV) Compounds
Two target compounds of triphenyltin(IV) 4-aminobenzoate (**2**) and triphenyltin(IV) 4-nitrobenzoate (**3**) were prepared by the reaction between the starting compound triphenyltin(IV) hydroxide (**1**) with 4-HABz and 4-HNBz using the published method (14,15, 20, 22, 24-28). The following procedure was performed:

Triphenyltin(IV) 4-aminobenzoate, [($C_6H_5)_3Sn$(4-$OCOC_6H_4NH_2$)] (Ph_3Sn4-ABz) (2)
1.1010 g of compound **1** in 20 mL of methanol was reacted with 0.4114 g 4-HABz in 10 mL of methanol (mole ratio was 1:1) and they were refluxed for 4 hours at 60-61 °C. The water formed in the synthesis process was separated by a Dean and

Stark apparatus. The remaining methanol solvent was evaporated by putting the synthesized solution into a vial and covered with aluminium foil that had been perforated and stored in a desiccator until it was obtained. The same procedure was applied in the preparation of compound, [Ph_3Sn(4-NBz)] (**3**). The compounds synthesized obtained were as follows:

[Ph_3Sn(4-HABz)] (**2**): yellow solid; UV $\lambda_{max.}$ (MeOH) nm (log ε): 234 and 278;   IR $\nu_{max.}$ (KBr) cm^{-1}: 3473.09 (NH), 3049.00 (C-H Phen), 1602.08 (C=O), 1528.02 (CO_2 asym), 1551.8; 730.8 (phen), 1177.08 (Sn-O-C), 782.07 (Sn-O); ^1H-NMR (in DMSO-D_6, 600 MHz) δ (ppm): $H_2 = H_6$ 7.440 (6H, d, Ar-H); H_3 & H_5 7.460 (6H, d, Ar-H); H in benzoate: $H_{9, 13} = $ 7.843-7.838 (6H, d); $H_{10,12} = $7.750-7.744 (6H, d); ^{13}C-NMR (in DMSO-D_6, 150 MHz): δ (ppm): C(phen): C_2 & $C_6 = $ 131.6, C_3 & $C_5 = $ 129.1 , $C_4 = $ 126.9; $C_7 = $ 163.8 (C7 C=O); C(NBz) $C_8 = $ 135.9; C_9 & $C_{13} = $ 130.2; C_{10} & $C_{12} = $ 129.1; $C_{11} = $ 129.5; microelemental analysis: found (calculated): C 61.52 (61.70), H 4.29 (4.32), N 2.80 (2.88).

Ph_3Sn(4-HNBz)] (**3**): white solid; UV $\lambda_{max.}$ (MeOH) nm (log ε): 234 and 290;   IR $\nu_{max.}$ (KBr) cm^{-1}: 3047.20 (C-H Phen), 1600.23 (C=O), 1520.08 (CO_2 asym), 1551.8; 730.8 (phen), 1334.50 (N-O),1170.04 (Sn-O-C), 723.53 (Sn-O); ^1H-NMR (in DMSO-D_6, 600 MHz) δ (ppm): $H_2 = H_6$ 7.508 (6H, d, Ar-H); H_3 & H_5 7.481 (6H, d, Ar-H); H in benzoate: $H_{9, 13} = $ 7.867-7.862 (6H, d); $H_{10,12} = $7.774-7.769 (6H, d); ^{13}C-NMR (in DMSO-D_6, 150 MHz): δ (ppm): C(phen): C_2 & $C_6 = $ 131.8, C_3 & $C_5 = $ 129.5, $C_4 = $ 127.3; $C_7 = $ 164.5 (C7 C=O); C(NBz) $C_8 = $ 136.9; C_9 & $C_{13} = $ 130.5; C_{10} & $C_{12} = $ 129.3; $C_{11} = $ 129.8; microelemental analysis: found (calculated): C 58.23 (58.14), H 3.84 (3.68), N 2.75 (2.71).

Disinfectant Bioactivity Test
The disinfectant bioactivity test was carried using procedure similar to the previous work (31) and as follows: Bacterial inoculum was made by taking one dose of rejuvenated *S. aureus* and *S. typhosa*, each bacteria was placed into 2 different Erlenmeyer flasks containing 100 mL of sterile Nutrient Broth media, and then they were shaker at room temperature for 24 hours. The optical density was measured at a wavelength of 600 nm using a UV-Visible Spectrophotometer. The tested solutions were prepared with varying concentrations of 5×10^{-3}, 1×10^{-3}, and 5×10^{-4} M and 5 mL of each compounds tested were placed into three different test tubes. Each tube was added with 500 μL of *S. aureus* and *S. typhosa* inoculums and then vortexed. At contact times of 0, 5, 10, and 15 minutes, the optical density of this mixture was measured using a UV-Visible Spectrophotometer instrument. Then, the same treatment was also carried out with a solution of methanol added with 5% dimethyl sulfoxide as a negative control, and a positive control solution of Wipol (2.5% pine oil).

RESULTS AND DISCUSSION

The synthesis of organotin(IV) compound

Two organotin(IV) compounds, [Ph$_3$Sn(4-HABz)] (**2**) and Ph$_3$Sn(4-HNBz)] compounds were obtained as yellow and white solid, respectively have been successfully synthesized from the reaction of compound **1** with 4-HABz and 4-HNBz based on the procedures described in the literature (14,15, 20, 22, 24-28). The schematic reaction for the synthesis of compounds **2** and **3** are shown in Figure 1, the products of the synthesis for compounds **2** and **3** were 84.09% and 80.70%, respectively. The elemental microanalyses of the compounds synthesized are in accordance with the calculated data.

(a)

1   4-aminobenzoic acid   **2**

(b)

1   4-nitrobenzoic acid   **3**
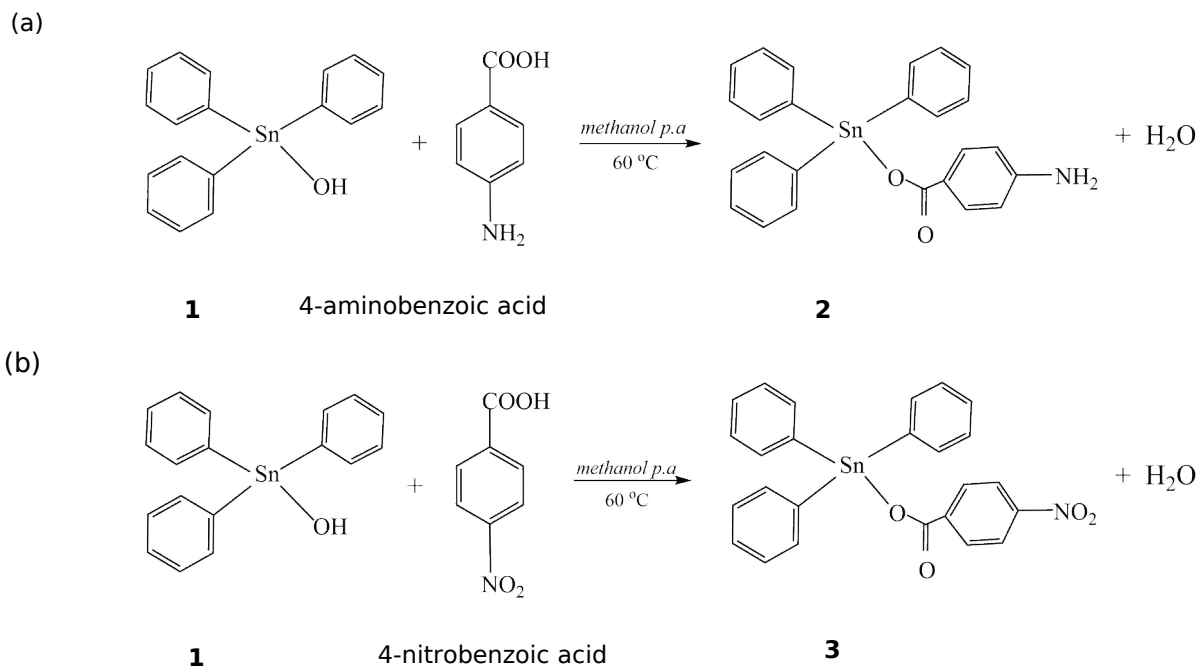
Figure 1: The preparation of **(a)** compound **2**; **(b)** compound **3**.

Characterization of Organotin(IV) Compounds

The success of the synthesis the targeted compounds was analyzed using some spectroscopy techniques. The result of IR characterization was proven by the appearance and disappearance of certain characteristic peaks. The appearance of the characteristic absorption in the two target compounds **2** and **3** is the presence of peak in the regions of 782.07 cm^{-1} and 723.53 cm^{-1} which are characteristics for the vibration of the Sn-O bond, and it is supported with the peaks from Sn-O-C bond in 1177.08 cm^{-1} and 1170. 04 cm^{-1} which indicated that the central atom of tin (Sn) has been bonded to the ligands of 4-HABz and 4-HNBz via oxygen (O) atom (3, 14).

The UV spectroscopic analysis produced the maximum wavelength (λ_{max}) of the compound measured. The data indicated there are several important shifts for each compound. The two compounds give two main characteristic bands of π→π* and n→π* transitions. For example, in compound **1**, there is π→π* transition at 234 nm, after conversion **1** to **2** there are changes in λ_{max} for the n→π* transition to 234 and 278 nm. The presence of a bathochromic shift is an indication that the substitution of ligand has occurred at the central atom because the 4-HABz ligand is a chromophore molecule, with the presence of a –C=O group and a -C=C- bond which causes a shift in wavelength towards a longer one and the effect of auxochrome with the presence of the –NH$_2$ group. Compound **3** also undergoes a change in max for the n→π* transition to 234 and 290 nm originating from the free electrons of O atoms such as –NO$_2$ and –COOH groups from 4-HNBz ligand.

The NMR data of the compounds synthesized were carefully analyzed to ascertain the successful in the synthesis of compounds **2** and **3**. The typical chemical shifts for compounds **2** and **3** prepared were characterized carefully and compared to the data available in the literature (14,15, 20, 22, 24-28). Based on the data of ^{1}H NMR spectrum for compound **2**, the chemical shifts of phenyl protons attached to tin metal appeared as expected in the range of 7.440 for H$_2$ and H$_6$ to 7.460 ppm for H$_3$ and H$_5$, while the protons in benzoate ring appeared at 7.744-7.843 ppm. The ^{13}C NMR values of the compounds synthesized were close to the values

reported by others (14,15, 20, 22, 24-28). The analyses are as follows the carbon in the carboxyl group as expected appeared in the region of 164 ppm. The δ of carbons in the phenyl ligand in compounds **2** and **3** are at 126.9-131.8 ppm and the carbons in the benzoate are in δ range of 129.1-136.9 ppm (14,15, 20, 22, 24-28).

The disinfectant bioactivity tests for compounds **2** and **3** at variation concentrations of 5×10^{-3}, 1×10^{-3}, and 5×10^{-4} M, solvent as negative control, and positive control with contact times of 0, 5, 10 and 15 minutes were carried. This is performed to find out the optical density of the disinfectant solutions that show the ability to inhibit the bacterial growth (Tables 1-3). The result clearly showed that compounds **2** and **3** have strong antibacterial activity against Gram-positive *S. aureus* and Gram-negative *S. typhosa* bacteria.

The compounds **2** and **3** have strong activity as a disinfectant, which characterized by the decrease in the absorbance value with variations from the maximum concentration to the minimum concentration where the longer the contact time to the disinfectant agent, the more disinfectant agent was absorbed by bacteria, and because of this process causing the destruction of bacteria and inhibits the growth of these bacteria, so that the absorbance value will decrease (31).

Compounds **2** and **3** were more capable in inhibiting *S. aureus* than *S. typhosa*, this was indicated by a greater decrease in the absorbance value when these compounds were tested against *S. aureus* bacteria. The difference in the decrease of absorbance values is because the two bacteria have different sensitivities and it was fount that *S. aureus* has a higher sensitivity than *S. typhosa*. This is due to fact that the differences in the structure of the cell walls of the two bacteria, causing differences in the decrease of optical density to the compounds tested in the intracellular bacteria. Gram positive bacteria *S. aureus* has a greater sensitivity level than Gram negative bacteria *S. typhosa* because the cell wall of Gram negative bacteria *S. typhosa* is composed of an outer membrane, an inner membrane and peptidoglycan with a more complex structure than that of Gram-positive bacteria (32-34).

Based on the test results, compound **3** has activity as a better disinfectant because it is characterized by a greater decrease in absorbance value than compound **2**, this is because compound **3** has the effect of electron withdrawing anion (NO_2) which causes the central atom of Sn to become more positive, so it is easier to penetrate the peptidoglycan layer on the bacterial cell wall which is electronegative, causing inhibition of bacterial cell growth.

The results of the bioactivity test of organotin disinfectant with a comparison of solvent as negative control and positive control against *S. aureus* and *S.typhosa* bacteria showed that both organotin compounds **2** and **3** had activity as effective disinfectants, compared to solvents and positive control characterized by a greater decrease in absorbance. large compared to the decrease in absorbance of the solvent and positive control. The MIC value (Minimum Inhibitory Concentration) of the two organotin compounds tested against *S. aureus* and *S. typhosa* was 5×10^{-4} M. This MIC value is stronger than fractions obtained from the stem roots extracts of *Archidendron jiringa* (35) or other synthetic products reported by others (36). The most effective contact time to inhibit the growth of the test bacteria was 15 minutes. This proves that the length of contact time has an effect on the magnitude of the inhibition of growth and reproduction of bacteria.

Table 1: The OD values of compounds **2** against *S. aureus* and *S. typhosa.*

Type of bacteria	Results											
	5 x 10^{-3} M				**1 x 10^{-3} M**				**5 x 10^{-4} M**			
	0´	5´	10´	15´	0´	5´	10´	15´	0´	5´	10´	15´
S. aureus (A$_{initial}$ = 0.655)	0.585	0.480	0.420	0.375	0.301	0.210	0.218	0.122	0.256	0.226	0.185	0.110
S.typhosa (A$_{initial}$ = 0.661)	1.112	0.452	0.330	0.133	0.300	0.252	0.260	0.110	0.235	0.193	0.195	0.102

Table 2: The OD values of compound **3** against *S. aureus* and *S. typhosa.*

Type of bacteria	Results											
	5 x 10^{-3} M				**1 x 10^{-3} M**				**5 x 10^{-4} M**			
	0´	5´	10´	15´	0´	5´	10´	15´	0´	5´	10´	15´
S. aureus (A$_{initial}$ = 0.655)	0.200	0.160	0.113	0.075	0.135	0.127	0.085	0.070	0.127	0.082	0.065	0.025
S.typhosa (A$_{initial}$ = 0.661)	0.172	0.157	0.110	0.080	0.113	0.089	0.077	0.045	0.089	0.073	0.055	0.032

Table 3: The OD values of solvent and positive control against *S. aureus* and *S. typhosa.*

Compound	Results							
	S. aureus (A$_{initial}$ = 0.655)				*S. typhosa* (A$_{initial}$ = 0.661)			
	0´	5´	10´	15´	0´	5´	10´	15´
P	0.522	0.494	0.492	0.490	0.598	0.486	0.480	0.484
KP	0.651	0.596	0.572	0.570	0.638	0.624	0.599	0.594

Note:
P   = solvent as negative control
KP = positive control

CONCLUSIONS

The synthesis of two organotin(IV) compounds, triphenyltin(IV) 4-aminobenzoate (**2**) and triphenyltin(IV) 4-nitrobenzoate (**3**) has been successfully carried out. The synthesized compounds, the ligands and the starting compounds **1** have been tested for their antibacterial activity. Based on optical density data, compound **3** showed the best antibacterial activity at a minimum inhibitory concentration value of 5×10^{-4} M and the most effective contact time to inhibit the growth of the test bacteria was 15 minutes. Organotin compounds **2** and **3** have activity as effective disinfectants, compared to the ligands, starting compound and positive control characterized by a greater decrease in absorbance compared to other substances during the test.

ACKNOWLEDGMENTS

CONFLICTS OF INTEREST

The authors declare no conflicts of interest.

REFERENCES

1. Sirajuddin M, Ali S, Tahir MN. Organotin(IV) derivatives based on 2-((2-methoxyphenyl)carbamoyl)benzoic acid: Synthesis, spectroscopic characterization, assessment of antibacterial, DNA interaction, anticancer and antileishmanial potentials. Journal of Molecular Structure. 2021 Apr;1229:129600.

2. Uddin N, Rashid F, Haider A, Tirmizi SA, Raheel A, Imran M, et al. Triorganotin (IV) carboxylates as potential anticancer agents: Their synthesis, physiochemical characterization, and cytotoxic activity against HeLa and MCF-7 cancer cells. Appl Organomet Chem [Internet]. 2021 Apr [cited 2022 Sep 14];35(4). Available from: https://onlinelibrary.wiley.com/doi/10.1002/aoc.6165

3. Rocha CS, de Morais BP, Rodrigues BL, Donnici CL, de Lima GM, Ardisson JD, et al. Spectroscopic and X-ray structural characterization of new organotin carboxylates and their in vitro antifungal activities. Polyhedron. 2016 Oct;117:35–47.

4. Pellerito L. Organotin(IV)n+ complexes formed with biologically active ligands: equilibrium and structural studies, and some biological aspects. Coordination Chemistry Reviews. 2002 Jan;224(1–2):111–50.

5. Tiekink ERT. Structural chemistry of organotin carboxylates: a review of the crystallographic literature. Appl Organometal Chem. 1991 Jan;5(1):1–23.

6. Szorcsik A, Nagy L, Gajda-Schrantz K, Pellerito L, Nagy E, Edelmann F. Structural studies on organotin(IV) complexes formed with ligands containing S,N,O donor atoms. Journal of Radioanalytical and Nuclear Chemistry. 2002;252(3):523–30.

7. Ahmed S, Ali S, Ahmed F, Bhatti MH, Badshah A, Mazhar M, et al. Synthesis, spectroscopic characterization, and biological applications of organotin(iv) derivatives of 2-(n-maleoyl)-3-phenylpropanoic acid. Synthesis and Reactivity in Inorganic and Metal-Organic Chemistry. 2002 Sep 26;32(8):1521–36.

8. Rocha C, De Morais B, Rodrigues B, Donnici C, De Lima G, Ardisson J, et al. Spectroscopic and X-ray structural characterization of new polymeric organotin (IV) carboxylates and their in vitro antifungal activities: Part II. Applied Organometallic Chemistry. 2017;31(7):e3645.

9. Muhammad N, Shah NA, Ali S, Elahi SN, Rehman W, Shujah S, et al. Theoretical and Experimental in vitro Antifungal and Antitumor Activities of Organotin(IV) Derivatives of 3-(4-nitrophenyl)-2-methylacrylic acid. Pharmaceutical Chemistry Journal. 2019 Nov 1;53(8):689–96.

10. Sari W, Qudus HI, Hadi S. The chemical reactivity study of organotin (IV) 4-aminobenzoates using cyclic voltammetry and antioxidant activity test by the DPPH method. Revista de Chimie. 2020;71(10):28–37.

11. Tyurin VYu, Yaohuan W, Prishchenko AA, Shpakovsky DB, Gracheva YuA, Antonenko TA, et al. Complexes of organotin compounds with bis- and trisphosphonate derivatives of 2,6-di-tert-butylphenol having antioxidant activity. Russian Chemical Bulletin. 2015 Jun 1;64(6):1419–29.

12. Hadi S, Qudus HI, Wattana-Amorn P. The Potency Study of Organotin (IV) 3-Nitrobenzoate Compounds as Antimalarial Agents. In IOP Publishing; 2019. p. 012012.

13. Hansch C, Verma RP. Larvicidal activities of some organotin compounds on mosquito larvae: A QSAR study. European Journal of Medicinal Chemistry. 2009 Jan;44(1):260–73.

14. Hadi S, Noviany N, Rilyanti M. In vitro antimalarial activity of some organotin (IV) 2-nitrobenzoate compounds against Plasmodium falciparum. Macedonian Journal of Chemistry and Chemical Engineering. 2018;37(2).

15. Hadi S, Fenska MD, Noviany N, Satria H, Simanjuntak W, Naseer MM. Synthesis and antimalarial activity of some triphenyltin (IV) aminobenzoate compounds against Plasmodium falciparum. Main Group Metal Chemistry. 2021;44(1):256–60.

16. Roner MR, Carraher Jr CE, Shahi K, Barot G. Antiviral activity of metal-containing polymers—Organotin and cisplatin-like polymers. Materials. 2011;4(6):991–1012.

17. Roner MR, Carraher CE, Miller L, Mosca F, Slawek P, Haky JE, et al. Organotin polymers as antiviral agents including inhibition of Zika and Vaccinia viruses. Journal of

Inorganic and Organometallic Polymers and Materials. 2020;30(3):684–94.

18. Rehman W, Badshah A, Khan S. Synthesis, characterization, antimicrobial and antitumor screening of some diorganotin (IV) complexes of 2-[(9H-Purin-6-ylimino)]-phenol. European journal of medicinal chemistry. 2009;44(10):3981–5.

19. Hadi S, Rilyanti M, Suharso S. In vitro activity and comparative studies of some organotin (iv) benzoate derivatives against leukemia cancer cell, l-1210. Indonesian Journal of Chemistry. 2012;12(2):172–7.

20. Syed Annuar SN, Kamaludin NF, Awang N, Chan KM. Cellular basis of organotin (IV) derivatives as anticancer metallodrugs: a review. Frontiers in chemistry. 2021;522.

21. Singh R, Chaudhary P, Kaushik N. A Review: Organotin compounds in corrosion inhibition. Reviews in Inorganic Chemistry. 2010;30(4):275–94.

22. Hadi S. The anticorrosion activity of dibutyltin (IV) and diphenyltin (IV) dihydroxybenzoate compounds towards HRP mild steel in NaCl. Journal of Chemical and Pharmaceutical Research. 2016;8(8):975–80.

23. Hazani NN, Mohd Y, Ghazali SAISM, Farina Y, Dzulkifli NN. Electrochemical studies on corrosion inhibition behaviour of synthesised 2-acetylpyridine 4-ethyl-3-thiosemicarbazone and its Tin (IV) complex for mild steel in 1 M HCl solution. Journal of Electrochemical Science and Technology. 2019;10(1):29–36.

24. Hadi S, Lestari S, Suhartati T, Qudus HI, Rilyanti M, Herasari D, et al. Synthesis and comparative study on the antibacterial activity organotin (IV) 3-hydroxybenzoate compounds. Pure and Applied Chemistry. 2021;93(5):623–8.

25. Hadi S, Simanjuntak W, Qudus HI, Yandri Y, Herasari D. In vitro antimicrobial activity study of some organotin (IV) chlorobenzoates against Staphylococcus aureus and Escherichia coli. Journal of Advanced Pharmacy Education & Research [JAPER]. 2021;11(2):17–22.

26. Hadi S, Qudus HI, Simanjuntak W. In vitro antibacterial activity of some of dibutyltin (IV) chlorobenzoate derivatives against Staphylococcus aureus and Escherichia coli. ARPN Journal of Engineering and Applied Sciences. 2021;16(15):1623–9.

27. Hadi S, Irianti NT, Noviany N. Sintesis, Karakterisasi, dan Uji Aktivitas Antibakteri Senyawa Organotimah (IV) 4-Nitrobenzoat. ALCHEMY Jurnal Penelitian Kimia. 2022;18(1):19–29.

28. Hadi S, Hermawati E, Noviany N, Suhartati T, Yandri Y. Antibacterial activity test of diphenyltin (IV) dibenzoate and triphenyltin (IV) benzoate compounds against Bacillus substilis and Pseudomonas aeruginosa. Asian Journal of Microbiology, Biotechnology & Environmental Sciences. 2018;20(1):113–9.

29. Annissa A, Suhartati T, Yandri Y. Antibacterial Activity of Diphenyltin (IV) and Triphenyltin (IV) 3-Chlorobenzoate Againts Pseudomonas aeruginosa and Bacillus subtilis. Oriental Journal of Chemistry. 2017;33(3):1133–9.

30. Hadi S, Suhartati T, Noviany N, Pandiangan KD, Yandri Y, Simanjuntak W, et al. Disinfecting activity of some diphenyltin (IV) benzoate derivative compounds. Pure and Applied Chemistry. 2022;

31. Chan ECS, Pelczar MJ. Instructor's manual to accompany Elements of microbiology. McGraw-Hill Book Company; 1981.

32. Lorian V, editor. In: Antibiotics in Laboratory Medicine. Baltimore: William and Wilkins co.; 1980. p. 1–22.

33. Lorian V, editor. In: Antibiotics in Laboratory Medicine. Baltimore: William and Wilkins co.; 1980. p. 170–8.

34. Lorian V, editor. In: Antibiotics in Laboratory Medicine. Baltimore: William and Wilkins co.; 1980. p. 511–2.

35. Amsterdam D. In: Antibiotics in Laboratory Medicine. 6th edition. Philadelphia: LWW Publishers; 2014. p. 807.

36. Noviany N, Sialdian D, Setiawan A, Irawan B, Azmi MN, Sutopo H. Bioassay-guided separation approach for characterization of new antibacterial fractions from the stem roots extracts of Archidendron jiringa. Journal of the Turkish Chemical Society Section A: Chemistry. 2021;8(2):391–402.

37. Sulaiman M, Hassan Y, TOK TT, Noundou XS. Synthesis, antibacterial activity and docking studies of benzyl alcohol derivatives. Journal of the Turkish Chemical Society Section A: Chemistry. 2020;7(2):481–8.

EPR-based study to monitor Free Radicals in Treated Silk Fibroin with Anthocyanins

Vefa Atayeva¹* (iD) **, Rasim Aslanov²** (iD)

¹Shaki Regional Scientific Center of Azerbaijan National Academy of Sciences, Shaki, AZ5500, Azerbaijan
²Institute of Biophysics, Azerbaijan National Academy of Sciences, Baku 1141, Azerbaijan

Abstract: Bioactive materials of natural origin have great demand in industry and medicine due to their versatility and useful properties. The main purpose of this work is to prepare biocomposites for the dual purpose of modified silk fibroin (*Bombyx mori* L.), which protects against the destructive effects of bioactive, antioxidant and ultraviolet rays. For this purpose, an aqueous extract of autumn leaves of the anthocyanin-rich smoke tree plant (*Cotinus coggygria* L.) was applied. 2% thiourea solution was used to increase the durability of the modified SF to external influences and for use in textiles. The intensity of free radicals in silk fibroin-anthocyanin (SFA) and silk fibroin-anthocyanin-thiourea (SFAT) biocomposites modified by the Electron Paramagnetic Resonance (EPR) method was studied. Maximum adsorption time was determined 20 minutes and the intensity of free radicals in SFA bio-composite was 80-85% and in SFAT biocomposite 50-55% in relation to silk fibroin untreated. For biomedical use of SFA, the radical scavenger activity kinetics were studied on a UV-2700 spectrophotometer and radical capture activity was calculated: RSA% $_{(bioextract)}$ = 73.52 ± 0.5, RSA% $_{(SF)}$ = 6.42 ± 0.4, RSA% $_{(SFA)}$ = 45.23 ± 0.8

INTRODUCTION

Preparation of eco-friendly biomaterials is one of the important fields in the materials science, industry and technology, medicine as well as for to reduce occurring in the production process harmful garbage and poisonous gases (1). Silk fibroin (SF) obtained from mulberry silkworm are wide using in the weaving industry and medicine as biomaterial. This is related to its fibrillar structure. In addition, silk fibroin materials have disadvantage peculiarity as wrinkling, aging, deformation and degradation due to arising from biocompatibility properties. A lot of attempts have been made for modification and functional of the silk fibroin fibers and silk fibroin cloths arising from market demands for natural and smart materials basing on the supply of raw materials sufficient raw materials in the world. Modification of the silk in form successful may be increase use quality in addition to eliminating internal deficiencies. Hong Liu and other researchers summarized the latest ideas, methodologies, and processing technologies for the surface modification and functionality of silk fibroin, taking into account the application of improved properties of silk fibroin. Based on the results of experimental studies, the researchers hoped that such success would be perspective in the field of application of both textiles and biomaterials. The largely application of silk is related to its luster properties, effective mechanical indicators, biocompatibility, and controllable degradation. SF fibers have superior mechanical properties with a breaking elongation ~ 15%, a specific tensile strength ~ 0.5 GPa, and a breaking energy of ~ 62.104 J kg⁻¹. There are 3 main kinds of secondary structures, namely: α-helix, β-sheet, and random coil. These structures can move from one structure to another as a result of external influences, such as temperature changes, pressure and chemical effects (2-5).

One of the most widespread and important representatives of fibrillar proteins is silk fibroin. Silk

fibroin consists of two phases, crystalline and amorphous. About 60% of content of the silk fibroin form the crystalline phase (Gly-Ala-Gly-Ala-Gly-Ser)n , and the rest amorphous phase. The formation of the crystalline and amorphous phases depends on the amino acid sequences. The fact that the crystalline phase is hydrophobic and the amorphous phase is hydrophilic also depends on the amino acid sequences. The content of *Bombyx mori* silk fibroin (in moles %) is mainly characterized by the predominance of five amino acids: Gly (42.9%), Ala (30.0%), Ser (12.2%), Tyr (4.8%) and Val (2.5) %) (6). *Bombyx mori* fibroin consists of two heavy-H chain and light-L chain proteins bound by disulfide bonds, as well as a glycoprotein called P25. The molecular weight of the H-chain is about 350 kDa, which is higher than that of the L-chains (26 kDa) and P25 (30 kDa). The H-heavy, L-light and P25 chains have a 6: 6: 1 molar mass ratio (7, 8). Anti-parallel β-sheets bound by hydrogen bonds form the second structure of fibroin. The predominance of β-structure in fibroin gives high mechanical strength to the materials obtained from it, and the amorphous part of the protein gives elasticity to fibroin. Silk fibers are superior to Kevlar (para-aramid), one of the best synthetic materials, in terms of their strength. Silk fibroin with a tensile strength of 740 MPa is widely used in the manufacture of hydrogels, various transparent layers, fibrous sponges, pipes, thin layers, and microlayers. Another advantage of fibroin-derived materials is that their mechanical strength is different from that of chemically-derived materials due to their low disintegration rate. They also indicate very good biocompatibility, even when implanted in living tissues (9).

Smoke tree is not only decorative, but also rich in anthocyanins (10). Anthocyanins occur naturally in plants in the form of glycosides, in the position bound glucose, galactose, rhamnose, xylose, or arabinose with the aglycone nucleus. Anthocyanins carry a positive charge in an acidic solution unlike other flavonoids. It dissolves well in water and is usually colored blue, purple, or red, depending on the pH and the presence of chelate-forming metal ions. Deglycosylation or aglycone forms of anthocyanins are known as anthocyanidins. The sugar components of anthocyanins are generally bound to the anthocyanin ring by the hydroxyl group in position 3 of the C-ring. The radical scavenging (antioxidant) activity of anthocyanins are mainly due to the presence of hydroxyl groups in the position 3 of the C ring and at the same time in the positions 3, 4 and 5 of the B ring of the molecule (Figure 1). The activity of anthocyanins (aglycones) is superior to the corresponding anthocyanins (glycosides) (11). The degree and position of hydroxylation and alkylation in the B ring, effects their stability and reaction activity, and in thus the antioxidant activity (12).
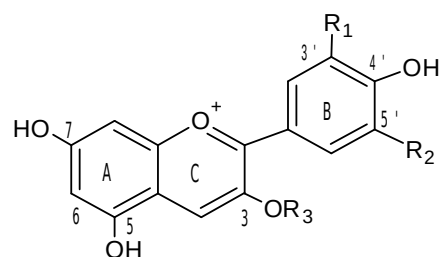
Anthocyanidin (aglycon)	R_1	R_2
Pelargonidin	H	H
Cyanidin	OH	H
Delphinidin	OH	OH
Peonidin	OCH_3	H
Petunidin	OCH_3	H
Malvidin	OCH_3	OCH_3

R_3=H or Glycoside

Figure 1: General structure of anthocyanins.

Free radicals are formed in living systems by various biochemical ways, serious oxidative effect to biomolecules and cause diseases. Indian researchers have confirmed the use of fenugreek-silk fibroin biocomposites nano-fibers as antioxidant scaffolds in wound healing applications. Fibroin scaffolds indicate the best porosity and high biocompatibility and can support better cell adhesion and proliferation. In vivo wound healing researches have indicated that they increase the rate of wound healing and collagen formation (13). Oguz Bayraktar and other researchers have proved that silk fibroin is a promising adsorbent for polyphenols based on its hydrophobic. The researchers confirmed the adsorption of antioxidant polyphenols in olive leaf on silk fibroin by FTIR. Modified silk fibroin has been shown to have antioxidant and antimicrobial activity (14).

The above-mentioned Turkish researchers made a comparative analysis of the adsorption process of silk fibroin from water and 70% ethanol extract of rutin and oleuropein in olive leaves. Achieved higher results in aqueous extract (15).

Antioxidant and antimicrobial active pads have been developed from the interaction of pomegranate peel powder and SF solution (16). Ethyl acetate extract of smoke tree leaves has been used in both biomedical research and the development of anti-cancer therapeutic strategies and has yielded high results (17). Researchers Halil Aksoy and others have used diabetic wounds on rats using from bioextract of smoke tree leaves extracted with 96% ethanol and have proven effective (18).

The main goal of this study was to improve the bioactive properties of SF with aqueous bioextract of autumn leaves with rich in anthocyanins. Because anthocyanins accumulate in the vacuoles of leaf cells, they dissolve well in water (19) and are better

extracted with water (15). The ecological usefulness and economic efficiency of water make it possible to use water as a solvent. The presented article determined the optimal time for joint processing of SF and anthocyanin pigments, had been studied the radical scavenger activity and kinetics of the obtained bioextract and biocomposite.

MATERIALS AND METHODS

Sample Preparation

The cocoon of SZEM-4 mulberry silkworm breed which it is belong *Bombyx mory* family, was removed from sericin according to accepted protocol (20). The degummed silk fibroin fibers have washed initially with tap water and in the end distilled water, and have dried at 25-30 °C. Eight silk fibroin samples weighing 0.4 g and one control sample for comparison have prepared for dyeing with smoke tree autumn leaf extract.

Getting of dye, adsorption process

The red leaves collected to extract the dye from autumn leaves of the smoke tree were dried until constant weight. The extracts were obtained by brew of ground leaves and distilled water in volume ratio of 2:1 at a temperature of 60 °C for 4 hours. From this extract, anthocyanins have treated with silk fibroin fibers at different times (15,21), and after the treatment process, the samples have been dried at room temperature. 4 samples have been taken from the obtained biocomposites and in 2% aqueous solution of thiourea ($CS(NH_2)_2$) for 30 minutes have been fixed.

Measurement in EPR

One of the most important aspects of EPR spectroscopy is to determine the concentration of radical species in special biological systems (22). All EPR spectra have been measured at room temperature using an ELEXSYS E580 spectrometer manufactured by Bruker. The G factors of free radicals have determined using the software provided with the device. The value of the G-factor is related not only to the electronic condition, but also to anisotropy (23).

Preparation of SF and SFA solution

SF and SFA were dissolved in LiBr (Sigma-Aldrich, USA) solution (9.3 M) at 60 °C for 4-5 h. The mixture solutions were dialyzed for 24 hours and centrifuged in Centrifuge 4500 rpm at 4 °C, 20 minutes, the concentration of both solutions was adjusted to 15 μM by using a UV-Vis spectrophotometric method (24).

Radical Scavenging Activity (RSA)

The free radical scavenging activity was evaluated by the 2,2-diphenyl-1-picrylhydrazyl (DPPH) (Sigma-Aldrich, USA) assay. In methanol, 60 μM 2,2-diphenyl-1-picrylhydrazyl (DPPH) solution were prepared and noted absorbance at 515 nm. The ability of the bioextract, SF and SFA biocomposite to act as free radical scavengers against DPPH radical was tested spectrophotometrically with UV-2700 spectrophotometer (Shimadzu) by measuring. The DPPH radical scavenging activity was calculated using the following equation: $RSA\% = (A_0 - A_s)/A_0$ (12).

RESULTS AND DISCUSSION

The adsorption process of SF samples in the bioextract was carried out at different times in pH = 4.5, T = 80 ± 5 °C and in the same concentration condition, in separately test tubes. Four samples dried at 20 °C were fixed in 2% thiourea solution for 30 min and were again dried. Finally, all samples were thoroughly washed in distillated water, dried and were prepared for EPR measurements. The spectra of the samples were monitored and the parameters were analyzed.

The frequency and the intersection of the magnetic field (3555 Gauss) that causes absorption are highly dependent on the nature of the radical and the concentration of the radicals (25). The values of the G-factors in the measured spectra have shown in Table 1. The value of the G-factor has determined on the basis of a program provided by Bruker.

Some researchers have determined with EPR using that free radicals in sik fibroin are stable state. Differential signals in EPR are caused by tyrosyl radicals. Tyrosyl radicals are present in the hydrophobic part and are functional for modification (26). In Figures 2 and 3, the amplitude of the EPR spectra of both treated with anthocyanin-rich extract silk fibroins, treated and $CS(NH_2)_2$ fixed fibroins show that, concentrations of free radicals characterized by the highest signal intensity in treated silk fibroin for 20 minutes and the weakest in treated silk fibroin for 40 minutes. Compared to the intensity of free radicals of untreated SF, the intensity of free radicals in SF treated with anthocyanins rich extract increased by 80-85% for 20 minutes (Figure 2). But in treated and fixed silk fibroins, this value is 50-55% (Figure 3). Experiments have shown that the intensity of EPR signals increases when silk modifies fibroin fibers. This helps to understand the function and application of free radicals in silk fibroids for biocomposites.

Table 1: G-factor of the samples.

Sample	Adsorption time, min.	G-factor
Silk fibroin		2.0049
Silk fibroin+anthocyanins (SFA)	10	2.0053
	20	2.0053
	30	2.0052
	40	2.00504
Silk fibroin+anthocyanins+CS(NH$_2$)$_2$ (SFAT)	10	2.00513
	20	2.00505
	30	2.00491
	40	2.00473
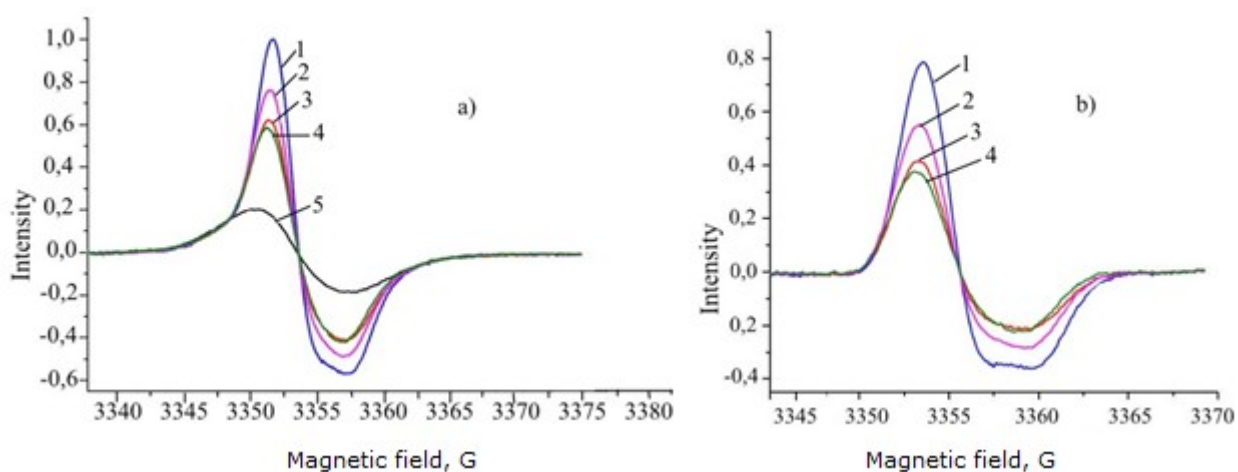
Figure 2: a) EPR spectra of silk fibroin treated with extract in various times: 1: 20 minutes, 2: 30 minutes, 3:10 minutes, 4: 40 minutes treated silk fibroin, 5: untreated silk fibroin. **b)** EPR spectra of anthocyanins obtained after subtracting untreated silk fibroin data from treated silk fibroin data in various times: 1: 20 minutes, 2: 30 minutes, 3: 10 minutes, 4: 40 minutes.
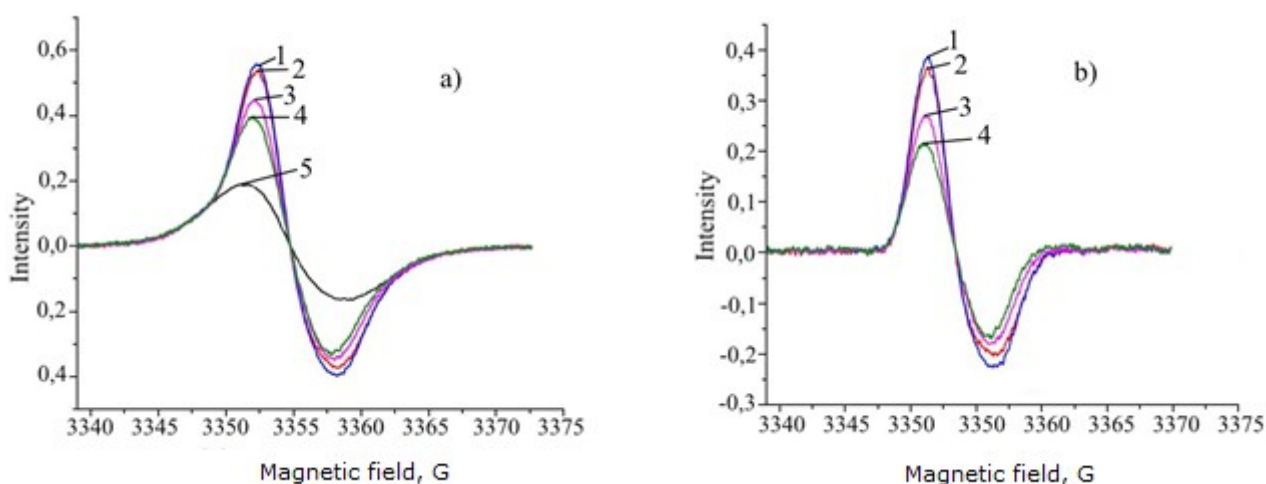
Figure 3: a) EPR spectra of silk fibroin treated with extract and fixed in various times:1: 20 minutes, 2: 30 minutes, 3: 10 minutes, 4: 40 minutes treated silk fibroin, 5: untreated silk fibroin **b)** EPR spectra of anthocyanins obtained after subtracting untreated silk fibroin data from treated and fixed silk fibroin data in various times: 1: 20 minutes, 2: 30 minutes, 3: 10 minutes, 4: 40 minutes.

The treatment process is based on the adsorption process. Since adsorption is a chemical (irreversible) and physical (reversible) process, van der Waals forces involve in physical adsorption, and chemical binding (covalent, hydrogen) occurs between fibroin and anthocyanins in chemical adsorption. In a range of 10-20 minutes, physical and chemical adsorption occur in parallel, in 30-40 minutes ranges only physical adsorption occur (27-29). The intermolecular H bonds and covalent bonds have been described in Figure 4 (30,31).

a)

b)
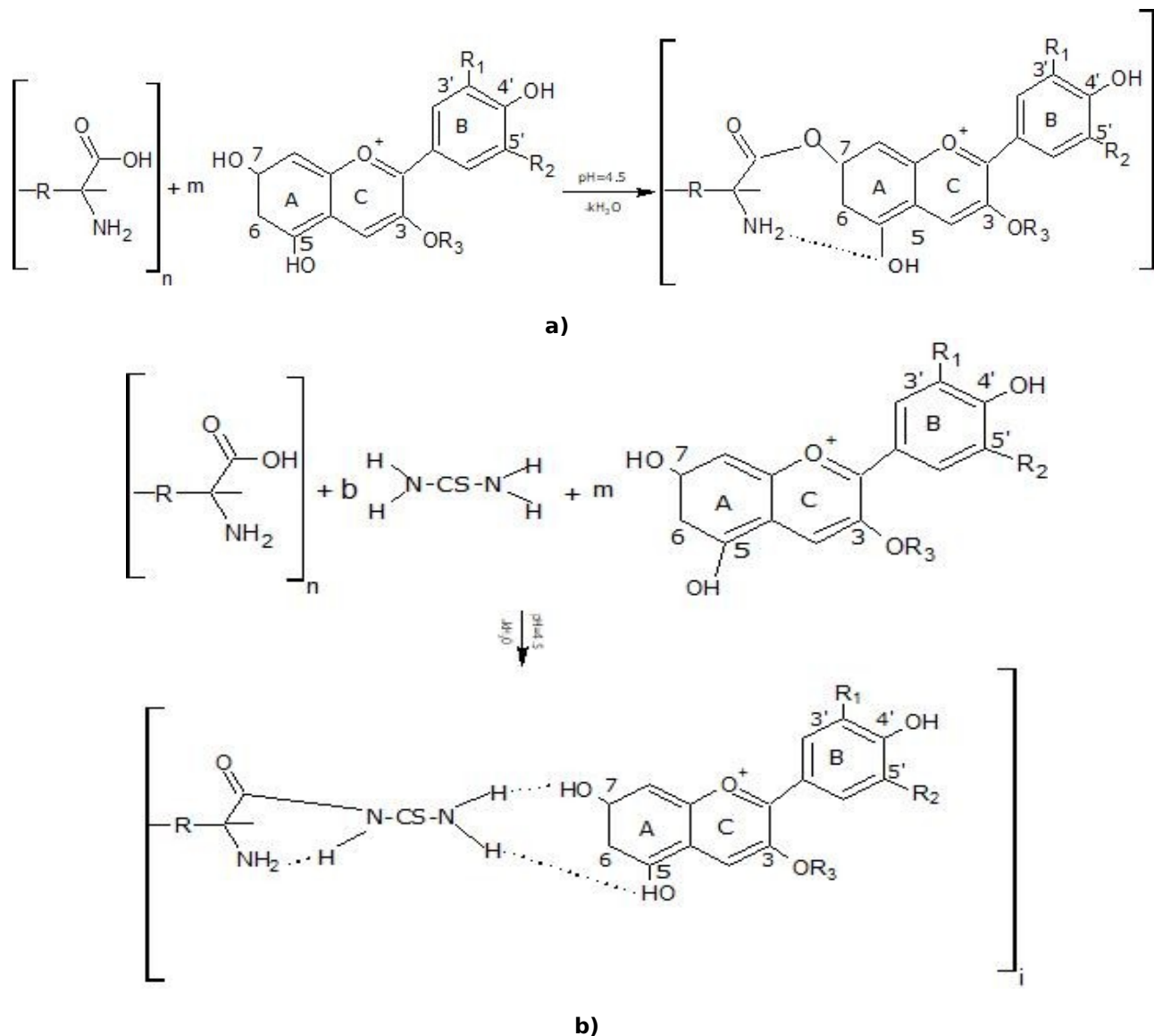
Figure 4: a) H-bond and covalent bond between anthocyanin and fibroin molecules, **b)** H- bond and covalent bond between anthocyanin, thiourea, and fibroin molecules.

The EPR analysis showed that the intensity of free radicals in the SFAT biocomposite was lower than that of the SFA. 20 minutes treated SFs were used to achieve the define goals. The resistance of SFAT biocomposite to detergents and sunlight, and SFA to 95% ethanol solution was tested for 24 months. These tests showed that the application of SFAT in textiles and SFA in biomedicine is considered appropriate. The SFA biocomposite can be stored in ethanol without any changes.

One of the goals of this study was to obtain a natural fibroin-based bioactive, antioxidant, antimicrobial biomaterial. For this purpose, the free radical capture activity of bioextract, SF and SFA solutions by DPPH was analyzed on a UV-2700 spectrophotometer. In a cuvette, 2950 µL of 60 µM methanolic DPPH solution was mixed with 50 µL of bioextract to start the reaction, kinetics was monitored for 30 minutes. The experiment was repeated for SF and SFA solutions with same way and in result: Bioextract > SFA > SF (Figure 5) (32). Then, absorbance of mixture solution was measured

at end of each process. The absorption data at 515 nm were recorded and the RSA (%) were calculated: RSA%$_{(bioextract)}$=73.52±0.5, RSA%$_{(SF)}$=6.42±0.4 and RSA%$_{(SFA)}$=45.23±0.8
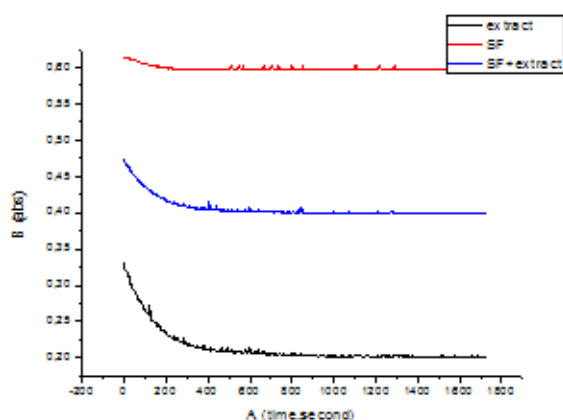
Figure 5: Kinetics of samples on UV-Vis spectophotometer.

CONCLUSION

It was determined in result of research that the free radical scavenger activity of silk fibroin increased from RSA% $_{(SF)}$ = 6.42 ± 0.4 to RSA% $_{(SFA)}$ = 45.23 ± 0.8 using an anthocyanin-rich bioextract obtained from the autumn leaves of the smoke tree.

The EPR method is determined that the intensity of free radicals and the amount of anthocyanins were higher in silk fibroins adsorbed for 20 minutes at a temperature of 80 ± 5 °C.

SFA can be used in biomedicine due to the intensity of free radicals, RSA and long-term (24 months) resistance in 95% ethanol and SFAT can be used in textiles due to resistance to detergents and sunlight.

EPR spectra showed that, according to the laws of the adsorption process, the combination between silk fibroin and anthocyanins in the autumn leaf extract of the smoke tree is obtained by hydrogen, covalent bonding and van-der-Waals forces.

REFERENCES

1. Hou TC, Jeng SC. Application of Bombyx mori Silk Fibroin Films for Liquid-Crystal Devices. ACS Appl Bio Mater [Internet]. 2020 Dec 21 [cited 2022 Sep 18];3(12):8575–80. Available from: <URL>.

2. Li G, Liu H, Li T, Wang J. Surface modification and functionalization of silk fibroin fibers/fabric toward high performance applications. Materials Science and Engineering: C [Internet]. 2012 May [cited 2022 Sep 18];32(4):627–36. Available from: <URL>.

3. Sun W, Gregory DA, Tomeh MA, Zhao X. Silk Fibroin as a Functional Biomaterial for Tissue Engineering. IJMS [Internet]. 2021 Feb 2 [cited 2022 Sep 18];22(3):1499. Available from: <URL>.

4. Patil PP, Reagan MR, Bohara RA. Silk fibroin and silk-based biomaterial derivatives for ideal wound dressings. International Journal of Biological Macromolecules [Internet]. 2020 Dec [cited 2022 Sep 18];164:4613–27. Available from: <URL>.

5. Murugesh Babu K, Sahana N, Anitha DV, Kavya BS. Silk fibroin coated antimicrobial textile medical products. The Journal of The Textile Institute [Internet]. 2021 Aug 3 [cited 2022 Sep 18];112(8):1199–207. Available from: <URL>.

6. Cilurzo F, Gennari CGM, Selmin F, Marotta LA, Minghetti P, Montanari L. An investigation into silk fibroin conformation in composite materials intended for drug delivery. International Journal of Pharmaceutics [Internet]. 2011 Jul [cited 2022 Sep 18];414(1–2):218–24. Available from: <URL>.

7. Fu C, Shao Z, Fritz V. Animal silks: their structures, properties and artificial production. Chem Commun [Internet]. 2009 [cited 2022 Sep 18];(43):6515. Available from: <URL>.

8. Shera SS, Kulhar N, Banik RM. Silk and silk fibroin-based biopolymeric composites and their biomedical applications. In: Materials for Biomedical Engineering [Internet]. Elsevier; 2019 [cited 2022 Sep 18]. p. 339–74. Available from: <URL>.

9. Huseynova E, Hetemzade N, Aslanov R, Qasımov O. Polimerlerin mexaniki mohkemlik xasselerini olcmek ucun universal qurgu. Azerbaijan journal of Physics. 2016;

10. Wang F, Xing S, Ji Y, Yan L, Liu F, Dong Y, et al. Leaf structural reddening in smoke tree and its significance. Urban Forestry & Urban Greening [Internet]. 2015 [cited 2022 Sep 18];14(1):80–8. Available from: <URL>.

11. Wang LS, Stoner GD. Anthocyanins and their role in cancer prevention. Cancer Letters [Internet]. 2008 Oct [cited 2022 Sep 18];269(2):281–90. Available from: <URL>.

12. Kähkönen MP, Heinonen M. Antioxidant Activity of Anthocyanins and Their Aglycons. J Agric Food Chem [Internet]. 2003 Jan 1 [cited 2022 Sep 18];51(3):628–33. Available from: <URL>.

13. Selvaraj S, Fathima NN. Fenugreek Incorporated Silk Fibroin Nanofibers—A Potential Antioxidant Scaffold for Enhanced Wound Healing. ACS Appl Mater Interfaces [Internet]. 2017 Feb 22 [cited 2022 Sep 18];9(7):5916–26. Available from: <URL>.

14. Altıok E, Bayçın D, Bayraktar O, Ülkü S. Isolation of polyphenols from the extracts of olive leaves (Olea europaea L.) by adsorption on silk fibroin. Separation and Purification Technology [Internet]. 2008 Sep 1 [cited 2022 Sep 18];62(2):342–8. Available from: <URL>.

15. Bayçın D, Altıok E, Ülkü S, Bayraktar O. Adsorption of Olive Leaf (Olea europaea L.) Antioxidants on Silk Fibroin. J Agric Food Chem [Internet]. 2007 Feb 1 [cited 2022 Sep 18];55(4):1227–36. Available from: <URL>.

16. Giannelli M, Lacivita V, Posati T, Aluigi, Conte A, Zamboni R, et al. Silk Fibroin and Pomegranate By-Products to Develop Sustainable Active Pad for Food Packaging Applications. Foods. 2021;10:2921.

17. Iliev I, Ivanov I, Todorova K, Dimitrova M. Effects of a Cotinus coggygria ethyl acetate extract on two human normal cell lines. Acta morphol anthropol. 2020;27(3–4):25–9.

18. Aksoy H, Sen A, Sancar M, Sekerler T, Akakin D, Bitis L, et al. Ethanol extract of Cotinus coggygria leaves accelerates wound healing process in diabetic rats. Pharmaceutical Biology [Internet]. 2016 Nov [cited 2022 Sep 18];54(11):2732–6. Available from: <URL>.

19. Poustka F, Irani NG, Feller A, Lu Y, Pourcel L, Frame K, et al. A Trafficking Pathway for Anthocyanins Overlaps with the Endoplasmic Reticulum-to-Vacuole Protein-Sorting Route in Arabidopsis and Contributes to the Formation of Vacuolar Inclusions. Plant Physiology [Internet]. 2007 Dec 4 [cited 2022 Sep 18];145(4):1323–35. Available from: <URL>.

20. Aslanov RB, Dashdemirova LM, Alekperov OZ, Abdurahimov AR, Gasymov OK. Dynamics of Proteins by Thermal Decay of Free Radicals Induced by Ultraviolet Irradiation. Journal of Spectroscopy [Internet]. 2018 Jun 28 [cited 2022 Sep 18];2018:1–6. Available from: <URL>.

21. Chandrasekhar J, Madhusudhan MC, Raghavarao KSMS. Extraction of anthocyanins from red cabbage and purification using adsorption. Food and Bioproducts Processing [Internet]. 2012 Oct [cited 2022 Sep 18];90(4):615–23. Available from: <URL>.

22. Tena N, Martín J, Asuero AG. State of the art of anthocyanins: Antioxidant activity, sources, bioavailability, and therapeutic effect in human health. Antioxidants. 2020;9(5):451.

23. Zhao P. EPR - Interpretation [Internet]. Libretexts, Chemistry; 2022. Available from: <URL>.

24. Rockwood DN, Preda RC, Yücel T, Wang X, Lovett ML, Kaplan DL. Materials fabrication from Bombyx mori silk fibroin. Nat Protoc [Internet]. 2011 Oct [cited 2022 Sep 18];6(10):1612–31. Available from: <URL>.

25. Davies MJ. Detection and characterisation of radicals using electron paramagnetic resonance (EPR) spin trapping and related methods. Methods [Internet]. 2016 Oct [cited 2022 Sep 18];109:21–30. Available from: <URL>.

26. Deng YB, Cai JH, Zhou P. Naturally Stable Free Radical in the Silk Fibroin and Its Structure Environment Studied by EPR and DFT. Spectroscopy Letters [Internet]. 2012 May [cited 2022 Sep 18];45(4):285–95. Available from: <URL>.

27. Rastogi S, Kandasubramanian B. Progressive trends in heavy metal ions and dyes adsorption using silk fibroin composites. Environ Sci Pollut Res [Internet]. 2020 Jan [cited 2022 Sep 18];27(1):210–37. Available from: <URL>.

28. Hu H, Xu K. Physicochemical technologies for HRPs and risk control. In: High-Risk Pollutants in Wastewater [Internet]. Elsevier; 2020 [cited 2022 Sep 18]. p. 169–207. Available from: <URL>.

29. Bedelbeyli-Agdamski T. Fiziki ve kolloid kimya. Baku, Azerbaijan; 2017.

30. Steppeler F, Iwan D, Wojaczyńska E, Wojaczyński J. Chiral Thioureas—Preparation and Significance in Asymmetric Synthesis and Medicinal Chemistry. Molecules [Internet]. 2020 Jan 18 [cited 2022 Sep 18];25(2):401. Available from: <URL>.

31. Prabhu K, Bhute AS. Plant based natural dyes and mordants: A Review. J Nat Prod Plant Resour. 2012;2(6):649–64.

32. Sanna D, Delogu G, Mulas M, Schirra M, Fadda A. Determination of Free Radical Scavenging Activity of Plant Extracts Through DPPH Assay: An EPR and UV–Vis Study. Food Anal Methods [Internet]. 2012 Aug [cited 2022 Sep 18];5(4):759–66. Available from: <URL>.

Phytochemical Investigation of *Rumex Abyssinicus* Root Barks and *In Vitro* Evaluation of Its Antibacterial Activities

Zelalem Abdisa[1]*, Zelalem Gudeta[2]

[1]Wollega University, Department of Chemistry, Nekemte, Ethiopia
[2]Metu College of Teacher Education, Department of Chemistry, Metu, Ethiopia

Abstract: Different parts of *Rumex abyssinicus* have been used as a traditional medicine by local community in Ethiopia. Root and root barks of this plant are used traditionally by people of Ilu Ababor (Ethiopia) to lower blood pressure, heal wound and treat stomach ache. This paper presents the isolation and characterization of compound from the root barks of *Rumex abyssinicus* and evaluation of its antibacterial activity. The powdered plant material was sequentially extracted using *n*-hexane, chloroform, acetone and methanol. The crude extracts and the isolated compound (**RA-3**) were evaluated against four bacterial strains: *Staphylococcus aureus*, *Escherichia coli*, *Pseudomonas aeruginosa* and *Salmonella thyphimurium* as a potential antibacterial agent. Both the acetone and methanol crude extracts showed promising inhibitory effects against all the tested bacterial strains. The strongest inhibitory activity was observed for acetone extract against *Staphylococcus aureus* (21 mm) as compared to the standard Gentamicin (25 mm). The isolated compound showed inhibitory effect only on *Staphylococcus aureus* and *Pseudomonas aeruginosa*. The acetone extract was subjected to column chromatographic separation and resulted in the isolation of one pure compound (**RA-3**). The structure of this compound was characterized with the help of spectroscopic methods (IR and NMR). The isolated compound was characterized as Emodin based on spectroscopic data and in comparison with literature reports.

INTRODUCTION

Plants contain chemical compounds called natural products that almost every plant can produce. Although any biological molecule is a natural product, the term is more precisely used for secondary metabolites which are not strictly required for the survival of the organism (1). They are derived by unique biosynthetic pathways from primary metabolites and intermediates. In Ethiopia, different plant varieties are used in the traditional health care system and remain to be the main resource of treatment for a large majority (80%) of the people (2).

Rumex abyssinicus (*R. abyssinicus*), which belongs to the family polygonaceae, is a perennial herb, up to 3m tall. It is locally called Dhangaggoo in Afan Oromo (Figure 1). It is one of the medicinal plants used in Ethiopia and is a common weed of cultivated lands or disturbed grounds ranging from North Africa to Ethiopia (3). Different parts of this plant, including root and root bark are used as a traditional medicine among Ilu Ababor people (Ethiopia) to lower blood pressure, heal wound and treat stomach ache. The rhizomes are used to treat malaria, gonorrhea, hepatitis, constipation, hypertension, migraine, rheumatism, breast cancer, stomach distention, earache, liver diseases, hemorrhoids, typhus, rabies and wound (4-7). Decoction of leaf or root powder of the plant was

taken as vermifuge. The rhizomes yield a yellow and red dye which is also used to impart a red color to the feet and hands of women of this area. The

rhizomes are also used to refine butter and give it a rich yellow color.

Figure 1: Aerial part of *Rumex abyssinicus*.

Getie *et al*., (8) reported that the 80% methanol extract of the rhizomes of *R. abyssinicus* demonstrated antimicrobial and *in vitro* anti-inflammatory activities. Similarly, extracts of the plant have been proved to have diuretic and analgesic (3), and antimalarial (9) activities. *Rumex* species are known to be rich in anthraquinones, particularly in the roots (10). Betulone and Oleic acid were recently isolated from acetone extracts of the roots of *Rumex abyssinicus* (11). This research reports the phytochemical investigation of the extracts from the root bark of *R. abyssinicus* and evaluation of the antibacterial activities of the crude extracts as well as the purified compound.

EXPERIMENTAL SECTION

Plant material
Botanical identification was made by Mr. Etana Tolesa (a botanist) and a specimen was deposited (voucher number Ze01) in the Herbarium of Department of Biology, Wollega University. Then after authentication, fresh root barks of *Rumex abyssinicus* were collected from Oromia region around Ilu Ababor Zone, Metu College of Teachers' Education campus. The collected plant root barks were washed with distilled water and dried under shade in laboratory at room temperature. The dried root bark was ground with manual grinder so as to enhance effective contact of solvent with plant material.

Materials/Instruments
Pestle and mortar was used to powder the dried plant material. Rotary evaporator (RE 52-F) was employed to remove solvents from extracts. Thin-layer chromatography (TLC) analysis was performed on alumina plates precoated with silica gel (Merck 60 F_{254}). Spots were determined using UV lamp

under UV radiation (λ_{max} = 254 and λ_{max} = 365 nm). Infrared (IR) spectra (KBr) were obtained from Perkin-Elmer BX infrared spectrophotometer (400-4000 cm^{-1}). One dimensional nuclear magnetic resonance (NMR) spectra were recorded on Bruker 400 MHz Avance spectrometer at Addis Ababa University, Ethiopia using DMSO-d_6 as a solvent.

Chemicals and Reagents
Solvents used for extraction were *n*-hexane, chloroform, acetone and methanol. Petroleum ether and ethyl acetate were utilized for elution. Column was packed with silica gel (100-120 mm mesh size). Chromatograms were visualized on TLC by spraying with 10% H_2SO_4 and heating on hot plate. Dimethyl sulfoxide (as a solvent), Mueller Hinton agar, nutrient broth and standard antibiotic drug gentamicin were used as a culture media during antibacterial test. All the chemicals and reagents of analytical grade were used.

Extraction and Isolation
Air dried and powdered root barks of *Rumex abyssinicus* (670 g) were sequentially extracted with *n*-hexane, chloroform, acetone and methanol by cold maceration method. The powdered material was socked with *n*-hexane (3350 mL) for 72 hours with occasional shaking and filtered first using cotton plug followed by Whatmann No.1 filter paper and concentrated by means of rotary evaporator. The marc was air dried and then socked with similar volume of chloroform for 72 hours. The extract was again filtered and concentrated. The same steps were repeated for acetone and methanol.

The crude acetone extract of *R. abyssinicus* root barks was subjected to chromatographic separation using petroleum ether/ethyl acetate solvent combinations. Crude extract (2.5 g) was adsorbed

onto 7 g of silica gel. The dry adsorbed sample was applied onto the top of column that was packed with 80 g silica gel (100-120 mesh size) slurry dissolved in petroleum ether. The column was eluted with petroleum ether and ethyl acetate mixture in different ratio with increasing polarity (Table 1).

Table 1: Column purification for acetone extract of *Rumex abyssinicus root* bark.

Fractions	Solvent ratio	Solvent used (mL)
F1-F17	Pet. ether 98:2 ethyl acetate	340
F18-F34	Pet. ether 95:5 ethyl acetate	340
F35-F51	Pet. ether 90:10 ethyl acetate	340
F52-F68	Pet. ether 85:15 ethyl acetate	340
F69-F85	Pet. ether 80:20 ethyl acetate	340
F86-F102	Pet. ether 75:25 ethyl acetate	340
F103-F119	Pet. ether 70:30 ethyl acetate	340
F120-F136	Pet. ether 65:35 ethyl acetate	340
F137-F152	Pet. ether 60:40 ethyl acetate	320

A total of 152 fractions each with 20 mL were collected. Fractions F120-F136 were combined and purified on silica gel column chromatography eluting with petroleum ether: ethyl acetate (65:35) and a total of 52 (f1-f52) fractions were collected each with 20 mL. Fractions f23-f52 were combined, solvent removed and resulted in an orange crystal solid (**RA-3**; 25mg) with R_f value of 0.57 (petroleum ether/ethyl acetate; 65:35).

Antibacterial assay

Test organisms
Four pathogenic bacterial strains, one Gram-positive (*Staphylococcus aureus* (ATCC25923)) and three Gram-negative (*Pseudomonas aeruginosa* (ATCC27853), *Escherichia coli* (ATCC25922) and *Salmonella typhimurium* (ATCC13311)) were obtained from Department of Biology, Wollega University and used to test the antibacterial activities of the root bark extracts of *R. abyssinicus* using agar well diffusion method (12)*.*

Preparation of test samples
The test solutions were prepared by dissolving known weight of crude extract by serial dilution methods (400, 200, 100 and 50 mg) in 1 mL of Dimethyl Sulfoxide (DMSO) to achieve final stock concentration of 400, 200, 100 and 50 mg/mL, respectively. Stock bacterial cultures were maintained at 4 °C on slants of nutrient agar. Active cultures for experiments were prepared by transferring a loop full of bacterial cells from the stock cultures to test tubes of Mueller-Hinton broth (MHB) that was incubated without agitation for 24 hrs at 37 °C. A cell suspension of each organism was freshly prepared by transferring isolated colonies selected from a 24 hrs agar plate in to a broth and the suspension turbidity adjusted to a 0.5 McFarland turbidity standard ($1x10^8$ CFU/mL) in sterile saline solution (13). About 100 µL of bacterial suspensions obtained above was spread over the 90 mm Petri dishes containing Mueller-Hinton agar using a sterile cotton swab. Then 20 µL each test solutions were applied onto 6 mm diameter sterile discs, the extract was allowed to diffuse for about 10 minutes and then the plates were kept in incubator at 37 °C for 24 hrs. The antibacterial activity was evaluated by measuring the zone of growth inhibition surrounding the discs in millimeter with ruler (14). Control wells containing neat solvent (DMSO) and gentamicin were run parallel in the same plate as negative and positive controls, respectively.

RESULTS AND DISCUSSION

Extraction yield
The crude extraction yields obtained for *n*-hexane, chloroform, acetone and methanol were 5.06g (0.75%), 8.37g (1.25%), 10.02g (1.52%) and 7.5g (1.16%), respectively (Table 2).

Table 2: Percentage yields of *Rumex abyssinicus* root barks extract.

Extraction solvents	Mass extracted (g)	% Yield
n-hexane	5.06	0.75
Chloroform	8.37	1.25
Acetone	10.02	1.52
Methanol	7.50	1.16

Structural elucidation of RA-3
The IR spectrum of **RA-3** (**S-1**) showed absorption band at 3424 cm^{-1} corresponding to the stretching vibration peak of the hydroxyl (OH) group. The band at 2936 cm^{-1} indicates the C-H stretching of methyl and the bands at 1680 cm^{-1} and 1650 cm^{-1} correspond to the unchelated and chelated carbonyl carbons absorption, respectively.

The ^{1}H-NMR (DMSO-d_6, 400 MHz) of **RA-3** (**S-2**) exhibited two hydroxyl protons at δ 11.87 (OH-1) and δ 11.95 (OH-8), two *meta*-coupled doublets at δ 6.49 (H-7) and δ 6.98 (H-5), two broad singlet signals at δ 7.01(H-2) and δ 7.31 (H-4) and one methyl proton group at δ 2.33. The result is also comparable with the ^{1}H-NMR spectral data of Emodin from literature (15) as shown in Table 3 below.

Table 3:^{1}H-NMR (DMSO-d_6, 400 MHz) data of **RA-3** with reported data of Emodin (15).

Nature/position of Proton	^{1}H-NMR data of **RA-3**(δ_H, ppm)	Reported data for Emodin (2:1 CDCl$_3$ + MeOH-d_4) (δ_H, ppm)
OH-1	11.87 s	-
H-2	7.01 br. s	7.06 s
CH$_3$-3a	2.33 s	2.44 s
H-4	7.31 br. s	7.56 br. s
H-5	6.98 d, J = 2.4 Hz	7.21 d, J = 2.5 Hz
OH-6	-	-
H-7	6.49 d, J = 2.4 Hz	6.58 d, J =2.2 Hz
OH-8	11.95 s	-

The ^{13}C-NMR (DMSO-d_6, 100 MHz) (Table 4, **S-3**) spectrum of **RA-3** showed one methyl carbon signal at δ 21.9 and three oxygenated carbons at δ 161.9 (C-1), δ 165.8 (C-6) and δ 164.7 (C-8). The ^{13}C-NMR also showed two carbonyl carbons at δ 189.9 (C-9) and δ 181.4 (C-10) and one methyl substituted carbon at δ 148.5 (C-3). According to the DEPT-135 spectra (**S-4**) the peaks at δ 135.3 (C-11), δ 109.1 (C-12), δ 113.4 (C-13) and δ 133.0 (C-14) belong to the quaternary carbons and the peaks at δ 124.5 (C-2), δ 121.1 (C-4), δ 109.1 (C-5) and δ 108.0 (C-7) are characteristics of one proton carbons. The chemical shift of carbon at δ 165.8 (C-6) indicates the presence of hydroxyl group on the benzene ring at this position.

Based on the above spectroscopic data and comparison of this data with the literature values, the compound **RA-3** is a hydroxyl anthraquinone known as Emodin (Figure 2). Emodin forms the basis of a purgative anthraquinone derivative and from ancient times has been widely used as a laxative compound (16-17). It is believed that the presence of hydroxyl groups in position 1 and 8 of the aromatic ring system is essential for the purgative action of this compound (18).

Table 4: Comparison of the observed ^{13}C-NMR and DEPT-135 spectroscopic data (DMSO-d_6) of **RA-3** and Emodin (2:1 CDCl$_3$ + MeOH-d_4) from literature (15).

Position of carbon	^{13}C NMR data of **RA-3** (δc in ppm)	DEPT-135 data of **RA-3** (δc in ppm)	^{13}C-NMR of Emodin (δc in ppm)	DEPT-135 of Emodin (δc in ppm)	Appearance
C-1	161.9	-	161.6	-	Quaternary
C-2	124.5	124.5	123.6	123.6	CH
C-3	148.5	-	147.5	-	Quaternary
C-4	121.1	121.1	120.3	120.3	CH
C-5	109.1	109.1	108.7	108.7	CH
C-6	165.8	-	165.6	-	Quaternary
C-7	108.0	108.0	107.6	107.6	CH
C-8	164.7	-	164.7	-	Quaternary
C-9	189.9	-	189.8	-	Quaternary
C-10	181.4	-	181.9	-	Quaternary
C-11	135.3	-	134.8	-	Quaternary
C-12	109.1	-	109.0	-	Quaternary
C-13	113.4	-	113.1	-	Quaternary
C-14	133.0	-	132.7	-	Quaternary
3a-CH$_3$	21.9	21.9	20.9	20.9	CH3
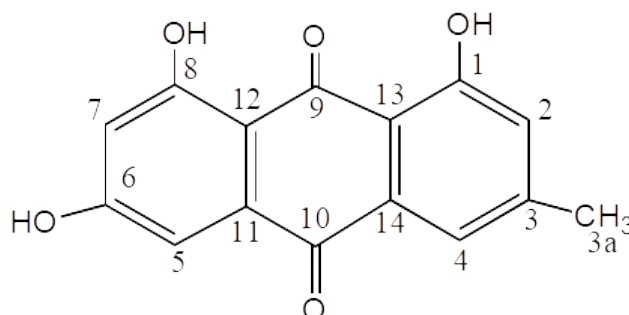
Figure 2: Proposed structure of **RA-3**.

Spectral data

The compound **RA-3** is an orange crystal, R_f 0.57 in petroleum ether: EtOAc (65:35), IRv$_{max}$ (KBr) cm^{-1}: 2936, 1680, 1724, ^{1}H-NMR (DMSO-d_6) at δ 2.33 (3H, s, CH$_3$), 6.49 (1H, d, J = 2.4 Hz, H-7), 6.98 (1H, d, J = 2.4 Hz, H-5), 7.01 (1H, br s, H-2), 7.31 (1H, br s, H-4), 11.87 (OH, s, OH-1), 11.95 (OH, s, OH-8); ^{13}C-NMR (DMSO-d_6) δ: 21.9 (CH$_3$), 108.0 (C-7), 109.1 (C-5, C-12), 113.4 (C-13), 121.1 (C-4), 124.5 (C-2), 133.0 (C-14), 135.3 (C-11), 148.5 (C-3), 161.9 (C-1), 164.7 (C-8), 165.8 (C-6), 181.4 (C-10), 189.9 (C-9).

Antibacterial activity

The *in vitro* antibacterial activity test result of the root barks extract of *R. abyssinicus* and the isolated the compound **RA-3** was shown in Table 5 (**S-5** and **S-6**). The result indicated that the acetone crude extract showed relatively better antibacterial activity followed by methanol extract as compared to the reference drug gentamicin. However, the activity of the pure compound **RA-3** was observed to be lower than the crude extracts. This showed that either the more active ingredient was not isolated or the activity might result from the joint effect of the constituents. *E. coli* and *S. typhimurium* were found to be resistant against **RA-3.** This and the anti-inflammatory effect of *R. abyssinicus* could justify its traditional use for the treatment of several skin diseases (8).

Table 5: Inhibition zone of the crude extracts and **RA-3** (Conc. 100 mg/mL).

Extract/**RA-3**/control	Zone of inhibition (mm)			
	E. coli	*S. aureus*	*S. typhimurium*	*P. aeruginosa*
n-Hexane extract	NA	NA	NA	NA
Chloroform extract	NA	NA	NA	NA
Acetone extract	17	21	19	19
Methanol extract	16	20	13	19
RA-3	NA	14	NA	12
Gentamicin	25	25	21	21
DMSO	NA	NA	NA	NA

NA – not active

CONCLUSION

Herbal remedies have been used for centuries but more recently, the compounds that are active have been identified, extracted and purified. The increase in drug resistance bacteria also urges chemists and other scientists to find more and more bioactive chemicals from medicinal plants. Several species of Rumex have important medicinal properties and they have been the subject of several pharmacological investigations. In the work presented herein one compound namely Emodin was isolated from the crude acetone extract of root barks of *R. abyssinicus*. Acetone crude extract demonstrated better bioactivity against the tested bacterial strains. However; the isolated compound **RA-3** showed moderate activity only on two of the tested pathogens at the tested concentration.

CONFLICT OF INTEREST

The authors declare that there are no conflicts of interest.

Supplementary Materials

The IR spectrum, ^{1}H-NMR, ^{13}C-NMR, and DEPT-135 spectra generated for identifying **RA-3** (Emodin) are annexed as supporting material **S-1** to **S-4**. Zone of bacterial growth inhibition of the crude extracts and isolated compound are attached as supporting material **S-5** and **S-6**, respectively. **S-1**: IR spectrum of **RA-3**. **S-2**: 1H-NMR spectrum of **RA-3**. **S-3**: 13C-NMR spectrum of **RA-3**. **S-4**: DEPT-135

spectrum of **RA-3**. **S-5**: Zone of bacterial growth inhibition of crude extracts of root of *R. abyssinicus*. **S-6**: Zones of bacterial growth inhibition of the isolated compound **RA-3**.

REFERENCES

1. Borris RP. Natural products research: perspectives from a major pharmaceutical company. Journal of Ethnopharmacology [Internet]. 1996 Apr [cited 2022 Sep 18];51(1–3):29–38. Available from: <URL>.

2. Teklehaymanot T. Ethnobotanical study of knowledge and medicinal plants use by the people in Dek Island in Ethiopia. Journal of Ethnopharmacology [Internet]. 2009 Jul [cited 2022 Sep 18];124(1):69–78. Available from: <URL>.

3. Mekonnen T, Urga K, Engidawork E. Evaluation of the diuretic and analgesic activities of the rhizomes of Rumex abyssinicus Jacq in mice. Journal of Ethnopharmacology [Internet]. 2010 Feb [cited 2022 Sep 18];127(2):433–9. Available from: <URL>.

4. Teklehaymanot T, Giday M, Medhin G, Mekonnen Y. Knowledge and use of medicinal plants by people around Debre Libanos monastery in Ethiopia. Journal of Ethnopharmacology [Internet]. 2007 May [cited 2022 Sep 18];111(2):271–83. Available from: <URL>.

5. Mulisa E, Asres K, Engidawork E. Evaluation of wound healing and anti-inflammatory activity of the rhizomes of Rumex abyssinicus J. (Polygonaceae) in mice. BMC Complement Altern Med [Internet]. 2015 Dec [cited 2022 Sep 18];15(1):341. Available from: <URL>.

6. Vasas A, Orbán-Gyapai O, Hohmann J. The Genus Rumex: Review of traditional uses, phytochemistry and pharmacology. Journal of Ethnopharmacology [Internet]. 2015 Dec [cited 2022 Sep 18];175:198–228. Available from: <URL>.

7. Shifa M, Abdïssa D, Asere TG. Chemical Constituents of Rumex abyssinicus Roots and Evaluation of Its Antimicrobial Activities. Journal of the Turkish Chemical Society Section A: Chemistry [Internet]. 2020 Nov 27 [cited 2022 Sep 18];21–46. Available from: <URL>.

8. Getie M, Gebre-Mariam T, Rietz R, Höhne C, Huschka C, Schmidtke M, et al. Evaluation of the anti-microbial and anti-inflammatory activities of the medicinal plants Dodonaea viscosa, Rumex nervosus and Rumex abyssinicus. Fitoterapia [Internet]. 2003 Feb [cited 2022 Sep 18];74(1–2):139–43. Available from: <URL>.

9. Muganga R, Angenot L, Tits M, Frédérich M. Antiplasmodial and cytotoxic activities of Rwandan medicinal plants used in the treatment of malaria. Journal of Ethnopharmacology [Internet]. 2010 Mar [cited 2022 Sep 18];128(1):52–7. Available from: <URL>.

10. Rao K, Sunitha C, Banji D, Sandhya S, Mahesh V. A study on the nutraceuticals from the genus Rumex. HygeiaJDMed [Internet]. 2011;3(1):76–88. Available from: <URL>.

11. Fufa F M, R P, Gt G. Phytochemical Investigation and In Vitro Antibacterial Evaluation on Root Extracts of Rumex abyssinicus. Nat Prod Chem Res [Internet]. 2016 [cited 2022 Sep 18];04(06). Available from: <URL>.

12. Sulaiman SF, Yusoff NAMd, Eldeen IM, Seow EM, Sajak AAB, Supriatno, et al. Correlation between total phenolic and mineral contents with antioxidant activity of eight Malaysian bananas (Musa sp.). Journal of Food Composition and Analysis [Internet]. 2011 Feb [cited 2022 Sep 18];24(1):1–10. Available from: <URL>.

13. Priya K, Ganjewala D. Antibacterial Activities and Phytochemical Analysis of Different Plant Parts of Nyctanthes arbor-tristis (Linn.). Research J of Phytochemistry [Internet]. 2007 Feb 1 [cited 2022 Sep 18];1(2):61–7. Available from: <URL>.

14. Nascimento GGF, Locatelli J, Freitas PC, Silva GL. Antibacterial activity of plant extracts and phytochemicals on antibiotic-resistant bacteria. Braz J Microbiol [Internet]. 2000 Oct [cited 2022 Sep 18];31(4). Available from: <URL>.

15. Meselhy M. Constituents from Moghat, the Roots of Glossostemon bruguieri (Desf.). Molecules [Internet]. 2003 Jul 31 [cited 2022 Sep 18];8(8):614–21. Available from: <URL>.

16. Evans WC. Trease and Evans' pharmacognosy. 14. ed. London: WB Saunders; 1996. 612 p.

17. Bruneton J, Bruneton J. Pharmacognosy, phytochemistry, medicinal plants. 2. ed., repr. Paris: Lavoisier Tec & Doc [u.a.]; 2001. 1119 p.

18. Paneitz A, Westendorf J. Anthranoid contents of rhubarb (Rheum undulatum L.) and other Rheum species and their toxicological relevance. European Food Research and Technology [Internet]. 1999 Dec 2 [cited 2022 Sep 18];210(2):97–101. Available from: <URL>.

Phytochemical Investigation of *Rumex Abyssinicus* Root Barks and *In Vitro* Evaluation of Its Antibacterial Activities

Zelalem Abdisa[1]*, Zelalem Gudeta[2]

Supplementary Information
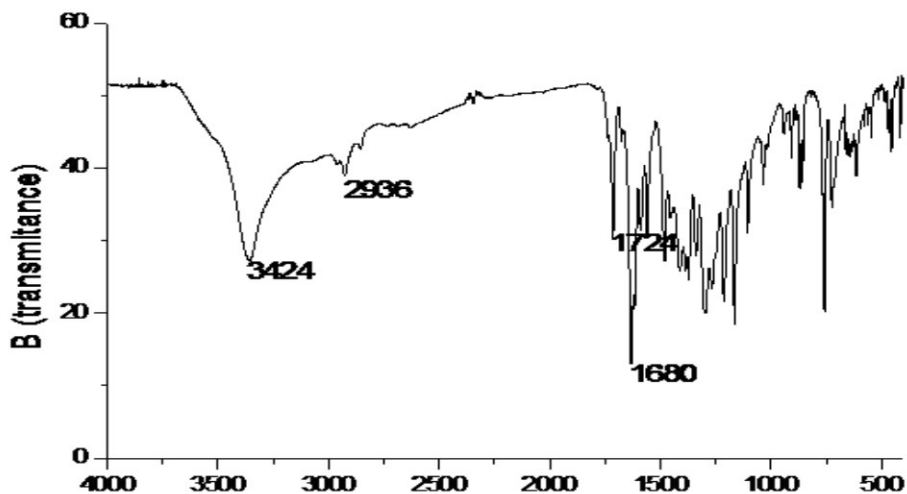
Figure S-1: IR spectrum of RA-3.
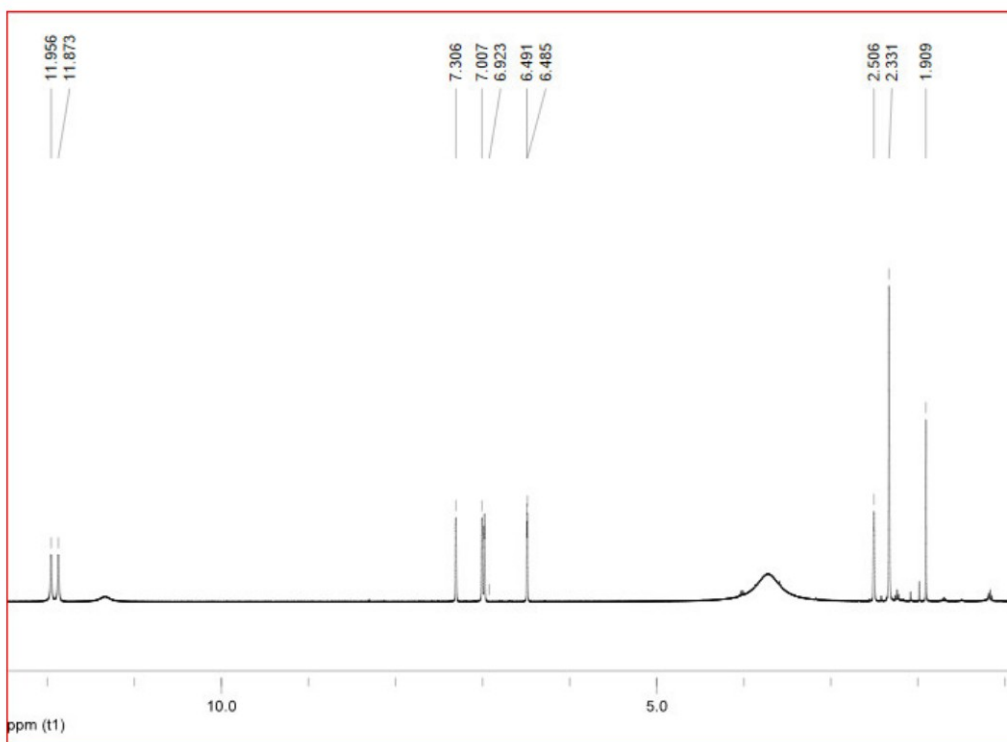
Figure S-2: ^{1}H NMR (DMSO-d$_6$) spectrum of RA-3.
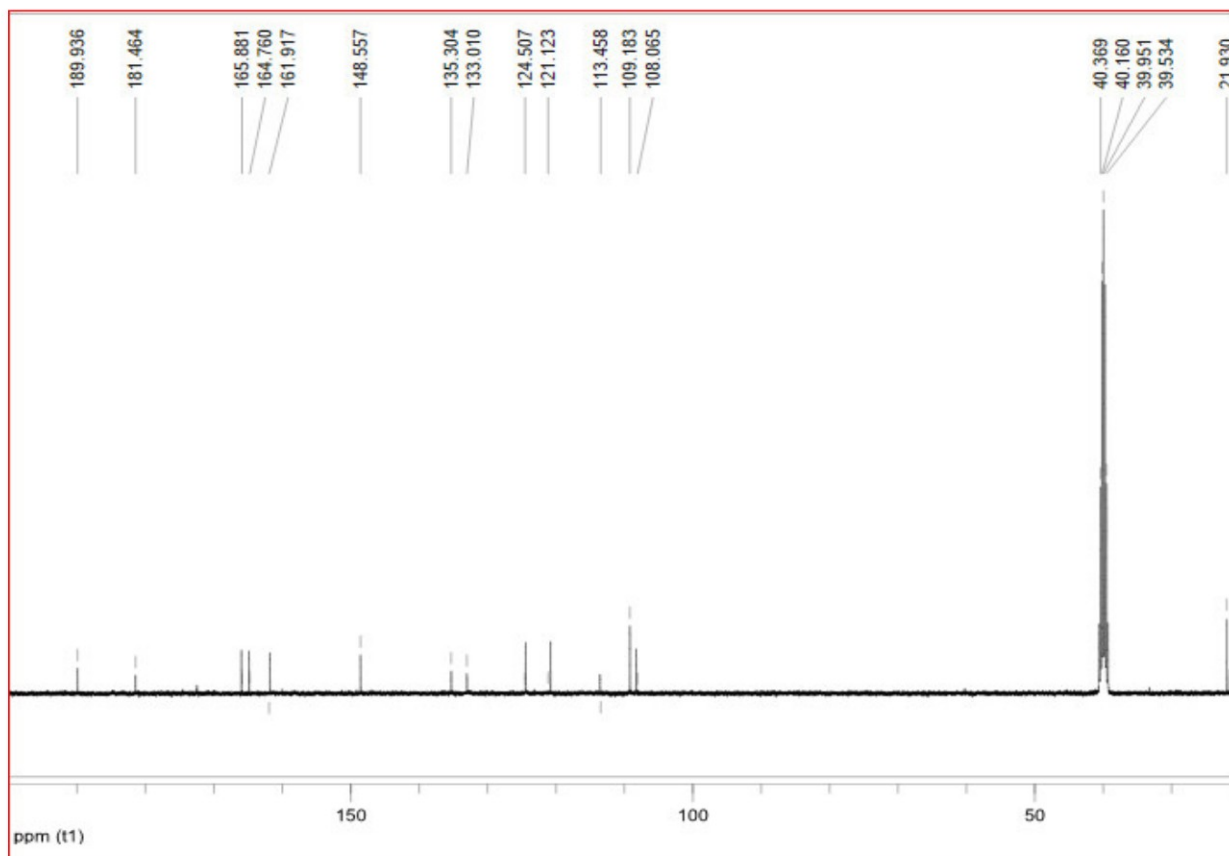
Figure S-3: ^{13}C NMR (DMSO-d$_6$) spectrum of RA-3.
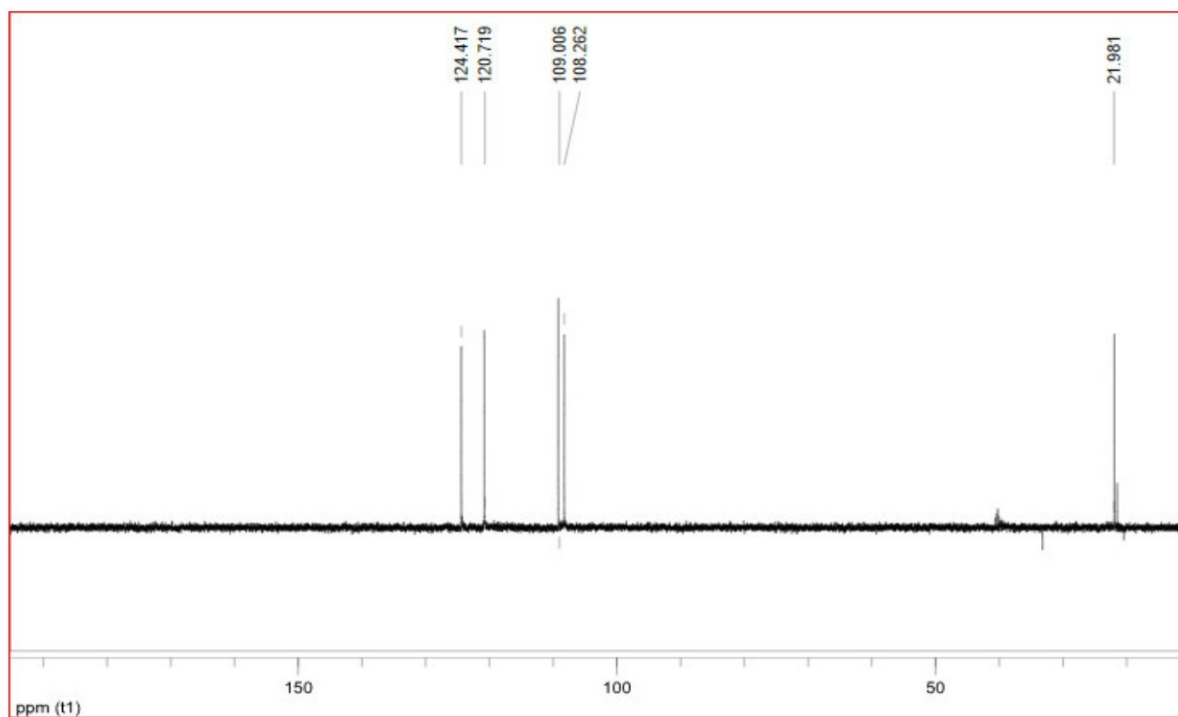
Figure S-4: DEPT-135(DMSO-d6) spectrum of RA-3.

Salmonella thyphimurium   *Staphylococcus aureus*

Pseudomonas aeruginosa   *Escherichia coli*
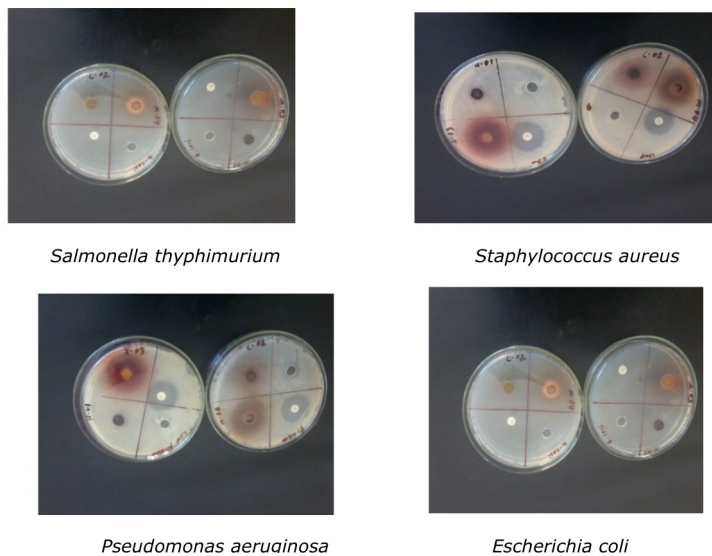
Figure S-5: Antibacterial activity of crude extracts of the root barks of *R. abyssinicus*.

Salmonella thyphimurium   *Staphylococcus aureus*

Pseudomonas aeruginosa   *Escherichia coli*
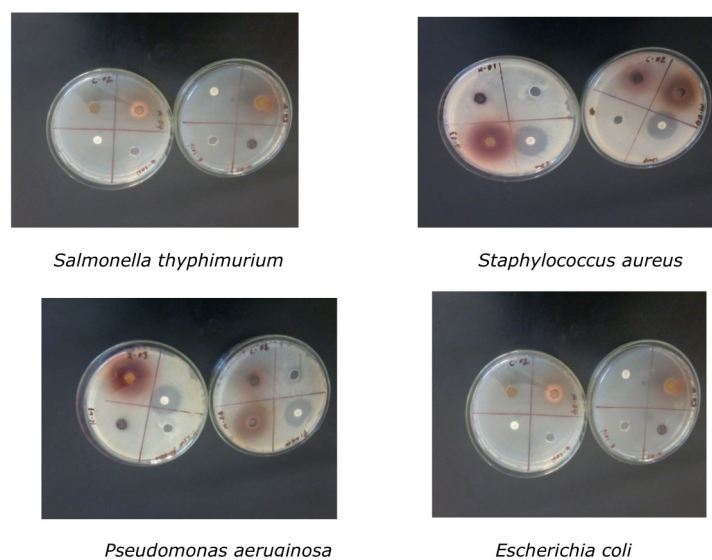
Figure S-6: Zone of bacterial growth inhibition of RA-3.

RESEARCH ARTICLE

Character Comparison Visualization of Natural Indicators in Alkalimetric Titration

Tias Ernawati[1,2]* iD **, Heru Kuswanto[3], Susanti[2]**

[1]Universitas Negeri Yogyakarta, Science Education Postgraduate Program, , Yogyakarta, 55281, Indonesia
[2]Universitas Sarjanawiyata Tamansiswa, Science Education Program, Yogyakarta, 55167, Indonesia
[3]Universitas Negeri Yogyakarta, Physics Education Postgraduate Program, Yogyakarta, 55281, Indonesia

Abstract: The use of natural materials began to be developed on a large scale in chemistry. Natural substances are safe to use, easy to find, and cheaper. Biological indicators in volumetric titration are the focus of experts. This study presented a visualization of the alkalimetric titration of a weak acid with a strong base with the addition of natural indicators. *Hibiscus rosa-sinensis* L. and *Clitoria ternatea* L. flowers were used as titration indicators for diprotic acid, namely oxalic acid, with a strong base, sodium hydroxide. The phenolphthalein indicator was chosen as an indicator to compare. Maceration of flower crowns aimed to obtain biological indicator extracts. The titration was held three times for the Hibiscus flower, Clitoria flower, and phenolphthalein. The addition of flower crown extract to oxalic acid gave a pink color to the solution. There was a color change to clear when titrated. The color change indicated the endpoint of the titration. The addition of the flower crown extract indicator showed a relatively similar curve to the phenolphthalein indicator during titration. This result showed that the two flower crown extracts had the same function as phenolphthalein as an indicator for alkalimetric titration of a weak acid with a strong base.

INTRODUCTION

The concentration of a chemical species can be determined by a straightforward method, namely volumetric analysis or titration. A certain amount of a solution is reacted with a standard solution of known concentration (1–3). The titration is carried out according to the solubility equilibrium (4). Titration conditions are made in such a way as to ensure that the results meet the accuracy requirements.

A virtual laboratory has been developed for titration activities. It is a very remarkable discovery. Virtual laboratories can overcome the lack of equipment when titrating in nonvirtual laboratories, improve understanding of concepts, thinking skills and motivation, and are practical

and virtually effective for online and blended learning (3–7). However, this still has the problem of what if students are faced with contextual conditions? Carrying out a titration requires good observation, patience, and vigilance. Titration activities are intended so that students are skilled in one of the laboratory activities and scientific work practices and can apply concepts or theories in chemistry practicum activities. Some of the skills expected to include measuring volume with the proper glassware, differentiating the use of glassware with different accuracy, practicing titration, processing experimental data into intelligible data, concluding experimental results, and communicating in written form.

Alkalimetric titration of a weak acid with a strong base will produce an equivalence point at pH > 7 due to excess hydroxide ions after the reaction.

$$H_2C_2O_{4\ (aq)} \circ H^+ + HC_2O_4^-{}_{(aq)}$$
$$HC_2O_4^-{}_{(aq)} \circ H^+ + C_2O_4^{2-}{}_{(aq)}$$
$$H_2C_2O_{4\ (aq)} + 2\ NaOH_{\ (aq)} \heartsuit Na_2C_2O_{4\ (aq)} + 2\ H_2O$$
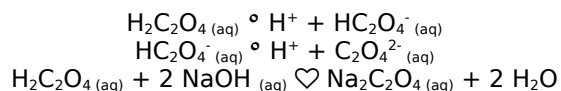
The above reaction shows that the oxalate ion is partially ionized as a weak acid. When a solution is titrated with NaOH, a certain amount of acid is neutralized by a certain amount of base. This condition is called the equivalence point. There is an excess of hydroxide ions at equilibrium. The remaining ions cause the solution to be basic with a pH > 7.

Common difficulties experienced by students when doing titrations include: how to determine the right indicator for titration, how to write the following reaction equation by balancing the reaction, how to draw a titration curve, determine the type of titration, and difficulty determining the equivalence point (4,8–10). It takes the help of an indicator added in a solution that will have a striking color difference when in an acid or alkaline medium (11,12). The condition at which the indicator provides visual information is called the end point of the titration (13). The endpoint of the titration should be observed close to the equivalence point (11). Volume and pH data obtained during the titration become the basis for determining the concentration of the solution sought.

Several alkalimetric titration indicators that have been clinically tested and work over a wide range of pH can be found at chemical stores. These indicators include thymolphthalein (pH 9.3 – 10.5), phenolphthalein (pH 8.3 – 10), thymol blue (pH 8 – 9.6), alizarin yellow R (pH 10.2 – 12), cresol Red (pH 9.3 – 10.5). The process of synthesizing chemicals often produces chemical derivatives and other pollutants that are harmful to the environment, the cost of which is also expensive (14). Many natural materials have begun to be investigated for acid-base titration indicators by utilizing dyes found in plant parts (15). Extracts of natural compounds tend to be safe, inexpensive, and abundantly available around the environment. Natural materials that can be used as indicators include hibiscus flowers (*Hibiscus rosa-sinensis* L.), roses (*Rosa Setigera*), allamanda flowers (*Allamanda Cathartica*) (16), butterfly flowers (*Clitoria ternatea* L.) (12)(17), purple cabbage leaf (*Brassica Oleracea*) (18), batang kayu secang (*Caesalpinia Sappan* L.) (14), rosella flower (*Hibiscus sabdariffa* L.) (13)(19), red spinach (Basella Alba) (20).

Figure 1: *Hibiscus rosa-sinensis* L. flower.

Figure 2: *Clitoria ternatea* L. flower.

This study used hibiscus and clitoria flowers extract. Figures 1 and 2 show the flower plants. The flower crowns that are still fresh and old in color are selected for use (14). The pigments that hibiscus and clitoria flowers have are anthocyanins (12,16,17,21,22). The chemical structure of anthocyanins is shown in Figure 3. Its color range between red, violet, and blue in acidic and basic solutions. The color change is due to a change in the pH of the solution. Based on these data, hibiscus flowers and clitoria flowers can be used as indicators of alkalimetric titrations.
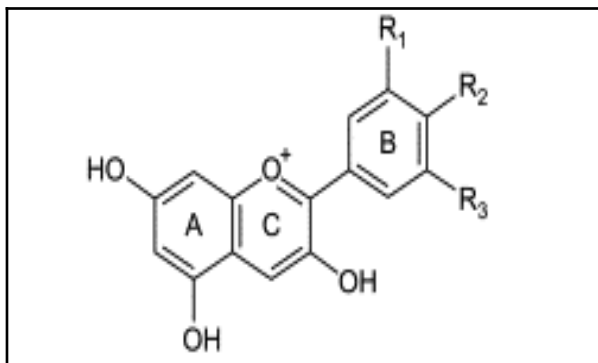
Figure 3: Anthocyanin structure.

Our study was unique because it directly compared the pH-volume curve of alkalimetric titration of a diprotic weak acid with a strong base. This study used natural indicators of *Hibiscus rosa-sinensis* L. and *Clitoria ternatea* L. flowers with phenolphthalein as a comparison indicator. Spreadsheets are used to visualize titration graphs due to their ease of use and data interpretation (23) through better graphic visualization (1,24,25). Previous research shows various flowers as alkalimetric titrations indicators by using monoprotic acid, acetic acid with a strong base, sodium hydroxide (11–13,16,17,21,22,26,27). In this study, the use of diprotic acid, oxalic acid is expected to be another alternative for selecting an acid solution for alkalimetric titration of a weak acid with a strong base.

EXPERIMENTAL SECTION

Material
0.1 M NaOH solution, 0.1 M oxalic acid solution, phenolphthalein indicator, hibiscus (*Hibiscus rosa-sinensis* L.) flower, clitoria (*Clitoria ternatea* L.) flower, ethanol 96%.

Extraction of Natural Indicators for Titration
The maceration technique carried out the extraction of anthocyanin pigments on the flower indicators of Hibiscus and Clitoria flowers (12,17,19). Hibiscus flower crowns and Clitoria flowers were chosen which have the brightest colors. Then the material was washed. Weigh 5 grams of flower crown, cut into small pieces. Put it in a dark glass bottle and soak it with 50 mL of 96% ethanol for 2 x 24 hours at room temperature in a closed state. Storage of extracts in dark bottles follows the results of previous studies (17,19).

Titration
Alkalimetric titration was performed against 10 mL of the oxalic acid solution, $H_2C_2O_4$, 0.1 M with solution NaOH 0.1 M. Three types of alkalimetric titration of a weak acid and strong were applied: 1) phenolphthalein indicator, 2) Hibiscus flower extract indicator, and 3) Clitoria flower extract indicator. The titration was held in triplicate.

Observation of the endpoint of the titration is carried out accurately. The titration produces data, namely the volume of the NaOH solution and the pH value of the neutralization reaction. We used the digital pH meter ATC 2011 to measure the pH. An excel spreadsheet describes the data and then performs a qualitative descriptive analysis.

RESULTS AND DISCUSSION

Three kinds of titrations were carried out by a strong base of NaOH against 10 mL of 0.1 M oxalic acid. Oxalic acid was used as the primary raw material because of its high purity, ease of purification, stability for a long time, strength in solution form, can be stored for a relatively long time, and has a definite relative molecular mass (28). This study chose the phenolphthalein indicator as a comparison indicator for the two natural indicators, namely the hibiscus flower and clitoria flower. Phenolphthalein was used because it has been tested as an indicator for alkalimetric titration of a weak acid with a strong base. The pink color produced by phenolphthalein indicator as a marker has ended the alkalimetric titration of a weak acid with a strong base (26,29). The addition of phenolphthalein indicator in the alkalimetric titration of oxalic acid with NaOH is shown in Figure 4.

Figure 4: The addition of phenolphthalein indicator produced a pink color at the end of the alkalimetric titration of a weak acid with a strong base.

The use of natural indicators in the identification of acids and bases has begun to be developed because they are easy to obtain, safe, and have cheaper production costs, and the results are no different when compared to the use of artificial indicators (29–31). The titration in this study used flower extract indicators that are easily found in the environment, namely Hibiscus flowers and Clitoria flowers. Extracts of both flower crowns could produce color changes when interacting with acids or bases. They are shown in Figure 5. A good indicator is an indicator that has a pH change trajectory around the equivalence point or at the

equivalence point and can show clear and sharp color changes (11,26).

Figure 5: The result of maceration of hibiscus (top) and clitoria (bottom) flower crowns.

Hibiscus and butterfly flower crowns contain anthocyanin pigments. Both hibiscus and clitoria flowers indicator gave a pink color when interacting with weak acids. The color slowly faded after titration with a strong base. Figure 6 shows the results of the titration of oxalic acid with NaOH using the hibiscus indicator and clitoria flowers.

Figure 6: Changes in the color of the solution after titration due to the addition of hibiscus (top) and clitoria (bottom) flowers indicators.

This study compared the visualization of alkalimetric titration results using natural indicators of flower crown extract against Phenolphthalein as an indicator. Titration used a weak diprotic acid in which there are two values of Ka. Oxalic acid used in this titration undergoes double ionization in the solution, resulting in the values of $Ka_1 = 5.6 \times 10^{-2}$ and $Ka_2 = 5.4 \times 10^{-4}$. These two values of Ka explain that oxalic acid has the ability to produce two hydrogen ions per molecule. While the strong base NaOH is only able to produce one hydroxide ion per molecule. Thus, when NaOH was titrated with oxalic acid, two hydrogen ions were equivalent to 1 mole of hydroxide ions. Or in other words, two hydrogen ions from oxalic acid were exactly neutralized by one hydroxide ion from NaOH.

The results of the study obtained that the alkalimetric titration data of a strong base NaOH against a weak diprotic acid, oxalic acid using indicators namely phenolphthalein (P), hibiscus flower (H), and clitoria flower (C), are presented in Table 1.

Table 1: Titration pH and NaOH Volume.

Vol NaOH (mL)	pH (T1-P) 1	pH (T2-P) 2	pH (T3-P) 3	pH (T2-H) 5	pH (T3-H) 6	pH (T1-C) 7	pH (T2-C) 8	pH (T3-C) 9
0	1.72	1.72	1.71	1.69	1.7	1.57	1.57	1.6
2	1.78	1.77	1.78	1.9	1.9	1.69	1.67	1.74
4	1.95	1.88	1.85	2.03	2.01	1.7	1.86	1.86
6	2.11	2.08	2.07	2.07	2.09	1.79	1.9	1.99
8	2.48	2.57	2.42	2.16	2.47	1.9	2.05	2.09
10	3.05	3.19	3.12	2.67	2.83	2.02	2.47	2.39
12	3.46	3.74	3.64	3.12	3.12	2.47	2.89	2.83
14	3.87	4.05	3.96	3.47	3.52	2.91	3.23	3.29
16	4.5	4.9	5	3.8	3.79	3.21	3.51	3.52
18	9.77	9.77	10.13	4.13	4.17	3.52	3.77	3.79
20	10.5	10.12	10.87	4.87	4.86	3.77	4.17	4.17
22	10.81	10.61	10.94	9.88	9.89	5.2	5.22	5.22
24	10.88	10.66	10.96	10.12	10.12	9.72	9.72	9.71
26	10.98	10.75	10.96	10.3	10.3	10.25	10.26	10.12
27	11	10.96	11	10.42	10.4	10.4	10.26	10.28

Visualization of the alkalimetric titration curve for a weak acid and a strong base was performed using an excel spreadsheet, presented in Figure 7. The graph of the alkalimetric titration results through a spreadsheet application provided convenience in data interpretation. The interaction of a volume of acid with a base produced plots of pH values. The graph was identical to the graph of an alkalimetric titration of a weak acid with a strong base, which is in the form of an S.
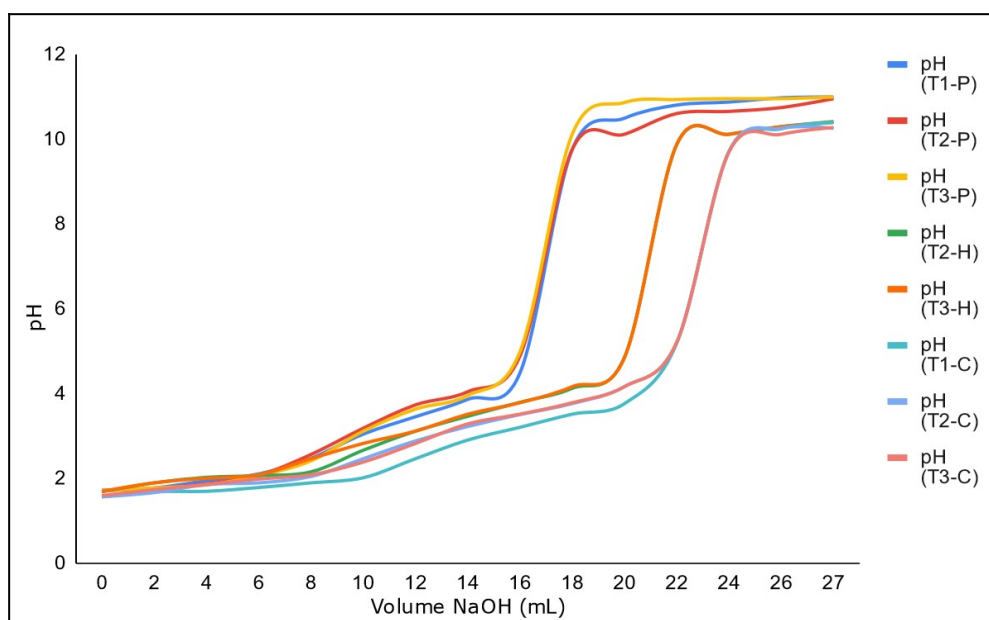
Figure 7: Alkalimetric titration (T) with phenolphthalein (P) indicator, hibiscus (H) flower and clitoria (C) flower.

Data were obtained from first to ninth titrations. Data for alkalimetric titrations with phenolphthalein indicator were displayed in data first to third. Alkalimetric titrations with the hibiscus flower indicator were established in the fourth, fifth, and sixth data. The fourth data revealed an erroneous

result, not so for the fifth and sixth data. The fifth and sixth data indicated relatively the same results. The clitoria flower indicator's titration was shown in the seventh, eighth, and ninth data.

The fourth data had the most different values from the fifth and sixth data. It could be caused by human error that occurred during the titration. When carrying out titration, some things that must consider include preparing the equipment correctly. Glassware must be completely clean of impurities. Pay attention to the burette used for the titration. Check the readiness of the burette. Replace if the burette is cracked, broken, or leaks at the faucet or valve. Next is to prepare the materials used, namely titrant and indicator. Use standard solutions and be free from other impurities. Prepare yourself before doing the titration. Use personal protective equipment. Confidently perform the titration, not in rush, but thorough. Pay attention to the addition of the titrant volume and pH value when you carry out the titration.

Oxalic acid reacted with the addition of NaOH shows a graph trend that increases from pH 2 to pH 4. Table 2 presents graphs, line equations, and coefficients of determination for the entire titration using phenolphthalein, hibiscus, and clitoria flowers as indicators. A strong coefficient of determination shows that the change in pH value is correct due to adding of a certain amount of NaOH. It indicates that the titration has been carried out correctly. There is no significant difference between the three gradients of the line equation.

Table 2: Graph of Oxalic Acid with NaOH Reaction at pH 2 to pH 4.

Figure	Indicator
	phenolphthalein $y = 0.2639x + 0.4426$ $R^2 = 0.9881$
	hibiscus $y = 0.1915x + 0.8311$ $R^2 = 0.9871$

clitoria
$y = 0.1618x + 0.7991$
$R^2 = 0.99$
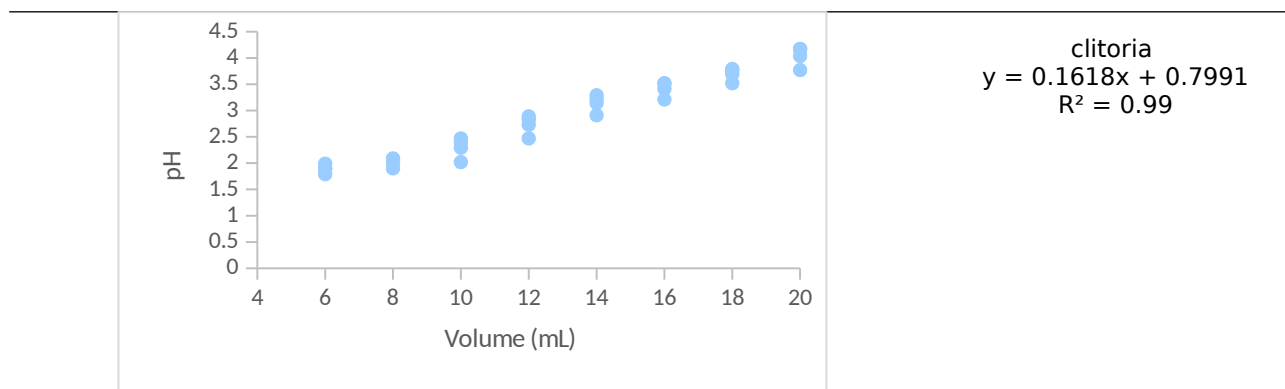
Table 2 provides information about alkalimetric titration using phenolphthalein indicator. The addition of NaOH volume from 16 mL to 18 mL showed a significant increase in the pH value, namely pH 4.5 - 5 to pH 9.77 - 10.13. In the alkalimetric titration using a hibiscus indicator, there was a significant change in the pH value from pH 4.86 to pH 9.89 for the addition of NaOH volume from 20 mL to 22 mL. As for the titration with the clitoria flower indicator, the change in pH 5.22 to pH 9.72 was indicated by the addition of NaOH volume from 22 mL to 24 mL. Such conditions implied that the titration was approaching the equivalence point. The pH value rose faster at first, but the increase became slower until it approached the equivalence point.

The equivalence point of the titration indicated that a certain amount of acid had been neutralized by the addition of a certain amount of base. Visualization of the pH equivalence point of the titration of a weak acid with a strong base was not correct in 7. The effect of the hydroxide ion possessed by the strong base used NaOH gives a pH value of > 7. There were still residual hydroxide ions when equilibrium occurred. The pH value increased more rapidly at the equivalence point. The three types of titrations produced almost the same equivalence point pH values, namely in the pH range of 9.72 – 9.89. This event follows the fact that the equivalence point of the alkalimetric titration of a weak acid with a strong base is at pH 8 – 10 (11,21).

In the pH range of 4.13 – 5.22, the color of the solution began to change in the three titrations. The pink color disappeared and then reappeared. And in the pH range of 9.71 - 10.13, the color of the solution no longer changed. Titration with phenolphthalein, the color of the solution changed from clear to pink. Meanwhile, in the titration with the indicator, both the Hibiscus flower and the Clitoria flower changed color from pink to clear. This indicated that the endpoint of the titration had occurred. It was advisable to stop the titration immediately.

In general, the increase in the value of pH 9 to pH 10 occurred very slowly, even though repeated amounts of NaOH were added. This slow increase could be explained because the solution formed a buffer system. Buffer solutions are produced by adding a small amount of a strong base to a weak acid. The buffer solution will maintain its pH value to a certain extent (2,11,15). At pH 10.12, the solution was even more difficult to raise the pH value. In this condition, there was an excess of hydroxide ions after equilibrium, so the pH of the solution became very basic.

CONCLUSION

The extraction of the hibiscus flower and clitoria flower could be obtained by curing the flower crown for 48 hours using ethanol. The extract obtained could be used as a titration indicator because it gave a clear and sharp color change. The pink color appeared when the flower crown extract was added to the oxalic acid solution. The endpoint of the titration was indicated when the pink color had changed to clear. The pH trajectory produced when the hibiscus flower and clitoria flower indicators work had similarities with the addition of phenolphthalein which had been tested as an indicator for alkalimetric titration of a weak acid with a strong base.

REFERENCES

1.   Okezue MA, Clase KL, Byrn SR. An Effort at Improving Reliability of Laboratory Data in Titrimetric Analysis for Zinc Sulphate Tablets Using Validated Spreadsheet Calculators. Int J Pharmacol Pharm Sci . 2021;15(5):182–9. Available from: <URL>..

2.   Asuero AG, Michalowski T. Comprehensive Formulation of Titration Curves for Complex Acid-Base Systems and Its Analytical Implications. Crit Rev Anal Chem . 2011;41(2):151–87. Available from: <URL>..

3.   Susatyo EB, Damanik YF. Pengembangan E-Laboratory Instruction Model Guided Inquiry Berbasis Blended Learning Pada Materi Titrasi Asam Basa. Inov Pendidik Kim. 2021;15(1):2754–63.

4.   Liu L, Ling Y, Gao Q, Fu Q. Supporting students' inquiry in accurate precipitation titration conditions with a virtual laboratory tool as learning scaffold. Educ Chem Eng . 2022;38:78–85. Available from: <URL>..

5.   Erni E, Copriady J, Linda R. The Use Of Vırtual

Laboratory To Improve Students' Conceptual Understandıng In Acıd Base Tıtratıon Subject. Int J Educ Best Pract . 2019;3(1):43–9. Available from: <URL>..

6.   Putri ZS, Kurniawati Y. The Effectiveness of Learning Using Virtual Laboratory Toward Student Critical Thinking Ability on Acid-Base Titration Lesson. J Indones Soc Integr Chem (On Progress) . 2021;13(1):14–20. Available from: <URL>..

7.   Sary SP, Tarigan S, Situmorang M. Development of Innovative Learning Material with Multimedia to Increase Student Achievement and Motivation in Teaching Acid Base Titration. In: 3rd Annual International Seminar on Transformative Education and Educational Leadership (AISTEEL 2018) Development . 2018. p. 422–5. Available from: <URL>..

8.   Sheppard K. High school students' understanding of titrations and related acid-base phenomena. Chem Educ Res Pract . 2006 Jan 1;7(1):32–45. Available from: <URL>..

9.   Astuti RT, Marzuki H. Analisis Kesulitan Pemahaman Konsep Pada Materi Titrasi Asam Basa Siswa SMA. Orbital J Pendidik Kim . 2017;1(1):22–7. Available from: <URL>..

10.   Wahyuni TS, Purwanto KK. Students' conceptual understanding on acid-base titration and its relationship with drawing skills on a titration curve. J Phys Conf Ser . 2020; Available from: <URL>..

11.   Pattarapongdilok N, Malichim P, Simmee N, Sichaem J. Senna Flower Extract As An Indicator For Acid-Base Titration. Rasayan J Chem . 2021;14(2):20211402–7. Available from: <URL>..

12.   Wiyantoko B, Astuti A. Butterfly Pea (Clitoria Ternatea L.) Extract as Indicator of Acid-Base Titration. Ind J Chem Anal . 2020;3(1):22–32. Available from: <URL>..

13.   Yazid EA, Munir MM. Potensi Antosianin Dari Ekstrak Bunga Rosella (Hibiscus sabdariffa L.) Sebagai Alternatif Indikator Titrasi Asam Basa. J Sains . 2018;8(15):1–7. Available from: <URL>..

14.   Padmaningrum RT, Marwati S, Wiyarsi A. Karakter Ekstrak Zat Warna Kayu Secang (Caesalpinia Sappan L) Sebagai Indikator Titrasi Asam Basa. In: Prosiding Seminar Nasional Penelitian, Pendidikan dan Penerapan MIPA. Yogyakarta; 2012. p. K1–9.

15.   Ramadhani R, Octarya Z, Tarbiyah F, Uin K, Riau S. Pemanfaatan Ekstrak Buah Senduduk (Melastoma malabathricum L.) sebagai Alternatif Indikator Alami Titrasi Asam Basa dan Implementasinya dalam Praktikum di Sekolah. Konfigurasi   J Pendidik Kim dan Terap . 2017;1(1):57–64. Available from: <URL>..

16.   Okoduwa SIR, Mbora LO, Adu ME, Adeyi AA. Comparative analysis of the properties of acid-base indicator of rose (Rosa setigera), Allamanda (Allamanda cathartica), and hibiscus (Hibiscus rosa-sinensis) flowers. Biochem Res Int . 2015;2015:1–6. Available from: <URL>..

17.   Fitri CBS, Fikroh RA. The Potential of Clitoria ternatea L. Extracts as an Alternative Indicator in Acid-Base Titration. JIPI . 2021;5(4):340–52. Available from: <URL>..

18.   Widyabudiningsih D, Sularasa A. Penggunaan Indikator Kubis Ungu Pada Analisis Asam Lemak Bebas dengan Metode Titrasi. Indones J Chem Anal . 2020;3(2):56–64. Available from: <URL>..

19.   Amperawati S, Hastuti P, Pranoto Y, Santoso U. Efektifitas Frekuensi Ekstraksi Serta Pengaruh Suhu dan Cahaya Terhadap Antosianin dan Daya Antioksidan Ekstrak Kelopak Rosella (Hibiscus sabdariffa L.). J Apl Teknol Pangan . 2019;8(1):38–45. Available from: <URL>..

20.   Chaurasiya A, Kumar Pal R, Kumar Verma P, Katiyar A, Kumar N, Author C. An Updated Review on Malabar Spinach (Basella alba and Basella rubra) and Their Importance. J Pharmacogn Phytochem . 2021;10(2):1201–7. Available from: <URL>..

21.   Saptarini M, Suryasaputra D, Nurmalia H. Application of Butterfly Pea Extract (Clitoria ternatea Linn) as An Indicator of Acid-Base Titration Application of Butterfly Pea (Clitoria ternatea Linn) extract as an indicator of acid-base titration. J Chem Pharm Res . 2015;7(2):275–80. Available from: <URL>..

22.   Madushan R, Vidanarachchi JK, Prasanna PHP, Werellagama S, Priyashantha H. Use of natural plant extracts as a novel microbiological quality indicator in raw milk: An alternative for resazurin dye reduction method. LWT - Food Sci Technol . 2021;144:1–9. Available from: <URL>..

23.   José Baeza-Baeza J, Pini O, Pérez-Pla FF, García-Álvarez-Coque MC, García-Álvarez MC. Solving Chemical Equilibria in Titrimetry with the Inclusion of Ionic Strength Using OCTAVE and EXCEL. World J Chem Educ . 2021;9(3):81–7. Available from: <URL>..

24.   Walkowiak M, Nehring A. Using ChemDuino, Excel, and PowerPoint as Tools for Real-Time Measurement Representation in Class. J Chem Educ . 2016;93(4):778–780. Available from: <URL>..

25.   Whiteley R V. The Simulation of an Oxidation−Reduction Titration Curve with Computer Algebra. J Chem Educ . 2015;92(5):950–3. Available from: <URL>..

26.   Kapilraj N, Keerthanan S, Sithambaresan M. Natural Plant Extracts as Acid-Base Indicator and Determination of Their pKa Value. J Chem . 2019;2019. Available from: <URL>..

27.   Riniati R, Sularasa A, Febrianto AD. Ekstraksi Kembang sepatu (Hibiscus Rosa Sinensis L) Menggunakan Pelarut Metanol dengan Metode Sokletasi untuk Indikator Titrasi Asam Basa. Indones J Chem Anal . 2019;2(01):34–40. Available from: <URL>..

28.   Colmenero F. Mechanical Properties of Anhydrous Oxalic Acid and Oxalic Acid Dihydrate. Phys Chem Chem Phys . 2019;21(5):2673–90. Available from: <URL>..

29.   Leshe S, Baye H. Extraction of Green Acid-Base Indicators From Acanthus Pubescens Flower for Use in the School Laboratory. Int J Chem . 2020;12(2):35. Available from: <URL>..

30.   Owolabi RU, Usman MA, Adejumo LA, Aderibigbe FA, Chinazom, Uba M, et al. An Investigation of the Analytical Potentials of Flower Extracts as Bio-Indicators in Acid Base Titration. SEU J Sci Eng. 2018;12(2).

31.   Payal R, Jain A, Malhotra P. Use of Cost Effective Kitchen Ingredients in Acid-Base Titrations: A Greener Approach. Green Chem Environ Sustain Chem Educ . 2018;147–51. Available from: <URL>..

Electrochemistry, DFT Calculations, and Antioxidant Capability of Cobalt Cefazolin Complex

Elif Turker ACAR (iD)

Istanbul University-Cerrahpaşa, Department of Chemistry, Engineering Faculty, Avcılar, Istanbul, 34320, Turkey

Abstract: The synthesis, characterization, electrochemistry, theoretical investigation and antioxidant capability of cobalt cefazolin [Co(Cefaz)Cl] complex are reported here. Electrochemical characterization of the complex was carried out by using cyclic voltammetry (CV) and Linear Sweep Voltammetry (LSV) methods. Two irreversible oxidative responses and one quasi-reversible reduction couple were observed for the complex on the voltammograms. The ground state energies of the molecules have been estimated using B3LYP functional with LanL2DZ basis set based on time dependent density functional theory (TD-DFT). According to the theoretical calculation, [Co(Cefaz)Cl] complex can be expected to exhibit greater reactivity from Cefazolin (Cefaz) ligand, and the higher antioxidant properties were observed for the complex. The experimental results are in good agreement with the theoretical calculations.

Keywords: Cefazolin complex, electrochemistry, DFT calculation, antioxidant capability.

INTRODUCTION

Cephalosporins are one group of beta-lactam antibiotics (1). The basis of the cephalosporin molecule forms from beta-lactam and dihydrothiazine rings attached to the cefem group. The cefem group leads to the complete loss of antimicrobial properties of cephalosporins with the cleavage of the rings and determines the antimicrobial activity of cephalosporins.

Cephalosporins cefazolin (CEF), ceftriaxone (CTRX), moxalactam (MXLM), cefuroxime (CFXM), and cefotaxime (CFTM) are first, second, and third generation cephalosporin derivatives, which are widely used in clinical therapy of severe infections (2).

Cefazolin, which is a first generation of cephalosporin antibiotics, consist of β-lactam ring, is mainly used to treat bacterial infections of the lung, stomach, skin, bone, heart valve, and blood (3-4). Especially, it is clinically effective against infections caused by *Staphylococci* and *Streptococci* of gram-positive bacteria (5). Generally, the interaction of β-lactam antibiotics with metal ions is of a complex nature (6). Toxicological and pharmacological properties of many drugs have been changed when they are in the form of metal complexes.

In the present study, [Co(Cefaz)Cl] complex was synthesized via a procedure in the literature. Redox properties of the complex were determined with cyclic voltammetry and linear sweep voltammetry methods. The relationship between the theoretical calculation and antioxidant capacity was investigated to confirm the experimental findings.

EXPERIMENTAL SECTION

Synthesis
The synthesis of [Co(Cefaz)Cl] was achieved according to published literature (7-8). The [Co(Cefaz)Cl] complex was prepared by mixing 1 mmol $CoCl_2 \cdot 6H_2O$ salt and 2 mmol cefazolin ligand in methanol (MeOH). 0.5 M NaOH was added dropwise to adjust the pH of the solution to 8.0. The solution mixture was aproximately stirred for 2 h at room temperature. The precipitated complex was filtered off, washed with diethyl ether and dried in a desiccator at room temperature. The melting point of the complex was found to be higher than 360°C. The formed [Co(Cefaz)Cl] complex is highly soluble in dimethylsulfoxide (DMSO) and DMF.

Computational Details
The complete geometry optimizations of Cefaz and [Co(Cefaz)Cl] complex were performed using the Density Functional Theory (9). The Becke three parameter hybrid exchange functional and the Lee-Yang- Parr correlation functional (B3LYP) (10-11) with LanL2DZ basis set were used for all the atoms of Cefaz and [Co(Cefaz)Cl] complex in TD-DFT calculations of HOMO-LUMO energy and molecular orbital analyses. The results are reported in Table 4. All the energy calculations were performed by the GAUSSIAN 09 package program (12).

Quantum chemical descriptors were approximated in terms of the one-electron energies of the frontier molecular orbitals (FMO), HOMO and LUMO, E_H and E_L, using the following equations (1)–(5):

$$\Delta_{gap} = E_L - E_H \tag{1}$$

$$\mu = \frac{-(E_H + E_L)}{2} \tag{2}$$

$$\eta = \frac{E_L - E_H}{2} \tag{3}$$

$$\omega = \frac{\mu^2}{2\eta} \tag{4}$$

$$\chi = -\mu \tag{5}$$

Here, η is chemical hardness, μ is electronic chemical potential, ω is electrophilicity index, and χ is electronegativity (13-15).

Electrochemistry
Cyclic Voltammetry (CV) and Linear Sweep Voltammetry (LSV) experiments were carried out using an Ivium Vertex potentiostat/galvanostat system. A conventional three electrode cell consisting of glassy carbon (3.0 mm diameter) working electrode (GCE), Ag/AgCl reference electrode and a platinum wire counter electrode were used for all electrochemical experiments. The GCE used as working electrode was polished with alumina slurry (Buehler Micropolish) using a polishing pad (Buehler-102 mm) and rinsed with water before each run. Measurements were performed in 1×10^{-3} M [Co(Cefaz)Cl] complex solution in DMSO containing 0.1 M of tetrabutylammonium perchlorate (TBAP) as supporting electrolyte. Before all electrochemical measurements, the solutions were saturated with pure nitrogen gas for 10 min.

Antioxidant Efficiency Assays

CUPRAC Assay
1 mL of 10 mM $CuCl_2 \cdot 2H_2O$, 1 mL of 7.5 mM Nc (neocuproine), 1 mL of 1.0 M pH 7 NH_4Ac buffer solution, x mL antioxidant sample solution and (1.1-x) mL H_2O were added to test tube, in this order. After the mixture, in a total volume of 4.1 mL, was incubated for 30 min, the absorbance spectra was recorded at 450 nm (16). The TEAC coefficients (trolox equivalent antioxidant capacities) were calculated from the ratio of the molar absorptivity of each compound to that of the trolox reaction (ε_{trolox}: 1.58×10^4 L mol^{-1} cm^{-1}).

DPPH Radical Scavenging Assay
The radical scavenging activities of the Cefaz ligand and [Co(Cefaz)Cl] complex were tested at different concentrations (12.5, 25, 37.5, 50, and 62.5 µM). Appropriate volume of the compound solution was mixed with 2 mL of 100 µM DPPH solution, and it made up to a final volume of 4 mL using methanol. After solution was stirred gently, the mixture was incubated for 30 min in the dark. The absorbance was measured at 515 nm (17) and the scavenging activity percentage was determined by the following equation:

DPPH radical scavenging activity (%) = [($A_{control}$ − A_{sample})/ $A_{control}$] x 100

Where $A_{control}$ and A_{sample} are absorbance of control and sample, respectively. IC_{50} values were calculated from the graph plotted between DPPH radical scavenging activity percentages and different solution concentrations. Ascorbic acid was used as standard.

Table 1: ATR-FTIR spectral findings of the Cefaz and [Co(Cefaz)Cl] complex.

	v (N-H)	v (C=O) lactam	v (C=O) amide	v (COO) asym	v (COO) sym	v (C-N)	v (C-O) stretch
Cefaz	3289	1758	1667	1540	1386	1490	1008
[Co(Cefaz)Cl]	3287	1765	1672	1547	1390	1497	1013

RESULTS AND DISCUSSION

Infrared Spectrum
FT-IR data were obtained by an Agilent Cary 630 spectrometer with an Attenuated Total Reflectance (ATR) unit in the 4000–600 cm^{-1} range. A comparison of the ATR-FTIR spectral findings of the Cefaz and [Co(Cefaz)Cl] complex are shown in Table 1. The similar spectral values observed for Cefaz and [Co(Cefaz)Cl] complex in the ATR-IR spectra. The main vibrational frequency values are 3289 v(N-H), 1758 v(C=O)lactam, 1667 v(C=O)amide, 1540 v(COO)asym, 1386 v(COO)sym, 1490 v(C-N), 1008 v(C-O)stretch for Cefaz Ligand. FTIR spectral values

of the [Co(Cefaz)Cl] complex are 3287 v(N-H), 1765 v(C=O)lactam, 1672 v(C=O)amide, 1547 v(COO)asym, 1390 v(COO)sym, 1497 v(C-N), 1013 v(C-O)stretch. Slight shifts (5-25 cm^{-1}) were observed in the spectrum of Cefaz and [Co(Cefaz)Cl] complex. Cobalt makes coordination bond with amide carbonyl group, COO group and nitrogen atoms. The coordination of metal atom is completed with the chloride ion. The ATR-FTIR spectral results of the Cefaz and [Co(Cefaz)Cl] complex proved the proposed structure. The results are in good agreement with literature (7-8).

Electrochemistry
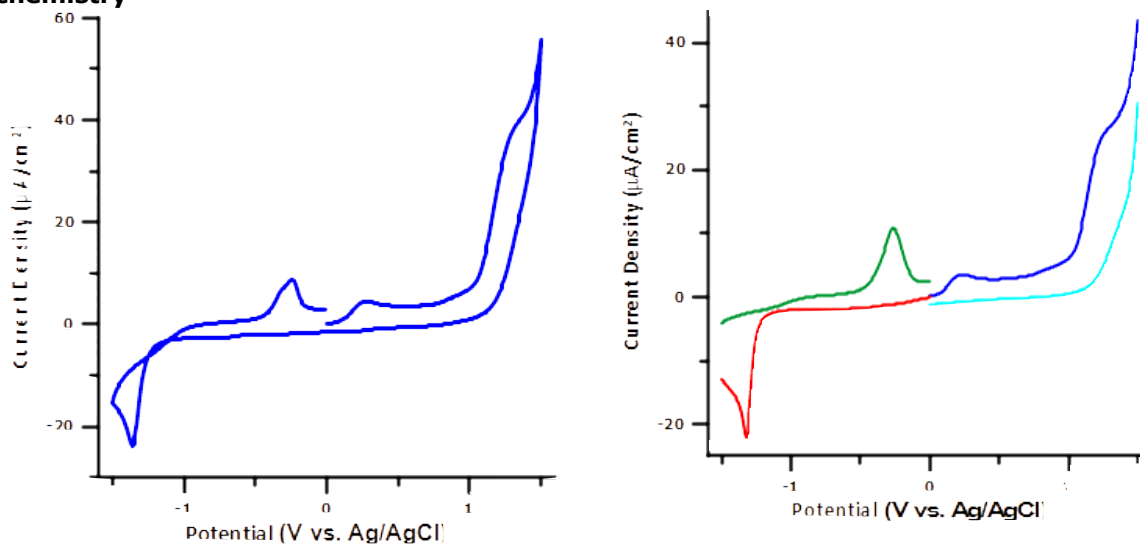
Figure 1. Left) CV and right) LSV of [Co(Cefaz)Cl] complex in 0.1 M TBAP/DMSO solution.

Electrochemical measurements of [Co(Cefaz)Cl] complex were used to estimate its electron transfer ability in DMSO. The CV and LSV of the complex were recorded in the potential range of (-1.5) – 1.5 V versus Ag/AgCl (Fig. 1). The [Co(Cefaz)Cl] complex showed three redox processes in DMSO. One quasi-reversible transfer process was observed with a reduction peak at E_{pc}=-1.36 V with a corresponding oxidation peak at E_{pa} = -0.24 V at a 50 mV/s scan rate in the CV curve of the complex (18). The peak separation (ΔEp) of this Co^{II}/Co^{I} couple is 1.1 V. Positive potential scans for [Co(Cefaz)Cl] showed two irreversible oxidative responses at 0.28 V and 1.27 V

attributed to the metal based Co^{II}/Co^{III} and the ligand based (L/L$^+$) oxidative responses, respectively. Similar voltammetric responses were observed in the Linear Sweep voltammetry method (Fig 1b) for the complex.

Antioxidant Efficiency
The antioxidant efficiencies of Cefaz and [Co(Cefaz)Cl] complex were assayed by using the CUPRAC (cupric reducing antioxidant capacity) method. Antioxidant activity deals with reaction kinetics and the chemical oxidation rate of the antioxidant or the rate of quenching of the reactive species by the antioxidant (16,19). The TEAC coefficients of ascorbic acid used

as a reference and compounds are shown in Table 2.

The order of in vitro antioxidant capacity of the compounds was [Co(Cefaz)Cl] > Cefaz in the assay (20). The antioxidant activity of Cefaz was found to be less than those of [Co(Cefaz)Cl] and Ascorbic Acid.

Table 2: The TEAC coefficients of the compounds.

Compounds	TEAC

Cefaz	0.80±0.058
[Co(Cefaz)Cl]	1.17±0.201
Ascorbic Acid	1.00 ± 0.01

The Cefaz and [Co(Cefaz)Cl] complex were tested for DPPH (1,1-Diphenyl-2-picrylhydrazyl) radical scavenging activity. DPPH has a strong absorption bond at 515 nm due to having an odd electron. When this electron becomes paired off, the absorption value decreases stoichiometrically according to the number of electrons taken up (21).
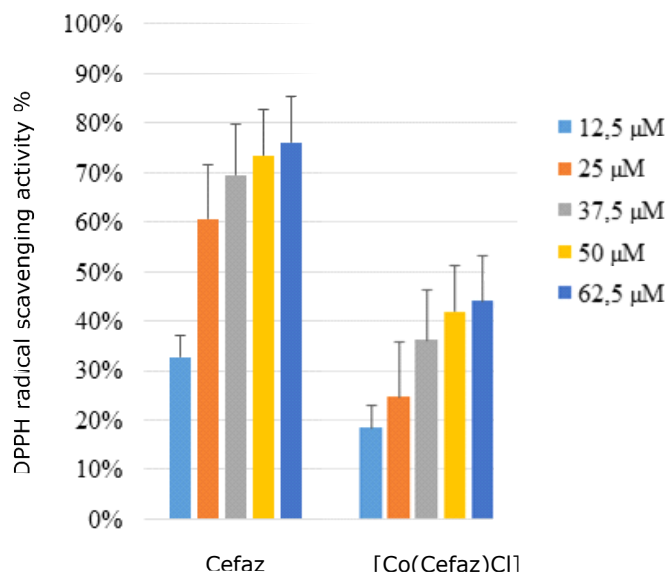
Figure 2. The free radical scavenging activity of the compounds (%).

Table 3. The radical scavenging activities of the compounds, as IC_{50}.

Compounds	DPPH IC_{50} (µM)
Cefaz	43.5
[Co(Cefaz)Cl]	136.8

A lower IC_{50} value indicates better scavenging activity.

According to this, Cefaz > [Co(Cefaz)Cl].
Cefaz ligand has moderate antioxidant activity when compared to ascorbic acid which used as standard. The DPPH radical scavenging activity results of Cefaz could not be supported by the TEAC value (0.80) obtained by the CUPRAC method. The differences between the two methods are due to the fact that the methods run with different reactions (22).

DFT Calculations
Table 4. Optimized geometry and frontier molecular orbital density distribution of the Cefaz and [Co(Cefaz)Cl] complex calculated at B3LYP/LanL2DZ.

	Structure	HOMO	LUMO
Cefaz			
[Co(Cefaz)Cl]			
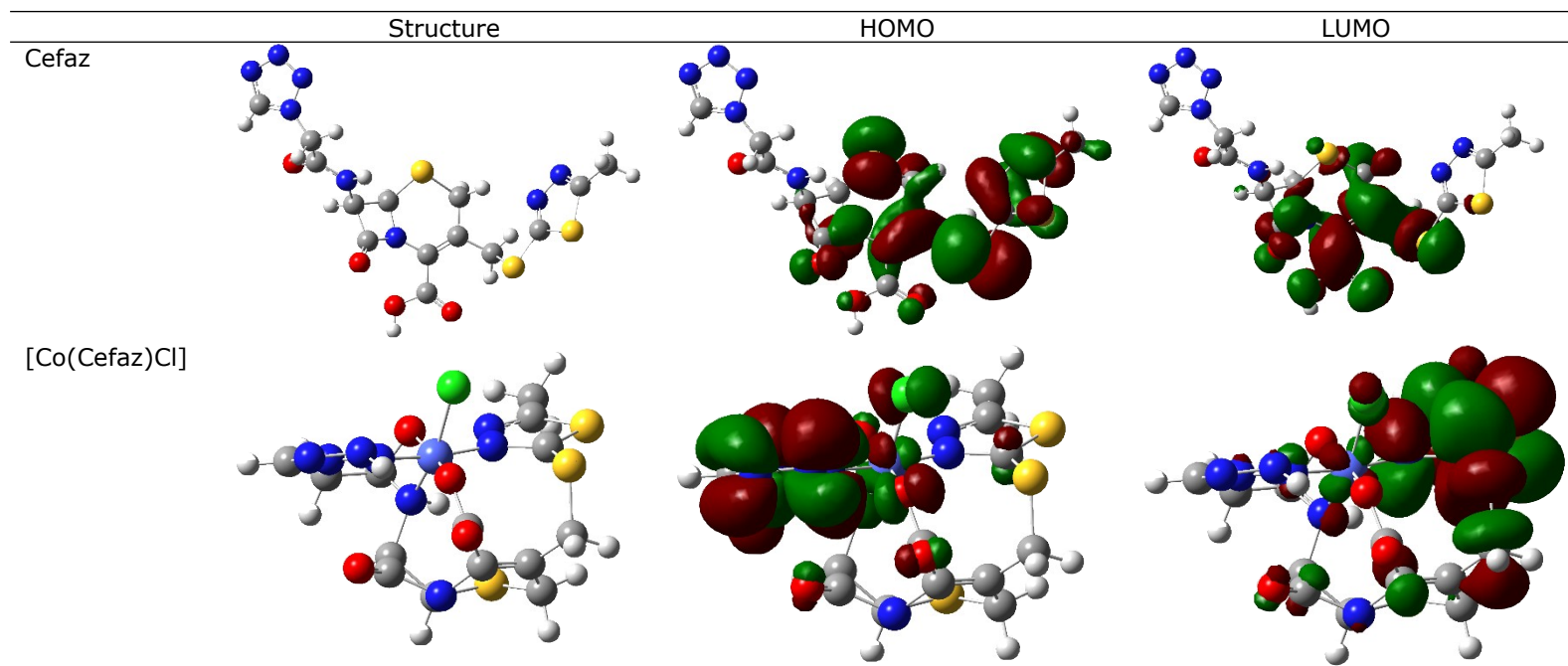
The energy differences of the frontier orbitals of the donor and acceptor, which correspond to the charge transfer transition, (ΔE_{gap}=LUMO$_{acceptor}$-HOMO$_{donor}$) (23) for the compounds were calculated from the HOMO and LUMO energies, which reflect the chemical activity of the molecule. The sample contour plots and 3D structures of the frontier orbitals (HOMOs and LUMOs) of the Cefaz and [Co(Cefaz)Cl] complex and their corresponding energy levels and gaps calculated with B3LYP/ LanL2DZ basis set are shown in Table 4.

The HOMO density for the Cefaz molecule is localized on the whole molecule surface, except for the some carbon and nitrogen atoms, and tetrazole group. The LUMO is distributed on the locally oxygen and sulfur heteroatoms and aromatic ring. On the other hand, as can be seen from Table 4, the LUMO extends over thiadiazole group and locally chlorine atom on the molecular surface for the [Co(Cefaz)Cl] complex. However, HOMO is located mainly on the chlorine atom and tetrazole group on the molecule surface. According to this findings, heteroatoms can be regarded as the active sites of compounds.

Table 5. Some Quantum chemical descriptors of the Cefaz and [Co(Cefaz)Cl] compounds calculated at B3LYP/LanL2DZ.

	E$_{HOMO}$ (eV)	E$_{LUMO}$ (eV)	ΔE_{gap}	ω(eV)	μ (eV)	η (eV)	χ
Cefaz	-6.974	-2.768	4.206	5.641	4.871	2.103	-4.871
[Co(Cefaz)Cl]	-4.460	-2.780	1.680	7.800	3.620	0.840	-3.620

The effect of the complexation reaction was investigated theoretically in determining both the antioxidant and electronic properties of the compounds. The HOMO-LUMO energy gap (ΔE_{gap}) of [Co(Cefaz)Cl] complex was found to be lower than Cefaz ligand (Table 5). It is estimated that the nitrogen atoms increase the HOMO density on the substituted tetrazole ring and also cause a decrease in ΔE_{gap} by raising the HOMO energies of the complex (Table 4). Accordingly, the [Co(Cefaz)Cl] complex can be expected to show greater reactivity, and higher antioxidant properties were observed in the experimental studies for the complex (Table 2).

On the other hand, the complexation reaction increases the electrophilic index (ω) and electronegativity (χ) of the synthesized [Co(Cefaz)Cl] complex. Therefore [Co(Cefaz)Cl] complex was found to be more reactive than Cefaz ligand in terms of antioxidant properties.

CONCLUSION

Electrochemical measurements of the [Co(Cefaz)Cl] complex show that the complex has two irreversible metal- and ligand-centered one-electron transfer response on the oxidation side and one quasi-reversible Co$^{II/I}$ couple indicating metal centered one-electron transfer on the reduction side in the CV and LSV voltammograms. The antioxidant activity of Cefaz was found to be less than [Co(Cefaz)Cl] complex and ascorbic acid. The HOMO-LUMO energy gap (ΔE_{gap}) of [Co(Cefaz)Cl] complex was found to be lower than Cefaz ligand. According to the theoretical calculations,

[Co(Cefaz)Cl] complex is expected to exhibit greater reactivity. The higher antioxidant property was observed for this complex in the experimental studies. The experimental results are in good agreement with the theoretical calculations.

CONFLICT OF INTEREST

No conflict and interest.

REFERENCES

1. Lancini D, Parenti F. Antibiotics (Russian translation). Moscow, Russia: Mir publishing; 1985.

2. Garzone P, Lyon J, Yu VL. Third-Generation and Investigational Cephalosporins: I. Structure-Activity Relationships and Pharmacokinetic Review. Drug Intelligence & Clinical Pharmacy [Internet]. 1983 Jul [cited 2022 Sep 21];17(7–8):507–15. Available from: <URL>.

3. Dajani AS. Prevention of Bacterial Endocarditis: Recommendations by the American Heart Association. JAMA [Internet]. 1997 Jun 11 [cited 2022 Sep 21];277(22):1794. Available from: <URL>.

4. Gentry LO, Zeluff BJ, Cooley DA. Antibiotic Prophylaxis in Open-Heart Surgery: A Comparison of Cefamandole, Cefuroxime, and Cefazolin. The Annals of Thoracic Surgery [Internet]. 1988 Aug [cited 2022 Sep 21];46(2):167–71.

Available from: <URL>.

5. Casanova J, Alzuet G, Borrás J, Timoneda J, García-Granda S, Cándano-González I. Coordination behavior of sulfathiazole. Crystal structure of dichloro-disulfathiazole ethanol Cu(II) complex. Superoxide dismutase activity. Journal of Inorganic Biochemistry [Internet]. 1994 Nov [cited 2022 Sep 21];56(2):65–76. Available from: <URL>.

6. Aravind L. An evolutionary classification of the metallo-beta-lactamase fold proteins. In Silico Biol. 1999;1(2):69–91.

7. Anacona JR, Alvarez P. Synthesis and Antibacterial Activity of Metal Complexes of Cefazolin. Transition Metal Chemistry [Internet]. 2002 [cited 2022 Sep 21];27(8):856–60. Available from: <URL>.

8. Anacona JR. Synthesis And Antibacterial Activity Of Some Metal Complexes Of Beta-Lactamic Antibiotics. Journal of Coordination Chemistry [Internet]. 2001 Nov 1 [cited 2022 Sep 21];54(3–4):355–65. Available from: <URL>.

9. Malkin V, Malkina O, Eriksson L, Salahub D. Modern Density Functional Theory. A Tool for Chemistry. Seminario J, Politzer P, editors. Amsterdam, the Netherlands: Elsevier; 1995.

10. Becke AD. Density-functional thermochemistry. III. The role of exact exchange. The Journal of Chemical Physics [Internet]. 1993 Apr [cited 2022 Sep 21];98(7):5648–52. Available from: <URL>.

11. Lee C, Yang W, Parr RG. Development of the Colle-Salvetti correlation-energy formula into a functional of the electron density. Phys Rev B [Internet]. 1988 Jan 15 [cited 2022 Sep 21];37(2):785–9. Available from: <URL>.

12. Frisch M, Trucks G, Schlegel H, Scuseria G, Robb M, Cheeseman J, et al. Gaussian 09, Revision A.02. Gaussian, Inc.; 2016.

13. Parr RG, Szentpály L v., Liu S. Electrophilicity Index. J Am Chem Soc [Internet]. 1999 Mar 1 [cited 2022 Sep 21];121(9):1922–4. Available from: <URL>.

14. Parr RG, Pearson RG. Absolute hardness: companion parameter to absolute electronegativity. J Am Chem Soc [Internet]. 1983 Dec [cited 2022 Sep 21];105(26):7512–6. Available from: <URL>.

15. Pearson RG. Absolute electronegativity and hardness correlated with molecular orbital theory. Proc Natl Acad Sci USA [Internet]. 1986 Nov [cited 2022 Sep 21];83(22):8440–1. Available from: <URL>.

16. Apak R, Güçlü K, Özyürek M, Karademir SE. Novel Total Antioxidant Capacity Index for Dietary Polyphenols and Vitamins C and E, Using Their Cupric Ion Reducing Capability in the Presence of Neocuproine: CUPRAC Method. J Agric Food Chem [Internet]. 2004 Dec 1 [cited 2022 Sep 21];52(26):7970–81. Available from: <URL>.

17. Sánchez-Moreno C, Larrauri JA, Saura-Calixto F. A procedure to measure the antiradical efficiency of polyphenols. Journal of the Science of Food and Agriculture [Internet]. 1998;76(2):270–6. Available from: <URL>.

18. Shiekh R, Rahman I, Malik M, Masudi S, Luddin N. Synthesis, Spectral, Electrochemical and Biological Studies of Nitrogen Donor Macrocyclic Ligand and its Transition Metal Complexes. 2012;7:12829–45. Available from: <URL>.

19. Apak R. Current Issues in Antioxidant Measurement. J Agric Food Chem [Internet]. 2019 Aug 21 [cited 2022 Sep 21];67(33):9187–202. Available from: <URL>.

20. Damena T, Zeleke D, Desalegn T, Demissie TB, Eswaramoorthy R. Synthesis, Characterization, and Biological Activities of Novel Vanadium(IV) and Cobalt(II) Complexes. ACS Omega [Internet]. 2022 Feb 8 [cited 2022 Sep 21];7(5):4389–404. Available from: <URL>.

21. Brand-Williams W, Cuvelier ME, Berset C. Use of a free radical method to evaluate antioxidant activity. LWT - Food Science and Technology [Internet]. 1995 [cited 2022 Sep 21];28(1):25–30. Available from: <URL>.

22. İlhan Ceylan B, Deniz NG, Kahraman S, Ulkuseven B. cis-Dioxomolybdenum(VI) complexes of a new ONN chelating thiosemicarbazidato ligand; Synthesis, characterization, crystal, molecular structures and antioxidant activities. Spectrochimica Acta Part A: Molecular and Biomolecular Spectroscopy [Internet]. 2015 Apr [cited 2022 Sep 21];141:272–7. Available from: <URL>.

23. Liao MS, Lu Y, Parker VD, Scheiner S. DFT Calculations and Spectral Measurements of Charge-Transfer Complexes Formed by Aromatic Amines and Nitrogen Heterocycles with Tetracyanoethylene and Chloranil. J Phys Chem A [Internet]. 2003 Oct 1 [cited 2022 Sep 21];107(42):8939–48. Available from: <URL>.

Molecular Dynamics Simulation of E412 Catalytic Residue Mutation of GOx-IPBCC

Asrul Fanani[1] (iD), **Popi Asri Kurniatin[1]** (iD), **Setyanto Tri Wahyudi[2,3]** (iD), **Waras Nurcholis[1,3]** (iD), and **Laksmi Ambarsari[1*]** (iD)

[1]Department of Biochemistry, Faculty Mathematics and Natural Sciences, IPB University, Bogor, West Java, Indonesia.
[2]Department of Physics, Faculty Mathematics and Natural Sciences, IPB University, Bogor, West Java, Indonesia.
[3]Tropical Biopharmaca Research Center, IPB University, Bogor, West Java, Indonesia.

Abstract: The enzyme glucose oxidase from *Aspergillus niger* has a homodimeric structure, consisting of two identical subunits with a molecular weight of 150,000 Daltons. In this study, we used the structure of the enzyme glucose oxidase from *Aspergillus niger* IPBCC.08.610 (GOx-IPBCC), this enzyme had a total activity of 92.87 U (μmol/min) and a Michaelis-Menten constant (*Km*) of 2.9 mM (millimolar). This study was conducted to predict the molecular dynamics of E412 (Glu412) residue catalytic mutation belonging to the GOx-IPBCC enzyme was determine the effect of changes in the catalytic residue on substrate binding (β-D-glucose). The results of molecular docking of 19 mutant structures, six E412 mutant homologous structures were selected (E412C, E412K, E412Q, E412T, E412, E412V, and E412W), which were evaluated using molecular dynamics simulation for 50 ns. The results showed a decrease in *ΔG* values in two mutant structures is E412C and E412T, and there is one mutant structure that increased *ΔG* values, namely E412W, these three mutant structures showed the best stability, bond interaction, and salt bridge profile according to molecular dynamics simulation.

INTRODUCTION

Glucose oxidase (GOx) is an enzyme that catalyzes the oxidation of β-D-glucose to gluconic acid. This enzyme works to convert glucose into gluconic acid and hydrogen peroxide with the help of oxygen (1). GOx is used industrially both to maintain glucose and to remove oxygen. An exciting application is also a unique test reagent for glucose (2). This enzyme was mainly isolated from *Aspergillus niger* (3) and *Penicillium sp* (4). GOx from Aspergillus niger has a homodimeric structure, consisting of two identical subunits with a molecular weight of 150,000 Daltons. Each subunit molecule is tightly bound to the coenzyme flavin adenine dinucleotide (FAD), which acts as a redox carrier in its catalytic reaction (5).

Until now, GOx enzymes have been widely applied in the pharmaceutical (6), chemical, and food industries, including gluconic acid production, food preservatives, and the development of biofuel cells (7). The glucose oxidase enzyme is the most widely used in daily and continuous blood glucose sensor materials (8). Glucose oxidase can also be applied in biofuel cells or self-power sensors because glucose oxidase has high specificity for glucose, low redox potential (~-0.42 V vs. Ag/AgCl at pH 7.4), and good thermostability (9,10).

In this study, we used the GOx enzyme structure of *Aspergillus niger* IPBCC.08.610 (GOx-IPBCC). This enzyme has a total activity of 92.87 U and a Km value of 2.9 mM (11,12). The 3-dimensional structure of the GOx-IPBCC enzyme was successfully predicted from the sequence of its constituent genetic code (https://www.ncbi.nlm.nih.gov/ with access number MH593586.1) (13,14). This study was conducted to predict the molecular dynamics of E412 residue catalytic mutation belonging to the GOx-IPBCC enzyme. Mutations in catalytic residues are used to determine the extent of changes in substrate binding efficiency from the dynamics of mutation changes carried out on catalytic residues, so it is hoped that this research can help the development of science related to modification of the GOx enzyme structure. The analyzes used to support the results of this study are molecular dynamics simulation (MD) and molecular mechanics Poisson Boltzmann (MMPBSA) to determine the stability of the mutant structure and to determine the bond free energy (ΔG) (15,16). Until now, there have been many computational-based studies (bioinformatics) to predict the improvement of enzyme structures that can increase the stability and work of enzymes (17–19).

EXPERIMENTAL SECTION

Molecular Docking Simulation
Molecular docking simulation in this study was performed using Autodock Vina 1.1.2, with free energy (kcal/mol) value calculation parameters. 3-dimensional structure files of GOx-IPBCC enzymes and ligands were prepared using the AutoDockTools 1.5.6 tool and saved in *pdbqt format (GOx.pdbqt and ligand.pdbqt). The coordinates of the ligand-binding region (Grid box) were determined using the help of the AutoDockTools 1.5.6 tool. Furthermore, to analyze the bonding interactions ($\mathring{A}$) between GOx-IPBCC and the molecular docking ligands, the Ligplot+ 1.4.5 was used to analyze results in 2D format (hydrophobic interactions and hydrogen bonds with long bond distances).

Structural Mutation of GOx-IPBCC Enzyme
In this study, the structure of the GOx-IPBCC enzyme was mutated in the E412 catalytic region with 19 mutations. Mutations were performed using the Chimera 1.14 software following the computational mutation. The energy minimization of the mutants structures was carried out to obtain a 3-dimensional conformation in the normal state (20).

Table 1: The type of E412 residue mutation (glu412) of the GOx-IPBCC enzyme.

Mutant	Mutant	Mutant
E412A (Ala)	E412K (Lys)	E412R (Arg)
E412C (Cys)	E412L (Leu)	E412S (Ser)
E412D (Asp)	E412M (Met)	E412T (Thr)
E412F (Phe)	E412N (Asn)	E412V (Val)
E412G (Gly)	E412P (Pro)	E412W (Trp)
E412H (His)	E412Q (Gln)	E412Y (Tyr)
E412I (Ile)		

Molecular Dynamics (MD) Simulation
Molecular dynamics simulations were run using the Amber 18 (21). The ligand and protein complexes were prepared from the best models, removing unnecessary hydrogen atoms and other molecules. Next, a new hydrogen atom is added, and the protonated state of the side chain can be titrated using the Virginia Tech H++ server (http://biophysics.cs.vt.edu/H++) (22,23). After that, energy minimization was carried out for six repetitions. In the end, the system was heated gradually from 0-300 K. After the desired temperature was reached, six equilibrium steps were carried out to ensure the stability of the time-related structural properties in the initial equilibration. The first step of limiting was applied in fixed volume (NVT) for 50 ps and the subsequent phase under constant pressure (NPT). The restriction is then slowly removed for 300 ps in total. This allows the system to get the proper density and also to avoid aggregation. The final step of the simulation is a lengthy production process in which the dissolved protein is run for 50 ns of simulation in 25 separate stages of 2.0 ns each (2.0 fs timestep).

The free energy of ligand binding by proteins was calculated using the MMPBSA approach (kcal/mol) (24). The free energy is calculated using a single pass procedure, agreeing with the results obtained from molecular dynamics simulations, operating with high structural stability. This approach uses the potential energy of molecular dynamics (VDW + EEL) and the free energy of the solvent (nonpolar + polar) (16).

RESULTS AND DISCUSSION

Molecular Docking Validation

The 3-dimensional structure of the GOx-IPBCC enzyme did not contain ligand structure that bind to its binding site. To compare and validate the binding site, the 3-dimensional structure of the GOx-IPBCC enzyme and the 3-dimensional structure of the GOx 1CF3 enzyme with known binding site was aligned (25). On the other hand, the use of the 1CF3 structure is based on the position of this structure as the template structure for the GOx-IPBCC builder (13).

Based on the analysis results, it was found that the anchorage area was suitable and had the best results from the alignment of the GOx-IPBCC and 1CF3 structures with binding energy values of 6.0 kcal/mol and 6.6 kcal/mol. Moreover, the results of redocking with 10 repetitions obtained a binding RMSD value of 0.7.
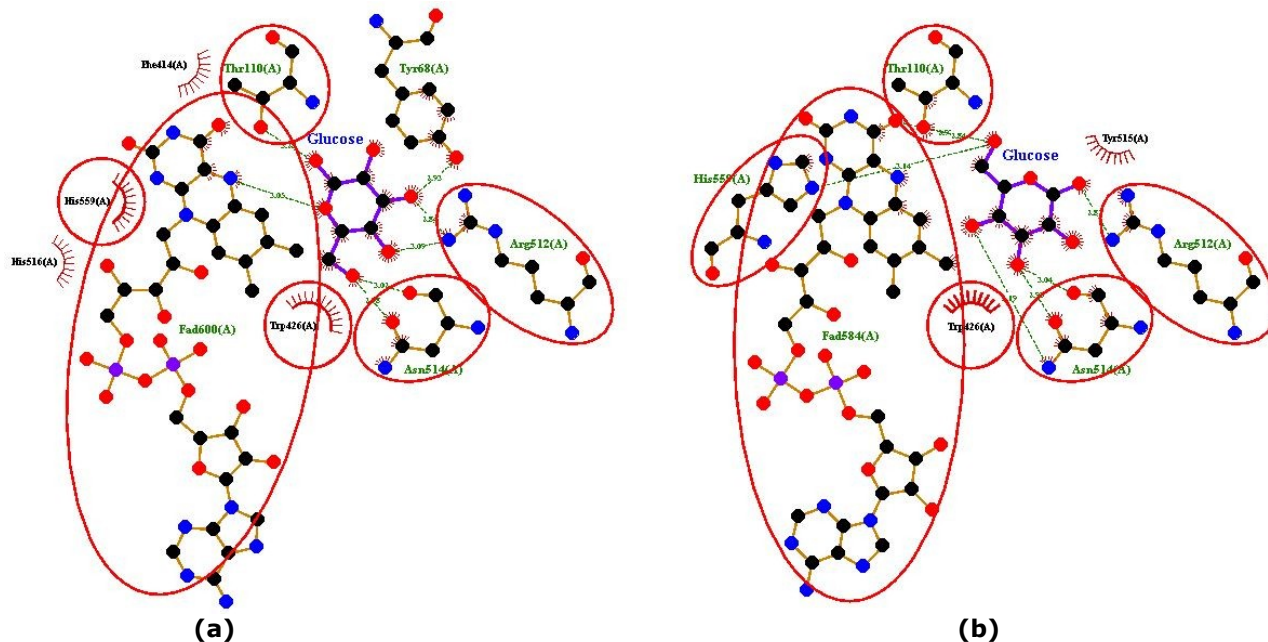
Figure 1: Comparison of visualization of β-D-glucose ligand binding interaction by the structures of **(a)** 1CF3 and **(b)** GOx-IPBCC.

Structural Mutations of GOx-IPBCC Enzyme

The study of mutagenesis has a broad impact on the development of science in enzymes (26). Mu et al., (2019) reported that the mutation of the GOx enzyme structure could increase the stability of the enzyme up to a temperature of 70℃ and a pH of 4.5-7.0 and was able to convert 98% of glucose into gluconic acid. In this study, the structure of the GOx-IPBCC enzyme was single-mutated at the catalytic residue E412. There are 19 mutant structures in all (Table 1). The parameter used to compare the quality of the mutant structure are the value of $ΔG$ and residue binding interactions with ligands. Based on the data obtained from the molecular docking simulation on the mutant structure, the mutation of the E412 residue in the GOx-IPBCC structure affects the binding energy of the ligand. Table 2 shows the changes in the value of $ΔG$ that occur in each mutant structure.

Table 2: Comparative data from molecular docking simulation analysis on residue E412.

Mutant	$ΔG$ (kcal/mol)	Hydrogen bond	Hydrophobic bond
Wild-type	−6.0		
E412A	−6.0		
E412C	−5.9	Thr110, Arg512, Asn514, His559, FAD	Trp426, Tyr515
E412D	−5.9		
E412H	−5.9		
E412K	−6.0		
E412M	−5.9		
E412N	−6.0		
E412P	−5.7	Thr110, Arg512, Asn514, His559, Asp424 FAD	Trp426

1093

E412S	−5.9	Thr110, Arg512,	
E412V	−5.7	Asn514, His559,	Trp426, Tyr515
E412W	−6.1	FAD	
E412F	−5.5	Thr110, Arg512, Asn514, FAD	Trp426, Tyr515, His559
E412G	−5.9	Thr110, Arg512, Asn514, FAD	Trp426, His559
E412I	−5.7	Thr110, Arg512,	Trp426, Tyr515,
E412L	−5.7	Asn514, FAD	His559
E412Q	−5.9		
E412R	−6.0	Arg512, Asn514, His559, FAD	Thr110, Trp426
E412T	−5.8	Thr110, Arg512,	Trp426, His559
E412Y	−5.7	Asn514, FAD	

Based on the profile of the *ΔG* values of 19 mutant structures, explicated that the mutation of the E412 residue had a significant effect on the binding energy of the receptor (GOx-IPBCC). Furthermore, were selected six mutant structures for further molecular dynamics analysis. This analysis serves to obtain further data regarding the characteristics of the mutant structure at the molecular level and its stability. The mutant structures selected were E412C, E412K, E412Q, E412T, E412V, and E412W. These six selected structures are based on the *ΔG* value and the best ligand-binding mode that is close to the wild-type structure.

Molecular Dynamics Simulation
Molecular dynamics is simulated to obtain molecular data statistically and dynamically to validate the data of a structure (27). The molecular dynamics simulation of the GOx-IPBCC mutant enzyme was run for 50 ns at 300 K. The RMSD data obtained in the molecular dynamics simulation describe the structure of the E412C, E412K, E412Q, E412T, E412V, and E412W mutants. That have RMSD values that are not much different from the wild type (WT) structure

(Figure 2); these results confirm that the mutant structure has good structural stability, as does not have an RMSD value that is much different from the WT structure.

The following simulation data obtained is the RMSF plot. These data describe fluctuations in electron movement that occur at the level of residues (amino acids) of the GOx-IPBCC structure having high fluctuations in the N terminal and C terminal residues. However, this increase in fluctuation does not affect the stability level of the GOx-IPBCC structure. In addition, there are high enough fluctuations that also occur in the sequence residues 269-272, 255, and 259 (Figure 3). Based on the comparison data of the RMSF plot of the GOx-IPBCC mutant structure with the wild-type structure, there were quite clear differences in the fluctuations in the sequence of residues 61-73. The mutant structure experienced an increase in fluctuations in the RMSF plot of residue area 61-73. This increase occurred significantly in the E412K, E412Q, E412V, and E412W mutant structures, while in the E412C and E412T mutants, the increase was not significant (Figure 3).
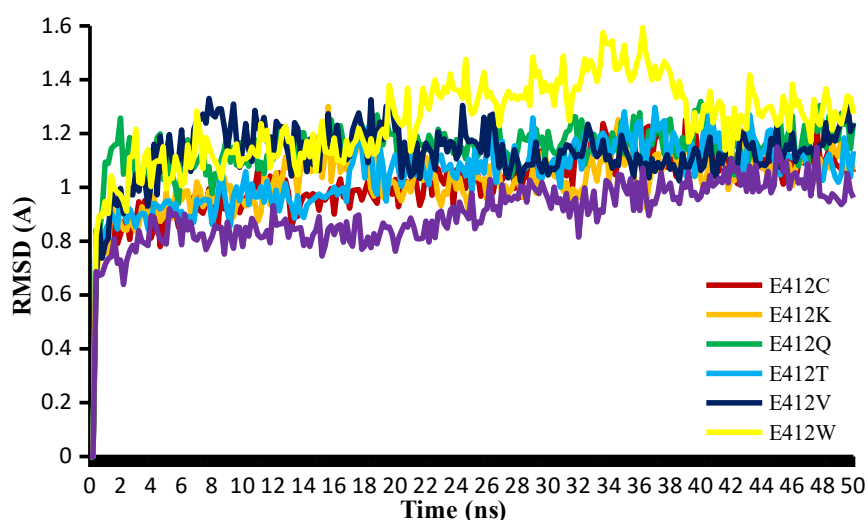
Figure 2: Comparative profile of the RMSD value of the GOx-IPBCC enzyme mutant structure from the 50 ns molecular dynamics simulation.
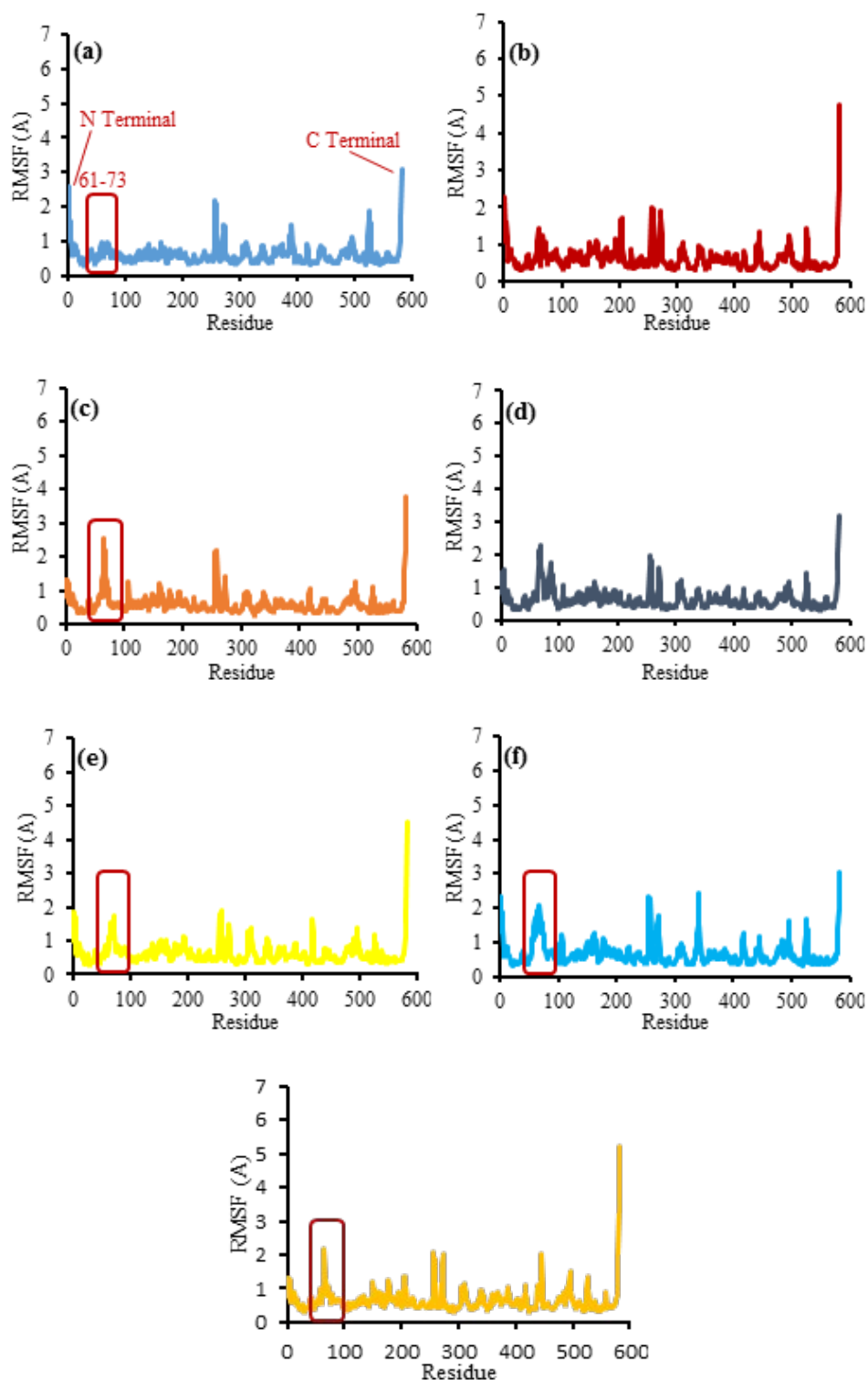
Figure 3: RMSF profile of GOx-IPBCC mutant during 50 ns molecular dynamics simulation at residue E412 (a) WT (b) E412C (c) E412K (d) E412Q (e) E412T (f) E412V (g) E412W.

The increase in fluctuations indicates that the level of flexibility of the residue structure increases, and residues that have low fluctuations are stiffer and, therefore, more stable (28). High fluctuations can affect the stability of the structure. The dynamics of fluctuations in the structure of the GOx-IPBCC mutant illustrate the effect of changes in the structure of one amino acid residue that can affect fluctuations in other amino acid residues. The fluctuation changes that occur are not significant, and it is difficult to determine whether the enzyme structure's stability well maintained. Thus,

secondary structure analysis needs to be carried out to determine the effect of increasing fluctuations on the secondary structure profile of the GOx-IPBCC enzyme.

Profile of GOx-IPBCC. Mutant Secondary Structure

Based on the analysis results obtained from the RMSF plot data, there are differences in fluctuations between the mutant and wild-type structures. This difference occurs mainly in the increasing sequence region of the residue from 61 to 73. The analysis results revealed that the residue sequence region 61-73 formed a secondary structure conformation of 3-10 helices. The 3-10 helix conformation has three rotating residues, with an angle of 120° between successive residues, the helix increment per residue 1.93–2.0. Simply put, the 3-10 helices have a tighter, longer,

and thinner coil than the -helices, with the same number of residues (29).

In the wild-type structure, this conformation was maintained until the end of the simulation time (50 ns) (Figure 4). The secondary structure of the E412C and E412V mutants shows that the two mutant structures do not undergo a 3-10 helix conformational change in the residue region 61-73. The mutant structures E412K, E412Q, E412T, and E412W gave different results (Figure 5), namely that these mutant structures have 3-10 helix conformational changes during the simulation time. Mutant E412K underwent a 3-10 helix conformational change when the simulation entered 23 ns, and at 43 ns, the 3-10 helix conformation reappeared. In the E412Q, E412T and E412W mutants, there was a 3-10 helix conformational change from the beginning of the simulation time to the end of the simulation time.
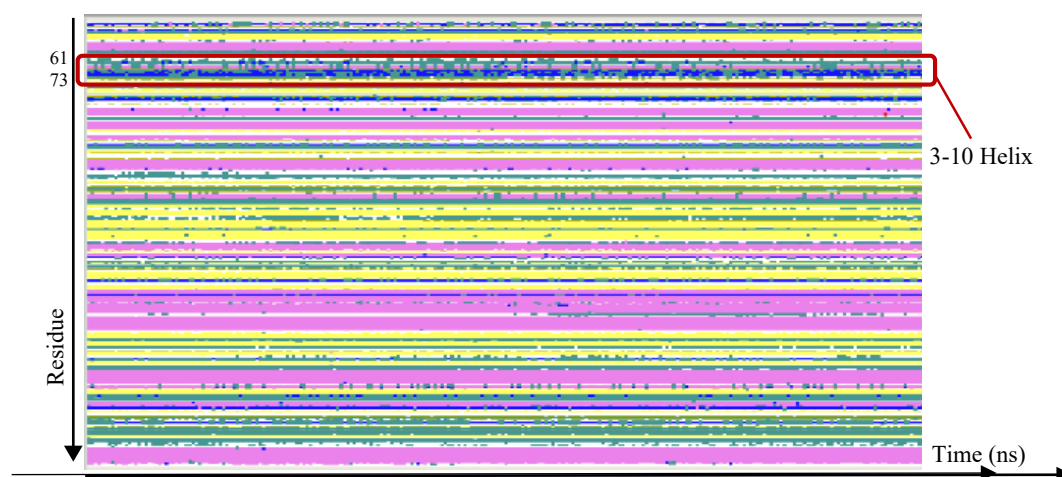
Figure 4: The results of analysis secondary structure enzyme GOD_IPBCC_1CF3 (wild type) during the molecular dynamics simulation time of 50 ns. ■ *turn,* ■ *isolated bridge,* ■ α-helix, ■ 3-10 helix, ■ Pi-helix, ■ *Extended configuration,* □ *coil.*

The 3-dimensional visualization was intended to determine the proximity of the 3-10 helix conformation to the mutant residue 412 (m412) and determine the effect of mutations on the interactions between amino acids in the 3D structure of the GOD-IPBCC mutant and to compare its interaction structure with the wild-type

conformation (Figure 6). Based on the observations, it is obtained an image of the close interaction between the residues of the 3-10 helix conformation and the residues of mE412 in the wild type structure, which is not too far apart, and the residues of the 3-10 helix conformation are also close to the FAD cofactor.
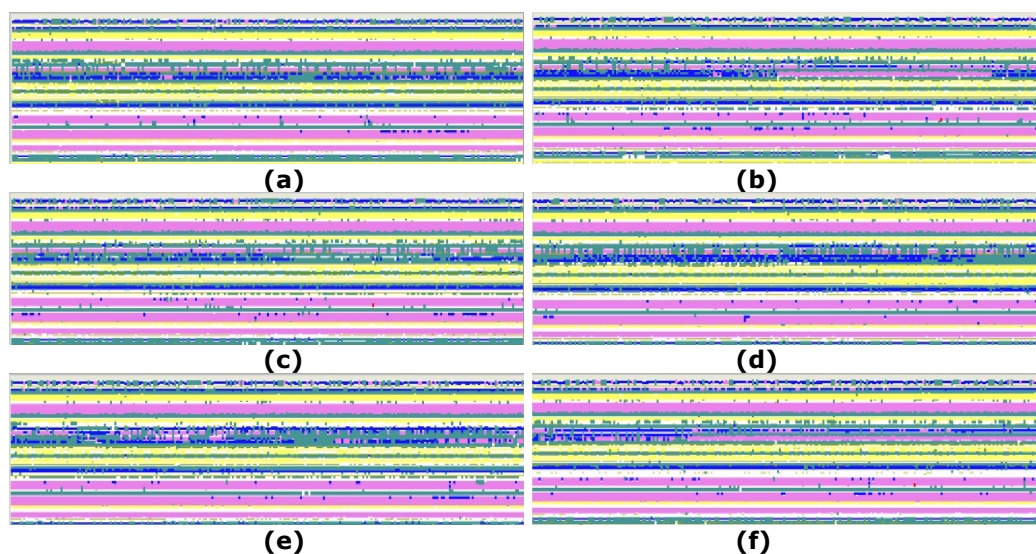
Figure 5: Visualization of the results of secondary structure analysis of 3-10 helix mutant residue E412 enzyme GOD_IPBCC_1CF3. (a) E412C, (b) E412K, (c) E412Q, (d) E412T, (e) E412V, (f) E412W.
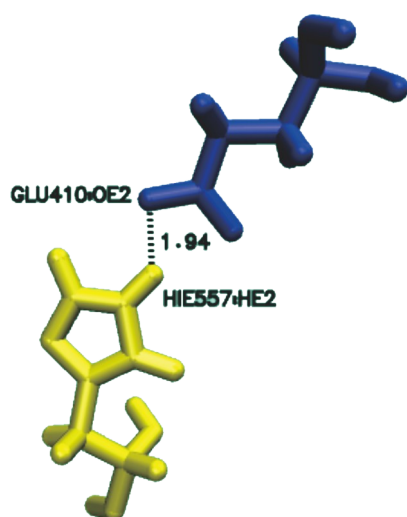
Figure 6: Visualization of the interaction between E412 and H559 mutant residues in the structures wild-type GOx-IPBCC.

From the observations on the structure of the GOD-IPBCC mutant, shown that what affects the stability of the 3-10 helix conformation is the proximity to residues H559 and m412. When the bond distance between residues m412 and H559 is stretched, the residue H559 tends to be unstable and closer to the 3-10 helix conformational region. Thus, the 3-10 helix conformation becomes unstable as it is disturbed by the activity of the closer H559 residue. This occurred in the E412T mutant (Figure 7d) because the bond distance between H559 and m412 became 6.61.

In contrast to what happened to the E412K, E412Q, and E412W mutants (Figure 7b, 7c, 7f). The three mutant structures had close interaction distances between H559 and m412 residues, which were 3.15, 2.95 and 2.02, respectively. However, the 3-10 helix structure was unstable. This is because the interaction of the H559-m412 residue tends to be closer to the 3-10 helix conformation when compared to the wild-type structure. This is caused by a change in the -R group of the m412 amino acid, which results in a shift closer to the 3-10 helix conformation.
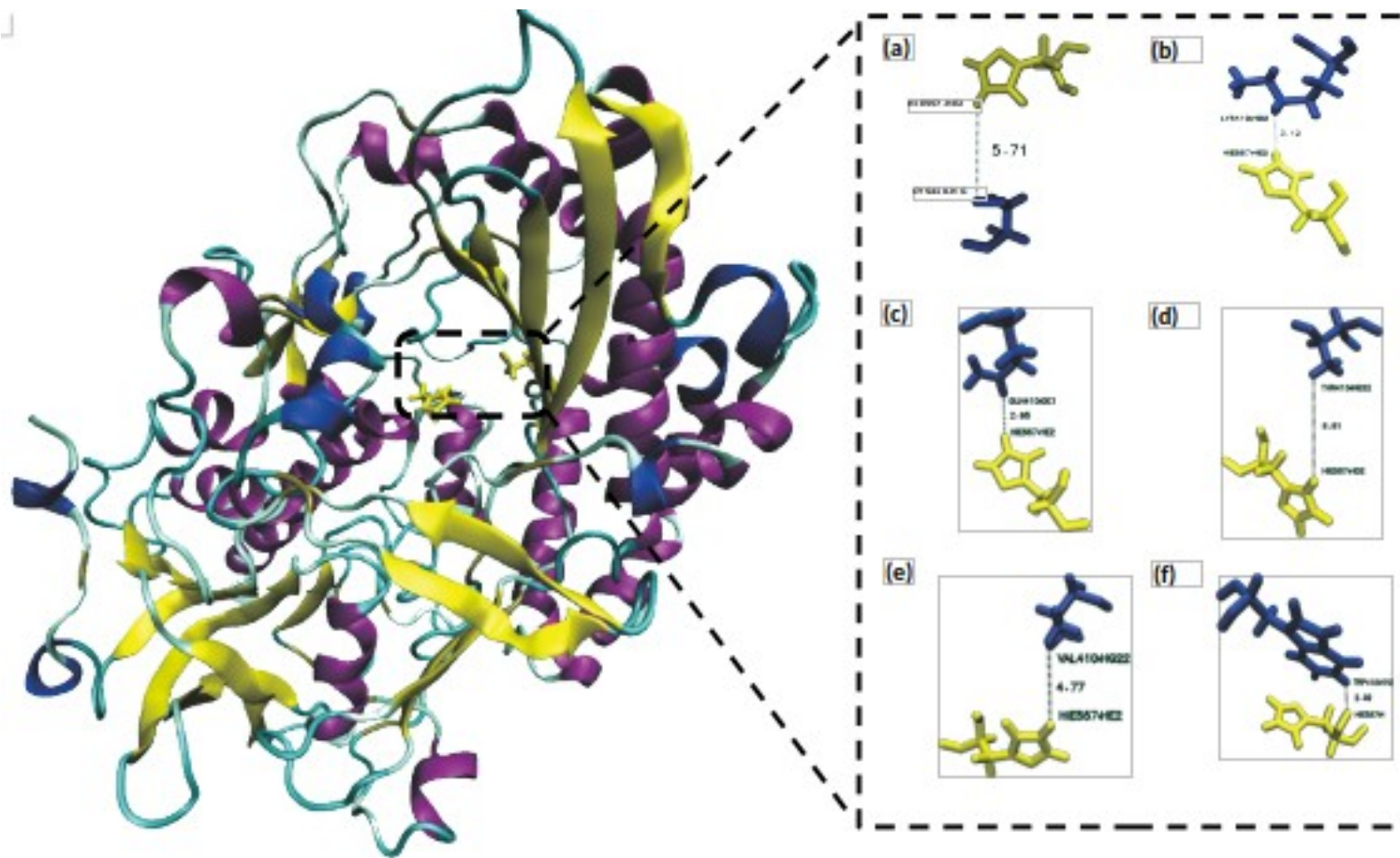
Figure 7: Visualization of the interaction between E412 and H559 mutant residues in the mutant structures (a) E412C, (b) E412K, (c) E412Q, (d) E412T, (e) E412V, (f) E412W.

(a)

(b)
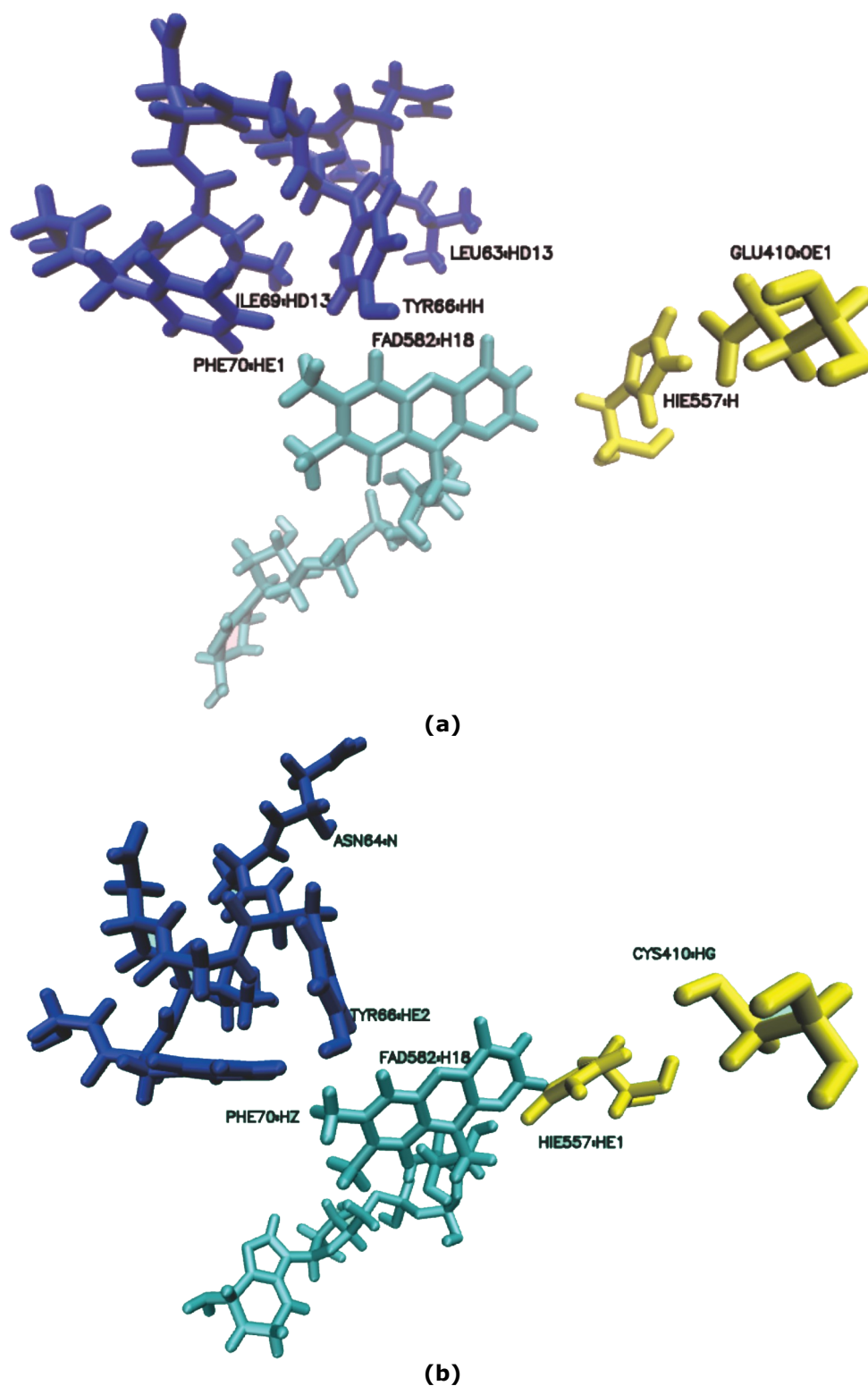
Figure 8: Visualization of the interaction distance between H559-m412 residues and 3-10 helix motif residues. (a) wild-type (b) E412C (c) E412K (d) E412Q (e) E412T (f) E412V (g) E412W.

(c)

(d)

Figure 8 (contd.): Visualization of the interaction distance between H559-m412 residues and 3-10 helix motif residues. (a) wild-type (b) E412C (c) E412K (d) E412Q (e) E412T (f) E412V (g) E412W.

(e)

(f)
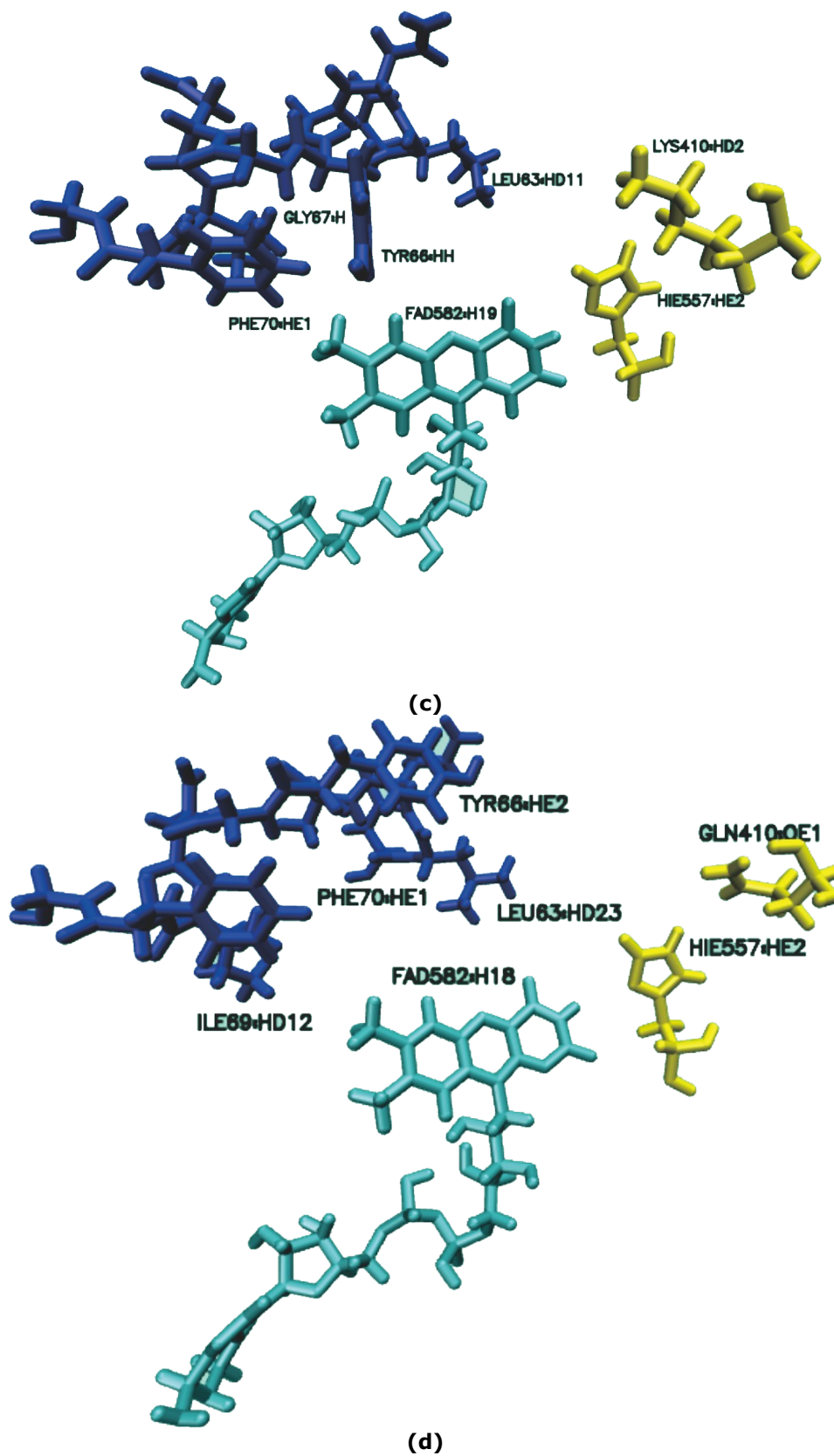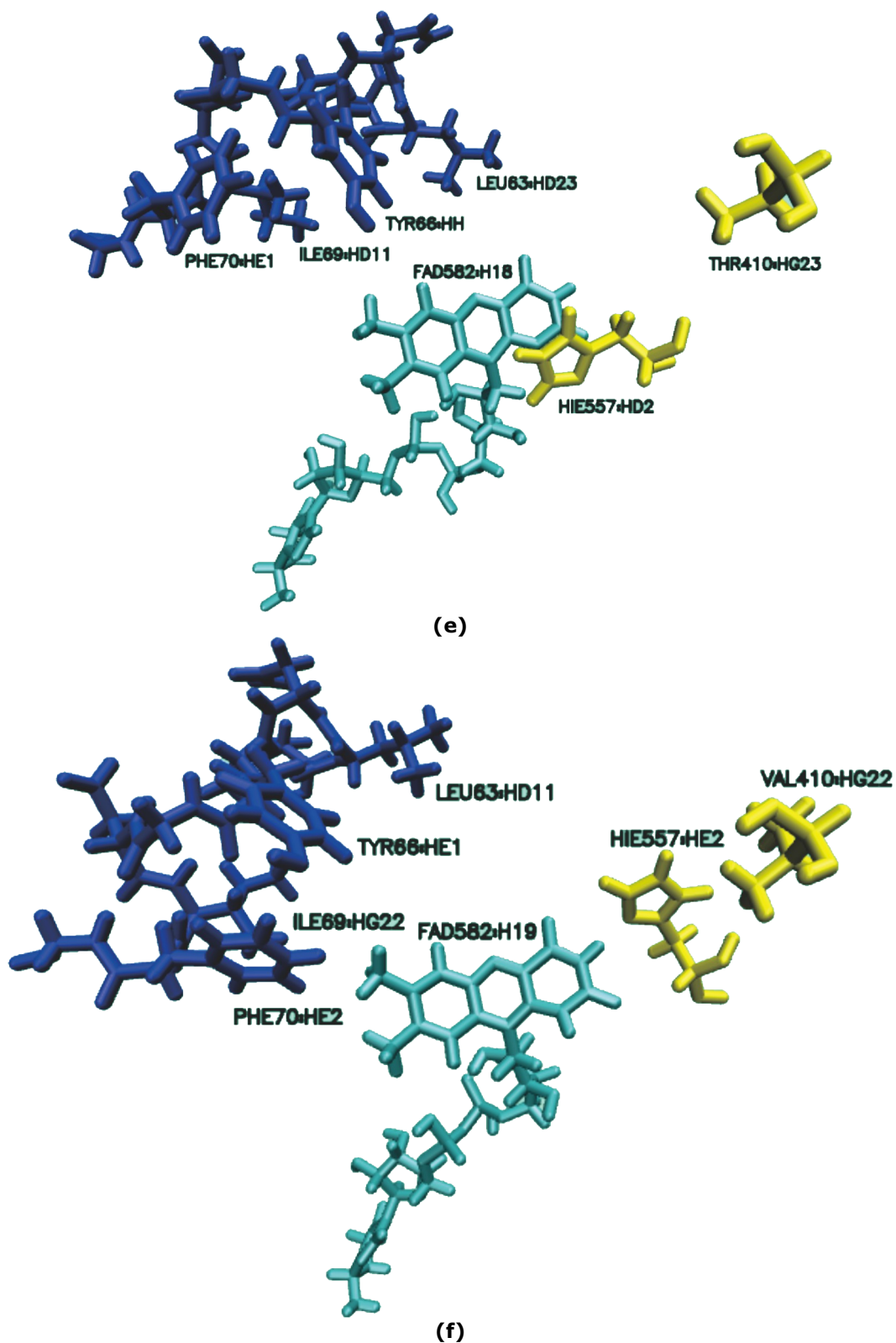
Figure 8 (contd.): Visualization of the interaction distance between H559-m412 residues and 3-10 helix motif residues. (a) wild-type (b) E412C (c) E412K (d) E412Q (e) E412T (f) E412V (g) E412W.
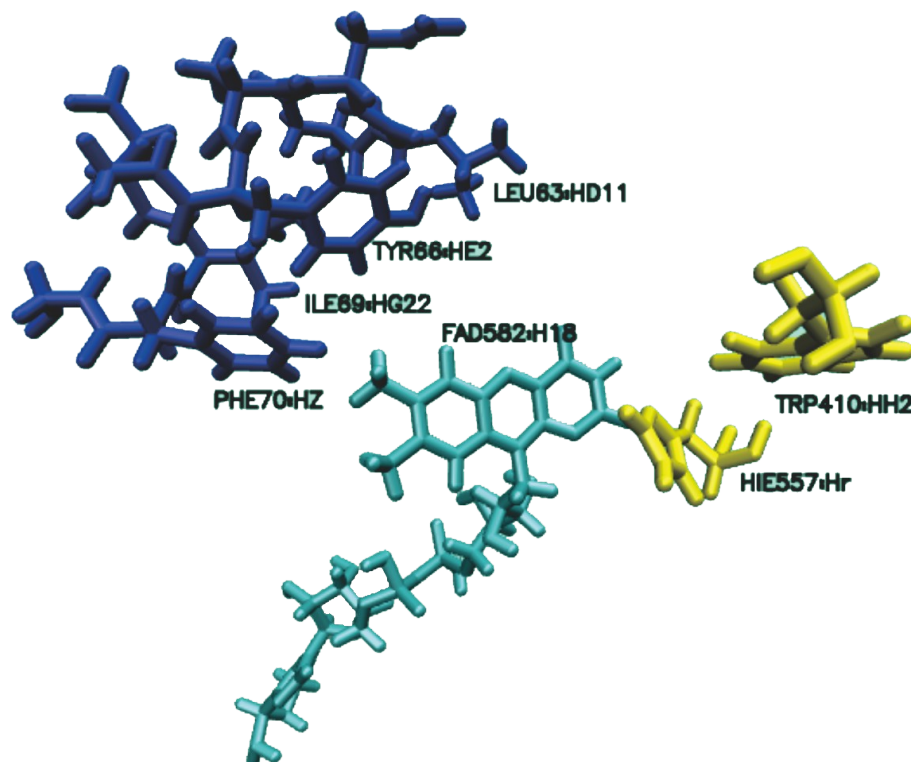
(g)

Figure 8 (contd.): Visualization of the interaction distance between H559-m412 residues and 3-10 helix motif residues. (a) wild-type (b) E412C (c) E412K (d) E412Q (e) E412T (f) E412V (g) E412W.

GOx-IPBCC Mutant Structure Stability Based on Salt Bridge

The stability of the GOx-IPBCC mutant structure was further evaluated using salt bridge analysis that emerged during a simulation time of 50 ns. As a probability from molecular dynamics simulations, the salt bridge bond interactions are formed by chance (30). The analysis results show approximately 45 pairs of salt bridges formed during the simulation time and 21 pairs of salt bridges that always appear in each mutant structure (Table 3). The probability of the emergence of salt bridge interactions plays a vital role in the thermal stability of proteins (31).

Several pairs of salt bridges appear to be broken or not maintained by the mutant structure, including the E372-R398 salt bridge pairs (Table 3); the salt bridge pair D317-K304 failed to maintain by the E412Q and E412T mutants. Maulana et al., (2019) revealed that the GOx-IPBCC structure has thermal stability, which is influenced by the formation of salt bridges.

Table 3: Comparison of the results of the analysis of the salt bridge pairs that emerged in the 50 ns simulation of the mutant structure of the GOx-IPBCC enzyme.

Wild-type	E412C	E412K	E412Q	E412T	E412V	E412W
D19-K280	D19-K280	D19-K280	D19-K280	D19-K280	D19-K280	D19-K280
E38-R237	E38-R237	E38-R237	E38-R237	E38-R237	E38-R237	E38-R237
D55-R228	D55-R228	D55-R228	D55-R228	D55-R228	-	D55-R228
E61-R228	E61-R228	E61-R228	E61-R228	E61-R228	E61-R228	E61-R228
D75-R93	D75-R93	D75-R93	D75-R93	D75-R93	D75-R93	D75-R93
D132-K114	D132-K114	D132-K114	D132-K114	D132-K114	D132-K114	D132-K114
E142-R111	E142-R111	E142-R111	E142-R111	E142-R111	E142-R111	E142-R111
D175-K150	D175-K150	D175-K150	D175-K150	D175-K150	D175-K150	D175-K150
D179-K150	D179-K150	D179-K150	D179-K150	D179-K150	D179-K150	D179-K150
E219-R145	E219-R145	E219-R145	E219-R145	E219-R145	E219-R145	E219-R145
E266-K250	E266-K250	E266-K250	E266-K250	E266-K250	E266-K250	E266-K250
E282-R543	E282-R543	E282-R543	E282-R543	E282-R543	E282-R543	E282-R543

Wild-type	E412C	E412K	E412Q	E412T	E412V	E412W
D317-K524	D317-K524	D317-K304	-	D317-K304	D317-K304	D317-K524
D317-K304	D317-K304	D317-K524	-	-	D317-K524	D317-K304
E372-R398	-	-	-	-	-	E372-R398
D422-R510	D422-R510	D422-R510	-	A422-R510	A422-R510	D422-R510
D440-K271	D440-K271	D440-K271	D440-K271	D440-K271	D440-K271	D440-K271
E456-K370	E456-K370	E456-K370	E456-K370	E456-K370	E456-K370	E456-K370
D571-R35	D571-R35	D571-R35	D571-R35	D571-R35	D571-R35	D571-R35
D576-R535	D576-R535	D576-R535	D576-R543	D576-R535	D576-R535	D576-R535
D576-R543	D576-R543	D576-R543	D576-R535	D576-R543	D576-R543	D576-R543

The stability of the GOx-IPBCC mutant structure based on RMSD data describes fairly good stability during the simulation time. However, the RMSF and secondary structure data revealed that the GOx-IPBCC structure was unstable at the residue region 61-73, namely, the conformation of the 3-10 helix structure changed. Especially in the mutant structure E412K, E412Q, E412V and E412W, which undergo structural conformational changes during the simulation time.

MMPBSA Calculation and Hydrogen Bond Interaction
Hydrogen bonding interactions between β-D-glucose and GOx-IPBCC enzymes were also analyzed to obtain information about the effect of mutations on the substrate-binding site (Table 4). Based on the analysis results, the dynamics of changes in substrate binding by the GOx-IPBCC mutant structure did not change significantly. Residues that appear on the results of the analysis of the wild-type structure can still be found in the mutant structure; in the mutant structure, the hydrogen bonding interactions of the other residues even increased, especially in the E412K and E412T mutants. On the other hand, in the E412C, E412Q, E412V and E412W mutant structures, the number of residues interacting with hydrogen bonds was reduced. The E412 residue is a catalytic residue that stabilizes the H559 catalytic residue to bind the substrate. Thus, some of the mutations in this study affect the substrate binding-pose, especially on hydrogen interactions.

Based on the results of molecular dynamics simulations, the ligand complex and structure of the GOx-IPBCC mutant analyzed using the MMPBSA simulation method. This method is the final method widely used to validate molecular docking data by calculating the value of free energy (ΔG) (32,33). The free energy of ligand binding by proteins is measured by calculating the entropic contribution during the reaction. Another approach to estimating binding affinity is calculating the free energy along the path connecting the two thermodynamic states: the ligand in its bound and unbound state (34).

The MMPBSA simulation was run using the Amber 18. The results revealed that the free energy data of ligand binding during the molecular dynamics simulation time showed that the mutant structures E412C, E412K, E412Q, E412T, and E412V. Has higher free energy values (ΔG) compared to the wild type structures (20.63 kcal/mol) or has a weaker free energy value because the more negative the binding energy of the ligand, and there is one mutant structure that has a negative free energy value or better, that is -22.79 in the E412W mutant. These results indicate that the analyzed mutant structure largely reduces the interaction or ligand binding free energy by the GOx-IPBCC enzyme.
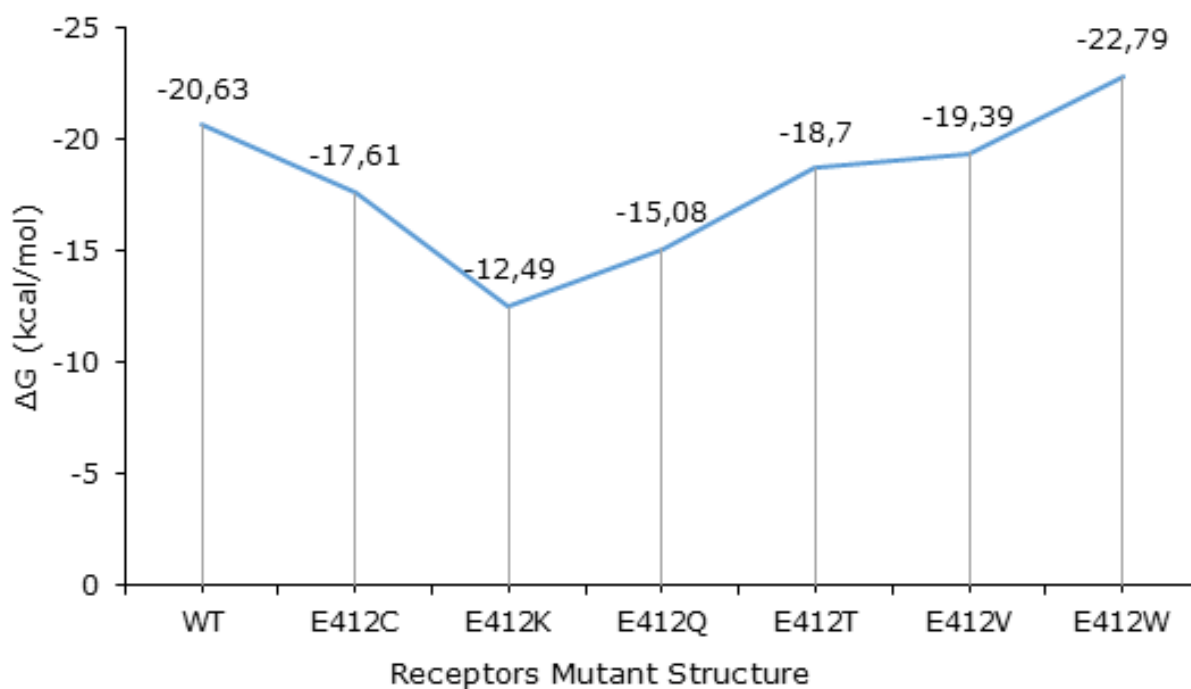
Figure 9: Comparative profile of free energy value (*ΔG*) of β-D-glucose ligand binding by GOx-IPBCC mutant structure.

The bond interaction profile formed during the simulation time of 50 ns between the mutant structure and the β-D-glucose ligand gave quite different results. There is a loss of interacting catalytic residues. The loss of this interaction is predicted that the enzyme structure loses its catalytic ability. The mutants that experienced a loss of interaction of H516 and H5559 catalytic residues were E412K and E412V mutants, while the E412C and E412T mutants lost one interaction of H516 catalytic residues, and the E412W mutant did not lose interaction with the two catalytic residues.

Table 4: Residual data that interacts hydrogen bonding with the substrate (β-D-glucose) during the molecular dynamics simulation time of 50 ns.

Receptor	Hydrogen Bond	Payload Mutant
Wild-type	Tyr66, Thr108, Gln327, Thr329, Arg510, Asn512, His514, His557, FAD	Polar
E412C	Tyr66, Thr108, Asp422, Arg510, Asn512, His557, FAD	Polar
E412K	Tyr66, Asp68, Gly107, Thr108, Thr329, Ile336, Asp414, Ala416, Ser420, Asp422, Arg510, Asn512, FAD	Positive
E412Q	Tyr66, Thr108, Asp422, Arg510, Asn512, His514, His557, FAD	Polar
E412T	Tyr66, Thr108, Thr329, Asp422, Arg510, Pro511, Asn512, His557, FAD	Polar
E412V	Tyr66, Val104, Gly106, Asp422, Arg510, Asn512, FAD	Nonpolar
E412W	Thr108, Arg510, Asn512, His514, His557	Nonpolar

CONCLUSION

The results showed that the catalytic mutation of residue E412 in the GOx-IPBCC enzyme significantly affected the structural stability and binding of the GOx-IPBCC enzyme to the ligand. These results were confirmed by the molecular dynamics analysis method, which showed that the structure of the mutant increased and decreased in the binding energy value, in the E412W mutant,

which decreased, and the E412C, E412K, E412Q, E412T, and E412V mutants increased. In addition, based on RMSF and salt bridge data, it is known that the structure of the E412C, E412T and E412W mutants are the mutants that have the best structural stability. These results are expected to add information about increasing the utilization of GOx-IPBCC enzymes, especially those that require enzyme activity with higher ΔG values, such as EFC (enzymatic fuel cell) for E412C and E412T mutant types, or to improve molecular quality-holding energy, namely E412W.

CONFLICT OF INTEREST

There is no conflict to declare.

REFERENCES

1.   Obut S, Bahar T. Glucose oxidase immobilized biofuel cell flow channel geometry analysis by CFD simulations. Turkish J Chem. 2019;43(5):1486–502. Available from: <URL>.

2.   Sumaiya A, Trivedi R. A Review on Glucose OxidaseDepartment of Microbiology. Shree Ramkrishna Institute of Applied Sciences. int J curr Microbiol App sci. 2015;4:636–40.

3.   Kriaa M, Kammoun R. Producing Aspergillus tubingensis CTM507 Glucose oxidase by Solid state fermentation versus submerged fermentation: Process optimization and enzyme stability by an intermediary metabolite in relation with diauxic growth. J Chem Technol Biotechnol. 2016;91(5):1540–50. Available from: <URL>.

4.   Anas A, Gunny N. Studies on the production of Glucose oxidase by Aspergillus terreus UniMAP AA-1. Universiti Malaysia Perlis (UniMAP); 2011.

5.   Gutierrez A, Wallraf A, Balaceanu A, Bocola M, Davari M, Meier T, et al. How to engineer glucose oxidase for mediated electron transfer. Biotechnol Bioeng. 2018;115(10):2405–15. Available from: <URL>.

6.   Subiyono S, Martsiningsih MA, Gabrela D. Gambaran Kadar Glukosa Darah Metode GOD-PAP (Glucose Oxsidase–Peroxidase Aminoantypirin) Sampel Serum dan Plasma EDTA (Ethylen Diamin Terta Acetat). J Teknol Lab. 2016;5(1):45–8.

7.   Ostafe R, Fontaine N, Frank D, Ng Fuk Chong M, Prodanovic R, Pandjaitan R, et al. One-shot optimization of multiple enzyme parameters: Tailoring glucose oxidase for pH and electron mediators. Biotechnol Bioeng. 2020;117(1):17–29. Available from: <URL>.

8.   Mano N. Engineering glucose oxidase for bioelectrochemical applications. Bioelectrochemistry [Internet]. 2019;128:218–40. Available from: <URL>.

9.   Leech D, Kavanagh P, Schuhmann W. Enzymatic fuel cells: Recent progress. Electrochim Acta [Internet]. 2012;84:223–34. Available from: <URL>.

10.   Vogt S, Schneider M, Schäfer-Eberwein H, Nöll G. Determination of the pH dependent redox potential of glucose oxidase by spectroelectrochemistry. Anal Chem. 2014;86(15):7530–5. Available from: <URL>.

11.   Triana R. Pemurnian dan karakterisasi enzim glukosa oksidase dari isolat lokal Aspergillus niger (IPBCC.08610). Institut Pertanian Bogor; 2013.

12.   Indriani A. Pemurnian dengan kromatografi penukar anion dan karakterisasi glukosa oksidase dari aspergillus niger IPBCC 08.610. Institut Pertanian Bogor; 2018.

13.   Maulana FA, Ambarsari L, Wahyudi ST. Homology modeling and structural dynamics of the glucose oxidase. Indones J Chem. 2019;20(1):43–53.

14.   Kurniatin PA, Ambarsari L, Khanza ADA, Setyawati I, Seno DSH, Nurcholis W. Characteristics of glucose oxidase gene (GGOx) from Aspergillus niger IPBCC 08.610. J Kim Val. 2020;6(1):10–9.

15.   Dwiastuti R, Radifar M, Marchaban M, Noegrohati S, Istyastono E., Dwiastuti R, et al. Molecular Dynamics Simulations and Empirical Observations on Soy Lecithin Liposome Preparation. Indones J Chem. 2016;16(2):222–8.

16.   Sharma P, Joshi T, Mathpal S, Joshi T, Pundir H, Chandra S, et al. Identification of natural inhibitors against Mpro of SARS-CoV-2 by molecular docking, molecular dynamics simulation, and MM/PBSA methods. J Biomol Struct Dyn [Internet]. 2020;0(0):1–12. Available from: Available from: <URL>.

17.   Petrović D, Frank D, Kamerlin S, Hoffmann K, Strodel B. Shuffling active site substate populations affects catalytic activity: The case of glucose oxidase. ACS Catal. 2017;7(9):6188–6197. Available from: <URL>.

18.   Mu Q, Cui Y, Tian Y, Hu M, Tao Y, Wu B. Thermostability improvement of the glucose oxidase from Aspergilus niger for efficient gluconic acid production via computational design. Biol Macromol. 2019;136:1060–8. Available from: <URL>.

19.   Tu T, Wang Y, Huang H, Wang Y, Jiang X, Wang Z, et al. Improving the thermostability and catalytic efficiency of glucose oxidase from Aspergillus niger by molecular evolution. Food Chem. 2019;281:163–70. Available from: <URL>.

20.   Kaczmarski JA, Mahawaththa MC, Feintuch A, Clifton BE, Adams LA, Goldfarb D, et al. Altered conformational sampling along an evolutionary trajectory changes the catalytic activity of an enzyme. Nat Commun [Internet]. 2020;11(1):1–14. Available from: <URL>.

21.   Case I, Ben-Shalom S, Brozell D, Cerutti T, Cheatham I, Cruzeiro T, et al. AMBER 2018. San Francisco: University of California; 2018.

22.   Myers J, Grothaus G, Narayanan S, Onufriev A. A simple clustering algorithm can be accurate enough for use in calculations of pKs in macromolecules. Proteins Struct Funct Bioinforma. 2006;63(4):928–38. Available from: <URL>.

23.   Anandakrishnan R, Aguilar B, Onufriev A V. H++ 3.0: Automating pK prediction and the preparation of biomolecular structures for atomistic molecular modeling

and simulations. Nucleic Acids Res. 2012;40(W1):W537–41. Available from: <URL>.

24.   Miller BR, McGee TD, Swails JM, Homeyer N, Gohlke H, Roitberg AE. MMPBSA.py: An efficient program for end-state free energy calculations. J Chem Theory Comput. 2012;8(9):3314–21. Available from: <URL>.

25.   Wohlfahrt G, Witt S, Hendle J, Schomburg D, Kalisz H, Hecht H. 1.8 and 1.9 Å resolution structures of the Penicillium amagasakiense and Aspergillus niger glucose oxidases as a basis for modelling substrate complexes. Acta Crystallogr Sect D Biol Crystallogr. 1999;969–77. Available from: <URL>.

26.   Singh R, Tiwari M, Singh R, Lee J. From protein engineering to immobilization: promising strategies for the upgrade of industrial enzymes. Int J Mol Sci. 2013; (14):1232–77. Available from: <URL>.

27.   Guterres H, Im W. Improving protein-ligand docking results with high-throughput molecular dynamics simulations. J Chem Inf Model. 2020;60(4):2189–98. Available from: <URL>.

28.   Yu H, Yan Y, Zhang C, Dalby PA. Two strategies to engineer flexible loops for improved enzyme thermostability. Sci Rep. 2017;7(1):1–15. Available from: <URL>.

29.   Vieira P, Simão R, Morais C, Henrique J. 3_{10} Helices in channels and other membrane proteins. J Gen Physiol. 2010;136(6):585–92. Available from: <URL>.

30.   Basu S, Biswas P. Salt-bridge dynamics in intrinsically disordered proteins: A trade-off between electrostatic interactions and structural flexibility. Biochim Biophys Acta - Proteins Proteomics [Internet]. 2018;1866(5–6):624–41. Available from: <URL>.

31.   Chen L, Li X, Wang R, Fang F, Yang W, Kan W. Thermal stability and unfolding pathways of hyperthermophilic and mesophilic periplasmic binding proteins studied by molecular dynamics simulation. J Biomol Struct Dyn. 2016;34(7):1576–89. Available from: <URL>.

32.   Anuar NFSK, Wahab RA, Huyop F, Amran SI, Hamid AAA, Halim KBA, et al. Molecular docking and molecular dynamics simulations of a mutant Acinetobacter haemolyticus alkaline-stable lipase against tributyrin. J Biomol Struct Dyn. 2020;1–13. Available from: <URL>.

33.   Ji B, Liu S, He X, Man VH, Xie XQ, Wang J. Prediction of the binding affinities and selectivity for CB1 and CB2 ligands using homology modeling, molecular docking, molecular dynamics simulations, and MM-PBSA binding free energy calculations. ACS Chem Neurosci. 2020;11(8):1139–58. Available from: <URL>.

34.   Aldeghi M, Bodkin MJ, Knapp S, Biggin PC. Statistical analysis on the performance of molecular mechanics poisson-boltzmann surface area versus absolute binding free energy calculations: bromodomains as a case study. J Chem Inf Model. 2017;57(9):2203–21. Available from: <URL>.

Removal of Cu (II) Ions from Aqueous Solution Using Poly-Amidoxime Resin from Grafted Millet Husk Cellulose

Aminu Musa[1]*, Maryam Ibrahim Ifo[1] and Ahmed Salisu[1]

[1]Umaru Musa Yar'adua University, Department of Pure and Industrial Chemistry, Katsina 820001, Nigeria

Abstract: Poly-amidoxime ligand was synthesized on the cellulose isolated from millet husk through a graft copolymerization process for adsorption of Cu (II) ion from aqueous solution. The functional group, thermal degradation and morphology of the adsorbent were investigated by Fourier transform infrared (FTIR), thermal gravimetric analysis (TGA) and scanning electron microscope (SEM), respectively. The FTIR results showed that grafting was successful due to the presences of 2244 cm^{-1} for cyano group (CN) and also band at 1640 cm^{-1} and 1380 cm^{-1} that replaced 2244 cm^{-1} which successfully confirmed the synthesis of poly(amidoxime) functional group. The TGA showed two stages of thermal degradation 12 % weight loss observed in amidoxime at 240 ^{0}C which is due degradation of amidoxime functional group then it reduces to 2% in second stage at 530 ^{0}C which revealed the improved thermal stability of the material. The SEM image showed a clear morphology of the absorbent before adsorption and after adsorption. The Initial concentration, adsorbent dosage and contact time were taken as independent variables. The adsorption process was optimized by central composite design (CCD) in Response surface methodology (RSM). The predicted value is in good agreement with experimental value and also the ANOVA result showed that all the independent variables have significant impact with the adsorbent. The optimum condition achieved in the experiment was at initial concentration of 150 mg/L, adsorbent dosage of 0.3 g and contact time of 90 min for Cu^{2+} with percentage removal of 55.41 % predictably and 54.92 % experimentally.

INTRODUCTION

Heavy metals pollution is one of the reasons of industrial revolution that can human life, as well as the environment, in various regions around the world, especially in developing countries. The pollution of environment such as air, water, and land by toxic heavy metal ions such as mercury, cadmium, lead, and chromium, and their accumulation through the food chain has a raised in a number of diseases and disorders (1).

Copper is a component of many plant enzymes (oxidase for example) and is involved in many electron transfer processes. Copper is an essential element for human life, but excessive intake results in its accumulation in the liver and produces gastrointestinal problems, anemia, liver and kidney damage. Long-term exposure to copper can cause irritation of the nose, mouth and eyes and headaches, stomachaches, dizziness, vomiting, and diarrhea (2).

High abundance of heavy metal ions in environment can harm human health and living organism ecosystem, thus removal of heavy metal ions is highly needed. Various separation techniques have applied for the removal of heavy metals such as chemical precipitation, reverse osmosis, adsorption, ion exchange and coagulation. The frequently techniques that attracted many researchers around the world is adsorption which is due to its highly abundance, easy modification, and high adsorption performance (3, 4). As a result, researchers try

various absorbent that can be used economically and effectively. In recent years, various agricultural waste by-product could be considered as absorbent for removal of heavy metal ions from aqueous solution or contaminated water.

Many researchers encouraging adsorbent that contain amidoxime functional group for the removal of heavy metals from waste water (5-7). This associated with mixing nitrile group into the polymer matrix through graft polymerization reaction of acrylonitrile to a polymer substrate, then converting of the nitrile groups into amidoxime groups using the alkaline solution of hydroxylamine (8).

A fibrous adsorbent that contain amidoxime groups was synthesed through graft copolymerization of acrylonitrile (AN) onto poly (ethylene terephthalate) (PET) fibers using benzoyl peroxide (Bz_2O_2) as initiator in aqueous solution, and chemical modification of cyano groups by reaction with hydroxylamine hydrochloride in methanol (9). Also, synthesis of a chelating ion-exchange resin containing amidoxime functional group which was carried out by grafting polyacrylonitrile (PAN) sago starch. Were the PAN grafted copolymer was gained by free-radical initiating process using ceric ammonium nitrate as an initiator. Transformation of nitrile groups of the grafted copolymer into the amidoxime was carried out by treatment with hydroxylamine via alkaline solution (10). Similarly, acrylic acid–amidoxime and poly (maleic acid–amidoxime) resins were snythesed by the γ-radiation-induced copolymerization of acrylonitrile with acrylic acid and maleic acid, respectively. The obtained resins were amidoximated by reaction with hydroxylamine (11).

Various researchers have been reported the reaction mechanism of grafting which occurred by free radical initiation reaction of oxygen atom of hydroxyl group in cellulose unit by polymerization of vinyl or acrylic monomer. In this current study millet husk Cellulose (MHC) was grafted with acrylonitrile monomer by free radical initiation reaction with ceric ammonium nitrite as an initiator. By this process, ceric (IV) ion attack the OH group of cellulose to form complex ion which was reduced to cerium(III) ion where the hydrogen atom oxidized. To form Ce^{3+} from Ce^{4+} by forming free radicals of cellulose unit which undergo the addition reaction with acrylonitrile that induced the initiation reaction of grafting. Therefore, the formation of radical resulted in the propagation reaction. The termination of reaction of growing polymer chain on the cellulose monomer are resulted in combination reaction as shown in Scheme 1 (12).

The Millet Husk cellulose grafted cellulose which was merged with nitrile group was transferred to poly (amidoxime) where all the nitrile group reacted with alkaline solution of hydroxylamine to form polymeric ligand which consisted the poly (amidoxime) functional group. The poly (amidoxime) ligand functional group can participate in rising-up the binding properties with metal ions. The bi dentate poly (amidoxime) chelating ligand contributed five membered ring complexes with metal ions as shown in Scheme 1.

MATERIALS AND METHODS

Materials
All the reagent used throughout the research were of analytical grade and used as received. $CuSO_4 .5H_2O$ were used as source of Cu^{2+}, Sodium Hydroxide (97.5 %) and sodium hypochlorite (99 %) are from Kem light laboratories LTD Glacial acetic acid (99.5 %) BH15, 1TD England Sulfuric acid (98 %) Loba Chemie pvt. LTD Mumbai Ceric ammonium nitrate (CAN) (99 %) geetraj corporation Acrylonitrile (AN) A.S. Joshi and company Hydroxylamine hydrochloride ACS Chemicals and Methanol (99 %) reagent chemicals.

Methods
Extraction of Cellulose from Millet Husk
Millet husk was collected from a farm at Farun Bala village, Jibia Local Government Area of Katsina State. It was washed, dried, grinded and sieved into fine powder. Millet husk powder (100 g) was treated with 10 % NaOH (500 mL) and glacial acetic acid (500 mL) for 2 h and 1 h respectively at 75 ^{0}C with continuous stirring, and washed with deionized water several times. The alkali method was repeated twice and finally rinsed with deionized water to remove the lignin and hemicellulose. The resultant cellulose was used for bleaching treatment with 2 % NaOCl and 5 % NaOH (400 mL) boil for 3 h at 50 ^{0}C. The mixture was than filtered and washed with deionized water, the process was done twice until white cellulose was obtained. Then the cellulose was oven dried at 50 ^{0}C.

Graft Copolymerization
The reaction was carried out in 250 mL three-neck flask which was equipped with a condenser and magnetic stirrer, and then immersed into paraffin oil to maintain a constant temperature. 10 g of cellulose was put into the flask, 50 mL of distilled water was added to the sample and preheated for about 30 min at 80 ^{0}C with continues stirring. After 30 min, the flask was cool to 50 ^{0}C, then 4 mL of diluted sulphuric acid was added to the reaction (H_2SO_4: H_2O, 1:1), after 5 min 10 mL of diluted CAN was added (2 g in 10 mL of distilled water) the reaction was stirred continuously for 10 min. Exactly after 10 min 24 mL of (AN) was added to the mixture with continuous stirring for 90 min. All the reaction was done throughout under N_2 gas atm [8], with little modification.
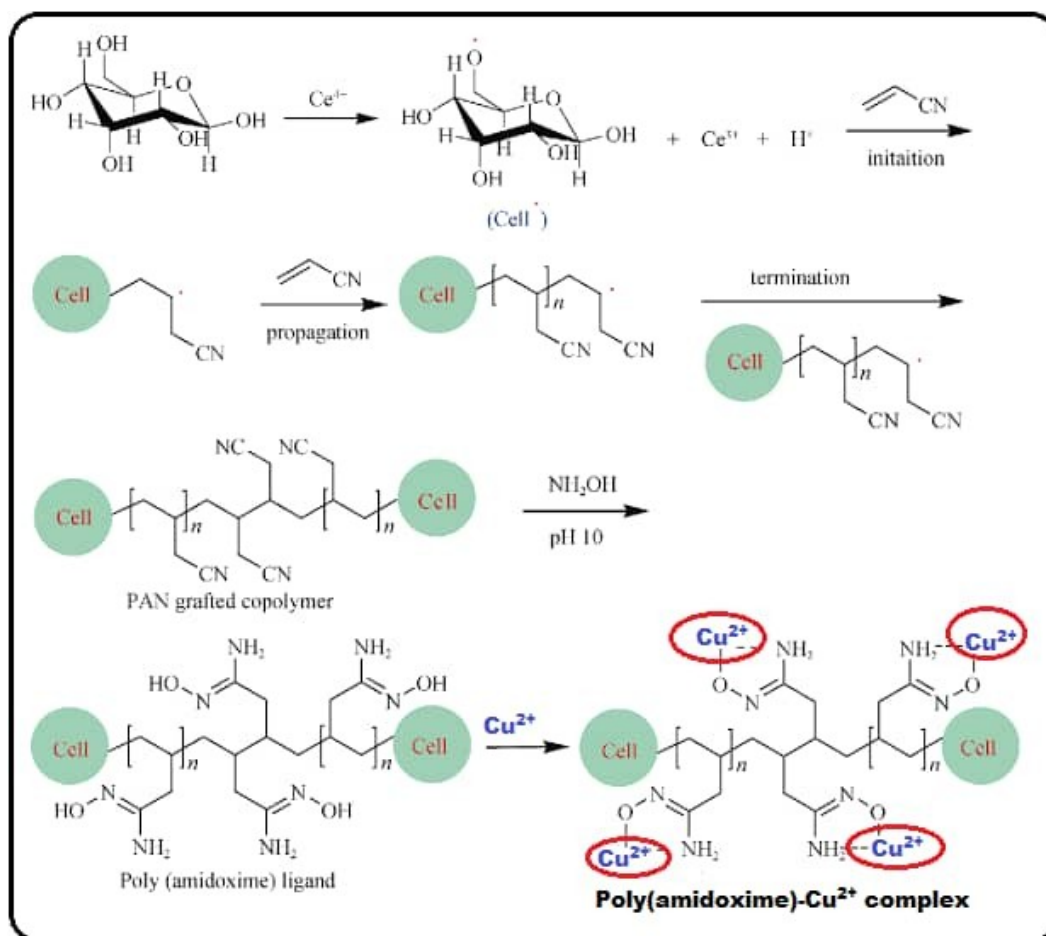
Scheme 1: Scheme of graft copolymerization of acrylonitrile onto cellulose to produce PAN-graft-cellulose, poly(amidoxime), and poly-amidoxime-Cu^{2+} complex.

When the reaction was completed the reaction flask was cool down under running tap water and the product was poured into 200 mL of methanol to induce the precipitation. The grafted product was washed several times with methanolic solution (CH_3OH: H_2O, 4:1) then oven dried the product at 50 ^0C to the constant weight.

The percentage of grafting was calculated via the following equation;

$$GP\% = \frac{W_1 - W_0}{W_0} \times 100 \qquad \text{(Eq. 1)}$$

Where W_0 is the weight of cellulose backbone W_1 is the weight of grafted cellulose.

Synthesis of Poly (Amidoxime) ligand
20 g of hydroxylamine hydrochloride was dissolved in 150 mL methanolic solution (CH_3OH; H_2O/5:1). The HCl of NH_2OH was neutralized by NaOH solution and the precipitate of NaCl was filtrated. The solution was adapted to pH 10 using NaOH solution. 10 g of millet husk grafted cellulose was put into the two-neck flask, which was set with a condenser and magnetic stirrer, and then immersed into paraffin oil to maintain a constant temperature [12].

Then the above-prepared hydroxylamine solution was added to the flask, and the reaction was carried out at 70 °C and 2 h. After 2 h of the reaction, the resin was filtered and washed multiple times with methanolic solution (methanol: water /4:1). Then, the resin was treated with 100 mL of methanolic 0.1 M HCl solution for 10 min. Finally, the resin was filtered and washed multiple times with methanolic solution (methanol±water /4:1), and then oven dried at 50 °C to a constant weight (10).

Experimental Design of (Cu^{2+}) Using Design Expert Software
The three parameters i.e. initial concentration of dye, adsorbent dosage and contact time were used as independent variables, nineteen runs of the "Central Composite RotaTable Design "(CCRD) experimental design consisted of eight factorial points, six axial points and also six center points, the three independent variables with (initial concentration (20-320 mg/L), contact time (10-190 min) and adsorbent dosage (0.05-0.6 g) for (Cu^{2+}) solution, according to RSM design.

The experimental data belong to second-order polynomial regression analysis and used to predict

the response as the function of independent variables. The equation below is a form of second order polynomial regression model that used to explain the (Cu^{2+}) removal.

$$Y = \beta_0 + \sum_{i=1}^{3} \beta_i \chi_i \chi_i + \sum_{i=1}^{3} \beta_{ii} \chi_i^2 + \sum_{j=i+1}^{3} \beta_{ij} \chi_i \chi_j \text{ (Eq. 2)}$$

Where β_0 is the offset term, β_i is the linear effect, β_{ii} is the squared effect, β_{ij} is the interaction effect, χ_i-dimensionless coded value of the variable χ_i. The analysis of variance (ANOVA) with p-value (<0.05), f-value, lack of fit, and R^2 value were used to determine the fitness of model. The 3-D plot and contour plot was used to show the influence between two variables and the interaction effects of the significant variables respectively.

Batch Adsorption Experiment
Batch adsorption experiment for both dye and metal ion were conducted at room temperature by shaking the required amount of adsorbents into 50 mL of (Cu^{2+}) aqueous working solution in 250 mL Erlenmeyer flasks and agitated at 200 rpm for a chosen contact time. The solution was filtered using filter paper and their initial and final concentration was analyzed using Atomic Absorption spectroscopy (AAS).

The experimental data with different mathematical models were analyzed and the ANOVA results showed that the reaction of removals was illustrated with a "2FI" polynomial model. The percentage removal of and (Cu^{2+}) was taken as response (Y) in experimental design and calculated using:

$$q_t = \frac{(C_0 - C_t)}{M} V \qquad \text{(Eq. 3)}$$

Where C_0 and C_t are the initial and final concentration in (mg/L) solutions respectively.

The adsorption capacity q_t (mg/g) at equilibrium condition per unit mass of adsorbent (m) was calculated by the following equation:

$$q_t = \frac{(C_0 - C_t)}{M} V \qquad \text{(Eq. 4)}$$

C_0 and C_t are the initial and final concentrations (mg/L). V is the volume of solution (L), and m is the mass of adsorbent (g)

Characterization
All the changes of functional group in cellulose, grafted cellulose and poly-amidoxime resin were verified using Fourier transform infrared (FTIR) were the spectral been recorded using spectrometer (Model 8400S) Shimadzu Japan from the range of 4000 – 650 cm^{-1}. The thermal behavior of cellulose, grafted cellulose and poly-amidoxime resin were analyze in thermogravimetric analyzer (TGA7 Perkin Elmer) at the temperature of 30 °C-950 °C with the constant heating rate 10 °C mn^{-1} under Nitrogen gas atmosphere at 20 mL/min. The changes in the morphology of poly- amidoxime ligand and poly-amidoxime ligand after adsorption of Cu^{2+} also were observed using scanning electron microscope (SEM-JEOL-JSM-7800F).

RESULTS AND DISCUSSION

FTIR Analysis
The FTIR spectral used to study the functional group in the prepared adsorbent. The main characteristics peaks of this study are assigned to be considered. The spectral for Millet Husk-cellulose, Millet Husk-cellulose grafted (PAN) and cellulose based poly (amidoxime) ligand are overlaid for comparison as shown in the Figure 1.

The spectrum of pure MH-cellulose showed the absorption band at 3327 cm^{-1} and 2895 cm^{-1} which represented the stretching of hydroxyl group and carbon- hydrogen stretching respectively. And also, the peaks at 1372 cm^{-1} and 1033 cm^{-1} belong to bending of hydroxyl and extending carbon-oxygen group. The α-glycosidic linkage between the cellulose unit carbon-hydrogen deformations weak which was present at 899 cm^{-1} which confirmed the structure of cellulose [10]. The IR spectrum of Millet Husk- cellulose (PAN) showed new adsorption band at 2244 cm^{-1} due to cyano group (CN) and the remaining peaks are retained from the Millet Husk-cellulose. The presence of band at 2244 cm^{-1} confirmed the grafting of acrylonitrile onto cellulose. The cyano group are observed from the range 2500-2000 cm^{-1} for the backbone of cellulose [13]. In IR-spectrum of poly(amidoxime) ligand the peak at 2244 cm^{-1} disappeared and formed new absorption band at 1640 cm^{-1} and 1380 cm^{-1} due to C=N stretch and N-H bending mode respectively. Also, the peak at 1380 cm^{-1} were both due to hydroxyl and amide group [14]. The band at 2244 cm^{-1} which was replaced with band at 1640 cm^{-1} and 1380 cm^{-1} was successful confirmed the synthesis of poly(amidoxime) functional group from MH-cellulose grafted (PAN).
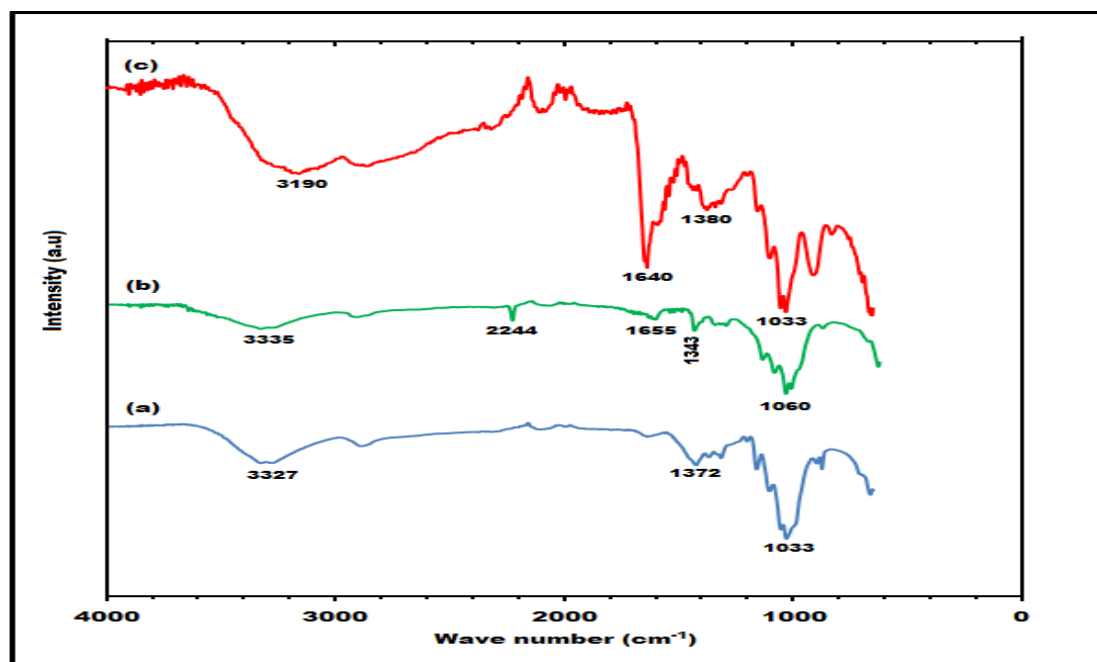
Figure 1: FTIR spectra of (a) cellulose (b) PAN-Grafted cellulose and (c) poly(amidoxime) ligand.

Thermal Gravimetric Analysis (TGA)

Thermal degradation of cellulose, (PAN) grafted cellulose and amidoxime ligand was measured by TGA with heating rate 10 ^{0}Cmin^{-1} under N$_2$ atmosphere and the result obtained are shown in the Figure 2 below. The weight loss occur in two stages throughout the experiment and the changes has been observed in the analysis. In cellulose the first stage of weight loss is observed at 257 ^{0}C which is about (10 %) and second stage is at 524 ^{0}C (70 %) due to degradation of hydroxyl OH and CH$_2$OH (14). In term of PAN-Grafted cellulose its loss almost 79.9 % at 224 ^{0}C-595 ^{0}C, were the first stage lost about 10.5 % at 250 ^{0}C and in second stage 8.99 % weight has been loss at 550 ^{0}C which is due to degradation of poly (acrylonitrile) and the volatile gases [14]. In amidoxime ligand peak the thermal stability has been observed with high water content which confirm the hydrophilicity of the amidoxime ligand. 12 % weight loss observed in amidoxime at 240 ^{0}C which is due degradation of amidoxime functional group then it reduces to 2 % in second stage at 530 ^{0}C.
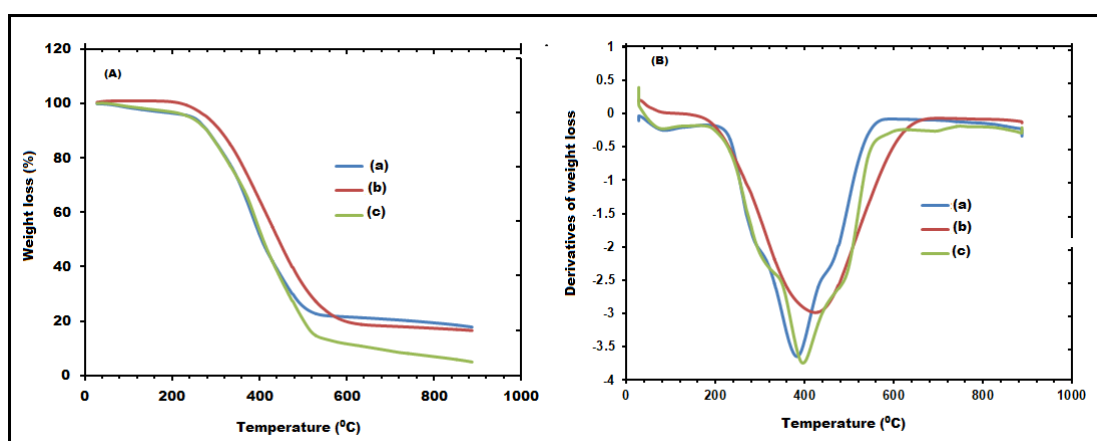
Figure 2: TGA-DTA of (a) cellulose (b) PAN-Graft-cellulose and (c) poly(amidoxime) ligand.

Scanning Electron Microscope (SEM)

The SEM micrographs of the amidoxime ligand, before and after adsorption are shown in Figure 3 (a and b) .The morphology of amidoxime ligand before adsorption (Figure 3 a) shows many pores and white material on the surface which may be important for adsorption. After adsorption, the ligand surface became packed and almost all the white material also disappeared, the change in shape and size also been observed after metal adsorption as shown in Figure 3 (b).
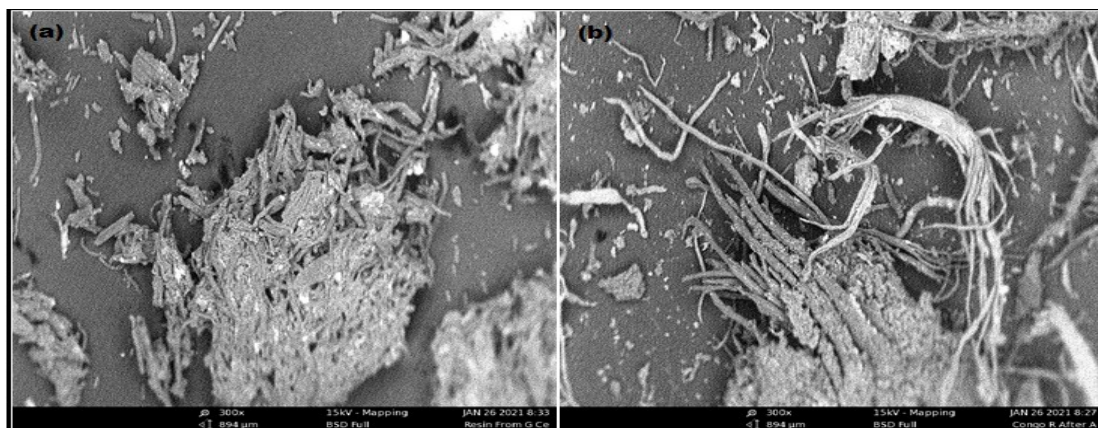
Figure 3: SEM image of (a) poly (amidoxime) ligand, (b) poly(amidoxime) ligand after cu²⁺ adsorption.

Design of Experiment

Central Composite Design (CCD) and Statistical Analysis from RSM

The chosen three-factors and design from CCD produce by software and the experimental data obtained in batch adsorption of Cu^{2+} ion is summarized in Table 1 were the experimental and predicted value has been shown and the designs are properly fitted considering the value of co-efficient determination R^2 (R^2 of Cu^{2+} = 0.9976).

The final equation in terms of coded factor relating the removal efficiency and process parameters that are developed for Cu^{2+} shown in equation (5) and the equation is 2FI model.

%Removal (Cu^{2+}) = 54.92-19.04A+20.1B+4.1C+0.098AB+0.91AC-1.5BC (5)

Table 1: Result obtained from the removal of Cu^{2+} by amidoxime ligand from RSM.

Std	Run	Factor 1 A: Initial Concentration (mg/L)	Factor 2 B: Contact Time (Minutes)	Factor 3 C: Adsorbent Dosage (g)	Response Removal of Cu²⁺ (%)	
					Exp. Value	Pred. value
1	12	50	30	0.1	50.21	49.26
2	15	250	30	0.1	9.28	9.17
3	1	50	30	0.5	93.22	92.28
4	11	250	30	0.5	53.09	52.58
5	7	50	150	0.1	58.52	58.66
6	5	250	150	0.1	21.62	22.19
7	10	50	150	0.5	95.92	95.66
8	9	250	150	0.5	59	59.58
9	13	20	90	0.3	78.86	79.68
10	19	320	90	0.3	23.42	22.55
11	8	150	90	0.05	30.69	29.79
12	17	150	90	0.6	85.3	85.07
13	4	150	10	0.3	46.71	49.45
14	16	150	190	0.3	61.69	61.76
15	18	150	90	0.3	55.41	54.92
16	2	150	90	0.3	57.28	54.92
17	3	150	90	0.3	53.29	54.92
18	14	150	90	0.3	55.33	54.92
19	6	150	90	0.3	53.43	54.92

Statistical Analysis Using (ANOVA)

The analysis of variance (ANOVA) was used to determine the adequacy of the model. The ANOVA statistics for the response % removal is shown in Table 2 for Cu^{2+}.

The ANOVA result of Cu^{2+} is 2FI model which indicated that the models could be used to navigate the design space, according to the ANOVA (Table 2) the F-value of Cu^{2+} is 815.16 which suggest the fitness of model. So, the significance of model was evaluated using probability of error value P-value (prob>F). in (Table 2) the value of (prob>F) is less

than 0.0500 these indicated that the models are significant (15, 16). Also, it found that A, B, C, AB, AC and BC are significant model term for adsorption capacity of Cu^{2+} using Amidoxime ligand.

In Cu^{2+} models based on F-value has significant effect on adsorption capacity, were the adsorbent dosage has the highest F-value of 2438.66 which implies that they have the most significant influence on the adsorption capacity compared to initial concentration and contact time, (16, 17). Also, in (Table 4.2) the lack of fit F-value is not significant relative to the pure error. The coefficient of determination (R^2) was used to investigate the goodness of the model obtained (16). The high the

value of R^2 indicated that the model is more reliable. Furthermore, the difference between the R^2-adjusted and R^2-predicted is an indication of model adequacy, for good equate model the difference should not exceeded 0.2, according to (Table 2) the R^2 obtained is 0.9976 and the difference between adj.-R^2 and pred.-R^2 is 0.0019 Cu^{2+} which confirm the model adequacy. Moreover, the value of adequate precision that measures the signal to noise and a ratio greater than 4 is desirable. The adequate precision of this study is high which is 101. 864 for Cu^{2+}. These high adequacy precisions confirmed that the models are significant that can be used to navigate the design space.

Table 2: ANOVA result for quadratic model, data analyzing and modeling of Cu^{2+}.

Source	Mean Square	DF	F Value	p-value (Prob > F)	
			Removal of Cu^{2+} (%)		
Model	1595.15	6	815.16	< 0.0001	significant
A-Initial Concentration	4558.57	1	2329.55	< 0.0001	
B-Contact Time	4772.09	1	2438.66	< 0.0001	
C-Adsorbent Dosage	211.06	1	107.86	<0.0001	
AB	0.076	1	0.039	0.847	
AC	6.55	1	3.35	0.0922	
BC	18.12	1	9.26	0.0102	
Residual	1.96	12	2329.55	< 0.0001	Not significant
Lack of Fit	1.58	8	2438.66	< 0.0001	
Pure Error	2.71	4			
Cor total	9594.35	18			
Adeq.Precision= 101.864 R^2= 0.9976	R^2(Adj.)=0.9963	R^2(Pred.) =0.9944			

Interpretation of 3-Dimentional Response Surface Plot (3D-Plot) and Contour Plot of Cu^{2+}
The 3D and contour plot are used to estimate the percentage removal efficiency over independent variables. Each plot represents an infinite number of two tested combination variables while the one variable kept constant.

In this study the 3D and contour plot clearly showed the interaction between the variables which are significant as shown in Figure 4. Figure 4 shows the 3D and contour plot of Cu^{2+} were Figure 4(a) show interaction between initial concentration and adsorbent dosage while contact time is constant at

90 min, Figure 4(b) show interaction between initial concentration and contact time while adsorbent dosage is constant at 0.3 g and Figure 4(c) show interaction between adsorbent dosage and contact time while initial concentration is constant at 150 mg/L.

These showed the evident from the figure that removal of Cu^{2+} increases when the adsorbent dosage increases and decreases when initial concentration increases. Also, removal attained its maximum value when the adsorbent dosage and contact time were at high value.
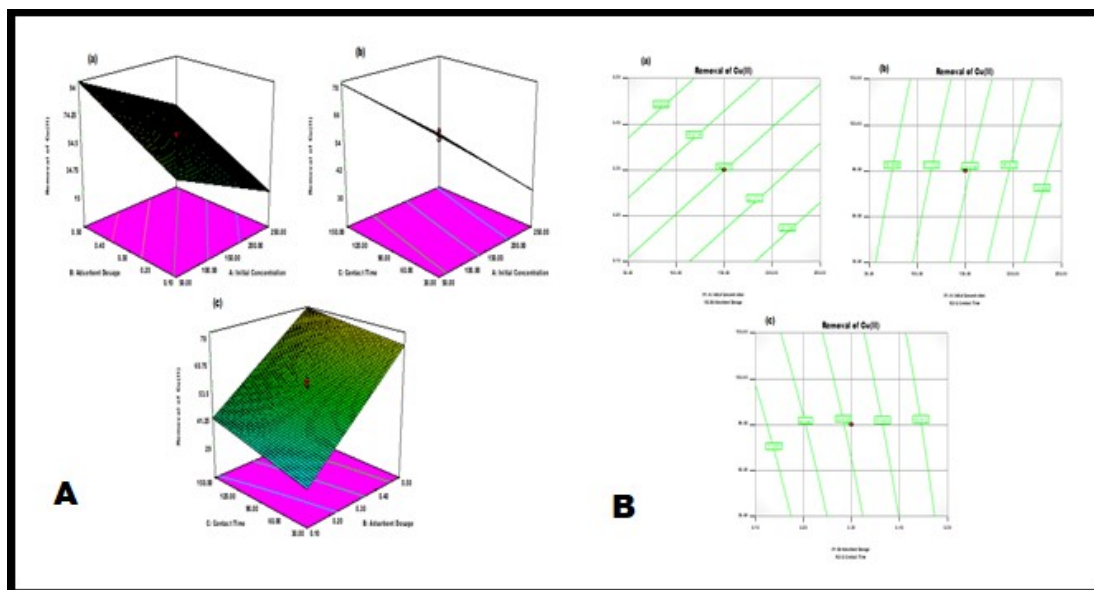
Figure 4: 3D-plot and contour plot of Cu^{2+} removal.

Optimization of the Adsorption Process

The optimization process was achieved using response surface methodology which is used to identify the maximum value of 3 independent factors and dependent factor (response) which gives the maximum removal for adsorption of Cu^{2+} by poly-amidoxime ligand from millet husk.

The target suggested is 100 % with upper and lower weight which was set as 1. The software predicted 54.92 % removal for Cu^{2+} and also the confirmation test for optimum condition carried out with the variables as set by model are shown under Table 3 the combination of factors that are setting in achieving the desired response was found to be at initial concentration of 150 mg/L, Adsorbent dosage of 0.3 g and contact time of 90 min with the predicted response of 54. 92 % for Cu^{2+}. Therefore, percentage removal achieved in this study indicated that the 2FI model was valid in predicting the response.

Table 3: Constraints and optimum condition for removal of Cu^{2+}.

Name	Goal	Lower Limit	Upper Limit	Lower Weight	Upper Weight
A: Initial conc.	is in range	50	250	1	1
B: Contact time	is in range	30	150	1	1
C: Adsorbent dosage.	is in range	0.1	0.5	1	1
% Removal of Cu^{2+}	Target= 100	54.22	55.62	1	1

Initial Conc. (mg/L)	Contact Time (min)	Adsorbent Dosage (g)	Removal of Cu (%)	
			Exp. Value	Pred. Value
150	90	0.3	55.41	54.92

CONCLUSION

In this study poly-amidoxime ligand have been synthesized using the millet husk cellulose through graft copolymerization process and used as adsorbent to investigate the removal of Cu^{2+} from aqueous solution. The functional group, thermal degradation and morphology of the adsorbent were investigated by Fourier transform infrared (FTIR), thermal gravimetric analysis (TGA) and scanning electron microscope (SEM) respectively. The FTIR results showed that grafting was successful due to the presences of 2244 cm^{-1} for cyano group (CN) and also band at 1640 cm^{-1} and 1380 cm^{-1} that replaced 2244 cm^{-1} which successfully confirmed the synthesis of poly(amidoxime) functional group. The TGA showed two stages of thermal degradation 12 % weight loss observed in amidoxime at 240 ^0C which is due degradation of amidoxime functional group then it reduces to 2% in second stage at 530 ^0C which revealed the improved thermal stability of the material. The SEM image showed a clear morphology of the absorbent before adsorption and after adsorption. The Initial concentration, adsorbent dosage and contact time were taken as independent variables. The adsorption process was

optimized by central composite design (CCD) in Response surface methodology (RSM). The predicted value is in good agreement with experimental value and also the ANOVA result showed that all the independent variables have significant impact with the adsorbent. The optimum condition achieved in the experiment was at initial concentration of 150 mg/L, adsorbent dosage of 0.3 g and contact time of 90 min for Cu^{2+} with percentage removal of 55.41 % predictably and 54.92 % experimentally.

Finally, it can be concluded that, poly-amidoxime ligand can be efficiently used in treatment of waste water contaminated with metal ions.

ACKNOWLEDGMENTS

REFERENCES

1. Bailey SE, Olin TJ, Bricka RM, Adrian DD. A review of potentially low-cost sorbents for heavy metals. Water Research. 1999 Aug;33(11):2469–79. <URL>.

2. Nuhoglu Y, Oguz E. Removal of copper(II) from aqueous solutions by biosorption on the cone biomass of Thuja orientalis. Process Biochemistry. 2003 Jun;38(11):1627–31. <URL>.

3. Crini G. Non-conventional low-cost adsorbents for dye removal: A review. Bioresource Technology. 2006 Jun;97(9):1061–85. <URL>.

4. Gupta VK, Suhas. Application of low-cost adsorbents for dye removal – A review. Journal of Environmental Management. 2009 Jun;90(8):2313–42. <URL>.

5. Seko N, Katakai A, Tamada M, Sugo T, Yoshii F. Fine Fibrous Amidoxime Adsorbent Synthesized by Grafting and Uranium Adsorption–Elution Cyclic Test with Seawater. Separation Science and Technology. 2004 Jan 12;39(16):3753–67. <URL>.

6. Kaya B. Amidoksime-polimer ağyapılar ile bakır(II) iyonu adsorpsiyonu. Int J Multidis Stud Innov Technol. 2019;3(2):151–6. <URL>.

7. Mahdavinia GR, Shokri E. Synthesis and characterization of magnetic amidoximated chitosan-g poly(polyacrylonitrile)/laponite RD nanocomposites with enhanced adsorption capacity for Cu^{2+}. Turk J Chem. 2017;41:135–52. <URL>.

8. Anirudhan TS, Divya L, Bringle CD, Suchithra PS. Removal of Copper(II) and Zinc(II) from Aqueous Solutions Using a Lignocellulosic-Based Polymeric Adsorbent Containing Amidoxime Chelating Functional Groups. Separation Science and Technology. 2010 Nov;45(16):2383–93. <URL>.

9. Coşkun R, Soykan C. Preparation of amidoximated polyester fiber and competitive adsorption of some heavy metal ions from aqueous solution onto this fiber. J Appl Polym Sci. 2009 May 5;112(3):1798–807. <URL>.

10. Rahman L, Silong S, Zin WM, Rahman MZA, Ahmad M, Haron J. Graft copolymerization of methyl acrylate onto sago starch using ceric ammonium nitrate as an initiator. J Appl Polym Sci. 2000 Apr 25;76(4):516–23. <URL>.

11. Abdel-Aziz HM. γ-radiation-induced preparation of polyamidoxime resins and their adsorption of methyl violet. J Appl Polym Sci. 2011 May 5;120(3):1547–54. <URL>.

12. Rahman ML, Sarkar S, Yusoff M, Kulkarni A, Chowdhury Z, Ali ME. Poly(amidoxime) from Polymer-Grafted Khaya Cellulose: An Excellent Medium for the Removal of Transition Metal Cations from Aqueous Solution. BioResources. 2016;11(3):6780–800. <URL>.

13. Pan Y, Wang F, Wei T, Zhang C, Xiao H. Hydrophobic modification of bagasse cellulose fibers with cationic latex: Adsorption kinetics and mechanism. Chemical Engineering Journal. 2016 Oct;302:33–43. <URL>.

14. Rahman ML, Fui CJ, Sarjadi MS, Arshad SE, Musta B, Abdullah MH, et al. Poly(amidoxime) ligand derived from waste palm fiber for the removal of heavy metals from electroplating wastewater. Environ Sci Pollut Res. 2020 Sep;27(27):34541–56. <URL>.

15. Garba ZN, Bello I, Galadima A, Lawal AY. Optimization of adsorption conditions using central composite design for the removal of copper (II) and lead (II) by defatted papaya seed. Karbala International Journal of Modern Science. 2016 Mar;2(1):20–8. <URL>.

16. Bayuo J, Abukari MA, Pelig-Ba KB. Optimization using central composite design (CCD) of response surface methodology (RSM) for biosorption of hexavalent chromium from aqueous media. Appl Water Sci. 2020 Jun;10(6):135. <URL>.

17. Gottipati R, Ecocarb G, Rourkela T. Application of response surface methodology for optimization of Cr (III) and Cr (VI) adsorption on commercial activated. Res J Chem Sci. 2012;2:40–8.

18. Basaleh AA, Al-Malack MH, Saleh TA. Methylene Blue removal using polyamide-vermiculite nanocomposites: Kinetics, equilibrium and thermodynamic study. Journal of Environmental Chemical Engineering. 2019 Jun;7(3):103107. <URL>.

RESEARCH ARTICLE

Biosynthesis and Characterization of Co₃O₄NPs Utilizing Prickly Pear Fruit Extract and its Biological Activities

Dharmalingam Nagajothi[1] iD **, Shanmugasundaram Gurusamy[2] and Vaseekaran Maheswari[1]*** iD

[1]Ayya Nadar Janaki Ammal College (Affiliated to Madurai Kamaraj University), Department of Chemistry, Sivakasi - 626124, Tamil Nadu, India.
[2]V.O.Chidambaram College, Department of Chemistry, Tuticorin. Tamil Nadu, India.

Abstract: In the current research, there is a low level of research and information about the interaction of cobalt oxide nanoparticles (Co₃O₄NPs) in biological systems. This research creates a very simple and cost-effective preparation of cobalt oxide nanoparticles by using prickly pear fruit extract as a reducing agent, which may be further used for biological applications like antimicrobial, antioxidant, DNA interaction and in-vitro anticancer activity. The use of prickly pear fruit extract acts as a good reducing agent and is responsible for easy preparation and reducing the toxicity of cobalt oxide nanoparticles. The fabricated biogenic nanoparticles were confirmed by microscopic and spectroscopic analytical techniques like Ultra Violet-Visible spectrometer, Fourier transforms infrared spectrometer (FTIR), X-ray Diffraction Method (XRD), Energy-dispersive X-ray spectroscopy (EDS), Scanning electron microscopy (SEM) and Transmission electron microscopy (TEM). The average size of the synthesized nanoparticles is 36.24 nm. In the MTT assay, the prepared cobalt oxide NPs haspotential mechanisms of cytotoxicity and in-vitro anticancer activity in Hepatocellular carcinoma cancer cells (HepG2). The microbial activities like antibacterial and antifungal studies of the biosynthesized nanoparticles were performed by the Disc method. The Co₃O₄NPs with DNA interaction were examined by UV-Visible and fluorescence spectroscopic methods. The binding constant value of biogenic Co₃O₄NPs with CT-DNA was observed by UV-Visible spectroscopy with a result of $2.57 \times 10^5 \text{mol}^{-1}$. The binding parameters and quenching constants were observed by fluorescence spectroscopic methods having values of $K_{sv} = 7.1 \times 10^3$, $k_q = 7.1 \times 10^8$, $K_a = 3.47.1 \times 10^5$, $n = 0.9119$. From the findings, Co₃O₄NPs may be utilized as a medicinal aid for their antibacterial, antifungal, antioxidant, DNA binding and in-vitro anticancer activities.

Keywords: Cobalt oxide nanoparticles, prickly pear, antibacterial, antifungal, antioxidant, DNA binding, in-vitro anticancer activity.

INTRODUCTION

The development of nanomaterials has a huge impact on the growth of different fields like biomedicine, medicine, engineering, pharmacy, etc. Cobalt is a vital metal of research interest, most often utilized in the preparation of nanoparticles for its biomedical applications like antibacterial, antifungal, antioxidant, anti-inflammatory, in-vivo and in-vitro anticancer studies. The biosynthesis reactions are performed by suitable precursors and they depend on various parameters like temperature, pressure, pH and solvent (1, 2). The biogenic process of nanomaterials using various parts of plant extracts has increased their potential results because of their effective phytochemicals such as aldehydes, flavonoids, phenolic compounds, ketones, carboxylic acids, ascorbic acids, terpenoids and amides (3–5). In the previous studies, various plants like Aspalathuslinearis (6), Azadirachtaindica (7), Calotropisgiganta (8), Calotropisprocera (9), Euphorbia heterophylla (10), Ginkgo biloba (11), Hibiscusrasa (12), Helianthusannus (13), Manihotesculenta (14), Moringaoleifera (15),

Neriumindicum (16), Pipernigrum (17), Punicagrantum (18, 19), Sageretiathea (20), Sechiumedule (21), Tamarind (22), and Taraxacum officinal (23) were used for nanoparticle synthesis. Phytochemicals can condense metal salts into metal nanoparticles. Among the nanomaterials, the metallic nanoparticles, which have antibacterial and antitumor properties, open new avenues to combat and prevent different types of tumors and other infectious diseases. Hence, research on nanomaterials in bacteria has become important and there is a topical increase in the challenging strains of microorganisms to the potent antibiotics and the vital role of bactericidal nanomaterials as potential anticancer agents (24). Its inexpensive nature, environment friendliness, and its considerable role in the synthesis and production of cobalt nanoparticles are in wide use in various sectors.

Cobalt oxide nanoparticles are common industrial nanoparticles that are utilized in various applications due to their cost-effectiveness, eco-friendly, larger surface area per unit and weight than their bulk counterpart materials. Nano-cobalt oxide is an important magnetic material because of its innate role in electrochemical and biological applications (25).The biosynthesized nanoparticles with plant extract are biocompatible and have low toxicity in the physicochemical process. The antibacterial effect can be assessed by two methods like disc diffusion method and growth curve analysis. The antibacterial activities of Co3O4NPs were investigated using gram-positive and gram-negative bacteria in the agar disc diffusion method (26). Previous literature reports discussed a comparative study of gram-positive and gram-negative bacterial strains and the nanoparticles were higher against gram-positive strain than gram-negative strain (27). The nanocomposite of these nanoparticles increases the antibacterial activity against the pathogenic strains (28, 29). The biogenic Co3O4NPs were examined by the biocompatibility and the toxicity of Co3O4NPs toward the cancerous cells and normal human cells and points out the green synthesis of metal oxide nanoparticles with numerous biological applications (30). Hence, the study investigates the biosynthesis and biological applications of Co3O4NPs for their potential effect on the HepG2 tumour cell lines and their lower cytotoxicity in normal cells.

Compared with the other chemical methods, phytochemical mediated nanoparticles have beneficial efficiency, biocompatibility and useful biological applications. Medicinal plants are used as an alternative source to synthesize the nanoparticles to satisfy the limitations of the biological field (31). Opuntia ficus-indica is the botanical name for the prickly pear. The fruit is grown widely and is easy to obtain on the outskirts

of the Virudhunagar city, Tamil Nadu, India. The prickly pear fruits have a good source of nutrients and antioxidants with excellent health benefits, such as protective effects of the hepatoprotector, cardiovascular system, chemopreventive, anticancer, antiproliferative, and neuroprotective [32, 33]. The objectives of this study are (i) to synthesize Co3O4NPs from the stabilizing and reducing agents present in the aqueous extract of the prickly pear fruit. (ii) to find the characterization of the biosynthesized Co3O4NPs, and (iii) to evaluate their therapeutic properties such as antibacterial, antioxidant, DNA interaction, and anticancer activities under in-vitro conditions. Recently, the synthesis of copper oxide and silver nanoparticles using prickly pear fruit extract has been reported. According to past literature surveys, the fruit extract of this plant has not been used for the synthesis of Co3O4-NPs so far (34–36).

MATERIALS AND METHODS

Materials
Cobalt Nitrate hexahydrate (Co(NO3)2.6H2O) as a precursor was purchased from Merck, National Scientific Company, Madurai. Methyl thiazolyl diphenyl tetrazolium bromide (MTT), diphenyl picrylhydrazyl (DPPH), methanol, Dimethylsulfoxide (DMSO) and ethanol were purchased from Alpha lab supplies, Thermo Fisher Brand, Madurai, Tamil Nadu, India.

Prickly Pear collection and aqueous extract preparation
The sample fruits of prickly pear were collected from the outskirts of Virudhunagar city, Tamil Nadu and the collected fresh fruits were washed three to four times and cut into tiny pieces. Twenty-five grams of fruits were mixed with 300mL of water: ethanol (2:1, v:v) and was refluxed at 70°C for 4-6 hrs, utilizing the soxhlet apparatus. After the reflux, the extract of the chemical mixture was collected.

Green synthesis of Co3O4NPs
The prepared cobalt oxide nanoparticles (Co3O4NPs) were prepared with 40mL of 0.1M cobalt precursor solution in the estimated ratio of ethanol: water (2:3, v:v) and were stirred for 15 min and were slowly added 20mL of fruits extracts with continuous stirring for half an hour. Additionally, adding five drops of ammonia solution drop wise with continuous stirring for the next 2h, then the potion was relocated to a 100mL autoclave at 120 °C for 6–7 hrs. After getting the mixture was subdued to the room temperature, the precipitate was collected and washed several times using water and ethanol and centrifuged for 15 min. Finally, the precipitate was dehydrated at 90 °C for two hours and then calcinated at 400–500 for three hours. The schematic diagram of the nanoparticle synthesis is given in Figure 1.
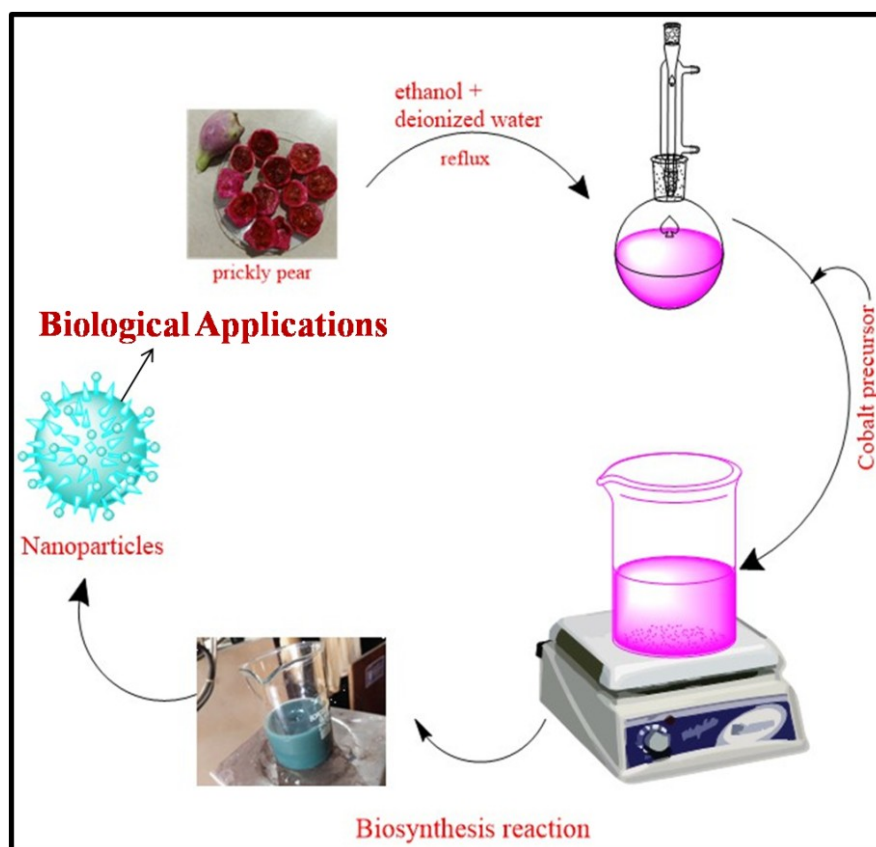
Figure 1: Preparation and mechanism of biogenic Cobalt oxide nanoparticles.

Physicochemical Characterization

The absorption properties of the biosynthesized Co_3O_4NPs and the fruit extract was examined by UV-Visible spectroscopic technique (UV-1601 Shimadzu spectrophotometer) using DMSO at a resolution of 1 nm, in the wavelength range of 400–800 nm. FT-IR measurement was done using FTIR8400S-spectrophotometer (Shimadzu, International, Co. Ltd, Tokyo, Japan) to determine the different types of chemical bonds between bioactive compounds of extract and cobalt oxide solution. Samples were scanned from 400–4000 cm-1 with potassium bromide pellets. The representative peaks of the cobalt oxide group with NP are expressed in a reciprocal wavelength (cm-1).The wide-angle X-ray diffraction (XRD, Bruker AXS D8) spectra were measured on a powder diffractometer with nickel-filtered Cu Ka, X-ray beam (l= 0.15418 nm).The morphology and the particle size of the nanoparticles were investigated by Scanning Electron microscope and Transmission Electron Microscope. The images were observed with the help of an electron microscope (VEGA3SB, TESCAN, and Czech). Energy Dispersive X-ray (EDS) spectroscopy (a part of SEM which was done using Quantax 200 with X Flash® 6130) was used for detecting the arrangement of elements in the sample. For the Transmission Electron Microscope (TEM) (Model: JEM-2010, JEOL, Japan) analysis, diluted and dispersed solutions of cobalt oxide nanoparticles were dropped onto a copper grid (~200 mesh), dried and observed at 200KV.

Biological Study

The antimicrobial activities of cobalt oxide nanoparticles were tested against bacterial species like three gram-negative (Staphylococcus aureus, Proteus vulgaris, Salmonella typhimurium) & two gram-positive (Escherichia coli, Bacillus subtilis) and fungal activity of these nanoparticles against fungi like Aspergillus flavus, Aspergillus niger, Candida albicans, Culvularia lunata and Rhizoctonia bataicolaby Well diffusion method. At room temperature, DNA interaction of nanoparticles in the presence or absence of DNA in Tris-HCl/NaCl (5 mM/50 mM) buffer solution at pH 7.4 was investigated by the use of the electronic absorption spectral titration method. The competitive binding of nanoparticles with ethidium bromide bound DNA in Tris-HCl buffer solution at pH 7.4 was investigated by fluorescence techniques (37, 38).The antioxidant activities of the nanoparticles were gauged by 2,2′-Diphenyl-1-picrylhydrazil (DPPH) method. The experiment was conducted using Visible spectrophotometer (39, 40). The Hepatocellular carcinoma cancer cells (HepG2) were purchased from National Centre for Cell Science, Pune, India. The procured HepG2 were incubated in an RPMI 1640 medium that was supplemented with L-glutamicin, 10% bovine serum, 100 U of penicillin, and 1 mg/mL of streptomycin. The cells were supplied with a fresh complete medium after four days of incubation in 5% CO2, 95% air, and 37°C environments. The HepG2 cell lines were also grown

in Dulbecco's Modified Eagle's Medium supplemented with sodium pyruvate and other components as mentioned earlier and incubated under similar growth conditions. All the reagents and growth media were purchased from Himedia, India. The cells were seeded at a density of 1×10^3 cells per well in 96-well plates and left overnight under similar growth conditions as mentioned previously. It was then treated at concentration levels of 50, and 100µg/mL of the tested compounds. The cells were treated with 10% MTT solution and incubated for 3 to 4 h at 37°C after 24 h of incubation. The spectrophotometric readingswere taken at wavelengths of 650 nm using a Multiskan EX instrument (Thermo Scientific, USA). The percentage of the viable cells was estimated using the following formula after subtracting the absorbance value at 650 nm (41).

Phytochemical Screening Tests

The phytochemicals of the fruit extract were analyzed with the help of available qualitative analysis. Wagner's test (alkaloids): 2 mL extract was added with some drops of Wagner's reagent. The alkaloid presence was calculated by the formation of the reddish-brown precipitate. Shinoda test (flavonoids): 2 mL extract was added to a pinch of magnesium, then added with 1–2 drops of concentrated HCl. The presence of flavonoids in the solution was confirmed by the formation of pink color. Lead acetate test (phenol and tannins): 2 mL extract was added with 0.5 mL of (1%) lead acetate solution and the presence of tannins and phenolic compounds was confirmed by the precipitate formation (42).

RESULTS AND DISCUSSION

Characterization of Co3O4NPs
UV –Vis Analysis

UV-Visible analysis is a common analytical technique employed to estimate the absorbance of nanoparticles. Figure 2 represents the UV spectrum of biosynthesizedcobalt oxide nanoparticles using prickly pear fruit extract. The peak at 513 nm is due to the inter-band transition of electrons in cobalt metalcores. The UV spectrum of the aqueous fruitextract did not show the type of excitation for these nanoparticlesin this region. The synthesis of aqueous fruit extracts mediatednanoparticles was validated by visual observation using prickly pear fruit extract and the reaction mixture from pink toblack showed the formation of cobalt oxide nanoparticles in Figure 2. Inthe UV spectrum, peaks at 536 nm and 513 nm are due to the absorptionof prickly pear fruit extract and cobalt oxide. The band of surface plasmon absorption at a maximum wavelength of 513 nm indicates the formation of CNPssimilar to the reports of previous literature. Cobalt oxide Nanoparticles formed by cobalt nitrate precursor with a mixture of prickly pear fruit extract act as reducing agents (43, 44). Figure 2 shows the clear UV Spectrum of prickly pear fruit extract-mediated cobalt oxide nanoparticles (45).
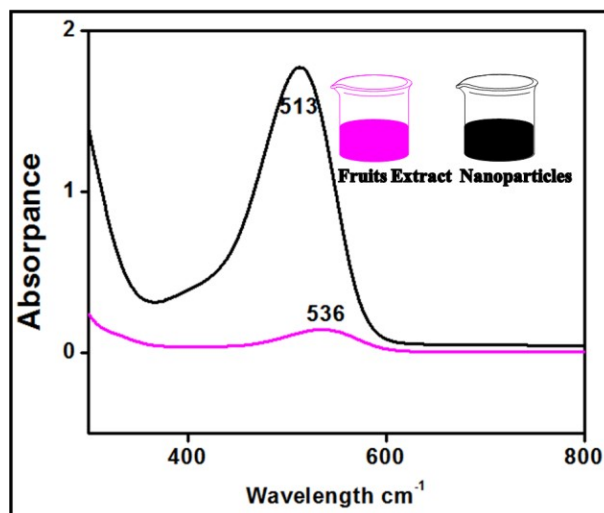
Figure 2: UV Spectrum of Prickly Pear fruit extract and Cobalt Oxide Nanoparticles.

Infrared Spectroscopic Analysis

The chemical composition and functional groups of these nanoparticles are determined by FTIR analysis. Figure 3 shows the FTIR spectrum of the prepared Co3O4NPs. The vibrational properties of Co3O4NPs were studied using Fourier Transform Infra-Red spectra and are in the range of 0 to 4000 cm-1 as pointed in Figure 3. The observed peaks are at 566cm-1 and 667cm1 and are represented with Co-O, O-Co-O stretching frequency that confirmed the configuration of Co3O4. Consequently, Co3+ located at the octahedral site is characterized by a peak at 566cm-1 and Co2+ located at the tetrahedral site is characterized by a peak at 667cm-1 respectively. The broadband at about 3450 cm−1 is assigned to the adsorbed water (46–48).
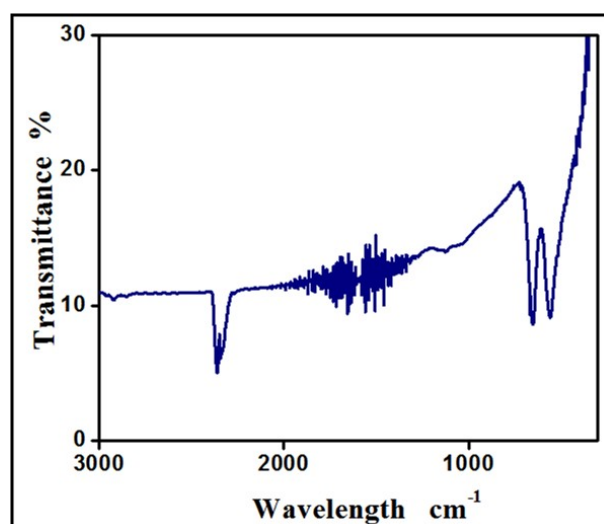
Figure 3: FTIR Spectrum of Co_3O_4NPs

XRD Analysis

The crystalline nature of the cobalt oxide nanoparticles was evaluated by X-ray diffraction analysis. In Figure 4, the XRD pattern of Co3O4

nanoparticles exhibits diffraction peaks with 2θ values of 30.84°, 36.31°, 37.99°, 44.16°, 54.89°, 58.53°, and 64.33° that are allocated to 220, 311, 222, 400, 422, 511, and 440 crystal planes of the crystalline Co3O4 phase correspondingly. These peaks are indexed to a pure cubic phase structure (JCPDS Card No. 80–1540). The average crystalline size of the nanoparticles was calculated using the Scherrer equation concerning the peaks(12).The average size of th synthesized Co3O4 nanoparticles was 36.24 nm.

Morphological Analysis

The size, shape, structure, morphology and microimaging of cobalt oxide nanoparticles were evaluated with the help of SEM and TEM analysis. Figure 5 shows SEM and TEM images of the prepared Co3O4NPs. Previous reports indicate that an increase in temperature up to 80°C forces the particles to agglomerate when nitrate was used as a counter ion of cobalt (49). The prepared Co3O4 nanoparticles showed a cubic spinel structure with a porous network. The pure nanosized crystal particles had an average size of 36.24 nm. Elemental analysis of cobalt oxide nanoparticles was performed using

EDS techniques. Elements such as Co and O identified by EDS indicates the high purity of the prepared Co3O4 nanomaterial as shown in Figure 5. The chemical composition results of Co3O4 by XRD and EDS analysis are in excellent agreement. The atomic percentage of Co & O is 63.76 and 36.24 respectively and it is close to the abstract ratio (3:4) of cobalt oxide.
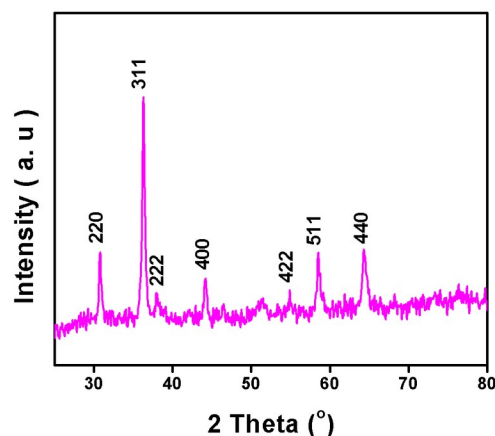
Figure 4: XRD Spectrum of Co3O4NPs
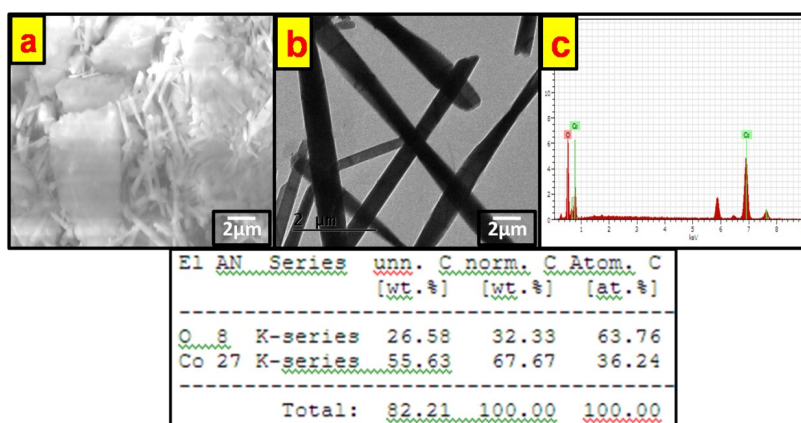
Figure 5: SEM, TEM& EDS Spectrum of Co3O4NPs.

Biological Applications of Co3O4NPs
Antimicrobial activity

The synthesized Co3O4NPs were estimated for their antimicrobial activity upon selected bacteria and fungi. The bacterial activity of these nanoparticles against three-gram negative (Staphylococcus aureus, Proteus vulgaris, Salmonella typhimurium) and two-gram positive (Escherichia coli, Bacillus subtilis) strains of bacteria was investigated. The minimum inhibition concentration (MIC) value of the synthesized cobalt oxide nanoparticles was summarized and compared to the control drug ciprofloxacin. The fungal activity of these nanoparticles against fungi like Aspergillus niger, Aspergillus flavus, Culvularia lunata, Rhizoctonia bataicola and Candida albicans was also investigated. In such treatments, fluconazol is the standard drug for treating fungi. The antimicrobial action of metal oxide nanoparticles (Co3O4NPs) shows potential antibacterial and antifungal

activities at MIC=2.7–6.1µg/mL and MIC=3.1–6.5 µg/mL respectively as shown in Table 1. This analysis of antimicrobial activity data points out the biosynthesized nanoparticles that exhibit higher antibacterial and antifungal activities and their activities are very close to that of the control drugs.

Antioxidant activity

The antioxidant activity of the biosynthesized Co3O4NPs was analyzed and estimated using a radical scavenging assay (RSA) free from diphenylpicrylhydrazyl (DPPH) with spectrophotometric methods. The capacity of DPPH free radical scavenging was estimated using a free radical scavenging assay in different concentrations. The concentration of Co3O4NPs was mixed with 180 µL of diphenylpicrylhydrazyl substance and incubated for up to 30min in a dark place. After that, the absorbance peak at 518 nm was recorded and

the free radical scavenging of samples are calculated using the formula.

Inhibition percentage of free radical scavenging =
$$\frac{\text{Absorbance of control}\,(A^\circ) - \text{Absorbance of sample}\,(A)}{\text{Absorbance of control}\,(A^\circ)}$$

When the Co3O4NPs concentration increases, it induces antioxidant activity. Figure 6 shows diphenylpicrylhydrazyl radical scavenging of a maximum of 59.9% at 450 mg/mL and minimum of 26.8% at 50 mg/mL. The results prove that are similar to the past research works (50–53).

Table 1: MIC value of the synthesized cobalt oxide nanoparticles against five bacterial growths (µg/mL).

Bacteria	*Staphylococcus aureus*	*Proteus vulgaris*	*Escherichia coli*	*Bacillus subtilis*	*Salmonella typhimurium*
cobalt oxide nanoparticles	2.7	3.5	4.1	5.8	5.6
ciprofloxacin	1.7	1.9	2.0	1.8	2.4

Fungi	*Aspergillus niger*	*Aspergillus flavus*	*Culvularia lunata*	*Rhizoctonia bataicola*	*Candida albicans*
cobalt oxide nanoparticles	3.1	4.2	4.8	5.8	6.5
Fluconazol	1.0	1.3	1.2	1.1	1.6
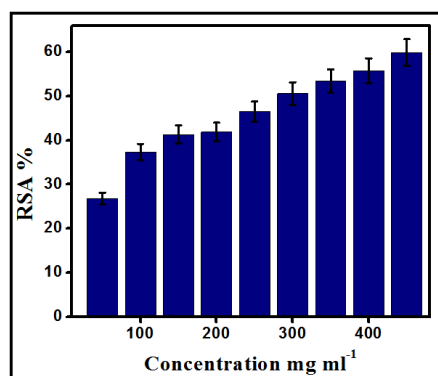
Figure 6: Antioxidant activity of cobalt oxide nanoparticles.

DNA Interaction / Binding Studies
The development of DNA technologies using functional nucleic acids is increasingly attractive with metal ions, proteins, small molecules, and cells (54, 55). The interfacing DNA with nanoparticle probes was based on the surface plasmon resonance, magnetic resonance signal, and fluorescence quenching (56, 57). DNA absorption in nanoparticles is robustly influenced by nucleotide properties. The first property is charge changeability where the nucleobases are uncharged when the pH value is 4–9. If the pH is lower than 4, cytosine and adenine become protonated and if the pH is higher than 9, thymine and guanine become deprotonated

because of monophosphate nucleotides losing their protons (58). The second property is hydrophobicity, the rank of hydrophobicity in nucleotide unit is of nitrogenous base> deoxyribose> phosphate group. The third property is absorption ability, DNA can interact with metal ions via chemisorptions (59). Nucleic acids with nanoparticles have great potential for nanoelectronics and nanomedicine (60).

The binding mechanism of DNA with nanoparticles and the interaction studies is usually carried out by different methods like electronic absorption spectroscopy, spectrofluorescence, colorimetry, and viscometry (61). This research work has utilized the first two methods to find the interaction of DNA with the use of Co3O4 nanoparticles. In interaction studies, various types of interactions present in nanoparticles in DNA are more important. There are four types of interaction processes such as groove binding, electrostatic binding, hydrophobic interactions (intercalation binding), and hydrogen bonding interaction. The chemical interaction of nanoparticles with DNA is intercalation binding, major and minor grooves of DNA interaction is groove binding, and electrically charged species of DNA interaction is electrostatic binding (62, 63).

Electronic Absorption Spectroscopy
The electronic absorption spectroscopy method is the most common for finding nanoparticle interactions with DNA using the 260–300 nm range of tris HCl/NaCl buffer solution of CT-DNA. The absorption spectra were obtained and the constant

nanoparticle concentration with increased DNA concentration (64–66). Figure 7 a illustrates the hyperchromic shift of the absorption spectrum that was observed with the electrostatic intercalation binding present in DNA with Co3O4 nanoparticles. Table 2 lists the calculated details of the binding constant and percentage of chromism. The binding constant of DNA with Co3O4NPs is 2.57x103 and 21.42% of hyperchromism.

Spectrofluorometric Methods
The competitive binding or fluorescence studies of DNA with Co3O4NPs were analyzed with the use of a spectrofluorometer. Figure 7 b demonstrates the fluorescence behavior of ethidium bromide (EB) in DNA that increases the intercalative interaction of

DNA. Then, EB fluorescence intensity is quenched by the addition of nanoparticles owing to the replacement of EB with NPs. The quenching constant is estimated by the utilization of the Stern-Volmer equation.

$$F_0 / F = 1 + K_{sv}[Q]$$

In the equation, F_0 is the absence of quencher fluorescence intensity, F is the presence of quencher fluorescence intensity, Stern-Volmer quenching constant is K_{sv} and [Q] represents the concentration of the quencher of Co3O4NPs (14). Ksv values of Co3O4NPs are 7.1×10^3. The quenching constant values obtained from the Co3O4NPs indicated beneficial CT-DNA binding activity (67–69).
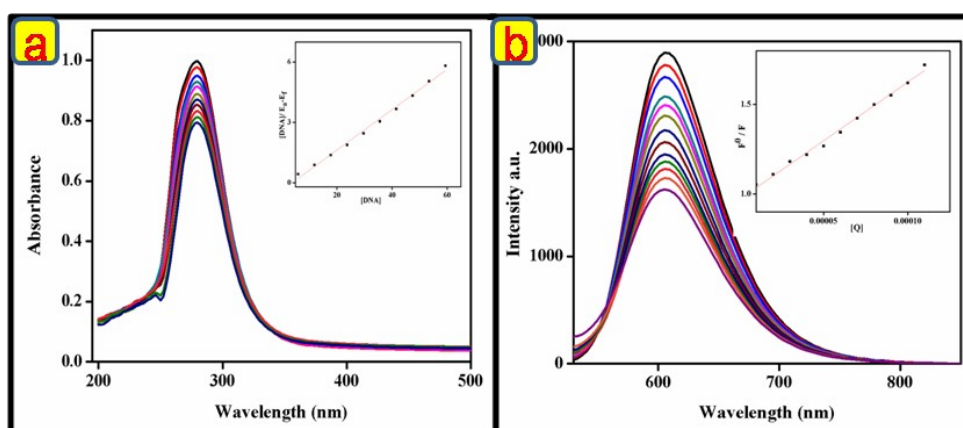
Figure 7: DNA interaction of cobalt oxide nanoparticles a) electronic absorption spectroscopy b) spectrofluorescence spectroscopy.

Table 2: Absorption spectral data and binding parameters of cobalt oxide nanoparticles.

λ_{max} (nm) free	bound	$\Delta\lambda$ (nm)	% chromism	K_b (m^{-1})	K_{sv} (L mol^{-1})	K_Q (L mol^{-1} S^{-1})	K_a (L mol^{-1})	n
278	265	13.0	21.42	2.57×10^3	7.1×10^3	7.1×10^8	$3.47.1 \times 10^5$	0.9119

Cytotoxicity Assay/Cell Viability
The cytotoxicity of the nanoparticles was calculated using colorimetric (MTT) assay using dimethylthiazol diphenyltetrazolium bromide with hepatocellular carcinoma cell lines, and the anticancer activity of nanoparticles was evaluated at IC50 against cancer cell lines as shown in figure 8. Drug concentration of IC50 value inhibits 50% cellular growth in 48 h of exposure to the drug. An average of three replicates from two determinations were acquired as result. The results specify that green synthesized Co3O4NPs have less toxicity and good in-vitro anticancer activity than the standard drug used for cancer applications (70). The cell viability value of the standard drug was 64.3%. The cell viability value of the Co3O4NPs at 50 µg mL-1 was 60.59% and the Co3O4NPs at 100 µg mL-1 was 48.41% respectively.

This research work demonstrates the phenomenal anticancer activity of the Co3O4 nanoparticles with an IC50 value of (70.17%). The results-oriented to the past research works indicate that Co3O4NPs are biocompatible and have potential in-vitro anticancer activity (71).
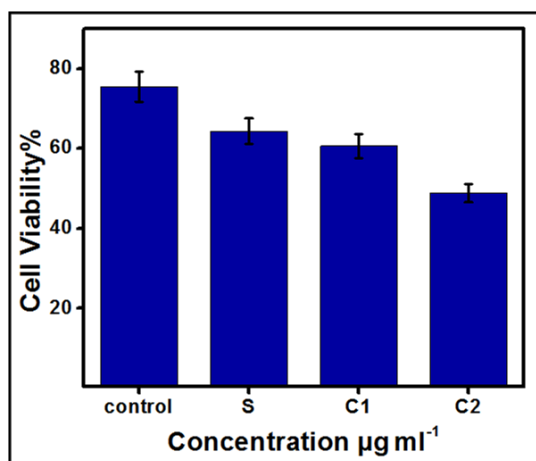
Figure 8: Cell Viability, S- standard drug (cisplatin), C1- cell treated Co3O4NPs at 50 µg mL-1, C2- cell treated Co3O4NPs at 100 µg mL-1

In-vitro Anticancer Activity

The in-vitro anticancer study of Co3O4NPs was evaluated by treating hepatocellular carcinoma cell staining method. The use of Co3O4NPs demonstrates early apoptotic presence with late apoptotic cells with fragment apoptotic bodies. The nuclear staining results indicate the stimulation of apoptosis continued by necrosis in hepatocellular carcinoma cells by cobalt oxide nanoparticles (72–75). The control group of untreated HepG2 cells showed full spherical shaped and homogeneous pink nuclear staining. While the cells treated with cobalt oxide nanoparticles (50 µg mL-1) indicated an irregular shape nucleus, cell shrinkage and scattering of nuclear granules. It suggested the indication of nuclear fragmentation (figure 9). Hence, the treatment of Co3O4NPs induces cell death in HepG2 cells. The observations indicate that synthesized Co3O4NPs have favorable in-vitro anti-cancer activity on Hepatocellular carcinoma cancer cells.
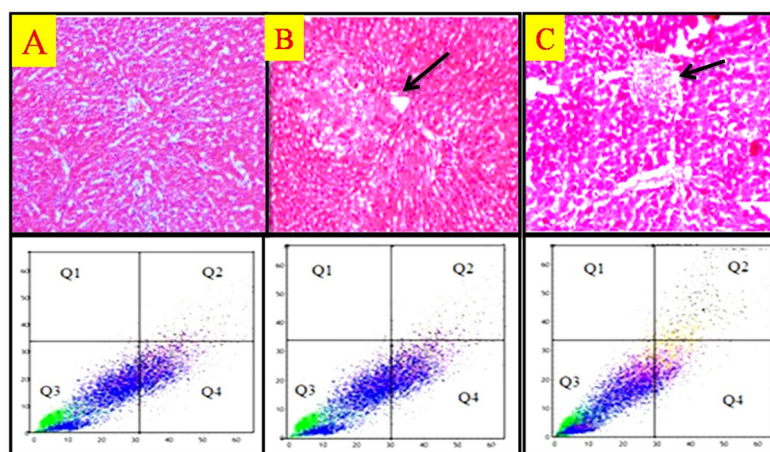
Figure 9: Detection of in-vitro anticancer activity in Hepatocellular carcinoma cells A. Control, B. treated with standard drug, C. cells treated with cobalt oxide nanoparticles (Co3O4NPs). Dot plots indicate increases in early and late apoptosis in hepatocellular carcinoma cell lines, respectively.

CONCLUSION

This study developed a green synthesis of Co3O4NPs utilizing prickly pear fruit extract to decrease the toxicity that arises while biological applications. This research successfully fabricated cobalt oxide nanoparticles Co3O4NPs and characterized them using various techniques and methods like UV, FTIR, XRD, SEM, EDX and TEM. The UV-Visible analysis shows the optical density and absorbance of Co3O4 NPs formed from cobalt nitrate precursor in addition to prickly pear fruit extract. FTIR analysis proves the functional group of cobalt oxide nanoparticles by the peak at 566cm-1 for the octahedral site and the peak at 667cm-1 for the tetrahedral site, which is confirmed by the formation of cobalt oxide nanoparticles. The crystal structure and crystalline nature of cobalt oxide (Co3O4) nanoparticles were confirmed by X-ray diffraction analysis and the major diffraction peak values of

crystalline Co3O4 are30.84°, 36.31°, 44.16°, 64.33° assigned to (220), (311), (400), (440). These peaks were indexed to pure cubic phase structure and the average particle size (36.24nm), and lattice parameter values of cobalt oxide nanoparticles were also determined using XRD analysis. The SEM and TEM images showed the surface morphology and particle size of the Co3O4NPs. EDS indicates the purity and chemical composition of Co3O4 nanoparticles, exhibiting the atomic percentage of Co & O is 63.76% and 36.24%. Antimicrobial activity data indicated that the biosynthesized nanoparticles exhibit higher antifungal and antibacterial activities and are potential like the control drugs. The maximum and minimum mean bacterial activity of Co3O4 nanoparticles was found for A.niger (3.1) and S.aureus (2.7) (73).The maximum and minimum mean fungal activity of Co3O4 nanoparticles was found for B.subtilis (5.8) and C.albicans (6.5). In DPPH assay findings, Co3O4 NPs concentration

increased antioxidant activities also increased. The maximum and minimum radical scavenging activity of these nanoparticles is 59.9% at 450mg/mL and 26.8% at 50mg/mL. Anticancer activity and cytotoxicity assay affirm nuclear disintegration and cancerous cell death by the potential effect of the Co3O4 nanoparticles. The administration of Co3O4 NPs demonstrates the early presence of apoptosis and late apoptotic cells with fragment apoptotic bodies. In DNA binding, electronic absorption spectroscopy, and spectrofluorescence yielded positive results. The intrinsic binding constant of DNA with Co3O4 NPs is 2.57x103 and 21.42% of hyperchromism. Hence, the results show that Co3O4 NPs may be used as an excellent nanomaterial to administer HepG2 cancerous cell lines for its antimicrobial, antioxidant, DNA interaction properties.

CONFLICT OF INTEREST

There is no conflict of interest.

ACKNOWLEDGEMENT

REFERENCES

1. Gibbs RD. Comparative chemistry and phylogeny of flowering plants. In Royal Society of Canada; 1954.

2. Esa YAM, Sapawe N. A short review on biosynthesis of cobalt metal nanoparticles. Materials Today: Proceedings. 2020;31:378–85. <URL>.

3. Harborne JB. Phytochemical methods: a guide to modern techniques of plant analysis. 3rd ed. London ; New York: Chapman and Hall; 1998. 302 p. ISBN :978-0-412-57260-9.

4. Trease G, Evans W. Textbook of pharmacognosy. 14th edition. London; 1989.

5. Vijayakumar S. Eco-friendly synthesis of gold nanoparticles using fruit extracts and in vitro anticancer studies. Journal of Saudi Chemical Society. 2019 Sep;23(6):753–61. <URL>.

6. Diallo A, Beye AC, Doyle TB, Park E, Maaza M. Green synthesis of Co 3 O 4 nanoparticles via Aspalathus linearis : Physical properties. Green Chemistry Letters and Reviews. 2015 Oct 2;8(3–4):30–6. <URL>.

7. Sivachidambaram M, Vijaya JJ, Kaviyarasu K, Kennedy LJ, Al-Lohedan HA, Jothi Ramalingam R. A novel synthesis protocol for Co 3 O 4 nanocatalysts and their catalytic applications. RSC Adv. 2017;7(62):38861–70. <URL>.

8. Sharma JK, Srivastava P, Singh G, Akhtar MS, Ameen S. Green synthesis of Co3O4 nanoparticles and their applications in thermal decomposition of ammonium perchlorate and dye-sensitized solar cells. Materials Science and Engineering: B. 2015 Mar;193:181–8. <URL>.

9. Dubey S, Kumar J, Kumar A, Sharma YC. Facile and green synthesis of highly dispersed cobalt oxide (Co3O4) nano powder: Characterization and screening of its eco-toxicity. Advanced Powder Technology. 2018 Nov;29(11):2583–90. <URL>.

10. Mulya Dewi NO, Yulizar Y, Bagus Apriandanu DO. Green synthesis of Co 3 O 4 nanoparticles using Euphorbia heterophylla L. leaves extract: characterization and photocatalytic activity. IOP Conf Ser: Mater Sci Eng. 2019 May 3;509:012105. <URL>.

11. Han L, Yang DP, Liu A. Leaf-templated synthesis of 3D hierarchical porous cobalt oxide nanostructure as direct electrochemical biosensing interface with enhanced electrocatalysis. Biosensors and Bioelectronics. 2015 Jan;63:145–52. <URL>.

12. Anuradha CT, Raji P. Effect of annealing temperature on antibacterial, antifungal and structural properties of bio-synthesized Co 3 O 4 nanoparticles using Hibiscus Rosa-sinensis. Mater Res Express. 2019 Jul 17;6(9):095063. <URL>.

13. Saeed M, Akram N, Atta-ul-Haq, Naqvi SAR, Usman M, Abbas MA, et al. Green and eco-friendly synthesis of Co3O4 and Ag-Co3O4: Characterization and photo-catalytic activity. Green Processing and Synthesis. 2019 Jan 28;8(1):382–90. <URL>.

14. Ikhuoria EU, Omorogbe SO, Sone BT, Maaza M. Bioinspired shape controlled antiferromagnetic Co3O4 with prism like-anchored octahedron morphology: A facile green synthesis using Manihot esculenta Crantz extract. Science and Technology of Materials. 2018 May;30(2):92–8. <URL>.

15. Matinise N, Mayedwa N, Fuku XG, Mongwaketsi N, Maaza M. Green synthesis of cobalt (II, III) oxide nanoparticles using Moringa Oleifera natural extract as high electrochemical electrode for supercapacitors. In Stellenbosch, South Africa; 2018 [cited 2022 Oct 3]. p. 040005. <URL>.

16. Sebeia N, Jabli M, Ghith A. Biological synthesis of copper nanoparticles, using Nerium oleander leaves extract: Characterization and study of their interaction with organic dyes. Inorganic Chemistry Communications. 2019 Jul;105:36–46. <URL>.

17. Ullah M, Naz A, Mahmood T, Siddiq M, Bano A. Biochemical synthesis of nickel & cobalt oxide nano-particles by using biomass waste. International Journal of Enhanced Research in Science Technology & Engineering. 2014;3:415–22.

18. Bibi I, Nazar N, Iqbal M, Kamal S, Nawaz H, Nouren S, et al. Green and eco-friendly synthesis of cobalt-oxide nanoparticle: Characterization and photo-catalytic activity. Advanced Powder Technology. 2017 Sep;28(9):2035–43. <URL>.

19. Saravanakumar P, Muthukumar M, Muthuchudarkodi R, Ramkumar P. Piper nigrum mediated green synthesis, characterization of undoped cobalt oxide and cerium ion doped cobalt oxide nanoparticles. Int J Recent Res Aspects. 2018;918–23.

20. Khalil AT, Ovais M, Ullah I, Ali M, Shinwari ZK, Maaza M. Physical properties, biological applications and biocompatibility studies on biosynthesized single phase cobalt oxide (Co3O4) nanoparticles via Sageretia thea (Osbeck.). Arabian Journal of Chemistry. 2020 Jan;13(1):606–19. <URL>.

21. Das RK, Golder AK. Co3O4 spinel nanoparticles decorated graphite electrode: Bio-mediated synthesis and electrochemical H2O2 sensing. Electrochimica Acta. 2017 Oct;251:415–26. <URL>.

22. Mindru I, Gingasu D, Patron L, Ianculescu A, Surdu VA, Culita DC, et al. A new approach: Synthesis of cobalt aluminate nanoparticles using tamarind fruit extract. Materials Science and Engineering: B. 2019 Jul;246:42–8. <URL>.

23. Rasheed T, Nabeel F, Bilal M, Iqbal HMN. Biogenic synthesis and characterization of cobalt oxide nanoparticles for catalytic reduction of direct yellow-142 and methyl orange dyes. Biocatalysis and Agricultural Biotechnology. 2019 May;19:101154. <URL>.

24. Majeed S, Abdullah MS bin, Nanda A, Ansari MT. In vitro study of the antibacterial and anticancer activities of silver nanoparticles synthesized from Penicillium brevicompactum (MTCC-1999). Journal of Taibah University for Science. 2016 Oct;10(4):614–20. <URL>.

25. Khan S, Ansari AA, Khan AA, Ahmad R, Al-Obaid O, Al-Kattan W. In vitro evaluation of anticancer and antibacterial activities of cobalt oxide nanoparticles. J Biol Inorg Chem. 2015 Dec;20(8):1319–26. <URL>.

26. Stankic S, Suman S, Haque F, Vidic J. Pure and multi metal oxide nanoparticles: synthesis, antibacterial and cytotoxic properties. J Nanobiotechnol. 2016 Dec;14(1):73. <URL>.

27. Hafeez M, Shaheen R, Akram B, Zain-ul-Abdin, Haq S, Mahsud S, et al. Green synthesis of cobalt oxide nanoparticles for potential biological applications. Mater Res Express. 2020 Feb 1;7(2):025019. <URL>.

28. Bhushan M, Kumar Y, Periyasamy L, Viswanath AK. Antibacterial applications of α-Fe2O3/Co3O4 nanocomposites and study of their structural,

optical, magnetic and cytotoxic characteristics. Appl Nanosci. 2018 Feb;8(1–2):137–53. <URL>.

29. Rajeswari VD, Khalifa AS, Elfasakhany A, Badruddin IA, Kamangar S, Brindhadevi K. Green and ecofriendly synthesis of cobalt oxide nanoparticles using Phoenix dactylifera L: antimicrobial and photocatalytic activity. Appl Nanosci [Internet]. 2021 Aug 30 [cited 2022 Oct 3]; <URL>.

30. Mauro M, Crosera M, Pelin M, Florio C, Bellomo F, Adami G, et al. Cobalt Oxide Nanoparticles: Behavior towards Intact and Impaired Human Skin and Keratinocytes Toxicity. IJERPH. 2015 Jul 17;12(7):8263–80. <URL>.

31. Kamaraj M, Nithya TG, Santhosh P, Mulugeta K. Rapid Green Synthesis of Silver Nanoparticles Using Ethiopian Cactus Pear Fruit Peel Infusions and Evaluation of Its In Vitro Clinical Potentials. J Inorg Organomet Polym. 2020 Sep;30(9):3832–6. <URL>.

32. El-Mostafa K, El Kharrassi Y, Badreddine A, Andreoletti P, Vamecq J, El Kebbaj M, et al. Nopal Cactus (Opuntia ficus-indica) as a Source of Bioactive Compounds for Nutrition, Health and Disease. Molecules. 2014 Sep 17;19(9):14879–901. <URL>.

33. Livrea MA, Tesoriere L. Health benefits and bioactive components of the fruits from Opuntia ficus-indica [L.] Mill. Journal of the Professional Association for cactus Development. 2006;8(1):73–90.

34. Badri A, Slimi S, Guergueb M, Kahri H, Mateos X. Green synthesis of copper oxide nanoparticles using Prickly Pear peel fruit extract: Characterization and catalytic activity. Inorganic Chemistry Communications. 2021 Dec;134:109027. <URL>.

35. Muñoz-Carrillo MG, Garcidueñas-Piña C, Valerio-García RC, Carrazco-Rosales JL, Morales-Domínguez JF. Green Synthesis of Silver Nanoparticles from the Opuntia ficus-indica Fruit and Its Activity against Treated Wastewater Microorganisms. Chauhan BPS, editor. Journal of Nanomaterials. 2020 Nov 17;2020:1–10. <URL>.

36. Pooja S, Vidyasagar G. Biosynthesis of Silver Nanoparticles from Three Opuntia Sps. Int J Adv Sci Res Manag. 2019;4:1–11.

37. Sankarganesh M, Dhaveethu Raja J, Sakthikumar K, Solomon RV, Rajesh J, Athimoolam S, et al. New bio-sensitive and biologically active single crystal of pyrimidine scaffold ligand and its gold and platinum complexes: DFT, antimicrobial, antioxidant, DNA interaction, molecular docking with DNA/BSA and anticancer studies. Bioorganic Chemistry. 2018 Dec;81:144–56. <URL>.

38. Sankarganesh M, Adwin Jose P, Dhaveethu Raja J, Kesavan MP, Vadivel M, Rajesh J, et al. New

pyrimidine based ligand capped gold and platinum nano particles: Synthesis, characterization, antimicrobial, antioxidant, DNA interaction and in vitro anticancer activities. Journal of Photochemistry and Photobiology B: Biology. 2017 Nov;176:44–53. <URL>.

39. Sakthikumar K, Dhaveethu Raja J, Vijay Solomon R, Sankarganesh M. Density functional theory molecular modelling, DNA interactions, antioxidant, antimicrobial, anticancer and biothermodynamic studies of bioactive water soluble mixed ligand complexes. Journal of Biomolecular Structure and Dynamics. 2019 Jul 3;37(10):2498–514. <URL>.

40. Vadivel M, Sankarganesh M, Raja JD, Rajesh J, Mohanasundaram D, Alagar M. Bioactive constituents and bio-waste derived chitosan / xylan based biodegradable hybrid nanocomposite for sensitive detection of fish freshness. Food Packaging and Shelf Life. 2019 Dec;22:100384. <URL>.

41. Jeyaraj M, Praphakar RA, Rajendran C, Ponnamma D, Sadasivuni KK, Munusamy MA, et al. Surface functionalization of natural lignin isolated from Aloe barbadensis Miller biomass by atom transfer radical polymerization for enhanced anticancer efficacy. RSC Adv. 2016;6(56):51310–9. <URL>.

42. Madasamy S, Sundan S, Krishnasamy L. Preparation Of Cold Cream Against Clinical Pathogen Using Caralluma Adscendens Var. Attenuata. Asian J Pharm Clin Res. 2020 Jun 29;120–3. <URL>.

43. Bibi I, Nazar N, Iqbal M, Kamal S, Bhatti HN, Nouren S, et al. Corrigendum to 'Green and eco-friendly synthesis of cobalt-oxide nanoparticle: Characterization and photo-catalytic activity' [Adv. Powder Technol. 28 (2017) 2035–2043]. Advanced Powder Technology. 2017 Oct;28(10):2796. <URL>.

44. Iravani S, Varma RS. Sustainable synthesis of cobalt and cobalt oxide nanoparticles and their catalytic and biomedical applications. Green Chem. 2020;22(9):2643–61. <URL>.

45. Rajasekar K, Muthukumaravel K, Ashok K, Babu M. Phytosynthesis of copper oxide nanoparticles from Opuntia ficus and its antibreast cancer activity against MCF-7 cell line (invasive ductal carcinoma). Malaya J Matematik S (2). 2020;4414–9.

46. Dubey S, Kumar J, Kumar A, Sharma YC. Facile and green synthesis of highly dispersed cobalt oxide (Co3O4) nano powder: Characterization and screening of its eco-toxicity. Advanced Powder Technology. 2018 Nov;29(11):2583–90. <URL>.

47. Salavati-Niasari M, Davar F, Mazaheri M, Shaterian M. Preparation of cobalt nanoparticles from [bis(salicylidene)cobalt(II)]–oleylamine complex by thermal decomposition. Journal of Magnetism and Magnetic Materials. 2008 Feb;320(3–4):575–8. <URL>.

48. Herrero M, Benito P, Labajos F, Rives V. Nanosize cobalt oxide-containing catalysts obtained through microwave-assisted methods. Catalysis Today. 2007 Oct 30;128(3–4):129–37. <URL>.

49. Manteghi F, Kazemi SH, Peyvandipour M, Asghari A. Preparation and application of cobalt oxide nanostructures as electrode materials for electrochemical supercapacitors. RSC Adv. 2015;5(93):76458–63. <URL>.

50. Bhushan M, Kumar Y, Periyasamy L, Viswanath AK. Antibacterial applications of α-Fe2O3/Co3O4 nanocomposites and study of their structural, optical, magnetic and cytotoxic characteristics. Appl Nanosci. 2018 Feb;8(1–2):137–53. <URL>.

51. Moradpoor H, Safaei M, Rezaei F, Golshah A, Jamshidy L, Hatam R, et al. Optimisation of Cobalt Oxide Nanoparticles Synthesis as Bactericidal Agents. Open Access Maced J Med Sci. 2019 Aug 30;7(17):2757–62. <URL>.

52. Wang Y, Aker WG, Hwang H min, Yedjou CG, Yu H, Tchounwou PB. A study of the mechanism of in vitro cytotoxicity of metal oxide nanoparticles using catfish primary hepatocytes and human HepG2 cells. Science of The Total Environment. 2011 Oct;409(22):4753–62. <URL>.

53. Ajarem JS, Maodaa SN, Allam AA, Taher MM, Khalaf M. Benign Synthesis of Cobalt Oxide Nanoparticles Containing Red Algae Extract: Antioxidant, Antimicrobial, Anticancer, and Anticoagulant Activity. J Clust Sci. 2022 Mar;33(2):717–28. <URL>.

54. Abbasi BA, Iqbal J, Mahmood T, Qyyum A, Kanwal S. Biofabrication of iron oxide nanoparticles by leaf extract of Rhamnus virgata : Characterization and evaluation of cytotoxic, antimicrobial and antioxidant potentials. Appl Organometal Chem [Internet]. 2019 Jul [cited 2022 Oct 4];33(7). <URL>.

55. Mianai RS, Ghasemzadeh MA, Monfared MRZ. Green Fabrication of Cobalt NPs using Aqueous Extract of Antioxidant Rich Zingiber and Their Catalytic Applications for the Synthesis of Pyrano[2,3-c]pyrazoles. CCHTS. 2019 May 3;22(1):18–26. <URL>.

56. Chattopadhyay S, Dash SK, Tripathy S, Das B, Kar Mahapatra S, Pramanik P, et al. Cobalt oxide nanoparticles induced oxidative stress linked to activation of TNF-α/caspase-8/p38-MAPK signaling in human leukemia cells: Anticancer activity of CoO nanoparticles in vitro and in vivo. J Appl Toxicol. 2015 Jun;35(6):603–13. <URL>.

57. Abamor ES. Antileishmanial activities of caffeic acid phenethyl ester loaded PLGA nanoparticles against Leishmania infantum promastigotes and amastigotes in vitro. Asian Pacific Journal of Tropical Medicine. 2017 Jan;10(1):25–34. <URL>.

58. Ebrahiminezhad A, Zare-Hoseinabadi A, Sarmah AK, Taghizadeh S, Ghasemi Y, Berenjian A. Plant-Mediated Synthesis and Applications of Iron Nanoparticles. Mol Biotechnol. 2018 Feb;60(2):154–68. <URL>.

59. Matinise N, Fuku XG, Kaviyarasu K, Mayedwa N, Maaza M. ZnO nanoparticles via Moringa oleifera green synthesis: Physical properties & mechanism of formation. Applied Surface Science. 2017 Jun;406:339–47. <URL>.

60. Jin C, Fu T, Wang R, Liu H, Zou J, Zhao Z, et al. Fluorinated molecular beacons as functional DNA nanomolecules for cellular imaging. Chem Sci. 2017;8(10):7082–6. <URL>.

61. Morris DL. DNA-bound metal ions: recent developments. Biomolecular Concepts. 2014 Oct 1;5(5):397–407. <URL>.

62. Yang D, Hartman MR, Derrien TL, Hamada S, An D, Yancey KG, et al. DNA Materials: Bridging Nanotechnology and Biotechnology. Acc Chem Res. 2014 Jun 17;47(6):1902–11. <URL>.

63. Sun H, Ren J, Qu X. Carbon Nanomaterials and DNA: from Molecular Recognition to Applications. Acc Chem Res. 2016 Mar 15;49(3):461–70. <URL>.

64. Liu B, Liu J. Methods for preparing DNA-functionalized gold nanoparticles, a key reagent of bioanalytical chemistry. Anal Methods. 2017;9(18):2633–43. <URL>.

65. Izatt RM, Christensen JJ, Rytting JH. Sites and thermodynamic quantities associated with proton and metal ion interaction with ribonucleic acid, deoxyribonucleic acid, and their constituent bases, nucleosides, and and nucleotides. Chem Rev. 1971 Oct;71(5):439–81. <URL>.

66. Pershina AG, Sazonov AE, Filimonov VD. Magnetic nanoparticles–DNA interactions: design and applications of nanobiohybrid systems. Russ Chem Rev. 2014 Apr 30;83(4):299–322. <URL>.

67. Chaurasia M, Tomar D, Chandra S. Synthesis, spectroscopic characterization and DNA binding studies of Cu(II) complex of Schiff base containing benzothiazole moiety. Journal of Taibah University for Science. 2019 Dec 11;13(1):1050–9. <URL>.

68. Thulasiram B, devi CS, Kumar YP, Aerva RR, Satyanarayana S, Nagababu P. Correlation Between Molecular Modelling and Spectroscopic Techniques in Investigation With DNA Binding Interaction of

Ruthenium(II) Complexes. J Fluoresc. 2017 Mar;27(2):587–94. <URL>.

69. Chaurasia M, Tomar D, Chandra S. Synthesis, spectral characterization, and DNA binding studies of Co(II), Ni(II), Cu(II) and Zn(II) complexes of Schiff base 2-((1H-1,2,4-triazol-3-ylimino)methyl)-5-methoxyphenol. Journal of Molecular Structure. 2019 Mar;1179:431–42. <URL>.

70. Park SY, Lytton-Jean AKR, Lee B, Weigand S, Schatz GC, Mirkin CA. DNA-programmable nanoparticle crystallization. Nature. 2008 Jan;451(7178):553–6. <URL>.

71. Shaban NZ, Aboelsaad AM, Shoueir KR, Abdulmalek SA, Awad D, Shaban SY, et al. Chitosan-based dithiophenolato nanoparticles: Preparation, mechanistic information of DNA binding, antibacterial and cytotoxic activities. Journal of Molecular Liquids. 2020 Nov;318:114252. <URL>.

72. Sankarganesh M, Adwin Jose P, Dhaveethu Raja J, Kesavan MP, Vadivel M, Rajesh J, et al. New pyrimidine based ligand capped gold and platinum nano particles: Synthesis, characterization, antimicrobial, antioxidant, DNA interaction and in vitro anticancer activities. Journal of Photochemistry and Photobiology B: Biology. 2017 Nov;176:44–53. <URL>.

73. Han MS, Lytton-Jean AKR, Oh BK, Heo J, Mirkin CA. Colorimetric Screening of DNA-Binding Molecules with Gold Nanoparticle Probes. Angew Chem Int Ed. 2006 Mar 6;45(11):1807–10. <URL>.

74. Mirzaei-Kalar Z, Yavari A, Jouyban A. Increasing DNA binding affinity of doxorubicin by loading on Fe3O4 nanoparticles: A multi-spectroscopic study. Spectrochimica Acta Part A: Molecular and Biomolecular Spectroscopy. 2020 Mar;229:117985. <URL>.

75. Zhang NN, Bigdeli F, Miao Q, Hu ML, Morsali A. Ultrasonic-assisted synthesis, characterization and DNA binding studies of Ru(II) complexes with the chelating N-donor ligand and preparing of RuO2 nanoparticles by the easy method of calcination. Journal of Organometallic Chemistry. 2018 Dec;878:11–8. <URL>.

76. Hafeez M, Shaheen R, Akram B, Zain-ul-Abdin, Haq S, Mahsud S, et al. Green synthesis of cobalt oxide nanoparticles for potential biological applications. Mater Res Express. 2020 Feb 1;7(2):025019. <URL>.

RESEARCH ARTICLE

Influence of Europium Doping on the Crystallization, Morphology, and Cathodoluminescent Properties of PbNb$_2$O$_6$:Eu^{3+} Phosphors

Mete Kaan Ekmekçi[*] (iD)

[*]Department of Chemistry, Faculty of Sciences, Marmara University, Göztepe Campus, Kadıköy, 34722, İstanbul, Turkey

Abstract: Undoped PbNb$_2$O$_6$ and Eu^{3+} ion doped PbNb$_2$O$_6$ samples were synthesized by high temperature mixed oxide method, applying a heat treatment temperature of 1250°C and an annealing time of 6 hours. In order to elucidate the structural and optical behavior of PbNb$_2$O$_6$:Eu^{3+} phosphors, XRD (X-ray diffraction), SEM (scanning electron microscopy), EDS (energy dispersive spectroscopy), CL (cathodoluminescence) and absoption analyses were performed. The X-ray diffraction results showed that the undoped PbNb$_2$O$_6$ sample crystallized in a rhombohedral symmetry while Eu^{3+} doped samples formed in orthorhombic symmetry. The morphologies of the rhombohedral and orthorhombic grains were examined by SEM-EDS. The CL spectra showed spectral profiles between 580 and 780 nm in relation to the 4f–4f transitions of Eu^{3+}. A strong emission was observed at about 620 nm, corresponding to the red color and associated with the $^5D_0 \rightarrow {}^7F_2$ transition of Eu^{3+}, while the undoped sample did not exhibit CL emission of the host which is probably due to the presence of lead in the host structure. In addition, the CL analysis results showed that the emission intensity increased with the increase of Eu^{3+} ion concentration. The increase in magnetic dipole transition caused by the electron beam radiation effect of the CL with increasing doping concentration is associated with the change of dipole moments of the Eu^{3+} doped tungsten bronze host and thus differentiating the emission spectrum. UV lamp excited photograph of undoped sample showed blue-violet color while Eu^{3+} doped phosphors with red color became more significant with increasing Eu^{3+} concentration.

INTRODUCTION

Trivalent lanthanide (Ln^{3+}) ions exhibiting 4f–4f inner-shell transitions have certain properties such as high luminescence efficiency, narrow emission line, and long decay time constant. Due to their advantages, such as reliability and environmental friendliness, they have attracted great attention as new generation solid-state lighting sources in recent years (1–9). Among these materials, trivalent europium, which is used as a dopant in the production of inorganic-based red light emitting phosphors (LEDs), is known as an effective activator due to its characteristic $^5F_0 \rightarrow {}^7F_J$ (J = 0, 1, 2, 3, 4, 5) band transitions. In addition, the Eu^{3+} is well

known for its strong luminescence in the red region of the spectrum, and also has a great advantage over other rare earth ions with an even number of 4f electrons in that the initial levels of transitions in both the absorption and luminescence spectrum are non-degenerate (10). The magnetic dipole transition of $^5F_0 \rightarrow {}^7F_1$ and the electric dipole transition of $^5F_0 \rightarrow {}^7F_2$ show emissions at wavelengths of 590–600 nm and 610–630 nm, respectively. Moreover, trivalent Eu, as a potential emission activator, provides important information about spectroscopic characterization when used as a dopant in different host structures (6-10).

Cathodoluminescence (CL) is a method used in the optical characterization resulting from the interaction of the material with an electron beam provided by an electron gun. The CL analysis can be interpreted via spectral lines that are similar to those from other luminescence techniques, and characteristically dominate the spectrum with bound excitonic states and changes from emission lines, donor-acceptor double bands, and defect-related properties (11–16).

The synthesis, structural, and optical properties of several AB_2O_6-type niobate compounds have been investigated (17-21). Among the lead-based niobates, $PbNb_2O_6$ ceramics have been studied recently for their photocatalytic (22), dielectric and piezoelectric (23), ferroelectric (24-29), and thermal properties (30). Furthermore, lhan et al. (17, 18) investigated the photoluminescence properties of rhombohedral $PbNb_2O_6$:Eu^{3+} phosphor, as well as the thermoluminescence kinetic parameters, Judd-Ofelt analysis and radioluminescence properties of orthorhombic $PbNb_2O_6$:Eu^{3+} phosphor.

$PbNb_2O_6$ exhibits three different structures in PbO-Nb_2O_5 system. The stable forms of $PbNb_2O_6$ are the rhombohedral and tetragonal polymorphs, which occur at low and high temperatures, respectively. The rhombohedral and tetragonal are not ferroelectric and piezoelectric. The only metastable orthorhombic polymorph of $PbNb_2O_6$ is an important high-temperature piezoelectric material (30) that can act as actuators that can convert electrical pulses to motion or sensors that can convert motion/pressure pulses to electrical voltage. This actuator and sensor property of piezoelectric materials can be combined in applications in the medical and engineering

fields, for example, with the imaging technique of ultrasonography, for the diagnosis of diseases and for the structural imaging of engineering materials. $PbNb_2O_6$ with high Curie temperature is used as a rocket and automobile exhaust sensor material (31). In addition, $PbNb_2O_6$ synthesized by high temperature solid state method was evaluated in terms of lithium storage in rechargeable batteries (32, 33). The ferroelectric phase transition properties of lead meta niobate ($PbNb_2O_6$) with a single crystal under gamma rays radiation have been investigated (34). Samarium doped lead based ceramic materials with rhombohedral structure were produced by a high temperature conventional solid state synthesis and examined for their dielectric and piezoelectric properties (35). Due to investigating the tunable dielectric properties of $PbNb_2O_6$ via calcium substitution, $Pb_{1-x}Ca_xNb_2O_6$ perovskite structures were synthesized via sol-gel auto-combustion method (36). Due to the high piezoelectric constant, the high Curie temperature of Ca, and excess Ti doped high density $PbNb_2O_6$ (PN), ferroelectric ceramics produced by the traditional powder synthesis method and their use in ultrasonic applications as piezoelectric material have been investigated (37). $PbNb_2O_6$ ferroelectric ceramics with orthorhombic structure have been synthesized by solid state reaction route and evaluated in terms of their dielectric properties in the frequency range of 20 Hz to 2 GHz (38).

Undoped and Eu^{3+} doped $PbNb_2O_6$ ceramic phosphors have been synthesized via solid state synthesis. The structural and cathodolumi-nescence properties of the samples were investigated. In addition, the effect of europium doping on the crystallization, morphology, structural and cathodolumi-nescence properties of the samples has also been researched and evaluated. The microphase morphology, crystalline structure and cathodoluminescence properties of the samples were carried out by XRD, SEM, EDS, CL, and absorption analyses.

EXPERIMENTAL SECTION

Undoped $PbNb_2O_6$ and Eu^{3+} doped $PbNb_2O_6$:$x$$Eu^{3+}$ (x = 0.5, 1, 3, and 6 mol%) samples were produced by using the solid state reaction route, where x represents 2 atomic value due to Eu_2O_3. For this, $Pb(NO_3)_2$ and Nb_2O_5 powders were taken as starting materials, with purities of 99% (Sigma-Aldrich) and 99.9% (Alfa Aesar), respectively. Eu_2O_3 powder

was used as a dopant with a purity of 99.9% (Alfa Aesar). $Pb(NO_3)_2$ and Nb_2O_5 powders were taken and mixed according to $PbNb_2O_6$ stoichiometry. Eu_2O_3 was subsequently added to this mixture in different molar ratios. Later on, these powder mixtures were homogenized by grinding in an agate mortar and subsequently sintered in an electric furnace at 1250 °C in an air atmosphere for 6 hours after pelleting. The crystalline phases of the ceramic samples were identified by X-ray diffractometry (XRD, Rigaku Corp., D-MAX 2200) using Cu-Kα radiation and Ni filter at a scanning rate of 2°/min between 20 and 65°. SEM observations were performed by SEM (FEI, Oregon, Inspect S50, USA). The elemental contents of the ceramic samples were examined by using an energy dispersive spectrometer (EDS, OXFORD Industries INCAxSight 7274; 133-eV resolution 5.9 keV)

which integrated to scanning electron microscope (SEM, JEOL Ltd., JSM-5910LV). The CL (cathodoluminescence) spectra were taken by a SEM (NOVA-NANOSEM 650), that is operated at 15 kV (spot size 3.5, work distance 6.6 mm, and high vacuum) equipped with field emission gun at room temperature. The CL system is equipped with a spectrometer (DATAN-Mono CL4), which allows monochromatic CL imaging as well as the acquisition of CL spectra on very localized spots of a sample. The absorptions of the samples were taken by a Perkin-Elmer Lambda spectrophotometer (USA).

RESULTS AND DISCUSSION

Morphological and Structural Characterization
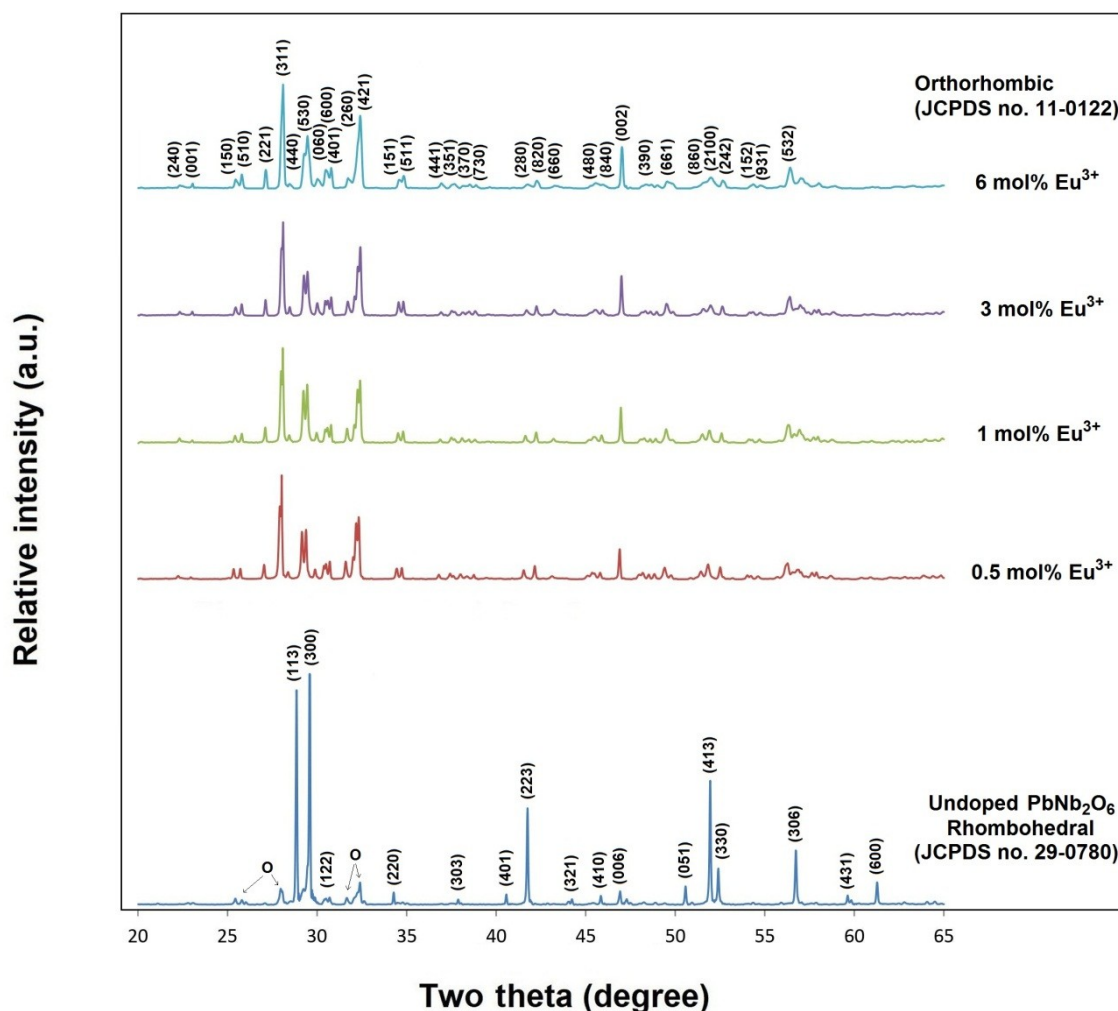
Figure 1: X-ray diffractions of undoped and Eu^{3+} doped $PbNb_2O_6$ samples.
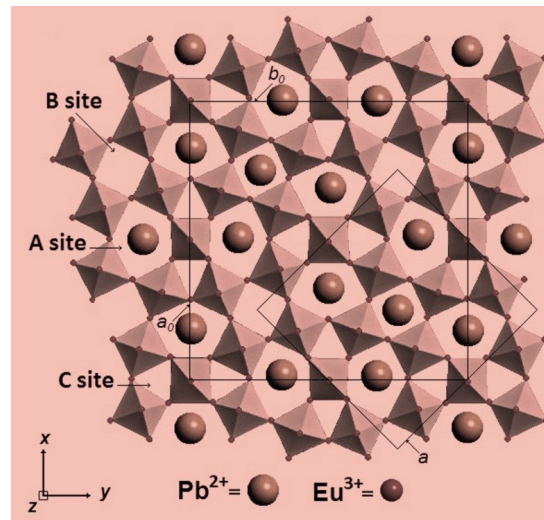
Figure 2: Relationship of orthorhombic and tetragonal in $PbNb_2O_6$ structure.

The results of X-Ray Diffraction for undoped and doped samples that sintered at 1250 °C for 6 hours are shown in Figure 1. XRD analysis also showed the undoped $PbNb_2O_6$ sample crystallized in rhombohedral (hexagonal) symmetry (JCPDS card No. 29–0780) with space group $R3/m$ (no.160) while Eu^{3+} doped samples formed in orthorhombic symmetry (JCPDS card no. 11–0122) with space group $Cmm2$ (no.35). The lattice parameters of rhombohedral were reported as a = 10.501 Å, b = 10.501 Å, c = 11.555 Å, V = 1103 Å^3 (28). The orthorhombic $PbNb_2O_6$ cell data have been reported as a_0=17.65 (Å), b_0=17.91 (Å) and c_0=7.736 (Å) (24). Interestingly, as seen from the XRD model of the $PbNb_2O_6$ samples, the Eu^{3+} doped samples changed to a different symmetry than the undoped sample. In the XRD pattern of the undoped sample, the rhombohedral phase, which normally crystallizes at 1150 °C, also formed at 1250 °C, and there is an orthorhombic phase indicated by "O" in the form of impurity in the rhombohedral phase. As stated in different studies (18,37), orthorhombic polymorph can be obtained by rapid cooling of tetragonal at temperatures between 1200-1250 °C. In this study, the average cooling rate is about 6 K/min, which is not sufficient for the transformation of the pure orthorhombic phase. However, the lack of rhombohedral polymorph with Eu^{3+} doping and the ease with which the orthorhombic polymorph was obtained indicate that an anisotropic phase transformation occurred as a result of thermal shock in the lattice caused by Eu^{3+} ions doping (18). The tetragonal ($a{\approx}b,c$) and orthorhombic (a_0,b_0,c_0) polymorphs have tungsten bronze symmetry (24, 39, 40), where the lattice data of them are associated with $a_0=a\sqrt{2}$, $b_0{\approx}a\sqrt{2}$, $c_0=2c$. Accordingly, the b/a ratio is approximately equal to 1.015 where a, b constants are fairly close. So, due to a small distortion in orthorhombic, the XRD pattern of the orthorhombic $PbNb_2O_6$ can be indexed based on tungsten bronze symmetry (24, 25). The relationship between orthorhombic and tetragonal polymorphs is illustrated in Figure 2, where tetragonal shows the small square and its corners located in the B tunnels, while orthorhombic represents the large square and its corners located in the octahedral sites (18).
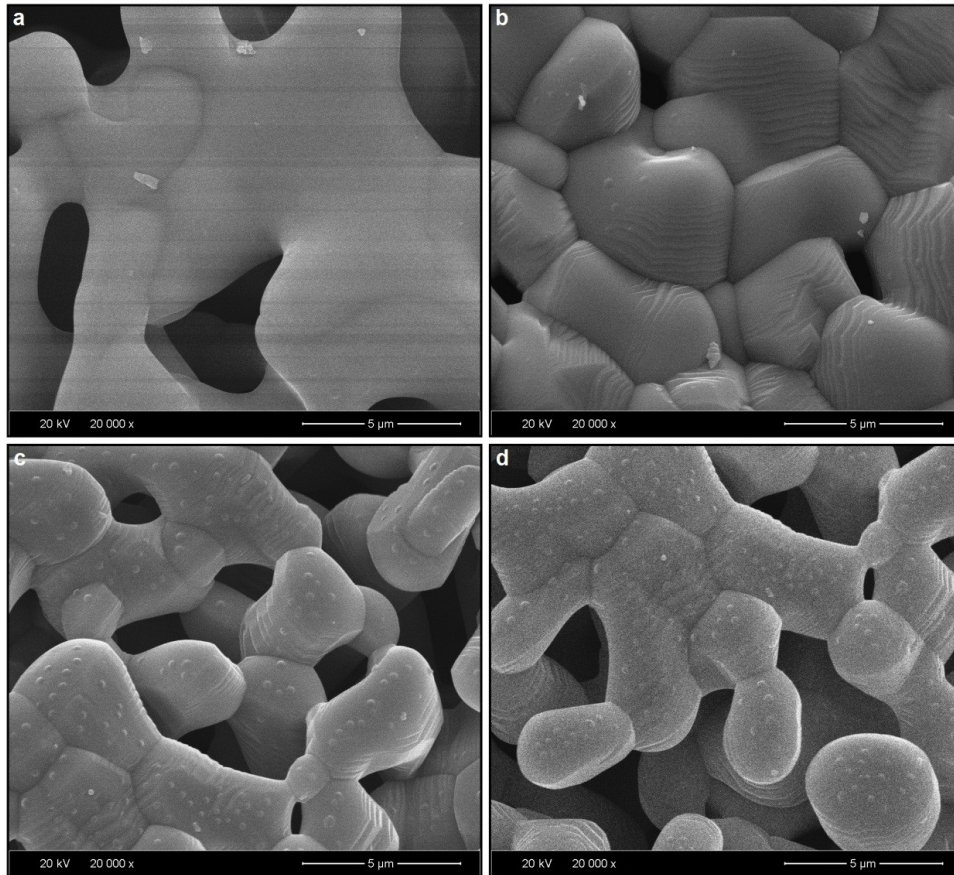
Figure 3: SEM micrographs of (a) undoped and (b) 0.5, (c) 3, (d) 6 mol% Eu^{3+} doped samples at 20 kV acceleration voltage, and 20.000x magnification.

SEM micrographs of undoped sample (rhombohedral) and 0.5, 3, 6 mol% Eu^{3+} doped ones (orthorhombic) are shown in Figure 3(a–d), respectively. The morphology of the grains was examined by the SEM. The grain morphology of the undoped sample showed smooth surface and an amorphous shape, while the boundaries of the grains were hard to see. Depending on concentration, the grain shapes of the doped samples exhibited an oval and wavy morphology, which are more common for 3 and 6 mol% samples. SEM findings uncovered a terraced morphology that can be ascribed to the angular structure of tungsten bronze. SEM results may also be associated with how morphological transformation between

orthorhombic and rhombohedral. The decrease in the grain size with the increase in Eu^{3+} concentration can be explained by the restriction of grain growth due to suppression in the lattice (41,42). The grain sizes for 0.5 and 6 mol% were detected between 3-11 and 1.5-6.5 µm, respectively.

EDS analysis was applied to the samples in order to define the composition change of the elements. EDS results (weight% and atomic%) for 6 mol% Eu^{3+} doped sample are given in Figure 4. As seen in the tabulated EDS results in Figure 4, the atomic% compositions of the elements are in agreement with the theoretical atomic amounts%.
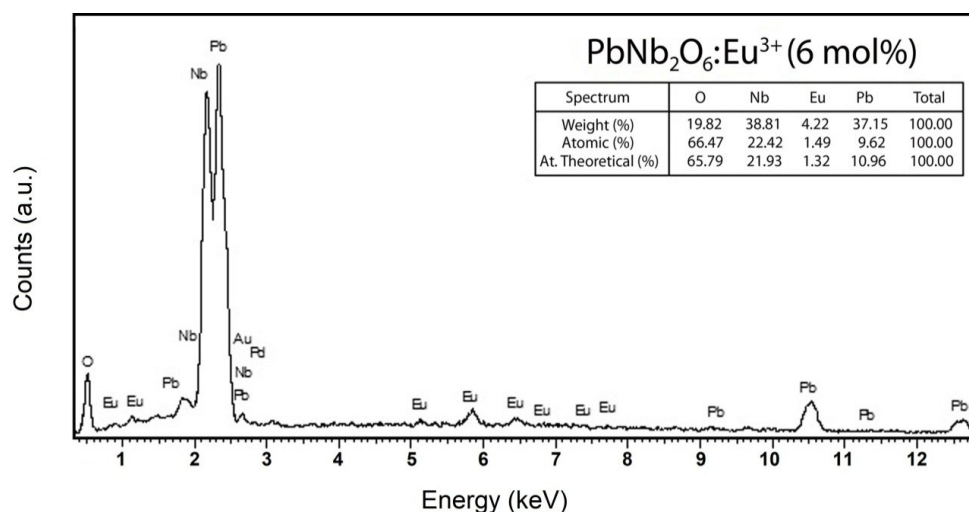
Figure 4: EDS spectrum and elemental analysis results (wt.%, at.%) and theoretical atomic percentages for 6 mol% Eu^{3+} doped sample.

Cathodoluminescence Analysis

Figure 5(a-e) shows the CL spectra of undoped PbNb$_2$O$_6$ (rhombohedral) and 0.5, 1, 3 and 6 mol% Eu^{3+} doped phosphors (orthorhombic) sintered at 1250 °C. In Fig. 4a, the CL spectrum of the undoped sample has a CL emission of around 640 nm. The observed CL emission of undoped PbNb$_2$O$_6$ is probably associated with the defect emission, which can be attributed to the recombination of electrons in the non-bridging oxygen band-gap state with holes in the valence band (43). Generally, considering lead niobate as a host structure, a weakness in CL emissions was observed. This is probably related to the presence of lead in the compound. Lead has the ability to stop gamma and X-ray radiation due to lead's high atomic number and stable isotopes (44).

A weak CL emission observed around 420 nm may probably be related to the rhombohedral host, and a peak around 440 nm observed in Eu^{3+} doped samples is associated with the orthorhombic polymorph. The illustration of rhombohedral PbNb$_2$O$_6$ structure is shown in Figure 6, where the rhombohedral has an edge-sharing crystal arrangement (28) while the orthorhombic (in Figure 2) has a corner-sharing structure. The edge-shared octahedral structure

is associated with a higher band gap compared to the corner-shared octahedral structure (45), which can be ascribed to a lower wavelength shift of rhombohedral or a larger wavelength shift of octahedral. Therefore, a change in wavelength is likely to occur with the rhombohedral-orthorhombic phase transformation, where the peak of the edge-shared rhombohedral host at about 420 nm, shifted to the peak of the corner-shared orthorhombic host at about 440 nm. The shift between the two polymorphs was also studied by absorption analysis, which is given in Figure 7. PL host absorption for rhombohedral PbNb$_2$O$_6$ has been previously reported around 385 nm (17), but it was not clearly observed in the same spectral range. The absorption peaks of the Eu^{3+} doped PbNb$_2$O$_6$ and undoped PbNb$_2$O$_6$ samples are around 370-375 nm. As seen in the spectral profiles, the absorption of the Eu^{3+} doped samples decreases with the increasing doping concentration. On the other hand, when compared to undoped and Eu^{3+} doped samples, it is seen that the undoped sample slightly shifts towards higher energy. Accordingly, based on the absorbance results where a slightly higher energy shift occurred, this supports the shift of rhombohedral host emission.
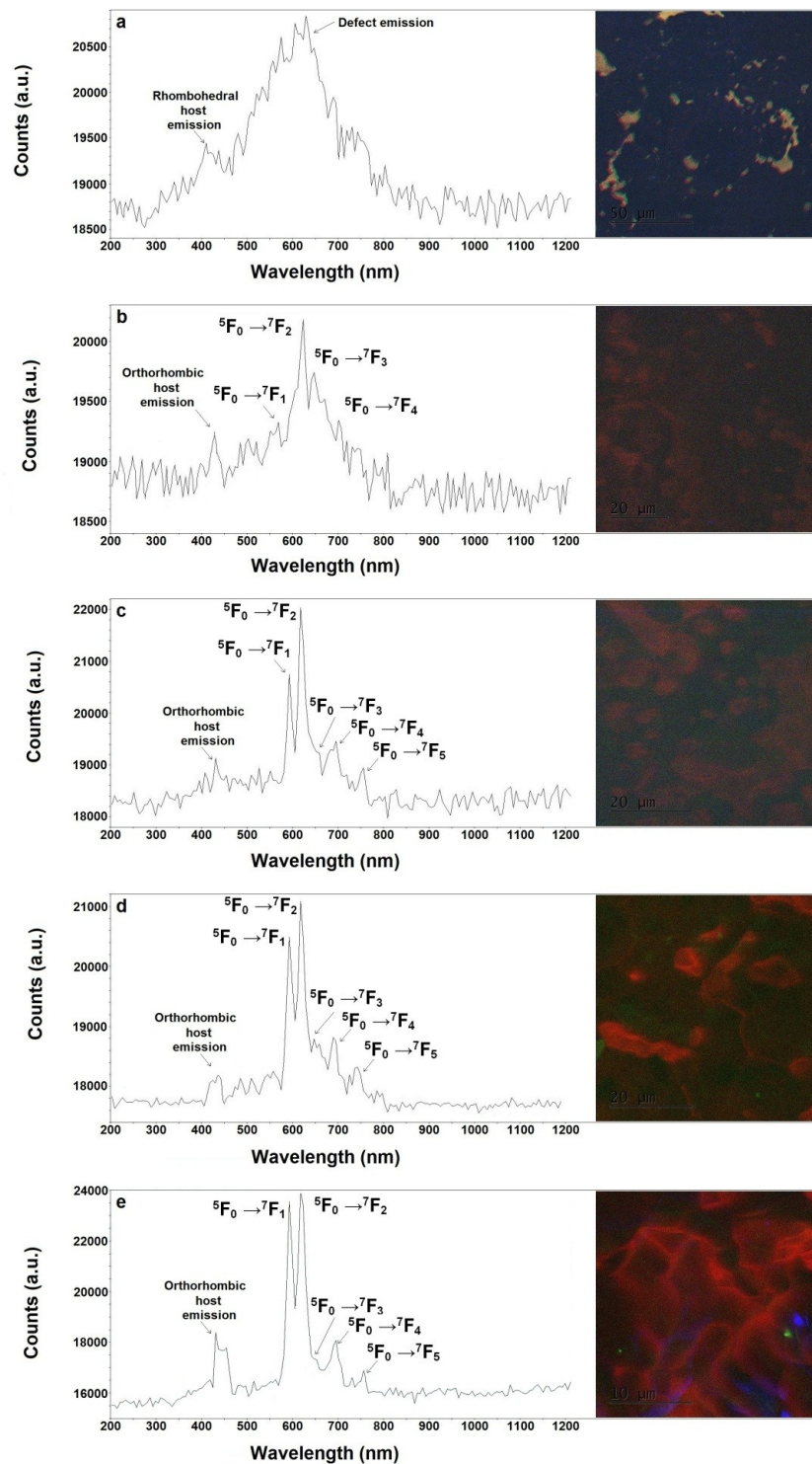
Figure 5: CL emission spectra and CL micrographs (inset figures) for (a) undoped PbNb$_2$O$_6$, and (b) 0.5, (c) 1, (d) 3, (e) 6 mol Eu^{3+} doped PbNb$_2$O$_6$ phosphors.
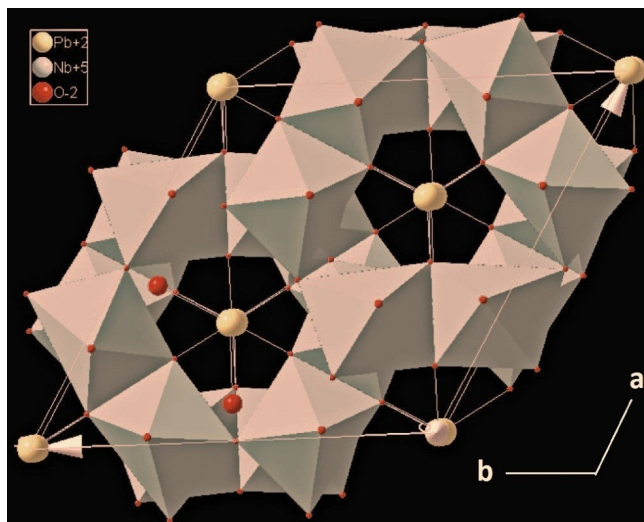
Figure 6: Illustration of rhombohedral (hexagonal) $PbNb_2O_6$ structure.

The CL emissions of Eu^{3+} doped phosphors were monitored for the CL peaks of 592, 618, 650, 695 and 755 nm corresponding to $^5F_0\rightarrow{}^7F_1$, $^5F_0\rightarrow{}^7F_2$, $^5F_0\rightarrow{}^7F_3$, $^5F_0\rightarrow{}^7F_4$, and $^5F_0\rightarrow{}^7F_5$ transitions, respectively. Increasing the Eu^{3+} concentration increased the $^5F_0\rightarrow{}^7F_J$ (J = 0, 1, 2, 3, 4, 5) transition intensities, while the highest CL intensity was reached at 6 mol% concentration. CL micrographs of undoped $PbNb_2O_6$ and Eu^{3+} doped phosphors are shown in the inset figures of Figure 4(a-e). As seen as in CL spectra, the asymmetry ratio ($^5F_0\rightarrow{}^7F_2/^5F_0\rightarrow{}^7F_1$) decreased or the symmetry of phosphor increased with increasing Eu^{3+} concentration. Among Eu^{3+} ion transitions, it is well known that the $^5D_0\rightarrow{}^7F_1$ magnetic dipole transition hardly changes with the crystal field around the Eu^{3+} ions whereas $^5D_0\rightarrow{}^7F_2$ electric dipole transition is very sensitive to the crystal field changes (42). In radioluminescence (RL) mechanism, the excitation of holes and electrons by high-energy X-rays may create asymmetry differences with the UV-Vis excitation mechanism of PL, where X-ray excitation with a volumetric character can change the asymmetric ratio due to its deeper penetration (46-48). On the basis of the similarity of the CL mechanism to the RL mechanism due to the high-energy electron beam, it is possible that electron beam irradiation changed the dipole moments in the Eu^{3+} doped host and caused the emission spectrum change. Therefore, when $PbNb_2O_6$:Eu^{3+} phosphor was exposed to irradiation with high-energy electrons of CL, the symmetry of the Eu^{3+} local environment probably increased (46-48).
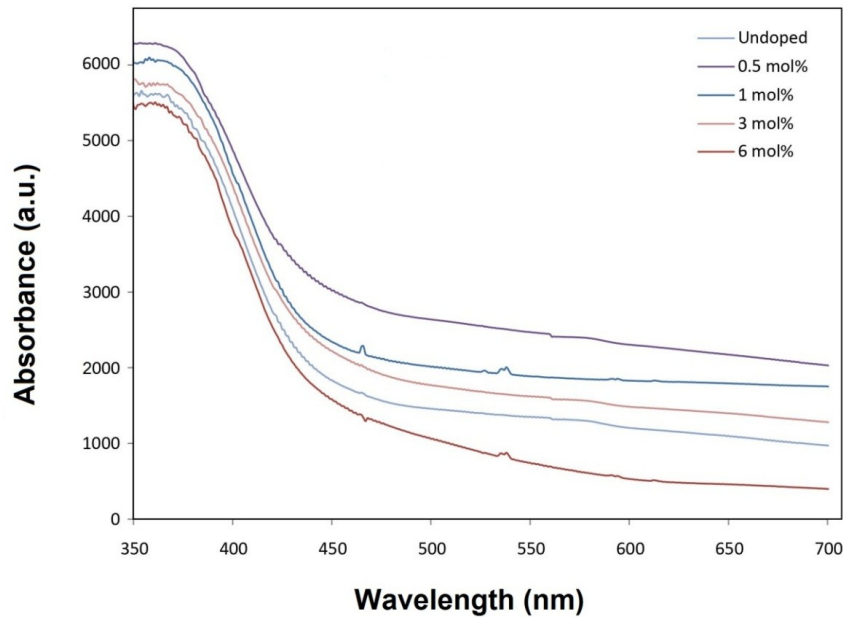
Figure 7: Absorption spectrums of undoped $PbNb_2O_6$ (rhombohedral) and Eu^{3+} doped $PbNb_2O_6$ (orthorhombic) samples.

In inset photographs of Figure 5(a-e), the CL micrograph of the undoped sample has different regions such as blue-yellow-green-red due to the broad peak between 400-800 nm, while the Eu^{3+} doped samples have red regions due to Eu^{3+} emissions. The UV lamp photographs of $PbNb_2O_6$ and $PbNb_2O_6$:Eu^{3+} phosphors under 254 nm are shown in Figure 8. The UV lamp photograph of the undoped sample has blue-violet emission that supports the peak around 420 nm. The Eu^{3+} doped samples with red color became brighter with increasing Eu^{3+} concentration, and 6 mol% doped sample has the brightest appearance, as seen in CL results, which show the highest emission intensity.
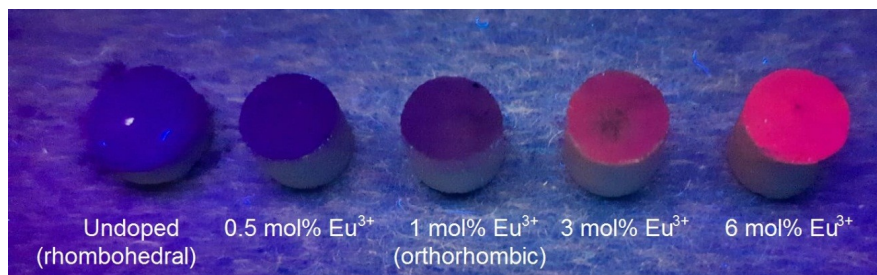
Figure 8: UV lamp photograph of undoped and Eu^{3+} doped $PbNb_2O_6$ ceramics phosphors with excitation of 254 nm or short wavelength.

CONCLUSION

By solid state reaction, Eu^{3+} doped orthorhombic $PbNb_2O_6$ phosphors with tugsten bronze symmetry were fabricated. According to X-ray diffraction results, undoped $PbNb_2O_6$ has a rhombohedral symmetry, while the Eu^{3+} presence between 0.5 and 6 mol% led to the orthorhombic phase transformation. SEM analysis revealed that the grains of the undoped sample have an amorphous shape and a smooth surface such that the boundary of grains is hardly seen. The grain shapes of Eu^{3+} doped samples for 3 and 6 mol% samples showed an oval and wavy morphology. CL emission of the undoped sample has a peak at around 640 nm, which is related to defect emission. The CL emission of rhombohedral $PbNb_2O_6$ host was not clearly observed in the CL spectral profiles. This can be associated with

the presence of lead in $PbNb_2O_6$, which has the ability to stop gamma and X-ray radiation. The rhombohedral-orthorhombic phase transformation led to a shift in the rhombohedral and orthorhombic CL host peaks, in which the edge-shared rhombohedral host and the corner-shared orthorhombic host have CL peaks at wavelengths of about 420 and 440 nm, respectively. The Eu^{3+} doped $PbNb_2O_6$ and undoped $PbNb_2O_6$ samples exhibited absorption peaks of around 370-375 nm, where the slightly higher energy of the undoped sample supports a high energy shift of the rhombohedral host emission. The CL emissions of $PbNb_2O_6$:Eu^{3+} phosphors exhibited the $^5F_0 \rightarrow ^7F_J$ (J = 0, 1, 2, 3, 4, 5) characteristic transitions of Eu, and the highest CL intensity was observed at 6 mol% concentration. The decrease in the asymmetry ratio or the increase in magnetic dipole transition with the increase in doping concentration showed that the electron beam radiation of CL changes the dipole moments of the Eu^{3+} doped tungsten bronze host and causes a difference in the emission spectrum. UV lamp photograph of undoped $PbNb_2O_6$ exhibited blue-violet emission that supports the peak around 420 nm, while Eu^{3+} doped samples exhibited red color that became more evident with increasing Eu^{3+} concentration.

CONFLICT OF INTEREST

There is no conflict of interest.

REFERENCES

1. Ekmekçi MK, İlhan M, Güleryüz LF, Mergen A. Study on molten salt synthesis, microstructural determination and white light emitting properties of CoNb2O6:Dy3+ phosphor. Optik [Internet]. 2017 Jan [cited 2022 Oct 9];128:26–33. Available from: <URL>.

2. İlhan M, Ekmekçi MK, Keskin İÇ. Judd–Ofelt parameters and X-ray irradiation results of MNb 2 O 6 :Eu 3+ (M = Sr, Cd, Ni) phosphors synthesized via a molten salt method. RSC Adv [Internet]. 2021 [cited 2022 Oct 9];11(18):10451–62. Available from: <URL>.

3. Ekmekçi MK, İlhan M, Başak AS, Deniz S. Structural and Luminescence Properties of Sm3+ Doped TTB -Type BaTa2O6 Ceramic Phosphors. J Fluoresc [Internet]. 2015 Nov [cited 2022 Oct 9];25(6):1757–62. Available from: <URL>.

4. İlhan M, Ekmekçi MK, Oraltay RG, Başak AS. Structural and Near-Infrared Properties of Nd3+ Activated Lu3NbO7 Phosphor. J Fluoresc [Internet].

5. İlhan M, Ekmekçi MK, Mergen A, Yaman C. Photoluminescence characterization and heat treatment effect on luminescence behavior of BaTa 2 O 6 :Dy 3+ phosphor. Int J Appl Ceram Technol [Internet]. 2017 Nov [cited 2022 Oct 9];14(6):1134–43. Available from: <URL>.

6. Ekmekçi MK, Erdem M, Başak AS, İlhan M, Mergen A. Molten salt synthesis and optical properties of Eu3+, Dy3+or Nd3+ doped NiNb2O6 columbite-type phosphors. Ceramics International [Internet]. 2015 Sep [cited 2022 Oct 9];41(8):9680–5. Available from: <URL>.

7. Ekmekçi MK, Erdem M, Başak AS. Molten salt synthesis, visible and near-IR region spectral properties of europium or neodymium doped CoNb 2 O 6 columbite niobate. Dalton Trans [Internet]. 2015 [cited 2022 Oct 9];44(12):5379–85. Available from: <URL>.

8. İlhan M. Synthesis, Structural Properties and Visible–Near Infrared Photoluminescence of Trivalent Erbium (Er3+) Doped BaTa2O6 Phosphor. AKU-J Sci Eng [Internet]. 2017 Aug 1 [cited 2022 Oct 9];17(2):675–82. Available from: <URL>.

9. Ekmekçi MK, İlhan M, Ege A, Ayvacıklı M. Microstructural and Radioluminescence Characteristics of Nd3+ Doped Columbite-Type SrNb2O6 Phosphor. J Fluoresc [Internet]. 2017 May [cited 2022 Oct 9];27(3):973–9. Available from: <URL>.

10. Binnemans K. Interpretation of europium(III) spectra. Coordination Chemistry Reviews [Internet]. 2015 Jul [cited 2022 Oct 9];295:1–45. Available from: <URL>.

11. Mitsui T, Yamamoto N, Tadokoro T, Ohta S. Cathodoluminescence image of defects and luminescence centers in ZnS/GaAs(100). Journal of Applied Physics [Internet]. 1996 Dec 15 [cited 2022 Oct 9];80(12):6972–9. Available from: <URL>.

12. Yacobi BG, Holt DB. Cathodoluminescence scanning electron microscopy of semiconductors. Journal of Applied Physics [Internet]. 1986 Feb 15 [cited 2022 Oct 9];59(4):R1–24. Available from: <URL>.

13. İlhan M, Güleryüz LF. Cathodoluminescence and photoluminescence of BaTa2O6:Sm3+ phosphor depending on the sintering temperature. Chem Pap [Internet]. 2022 Jul 31 [cited 2022 Oct 9]; Available from: <URL>.

14. Edwards PR, Martin RW. Cathodoluminescence nano-characterization of semiconductors. Semicond Sci Technol [Internet]. 2011 Jun 1 [cited 2022 Oct 9];26(6):064005. Available from: <URL>.

15. Dierre B, Yuan X, Sekiguchi T. Low-energy cathodoluminescence microscopy for the characterization of nanostructures. Science and Technology of Advanced Materials [Internet]. 2010 Feb [cited 2022 Oct 9];11(4):043001. Available from: <URL>.

16. Ma DDD, Lee ST, Mueller P, Alvarado SF. Scanning Tunneling Microscope Excited Cathodoluminescence from ZnS Nanowires. Nano Lett [Internet]. 2006 May 1 [cited 2022 Oct 9];6(5):926–9. Available from: <URL>.

17. İlhan M, Ekmekçi MK, Demir A, Demirer H. Synthesis and Optical Properties of Novel Red-Emitting PbNb2O6: Eu3+ Phosphors. J Fluoresc [Internet]. 2016 Sep [cited 2022 Oct 9];26(5):1637–43. Available from: <URL>.

18. İlhan M, Keskin İÇ. Evaluation of structural behaviour, radioluminescence, Judd-Ofelt analysis and thermoluminescence kinetic parameters of Eu3+ doped TTB–type lead metaniobate phosphor. Physica B: Condensed Matter [Internet]. 2020 May [cited 2022 Oct 9];585:412106. Available from: <URL>.

19. Başak AS, Ekmekçi MK, Erdem M, Ilhan M, Mergen A. Investigation of Boron-doping Effect on Photoluminescence Properties of CdNb2O6: Eu3+ Phosphors. J Fluoresc [Internet]. 2016 Mar [cited 2022 Oct 9];26(2):719–24. Available from: <URL>.

20. Francombe MH. Polymorphism in lead metaniobate. Acta Cryst [Internet]. 1956 Aug 1 [cited 2022 Oct 9];9(8):683–4. Available from: <URL>.

21. Roth RS, Waring JL. Phase equilibrium relations in the binary system barium oxide-niobium pentoxide. J RES NATL BUR STAN SECT A [Internet]. 1961 Jul [cited 2022 Oct 9];65A(4):337. Available from: <URL>.

22. Xiao Q, Zhou Q, Zhang J, Ouyang L. Photocatalytic decolorization of methylene blue over monoclinic pyrochlore-type Pb2Nb2O7 under visible light irradiation. Journal of Alloys and Compounds [Internet]. 2009 Jan [cited 2022 Oct 9];468(1–2):L9–12. Available from: <URL>.

23. Sahini MG, Grande T, Fraygola B, Biancoli A, Damjanovic D, Setter N. Solid Solutions of Lead Metaniobate-Stabilization of the Ferroelectric Polymorph and the Effect on the Lattice Parameters, Dielectric, Ferroelectric, and Piezoelectric Properties. Viehland D, editor. J Am Ceram Soc [Internet]. 2014 Jan [cited 2022 Oct 9];97(1):220–7. Available from: <URL>.

24. Francombe MH, Lewis B. Structural, dielectric and optical properties of ferroelectric lead metaniobate. Acta Cryst [Internet]. 1958 Oct 1 [cited 2022 Oct 9];11(10):696–703. Available from: <URL>.

25. Subbarao EC, Shirane G, Jona F. X-ray dielectric, and optical study of ferroelectric lead metatantalate and related compounds. Acta Cryst [Internet]. 1960 Mar 1 [cited 2022 Oct 9];13(3):226–31. Available from: <URL>.

26. Goodman G. Ferroelectric Properties of Lead Metaniobate. J American Ceramic Society [Internet]. 1953 Nov [cited 2022 Oct 9];36(11):368–72. Available from: <URL>.

27. Subbarao EC. X-Ray Study of Phase Transitions in Ferroelectric PbNb2O6 and Related Materials. J American Ceramic Society [Internet]. 1960 Sep [cited 2022 Oct 9];43(9):439–42. Available from: <URL>.

28. Chakraborty KR, Sahu KR, De A, De U. Structural Characterization of Orthorhombic and Rhombohedral Lead Meta-Niobate Samples. Integrated Ferroelectrics [Internet]. 2010 Nov 12 [cited 2022 Oct 9];120(1):102–13. Available from: <URL>.

29. Haertling GH. Ferroelectric Ceramics: History and Technology. Journal of the American Ceramic Society [Internet]. 1999 Apr [cited 2022 Oct 9];82(4):797–818. Available from: <URL>.

30. Sahu KR, De U. Thermal characterization of piezoelectric and non-piezoelectric Lead Meta-Niobate. Thermochimica Acta [Internet]. 2009 Jun [cited 2022 Oct 9];490(1–2):75–7. Available from: <URL>.

31. Sahu KR, De U. Impedance Spectroscopy of Piezoelectric 0.963PbNb2O6 – 0.037Ca0.6TiO3. Materials Today: Proceedings [Internet]. 2019 [cited 2022 Oct 9];11:859–68. Available from: <URL>.

32. Fang R, Zhou Z, Liang R, Dong X. Effects of CuO addition on the sinterability and electric properties in PbNb2O6-based ceramics. Ceramics International [Internet]. 2020 Oct [cited 2022 Oct 9];46(15):23505–9. Available from: <URL>.

33. Yu H, Liu Y, Deng C, Xia M, Zhang X, Zhang L, et al. Lithium storage behaviors of PbNb2O6 in rechargeable batteries. Ceramics International [Internet]. 2021 Oct [cited 2022 Oct 9];47(19):26732–7. Available from: <URL>.

34 Yoel A, Michael PEP, Kokate MV, Tabhane VA. Effect of gamma rays irradiation on ferroelectric phase transition and domain defect interaction in lead meta niobate single crystal. Physica B: Condensed Matter [Internet]. 2012 Feb [cited 2022 Oct 9];407(4):576–80. Available from: <URL>.

35. Raghavendra V, Viswarupachary P, Suryanarayana B, Chandra Mouli K, Vikram GNVR, Murali N. Dielectric and piezoelectric properties of Sm3+ doped lead barium niobate (PBN) ceramics. Physica B: Condensed Matter [Internet]. 2019 Mar [cited 2022 Oct 9];556:75–81. Available from: <URL>.

36. Aslam S, Rafique HM, Ramay SM, Akhtar N, Mustafa GM, Siddig AA, et al. Tuning the dielectric properties of PbNb2O6 perovskite through calcium substitution. Physica B: Condensed Matter [Internet]. 2022 Jun [cited 2022 Oct 9];635:413840. Available from: <URL>.

37. Li YM, Cheng L, Gu XY, Zhang YP, Liao RH. Piezoelectric and dielectric properties of PbNb2O6-based piezoelectric ceramics with high Curie temperature. Journal of Materials Processing Technology [Internet]. 2008 Feb [cited 2022 Oct 9];197(1–3):170–3. Available from: <URL>.

38. Guerrero F, Leyet Y, Venet M, de Los S. Guerra J, Eiras JA. Dielectric behavior of the PbNb2O6 ferroelectric ceramic in the frequency range of 20Hz to 2GHz. Journal of the European Ceramic Society [Internet]. 2007 Jan [cited 2022 Oct 9];27(13–15):4041–4. Available from: <URL>.

39. Neurgaonkar RR, Cory WK. Progress in photorefractive tungsten bronze crystals. J Opt Soc Am B [Internet]. 1986 Feb 1 [cited 2022 Oct 9];3(2):274. Available from: <URL>.

40. Xu Y. Ferroelectric tungsten-bronze-type niobate crystals. In: Ferroelectric materials and their applications [Internet]. Amsterdam ; New York : New York, NY, USA: North-Holland ; Sole distributors for the USA and Canada, Elsevier Science Pub. Co; 1991. p. 247–9. Available from: <URL>.

41. İlhan M, Keskin İÇ, Gültekin S. Assessing of Photoluminescence and Thermoluminescence Properties of Dy3+ Doped White Light Emitter TTB-Lead Metatantalate Phosphor. Journal of Elec Materi [Internet]. 2020 Apr [cited 2022 Oct 9];49(4):2436–49. Available from: <URL>.

42. İlhan M, Ekmekçi MK, Mergen A, Yaman C. Synthesis and Optical Characterization of Red-Emitting BaTa2O6:Eu3+ Phosphors. J Fluoresc

[Internet]. 2016 Sep [cited 2022 Oct 9];26(5):1671–8. Available from: <URL>..

43. Coenen T, Haegel NM. Cathodoluminescence for the 21st century: Learning more from light. Applied Physics Reviews [Internet]. 2017 Sep [cited 2022 Oct 9];4(3):031103. Available from: <URL>.

44. Li Z, Zhou W, Zhang X, Gao Y, Guo S. High-efficiency, flexibility and lead-free X-ray shielding multilayered polymer composites: layered structure design and shielding mechanism. Sci Rep [Internet]. 2021 Dec [cited 2022 Oct 9];11(1):4384. Available from: <URL>.

45. Kamminga ME, de Wijs GA, Havenith RWA, Blake GR, Palstra TTM. The Role of Connectivity on Electronic Properties of Lead Iodide Perovskite-Derived Compounds. Inorg Chem [Internet]. 2017 Jul 17 [cited 2022 Oct 9];56(14):8408–14. Available from: <URL>.

46. İlhan M, Katı Mİ, Keskin İÇ, Güleryüz LF. Evaluation of structural and spectroscopic results of tetragonal tungsten bronze MTa2O6:Eu3+ (M = Sr, Ba, Pb) phosphors and comparison on the basis of Judd-Ofelt parameters. Journal of Alloys and Compounds [Internet]. 2022 Apr [cited 2022 Oct 9];901:163626. Available from: <URL>.

47. İlhan M, Keskin İÇ, Güleryüz LF, Katı Mİ. A comparison of spectroscopic properties of Dy3+-doped tetragonal tungsten bronze MTa2O6 (M = Sr, Ba, Pb) phosphors based on Judd–Ofelt parameters. J Mater Sci: Mater Electron [Internet]. 2022 Jul [cited 2022 Oct 9];33(20):16606–20. Available from: <URL>.

48. İlhan M, Keskin İÇ. Analysis of Judd–Ofelt parameters and radioluminescence results of SrNb 2 O 6 :Dy 3+ phosphors synthesized via molten salt method. Phys Chem Chem Phys [Internet]. 2020 [cited 2022 Oct 9];22(35):19769–78. Available from: <URL>.

RESEARCH ARTICLE

Synthesis, Characterization and Cytotoxicity Activity Study of Some Chalcones Derived from 2-(1,1-dimethyl-1,3-dihydro-2H-benzo[e]indol-2-ylidene)malonaldehyde

Dhuha S. Mohammad¹* (iD) **, Wassan B. Ali¹** (iD)

¹University of Diyala, Department of Chemistry, Diyala Governorate, Iraq

Abstract: In this work, series of new chalcones derived from indole compounds were synthesized. In the first the compound 2-(1,1-dimethyl-1,3-dihydro-2H-benzo[e]indol-2-ylidene)malonaldehyde was synthesized from the reaction of 1,1,2-trimethyl-1H-benzo[e]indole with Phosphoryl chloride in in the presence of (DMF). Schiff base (C₂) was prepared by reaction of 2-(1,1-dimethyl-1,3-dihydro-2H-benzo[e]indol-2-ylidene) malonaldehyde with 3-amino acetophenone and then the compounds (C₃-C₆) were synthesized by reacting compound (C₂) with a different aryl aldehyde in the presence of potassium hydroxide. The chemical composition of the compounds was confirmed and characterized by spectroscopic techniques (FT-IR, ¹H-NMR and¹³C-NMR). Target compounds with different concentrations were investigated for their cytotoxic activity against the human breast cancer cell line MCF7. The results showed that the compounds had promising cytotoxic activity against MCF7 cell line especially compound (2) which showed the highest inhibition at the rate of 100 µg/mL among the tested compounds at varied concentrations.

INTRODUCTION

There are many biological active compounds that have been synthesized and reported from different heter°Cyclic compounds. As breast cancer has become dangerous for many people, the need to modify and find new biologically active compounds to overcome this problem has become important and has a wide interest of scientists. Generally, heter°Cycles °Ccupy a prominent place in chemistry due to their wide range of applications in the fields of drug design, phot°Chemistry, agr°Chemicals, dyes and so on. Among them, indole scaffolds have been found in most of the important synthetic drug molecules and paved a faithful way to develop effective targets. Privileged structures bind to multiple receptors with high affinity, thus aiding the development of novel biologically active compounds (1). Recently, indoles are considered interesting heter°Cyclic compounds due to their wide range of biological activities (2). The derivatives of indoles and indazoles exhibits antibacterial, anticancer, antionidants, anti-inflammatory, antidiabetic, antiviral, atniproliferative, antituberculosis, antispermetogenic activity, antipsychotic drugs etc (3). Schiff bases/imines are a substantial class of organic compounds achieved via condensation of carbonyl compounds (aldehydes or ketones) and primary amines to generate an azomethine (−C=N−) functionality (4) Compounds of this class have shown significant applications in the field of

analytical, coordination, and pharmaceutical chemistry (5) . It has several applications, including Nafia R. A. et. al.(2019). Synthesis and characterization of new indole schiff bases and study effect of the compounds on lymphatic cell in metaphase in human blood (6). Chalcones are known as α, β-unsaturated ketones, characterized by having the presence of two aromatic rings that are joined by a three-carbon chain, they are a class of compounds considered an exceptional model due to chemical simplicity and a wide variety of biological activities (7). Chalcones are a group of polyphenolic compounds derived from plants which belong to the flavonoids family and owna wide variety of modulatory and cytoprotective functions. They have been linked with anti-bacterial, anti-fungal, antiinflammatory, anti-oxidant, anti-cancer and anti-diabetic activities (8). a family of small molecules that are naturally abundant in edible plants, have been found to have antitumor properties for specific cancer cell lines and to interfere in each step of carcinogenesis, including apoptosis (9). Özdemir, Ahmet, et al. new indole-based chalcone derivatives were obtained via the reaction of 5-substituted-1H-indole-3-carboxaldehydes/1-methylindole-3-carboxaldehyde with appropriate acetophenones. The synthesized compounds were investigated for their in vitro inhibitory activity. According to in vivo studies, these compounds displayed antiinflammatory and antioxidant activities (10). In the present work, As a result of the importance of the compound indole, schiff and chalcone, and in order to continue to find a new modification to the compound (1,1,2-trimethyl-1H-benzo[e]indole). We therefore synthesized them as well as measure the biological effectiveness of these compounds to know their importance, also to allow the possibility of using them in other uses.

MATERIALS AND METHODS

Chemical Part
All chemicals and solvents used during synthesis compounds were obtained from a numeral of different companies such as Merck, BDH, Fluka and Sigma Aldrich.

Melting points were determined by utilizing the device Melting point SMP10. Diyala University, College of Science. FT-IR spectra was recorded using PERKIN ELMER SPECTRUM-65, JASCO, Infrared spectrometer, within the range (4000-400) using KBr Disc, Diyala University, College of Science.

The ^{1}H-NMR and ^{13}C-NMR spectra was recorded by Varian 400 MHz spectrometer with TMS as internal standard and deuterated DMSO was used as a solvent, measurements were made at Central

Lab., School of Chemistry, College of Science, University of Tehran, Iran.

Synthesis of Malonaldehyde 2-(1,1-dimethyl-1,3-dihydro-2Hbenzo[e]indol-2-ylidene) (C₁).
N,N-dimethyl formamide (DMF) (3 mL) was cooled in an ice bath then added drop wise of (1.3 mL) Phosphoryl chloride (POCl₃) with stirring under 5°C, then a solution of (1 g, 0.0047 mole) 1,1,2-trimethyl-1H-benzo[e]indole in DMF (3 mL) was cooled under 5 °C and added dropwise, the reaction mixture was stirred in ice path for 1h. then reflux for 3h. at 88 °C. The resulting solution was added to icy distilled water and neutralized with 25% NaOH aqueous, the yellow precipitate was formed filtered off and dried in oven. Recrystallized from ethanol to afford pure yellow precipitate. Yield: (1.243 g, 98%). m.p. 202-203 ºC.(11,12)

Synthesis of (2E)-3-((3-acetylphenyl)imino)-2-(1,1-dimethyl-1,3-dihydro-2H-benzo[e]indol-2-ylidene)propanal. (C₂)
A solution of 2-(1,1-dimethyl-1,3-dihydro-2H-benzo[e]indol-2-ylidene) malonaldehyde (3 g, 0.011 mole) in (20 mL of ethanol +5 mL of DMF) is mixed with 3-aminoacetophenone (1.48 g, 0.011 mole), to which 5-6 drops of glacial acetic acid was added, and the reaction mixture was refluxed for 12 hours. The completion of the reaction was checked by using TLC (3:1) hexane: ethyl acetate with pre-coated silica gel, which gave one spot. After cooling at room temperature the product was filtered and recrystallized from a suitable solvent. Yield: (2.8g, 64 %), M.P.(220 °C).

FT-IR data (cm⁻¹): 3458 υ (N-H), 3049 υ (CH aromatic),2932 υ (C-H aliphatic), 1688 υ (CH=O), 1668 υ (C°CH₃) 1621 υ (CH=N), 1579-1486 υ (C=C), 1208 υ (C-N), 759 υ (C-H bending). ^{1}H NMR (400 MHz, DMSO, δ in ppm): δ =14.24 (s,1H,NH) 9.56(s,1H, CHO), 8.81 (s, 1H, CH=N), 7.82-8.17 (m, 10 Ar-H), 2.69 (s, 3H, COCH₃) , 1.89 (s, 6H, 2xCH₃). The ^{13}C-NMR spectra of this compound, exhibits the signals (400 MHz, DMSO-d6, δ in ppm): δ = 198.15(C=O),147.98(C=N),140.86(C-NH), 109.11(C=C),(138.79-123.34) C-Ar, 27.52, 20.95 (2CH₃), 56.02(C(CH₃)₂).

Synthesis of Compounds (C₃-C₆)
Equimolar quantity (0.5g,0.0013 mole) of (2E)-3-((3-acetylphenyl)imino)-2-(1,1-dimethyl-1,3-dihydro-2H-benzo[e]indol-2-ylidene)propanal and appropriate aryl aldehyde (0.0013 mole) mixed and dissolved in 25 mL of ethanol absolute. To this, 40% potassium hydroxide solution (1 mL) added slowly and mixed occasionally for (3 hrs) at room temperature. the resulted mixture was refluxed for (6-8 hrs) at (78 °C). Completion of the reaction was identified by TLC using Silica gel-

G. (3:1) hexane: ethyl acetate, which gave one spot.

FT-IR data in (cm^{-1}) of compound **(C$_3$)**: 3131 υ (NH), 2885 υ (CH aliphatic),1681 υ (CHO),1656 υ (C°CH=CH), 1609 υ (CH=N),1598-1457 υ (C=C),1210 υ (CN), and751 υ (CH bending).^{1}H NMR (400 MHz, DMSO, δ in ppm) of compound **(C$_3$)**: δ =13.46(NH), 9.84 (CHO), 8.65 (CH=N), 7.63(CH=C), 7.51 (CH=CO), 7.66-8.19 (Ar-H, 14H), 3.04 (s,6H,N(CH$_3$)$_2$), 1.99 (s, 6H, 2xCH$_3$).

FT-IR data in (cm^{-1}) of compound **(C$_4$)**: 3134 υ (NH),2928 υ (CH aliphatic),2728 υ (CH aldehyde),1681 υ (CHO),1655 υ (C°CH=CH),1609 υ (CH=N),1598-1456 υ (C=C),1399-1512 υ (NO$_2$), 1210 υ (CN), and 751 υ (CH bending). ^{1}H NMR (400 MHz, DMSO, δ in ppm) of compound **(C$_4$)**: δ =13.46 (s,1H,NH), 9.80 (s,1H,CHO), 8.81 (s,1H, CH=N) ,7.61 (d, 1H, C=CH), 7.52 (d, 1H, COCH), 7.83-8.19 (m , 14H, Ar-H) , 1.99 (s, 6H, 2xCH$_3$).

FT-IR data in (cm^{-1}) of compound **(C$_5$)**:3650 υ(OH),3131υ(NH),2968 υ(CH aliphatic),2740 υ(CH aldehyde),1681 υ(CHO),1655 υ (COCH=CH),1612 υ(CH=N),1598-1400 υ(C=C), 1210 υ(CN),and751 υ(CH bending). ^{1}H NMR (400 MHz, DMSO, δ in ppm) of compound **(C$_5$)**: δ =13.47 (s, 1H , NH) , 9.84 (s, 1H, CHO), 9.52 (S, 1H, OH) , 8.79 (s, 1H, CH=N), 7.63-8.19 (m. 14H, Ar – H) , 7.52 (d, 1H, C=CH) 7.51 (d, 1H, C°CH), , 1.99 (s, 6H, 2xCH$_3$)

FT-IR data in (cm^{-1}) of compound **(C$_6$)**:3136 υ (NH),2978 (Charomatic), 2930 υ (Chaliphatic), 1681 υ (CHO),1656 υ (C-CH=CH),1610 υ (CH=N), 1598-1455 υ (C=C), 1210 υ (CN), and 750 υ (CH bending),714 υ (C-Cl).^{1}H NMR (400 MHz, DMSO, δ in ppm) of compound **(C$_6$)**:δ=13.47 (NH), 9.79 (CH=O), 8.20 (CH=N), 7.93 (CH=C), 7.50 (CH=CO), 7.63-8.17 (Ar-H,14H), 1.93 (s, 6H, 2xCH$_3$). The ^{13}C-NMR spectra of this compound **(C$_6$)**, exhibits the signals (400 MHz, DMSO-d6, δ in ppm):δ=179.79(C=O), 138.05(C=N), 133.98(C-NH), 132.18-122.86(C-Ar), 114.74 (COC=C), 109.16 (C=C), 24.06, 22.25 (2CH$_3$), 52.96 (C(CH$_3$)$_2$).
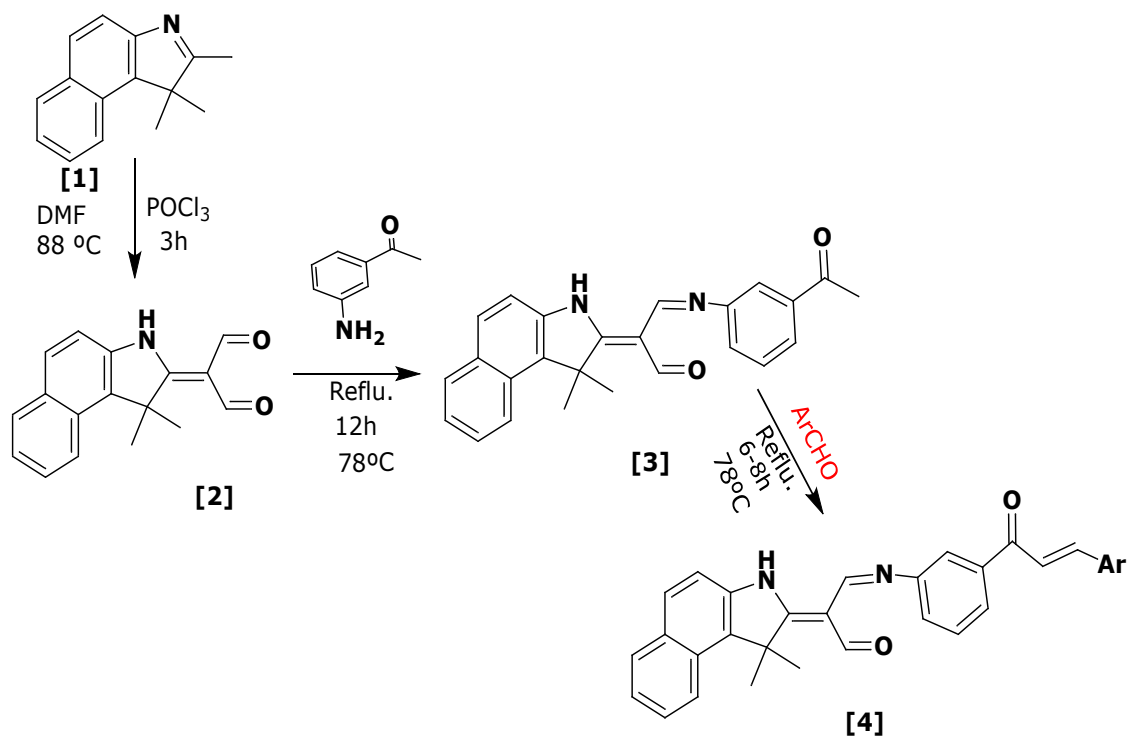
ArCHO=4-(dimethylamino)benzaldehyde, 4-nitrobenzaldehyde, 4-hydroxybenzaldehyde, 4-chlorobenzaldehyde

Scheme 1: Synthesis of (C1-C6).

Biological Part
Determination of solubility of compounds tested for in vitro cytotoxicity. The cytotoxicity assay was carried out using the crystal violate stain according to the method of Freshney (2012) (13). In brief, the organic compounds were dissolved in DMSO and diluted by serum free media (SFM) to prepare different concentrations range of (50,100) µg/mL. Two types of cell lines were used in human breast cancer cell line MCF7, and normal human (MEF) cell lines. The tumor cells (1 x 10^5 cell/mL) were seeded in 96-well microplate and incubated for 24 h at 37 °C, then old media was changed with a new serum-free medium (SFM) containing concentrations of each compound. Plate was incubated for 24 h in humidified incubator at 37 °C containing 5% CO_2. After incubation, the culture medium was discarded and 100 mL of crystal violate was into each well and re-incubated for 20 min at 37 °C. The inhibition percentage was calculated by the following formula (1):

$$\text{Inhibition (\%)} = (A-B/A) \times 100 \qquad \text{(Eq. 1)}$$

Where,
A = Absorbance of the control
B = Absorbance of the sample

RESULTS AND DISCUSSION

New indole containing Schiff bases and chalcones were synthesized and characterized with spectral studies (^{1}H-NMR,^{13}C-NMR, and FT-IR), physical properties such as melting point and yields of the new compounds are mentioned in Table 1.

Table 1: Physical properties of the synthesized compounds.

Comp. No.	Molecular formula	%Yield	Melting Point, °C
1	$C_{17}H_{15}NO_2$	98%	207
2	$C_{25}H_{22}N_2O_2$	64%	220
3	$C_{34}H_{31}N_3O_2$	52%	154
4	$C_{32}H_{25}N_3O_4$	62%	180
5	$C_{32}H_{26}N_2O_3$	59%	203
6	$C_{32}H_{25}ClN_2O_2$	68%	140

Table 2: The newly synthesized compounds.

Comp No.	Comp. Structure	Comp. Name
C$_1$		2-(1,1-dimethyl-1,3-dihydro-2H-benzo[e]indol-2-ylidene)malonaldehyde
C$_2$		3-((3-acetylphenyl)imino)-2-(1,1-dimethyl-1,3-dihydro-2H-benzo[e]indol-2-ylidene)propanal
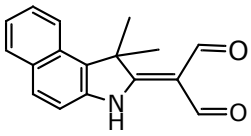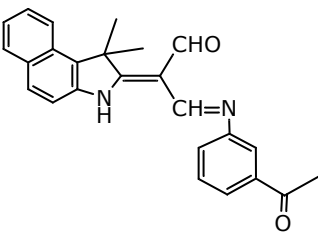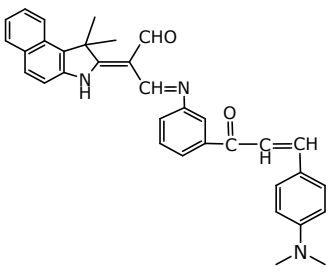
C₃		2-(1,1-dimethyl-1,3-dihydro-2H-benzo[e]indol-2-ylidene)-3-((3-(3-(4-(dimethylamino)phenyl)acryloyl)phenyl)imino)propanal
C₄		2-(1,1-dimethyl-1,3-dihydro-2H-benzo[e]indol-2-ylidene)-3-((3-(3-(4-nitrophenyl)acryloyl)phenyl)imino)propanal
C₅		2-(1,1-dimethyl-1,3-dihydro-2H-benzo[e]indol-2-ylidene)-3-((3-(3-(4-hydroxyphenyl)acryloyl)phenyl)imino)propanal
C₆		3-((3-(3-(4-chlorophenyl)acryloyl)phenyl)imino)-2-(1,1-dimethyl-1,3-dihydro-2H-benzo[e]indol-2-ylidene)propanal
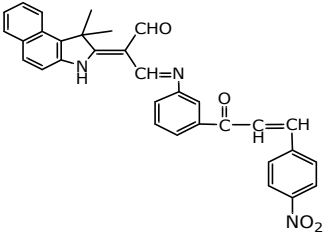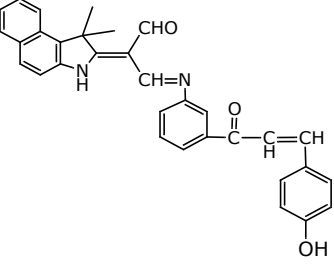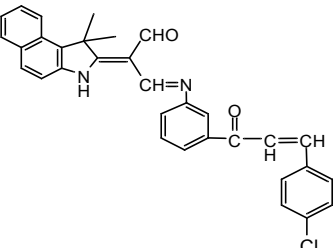
FT-IR study

The FT-IR spectra of the new five synthesized compounds showed the absorption band of the new functional group (imine group CH=N) at 1621, 1609, 1609, 1612, and 1610 cm⁻¹ for the compounds 2, 3, 4, 5, and 6, respectively which approved the chemical structure of the synthesized compounds. A strong absorption band appeared at 1681-1688 cm⁻¹ for all compounds (2, 3, 4, 5, and 6) related to the carbonyl group CH=O of aldehyde. Whereas 1655-1656 cm⁻¹ for stretching of C= O due to the conjugated with double bonds for the mentioned compounds. Also an absorption band at 1598-1400 cm⁻¹ which belonged to C=C group. All of these bands are confirmed the chemical structures of the synthesized compounds (C₂-C₆).

NMR Study

¹H-NMR spectra were reported in DMSO (dimethyl sulfoxide) with chemical shifts in ppm and using TMS (tetramethylsilane) as standard. The ¹H-NMR results for compound (1) shown single signals at 13.14 ppm was belonged to proton of (N̲H̲) of indole ring. A singlet signal at 9.79 ppm was referred to proton of aldehyde (C̲H̲=O) group. Signals were appeared in the region between (7.69-7.38) ppm were assigned to protons of aromatic ring for (2) compound. Finally, a peak at 1.96 ppm belonged to six protons of two methyl groups. The ¹H-NMR results for compound (C₂) Figure 1 showed single signals at 14.24 ppm which belonged to proton of (N̲H̲) of indole ring. A singlet signal at 9.56 ppm referred to the proton of aldehyde (C̲H̲=O) group. A singlet signal at 8.81

ppm was referred to the proton of Schiff base group (CH=N). Signals were appeared in the region between (7.82-8.17) ppm were assigned to protons of aromatic and singlet signal at 2.69 ppm was attributed to (COCH_3). The peak at 1.89 ppm belonged to six protons of two methyl groups. Whereas the ^{1}H-NMR of compound (C$_3$) Figure (3) showed singlets at 13.46 ppm that belonged to the proton of (NH) of indole ring. A singlet signal at 9.84 ppm was referred to proton of the aldehyde (CH=O) group. A singlet signal at 8.65 ppm was referred to proton of Schiff base group (CH=N). Signals was appeared in the 7.63 was attributed to (CH=C) and signals was appeared in the 7.51 was attributed to (CH=CO), Signals were appeared in the region between (7.66-8.19) ppm were assigned to protons of aromatic and singlet signal at 3.04 ppm was attributed to (N(CH_3)$_2$). Finally peak at 1.99 ppm was referred to six protons of two methyl groups. ^{1}H NMR results of other compounds are listed in Table (3).

^{13}C-NMR results were used to characterize this new compound and support the results of 1H- NMR.

Figure (2) results of compound (C$_2$) A signal at 198.15 ppm were assigned to the carbonyl group C=O and, while a signal of CH=N group detected at 147.98 ppm. The signals were appear in the range between 123.34- 138.79 ppm were belonged to the carbon atoms of aromatic rings. In addition, two signals appeared at 109.11 ppm and 56.02 ppm were assigned to C=C and CH3-C-CH3 groups respectively. Finally, signal at(27.52 and 20.95) ppm was belongs to the rest two methyl groups.^{13}C NMR results of other compound (C$_6$) Figure (7) are discussed A signal at 179.79 ppm were assigned to the carbonyl group C=O and, while a signal of CH=N group detected at 138.05 ppm. The signals were appear in the range between 122.86- 133.08 ppm were belonged to he carbon atoms of aromatic rings. In addition, to appearing COC=C at 114.74 .two signals appeared at 109.16 ppm and 52.96 ppm were assigned to C=C and CH3-C-CH3 groups respectively. Finally, signal at (24.06 and 22.25) ppm was belongs to the rest two methyl groups.

Table 3: The chemical shift in ppm to ^{1}H NMR results of compounds.

No	NH	HC=O	CH=N	CH=C	CH=CO	Ar-H	2xCH$_3$	Other
1	13.14	9.79	-	-	-	7.69-7.38	1.68	-
2	14.24	9.56	8.81	-	-	7.82-8.17		2.69 C-CH$_3$
3	13.46	9.84	8.65	7.63	7.51	7.66-8.19	1.99	3.04 N(CH_3)$_2$
4	13.46	9.80	8.81	7.61	7.52	7.83-8.19	1.99	-
5	13.47	9.84	8.79	7.52	7.51	7.63-8.19	1.99	9.52 OH
6	13.47	9.79	8.20	7.93	7.50	7.63-8.17	1.93	-

In vitro cytotoxic activity
The new Prepared compounds (2, 3 ,4 and 5) in vitro to study cytotoxicity Activity against the human breast cancer cell line MCF7 in two different concentrations 50 and 100 mcg/mL with an exposure time of 24 hours and a temperature of 37. Results that we obtained showed compound (C$_2$) Highest cytotoxic activity with inhibition rate 66.40% at a concentration of 100 µg/mL Among the rest of the vehicles installed with Diverse concentrations. In the case of compound (C$_3$), the results were revealed Reliance on them to focus regularly, the inhibition rates were 20.07 and 56.45% for 50 and 100 µg/mL concentrations, respectively. While compound (C$_4$) showed inhibition rate and the inhibition rates were (30.13 and 48.46%) for 50 concentrations and 100 µg/mL, respectively. The compound (C$_5$) gave inhibition rates of 40.17 and 46.33% for concentrations 50 and 100 µg/mL, respectively.

Table 4 : The in vitro cytotoxicity effect of prepared organic compounds on different cell lines at 50 and 100 µg/mL after 24 h incubation at 37 °C.

Derivatives No.	Inhibition ratio 100% Normal Cell Line MEF		Inhibition ratio 100% Cell Line cancer MCF7		Normal cell line(MEF) in 100 µg/m Images	Cell line(MCF7) in 100 µg/m Images
	Con. µg/mL		Con. µg/mL			
	50	100	50	100		
C$_2$	18.40	19.70	50.19	66.40		
C$_3$	9.12	11.78	20.07	56.45		
C$_4$	8.11	13.57	30.13	48.46		
C$_5$	10.12	16.22	40.17	46.33		
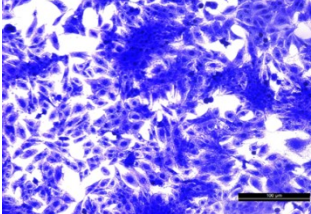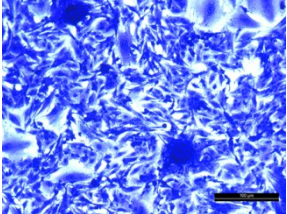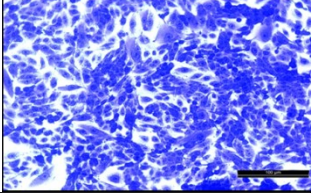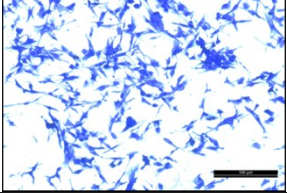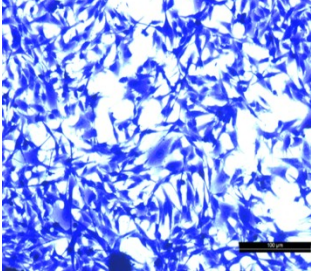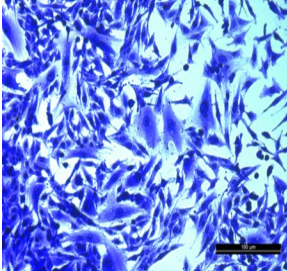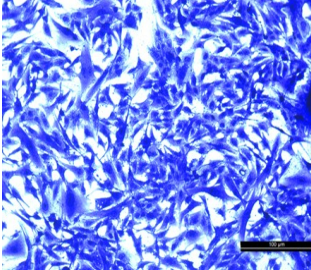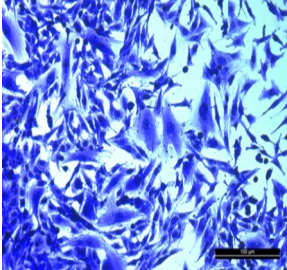
CONCLUSION

In the current work, synthesized new derivatives of Indole compounds categorized (C$_1$–C$_6$). These compounds were characterized utilizing diverse spectroscopic methods like FT-IR, ^{1}H-NMR and ^{13}C-NMR In addition to measurement some of their physical properties. Target compounds were investigated for their cytotoxic activity against the human breast cancer cell line MCF7. The results showed that the compounds had promising cytotoxic activity against MCF7 cell line especially compound (C$_2$) which showed the highest inhibition at the rate of 100 µg/mL among the tested compounds at varied concentrations.

REFERENCES

1. Sravanthi, T. V., & Manju, S. L. (2016). Indoles—A promising scaffold for drug development. *European Journal of Pharmaceutical Sciences*, *91*, 1-10.

2. Sayed, M., Kamal El-Dean, A. M., Ahmed, M., & Hassanien, R. (2018). Synthesis of some heter°Cyclic compounds derived from indole as antimicrobial agents. Synthetic Communications, 48(4), 413-421.

3.　Shafakat Ali, N. A., Ahmad Dar, B., Pradhan, V., & Farooqui, M. (2013). Chemistry and biology of indoles and indazoles: a mini-review. *Mini reviews in medicinal chemistry*, *13*(12), 1792-1800.

4.　Xavier, A., & Srividhya, N. (2014). Synthesis and study of Schiff base ligands. IOSR Journal of Applied Chemistry, 7(11), 06-15.

5.　Abu-Dief, A. M., & Mohamed, I. M. (2015). A review on application of transition metal complexes incorporating Schiff bases. REPLACE THIS REFERENCE, IT DOES NOT CONTAIN THE REQUIRED INFORMATION.

6.　Nafia, R. A., & Faraj, F. L. (2019). Synthesis and characterization of new indole schiff bases and study effect of the compounds on lymphatic cell in metaphase in human blood. Journal of Pharmaceutical Sciences and Research, 11(4), 1319-1326.

7.　Rocha, J. E., de Freitas, T. S., da Cunha Xavier, J., Pereira, R. L. S., Junior, F. N. P., Nogueira, C. E. S., ... & Coutinho, H. D. M. (2021). Antibacterial and antibiotic modifying activity, ADMET study and molecular d°Cking of synthetic chalcone (E)-1-(2-hydroxyphenyl)-3-(2, 4-dimethoxy-3-methylphenyl) prop-2-en-1-one in strains of Staphylococcus aureus carrying NorA and MepA efflux pumps. *Biomedicine & Pharmacotherapy*, *140*, 111768.

8.　Das, P., Srivastav, A. K., & Muthukannan, M. R. (2021). A study on molecular targeted approaches to cancer therapy and the role of chalcones in chemoprevention. *European Journal of Molecular & Clinical Medicine*, *8*(3), 3254-3267.

9.　Kedar, M. S., Shirbhate, M. P., Chauhan, R., Sharma, S., & Verma, A. (2020). Design Synthesis and Evaluation of Anticancer Pyrazole Derivatives of Chalcone Scaffold. *Research Journal of Pharmacy and Technology*, *13*(1), 342-346.

10.　Özdemir, A., Altıntop, M. D., Turan-Zitouni, G., Çiftçi, G. A., Ertorun, İ., Alataş, Ö., & Kaplancıklı, Z. A. (2015). Synthesis and evaluation of new indole-based chalcones as potential antiinflammatory agents. *European journal of medicinal chemistry*, *89*, 304-309.

11.　Khezri, M., Afghan, A., Roohi, L., & Baradarani, M. M. (2016). Vilsmeier-Haack Reaction with 2, 3, 3-Trimethyl-3H-benzo [g] indole and Its Conversion into 2-(1-aryl-1H-pyrazol-4-yl)-3, 3-dimethyl-3H-benzo [g] indoles. Organic Chemistry Research, 2(2), 120-126.

12.　Rothan, H. A., Amini, E., Faraj, F. L., Golpich, M., Teoh, T. C., Gholami, K., & Yusof, R. (2017). NMDA receptor antagonism with novel indolyl, 2-(1, 1-Dimethyl-1, 3-dihydro-benzo [e] indol-2-ylidene)-malonaldehyde, reduces seizures duration in a rat model of epilepsy. Scientific reports, 7(1), 1-10.

13.　Freshney, R. I. (2012) . Culture of animal cell. Sixth edition. Wily liss, New York. 5th edition.

Three-Dimensional Niobium Nanopillar based Electrode for Energy Storage Devices

Nevin Taşaltın [1,2,3*], Elif Tüzün[4], Selcan Karakuş[4*]

[1]Maltepe University, Dept. of Electrical and Electronics Eng., Istanbul, Turkey.
[2]Maltepe University, Dept. of Basic Sciences, Istanbul, Turkey.
[3]Maltepe University, Dept. of Renewable Energy Tech. and Management, Istanbul, Turkey.
[4]Istanbul University-Cerrahpasa, Dept. of Chemistry, Istanbul, Turkey.

Abstract: In this study, aluminum (Al) film with high purity was coated on the Niobium (Nb) sheet by thermal evaporation under ultra-high vacuum. An Anodic Aluminum Oxide (AAO) nanotemplate was prepared on the Nb sheet. During AAO nanotemplate preparation, three-dimensional (3D) Nb nanopillars were grown on the Nb sheet. We performed a simple 3D Artificial Intelligence (AI) analysis of Nb nanopillars. According to the experimental results, the width of the prepared Nb nanopillars is in the range of 100–120 nm, and the length is approximately 150 nm. The Electron Diffraction Spectroscopy (EDS) results confirmed that the nanopillars are Nb. The prepared Nb nanopillars can be a potential candidate for energy storage applications.

INTRODUCTION

Current global economic conditions make it essential that energy resources should not be consumed excessively. Environmental pollution should be prevented for a moment (1–3). Renewable energy resources should be used more frequently in order to meet the increasing energy demand. Energy should be stored effectively and energy storage technologies should be developed rapidly (4–6). Therefore, it is extremely urgent to develop sustainable and efficient materials for energy storage devices, especially for supercapacitors and lithium-ion batteries (7–9). Among the materials used in energy devices, Niobium (Nb)-based materials (10–12) constantly maintain their attractiveness due to their unique crystal structures and high performance. A number of researchers have

reported that the kinetics of anodic oxide film growth on the surface of Nb is commonly clarified with the high-field electrical conductivity measurements due to the hopping transmission between charged imperfections (13,14). This study set out with the aim of assessing the synthesis of the self-assembly Anodic Aluminum Oxide (AAO). In this study, high purity aluminum-Niobium (Al-Nb) was synthesized from the formation of barrier type Al_2O_3 layers on substrate metal using the controlled anodic oxidation method. It was experimentally observed that the metal film coating on the substrate metal during the controlled anodic oxidation process and the substrate metal was directed towards the finger-shaped alumina barrier layers due to the formation of Al_2O_3 layers (15,16). Nb nanostructures were prepared using the AAO

nanotemplate (17–21). The current study found that the shape of the prepared Nb nanostructure depended on the anodizing conditions. In reviewing the literature, a few studies have been reported on the preparation of Al-Nb (22–24). Inspired by the previous studies, in this study, Nb nanopillars were prepared via anodic oxide growing kinetics on the surface of Nb and characterized.

EXPERIMENTAL

The Nb sheet (99.99%) was purchased from American Elements Company (USA). Hydrofluoric acid (HF) (38–40%), oxalic acid (98%), and phosphoric acid (85%) were purchased from Merck Company (Germany). Scanning Electron Microscopy (SEM) and Electron Diffraction Spectroscopy (EDS) results of samples were obtained using a Quanta 250 FEG SEM model.

In this study, Nb sheet was chemically cleaned by immersion washers in a 10 to 90%

hydrofluoric acid (HF)/deionized water solution. After cleaning in HF/deionized water solution, the Al layer (thickness:700 nm) was evaporated on the Nb sheet under the ultra high vacuum (1x10^{-7} Pa) medium and annealed at 200 ^{0}C for 15 min. The controlled anodic oxidation treatment of the solution with a 0.3 M oxalic acid solution at constant 40 V for 15 min; the sample was immersed in a phosphoric acid solution (3 wt. %) at 25 ^{0}C for 15 min. Then, the second anodic oxidation was performed under the same experimental conditions to obtain a novel AAO nanotemplate on Nb sheet. During the formation of the AAO nanotemplate, Nb nanopillars were grown on the surface of the Nb sheet. The AAO nanotemplate/Nb sample was vertically dipped in a 0.1 M NaOH solution for 10 min to dissolve the AAO nanotemplate, and then Nb nanopillars were obtained. The schematic illustration of the preparation of the Nb nanopillars is given in **Figure 1**. SEM and EDS measurements were carried out for the morphological and compositional analysis of Nb nanopillars.
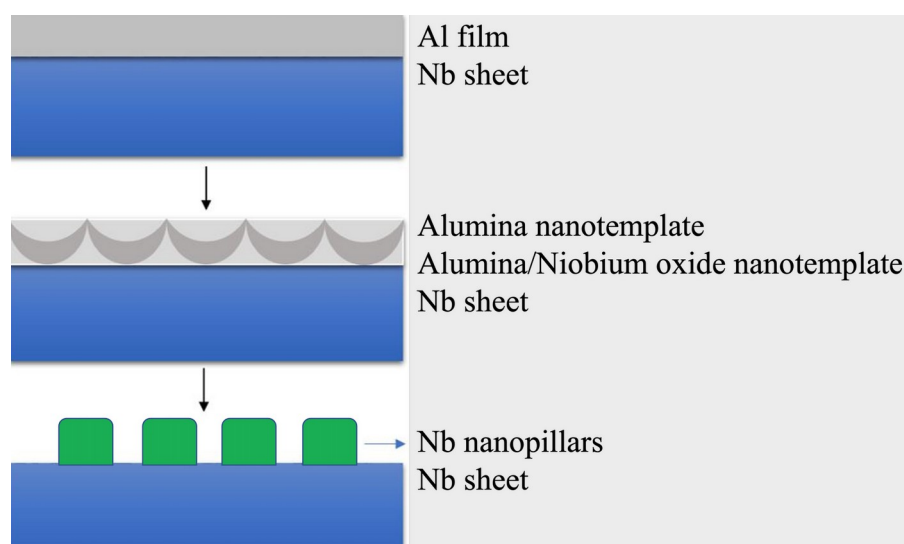
Figure 1: The schematic illustration of the preparation of the Nb nanopillars.

RESULTS AND DISCUSSION

The SEM image and EDS analysis of the obtained Nb nanopillars are shown in **Figure 2**. As clearly seen from the SEM image given in the inset of **Fig.2a-f**, the obtained Nb nanopillars are approximately 100 nm in diameter. Sometimes, material analysis techniques may not be sufficient for the analysis of materials, or the necessary infrastructure for the analysis is not available. In such cases, the Artificial

Intelligence (AI) technique really comes to the rescue. It was not possible to determine the size of the Nb nanopillars prepared in this study by SEM analysis due to the infrastructure. Therefore, we performed a 3D AI analysis of Nb nanopillars. According to the experimental results, the width of the prepared Nb nanopillars is in the range of 100–120 nm, and the length is approximately 150 nm (**Fig. 2f**). The EDS spectrum confirmed that the nanopillars are Nb (**Fig. 2c**).
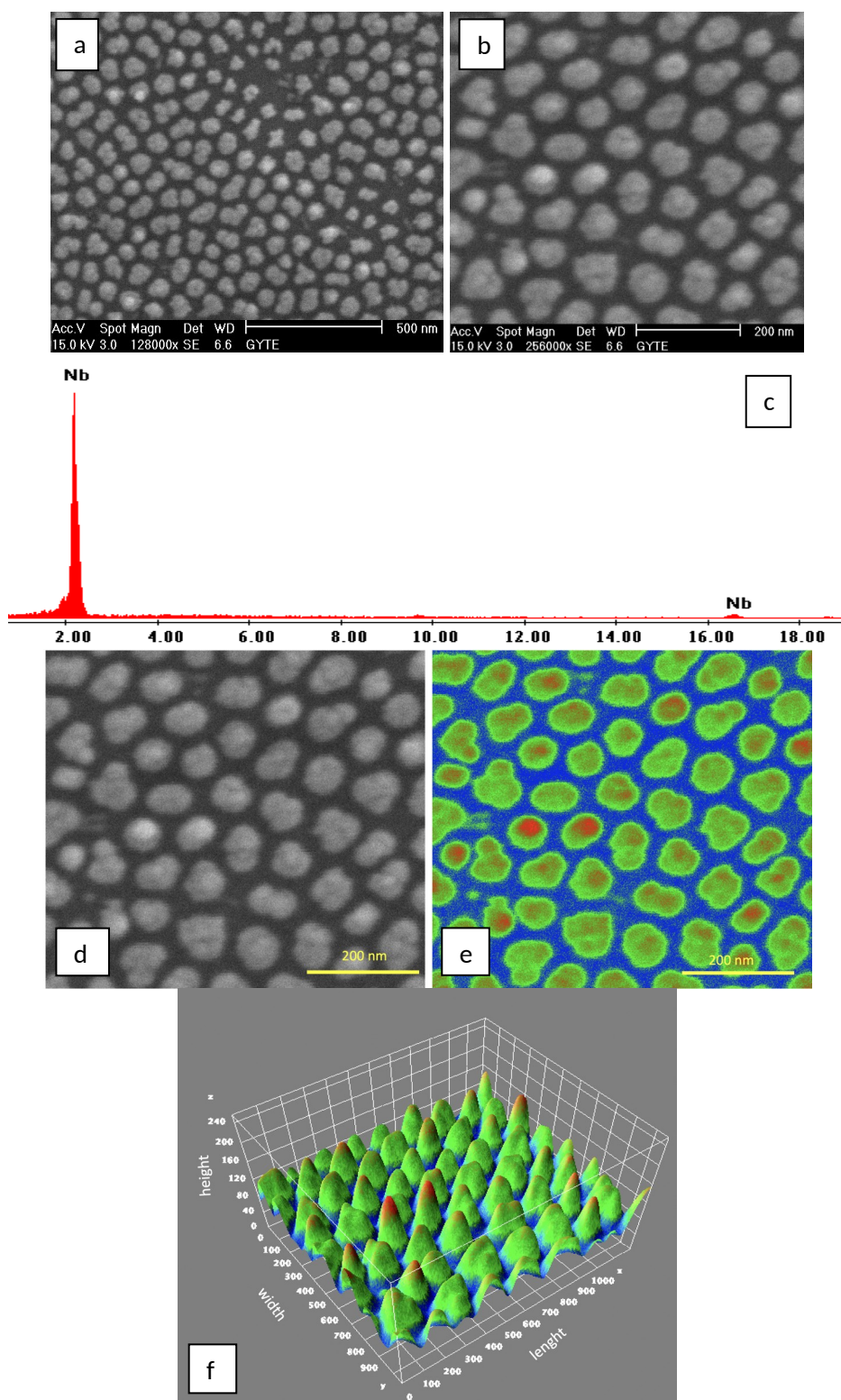
Figure 2. (a-b) SEM images and **(c)** EDS analysis of the prepared Nb nanopillars, **(d)** Artificial Intelligence (AI)-powered SEM image (8-bit) **(e)** SEM image (8-bit/rainbow RGB), and **(f)** 3D surface plot of Nb nanopillars.

When the two-step anodization technique (25) applied to Al film on Nb sheet, the anodic metal oxide was developed on the Nb_2O_5 layer by simultaneous growth at the Nb_2O_5 /Al_2O_3 interface by the migration of oxygen ions into the AAO layer (26). With the effect of anodization conditions, negative oxygen ions moved through the oxide layers in the direction of the Nb_2O_5 layers and the released Al^{+3} ions were expelled towards the electrolyte by passing through the barrier oxide layers. During the anodization of the metal substrate, some of Al^{+3} anions reacted with the O^{-2} ions at the interface of the AAO barrier layer/electrolyte and it was related to the formation of Al_2O_3 at the interface of metal oxide/electrolyte in the pores of AAO. Migrated electrolyte O^{-2} ions in the Nb_2O_5 layers were penetrated and oxidized the layer due to the formation of Nb_2O_5/Al_2O_3 using an electrochemical migration approach. At the same time, Nb^{+5} ions were directed outward to obtain new oxide layers at the interface of Nb_2O_5/Al_2O_3 by the electric field. Additionally, the thickness of the AAO barrier layer could be increased under the constant anodization voltage during the anodization due to the formation of the new oxide at the Nb_2O_5/Al_2O_3 and interfaces of Al_2O_3/electrolyte, and it was compensated by the ionic interface resistance of the interface of Al-Nb. It was also revealed that Nb_2O_5 were formed without direct contact between Nb metal and electrolyte due to the migration of O^{-2} ions and exition on the AAO barrier layer to Nb metal using a highly controlled process. At the beginning of the anodization process, the decrease in current was related to the O^{-2} ions on the Nb_2O_5 layer at the interface of Nb_2O_5/Al_2O_3 and the AAO layer on Al. Nb nanopillars with controlled morphologies could be easily achieved from AAO with the different electric field distribution. Finally, it was successfully presented the fabrication of a new the self-assembly AAO nanotemplate using a dilute NaOH solution, which yield the formation of Nb nanopillars with small nanopores.

CONCLUSIONS

The AAO nanotemplate was prepared on the Nb sheet. During AAO nanotemplate preparation, Nb nanopillars were grown on the Nb sheet. The proposed Nb nanopillars is a advanced energy storage material with superior advantages such as high surface area and electroactive regions. The diameter of Nb nanopillars is approximately 100–120 nm, and the length is approximately 150 nm. Nb-based materials are promising electrode materials for use in supercapacitors and batteries. The Nb nanopillar-based electrodes prepared in this study can overcome

the following problems. Nb nanopillars can shorten the diffusion distance between ions, provide a fast transfer path for ions, increase the contact surface between electrolyte and electrode, and expand the specific surface area, which improves the efficiency of the active material. In this way, volume expansion can be experienced. The large lattice parameter in Nb nanopillars can show a high Li^+ diffusion coefficient in Li-ion batteries, providing low electrode polarization and charge transfer resistance. Modification of Nb nanopillars with metal nanoparticles can achieve a more satisfactory crystal structure that increases the unit cell volume and lattice parameters. Thus, it can result in superior lithium diffusion kinetics in the Li-ion battery. Therefore, improved conductivity and increased Li^+ ion diffusion coefficients can be achieved, resulting in improved electrochemical performance. Modifying Nb nanopillars with carbon-based nanomaterials can greatly improve conductivity and contribute to enough active sites and efficient conductive contacts during the electrochemical reaction process. In summary, it is predicted that Nb-based materials will have a wider application area in supercapacitors and batteries in the future.

DECLARATION OF COMPETING INTEREST

The authors declare that they have no conflict of interest.

AUTHOR CONTRİBUTİONS

Nevin Taşaltın: Conceptualization, Methodology, Writing- Reviewing and Editing. Elif Tüzün: Methodology, Selcan Karakuş: Conceptualization, Methodology, Writing- Original draft preparation, Software.

CONFLICTS OF INTEREST

None.

DATA AVAILABILITY

The authors confirm that the data supporting the findings of this study are available within the article. Raw data that support the findings of this study are available from the corresponding author, upon reasonable request.

REFERENCES

1. Idrees M, Mukhtar A, Ata-ur-Rehman, Abbas SM, Zhang Q, Li X. Transition metal nitride electrodes as future energy storage devices: A review. Materials Today Communications. 2021 Jun;27:102363. <URL>.

2. Li Y, Xiao S, Qiu T, Lang X, Tan H, Wang Y, et al. Recent advances on energy storage microdevices: From materials to configurations. Energy Storage Materials. 2022 Mar;45:741–67. <URL>.

3. Pore OC, Fulari AV, Shejwal RV, Fulari VJ, Lohar GM. Review on recent progress in hydrothermally synthesized MCo2O4/rGO composite for energy storage devices. Chemical Engineering Journal. 2021 Dec;426:131544. <URL>.

4. Zhang Y, Liu J, Li SL, Su ZM, Lan YQ. Polyoxometalate-based materials for sustainable and clean energy conversion and storage. EnergyChem. 2019 Nov;1(3):100021. <URL>.

5. Lu T, Dong S, Zhang C, Zhang L, Cui G. Fabrication of transition metal selenides and their applications in energy storage. Coordination Chemistry Reviews. 2017 Feb;332:75–99. <URL>.

6. Raj A, Kumar M, Anshul A. Recent advancement in inorganic-organic electron transport layers in perovskite solar cell: current status and future outlook. Materials Today Chemistry. 2021 Dec;22:100595. <URL>.

7. Li WC, Lin CH, Ho CC, Cheng TT, Wang PH, Wen TC. Superior performances of supercapacitors and lithium-ion batteries with carboxymethyl cellulose bearing zwitterions as binders. Journal of the Taiwan Institute of Chemical Engineers. 2022 Apr;133:104263. <URL>.

8. Dai X, Zhang M, Li T, Cui X, Shi Y, Zhu X, et al. Effect of current on electrodeposited MnO2 as supercapacitor and lithium-ion battery electrode. Vacuum. 2022 Jan;195:110692. <URL>.

9. Natarajan S, Krishnamoorthy K, Kim SJ. Effective regeneration of mixed composition of spent lithium-ion batteries electrodes towards building supercapacitor. Journal of Hazardous Materials. 2022 May;430:128496. <URL>.

10. Zhang X, Peng N, Liu T, Zheng R, Xia M, Yu H, et al. Review on niobium-based chalcogenides for electrochemical energy storage devices: Application and progress. Nano Energy. 2019 Nov;65:104049. <URL>.

11. Mandal D, Jeong JY, Singu BS, Lee S, Mun WJ, Kim H. Flexible all solid-state niobium nitride//activated carbon lithium-ion hybrid capacitor with high volumetric power and energy densities. Journal of Energy Storage. 2022 Apr;48:104031. <URL>.

12. Vicentini R, Beraldo R, Aguiar JP, Oliveira FE, Rufino FC, Larrude DRG, et al. Niobium pentoxide nanoparticles decorated graphene as electrode material in aqueous-based supercapacitors: Accurate determination of the working voltage window and the analysis of the distributed capacitance in the time domain. Journal of Energy Storage. 2021 Dec;44:103371. <URL>.

13. Ma J, Guo X, Xue H, Pan K, Liu C, Pang H. Niobium/tantalum-based materials: Synthesis and applications in electrochemical energy storage. Chemical Engineering Journal. 2020 Jan;380:122428. <URL>.

14. Zhao Z, Xue Z, Xiong Q, Zhang Y, Hu X, Chi H, et al. Titanium niobium oxides (TiNb2O7): Design, fabrication and application in energy storage devices. Sustainable Materials and Technologies. 2021 Dec;30:e00357. <URL>.

15. Yao M, Chen J, Su Z, Peng Y, Li F, Yao X. Ionic transport and barrier effect of anodic oxide layer in a solid-state Al2O3 capacitor under high electric field. Electrochimica Acta. 2017 Jan;224:235–42. <URL>.

16. ur-rehman A, Ashraf MW, Shaikh H, Alhamidi A, Ramay SM, Saleem M. Yttrium incorporated BiFeO3 nanostructures growth on two step anodized Al2O3 porous template for energy storage applications. Ceramics International. 2020 Apr;46(6):7681–6. <URL>.

17. Remešová M, Tkachenko S, Kvarda D, Ročňáková I, Gollas B, Menelaou M, et al. Effects of anodizing conditions and the addition of Al2O3/PTFE particles on the microstructure and the mechanical properties of porous anodic coatings on the AA1050 aluminium alloy. Applied Surface Science. 2020 May;513:145780. <URL>.

18. Ahmad N, Khan S, Li WJ, Saddique M, Shah SA, Iqbal J, et al. Potential dependent tuning of magnetic and structural properties of electrodeposited NiZn nanowires in Al 2 O 3 templates. Journal of Magnetism and Magnetic Materials. 2017 Nov;441:696–701. <URL>.

19. Na HC, Sung TJ, Yoon SH, Hyun SK, Kim MS, Lee YG, et al. Formation of unidirectional nanoporous structures in thickly anodized aluminum oxide layer. Transactions of Nonferrous Metals Society of China. 2009 Aug;19(4):1013–7. <URL>.

20. Scisco GP, Haynes K, Jones KS, Ziegler KJ. Single step bonding of thick anodized aluminum oxide templates to silicon wafers for enhanced system-on-a-chip performance. Journal of Power Sources. 2020 Oct;474:228643. <URL>.

21. Patel Y, Janusas G, Palevicius A. Fabrication of nanoporous free standing anodic alumina using two-step anodization for applicability in microhydraulic system as nano filter using surface acoustics. Materials Today: Proceedings. 2021;45:5059–64. <URL>.

22. Ding H, Song Z, Zhang H, Zhang H, Li X. Niobium-based oxide anodes toward fast and safe energy storage: a review. Materials Today Nano. 2020 Aug;11:100082. <URL>.

23. Rasheed PA, Pandey RP, Banat F, Hasan SW. Recent advances in niobium MXenes: Synthesis,

properties, and emerging applications. Matter. 2022 Feb;5(2):546–72. <URL> .

24. Joslin Vijaya D, Pradeep Kumar J, Robinson Smart DS. Analysis of hybrid aluminium composite material reinforced with Ti and NbC nanoparticles processed through stir casting. Materials Today: Proceedings. 2022;51:561–70. <URL>.

25. Kikuchi T, Onoda F, Iwai M, Suzuki RO. Influence of sub-10 nm anodic alumina nanowire morphology

formed by two-step anodizing aluminum on water wettability and slipping behavior. Applied Surface Science. 2021 Apr;546:149090. <URL>.

26. Cigarroa-Mayorga OE, Gallardo-Hernández S, Talamás-Rohana P. Tunable Raman scattering enhancement due to self-assembled Au nanoparticles layer on porous AAO: The influence of the alumina support. Applied Surface Science. 2021 Jan;536:147674. <URL>.

A Review: Analysis of Metal and Mineral Content in the Complexity of Sidoarjo Hot Mud as a Source of Renewable Energy in Indonesia

Deni Ainur Rokhim[1,2]* (iD)**, Kafita Krisnatul Islamiyah*[1]** (iD)**, and Eli Hendrik Sanjaya[1]** (iD)

[1]Universitas Negeri Malang, Department of Chemistry, Semarang Street No. 5, Malang, 65145, Indonesia
[2]SMAN 3 Sidoarjo, Dr. Wahidin Street No. 130, Sidoarjo, 61215, Indonesia

Abstract: The Sidoarjo Hot Mud is a phenomenon of mudflow caused by exploration activities of PT. Lapindo Brantas since 2006. The purpose of this article is to provide information related to the empowerment of the Sidoarjo Hot Mud which has the potential as alternative source of renewable energy: source of electrical energy and biodiesel catalyst. Based on XRF results on samples at two locations: the center of the eruption and Lusi Island, it showed that there were various metallic elements and oxide minerals. Based on the results, the Sidoarjo Hot Mud from the center of the eruption resulted in potential difference of 8.8 V and electric power of 7.07135 watts/hour (8 circuits). The hot mud samples of Lusi Island produced potential difference of 4.38 V and electric power of 3.5196 watts/hour (3 circuits); 5.84 V and 4.6928 watts/hour (4 circuits). The silica mineral in the center of the eruption was 45.0% (radius 500 m), 45.3% (radius 1000 m), and 43.3% (radius 2000 m), while on Lusi Island it was 43.8%. Based on these results, the Sidoarjo mud has the potential to be used as a source of renewable energy in Indonesia, as a source of electrical energy and for synthesis for biodiesel catalyst.

INTRODUCTION

Sidoarjo Hot Mud is an ecological phenomenon of mudflow caused by the exploration activities of PT. Lapindo Brantas in Balongnongo, Renokenongo, Porong, Sidoarjo, East Java, which has occurred since November 2006. This phenomenon has included about 250 hectares of land i.e: 7 villages, rice fields, sugar cane plantations, irrigation canals, and transportation routes. The average volume of mudflow per day is around 50,000 – 120,000 m^3. The mudflow comes from a hole with a diameter of approximately 50 m (1). $\pm 60,000$ m^3 of $\pm 80,000$ m^3 volume of released mud is flowed into the sea through the Porong River (2). The overflow of mud into the Porong river causes the river to become shallow and the water flows slowly at high tide. The contained Sediment in river flow forms sedimentary deposits. Over time, these deposits formed a new island or better known as "Lusi Island" (3).

The Sidoarjo mudflow has had a tremendous impact in various fields, both for the life of the people around the center of the eruption and in East Java. In the economic field, it causes disruption of transportation facilities, namely the interruption of the main traffic routes of Surabaya-Malang and Surabaya-Banyuwangi. Disruption of aspects of education, where several formal and non-formal schools are flooded. Public health was also disrupted due to the toxic gas released from the hot mudflow. In addition, residents' houses were submerged in mud, causing economic losses. Therefore, the empowerment of the Sidoarjo mud is considered very important to minimize the impact (4).

Based on research by Utomo (2009), the results of the elemental content in Sidoarjo mud consisted of Si 25.67%, Na 1.17%, Mg 1.75%, Al 13.27%, Cl 0.91%, K 1.93%, Ca 1.54%, Fe 7.89%, Cd 0.3 %, Cu 0.4%, and Pb 0.73% (5). From these contents there are several metal elements that have the potential to be used as sources of electrical energy such as Na, Mg, Al, Fe, and Cd. This makes the Lapindo mud potential as a new renewable energy source to generate electricity by applying the study of chemistry "Voltaic Cell/Galvanic Cell". A voltaic cell or galvanic cell is an electrochemical cell that can generate electrical energy caused by a spontaneous oxidation-reduction reaction (6) (7).

Electrical energy is one of the essential basic needs in human life. Almost all human activities are related to electrical energy. In line with the increasing economic growth in Indonesia, the demand for electrical energy is also increasing. In the period 2013-2023 or the next 10 years, the Java-Bali electricity system is estimated to increase from 144 terra watts/hour (TWh) in 2013 to 375 TWh in 2022, which means a growth of 7.6%/year (8).

In addition to its elemental content, Sidoarjo hot mud also contained oxide minerals, including Al_2O_3 16%, SiO_2 49.9%, K_2O 2.51%, CaO 6.14%, TiO_2 1.74%, and Fe_2O_3 21.7% (9). Based on these data, silica content is one of the main mineral components in the Sidoarjo mud. Therefore, Sidoarjo hot mud has the potential to be used as a source of silica. One of the uses of silica is as a raw material for making synthetic zeolite to be used as a biodiesel/biofuel catalyst (10). The use of silica as a raw material for the manufacture of synthetic zeolite is carried out because the price of silica in the market isrelatively expensive (11).

Currently, the majority of energy needs in Indonesia are met by fossil fuels as non-renewable energy sources. Meanwhile, its availability in nature is increasingly depleting, this can be proven by the decline in the average oil reserves in Indonesia in the last five years, which is 22 billion barrels/year (12), (13). The continuous use of non-renewable energy sources causes a decrease in the quantity of petroleum resources. Based on data from the Minister of Energy and Mineral Resources (ESDM) in 2020, Arifin Tasrif in the Indonesian Energy Portrait Webiner on Tempo Energy Day (Wednesday 21/10/2020) said that without the discovery of alternative energy sources, oil in Indonesia will run out. in the next 9 years (2029), natural gas will run out in the next 22 years (2042), and coal will last for the next 65 years (14). These data indicated that Indonesia has limited energy and is in danger of experiencing an energy crisis in the future. Therefore, it is necessary to empower alternative energy sources to solve this problem. One alternative is empowering Sidoarjo hot mud which can be used as a potential source of electrical energy and biodiesel/biofuel.

Based on the above explanation, this article is expected to provide information to the public regarding the empowerment of Sidoarjo hot mud to be used as a renewable energy source (electric energy source and biodiesel catalyst source) in Indonesia. This idea can be a solution to the complex problem of the Sidoarjo hot mud, as well as a solution to the threat of the energy crisis in Indonesia.

MATERIAL AND METHODS

The used research method was the Systematic Literature Review (SLR) method. Using the SLR method, a systematic review and identification of journals can be carried out which followed the organized steps (31).

Research Question
Research questions were made based on the needs of the topic chosen by the author. The following were the research questions in this study, namely:
1.   What are the metals and minerals contained in the Sidoarjo hot mud sample?
2.   How the differences in the metal and mineral content contained in the Sidoarjo hot mud samples obtained from 2 different locations (eruption center and Lusi island)?
3.   How the potential sources of renewable energy that can be utilized from the Sidoarjo hot mud phenomenon?

Search Process
The search process was used to obtain relevant sources to answer Research Questions/research questions and other related references. The search process used the Google Scholar database. In this study, the authors conducted a search with several keywords. Each keyword and its search results are shown in Table 1.

Table 1: Search Results for Each Keyword in Indonesian Language.

Num.	Keyword	Search Result
1	"Potensi Energi Baru dan Terbarukan"	13.700 articles
2	"Menjadi energi listrik"	147.000 articles
3	"Lumpur Sidoarjo menjadi sumber energi"	1.530 articles
4	"Lumpur Sidoarjo menjadi sumber energi listrik"	792 articles

Inclusion and Exclusion Criteria
This stage is to determine the found data for use in Systematic Literature Review method. A study was eligible to be selected according to the following criteria:
Data used in the last 15 years.
1.   Data obtained through Google Scholar.
2.   The used data was only focused on problems regarding the analysis of Sidoarjo hot mud content as a potential source of renewable energy.

Data Collection and Data Analysis
Data collection is the stage where the research data was collected. The data collected in this study was secondary data. Secondary data obtain in journals and research articles. From all the articles obtained, the authors filter the results of the appropriate articles and journals to obtain accurate data for use in this study.

In this study, the researcher used 23 samples with details of 19 articles and 4 academic final reports. Researchers took data by reviewing existing information and facts, then re-paraphrasing and providing a thorough analysis.

RESULTS AND DISCUSSION

Analysis of Compound Content
Analysis of compound content in Sidoarjo hot mud samples consisted of elemental content analysis and analysis of oxide mineral compounds using XRF test. The principle of the XRF test is based on the interaction of the material with X-rays (15). This test is often used in mineral analysis, because of fast, accurate, non-destructive, and usually requires only minimal sample preparation (16).

XRF Test Results
In the study of this article, the samples studied were sourced from 2 locations, the mud sample at the center of the Sidoarjo hot mudflow (radius 500 m, 1000 m, and 2000 m) and the mud on Lusi Island.

Sidoarjo Hot Mudflow Center
The results of elemental content in the Sidoarjo hot mud at a radius of 500 m, 1000 m, and 2000 m from the center of the eruption are shown in Table 2.

Table 2: Results of Elemental Content Analysis in Sidoarjo Hot Mud Using XRF.

Element	% Radius 500 m	% Radius 1000 m	% Radius 2000 m	Element	% Radius 500 m	% Radius 1000 m	% Radius 2000 m
Al	11	11	9.9	Cu	0.15	0.14	0.16
Si	32.7	33.0	31.1	Zn	0.08	0.07	0.07
K	4.03	3.88	3.81	Br	0.39	0.31	-
Ca	7.78	8.19	7.99	Sr	1.1	1.1	0.86
Ti	2.13	2.11	2.20	Mo	5.1	5.1	5.4
V	0.081	0.087	0.087	Eu	0.59	0.58	0.67
Cr	0.100	0.099	0.11	Yb	0.1	-	-
Mn	0.45	0.47	0.53	Re	0.2	0.2	0.3
Fe	34.2	33.9	36.4	P	-	-	0.44
Ni	0.03	-	-				

Based on Table 2, the main elemental contents in Sidoarjo hot mud were Iron (Fe) 34.2% (radius 500 m), 33.9% (radius 1000 m), and 36.4% (radius 2000 m). The second main contents were silicon (Si) of 32.7% (radius 500 m), 33.0% (radius 1000 m), and 31.1% (radius 2000 m). The other elements were Al, K, Ca, Ti, V, Cr, Mn, Ni, Cu, Zn, Br, Sr, Mo, Eu, Yb, Re, and P. The content of silicon in this study was slightly higher. Larger than the results of the initial analysis conducted by Assolah (2015) which obtained an elemental Si content of 19.70%. In addition to analyzing the elemental content in the Sidoarjo mud, this XRF analysis also analyzes the oxide content which is shown in Table 3.

Based on Table 3, the main oxide content in Sidoarjo mud was silica of 45.0% (radius 500 m), 45.3% (radius 1000 m), and 43.3% (radius 2000 m). The second main content was iron oxide, namely 24.1% (radius 500 m), 23.7% (radius 1000 m), and 25.9% (radius 2000 m), the presence of iron content was correlated to the blackish gray color of the Sidoarjo hot mud. Other oxides contained in it were Al_2O_3, K_2O, CaO, TiO_2, VO_5, Cr_2O_3, MnO, NiO, CuO, ZnO, SrO, MoO_3, Eu_2O_3, Yb_2O_3, and Re_2O_7. Thus, this Sidoarjo hot mud has the potential to be used as a source of silica in the future and further exploration can also be carried out due to the presence of soil minerals that were rarely identified.

Table 3: Results of Oxide Content Analysis in Sidoarjo Mud Using XRF.

Oxide	% Radius 500 m	% Radius 1000 m	% Radius 2000 m	Oxide	% Radius 500 m	% Radius 1000 m	% Radius 2000 m
Al_2O_3	14	14	13	NiO	0.02	-	-
SiO_2	45.0	45.3	43.3	CuO	0.084	0.079	0.092
K_2O	2.76	2.64	2.64	ZnO	0.04	0.04	0.04
CaO	6.05	6.34	6.30	SrO	0.60	0.56	0.46
TiO_2	1.91	1.88	2.01	MoO_3	4.6	4.5	4.8
V_2O_5	0.076	0.081	0.083	Eu_2O_3	0.35	0.35	0.40
Cr_2O_3	0.077	0.076	0.085	Yb_2O_3	0.05	-	-
MnO	0.29	0.30	0.35	Re_2O_7	0.1	0.1	0.2
Fe_2O_3	24.1	23.7	25.9	P_2O_5	-	-	0.62

As for obtaining silica with a high level of purity, a synthesis method is needed that can significantly reduce the level of impurities in the sample. Research by Silvia & Zainuri has succeeded in synthesizing silica from Bancar beach natural sand which has the highest purity reaching 100% from an initial content of 81.7% using the coprecipitation method with NaOH solvent (17). This shows that the coprecipitation method or others can be applied to samples containing silica such as Sidoarjo hot mud to obtain high purity. Therefore, this Sidoarjo hot mud has the potential as a source of high purity silica.

Lusi Island
The results of the analysis of elemental content in Lusi Island are shown in Table 4.

Table 4: Results of Elemental Analysis on Lusi Island Using XRF.

Element	% Content	Element	% Content	Element	% Content
Al	12	Mn	0.75	Sr	-
Si	32.1	Fe	38.5	Mo	3.9
K	2.10	Ni	0.03	Eu	0.55
Ca	6.86	Cu	0.18	Yb	0.1
Ti	2.05	Zn	0.09	Re	0.2
V	0.088	Mn	0.75	P	-
Cr	0.083	Br	-	-	-

Based on Table 4 , the largest element content in Lusi Island was Iron (Fe) 38.5%. The second largest content was silicon (Si) 32.1%. Other elements contained in it were Al, K, Ca, Ti, V, Cr, Mn, Ni, Cu, Zn, Mo, Eu, Yb, and Re. The metal content of Fe in Lusi Island was slightly higher than the content of Fe in the Sidoarjo Mud which was 36.4% (radius 2000 m). Meanwhile, the silicon (Si) content in Lusi Island was slightly lower than that in Sidoarjo hot mud of 33.0% (radius 1000 m). In addition to analyzing the elemental content in Lusi Island, this XRF analysis also analyzed the oxide content as shown in Table 5.

Table 5: Results of Oxide Content Analysis in Lusi Island Using XRF.

Oxide	% Content	Oxide	% Content	Oxide	% Content
Al_2O_3	16	V_2O_5	0.083	CuO	0.10
SiO_2	43.8	Cr_2O_3	0.064	ZnO	0.05
K_2O	1.44	MnO	0.49	SrO	-
CaO	5.39	Fe_2O_3	26.9		
Al_2O_3	16	NiO	0.01		

Based on Table 5, the most dominant oxide content in Lusi Island was silica of 43.8%. The second dominant content was iron oxide, which was 26.9%. Other oxides contained in it were Al_2O_3, K_2O, CaO, TiO_2, VO_5, Cr_2O_3, MnO, NiO, CuO, ZnO, SrO, and MoO_3. The silica content in Lusi Island was slightly lower than that in Sidoarjo Mud, which is 45.3%.

Based on the results of the XRF test, it was found that the content of metallic elements and oxide minerals in the Sidoarjo hot Mudflow Center and Lusi Island had almost the same percentage. With this content, this mud has the potential to be used as a new renewable energy source (source of electrical energy and a source of silica as a biodiesel catalyst).

The Effectiveness of Utilizing Sidoarjo Mud as a Source of Electrical Energy
Based on the XRF test data, the Sidoarjo Hot Mud and Lusi Island have high metal content. Through the application of the principle of the voltaic cell, Sidoarjo Mud can be used as a source of environmental friendly electrical energy. By making a circuit, copper and magnesium as electrodes connected to a digital multimeter can be produced relatively large electric currents. Based on the research results of Rokhim the Sidoarjo mudflow at the center of the eruption can be produced a potential difference of 8.8 volts and an electric power of 7.07135 watts/hour (8 sets of cells). Meanwhile, in Lusi Island, 3 sets of cells produced a potential difference of 4.38 volts and an electrical power of 3.5196 watts/hour. In 4 series of cells it produced a potential difference of 5.84 volts and an electric power of 4.6928 watts/hour (8).

Utilization of Sidoarjo hot mud as a source of electrical energy has a high effectiveness. This referred to the results of research by (18), (19), and (19) concluding that Sidoarjo Hot Mud can be used as bioelectricity by using microbial fuel cells (MFC). Another study conducted by (20) concluded that Sidoarjo Hot Mud can be used as a potential source of new renewable energy based on SCL (Soil Cell) with hydrothermal technology.

Potential electrical energy that can be generated from Sidoarjo hot mud processing is an electric voltage of 163.83 Volt/m^2 and an electric current of 0.01 A/m^2 (18), while the results of the research by Saragih & Melaca produced an electric voltage of 210.25 volts/m^2, and an electric current of 51.75 A/m^2 (18).

Another effectiveness of the utilization of the Sidoarjo hot mud is that it can be used as a lithium battery with a large output and it can be used repeatedly until its lifetime runs out (21), (22), and (22). The results of this study were reinforced by the results of research by Noerochim, Satriawangsa, and Widodo that in the Sidoarjo Hot Mud geothermal fluid there was a lithium content of 5.81 mg/liter which can be used as the most potential source of lithium. By doing a rough calculation and assuming that the amount of sludge discharge and the content of Lithium is constant, Lusi can be produced at least 18 tons of Lithium every year (23). Extraction and Processing of Lithium from Sidoardjo Hot Mud can be used as a Lithium Battery Cathode Manufacturing.

Utilization of Sidoarjo Mud into alternative energy as Renewable Energy is a form of saving the environment, especially in the area around the Sidoarjo hot mud (2), (8). In addition, it is also an effort to overcome the use of non-renewable natural resources, especially in the problem of electrical energy in Indonesia.

Effectiveness of Utilizing Sidoarjo Mud as a Silica Source
The mineral composition of the Sidoarjo hot mud in the eruption Center and Lusi Island has almost the same percentage. Based on the data, the XRF test results showed that the highest and most dominant oxide percentage in both places were silica (SiO_2). The silica content in the Sidoarjo Hot Mud and Lusi Island, respectively, was 45.3% (radius 1000 m) and 43.8%. Therefore, these minerals have the most potential for exploitation. To obtain silica, several methods of silica extraction are necessary. Commonly, the used silica extraction methods on samples of the Sidoarjo hot mud type included continuous methods, sol gel, leaching, and coprecipitation as shown in Table 6.

Based on the literature review on the Table 6 , the majority of researchers used the continuous method in extracting silica contained in the Sıdoarjo hot mud. One of the potential silica can be used as a raw material in the manufacture of catalysts. For example, the catalyst is a synthetic zeolite which was the hydrated porous alumino-silicate crystals (28). The use of silica from natural materials as raw material for the manufacture of synthetic zeolite was carried out because the price of silica in the market is relatively expensive (28). Zeolite made from silica is useful as a catalyst for biodiesel and biofuel (10).
Biodiesel is a long chain methyl ester compound that can be produced through the esterification-transesterification process of vegetable oils or animal fats. The process usually use a homogeneous base or acid catalyst, so the process can reacts at low temperature and selective products (29).

The synthesis of biodiesel can use homogeneous catalysts, such as acids and bases. The use of this homogeneous catalyst causes problems in the resulting product, one of which still contained a catalyst that must be separated again. On the other hand, the use of base catalysts can also overcome side reactions, namely the saponification reaction, which affected the process of biodiesel synhtesis. So, the use of heterogeneous catalysts, such as activated synthetic zeolite, will facilitate the separation of the catalyst from the product (30). Biodiesel is an alternative fuel from renewable resources that has many advantages, including: environmentally friendly, relatively low emissions of air pollution, can be decomposed naturally (biodegradable), and can be used without the need for engine modification processes. Therefore, the use of silica as a raw material for the manufacture of zeolite (biodiesel catalyst) is a form of solution for using alternative energy as a new renewable energy source in Indonesia.

Table 6: Silica Extraction Method on the Sample.

Method	Starting material	Procedure Sequence	Product	Reference
Continuous	Dried mud solids	• Mud washed with distilled water • Soaked with 2 M HCl • Dry at 110 ℃ • Flowing with alkaline solution (KOH) • Conditioned under acidic conditions (pH =4)	Precipitated amorphous silica	(24)
Sol Gel	Dried mud solids	• Soaked with 2 M HCl (4 hours) • Filtration (took the sediment) • Washed with distilled water • Reacted with 7 M NaOH (5 hours, 80 ℃) • Filtration • The filtrate was heated T= 100 ℃, 10 minutes • Add 3 M HCl until the pH was close to 7	Silica white precipitate	(25)
Leaching	Dried mud solids	• Reacted with 6 M NaOH, T= 90 ℃, 5 hours • Titration with HCl (pH up to 8) • Washed and dried, T= 120 ℃, 10 hours	Xerogel Silica	(26)
Coprecipitation	Dried mud solids	• Reacted with NaOH • Heated and stirred • Filtration • The filtrate was dripped with HCl (pH up to 7)	Precipitated amorphous silica	(27)

CONCLUSION

Based on the XRF test results, it can be concluded that the metal and mineral oxide content of the Sidoarjo Hot Mud in two locations namely the center of the Sidoarjo Hot mudflow and the Lusi island have relatively the same content. The oxide contents in the Sidoarjo Hot Mud were SiO_2, Fe_2O_3, Al_2O_3, K_2O, CaO, TiO_2, VO_5, Cr_2O_3, MnO, NiO, CuO, ZnO, SrO, and MoO_3. The high metal content in the mud has the potential to be used as a source of environmentally friendly electrical energy. While the content of silica minerals can be used as the basic material for zeolites synthesis (biodiesel catalysts). So, the empowerment of the Sidoarjo Hot Mud can be used as an alternative solution for renewable energy.

CONFLICT OF INTEREST

All authors declare no conflict of interest.

REFERENCES AND NOTES

1. N. Herawati, "Analisis risiko Lingkungan Aliran Air Lumpur Lapindo Ke Badan Air(Studi Kasus Sungai Porong dan Sungai Aloo - Kabupaten Sidoarjo)," *Univ. Diponegoro*, 2007.

2. T. Winarno, Y. B. A. Gunawan, and J. Marin, "Analisis Mineralogi dan Kandungan Kimia Endapan Lumpur Sidoarjo dan Arah Pemanfaatannya," *Teknik*, vol. 40, no. 2, p. 91, 2019, <DOI>.

3. A. Rahardjanto and F. E. B. Setyawan, *Memahami Kearifan Lokal Pada Konservasi DAS Daerah Hulu*. 2021.

4. P. R. Indonesia, "Tentang U. P. Antara P. Pemerintah D. D. Provinsi dan kota." 2007.

5. Y. Utomo, *Lingkungan Hidup*. Malang: Pusat Penelitian Lingkungan Hidup Lembaga Penelitian, Universitas Negeri Malang, 2009.

6. H. Sastrohamidjojo, "No Title," 2018.

7. A. Harianto, S. Suryanti, and Y. Khery, "No Title," 2017.

8. D. A. Rokhim, "Sidoarjo Mudflow Electric (SMF-E): Optimalization of Sidoarjo Mudflow as an Electric Supplier Based on Electrochemical," *R.E.M. (Rekayasa Energi Manufaktur) J.*, vol. 5, no. 1, pp. 23–26, 2021, <DOI>.

9. A. Rosmawati, R. T. Tjahjanto, and Y. P. Prananto, "Variasi Metode Preparasi Gel Pada Sintesis Aerogel Silika Dari Lumpur Lapindo," *Kim. Student J.*, vol. 1, no. 2, pp. 161–167, 2013.

10. S. Norvia, Suhartana, and Pardoyo, "Dealuminasi Zeolit Alam Menggunakan Asam (HCl dan H2SO4)," *J. Kim. Sains dan Apl.*, vol. 19, no. 2, pp. 72–76, 2016.

11. D. H. Astuti *et al.*, "Kajian Kualitas Komposisi Adsorben Berbahan Baku Quality Study Of Adsorben Composition With Sidoarjo," 2020.

12. K. E. dan S. D. Mineral, "Minyak & Gas Bumi," p. 20, 2009.

13. H. Herliati, S. B. Prasetyo, and Y. Verinaldy, "Review: Potensi limbah Plastik dan Biomassa sebagai Sumber Energi Terbarukan Dengan Proses Pirolisis," *J. Teknol.*, vol. 6, no. 2, pp. 85–98, 2019, <DOI>.

14. H. EBTKE, "Menteri Arifin: Transisi Energi Mutlak Diperlukan," Jakarta, Indonesia.

15. D. R. Baharintasari, M. R. Asrori, and Y. F. Prakasa, "Kabupaten Blitar Menggunakan Xrf Dan Xrd," vol. 4, no. 2, pp. 52–55, 2019.

16. Jamaluddin, A. Darwis, and M. A. Massinai, "X-Ray Fluorescence (XRF) to identify chemical analysis of minerals in Buton island, SE Sulawesi, Indonesia," *IOP Conf. Ser. Earth Environ. Sci.*, vol. 118, no. 1, pp. 0–5, 2018, <DOI>.

17. L. Silvia and M. Zainuri, "Analisis Silika (SiO2) Hasil Kopresipitasi Berbasis Bahan Alam menggunakan Uji XRF dan XRD," *J. Fis. dan Apl.*, vol. 16, no. 1, p. 12, 2020, <DOI>.

18. I. Rozi and H. Habshi, "Pemanfaatan Lumpur Lapindo sebagai Biolistrik dengan Menggunakan Microbial Fuel Cells (Mfcs)," Institut Teknologi 10 Nopember Surabaya, 2017.

19. V. Saragih and K. M. Melaca, "Pengaruh Eksternal Resistansi dan Penambahan Molasses pada Lumpur Lapindo untuk Menghasilkan Biolistrik dengan Menggunakan Microbial Fuel Cells," Institut Teknologi 10 Nopember Surabaya, 2018.

20. N. A. Putri, N. Nabillah, U. L. Novianti, and M. R. Huseini, "Variasi Temperatur Dan Waktu Tinggal Hidrotemalisasi Terhadap Efektifitas Lumpur Lapindo Sebagai Sumber Energi Alternatif," 2019, pp. 1–5.

21. M. iqbal Akbar, P. Astuti, and D. Rahmawati, "Sistem Pembangkit Listrik Ramah Lingkungan Berbasis Teknologi Microbial Fuel Cell di Area Semburan Lumpur Panas Sidoarjo sebagai Sumber Energi Listrik Bagi Daerah Tertinggal di Jawa Timur," Bogor, 2011. [Online]. Available: Institut Pertanian Bogor.

22. W. P. Kistiyanto, "Pengaruh Variasi Temperatur Kalsinasi pada Sintesa Lithium Mangan Oksida dengan Rasio Mol Li/Mn 0,8 Terhadap Kemampuan Adsorpsi Lithium Lumpur Sidoarjo," Institut Teknologi 10 Nopember Surabaya, 2016.

23. G. Akbar Satriawangsa and L. Noerochim, "Pengaruh Rasio Mol Li/Mn Pada Proses Preparasi Lithium Mangan Oksida Terhadap Kemampuan Adsorbsi Lithium Dari Lumpur," *J. Tek. Pomits*, vol. 3, no. 2, pp. 6–11, 2014.

24. A. F. Fadli, R. T. Tjahjanto, and Darjito, "Ekstraksi Silika dalam Lumpur Lapindo Menggunakan Metode Kontinyu," *Kim. Student J.*, vol. 1, no. 2, pp. 182–187, 2013.

25. A. Assolah, "Sintesis dan Karakterisasi Zeolit X dari Lumpur Lapindo dengan Variasi Komposisi SiO2/Al2O3 Menggunakan Metode Sol-Gel," 2015.

26. M. A. S. Al Mubarok, L. P. Setiawan, M. Utami, and W. Trisunaryanti, "Study of acid leaching in the preparation of silicon from lapindo mud," *Int. J. Acad. Sci. Res.*, vol. 2,

no. 4, pp. 31–36, 2014.

27. I. F. Ulfindrayani, N. Ikhlas, Q. A'yuni, N. Fanani, B. L. Gaol, and D. Lestari, "Pengaruh Ekstraksi SiO2 dari Lumpur Lapindo Terhadap Daya Adsorpsinya pada Larutan," *Angew. Chemie Int. Ed. 6(11), 951–952.*, vol. 2, no. 2, pp. 5–24, 2019.

28. H. Hartati, "Sintesis Zeolit ZSM-5 dari Metakaolin Terdealuminasi Tanpa Cetakan Organik dengan Metode Desilikasi," *Akta Kim. Indones.*, vol. 4, no. 1, p. 63, 2019, <DOI>.

29. D. Y. C. Leung, X. Wu, and M. K. H. Leung, "A review on biodiesel production using catalyzed transesterification," *Appl. Energy*, vol. 87, no. 4, pp. 1083–1095, 2010, <DOI>.

30. I. Aziz, S. Nurbayti, and A. Rahman, "Penggunaan Zeolit Alam sebagai Katalis dalam Pembuatan Biodiesel," *J. Kim. Val.*, vol. 2, no. 4, pp. 511–515, 2012, <DOI>.

31. B. Kitchenham, O. Pearl Brereton, D. Budgen, M. Turner, J. Bailey, and S. Linkman, "Systematic literature reviews in software engineering - A systematic literature review," *Inf. Softw. Technol.*, vol. 51, no. 1, pp. 7–15, 2009, <DOI>.

RESEARCH ARTICLE

Investigation of Heavy Metal Concentrations in The Gulf of Izmit (Marmara Sea) Altinova Shipyard Region

Kübra Bayrak[1] (iD)**, Erol Kam[2]*** (iD)**, Zeki Ünal Yümün[3]** (iD)**, Melike Önce[3]** (iD)

[1]Akdeniz University, Dep. of Physics, Antalya, Türkiye
[2]Istanbul Technical University Department of Environmental Engineering, Istanbul, Türkiye
[3]Namik Kemal University, Engineering Faculty, Çorlu, Tekirdag, Türkiye

Abstract: In this study, heavy metal concentrations (Ca, Mg, Hg, As, Sb, Ag, Al, Co, Cr, Cu, Fe, Mn, Ni, Pb, V, Zn, Ti, Th, U, Mo, Cd) amounts were measured by examining marine sediment samples obtained from the coasts of the Izmit Bay Altınova shipyards region. The natural and anthropogenic pollution levels of the region were revealed by the analysis of sediment samples. The extent to which the marine ecosystem may have been affected by the shipyard activities that have been actively carried out in the region for the last ten years was also investigated. Heavy metal analyses of sediment samples were carried out by the XRF method. In addition, the morphological and surface features of the sediment grains were obtained by SEM analysis, and the element contents of seawater samples obtained from the region were determined with an ICP-OES device. The heavy metal pollution level of the region was revealed by evaluation of the data obtained as a result of the analysis. The results of the XRF analysis showed that the heavy metals, which are toxic for humans, such as cadmium (max 17.984 ppm), lead (max 31.302 ppm), nickel (max 71.725 ppm) and arsenic (max 13.852 ppm) were detected. According to the results of elemental analysis with ICP-OES, Hg, As, Sb, Ag, Al, Co, Cr, Ni, Pb, V, Ti, U, Mo, and Cd were below the measurable limit.

INTRODUCTION

Heavy metals have become one of the most accumulated pollutant groups with the development of industrial activities in marine ecosystems. Because these pollutants cannot be decomposed biologically and chemically, they accumulate in the sediment at the seabed. Environmental monitoring and evaluation of seacoasts is of critical importance in terms of the health of humans and sea creatures. In such monitoring, sediments are used as bioindicators for marine environments. The Sea of Marmara is exposed to chemical and biological pollution from various sources, including a dense population, excessive industrial activities, intense maritime traffic in the straits, marine accidents, and agricultural activities (1-5). This influx has caused pollution, not only in the Marmara Sea, but also in neighboring seas and rivers (1,6). In the marine environment, metals exist in dissolved forms or are adsorbed onto suspended particles (7,8). The movement of heavy metals in the marine environment is dependent on the primary minerals and on the silicate content in the sediment (9). Elements such as Cd, Pb, As, and Hg in marine environments are designated as potentially harmful elements (PHEs) and are reported as priority hazardous substances by Directive (AB) 2020/2184 of the European Commission (10-13). Sediment monitoring has been very important in revealing pollution in marine environments in recent years, and there have been studies on the subject (14-19).

In the study area, there are studies conducted in previous years regarding the pollution status of the region. Okay et al., (2001) showed that there were significant increases in Chlorophyll-a value, which is an indicator of primary producing organisms (phytoplankton) in the Gulf, compared to previous years (20). Morkoç et. al. (1995) studied the effects of wastewater on the water quality of the Bay. Pollution sources that put pressure on the Bay were determined and the situation of the Bay in terms of water quality was determined (21). Sur et al. (2010) determined that the area was polluted according to the metal values measured in the seafloor surface sediment of the study area. It has been determined that the biggest source of this pollution is port and shipyard activities (22). Bayrak et. al. (2018), showed the heavy metal densities of the marine sediments of the Izmit Bay Altinova region and it was determined that it was rich in metals such as Hg, Cu, Ni began (23). In 2007-2008, pollution-monitoring studies were carried out by TÜBİTAK / MAM in the Gulf. As a result of these studies, the water quality of the coastal areas was rated as poor or bad (24).

With these researches on heavy metals conducted in the study area, ways have been evaluated in which the marine ecosystem may have been affected by the shipyard activities, domestic and industrial waste disposal, as well as agricultural activities that have been actively carried out in recent years. Especially from shipyards; pollutants such as ship waste water, ballast water, ship repair oils, chemical paint wastes, wastes arising from leakage are mixed with marine environments. Discharge of these wastes to the marine environment without treatment puts the living life in the region in danger (25-29).

In this study, Marine sediment samples obtained from the shores of the Altınova shipyards region of the Gulf of Izmit were analyzed. Heavy metal analyses of marine sediment and seawater samples were carried out with XRF (wavelength-distributed X-ray fluorescence spectrometry), ICP-OES (inductively coupled plasma-optical emission spectrometry), SEM (scanning electron microscopy).

MATERIALS AND METHOD

Sampling Area
Yalova province is located in the south of Marmara Region, at the entrance of Izmit Bay (Figure 1). It is a developed region in terms of industry, shipbuilding facilities, and population, and there are side-by-side shipbuilding facilities along the coast of the study area. Altınova is built on the Hersek delta where agricultural activities are intense. The region is very active in terms of shipyard activities.
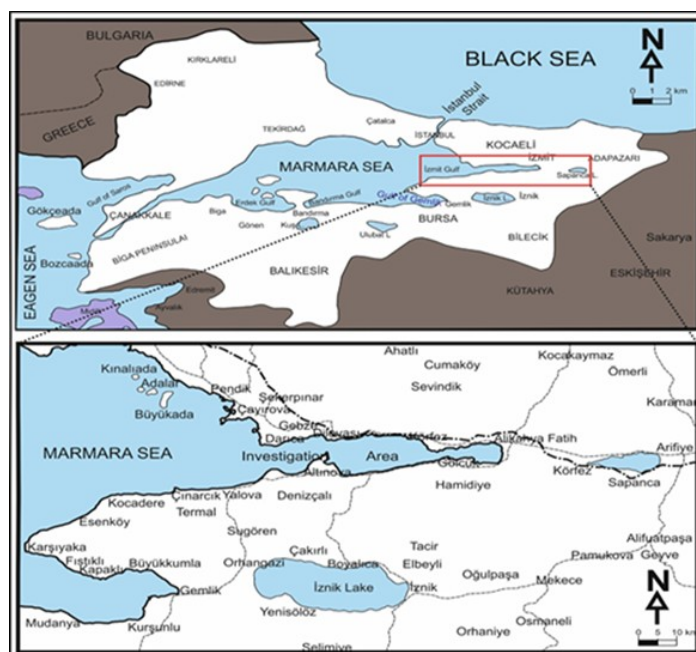
Figure 1: Location map of the study area.

Shipyard Pollution
In the shipbuilding and repair process, especially steel and metals, as well as paint and paint solvents (solvent), blast abrasives, machine oils and cutting oils are used as raw materials. It also contains chemical materials, heavy metals and cyanide used in surface preparation processes such as acid and alkaline cleaners, degreasing solvents and coating solutions. Shipyard wastes generally consist of organic compounds (VOCs), particles (PM), waste solvent materials, oil and resins, metal wastes, dirty water, dirty waste paint and abrasives (30).

Table 1: Shipyard processes and waste stream (30).

Process	Input Material	Air Emissions	Waste water
Surface Preparation	Abrasives (steel shot, grit, copper slag, paint removers and cleaners)	VOC emissions from solvent cleaners and paint removers	Paint chips, cleaning fluids, surface contaminants, oil and scrap oil from cargo and ballast tanks
Metal plating and surface finishing	Coating metals, cyanide solutions, cleaning solvents, rinses	Metal ion vapour, acid vapour, VOC emissions from solvents	Rinse water contaminated with metals, cyanide, acids, alkalis, organics and solvents
Painting	Paint, solvent and water	VOC emissions from paints and solvents and equipment being cleaned	Contaminated water from equipment cleaning and solvents
Fiberglass manufacture	Fiberglass, resin, catalysts, wood and plastic materials	VOC emissions during manufacturing	Waste water generation is very low
Machining and metal works	Cutting oils, solvents	VOC emissions from degreasers and cleaning solvents	Waste water contaminated with used solvents, cutting oils and cooling oils

Sampling and Preparation
Sea sediment samples were collected from sub-seafloor depths varying between 7 m and 38 m. A sediment sample and a seawater sample were taken with a ship at each of six points deemed appropriate for the region (Figure 2). The depths and coordinates of the six core samples obtained by drilling are recorded (Table 1).

Figure 2: Study area where sample locations are specified (31).

XRF Analysis of Sediment Samples
The analysis is based on excitation of atoms with a high-energy radiation such as X-rays. When the excited electrons return to their initial energy levels, they give back the excess energy they have gained in the form of X-rays with wavelengths of 0.1–50 Å. This secondary emission of X-rays is called fluorescence. The wavelengths of the radiations produced by the elements are specific to those elements (32). For XRF analysis, sediment samples were first ground into powder; then 9 grams of each sample was weighed and mixed homogeneously with 6 grams of cellulose. The obtained mixtures were transferred to a mold designed for that analysis and formed into pellets under high pressure. Pellets of approximately 15 grams each were prepared for analysis and were analyzed with the Pro-Trace program (Malvern Panalytical) for 116

minutes. The Pro-Trace program, which is a program that can count at the level of ppm (parts per million), is frequently used in elemental analysis studies today (33).

ICP-OES and Anion Analysis of Seawater Samples
The ICP-OES technique is based on the excitation of the elements in the sample by argon plasma, which is heated to a temperature of 10,000 K by electromagnetic induction, and measuring the optical emission of the excited elements according to their specific wavelengths (EPA Method 200.7) (34,35). ICP-OES analyses were performed on seawater samples taken from the study area. Seawater samples taken from the field were preserved and brought to the laboratory environment in accordance with sample storage standards (34,35). First, anion analyses were carried out on the water samples collected from the region. The device used in that analysis was an ICS-3000 DIONEX brand ion chromatography device. Results were obtained in ppm (3,5).

SEM Analysis of Sediment Samples
SEM images were taken with a JEOL brand JSM-6390LV scanning electron microscope. The sample to be SEM imaged first had to be resistant to

vacuum; that is, it must not evaporate, and it must be in the solid state (36). (Evaporation of samples under vacuum causes the microscope to become contaminated and may cause errors in the analysis result.) In SEM, a qualified image is obtained by scanning the sample surface in detail with electrons (33,37).

RESULTS AND DISCUSSION

XRF Analysis Results
XRF analysis results of the sediment samples are shown in Table 3.

In the qualitative analyses made with XRF, both element and compound determinations were made for the sediment composition. Because the sediments are composed of organic and inorganic deposits, the elements and compounds obtained in elemental analysis are quite diverse. The results of the analysis revealed that toxic heavy metals such as cadmium, lead, nickel, chromium, and arsenic were detected in high concentrations.

ICP-OES Analysis Results
The ICP-OES analysis results of the seawater samples are given in Table 5.

Table 2. Depths and coordinates of sediment samples obtained from the study area.

Sample No	Sample Depth (m)	Sample Coordinates (WGS-84, 6⁰)	
		Y (East)	X (North)
ALT-2	36	707472.83 d E	4508710.82 m N
ALT-3	25	708515.39 d E	4510087.64 m N
ALT-4	38	708213.88 d E	4510457.64 m N
ALT-5	7	710247.21 d E	4511234.23 m N
ALT-6	16	709718.67 d E	4511605.90 m N
ALT-8	27	706038.94 d E	4512214.84 m N

Table 3: Elemental or component concentrations of sediment samples.

	Sample No.						
Analyte	ALT-2 (ppm)	ALT-3 (ppm)	ALT-4 (ppm)	ALT-5 (ppm)	ALT-6 (ppm)	ALT-8 (ppm)	Average (ppm)
CaO	40,621.49	58,697.86	45,406.62	64,947.69	79,182.22	47,954.05	56,135
Sc	10.461	10.2	9.131	9.968	5.911	10.102	9.295
TiO$_2$	8995.155	8769.926	8915.32	8601.837	7829.54	8338.949	8575.11
V	98.913	104.746	97.119	111.393	105.338	104.23	103.6
Cr	78.331	72.632	74.615	99.909	109.665	79.99	85.86
Mn	411.705	431.44	404.828	854.884	658.978	443.219	534.18
Fe$_2$O$_3$	55,926.19	56,848.45	54,912.61	62,113.25	56,197.16	53,046.84	56,507.4
Co	30.654	32.384	29.87	28.35	31.592	24.921	29.63
Ni	19.448	15.031	19.078	61.294	71.725	18.162	34.12
Cu	22.823	102.799	21.295	85.177	100.921	80.478	68.915
Zn	76.986	86.662	69.79	90.52	85.467	86.211	82.606
Ga	14.037	13.95	13.595	16.086	14.733	13.677	14.35
Ge	-0.384	-0.726	-0.764	-0.889	-0.567	-0.82	-0.69
As	8.316	9.053	8.518	13.151	13.852	10.698	10.598
Se	0.365	0.819	-0.111	0.506	0.723	-0.174	0.3546
Br	61.64	59.981	49.375	14.268	22.251	63.709	45.204
Rb	79.757	76.005	79.025	92.643	87.778	72.75	81.326
Sr	156.675	262.375	172.795	185.423	216.609	168.63	193.75
Y	22.201	22.751	21.878	22.687	21.243	21.552	22.052
Zr	165.937	142.874	162.801	131.104	128.387	151.585	147.11
Nb	8.488	7.683	8.324	9.414	8.269	7.31	8.248
Mo	1.351	1.803	0.958	2.034	1.266	1.776	1.5313
Ag	-3.65	0.176	-0.923	-2.938	-6.226	-4.271	-2.972
Cd	17.984	18.436	21.026	17.478	17.705	16.412	18.174
Sn	3.232	7.535	5.031	6.784	7.991	8.024	6.432
Sb	4.823	0.802	2.257	5.958	5.761	5.663	4.077
Te	1.602	1.833	3.579	5.085	2.874	6.441	3.569
I	33.411	11.124	19.371	8.253	10.169	16.282	16.435
Cs	-14.354	-14.608	-13.98	-8.719	-7.968	-10.845	-11.75
Ba	199.893	196.735	190.162	253.518	271.294	196.469	218.011
La	34.585	30.899	23.762	26.434	25.248	23.102	31.57
Ce	44.173	47.583	47.242	50.167	39.931	76.717	50.968
Nd	30.514	31.69	26.618	41.402	25.894	33.3	31.569
Sm	0.261	-0.097	2.515	2.114	5.143	5.516	2.5753

			Sample No.				
Analyte	**ALT-2 (ppm)**	**ALT-3 (ppm)**	**ALT-4 (ppm)**	**ALT-5 (ppm)**	**ALT-6 (ppm)**	**ALT-8 (ppm)**	**Average (ppm)**
Yb	-18.848	-16.25	-16.46	-18.191	-16.651	-15.65	-17.008
Hf	-1.643	-3.609	-2.504	-4.73	-5.945	-3.971	-3.734
Ta	2.255	-0.058	0.02	-0.053	1.736	-2.017	0.3138
W	58.402	56.682	66.785	24.912	45.015	47.011	49.801
Hg	-118.182	-98.352	-117.369	-87.526	-86.553	-91.486	-99.911
Tl	2.002	0.367	1.911	1.27	2.012	1.06	1.437
Pb	24.174	29.202	21.006	31.302	33.893	30.856	28.405
Bi	-0.024	0.391	-1.202	-0.343	0.057	-0.692	0.302
Th	9.018	8.369	8.417	11.242	10.405	8.088	9.256
U	3.424	3.864	4.418	3.582	3.503	3.492	3.713

Table 4: Anion results of the seawater sample (ppm).

Sample	Fluoride [F$^-$]	Chloride [Cl$^-$]	Nitrite [NO$_2^-$]	Bromide [Br$^-$]	Nitrate [NO$_3^-$]	Sulfate [SO$_4^{2-}$]	Phosphate [PO$_4^{3-}$]
Seawater	0.9 ±0.1	12,9806 ±0.3	<MDL	36.5 ±0.2	9445.6 ±4.7	1778.2 ±0.3	<MDL

Minimum measurable limits of anions: MDL$_{[F^-]}$ = 0.37 ppb; MDL$_{[NO2^-]}$ = 3.66 ppb; MDL$_{[Cl^-]}$ = 1.62 ppb; MDL$_{[SO4]}$ = 2.83 ppb; MDL$_{[Br^-]}$ = 2.50 ppb; MDL$_{[PO4^{3-}]}$ = 6.97 ppb; MDL$_{[NO3^-]}$ = 7.83 ppb. The ICP-OES technique was used to determine the heavy metal contents of the water samples taken from the region. Analysis results are listed in Table 4.

Table 5: Result of ICP-OES analysis in seawater samples.

Analyte	Analysis result: $\mu = X_{Ort} \pm 2$ Stdev	Analysis Method	Std. Dev.	LOQ Measurement Limit (µg/L)	Calibration Standard Solution Range (ppb)
Ca	252.6 ± 12.2 mg/L	ICP-OES	6.10	12.96	0.20/0.50/1.0/2.0 mg/L
Mg	822.7 ± 10.9 mg/L	ICP-OES	5.45	1,168	0.20/0.50/1.0/2.0 mg/L
Hg	< Ö.L.	ICP-OES/Hydride	0.07549	0.8480	5.0/10/20 µg/L
As	< Ö.L.	ICP-OES/Hydride	0.26361	1.700	5.0/10/20 µg/L
Sb	< Ö.L.	ICP-OES/ Hydride	0.06259	0.354	5.0/10/20 µg/L

Analyte	Analysis result: $\mu = X_{Ort} \pm 2$ Stdev	Analysis Method	Std. Dev.	LOQ Measurement Limit (μg/L)	Calibration Standard Solution Range (ppb)
Ag	< Ö.L.	ICP-OES / Stand.	0.4484	2.729	25/50/100
Al	< Ö.L.	ICP-OES / Stand.	1.9685	6.256	25/50/100
Co	< Ö.L.	ICP-OES /Stand.	0.2107	1.427	25/50/100
Cr	< Ö.L.	ICP-OES/ Stand.	0.2047	1.428	25/50/100
Cu	2.914 ± 1.4338 μg/L	ICP-OES/ Stand.	0.7169	2.914	25/50/100
Fe	15.19 ± 0.46 μg/L	ICP-OES/ Stand.	0.2303	1.235	25/50/100
Mn	1.073 ± 0.46 μg/L	ICP-OES/ Stand.	0.0331	0.456	25/50/100
Ni	< Ö.L.	ICP-OES/ Stand.	0.454	2.240	25/50/100
Pb	< Ö.L.	ICP-OES/ Stand.	1.361	8.216	25/50/100
V	< Ö.L.	ICP-OES/ Stand.	0.5349	2.890	25/50/100
Zn	5.472 ± 0.284 μg/L	ICP-OES/ Stand.	0.1420	0.7064	25/50/100
Ti	< Ö.L.	ICP-OES/ Stand.	0.0924	1.233	25/50/100
Th	21.26 ± 4.78 μg/L	ICP-OES/ Stand.	2.3900	3.798	25/50/100
U	< Ö.L.	ICP-OES/ Stand.	8.689	65.86	25/50/100
Mo	< Ö.L.	ICP-OES/ Stand.	1.1415	3.985	25/50/100
Cd	< Ö.L.	ICP-OES/ Stand.	0.0000	0.9810	25/50/100

Table 6: General quality criteria of seawater (38).

Various metals	Maximum allowable result (mg/L)
Copper	0.01
Cadmium	0.01
Chromium	0.1
Lead	0.1
Nickel	0.1
Zinc	0.1
Mercury	0.004
Arsenic	0.1
Ammonia	0.02

By using the ion chromatography system in conjunction with the ICP-OES system, a much more sensitive and qualified element analysis was performed. According to the results of elemental analysis with ICP-OES, Hg, As, Sb, Ag, Al, Co, Cr, Ni, Pb, V, Ti, U, Mo, and Cd elements were below the measurable limit. The fact that elements such as mercury and cadmium, which are toxic to living beings, are present in very low concentrations indicates that heavy metal pollution does not pose a risk to the ecosystem of the region. It is also seen that the seawater is rich in magnesium and calcium. The elements copper and zinc were determined to be above the maximum limits according to the Water Pollution Regulation.

SEM-EDAX Analysis Results

In this part of the study, count density and elemental weight percentages (wt%) of sediment samples were determined by SEM imaging and EDAX (Energy dispersive X-ray spectroscopy) analysis. During the analysis, the relationships to each other of element groupings selected differently for each sample were examined. The SEM acceleration voltage chosen was 20 kV for all images of the sediments in order to keep the working conditions standard for all samples. SEM images were obtained at 100 times magnification on Sample ALT-2 (Figures 3, 5, 7, 9, 11). Then, the densities of a few elements selected as a result of the EDAX analysis were calculated (Figures 4, 6, 8, 10, 12).
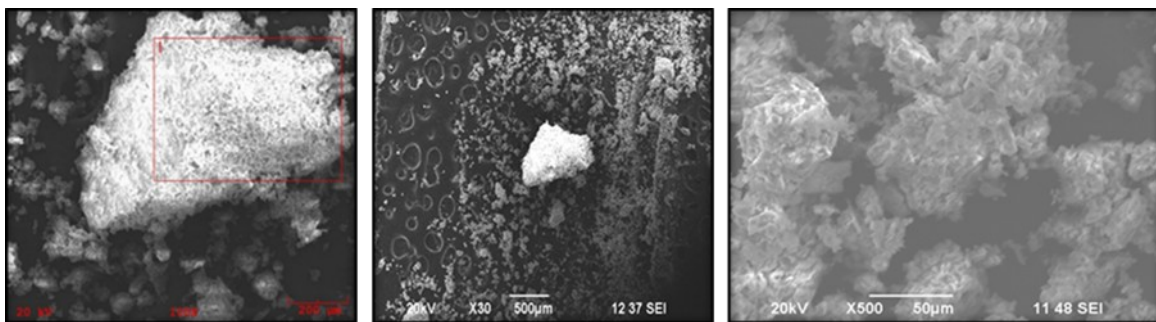
Figure 3: SEM images of Sample ALT-2.
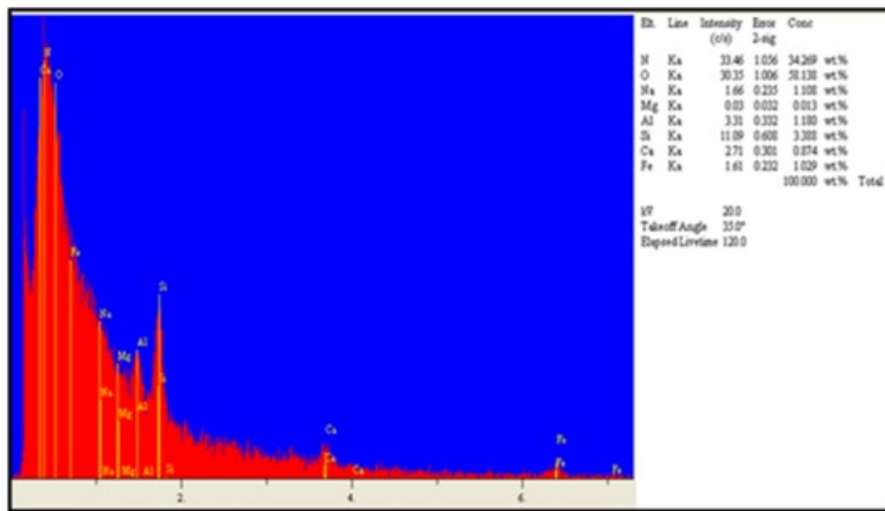
Figure 4: Results of EDAX spectrometric analysis of Sample ALT-2.

SEM images were obtained by 30X magnification of Sample ALT-3 (Figure 5). Then, in the EDAX analysis query, the densities of several selected elements were calculated (Figure 6).
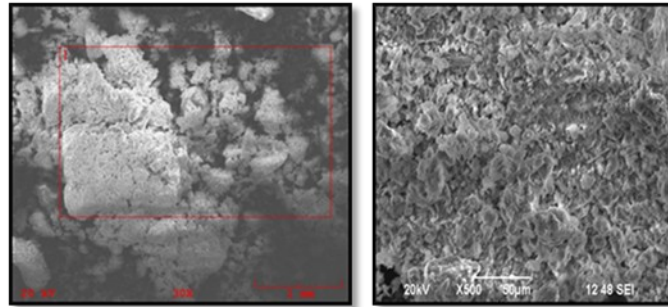
Figure 5: SEM images of Sample ALT-3.
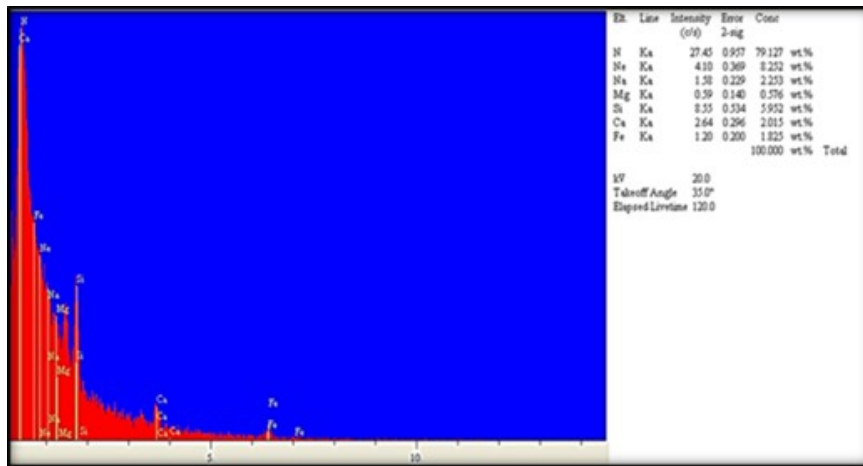
Figure 6: Results of EDAX spectrometric analysis of Sample ALT-3.

SEM images were obtained by magnifying Sample ALT-4 by 30 times (Figure 7). Then, in the EDAX analysis query, the densities of several selected elements were calculated (Figure 8).
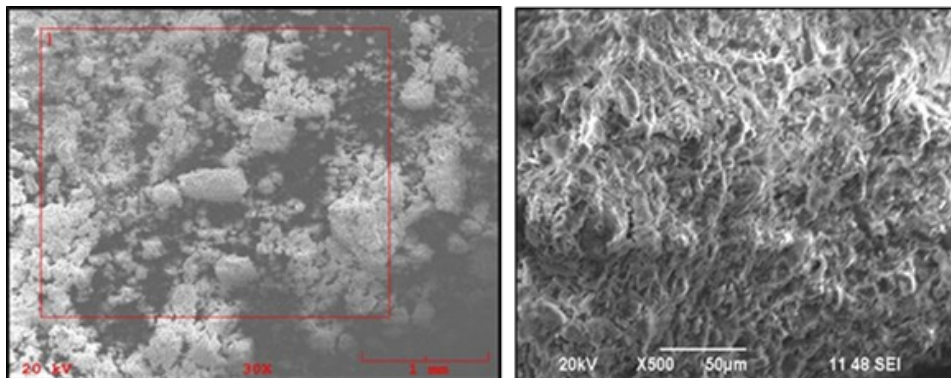
Figure 7: SEM images of Sample ALT-4.
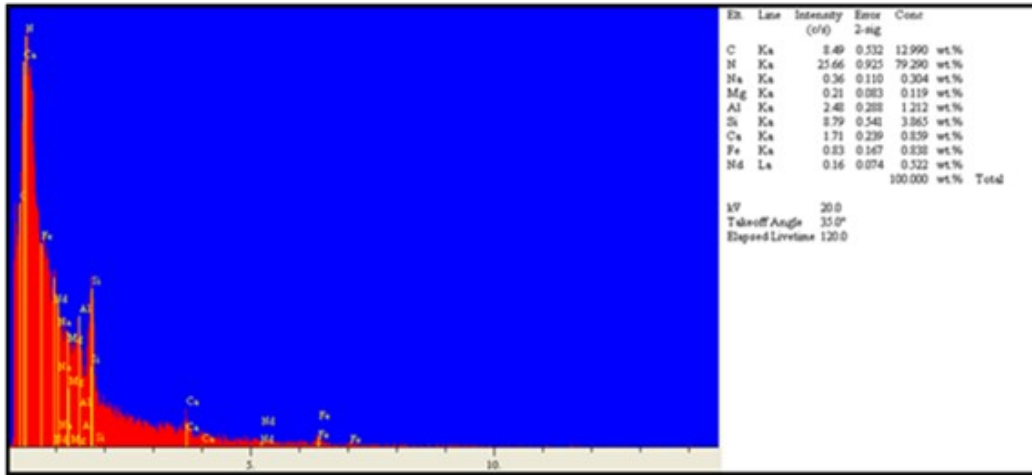
Figure 8: Results of EDAX spectrometric analysis of Sample ALT-4.

SEM images were obtained by 30X magnification of Sample ALT-5 (Figure 9). Then, in the EDAX analysis query, the intensities of several selected elements were calculated (Figure 10).
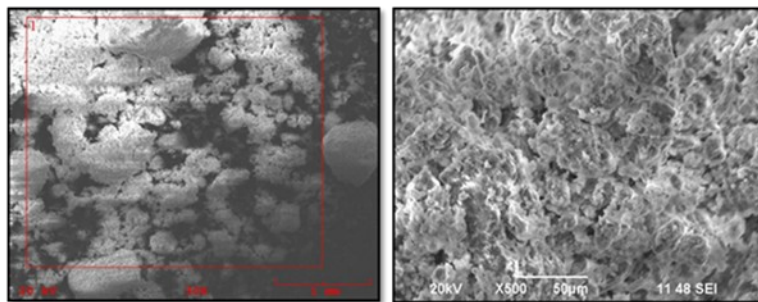
Figure 9: SEM images of Sample ALT-5.
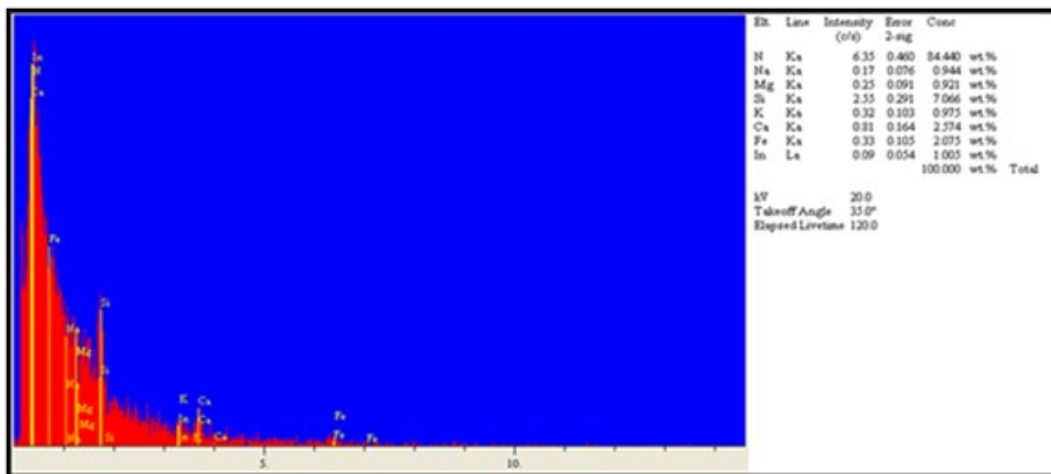
Figure 10: Results of EDAX spectrometric analysis of Sample ALT-5.

SEM images were also obtained by magnifying Sample ALT-6 by 30 times (Figure 11). Then, in the EDAX analysis query, the densities of several selected elements were calculated (Figure 12).
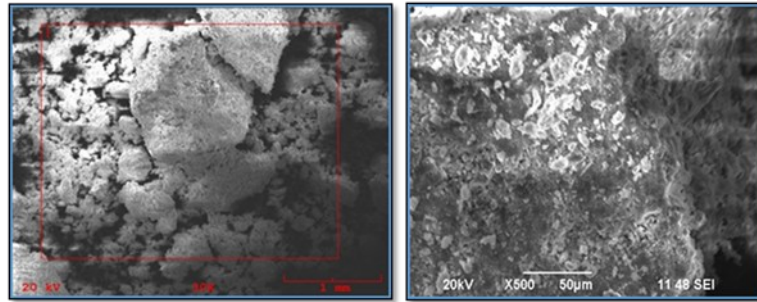
Figure 11: SEM images of Sample ALT-6.
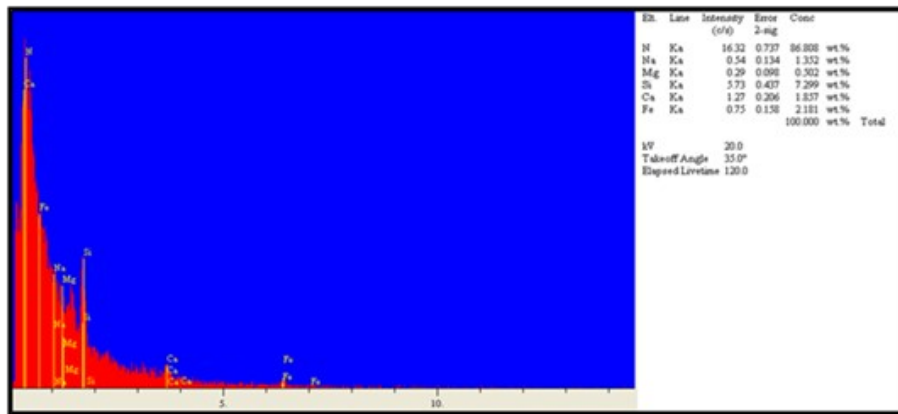
Figure 12: Results of EDAX spectrometric analysis of Sample ALT-6.

Finally, SEM images were obtained by 30X magnification of Sample ALT-8 (Figure 13). Then, as a result of the EDAX analysis, the densities of several selected elements were calculated (Figure 14).
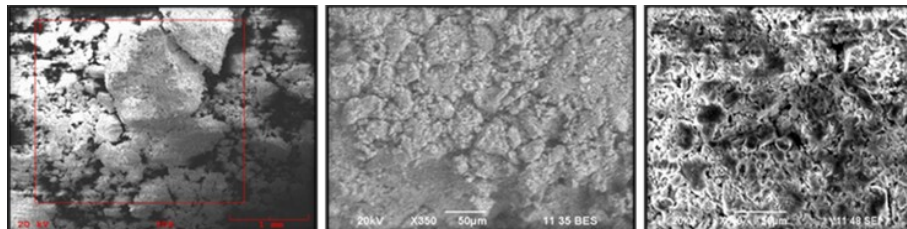
Figure 13: SEM images of Sample ALT-8.
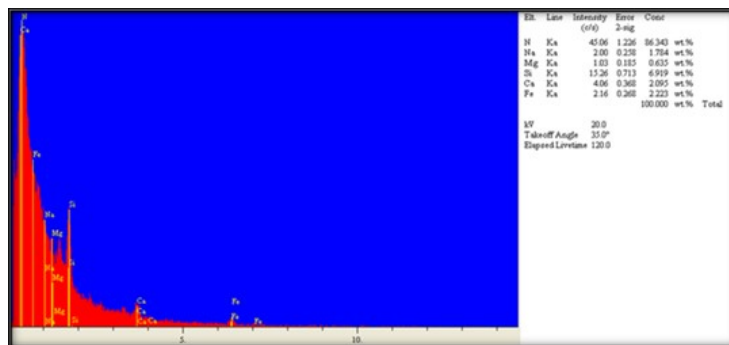
Figure 14: Results of EDAX spectrometric analysis of Sample ALT-8.

The selected elements in the analysis of Samples ALT-6 and ALT-8 were kept constant in the study and were compared for better interpretation of the SEM analysis. It was observed that the elemental abundance in Sample ALT-8 was higher. According to the analysis results, the element with the highest count was determined to be nitrogen (N). That situation is explained by the facts that some of the sediments are composed of organic materials and that the proteins in organic materials have nitrogen in their structures. Nitrogen also may have originated from the fertilizers used in the large agricultural lands in the hinterland of the study area. Another element that stands out in the results is silicon (Si). Silicon is one of the most abundant elements in nature, as 27.7% of the earth's crust by weight consists of silicon. Silicon, which is of vital importance for plants, is used in fertilizers to produce quality products on agricultural lands. It is thought that some of the silicon detected in the sediments may have originated from fertilizers (39). The percentage of the element neodymium (Nd) in the elemental composition of Sample ALT-4 sediment was investigated. Neodymium is one of the rare earth elements. According to the SEM results, the count was 0.16 c/s, while the XRF results were calculated as 0.22 c/s, so it is seen that the concentration results are almost in agreement with each other (40). When the SEM images were examined in terms of their topographic features, it was concluded that the sediments were not comprised of standard element compositions, which resulted in the images having complex structures.

CONCLUSION

In the study, heavy metal ratios were measured in sediment and seawater samples taken from the coasts of Altınova shipyards region of Yalova province. Heavy metal analyses were carried out in the sediment by XRF. In addition, the morphological and topographic properties of the sediments were obtained by SEM. Heavy metal contents in seawater were determined by ICP-OES. The study evaluated the extent to which the marine ecosystem may have been affected by the shipyard activities that have been actively carried out in the region for the past ten years. In future environmental studies, researches about this region will serve as a reference. Contamination on the coastline of the Altınova region originates from the regional sewage treatment plant, industrial zones, ferry piers, residences, a small number of restaurants, and, most importantly, the shipyards operating along the coast. In the qualitative analyses of the sediment content done with XRF, both elemental and compound determinations were made. As the sediments are both organic and inorganic deposits, the elements and compounds found in elemental analysis are quite diverse.

According to the results of the analysis, heavy metals that are toxic for humans (Arsenic poses a threat to the human body after 1 mg. Mercury and Cadmium are toxic even at very low concentrations such as 0.001 - 0.1 ppm. The lethal dose for mercury is in the range of 10 - 60 mg/kg. When lead is above 80mg/dl in the blood, it has toxicity (41).), such as cadmium (max 17.984 ppm), lead (max 31.302 ppm), nickel (max 71.725 ppm) and arsenic (max 13.852 ppm) were detected. By adding the ion chromatography system to the ICP-OES system, a much more sensitive and qualified element analysis was performed.

REFERENCES

1. Dökmeci AH. Concentrations of different macro and trace elements in sediment and fish samples from the coast of tekirdag marmara sea. Fresenius Environmental Bulletin. 2021;30(02A):1902–15.

2. Özden S, Aközcan S. Natural radioactivity measurements and evaluation of radiological hazards in sediment of Aliağa Bay, İzmir (Turkey). Arab J Geosci [Internet]. 2021 Jan [cited 2022 Oct 15];14(1):64. Available from: <URL>

3. Yümün ZÜ, Kam E. Effects of radionuclides on the recent foraminifera from the clastic sediments of the Çanakkale Strait-Turkey. Journal of African Earth Sciences [Internet]. 2017 Jul [cited 2022 Oct 15];131:179–82. Available from: <URL>

4. Yümün ZÜ, Önce M. Monitoring heavy metal pollution in foraminifera from the Gulf of Edremit (northeastern Aegean Sea) between Izmir, Balıkesir and Çanakkale (Turkey). Journal of African Earth Sciences [Internet]. 2017 Jun [cited 2022 Oct 15];130:110–24. Available from: <URL>

5. Yümün ZÜ, Kam E, Dinçer AR, Önce M, Yümün S. THE INVESTIGATION OF TOXIC ELEMENT POLLUTION AND RADIOACTIVITY ANALYSES OF MARINE SEDIMENTS IN THE GULF OF GEMLIK (BURSA, TURKEY). Appl Ecol Env Res [Internet]. 2021 [cited 2022 Oct 15];19(2):881–900. Available from: <URL>

6. Ranjan P, Ramanathan AL, Kumar A, Singhal RK, Datta D, Venkatesh M. Trace metal distribution, assessment and enrichment in the surface sediments of Sundarban mangrove ecosystem in India and Bangladesh. Marine Pollution Bulletin [Internet]. 2018 Feb [cited 2022 Oct 15];127:541–7. Available from: <URL>

7. Leivuori M, Joksas K, Seisuma Z, Kulikova I, Petersell V, Larsen B, et al. Distribution of heavy metals in sediments of the Gulf of Riga, Baltic Sea. Boreal Environment Research. 2000;5(2):165–85.

8. Yurkovskis A, Wulff F, Rahm L, Andruzaitis A, Rodriguez-Medina M. A Nutrient Budget of the Gulf of Riga; Baltic Sea. Estuarine, Coastal and Shelf Science [Internet]. 1993 Aug [cited 2022 Oct 15];37(2):113–27. Available from: <URL>

9. Masiol M, Facca C, Visin F, Sfriso A, Pavoni B. Interannual heavy element and nutrient concentration

trends in the top sediments of Venice Lagoon (Italy). Marine Pollution Bulletin [Internet]. 2014 Dec [cited 2022 Oct 15];89(1–2):49–58. Available from: <URL>

10. Kontas A, Uluturhan E, Alyuruk H, Darilmaz E, Bilgin M, Altay O. Metal contamination in surficial sediments of Edremit Bay (Aegean Sea): Spatial distribution, source identification and ecological risk assessment. Regional Studies in Marine Science [Internet]. 2020 Nov [cited 2022 Oct 15];40:101487. Available from: <URL>

11. N'guessan YM, Probst JL, Bur T, Probst A. Trace elements in stream bed sediments from agricultural catchments (Gascogne region, S-W France): Where do they come from? Science of The Total Environment [Internet]. 2009 Apr [cited 2022 Oct 15];407(8):2939–52. Available from: <URL>

12. El Nemr A, El-Said GF, Khaled A, Ragab S. Distribution and ecological risk assessment of some heavy metals in coastal surface sediments along the Red Sea, Egypt. International Journal of Sediment Research [Internet]. 2016 Jun [cited 2022 Oct 15];31(2):164–72. Available from: <URL>

13. Hussain T, Gondal MA. Monitoring and assessment of toxic metals in Gulf War oil spill contaminated soil using laser-induced breakdown spectroscopy. Environ Monit Assess [Internet]. 2007 Nov 22 [cited 2022 Oct 15];136(1–3):391–9. Available from: <URL>

14. Yang J, Cui Z, Dada OA, Yang Y, Yu H, Xu Y, et al. Distribution and enrichment of trace metals in surface marine sediments collected by the manned submersible Jiaolong in the Yap Trench, northwest Pacific Ocean. Marine Pollution Bulletin [Internet]. 2018 Oct [cited 2022 Oct 15];135:1035–41. Available from: <URL>

15. Sousa CAM, Delgado J, Szalaj D, Boski T. Holocene background concentrations and actual enrichment factors of metals in sediments from Ria Formosa, Portugal. Marine Pollution Bulletin [Internet]. 2019 Dec [cited 2022 Oct 15];149:110533. Available from: <URL>

16. Bakan G. Studies of environmental sedimentology and sediment quality criteria. Çevre Bilim ve Teknoloji. 2000;1(1):14–23.

17. Coban B, Balkıs N, Aksu A. Heavy metal levels in sea water and sediments of Zonguldak, TurkeyZonguldak deniz suyunda ve sedimentlerinde ağır metal seviyeleri. JOR. 2009;15(1).

18. Aydın B. Chemical Monitoring in Sediment According to Water Framework Directive and Evaluation of Turkey Applications. Presentation presented at; 2014; T.R. Ministry of Agriculture and Forestry.

19. Dinçer A, Dökmeci A. Concentrations of some heavy metals in the Gala Lake water, sediments and pollution sources. Journal of Environmental Protection and Ecology. 2006;7(4):759–65.

20. Okay OS, Tolun L, Tellı-Karakoç F, Tüfekçi V, Tüfekçi H, Morkoç E. İzmıt Bay (Turkey) Ecosystem after Marmara Earthquake and Subsequent Refinery Fire: the Long-term Data. Marine Pollution Bulletin [Internet]. 2001 May [cited 2022 Oct 15];42(5):361–9. Available from: <URL>

21. Morkoç E, Tüfekçi V, Okay O, Egesel L, Tüfekçi H, Orhon S. Izmit Bay Water Quality Characteristics. Gebze, Kocaeli: TÜBİTAK-MAM; 1995 p. 56.

22. Sur H, Apak R, Yüksek A, Altıok H, Taş S, Balkıs N, et al. Marmara Sea Pollution Monitoring Project Final Report. Ministry of Environment and Forestry; 2010 p. 60–3.

23. Bayrak K, Yümün ZÜ, Kam E. Determination of natural radiation levels in Izmit gulf Altınova shipyard area. J BIOL ENVIRON SCI. 2018;12(34):7–11.

24. Beken C, Aydöner C, Ediger D, Hüsrevoğlu S, Logicci M, Aydöner C, et al. Sea and Coast Determination of Water Quality Conditions and Classification (DEKOS) project final report. Gebze, Kocaeli: TÜBİTAK MAM; 2014.

25. Bergqvist R, Monios J, editors. Green ports: inland and seaside sustainable transportation strategies. Amsterdam, Netherlands ; Cambridge, MA, United States: Elsevier; 2019. 284 p.

26. Alkan G, İncaz S, Bakırcı E. Marine Pollution in International Legislation and Its Applications in Turkey. Istanbul, Turkey; 2005.

27. Klopott M. Restructuring of environmental management in Baltic ports: case of Poland. Maritime Policy & Management [Internet]. 2013 Sep [cited 2022 Oct 15];40(5):439–50. Available from: <URL>

28. Alnıpak S, Yorulmaz M. Sustainable Environmental Management in Our Ports: The Green Port Concept. In Istanbul, Turkey: Yıldız Technical University; 2019.
29. Baykal B, Öğüt A, Baykal M. Ships as Pollutant Source and Wastewater Management on Ships. In İzmir, Turkey;

30. Akanlar F. Investigation of Recycling of Waste Products in Shipbuilding [PhD Thesis]. [Istanbul, Turkey]: Yıldız Technical University; 2010.

31. Bayrak K. Investigation of Heavy Metal and Environmental Radioactivity in Marmara Sea, İzmit Bay, Altınova Shipyard Area [PhD Thesis]. [Istanbul, Turkey]: Yıldız Technical University;

32. Tanner PA, Leong LS, Pan SM. Contamination of Heavy Metals in Marine Sediment Cores from Victoria Harbour, Hong Kong. Marine Pollution Bulletin [Internet]. 2000 Sep [cited 2022 Oct 15];40(9):769–79. Available from: <URL>

33. Şimşek B, Ergın M, Evren M, Türkmen Ö, Palas S, Pehlıvan H, et al. GRAIN SIZE, TOTAL HEAVY MINERAL AND ELEMENT DISTRIBUTION AND CONTROL FACTORS OF CURRENT SEDIMENTS ON THE FLOOR OF HISARONU AND DATCA BAYS. Bulletin Of The Mineral Research and Exploration [Internet]. 2017 Apr 8 [cited 2022 Oct 15];154(154):59–82. Available from: <URL>

34. Baltas H, Kiris E, Sirin M. Determination of radioactivity levels and heavy metal concentrations in seawater, sediment and anchovy (Engraulis encrasicolus) from the Black Sea in Rize, Turkey. Marine Pollution Bulletin [Internet]. 2017 Mar [cited 2022 Oct 15];116(1–2):528–33. Available from: <URL>

35. Ghosh S, Prasanna VL, Sowjanya B, Srivani P, Alagaraja M, Banji D. Inductively coupled plasma–optical emission spectroscopy: a review. Asian J Pharm Ana. 2013;3(1):24–33.

36. Marathe R. XRD and SEM analysis of tapti river sediment: a case study. Archives of Applied Science Research. 2012;4(1):78–84.

37. Kucuksezgin F, Kontas A, Altay O, Uluturhan E, Darılmaz E. Assessment of marine pollution in Izmir Bay: Nutrient, heavy metal and total hydrocarbon concentrations. Environment International [Internet]. 2006 Jan [cited 2022 Oct 15];32(1):41–51. Available from: <URL>

38. Anonymous. Water Quality Control Regulation [Internet]. 2004. Available from: <URL>

39. Ma JF, Yamaji N. Silicon uptake and accumulation in higher plants. Trends in Plant Science [Internet]. 2006 Aug [cited 2022 Oct 15];11(8):392–7. Available from: <URL>

40. Yüksel C, Ankarali S, Aslan Yüksel N. The Use of Neodymium Magnets in Healthcare and Their Effects on Health. North Clin Istanbul [Internet]. 2018 [cited 2022 Oct 15];5(3):268–73. Available from: <URL>

41. Özbolat G, Tuli A. Effects of heavy metal toxicity on human health. Archives Medical Review Journal. 2016;25(4):502–21.

RESEARCH ARTICLE

Chemical Composition and Repellent Activity of Methyl Cinnamate-Rich Basil (*Ocimum basilicum*) Essential Oil

Azhari H. Nour¹, Abeer A. Idris¹, Omer A. Ishag¹*, Abdurahman H. Nour²

¹International University of Africa (IUA), Department of Applied and Industrial Chemistry, Khartoum, 12223, Sudan.
²Universiti Malaysia Pahang (UMP), College of Engineering Technology, Gambang, 26300, Malaysia.

Abstract: Basil (*Ocimum basilicum* L.) is an important culinary herb and essential oil source widely recognized worldwide. The oil of the plant is beneficial for medicinal uses, and it has many biological activities such as insect repellent, larvicidal, and bactericidal. This study aimed to investigate basil's essential oil for its chemical composition and repellent activity. The essential oil of basil was extracted from fresh leaves by steam distillation method, and the chemical composition of the oil was determined by using GC/MS. Also, the repellent activity of the oil was tested against American cockroaches. Ebeling Choice-Box test with a little modification used in repellence test. The obtained results of chemical composition revealed that the amount of the oil contained forty-one chemical constituents (~97.1%); the major constituents were methyl cinnamate (25.3%), linalool (19.1%) and estragole (12.3%) as the major oxygenated monoterpenes. While α-bergamoten (5.3%), germacrene (4.6%), γ-cadinene (2.8%), and β-elemene (2.4%) were the main compounds in sesquiterpene hydrocarbons. Whereas, in oxygenated sesquiterpenes, Tau-cadinol (4.3%) was an important compounds and ocimene the highest compound in monoterpene hydrocarbons. The obtained results also indicated that the essential oil had good activity against the P. American, at a 100% concentration of oil; the repellence reaches 100% after 1 h. The IC50 and IC90 values of basil essential oil against P. Americans were 53.0 and 83.0%, respectively. The major compound methyl cinnamate which exists in basil essential oil is a very important compound and could be used in a wide area of industrial applications as repellent products, medicinal products, and cosmetics.

INTRODUCTION

Natural products, especially plants, have served humanity as an important source for many uses. Humans use plants or their derivatives for many benefits, such as foods and medicines (1), antioxidant (2), rhizoremediation (3), fertilizers and pesticides (4), lipid-lowering potential, anti-malarial, anti-ulcer, antipyretic, anti-cancer, and anti-proliferation (5). The genus *Ocimum*, of *Ocimum basilicum* (Family: Lamiaceae formerly Labiatae), called basil has long been known worldwide as a diverse, rich source of essential oils and a significant culinary herb. Basils exhibit great variation in both morphology and diversity, such as inflorescence, leaf, and essential oil components (6). The

taxonomy of *O. basilicum* more complicated due to the numerous varieties, cultivars and chemotypes within the species that do not vary significantly in morphology. The essential oil composition was utilized to characterize the diversity among the most economically important *Ocimum* species (7). The essential oils of basils are used as a food flavoring, medicines, and in the perfumery industry. In addition, previous studies have reported very interesting biological activities of these oils, such as being bactericidal (8), mosquito repellent (9) and larvicidal (10), etc. Besides, it was used in traditional medicine to sooth pain, treat vomiting and stress, and as an insect repellent (11). The leaves and flower of basil are utilized in folk medicine as a tonic and vermifuge, also basil tea is good for treating

dysentery, nausea, and flatulence, its oil is useful for the mitigation of spasm, rhinitis, mental fatigue, cure of wasp stings and snake bites (12,13). It has used as a folk medicine for boredom and convulsion. Basil heals headache, improves digestion, and as well helpful for toothache, earache, and for curing epistaxis when used with camphor. The plant infusion is effective in cephalic, gouty joints, fever, otitis, and snakebite(12,14). In addition, it is efficient in remediation of stomach problems, fever, cough, gout, and given internally to cure cystitis, nephritis and interior piles. The plant is also used to keep away insects and snakes (12). The use of chemically synthetic repellents of insect control may result in disturbing natural ecosystems and resulted in the development of resistance to insecticides, and even adverse impact on non-target organisms. Hence, the idea of using natural repellent products as an alternative to develop new eco-friendly repellents could be a friendly solution for the reduction of adverse effects on the environment and human health. Therefore, this study aimed to investigate the chemical composition and repellent activity of *O. basilicum* essential oil.

MATERIALS AND METHODS

Plant Material
The fresh leaves of *O. basilicum* were collected in October 2017 from the Ministry of Agriculture and Forestry, General Directorate of Horticultural Production, Department of Medicinal and Aromatic Plants, Khartoum, Sudan.

Extraction of Essential oils
The fresh leaves of *O. basilicum* are used to obtain their essential oils. The extraction was conducted on a laboratory scale by Steam Distillation (SD) unit as the method described by Mesomo et al. (15) with slight modification. In brief, 100 g of fresh *O. basilicum* leaves were steam distilled for 4 h. Then, the extracted essential oils were dried over anhydrous sodium sulfate, filtered, stored in hermetically closed dark bottles, and kept at -4 °C for further studies. The percentage of extracted oils (v/w %) from the SD method was calculated according to the following formula:

$$\text{The Essential oil} \ (\%) = \frac{\text{volume of oil}}{\text{weight of sample}} \ \text{X } 100$$

Gas chromatography-mass Spectrometry Analysis
The chemical composition of extracted *O. basilicum* essential oils was determined using an Agilent 7890A GC-MS instrument equipped with column nonpolar capillary DB-1 of 100% dimethyl-polysiloxane (30 m, 0.25 mm i.d, film thickness 0.25 μm) and mass spectrophotometric detector. The carrier gas was helium with a flow rate of 1 mL/min, and the injector mode was splitless with an injection volume of 1μL/L and an injection temperature of 250 °C. The temperature program was 60 °C for 3 min, 240 °C at the rate of 3 °C/min, and held for 10 min.

The run time was 93 min, and the lab data system was NIST Library Chem Station software.

Cockroaches Collection and Repellent Test
About 600 adults (male and female) of American cockroaches (*P. Americana*) were collected from the University of Khartoum, Sudan. They were kept in boxes and reared in the laboratory by feeding on water and biscuits. The healthy nymphs and adults (male & female) cockroaches were used in this repellence test. The temperature was maintained at 28 ± 5 °C. The Ebeling choice box test, which describe by Ebeling (16) with some modification used in this experiment. The *O. basilicum* leaves essential oil was prepared in various concentrations (5, 25, 50, 75, and 100 v/v %) by dissolving in 1% DMSO. Ten adult and nymph cockroaches (male and female) were then released into the central choice box (untreated zone). Then, the choice boxes (treated and untreated location) were exposed to a photoperiod of 27 °C for 72 hrs. 1% DMSO and naphthalene were used as negative and positive controls, respectively. The cockroaches at the treated and untreated zone were carefully observed and counted for 0, 3, 6, 9, 12, 24, 48, and 72 hrs. of treatment. Each treatment with a different concentration was conducted in three replicates. The percentage of repellency is calculated as follows:

$$\text{Repellency \%} = 100 - \left(\frac{T}{N} \ \text{X } 100 \ \%\right)$$

Where T is the number of cockroaches located at the treated zone, and N stands for the total number (ten heads) of cockroaches been used in the repellency test. The mean percentage of the repellence was then calculated from the values obtained in three replicates.

Statistical Analysis
Statistical analysis of the obtained results conducted using MS Excel (2007) – version 12.0.4518.1014. The results performed in three repetitions and expressed as mean ± standard deviation.

RESULTS AND DISCUSSION

Yield of essential oil
The essential oil of the collected *O. basilicum* leaves was extracted using the steam distillation method, and the percentage yield of the oil was expressed on a fresh leaf weight basis (v/w %). The oil content was found to be 0.78%, and the color is light yellow with a camphor-like smell. Previously, reported *O. basilicum* had a yield of 1.56% essential oil with yellowish green color (17) and also a yield of 1.98 ± 0.01% with a pale yellow oil (18). In addition, a yield of 0.65 to 1.90% (19) and 0.9–1.7% essential oil (20), where these results were higher than the obtained results in this study. Whereas, the yields were found to be 0.05 to 0.55% (19), 0.6% (20) and 0.28% essential oil too (21); where these results were lower than the result obtained in this study. The variation in the results may be due to climate

and soil conditions, but the oil content is still in the range obtained in the previous studies.

Chemical Composition of Essential Oil

The chemical composition of the extracted *O. basilicum* essential oils was determined using GC-MS instrument and the obtained results were shown in Table 1. The obtained results were indicated forty-one chemical constituents (~97.1%); the major constituents were methyl cinnamate (25.3%), linalool (19.1%) and estragole (12.3%) as the major oxygenated monoterpenes. While sesquiterpenes hydrocarbons, α-bergamoten (5.3%), germacrene (4.6%), γ-cadinene (2.8%) and β-elemene (2.4%) were major constituents. Whereas, in oxygenated sesquiterpenes, Tau-cadinol (4.3%) was major

constituent and ocimene the major constituent in monoterpene hydrocarbons. In previous studies reported basil essential oils consisted of linalool were the most abundant component (56.7-60.6%), followed by epi-α-cadinol (8.6-11.4%), α-bergamotene (7.4-9.2%) and γ-cadinene (3.2-5.4%) (21,22). In addition, a total of 17 compounds were identified with linalool (70.44%) as the major compound, followed by an estragole (14.4%), tau-cadinol (4.1%) and α-bergamoten (3.7%) (23). Also reported the dominant components were methyl chavicol (81.8%), β-(*E*)-ocimene (2.9%), α -(*E*)-bergamotene (2.5 %), α -epi-cadinol (2.1%), 1,8-cineole (1.6%), methyl eugenol (1.1%) and camphor (1.1%) (24).

Table 1: Chemical composition of essential oil.

Compound	Formula	Area %
Monoterpene hydrocarbons		
alpha-Pinene	$C_{10}H_{16}$	0.2
Camphene	$C_{10}H_{16}$	0.0
Sabinene	$C_{10}H_{16}$	0.3
Pseudopinen	$C_{10}H_{16}$	0.5
Myrcene	$C_{10}H_{16}$	0.9
Limonene	$C_{10}H_{16}$	0.5
Ocimene	$C_{10}H_{16}$	1.5
Total monoterpene hydrocarbons		**3.9**
Oxygenated monoterpenes		
Cineole	$C_{10}H_{18}O$	5.6
Sabinene hydrate	$C_{10}H_{18}O$	0.3
Fenchone	$C_{10}H_{16}O$	0.9
Linalool	$C_{10}H_{18}O$	19.1
Fenchol	$C_{10}H_{18}O$	0.6
(a)	$C_{10}H_{14}O_2$	0.2
Camphor	$C_{10}H_{16}O$	0.4
Isoborneol	$C_{10}H_{18}O$	0.3
Terpinenol-4	$C_{10}H_{18}O$	0.1
Terpineol schlethin	$C_{10}H_{18}O$	0.9
Estragole	$C_{10}H_{12}O$	12.3
Beta-Citral	$C_{10}H_{16}O$	0.1
Geraniol	$C_{10}H_{18}O$	1.2
Alpha-Citral	$C_{10}H_{16}O$	0.2
Methyl cinnamate	$C_{10}H_{10}O_2$	25.3
3-Allylguaiacol	$C_{10}H_{12}O_2$	1.0
8-Hydroxylinalool	$C_{10}H_{18}O_2$	0.04
Total oxygenated monoterpenes		**68.5**
Sesquiterpene hydrocarbons		
Elixene	$C_{15}H_{24}$	0.3
Alpha-Ylangene	$C_{15}H_{24}$	0.1
Copaene	$C_{15}H_{24}$	0.2
b-Elemene	$C_{15}H_{24}$	2.4
Caryophyllene	$C_{15}H_{24}$	1.0
Alpha-Bergamoten	$C_{15}H_{24}$	5.3
(b)	$C_{15}H_{24}$	0.1
Beta-Farnesene	$C_{15}H_{24}$	0.2
Humulene	$C_{15}H_{24}$	0.6
Beta-Cubebene	$C_{15}H_{24}$	0.6
Germacrene	$C_{15}H_{24}$	3.6
Alpha-Bulnesene	$C_{15}H_{24}$	1.4
Gamma-Cadinene	$C_{15}H_{24}$	2.8
Total sesquiterpene hydrocarbons		**19.1**
Oxygenated sesquiterpenes		
Beta-Elemol	$C_{15}H_{26}O$	0.5

Cubedol	$C_{15}H_{26}O$	0.8
Tau-Cadinol	$C_{15}H_{26}O$	4.3
Total oxygenated sesquiterpenes		**5.5**
Others		**2.9**

(a): Oxirane,2-(hexyn-1-yl)-3-methoxymethylene, **(b):** Cis-Muurola-3,5-diene

The qualitative and quantitative composition of essential oils was quite different: *O. basilicum* var. purpureum essential oil contained 57.3% methyl-chavicol (estragol); *O. basilicum* var. thyrsiflora oil had 68.0% linalool; the main constituents of *O. citriodorum* oil were nerol (23.0%) and citral (20.7%) (25). Moreover, claimed the major compounds were: linalool (32.8%), linalyl acetate (16.0%), elemol (7.4%), geranyl acetate (6.2%), myrcene (6.1%), allo-ocimene (5.0%), *α*-terpineol (4.9%), (*E*)-*β*-ocimene (3.7%) and neryl acetate (3.5%) (18). Thus, the most of previously mentioned compounds were present in the obtained results.

The obtained results in Table 1 also showed that the total monoterpenes represents 72.4% of the oil, the ratio is hydrocarbon 3.9% and oxygenated monoterpene was 68.5%. While the total sesquiterpenes were 24.6%, representing 19.1% sesquiterpene hydrocarbon and 5.5% are oxygenated sesquiterpenes. The distribution of mono and sesquiterpenes in *O. basilicum* essential oil was shown in Figure 1. Previously, reported samples collected in winter were found to be richer in oxygenated monoterpenes (68.9%), compared to those collected in summer where were higher in sesquiterpene hydrocarbons (24.3%) (21,22).

Figure 1: Distribution of mono and sesquiterpenes in *O. basilicum* essential oil.

Repellent Activity of Essential Oil
Repellency activity of *O. basilicum* essential oil (100%) against A. cockroaches after 72 hrs. of treatment and the IC50 and IC90 values against A. cockroaches after 24 hrs. of treatment was tested in this study and the obtained result showed in Figure 2 and Figure 3. The obtained results indicated that the essential oil had a good activity against the cockroaches, at a 100% concentration of oil; the repellence reaches 100% up to 1 h of exposure; whereas the repellency reaches 80.0% for more than 4 h and more than 70.0% after 10 h. The IC50 and IC90 values of *O. basilicum* essential oil against cockroaches were 53.0% and 83.0%, respectively. Yoon (26) was tested the repellent efficacies of certain components and their obtained results indicated that the efficacies were varied with different doses and the cockroach species, and the major components responsible for the repellent activity of the essential oils were limonene, β-pinene and γ-terpinene.

Figure 2: Repellency activity of *O. basilicum* essential oil (100%) against cockroaches after 72 h of treatment.

Figure 3: The IC50 and IC90 values of *O. basilicum* essential oil against cockroaches after 24 h of treatment.

El-Seedi et al. (27) claimed that the *O. basilicum* oil with major compounds of 1,8-cineole, camphor, linalool, 4-terpineol, borneol, and carvone was the most repellent oil among many oils tested against cockroach. In addition a number of compounds were showed repellent activity against insects such as: linalool (28), Estragole (29), ocimene (30), cineole (31), -α-pinene (32), camphene (100%) against German cockroaches (33), camphor (34), limonene (35), sabinene (36), terpinene 4-ol (35), myrcene (34), geraniol was toxic to the cockroaches by contact or injection and repellency (32). Moreover, caryophyllene (34), fenchone (29), *β*-citral and *α*-citral (37), *β*-elemene (38), *β*-cubebene, fenchol, *α*-bergamoten, *α*-guaiene and *β*-farnesene (32), *α*-ylangene, *β*-elemol and *γ*-cadinene (35), germacrene (39), humulene (35), *β*-bulnesene (38),

β-cubebene (32), verbenone (33) and α-copaene (32). Nour et al. investigated the repellent activity of *Cyperus rotundus* rhizomes essential oil against American cockroaches; his obtained results indicated that the IC50 and IC90 values of *C. rotundus* rhizomes essential oil against American cockroaches were 57 and 88%, respectively (40). Sittichok et al. evaluated the repellent activity of the essential oils derived from Cymbopogon citratus (lemon grass), Cymbopogon nardus (citronella grass) and Syzygium aromaticum (clove) against adult American cockroach; in his results all of the essential oils in ethyl alcohol showed higher percent repellency (81-100%) against P. americana than all of the essential oils in soybean oil (66-84% repellency), The essential oil from C. citratus in ethyl alcohol exhibited the highest repellency (100%)

among the tested repellents and naphthalene (83% repellency)(41). The repellent activity of essential oil in this study could be due to the presence of compounds that had already demonstrated repellent activity against certain insects, including cockroaches.

CONCLUSION

The obtained results in this study indicated that the *O. basilicum* essential oil contained various chemical constituents include monoterpenes, oxygenated monoterpenes, sesquiterpenes, and oxygenated sesquiterpenes. Also indicated that oil had a repellent activity, and it could be attributed to the presence of compounds that have already demonstrated their repellent activity towards certain insects, including cockroaches.

CONFLICTS OF INTEREST

The authors declare no conflicts of interest exist.

ACKNOWLEDGMENTS

The authors are grateful to the laboratory staff of department of applied and industrial chemistry, international university of Africa for their supports.

REFERENCES

1. Che C-T, Zhang H. Plant natural products for human health. International journal of molecular sciences. 2019 Jan; 20(4):830 - 4. Available from: <URL>.

2. Saeed Z, Iqbal S, Younas U, Bukhari SM, Zaidi A. Variation in antioxidant potential of Vigna unguiculata grown in pure and amended soil. Kuwait Journal of Science. 2020;47(3), 2-14. Available from: <URL>.

3. Ubogu M, Odokuma LO. Growth and lolerance evaluation of selected plants to crude oil contamination for rhizoremediation potentials in the Niger Delta. Kuwait Journal of Science. 2019;46(4), 93-103. Available from: <URL>.

4. Elmi AO, Anderson AK, Albinali AA. Demand for organic food and public perception in the state of Kuwait: A Comparison of conventional and organic vegetable produce quality. Kuwait Journal of Science. 2019;46(4), 120-127. Available from: <URL>.

5. Lim PJ, Gan CS, Yusof A. Lipid lowering effect of Eurycoma longifolia Jack aqueous root extract in hepatocytes. Kuwait Journal of Science. 2019;46(2), 52-58. Available from: <URL>.

6. Telci I, Bayram E, Yılmaz G, Avcı B. Variability in essential oil composition of Turkish basils (Ocimum basilicum L.). Biochemical Systematics and Ecology. 2006;34(6):489–97. Available from: <URL>.

7. Abduelrahman A, Elhussein S, Osman NA, Nour A. Morphological variability and chemical composition of essential oils from nineteen varieties of Basil (Ocimum basilicum L.) growing in Sudan. International Journal of Chemical Technology. 2009;1(1):1–10. Available from: <URL>.

8. Nour A, Elhussein S, Osman N, Ahmed N, Abduelrahman A, Yusoff M. Antibacterial activity of the essential oils of Sudanese accessions of basil (Ocimum basilicum L.). Journal of Applied Sciences. 2009;9(23):4161–7. Available from: <URL>.

9. Nour A, Elhussein S, Osman N. Repellent activities of the essential oils of four Sudanese accessions of basil (Ocimum basilicum L.) against Anopheles mosquito. Journal of Applied Sciences. 2009;9(14):2645–8.

10. Nour AH, Elhussein SA, Osman NA, Yusoff M. A study of the essential oils of four Sudanese accessions of basil (Ocimum basilicum L.) against Anopheles mosquito larvae. American Journal of Applied Sciences. 2009;6(7):1359–63. Available from: <URL>.

11. Aidaross M, Kohob W, Galalb M. Evaluation of repellent and larvicidal activity of Ocimum basilicum L. and Cymbopogon citratus DC. Against Culex quinquefasciatus. Inti Chern. Pharm. Med J. 2005;2(2):243–6. Available from: <URL>.

12. Ch MA, Naz SB, Sharif A, Akram M, Saeed MA. Biological and pharmacological properties of the sweet basil (Ocimum basilicum). Journal of Pharmaceutical Research International. 2015;330–9. Available from: <URL>.

13. Baytop T. Therapy with medicinal plants in Turkey (Past and Present),(p. 189) Publication no 325. Istanbul University, Istanbul. 1984.

14. Kīrtikara KR, Basu BD, An I, Blatter E, Caius JF, Mhaskar K. Indian medicinal plants, with illustrations. 2001. Available from: <URL>.

15. Mesomo MC, Corazza ML, Ndiaye PM, Dalla Santa OR, Cardozo L, Scheer A de P. Supercritical CO2 extracts and essential oil of ginger (Zingiber officinale R.): Chemical composition and antibacterial activity. The Journal of Supercritical Fluids. 2013 Aug 1;80:44–9. Available from: <URL>.

16. Ebeling W, Wagner R, Reierson DA. Influence of repellency on the efficacy of blatticides. I. Learned modification of behavior of the German cockroach. Journal of Economic Entomology. 1966;59(6):1374–88. Available from: <URL>.

17. Bilal A, Jahan N, Ahmed A, Bilal SN, Habib S, Hajra S. Phytochemical and pharmacological studies on Ocimum basilicum Linn-A review. International Journal of Current Research and Review. 2012;4(23), 73-83. Available from: <URL>.

18. Hadj Khelifa L, Brada M, Brahmi F, Achour D, Fauconnier ML, Lognay G. Chemical composition and antioxidant activity of essential oil of Ocimum basilicum leaves from the northern region of Algeria. Journal of Herbal Medicine. 2012;1(2), 53–8. Available from: <URL>.

19. Beatovic D, Krstic-Milosevic D, Trifunovic S, Siljegovic J, Glamoclija J, Ristic M, et al. Chemical composition, antioxidant and antimicrobial activities of the essential oils of twelve Ocimum basilicum L. cultivars grown in Serbia. Records of Natural Products. 2015;9(1), 62-75. Available from: <URL>.

20. Koroch AR, Simon JE, Juliani HR. Essential oil composition of purple basils, their reverted green varieties (Ocimum basilicum) and their associated biological activity. Industrial crops and products. 2017;107,526–30. Available from: <URL>.

21. Hussain AI, Anwar F, Sherazi STH, Przybylski R. Chemical composition, antioxidant and antimicrobial activities of basil (Ocimum basilicum) essential oils depends on seasonal variations. Food chemistry. 2008;108(3), 986–95. Available from: <URL>.

22. Rubab S, Hussain I, Khan B, Unar A, Abbas K, Khichi Z, et al. Biomedical description of Ocimum basilicum L. Journal of Islamic International Medical College. 2017;12(1), 57–69. <URL>.

23. Nawaz H, Hanif MA, Ayub MA, Ishtiaq F, Kanwal N, Rashid N, et al. Raman spectroscopy for the evaluation of the effects of different concentrations of Copper on the chemical composition and biological activity of basil essential oil. Spectrochimica Acta Part A: Molecular and Biomolecular Spectroscopy. 2017;185, 130–8. Available from: <URL>.

24. Pripdeevech P, Chumpolsri W, Suttiarporn P, Wongpornchai S. The chemical composition and antioxidant activities of basil from Thailand using retention indices and comprehensive two-dimensional gas chromatography. Journal of the Serbian Chemical Society. 2010;75(11):1503–13. Available from: <URL>.

25. Avetisyan A, Markosian A, Petrosyan M, Sahakyan N, Babayan A, Aloyan S, et al. Chemical composition and some biological activities of the essential oils from basil Ocimum different cultivars. BMC complementary and alternative medicine. 2017;17(1):1–8. Available from: <URL>.

26. Yoon C, Kang SH, Yang JO, Noh DJ, Indiragandhi P, Kim GH. Repellent activity of citrus oils against the cockroaches Blattella germanica, Periplaneta americana and P. fuliginosa. Journal of Pesticide Science. 2009;34(2), 77–88. Available from: <URL>.

27. El-Seedi HR, Khalil NS, Azeem M, Taher EA, Göransson U, Pålsson K, et al. Chemical composition and repellency of essential oils from four medicinal plants against Ixodes ricinus nymphs (Acari: Ixodidae). Journal of medical entomology. 2014;49(5), 1067–75. Available from: <URL>.

28. Campos EV, Proença PL, Oliveira JL, Melville CC, Della Vechia JF, De Andrade DJ, et al. Chitosan nanoparticles functionalized with β-cyclodextrin: a promising carrier for botanical pesticides. Scientific reports. 2018;8(1), 1–15. Available from: <URL>.

29. Bedini S, Bougherra HH, Flamini G, Cosci F, Belhamel K, Ascrizzi R, et al. Repellency of anethole-and estragole-type fennel essential oils against stored grain pests: the different twins. Bull Insectol. 2016;69(1), 149–57. Available from: <URL>.

30. Dube FF, Tadesse K, Birgersson G, Seyoum E, Tekie H, Ignell R, et al. Fresh, dried or smoked, Repellent properties of volatiles emitted from ethnomedicinal plant leaves against malaria and yellow fever vectors in Ethiopia. Malaria Journal. 2011;10(1), 1–14. Available from: <URL>.

31. Cansian R, Astolfi V, Cardoso R, Paroul N, Roman S, Mielniczki-Pereira A, et al. Insecticidal and repellent activity of the essential oil of Cinnamomum camphora var. linaloolifera Y. Fujita (Ho-Sho) and Cinnamomum camphora (L.) J Presl. var. hosyo (Hon-Sho) on Sitophilus zeamaisMots.(Coleoptera, Curculionedae). Revista Brasileira de Plantas Medicinais. 2015;17(4), 769–73. Available from: <URL>.

32. Azhari H, Yap SS, Nour AH. Extraction and chemical compositions of ginger (Zingiber officinale Roscoe) essential oils as cockroaches repellent. Australian Journal of Basic and Applied Sciences. 2017;11(3), 1–8.

33. Athuman I, Innocent E, Machumi F, Augustino S, Kisinza W. Repellency properties of oils from plants traditionally used as mosquito repellents in Longido district, Tanzania. Int. J. Mosq. Res. 2016; 3(1): 04-08. Available from: <URL>.

34. Maia MF, Moore SJ. Plant-based insect repellents: a review of their efficacy, development and testing. Malaria journal. 2011;10(1), 1–15. Available from: <URL>.

35. Carroll JF, Tabanca N, Kramer M, Elejalde NM, Wedge DE, Bernier UR, et al. Essential oils of Cupressus funebris, Juniperus communis, and J. chinensis (Cupressaceae) as repellents against ticks (Acari: Ixodidae) and mosquitoes (Diptera: Culicidae) and as toxicants against mosquitoes. Journal of Vector Ecology. 2011;36(2), 258–68. Available from: <URL>.

36. Benelli G, Flamini G, Canale A, Molfetta I, Cioni PL, Conti B. Repellence of Hyptis suaveolens whole essential oil and major constituents against adults of the granary weevil Sitophilus granarius. Bulletin of Insectology. 2012;65(2), 177–83.

37. Baldacchino F, Tramut C, Salem A, Liénard E, Delétré E, Franc M, et al. The repellency of lemongrass oil against stable flies, tested using video tracking. Parasite. 2013;20, 21. Available from: <URL>.

38. Gokulakrishnan J, Kuppusamy E, Shanmugam D, Appavu A, Kaliyamoorthi K. Pupicidal and repellent activities of Pogostemon cablin essential oil chemical compounds against medically important human vector mosquitoes. Asian Pacific Journal of Tropical Disease. 2013;3(1), 26–31. Available from: <URL>.

39. Guo S, Zhang W, Liang J, You C, Geng Z, Wang C, et al. Contact and repellent activities of the essential oil from Juniperus formosana against two stored product insects. Molecules. 2016;21(4), 504-11. Available from: <URL>.

40. Nour A.H., Idris A.A., Ishag O.A., Nour A.H., Alara O.R. Chemical constituents and cockroach repellent activity of essential oil from Cyperus rotundus. J Res Pharm. 2022; 26(4): 920-930. Available from: <URL>.

41. Sittichok S, Phaysa W, Soonwera M. Repellency activity of essential oil on thai local plants against american cockroach (Periplaneta americana L.; Blattidae: Blattodea). Journal of Agricultural Technology. 2013;9(6):1613–20. Available from: <URL>.

Chemical Composition and Repellent Activity of Methyl Cinnamate-Rich Basil (*Ocimum basilicum*) Essential Oil

Azhari H. Nour[1], Abeer A. Idris[1], Omer A. Ishag[1*], Abdurahman H. Nour[2]

[1]International University of Africa (IUA), Department of Applied and Industrial Chemistry, Khartoum, 12223, Sudan.
[2]Universiti Malaysia Pahang (UMP), College of Engineering Technology, Gambang, 26300, Malaysia.

Abstract: Basil (*Ocimum basilicum* L.) is an important culinary herb and essential oil source widely recognized worldwide. The oil of the plant is beneficial for medicinal uses, and it has many biological activities such as insect repellent, larvicidal, and bactericidal. This study aimed to investigate basil's essential oil for its chemical composition and repellent activity. The essential oil of basil was extracted from fresh leaves by steam distillation method, and the chemical composition of the oil was determined by using GC/MS. Also, the repellent activity of the oil was tested against American cockroaches. Ebeling Choice-Box test with a little modification used in repellence test. The obtained results of chemical composition revealed that the amount of the oil contained forty-one chemical constituents (~97.1%); the major constituents were methyl cinnamate (25.3%), linalool (19.1%) and estragole (12.3%) as the major oxygenated monoterpenes. While α-bergamoten (5.3%), germacrene (4.6%), γ-cadinene (2.8%), and β-elemene (2.4%) were the main compounds in sesquiterpene hydrocarbons. Whereas, in oxygenated sesquiterpenes, Tau-cadinol (4.3%) was an important compounds and ocimene the highest compound in monoterpene hydrocarbons. The obtained results also indicated that the essential oil had good activity against the P. American, at a 100% concentration of oil; the repellence reaches 100% after 1 h. The IC50 and IC90 values of basil essential oil against P. Americans were 53.0 and 83.0%, respectively. The major compound methyl cinnamate which exists in basil essential oil is a very important compound and could be used in a wide area of industrial applications as repellent products, medicinal products, and cosmetics.

INTRODUCTION

Natural products, especially plants, have served humanity as an important source for many uses. Humans use plants or their derivatives for many benefits, such as foods and medicines (1), antioxidant (2), rhizoremediation (3), fertilizers and pesticides (4), lipid-lowering potential, anti-malarial, anti-ulcer, antipyretic, anti-cancer, and anti-proliferation (5). The genus *Ocimum*, of *Ocimum basilicum* (Family: Lamiaceae formerly Labiatae), called basil has long been known worldwide as a diverse, rich source of essential oils and a significant culinary herb. Basils exhibit great variation in both

morphology and diversity, such as inflorescence, leaf, and essential oil components (6). The taxonomy of *O. basilicum* more complicated due to the numerous varieties, cultivars and chemotypes within the species that do not vary significantly in morphology. The essential oil composition was utilized to characterize the diversity among the most economically important *Ocimum* species (7). The essential oils of basils are used as a food flavoring, medicines, and in the perfumery industry. In addition, previous studies have reported very interesting biological activities of these oils, such as being bactericidal (8), mosquito repellent (9) and larvicidal (10), etc. Besides, it was used in

traditional medicine to sooth pain, treat vomiting and stress, and as an insect repellent (11). The leaves and flower of basil are utilized in folk medicine as a tonic and vermifuge, also basil tea is good for treating dysentery, nausea, and flatulence, its oil is useful for the mitigation of spasm, rhinitis, mental fatigue, cure of wasp stings and snake bites (12,13). It has used as a folk medicine for boredom and convulsion. Basil heals headache, improves digestion, and as well helpful for toothache, earache, and for curing epistaxis when used with camphor. The plant infusion is effective in cephalic, gouty joints, fever, otitis, and snakebite(12,14). In addition, it is efficient in remediation of stomach problems, fever, cough, gout, and given internally to cure cystitis, nephritis and interior piles. The plant is also used to keep away insects and snakes (12). The use of chemically synthetic repellents of insect control may result in disturbing natural ecosystems and resulted in the development of resistance to insecticides, and even adverse impact on non-target organisms. Hence, the idea of using natural repellent products as an alternative to develop new eco-friendly repellents could be a friendly solution for the reduction of adverse effects on the environment and human health. Therefore, this study aimed to investigate the chemical composition and repellent activity of *O. basilicum* essential oil.

MATERIALS AND METHODS

Plant Material
The fresh leaves of *O. basilicum* were collected in October 2017 from the Ministry of Agriculture and Forestry, General Directorate of Horticultural Production, Department of Medicinal and Aromatic Plants, Khartoum, Sudan.

Extraction of Essential oils
The fresh leaves of *O. basilicum* are used to obtain their essential oils. The extraction was conducted on a laboratory scale by Steam Distillation (SD) unit as the method described by Mesomo et al. (15) with slight modification. In brief, 100 g of fresh *O. basilicum* leaves were steam distilled for 4 h. Then, the extracted essential oils were dried over anhydrous sodium sulfate, filtered, stored in hermetically closed dark bottles, and kept at -4 °C for further studies. The percentage of extracted oils (v/w %) from the SD method was calculated according to the following formula (Equation 1):

$$\text{The Essential oil}\ (\%) = \frac{\text{volume of oil}}{\text{weight of sample}} \text{ X 100}$$

(Eq. 1)

Gas chromatography-mass Spectrometry Analysis
The chemical composition of extracted *O. basilicum* essential oils was determined using an Agilent 7890A GC–MS instrument equipped with column nonpolar capillary DB-1 of 100% dimethyl-polysiloxane (30 m, 0.25 mm i.d, film thickness 0.25 µm) and mass spectrophotometric detector. The carrier gas was helium with a flow rate of 1 mL/min, and the injector mode was splitless with an injection volume of 1 µL/L and an injection temperature of 250 °C. The temperature program was 60 °C for 3 min, 240 °C at the rate of 3 °C/min, and held for 10 min. The run time was 93 min, and the lab data system was NIST Library Chem Station software.

Cockroaches Collection and Repellent Test
About 600 adults (male and female) of American cockroaches (*P. Americana*) were collected from the University of Khartoum, Sudan. They were kept in boxes and reared in the laboratory by feeding on water and biscuits. The healthy nymphs and adults (male & female) cockroaches were used in this repellence test. The temperature was maintained at 28±5 °C. The Ebeling choice box test, which describe by Ebeling (16) with some modification used in this experiment. The *O. basilicum* leaves essential oil was prepared in various concentrations (5, 25, 50, 75, and 100 v/v %) by dissolving in 1% DMSO. Ten adult and nymph cockroaches (male and female) were then released into the central choice box (untreated zone). Then, the choice boxes (treated and untreated location) were exposed to a photoperiod of 27 ºC for 72 hrs. 1% DMSO and naphthalene were used as negative and positive controls, respectively. The cockroaches at the treated and untreated zone were carefully observed and counted for 0, 3, 6, 9, 12, 24, 48, and 72 hrs. of treatment. Each treatment with a different concentration was conducted in three replicates. The percentage of repellency is calculated as follows (Equation 2):

$$\text{Repellency \%} = 100 - \left(\frac{T}{N} \text{ X 100 \%} \right) \quad \text{(Eq. 2)}$$

Where T is the number of cockroaches located at the treated zone, and N stands for the total number (ten heads) of cockroaches been used in the repellency test. The mean percentage of the repellence was then calculated from the values obtained in three replicates.

Statistical Analysis
Statistical analysis of the obtained results conducted using MS Excel (2007), version 12.0.4518.1014. The results performed in three repetitions and expressed as mean ± standard deviation.

RESULTS AND DISCUSSION

Yield of essential oil
The essential oil of the collected *O. basilicum* leaves was extracted using the steam distillation method, and the percentage yield of the oil was expressed on a fresh leaf weight basis (v/w %). The oil content

was found to be 0.78%, and the color is light yellow with a camphor-like smell. Previously, reported *O. basilicum* had a yield of 1.56% essential oil with yellowish green color (17) and also a yield of 1.98± 0.01% with a pale yellow oil (18). In addition, a yield of 0.65 to 1.90% (19) and 0.9–1.7% essential oil (20), where these results were higher than the obtained results in this study. Whereas, the yields were found to be 0.05 to 0.55% (19), 0.6% (20) and 0.28% essential oil too (21); where these results were lower than the result obtained in this study. The variation in the results may be due to climate and soil conditions, but the oil content is still in the range obtained in the previous studies.

Chemical Composition of Essential Oil
The chemical composition of the extracted *O. basilicum* essential oils was determined using GC-MS instrument and the obtained results were shown in Table 1. The obtained results were indicated forty-one chemical constituents (~97.1%); the major constituents were methyl cinnamate (25.3%),

linalool (19.1%) and estragole (12.3%) as the major oxygenated monoterpenes. While sesquiterpenes hydrocarbons, α-bergamoten (5.3%), germacrene (4.6%), γ-cadinene (2.8%) and β-elemene (2.4%) were major constituents. Whereas, in oxygenated sesquiterpenes, Tau-cadinol (4.3%) was major constituent and ocimene the major constituent in monoterpene hydrocarbons. In previous studies reported basil essential oils consisted of linalool were the most abundant component (56.7-60.6%), followed by epi-α-cadinol (8.6-11.4%), α-bergamotene (7.4-9.2%) and γ-cadinene (3.2-5.4%) (21,22). In addition, a total of 17 compounds were identified with linalool (70.44%) as the major compound, followed by an estragole (14.4%), tau-cadinol (4.1%) and α-bergamoten (3.7%) (23). Also reported the dominant components were methyl chavicol (81.8%), β-(E)-ocimene (2.9%), α-(E)-bergamotene (2.5 %), α-epi-cadinol (2.1%), 1,8-cineole (1.6%), methyl eugenol (1.1%) and camphor (1.1%) (24).

Table 1: Chemical composition of essential oil.

Compound	Formula	Area %
Monoterpene hydrocarbons		
alpha-Pinene	$C_{10}H_{16}$	0.2
Camphene	$C_{10}H_{16}$	0.0
Sabinene	$C_{10}H_{16}$	0.3
Pseudopinen	$C_{10}H_{16}$	0.5
Myrcene	$C_{10}H_{16}$	0.9
Limonene	$C_{10}H_{16}$	0.5
Ocimene	$C_{10}H_{16}$	1.5
Total monoterpene hydrocarbons		**3.9**
Oxygenated monoterpenes		
Cineole	$C_{10}H_{18}O$	5.6
Sabinene hydrate	$C_{10}H_{18}O$	0.3
Fenchone	$C_{10}H_{16}O$	0.9
Linalool	$C_{10}H_{18}O$	19.1
Fenchol	$C_{10}H_{18}O$	0.6
(a)	$C_{10}H_{14}O_2$	0.2
Camphor	$C_{10}H_{16}O$	0.4
Isoborneol	$C_{10}H_{18}O$	0.3
Terpinenol-4	$C_{10}H_{18}O$	0.1
Terpineol schlethin	$C_{10}H_{18}O$	0.9
Estragole	$C_{10}H_{12}O$	12.3
Beta-Citral	$C_{10}H_{16}O$	0.1
Geraniol	$C_{10}H_{18}O$	1.2
Alpha-Citral	$C_{10}H_{16}O$	0.2
Methyl cinnamate	$C_{10}H_{10}O_2$	25.3
3-Allylguaiacol	$C_{10}H_{12}O_2$	1.0
8-Hydroxylinalool	$C_{10}H_{18}O_2$	0.04
Total oxygenated monoterpenes		**68.5**
Sesquiterpene hydrocarbons		
Elixene	$C_{15}H_{24}$	0.3
Alpha-Ylangene	$C_{15}H_{24}$	0.1
Copaene	$C_{15}H_{24}$	0.2
b-Elemene	$C_{15}H_{24}$	2.4
Caryophyllene	$C_{15}H_{24}$	1.0
Alpha-Bergamoten	$C_{15}H_{24}$	5.3
(b)	$C_{15}H_{24}$	0.1

Beta-Farnesene	$C_{15}H_{24}$	0.2
Humulene	$C_{15}H_{24}$	0.6
Beta-Cubebene	$C_{15}H_{24}$	0.6
Germacrene	$C_{15}H_{24}$	3.6
Alpha-Bulnesene	$C_{15}H_{24}$	1.4
Gamma-Cadinene	$C_{15}H_{24}$	2.8
Total sesquiterpene hydrocarbons		**19.1**
Oxygenated sesquiterpenes		
Beta-Elemol	$C_{15}H_{26}O$	0.5
Cubedol	$C_{15}H_{26}O$	0.8
Tau-Cadinol	$C_{15}H_{26}O$	4.3
Total oxygenated sesquiterpenes		**5.5**
Others		**2.9**

(a): Oxirane,2-(hexyn-1-yl)-3-methoxymethylene, **(b):** Cis-Muurola-3,5-diene

The qualitative and quantitative composition of essential oils was quite different: *O. basilicum* var. purpureum essential oil contained 57.3% methyl-chavicol (estragol); *O. basilicum* var. thyrsiflora oil had 68.0% linalool; the main constituents of *O. citriodorum* oil were nerol (23.0%) and citral (20.7%) (25). Moreover, claimed the major compounds were: linalool (32.8%), linalyl acetate (16.0%), elemol (7.4%), geranyl acetate (6.2%), myrcene (6.1%), allo-ocimene (5.0%), *a*-terpineol (4.9%), (*E*)-*β*-ocimene (3.7%) and neryl acetate (3.5%) (18). Thus, the most of previously mentioned compounds were present in the obtained results.

The obtained results in Table 1 also showed that the total monoterpenes represents 72.4% of the oil, the ratio is hydrocarbon 3.9% and oxygenated monoterpene was 68.5%. While the total sesquiterpenes were 24.6%, representing 19.1% sesquiterpene hydrocarbon and 5.5% are oxygenated sesquiterpenes. The distribution of mono and sesquiterpenes in *O. basilicum* essential oil was shown in Figure 1. Previously, reported samples collected in winter were found to be richer in oxygenated monoterpenes (68.9%), compared to those collected in summer where were higher in sesquiterpene hydrocarbons (24.3%) (21,22).

Figure 1: Distribution of mono and sesquiterpenes in *O. basilicum* essential oil.

Repellent Activity of Essential Oil

Repellency activity of *O. basilicum* essential oil (100%) against A. cockroaches after 72 hrs. of treatment and the IC50 and IC90 values against A. cockroaches after 24 hrs. of treatment was tested in this study and the obtained result showed in Figure 2 and Figure 3. The obtained results indicated that the essential oil had a good activity against the cockroaches, at a 100% concentration of oil; the

repellence reaches 100% up to 1 h of exposure; whereas the repellency reaches 80.0% for more than 4 h and more than 70.0% after 10 h. The IC50 and IC90 values of *O. basilicum* essential oil against cockroaches were 53.0% and 83.0%, respectively. Yoon (26) was tested the repellent efficacies of certain components and their obtained results indicated that the efficacies were varied with different doses and the cockroach species, and the

major components responsible for the repellent activity of the essential oils were limonene, β-pinene and *γ*-terpinene.

Figure 2: Repellency activity of *O. basilicum* essential oil (100%) against cockroaches after 72 h of treatment.

Figure 3: The IC50 and IC90 values of *O. basilicum* essential oil against cockroaches after 24 h of treatment.

El-Seedi et al. (27) claimed that the *O. basilicum* oil with major compounds of 1,8-cineole, camphor, linalool, 4-terpineol, borneol, and carvone was the most repellent oil among many oils tested against cockroach. In addition a number of compounds were showed repellent activity against insects such as: linalool (28), Estragole (29), ocimene (30), cineole (31), α-pinene (32), camphene (100%) against

German cockroaches (33), camphor (34), limonene (35), sabinene (36), terpinene 4-ol (35), myrcene (34), geraniol was toxic to the cockroaches by contact or injection and repellency (32). Moreover, caryophyllene (34), fenchone (29), *β*-citral and *α*-citral (37), *β*-elemene (38), *β*-cubebene, fenchol, *α*-bergamoten, *α*-guaiene and *β*-farnesene (32), *α*-ylangene, *β*-elemol and *γ*-cadinene (35), germacrene (39), humulene (35), *β*-bulnesene (38), *β*-cubebene (32), verbenone (33) and α-copaene (32). Nour et al. investigated the repellent activity of *Cyperus rotundus* rhizomes essential oil against American cockroaches; his obtained results indicated that the IC50 and IC90 values of *C. rotundus* rhizomes essential oil against American cockroaches were 57 and 88%, respectively (40). Sittichok et al. evaluated the repellent activity of the essential oils derived from Cymbopogon citratus (lemon grass), Cymbopogon nardus (citronella grass) and Syzygium aromaticum (clove) against adult American cockroach; in his results all of the essential oils in ethyl alcohol showed higher percent repellency (81-100%) against P. americana than all of the essential oils in soybean oil (66-84% repellency), The essential oil from C. citratus in ethyl alcohol exhibited the highest repellency (100%) among the tested repellents and naphthalene (83% repellency)(41). The repellent activity of essential oil in this study could be due to the presence of compounds that had already demonstrated repellent activity against certain insects, including cockroaches.

CONCLUSION

The obtained results in this study indicated that the *O. basilicum* essential oil contained various chemical constituents include monoterpenes, oxygenated monoterpenes, sesquiterpenes, and oxygenated sesquiterpenes. Also indicated that oil had a repellent activity, and it could be attributed to the presence of compounds that have already demonstrated their repellent activity towards certain insects, including cockroaches.

CONFLICTS OF INTEREST

The authors declare no conflicts of interest exist.

ACKNOWLEDGMENTS

REFERENCES

1. Che C-T, Zhang H. Plant natural products for human health. International journal of molecular sciences. 2019 Jan; 20(4):830 - 4. Available from: <URL>.

2. Saeed Z, Iqbal S, Younas U, Bukhari SM, Zaidi A. Variation in antioxidant potential of Vigna unguiculata grown in pure and amended soil. Kuwait Journal of Science. 2020;47(3), 2-14. Available from: <URL>.

3. Ubogu M, Odokuma LO. Growth and lolerance evaluation of selected plants to crude oil contamination for rhizoremediation potentials in the Niger Delta. Kuwait Journal of Science. 2019;46(4), 93-103. Available from: <URL>.

4. Elmi AO, Anderson AK, Albinali AA. Demand for organic food and public perception in the state of Kuwait: A Comparison of conventional and organic vegetable produce quality. Kuwait Journal of Science. 2019;46(4), 120-127. Available from: <URL>.

5. Lim PJ, Gan CS, Yusof A. Lipid lowering effect of Eurycoma longifolia Jack aqueous root extract in hepatocytes. Kuwait Journal of Science. 2019;46(2), 52-58. Available from: <URL>.

6. Telci I, Bayram E, Yılmaz G, Avcı B. Variability in essential oil composition of Turkish basils (Ocimum basilicum L.). Biochemical Systematics and Ecology. 2006;34(6):489–97. Available from: <URL>.

7. Abduelrahman A, Elhussein S, Osman NA, Nour A. Morphological variability and chemical composition of essential oils from nineteen varieties of Basil (Ocimum basilicum L.) growing in Sudan. International Journal of Chemical Technology. 2009;1(1):1–10. Available from: <URL>.

8. Nour A, Elhussein S, Osman N, Ahmed N, Abduelrahman A, Yusoff M. Antibacterial activity of the essential oils of Sudanese accessions of basil (Ocimum basilicum L.). Journal of Applied Sciences. 2009;9(23):4161–7. Available from: <URL>.

9. Nour A, Elhussein S, Osman N. Repellent activities of the essential oils of four Sudanese accessions of basil (Ocimum basilicum L.) against Anopheles mosquito. Journal of Applied Sciences. 2009;9(14):2645–8.

10. Nour AH, Elhussein SA, Osman NA, Yusoff M. A study of the essential oils of four Sudanese accessions of basil (Ocimum basilicum L.) against Anopheles mosquito larvae. American Journal of Applied Sciences. 2009;6(7):1359–63. Available from: <URL>.

11. Aidaross M, Kohob W, Galalb M. Evaluation of repellent and larvicidal activity of Ocimum basilicum L. and Cymbopogon citratus DC. Against Culex quinquefasciatus. Inti Chern. Pharm. Med J. 2005;2(2):243–6. Available from: <URL>.

12. Ch MA, Naz SB, Sharif A, Akram M, Saeed MA. Biological and pharmacological properties of the sweet basil (Ocimum basilicum). Journal of Pharmaceutical Research International. 2015;330–9. Available from: <URL>.

13. Baytop T. Therapy with medicinal plants in Turkey (Past and Present),(p. 189) Publication no 325. Istanbul University, Istanbul. 1984.

14. Kīrtikara KR, Basu BD, An I, Blatter E, Caius JF, Mhaskar K. Indian medicinal plants, with illustrations. 2001. Available from: <URL>.

15. Mesomo MC, Corazza ML, Ndiaye PM, Dalla Santa OR, Cardozo L, Scheer A de P. Supercritical CO2 extracts and essential oil of ginger (Zingiber officinale R.): Chemical composition and antibacterial activity. The Journal of Supercritical Fluids. 2013 Aug 1;80:44–9. Available from: <URL>.

16. Ebeling W, Wagner R, Reierson DA. Influence of repellency on the efficacy of blatticides. I. Learned modification of behavior of the German cockroach. Journal of Economic Entomology. 1966;59(6):1374–88. Available from: <URL>.

17. Bilal A, Jahan N, Ahmed A, Bilal SN, Habib S, Hajra S. Phytochemical and pharmacological studies on Ocimum basilicum Linn-A review. International Journal of Current Research and Review. 2012;4(23), 73-83. Available from: <URL>.

18. Hadj Khelifa L, Brada M, Brahmi F, Achour D, Fauconnier ML, Lognay G. Chemical composition and antioxidant activity of essential oil of Ocimum basilicum leaves from the northern region of Algeria. Journal of Herbal Medicine. 2012;1(2), 53–8. Available from: <URL>.

19. Beatovic D, Krstic-Milosevic D, Trifunovic S, Siljegovic J, Glamoclija J, Ristic M, et al. Chemical composition, antioxidant and antimicrobial activities of the essential oils of twelve Ocimum basilicum L. cultivars grown in Serbia. Records of Natural Products. 2015;9(1), 62-75. Available from: <URL>.

20. Koroch AR, Simon JE, Juliani HR. Essential oil composition of purple basils, their reverted green varieties (Ocimum basilicum) and their associated biological activity. Industrial crops and products. 2017;107,526–30. Available from: <URL>.

21. Hussain AI, Anwar F, Sherazi STH, Przybylski R. Chemical composition, antioxidant and antimicrobial activities of basil (Ocimum basilicum) essential oils depends on seasonal variations. Food chemistry. 2008;108(3), 986–95. Available from: <URL>.

22. Rubab S, Hussain I, Khan B, Unar A, Abbas K, Khichi Z, et al. Biomedical description of Ocimum basilicum L. Journal of Islamic International Medical College. 2017;12(1), 57–69. <URL>.

23. Nawaz H, Hanif MA, Ayub MA, Ishtiaq F, Kanwal N, Rashid N, et al. Raman spectroscopy for the evaluation of the effects of different concentrations of Copper on the chemical composition and biological activity of basil essential oil. Spectrochimica Acta Part A: Molecular and Biomolecular Spectroscopy. 2017;185, 130–8. Available from: <URL>.

24. Pripdeevech P, Chumpolsri W, Suttiarporn P, Wongpornchai S. The chemical composition and antioxidant activities of basil from Thailand using retention indices and comprehensive two-dimensional gas chromatography. Journal of the Serbian Chemical Society. 2010;75(11):1503–13. Available from: <URL>.

25. Avetisyan A, Markosian A, Petrosyan M, Sahakyan N, Babayan A, Aloyan S, et al. Chemical composition and some biological activities of the essential oils from basil Ocimum different cultivars. BMC complementary and alternative medicine. 2017;17(1):1–8. Available from: <URL>.

26. Yoon C, Kang SH, Yang JO, Noh DJ, Indiragandhi P, Kim GH. Repellent activity of citrus oils against the cockroaches Blattella germanica, Periplaneta americana and P. fuliginosa. Journal of Pesticide Science. 2009;34(2), 77–88. Available from: <URL>.

27. El-Seedi HR, Khalil NS, Azeem M, Taher EA, Göransson U, Pålsson K, et al. Chemical composition and repellency of essential oils from four medicinal plants against Ixodes ricinus nymphs (Acari: Ixodidae). Journal of medical entomology. 2014;49(5), 1067–75. Available from: <URL>.

28. Campos EV, Proença PL, Oliveira JL, Melville CC, Della Vechia JF, De Andrade DJ, et al. Chitosan nanoparticles functionalized with β-cyclodextrin: a promising carrier for botanical pesticides. Scientific reports. 2018;8(1), 1–15. Available from: <URL>.

29. Bedini S, Bougherra HH, Flamini G, Cosci F, Belhamel K, Ascrizzi R, et al. Repellency of anethole-and estragole-type fennel essential oils against stored grain pests: the different twins. Bull Insectol. 2016;69(1), 149–57. Available from: <URL>.

30. Dube FF, Tadesse K, Birgersson G, Seyoum E, Tekie H, Ignell R, et al. Fresh, dried or smoked, Repellent properties of volatiles emitted from ethnomedicinal plant leaves against malaria and yellow fever vectors in Ethiopia. Malaria Journal. 2011;10(1), 1–14. Available from: <URL>.

31. Cansian R, Astolfi V, Cardoso R, Paroul N, Roman S, Mielniczki-Pereira A, et al. Insecticidal and repellent activity of the essential oil of Cinnamomum camphora var. linaloolifera Y. Fujita (Ho-Sho) and Cinnamomum camphora (L.) J Presl. var. hosyo (Hon-Sho) on Sitophilus zeamaisMots.(Coleoptera, Curculionedae). Revista Brasileira de Plantas Medicinais. 2015;17(4), 769–73. Available from: <URL>.

32. Azhari H, Yap SS, Nour AH. Extraction and chemical compositions of ginger (Zingiber officinale Roscoe) essential oils as cockroaches repellent. Australian Journal of Basic and Applied Sciences. 2017;11(3), 1–8.

33. Athuman I, Innocent E, Machumi F, Augustino S, Kisinza W. Repellency properties of oils from plants traditionally used as mosquito repellents in Longido district, Tanzania. Int. J. Mosq. Res. 2016; 3(1): 04-08. Available from: <URL>.

34. Maia MF, Moore SJ. Plant-based insect repellents: a review of their efficacy, development and testing. Malaria journal. 2011;10(1), 1–15. Available from: <URL>.

35. Carroll JF, Tabanca N, Kramer M, Elejalde NM, Wedge DE, Bernier UR, et al. Essential oils of Cupressus funebris, Juniperus communis, and J. chinensis (Cupressaceae) as repellents against ticks (Acari: Ixodidae) and mosquitoes (Diptera: Culicidae) and as toxicants against mosquitoes. Journal of Vector Ecology. 2011;36(2), 258–68. Available from: <URL>.

36. Benelli G, Flamini G, Canale A, Molfetta I, Cioni PL, Conti B. Repellence of Hyptis suaveolens whole essential oil and major constituents against adults of the granary weevil Sitophilus granarius. Bulletin of Insectology. 2012;65(2), 177–83.

37. Baldacchino F, Tramut C, Salem A, Liénard E, Delétré E, Franc M, et al. The repellency of lemongrass oil against stable flies, tested using video tracking. Parasite. 2013;20, 21. Available from: <URL>.

38. Gokulakrishnan J, Kuppusamy E, Shanmugam D, Appavu A, Kaliyamoorthi K. Pupicidal and repellent activities of Pogostemon cablin essential oil chemical compounds against medically important human vector mosquitoes. Asian Pacific Journal of Tropical Disease. 2013;3(1), 26–31. Available from: <URL>.

39. Guo S, Zhang W, Liang J, You C, Geng Z, Wang C, et al. Contact and repellent activities of the essential oil from Juniperus formosana against two stored product insects. Molecules. 2016;21(4), 504-11. Available from: <URL>.

40. Nour A.H., Idris A.A., Ishag O.A., Nour A.H., Alara O.R. Chemical constituents and cockroach repellent activity of essential oil from Cyperus rotundus. J Res Pharm. 2022; 26(4): 920-930. Available from: <URL>.

41. Sittichok S, Phaysa W, Soonwera M. Repellency activity of essential oil on thai local plants against american cockroach (Periplaneta americana L.; Blattidae: Blattodea). Journal of Agricultural Technology. 2013;9(6):1613–20. Available from: <URL>.

Fabrication of Textile-Based Flexible Supercapacitor with a Textile Dye on Polyaniline-Based Composite Electrode for Enhanced Energy Storage

Sibel Yazar (iD)

Istanbul University-Cerrahpasa, Engineering Faculty, Department of Chemistry, 34320 Avcilar, Istanbul, Turkey

Abstract: Polyaniline (PANI) is a promising conductive polymer for use in energy storage applications. Here, a one-step hydrothermal method of PANI polymerization on carbon felt electrode was synthesized using an azo dye, a bisulfonated dichloro anionic dye molecule to enhance an efficient textile-based flexible supercapacitor electrode material for energy storage applications. The electrode material synthesized at concentration of 2 mM AY17 exhibits 814.1 F g^{-1} at the scan rate of 5 mV s^{-1} with multiwall carbon nanotubes (MWCNTs). Due to electrostatic interaction with the polymer, the presence of high electronegativity Cl atoms in the dye molecule significantly improves the PANI structure's electron donor/acceptor properties. A symmetric supercapacitor exhibits an energy density of 11.7 W h kg^{-1} at a power density of 300 W kg^{-1}, and it is 4.5 W h kg^{-1} at 1800 W kg^{-1} in 3.0 M KCl aqueous electrolyte. The capacitance retention performance value of the symmetric supercapacitor exhibited 81.76% after 2500 cycles.

INTRODUCTION

The fast charge/discharge capabilities and high energy-power density of supercapacitors are good alternatives for energy storage devices (1). Electric double-layer capacitors, pseudocapacitors, and hybrid capacitors with both can be classified based on their energy storage system (2). In pseudocapacitors, a redox process occurs to store the charge, while in EDLCs, charges are electrostatically accumulated at the electrode/electrolyte interface (3). In hybrid supercapacitors, these two events co-occur on the electrode surface. Pseudocapacitors are commonly made of conductive polymers (CPs), and transition metal oxides/hydroxides (4). Carbonous materials is frequently used for EDLCs (5). Carbon-based materials or additives with redox behavior can be used to achieve high specific capacitance and long-cycling life for electrode materials (6).

PANI has unique properties in conducting polymers and easy polymerization. It has attracted some applications such as sensors, electronic devices, corrosion inhibitive materials, energy storage materials, and photonic devices (7). The polymerization of PANI, the aniline monomer exists in one of three oxidation states: leukoemeraldine, emerald, and pernigranilin. The fully oxidized form of PANI is known as pernigranilin. The totally reduced form of PANI is known as lecomeraldine, and half of the oxidized PANI is reduced to emerald (8). The physical/chemical properties of PANI-based supercapacitors can be significantly improved by doping process, and there are many studies combining carbon nanotubes and

carbonaceous materials such as graphene for their use in supercapacitors (9–11). The various compounds are utilized as dopants in supercapacitor electrodes as redox active chemicals, resulting in higher specific capacitance and energy density. Furthermore, when the conductive polymer structure is doped with large anions, since the polymer is immobile in the matrix, small electrolyte cations are involved in the charging/discharging process without large volume changes. Thus, the cyclic stability of the polymers is improved (3). The strong contact between the functional groups of the dye molecules as a counterion and the PANI improves capacitance performance (12). Dye molecules' anionic sulfonic groups interact electrostatically with the positively charged polymer structure. When previous research is examined, there are very few supercapacitor studies that have been studied with dye molecules. Q. F. Lu et al., reported the capacitance value of 579 F/g a dye-functional graphene/PANI (rGAP) electrode at the current density of 0.5 A/g in 1 M H_2SO_4 electrolyte solution. It has also been reported that 75% of the capacitance retention after 2000 cycles (13). With Alizarin Red S dye, Quanlu Wang et al. achieved a capacitance value of 461 F/g at 0.5 A/g current density (14). PANI doped with Prussion blue supercapacitor electrode was successfully constructed by Y. Xueying et al., that reported a specific capacitance of 218.4 F/g at a current density of 5 A/g. After 2000 cycles, they discovered that it had retained 94 percent of its capacitance (15).

The dyes used as energy storage materials in previous studies generally contain metals with redox behavior consisting of ring structures that provides electron delocalization, and also molecules with the highest degree of dissociation, such as sulfonic acid groups, are beneficial. Here, acid yellow 17 (AY17), because of the functional groups and the ring structures, assists the electron delocalization and improves the capacitance performance of the electrode materials. Furthermore, the inclusion of strong electronegativity of Cl atoms in the dye molecule, which is in electrostatic contact with the polymer, considerably enhances the electron donor/acceptor characteristics of the PANI structure (16).

In this study, an energy storage material of textile-based flexible electrode with a textile dye on multi-walled carbon nanotubes/polyaniline composite has been developed. PANI/MWCNT was synthesized on a carbon cloth electrode as a current collector in the presence of Acid Yellow 17 (AY17) counterion carrying an anionic sulfonate group. Disodium 2,5-dichloro-4-(5-hydroxy-3-methyl-4-(sulfophenylazo) pyrazol-1-yl) benzenesulfonate, namely acid yellow 17, is one of the basic color

dyes, textile, paper, paint, pharmaceutical cosmetics and cleaning materials such as detergent, soap (17). Cyclic voltammetry, galvanostatic charge/discharge, and electrochemical impedance spectroscopy experiments were used to investigate the influence of the electrochemical performance of PANI/MWCNT/AY-13(3mM) as supercapacitor electrode in half-cell and full-cell applications.

EXPERIMENTAL

Materials
Carbon nanotube (multi-walled, 50-90 nm diameter, >95% carbon basis) and Acid Yellow 17 were purchased from Sigma-Aldrich. Aniline, $FeCl_3.6H_2O$, HCl, ethanol (CH_2OH), nitric acid (HNO_3,%65), potassium chloride (KCl), and acetone were purchased from Merck Schuchardt OHG (Hogenbrunn, Germany). Carbon felt (Cft) was provided by Mersen Istanbul Industrial Products Inc.

Synthesis of AY17 modified PANI/MWCNTs
To remove impurities on the electrode surface, carbon felt electrodes were washed with acetone in an ultrasonic bath for 40 minutes and then dried at room temperature overnight. After that, it was soaked in HNO_3 and stored at ambient temperature for 72 hours. The treated carbon felt electrodes were rinsed in distilled water until they reached a neutral pH, then dried in a 40 °C oven. Hydrothermal synthesis was used to make polyaniline/multi-walled carbon nanotubes (PANI/MWCNTs). After ultrasonically adding 50 mg MWCNTs to 100 mL of 1.0 M HCl aqueous solution for 1 hour at room temperature, 10 mmol aniline was added to the solution. As an oxidant, 25 mmol $FeCl_3.6H_2O$ was added to the aforementioned solution (18,19). The prepared homogeneous solution and 4.0×5.0 cm^2 carbon felt electrode was added to the autoclave for hydrothermal synthesis for six h at 120 ºC (20). The electrodes were then rinsed in 1.0 M HCl solution and distilled water, then dried for 24 hours at 40 °C. The effect of counter ion concentration on the supercapacitor electrode was investigated in the presence of 1.0, 2.0, 3.0, 4.0, and 5.0 mM AY17 (see Table 1). PANI/MWCNTs were synthesized with 0.5 mg/L MWCNTs, and the remainder of the methods were the same as for PANI.

Characterization

The microstructure of the sample pictures of the electrode surface was examined using a Zeiss EVO® LS 10 (SEM) instrument (USA). Bruker Alpha-T DRIFT spectrometer with 30° reflection accessory (M112-06/08) was used to investigate the chemical structure of electrode material. A SII6000 Exstar TG/DTA 6300 apparatus was used to per-

form thermogravimetric analysis (TGA) of electrode materials. The phase and crystallinity of the samples were determined using the XRD pattern of the materials (XRD, PANalytical X'Pert PRO Cu at 45 kV).

The surface area and pore size volume parameters were calculated using the BET analysis (Quantachrome Instruments, USA). The active mass coated on the carbon felt electrode was measured with a balance (Radwag) with an accuracy of 0.01 mg before and after hydrothermal synthesis. The active substance was coated onto carbon felt at a quantity of 3.0 mg cm^{-2}.

Table 1. The ratio of raw materials used in supercapacitor electrode samples.

Sample	MWCNT (mg/L)	ANI (mmol)	AY17 (mM)
PANI	-	10.0	-
PANI/AY17	-	10.0	3.0
PANI/MWCNTs	0.5	10.0	-
PANI/MWCNTs/AY17-1	0.5	10.0	1.0
PANI/MWCNTs/AY17-2	0.5	10.0	2.0
PANI/MWCNTs/AY17-3	0.5	10.0	3.0
PANI/MWCNTs/AY17-4	0.5	10.0	4.0
PANI/MWCNTs/AY17-5	0.5	10.0	5.0

Electrochemical measurements
At room temperature, the electrochemical measurements of the acquired samples for the half-cell electrode system and the symmetric supercapacitor device (full-cell system) were performed using an Ivium Vertex Instruments Potentiostat/Galvanostat (Ivium Technologies B.V, The Netherlands). The reference electrode and counter electrode for the half-cell system were the Silver/Silver chloride (Ag/AgCl) electrode and Pt wire, respectively. The working electrode was a carbon felt electrode coated with an active substance.

The electrolyte was a 3.0 M KCl aqueous solution. At room temperature (252°C), the electrochemical characterizations were performed using cyclic voltammetry (CV) at various scan rates, galvanostatic charge/discharge test (GCD) at varied current densities, and electrochemical impedance spectroscopy (EIS) between 0.01-10,000 Hz. Equations (1) and (2) were used to compute the specific capacitance (C, F g^{-1}) of the electrodes based on the CV and GCD curves, respectively (21,22):

$$C = \frac{1}{mv(V_2 - V_1)} \int_{V_1}^{V_2} I(V) dV \qquad (1)$$

$$C = \frac{I \Delta t}{m \Delta V} \qquad (2)$$

where m is the mass of electroactive material; V_1 and V_2 are the cathodic and anodic voltage, respectively. The integral is calculated from the encircled area by cyclic voltammogram for a given

scan rate v, ΔV and Δt are the operating potential and the discharge time by GCD curve, respectively.

The active material for the flexible supercapacitor electrode was inserted into the carbon felt (1x1 cm^2). The sandwich form of supercapacitor was created by combining two identical flexible electrodes. A symmetric supercapacitor was also created utilizing a 1.0x1.0 cm^2 piece of filter paper wetted with 3.0 M KCl as a separator. The following formulas can be used to compute the energy density (E) and power density (P) of a half-cell system (6,23):

$$E = \frac{C \times (\Delta V)^2}{2 \times 4 \times 3.6} \qquad (3)$$

$$P = \frac{3600 \times E}{\Delta t} \qquad (4)$$

where C is the specific capacitance (F g^{-1}), ΔV, and Δt are the operating potential and discharge time during discharge of the device, respectively.

RESULTS AND DISCUSSION

Material Analysis
Figure 1a shows the FTIR spectra of PANI PANI/AY17, PANI/MWCNTs, and PANI/MWCNT/AY17-3 composite electrode material. All of the spectra's primary peaks revealed the characteristic PANI structural bands. The typical vibration peak of PANI was found in the FTIR spectrum at 3374 cm^{-1} for N–H stretching, 1563 cm^{-1} for C C stretching (quinoid rings), 1464 cm^{-1} for C C stretching (benzenoid rings), 1292 cm^{-}

[1] for C–N stretching (quinoid rings), and 1234 cm^{-1} for C–N stretching (benzenoid rings). The quinoid peak was a typical peak of electrical transport because it measured the degree of delocalization of electrons in the structure. The peaks at 1563 cm^{-1} and 1292 cm^{-1} gradually migrated to lower wave numbers (1559 cm^{-1}, 1232 cm^{-1}) in the PANI/AY17 spectra, with a noticeable increase in the intensity ratio of the quinoid to benzenoid ring peaks. When the materials, including MWCNTs in PANI/MWCNTs and PANI/MWCNTs/AY17-3 composite materials, were tested, the intensities of these peaks were shown to rise. Because of the oxidation effect of MWCNTs introduced to the media, interactions between PANI and carbon nanotubes may occur (24). In the spectrum of PANI/MWCNTs/AY17-3, the effect of acid yellow 17 on aniline polymerization was clearly seen. The asymmetric and symmetric stretching vibrations of the –SO3 groups were attributed to the peaks at 1118 and 1040 cm^{-1}, respectively (17). For PANI, PANI/AY17, PANI/MWCNTs, and PANI/MWCNT/AY17-3, a strong band was observed at 1069, 1106, 1117, and 1118 cm^{-1}, which was attributed to N=Q=N (Q, quinoid ring) (25). This strong peak also showed peaks at 1096 and 1040 cm^{-1} after doping with AY17. There would be an interaction of AY17 with quinoid diamine groups from PANI.
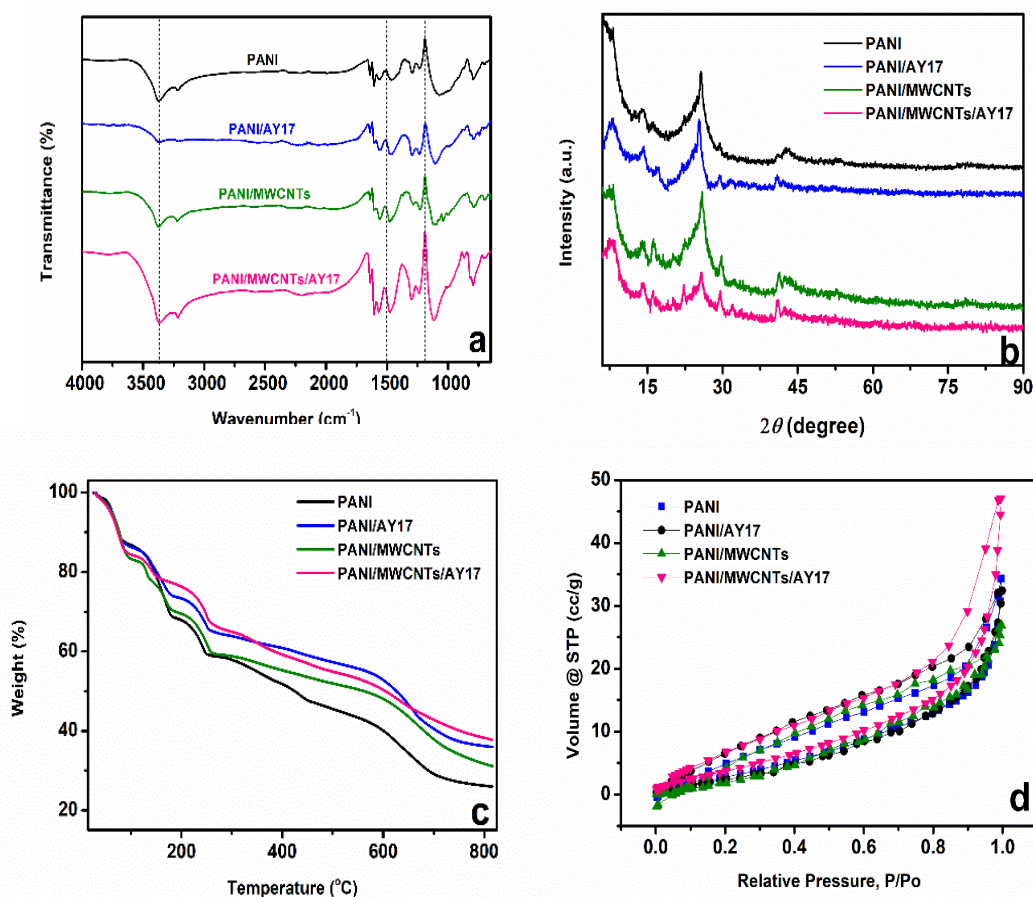
Figure 1: a) FTIR analysis, b) XRD patterns, c) TGA curves, and d) N_2 adsorption-desorption isotherms of PANI PANI/AY17, PANI/MWCNTs, PANI/MWCNT/AY17-3 composite electrode material.

Figure 1b shows the XRD analysis of PANI, PANI/AY17, PANI/MWCNTs, and PANI/MWCNT/AY17-3. The semi-crystalline polyaniline revealed three strong peaks at distinct diffraction angles, corresponding to crystal planes 121, 113, and 322 in Figure 1b, indicating that the majority of the chains structure of the resultant PANI was orientated in these three crystal planes (26). The PANI emeraldine salt showed a high peak at 2 = 25.57°, with a minor shoulder at 2 =

15 and 21, corresponding to the (322), (121), and (113) planes (27). PANI's XRD peaks showed a broad band around 25.57°, which was in good agreement with the literature. At 2 = 25.57°, PANI/AY17 showed a powerful and sharp peak. The crystal peaks for PANI/AY17 and PANI/MWCNTs were similar to those for PANI, showing that the PANI structure did not gain any additional crystalline structure. PANI/MWCNTs/AY17-3 XRD peaks were around 25.66°. In the case of composites, it was discovered that the PANI unit structure is intact, and peaks form around the peak shown in Figure 1b (28). The peaks of the PANI and the PANI/MWCNTs/AY17-3 nanocomposite were quite similar, indicating significant coverage of AY17-doped PANI onto MWNTs substrates (27). The MWCNTs also induced packing of the polymerization axis, thus maintaining a crystalline arrangement similar to that of PANI in the resulting composite (29).

Figure 1c represents the TGA thermograms of PANI, PANI/AY17, PANI/MWCNTs and PANI/MWCNT/AY17-3, which were performed under a nitrogen atmosphere. As seen in **Figure 1c**, the samples showed weight loss in three main stages; The elimination of moisture absorbed at the surface and polymer lattices was linked to the weight reduction in the first step (30). At 83.5 °C, PANI lost weight, while PANI/MWCNT/AY17-3 lost weight at 101.1 °C. Due to the elimination of

counter ion, the TGA curve for PANI drops drastically compared to PANI/MWCNT/AY17-3 (a weight loss of 6.5%), and the amount by weight was 19.65% in the second phase, and the polymer itself began to degrade (31,32). Finally, at the end of the third step, a polymer weight loss of 25.94% was observed for PANI at 815 °C and was higher than PANI/MWCNT/AY17-3 (37.78% at 816 °C). While PANI degrades at a faster rate with temperature, PANI/AY17, PANI/MWCNTs, and PANI/MWCNT/AY17-3 samples were observed to be more thermally stable. Because of the interaction of PANI with MWCNTs and AY17 dye molecules, the thermal stability of the PANI/MWCNT/AY17-3 sample was increased compared to pure PANI, as demonstrated by FTIR and XRD tests.

The effect of MWCNTs and AY17 dopant on the porosity and specific surface areas of the composite on PANI was examined by BET analysis, as shown in Figure 1d. The specific surface areas for PANI and the PANI/MWCNT/AY17-3 composite were 18.29 and 25.77 m^2/g, respectively, according to the BET study. The PANI electrode had a pore volume of 0.042 cc/g, whereas the PANI/MWCNT/AY17-3 composite electrode had a pore volume of 0.070 cc/g, and all electrodes were given in Table 2. In energy storage devices, increasing the surface area and pore volume allows redox active chemicals in the electrolyte seeping from the pore volumes to interact more with the electrode surface, allowing for easier mass transfer and thus improved energy and power density (33).

Table 2: BET surface analysis of PANI, PANI/AY17, PANI/MWCNTs, and PANI/MWCNT/AY17-3 Electrodes.

Electrode materials	PANI	PANI/AY17	PANI/MWCNTs	PANI/MWCNT/AY17
Surface area/m²/g	18.29	18.56	24.195	25.77
Pore volume/cc/g	0.042	0.048	0.040	0.072

Figure 2 depicts the surface morphology found in SEM images (a-d). The electrode surface was successfully coated with polymer by hydrothermal synthesis, and PANI gathered on the surface in cluster shapes. The polymer appears to be dispersed on the surface of the fibers in **Figures 2a and 2b** dispersed on the carbon felt for the PANI and PANI/AY17 electrodes. In the polymerization of PANI/MWCNT/AY17-3 on carbon felt medium, polymers with a larger porous feature and more compact structures were synthesized. A continuous matrix was also developed, which enhances the porosity of the composite and provides a large surface area for good electrode/electrolyte interface contact. This effect

could indicate that carbon nanotubes interact with MWCNTs, allowing for improved PANI deposition (34). In Figure 2d, it can also be shown that adding AY17 to the PANI and MWCNT medium reduces the development of huge agglomerated polymerized islands with unfavorable growth. Because the electrode-electrolyte interaction was stronger on such active surfaces, more electrolyte ions may move during charge-discharge operations in energy storage devices (35).

Electrochemical Analysis
Using cyclic voltammetry, galvanostatic charge–discharge, and electrochemical impedance techniques, the reversibility and redox

electrochemical properties of PANI and its composite with multi-wall carbon nanotubes and acid yellow 17 as a counter ion were investigated. Using a half-cell system in 3.0 M KCl electrolyte solution, the effect of AY17 concentration on electrode capacitive performance was investigated in the range of 1 to 5 mmol/L AY17. The cyclic voltammograms, galvanostatic charge-discharge tests, and capacitance values calculated from these tests, as well as electrochemical impedance measurements, are shown in **Figure 3(a-i).** PANI, PANI/AY17, PANI/MWCNTs, and PANI/MWCNT/AY17-3 were analyzed with the applied potential in the range of −0.8-0.5 V in **Figure 3a**. **Figure 3a** shows the voltammogram following the sequence PANI/MWCNT/AY17-3 > PANI/MWCNTs > PANI/AY17> PANI at a scan rate of 100 mV s^{-1} versus Ag/AgCl reference electrode. It can be noted that the PANI/MWCNT/AY17-3 and PANI/MWCNTs composite CV have larger areas of the encircled areas. The galvanostatic charge–discharge tests were recorded in a potential window of −0.8-0.5 V at the current density of 8.3 A g^{-1}. In **Figure 3b**, the discharge times were obtained at 17, 19, 46, and 50 seconds in 3.0 M KCl electrolyte solution, respectively. Figure 3c shows the values of gravimetric capacitances obtained from cyclic voltammograms and galvanostatic charge-discharge experiments. At a scan rate of 100 mV s^{-1}, the capacitance values for the PANI, PANI/AY17, PANI/MWCNTs, and PANI/MWCNT/AY17-3 were determined to be 55.0, 90.3, 151.1, and 177.9 F g^{-1}, respectively. At 8.3 current density, the capacitance values obtained from the GCD test were 109.0, 121.8, 301.3, and 320.5 F g^{-1} for PANI, PANI/AY17, PANI/MWCNTs, and PANI/MWCNT/AY17-3, respectively. When MWCNTs were added to PANI, the composite's specific capacitance rose when compared to PANI. According to the results of the BET surface area analysis, this leads to improved pore accessibility for electrode/electrolyte ion exchange. In addition, the functional groups of the AY17 dye enabled the development of redox behaviour of the PANI. In addition, -Cl bonds, N-N bonds in the ring structure, and sulfonate groups (SO_3^-) in the AY17 dye structure strengthened the delocalization in the chain structure, supporting the redox behavior of PANI (36).

PANI, PANI/AY17, PANI/MWCNTs, and PANI/MWCNT/AY17-3 electrode Nyquist curves fitted to a simple circuit model are shown in Figure 3d (inset in **Figure 3d**). Table 3 shows the impedance values of Rs, Rct, Cdl, and W obtained after fitting according to the simple circuit model. The results generated from the EIS analysis have error rates of less than 5%. The PANI/MWCNT/AY17-3 electrode had the lowest Rs value, while the PANI electrode showed the highest Rs value. The Rs values of PANI, PANI/AY17, PANI/MWCNTs, and PANI/MWCNT/AY17-3 electrodes were determined as 3.978 Ω, 3.458 Ω, 3.412 Ω, and 2.825 Ω, respectively. It caused a decrease in Rs and Rct values thanks to functional groups such as sulfonyl groups in the AY17 structure, which were added as counter-ions to the chain structure of PANI. In addition, Rs and Rct values were lower in the PANI/MWCNT/AY17-3 electrode since the benzenoid structure of PANI was supported by MWCNTs added to the medium during hydrothermal synthesis. The Rct values of PANI, PANI/AY17, PANI/MWCNTs, and PANI/MWCNT/AY17-3 electrodes were determined as 4.337 Ω, 4.171 Ω, 3.885 Ω, and 3.247 Ω, respectively. Small differences between Rs and Rct values were as expected since the EIS analyses of the electrodes were performed in the same electrolyte. The highest Cdl value was 577.4 e-6, and it belonged to the PANI/MWCNT/AY17-3 electrode synthesized together with AY17, and MWCNTs added to the medium during PANI synthesis. MWCNT, which improved the chain structure of PANI and caused an increase in delocalization in the benzenoid structure of PANI thanks to its strong electronic structure, caused the Rs and Rct to be lower in the PANI/MWCNT/AY17-3 electrode than the other electrodes and increased the Cdl value. Warburg impedance values (W) were determined as 308.8 e-6, 333.6 e-6, 476.7 e-6, and 553.5 e-6 for PANI, PANI/AY17, PANI/MWCNTs, and PANI/MWCNT/AY17-3 electrodes, respectively. The results obtained in the EIS analyses were also in agreement with the results of the CV and GCD analyzes of the electrodes. Here, the functional groups in the AY17 dye enabled the development of the PANI structure, while the MWCNTs added to the medium with AY17 reduced the resistance values of PANI, allowing the potential operating range to expand and displaying a more stable charge-discharge feature.
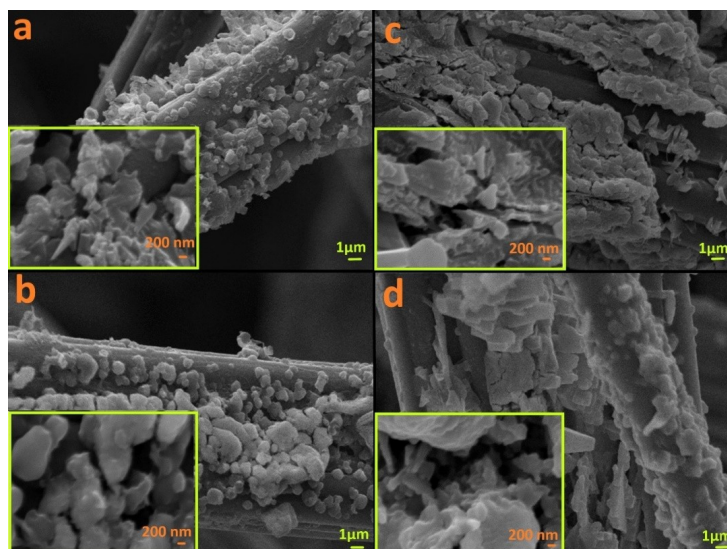
Figure 2: The SEM images of a) PANI, b) PANI/AY17, c) PANI/MWCNTs and d) PANI/MWCNT/AY17-3 electrode surfaces.
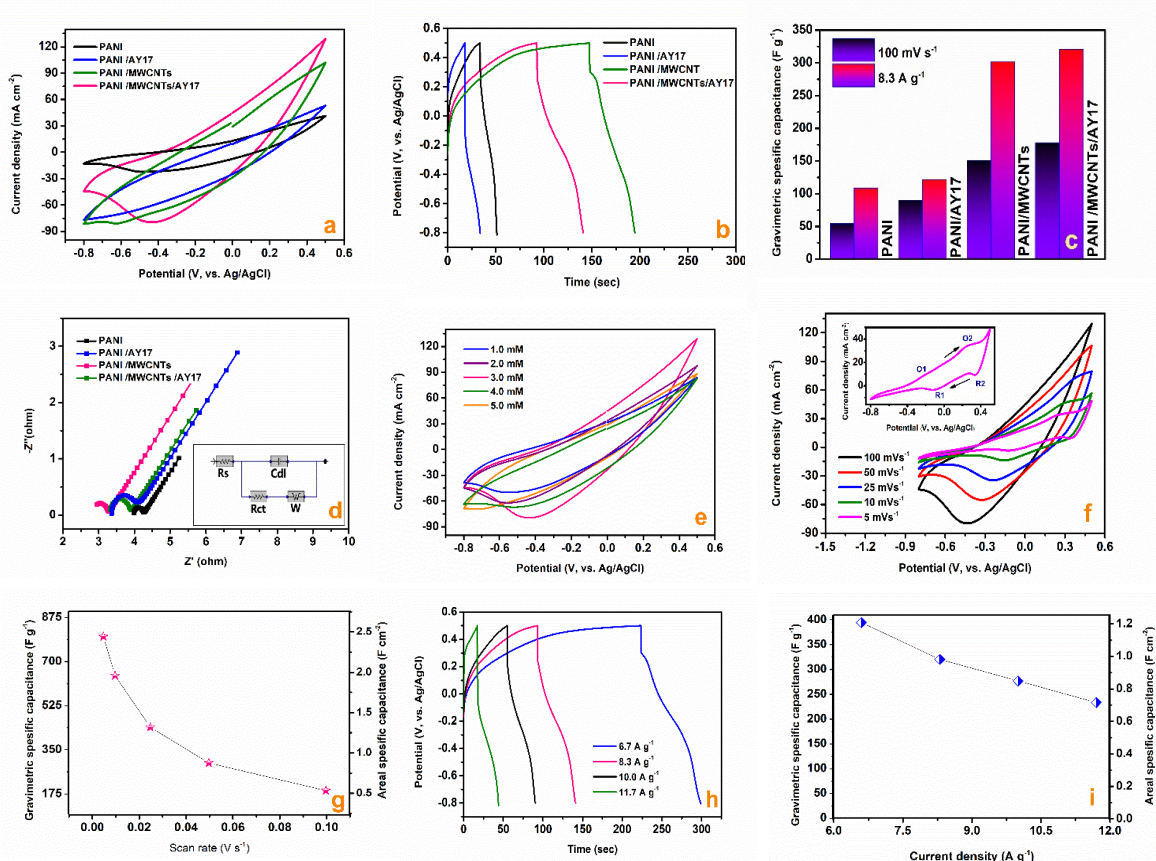
Figure 3: a) CVs at 100 mV s-1, b) GCD curves at 8.3 A g-1, c) Specific capacitance from CVs and GCD test, d) EIS Nyquist curves, the inset is equivalent circuit model, e) Effect of AY17 concentration on PANI/MWCNTs composite electrode, f) CV measurements of the PANI/MWCNT/AY17-3 electrode at different scan rates, g) Specific capacitance from CVs of the PANI/MWCNT/AY17-3 electrode, h) GCD profiles of the PANI/MWCNT/AY17-3 electrode at different current densities, i) Specific capacitance from GCD test of the PANI/MWCNT/AY17-3 electrode.

Table 3: Fitted impedance values of PANI, PANI/AY17, PANI/MWCNTs and PANI/MWCNT/AY17-3 electrodes.

Electrode Material	Rs / Ω	Rct / Ω	Cdl / F	W
PANI	3.978	4.337	245.1 e^{-6}	308.8 e^{-6}
PANI/AY17	3.548	4.171	417.5 e^{-6}	333.6 e^{-6}
PANI/MWCNTs	3.412	3.885	395.6 e^{-6}	476.7 e^{-6}
PANI/MWCNTs/AY17-3	2.825	3.247	577.4 e^{-6}	535.5 e^{-6}

In **Figure 3e**, the effect of different acid yellow 17 dye concentrations on the supercapacitor electrode of PANI/MWCNT on the flexible carbon felt was investigated using a half-cell system in 3.0 M KCl electrolyte solution, −0.8 V-(0.5) V vs Ag/AgCl operating potential window. An increase in the encircled area was observed in the CV of PANI/MWCNTs/AY17-3, indicating that the redox-active surface area at the electrode surface was more accessible (37,38). As a result, greater ion interaction at the electrolyte and electrode interface was found to improve charge storage performance.

The behavior of PANI/MWCNTs/AY17-3 supercapacitor electrodes at various scan rates of 5, 10, 20, 30, 50, and 100 mVs^{-1} was given in **Figure 3f.** The composite electrode showed two double redox peaks (-0.20/-0.11V and ~0.27/0.35V) at the scan rate of 5 mVs^{-1}. The conversion of the totally reduced leucoemeraldine base to partially oxidized emeraldine was linked with the first set of redox peaks, whereas the conversion of emeraldine to the fully oxidized pernigraniline form was related with the second set of redox peaks. (39). In **Figure 5g**, the value of specific capacitances was 814.1, 653.2, 439.8, 292.0, and 177.9 F g^{-1} at scan rates of 5 to 100 mV s^{-1}, respectively, calculated by the cyclic voltammograms from **Figure 5f**. This result showed that the PANI/MWCNTs/AY17-3 electrode has an excellent charge transfer process for energy storage systems. The charge-discharge profiles of the supercapacitor electrode were tested at various current densities of 6.6, 8.3, 10.0, and 11.7 Ag^{-1} in **Figure 3h**. The gravimetric and areal-specific capacitances of GCD test were presented in **Figure 3i**. The specific capacitances obtain at 394.9, 320.5, 276.9, and 233.3 F g^{-1} at the current densities of 6.6, 8.3, 10.0 and 11.7 Ag^{-1}, respectively. When we compared the SEM images of PANI and PANI/MWCNTs/AY17-3 electrode shown in **Figure 2**, the compactness and regular morphology of the PANI/MWCNTs/AY17-3 coated on a carbon felt surface was superior to the electrode made with PANI. Furthermore, when the surface area and pore volume features of PANI/MWCNTs/AY17-3 and other electrodes were examined using the N$_2$ adsorption-desorption

isotherms displayed in **Figure 1d**, the increase in electrode surface and electrochemical behavior were found to be consistent with the results. The morphology and electrochemical behavior of the PANI/MWCNTs/AY17-3 may be resulted from the electron-rich structure of disodium 2,5-dichloro-4-(5-hydroxy-3-methyl-4-(sulfophenylazo) pyrazol-1-yl) benzenesulfonate. Azo compounds enable electron delocalization as they contain both the benzene rings and the two nitrogen atoms connecting the rings (40). The presence of electron withdrawing and electron donating electrons can be very attractive for the use of these materials in textile-based energy storage studies. It also contains sulfonic groups with high protonation degree and electrical conductivity properties, which improves the capacitive property of the electrode. **Table 4** shows a literature search of capacitance values and other supercapacitor parameters using PANI polymer as the supercapacitor electrode.

The PANI/MWCNTs/AY17-3 electrode was used to build a symmetric supercapacitor device (full cell). Figures 4 and 5 illustrate the cell's electrochemical and capacitive performance in an aqueous 3.0 M KCl electrolyte solution (a-d). Figure 4a depicted the symmetric supercapacitor's cyclic voltammogram at various scan rates ranging from 5 to 200 mV s^{-1}. The operating potential of the supercapacitor was regulated between 0 and 0.9 V. Despite the higher scan rates, CV regions in cyclic voltammograms showed some coherence, depending on the scan rate. Figure 4b shows the gravimetric specific capacitance values calculated from the cyclic voltammograms in Figure 4a using Eq (1). As the scan rate ranged from 5-100 mV s^{-1}, the capacitance value fluctuated from 127.9 to 45.0 F g^{-1}. Figure 4c depicts charge–discharge testing at various current densities ranging from 0.3 to 2.0 A g^{-1}. The device's gravimetric specific capacitance value was estimated using the GCD test and Eq (2). In Figure 4d, the specific capacitance decreases from 103.7 to 40.0 F g^{-1} as the current density increases from 0.3 to 2.0 A g-1. At current densities of 0.3, 0.6, 1.0, 1.3, 1.7, and 2.0 A g^{-1}, IR drop values of 0.03, 0.05, 0.07, 0.09, 0.14, and 0.15 V were obtained from discharge curves at various current densities. In the galvanostatic discharge test, the electrode

retained 78.57 percent of its capacitance in the current density range of 0.3 to 1.7 A g^{-1}, indicating

excellent charge transfer and high capacitance.
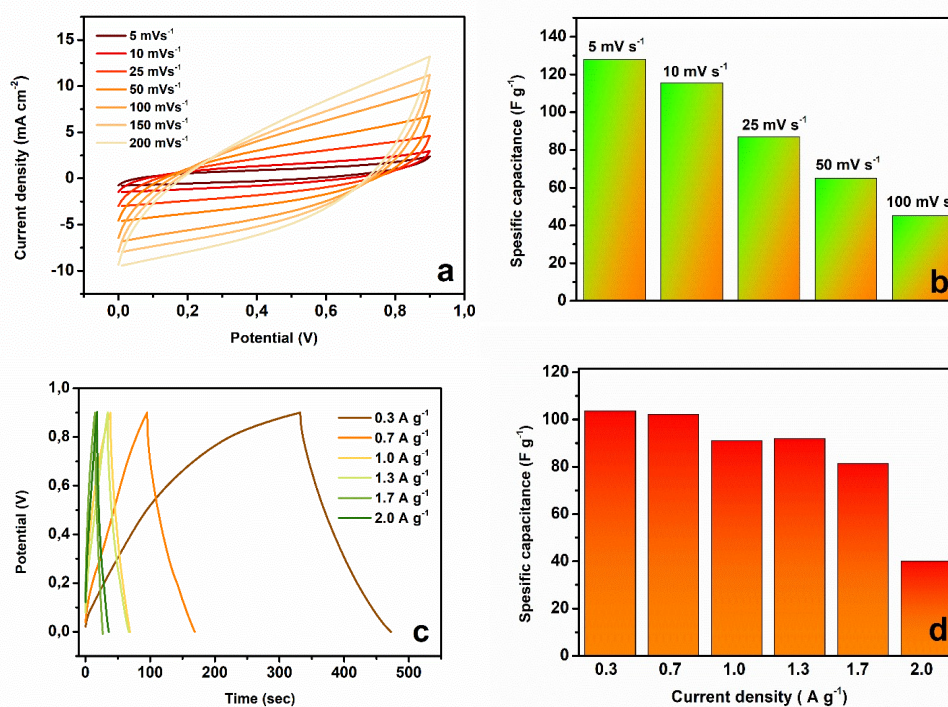
Figure 4: a) CVs at different scan rates, b) Specific capacitance values from CVs, c) GCD curves at different current densities, d) Specific capacitance values from GCD of symmetric supercapacitor.

Figure 5a shows a long-life cycling test of a symmetric supercapacitor. The capacitance retention of a symmetric supercapacitor was tested through 2,500 CV cycles at a scan rate of 200 mV s^{-1} with a potential window of 0.9 V. Despite using only polymeric and low-cost components and an aqueous electrolyte, the device demonstrated good capacitance retention of 81.76 percent after 2,500 cycles. As the number of cycles increased, the capacitance value decreased, indicating that sections of the electrode surface were no longer accessible to electrolyte ions.

Figure 5b shows the Nyquist curves obtained as a result of the EIS analysis of the PANI//MWCNTs/AY17-3 // PANI//MWCNTs/AY17-3 symmetric supercapacitor before the long cycle test and after 2,500 cycles. The equivalent circuit model was presented in the inset of **Figure 5b**.

While the Cdl value of the symmetrical supercapacitor device was 396.5 e^{-6} before charge-discharge, it decreased to 289.4 e^{-6} after 2500 cycles, as expected. According to the Cdl values, after 2,500 cycles, the PANI//MWCNTs/AY17-3 // PANI//MWCNTs/AY17-3 symmetric supercapacitor largely preserved its capacitance. The Warburg impedance value was initially 417.9 e^{-6}. After 2500 cycles, this value became 356.4 e^{-6}. The decrease in the Warburg impedance value was caused by partial deformation due to ion adsorption on the electrode surface over time after the long cycle test. The difference between the Rs and Rct values of the symmetric supercapacitor device before the long cycle test was lower than the difference between the Rs and Rct values after 2500 cycles. After 2500 cycles, the charge transfer resistance increased as the ions adsorbed on the electrode surface and the redox active regions reduced.

Table 4: The list of the maximum capacitance, electrolyte, and capacitance retention tests for PANI-based electrodes materials and devices.

Electrode materials	Electrolyte	Measurement type	Max. Capacitance	Cycling	Method	Ref
PANI/MWCNT	0.5 M H_2SO_4	3-electrode	590.7 F g^{-1} , 50 mVs^{-1}	500 (90%)	Chemical synthesis	(41)
PANI/MWCNTs (8 wt%)	PVA/H_2SO_4,	3-electrode	446.9 F g^{-1}, 40 mVs^{-1}	10,000 (84%)	Chemical synthesis	(42)
PANI/MWNTs	1.0 M $NaNO_3$	3-electrode	328 F g^{-1}, 5 mA cm^{-2}	1,000 (80%)	CVD/ Chemical synthesis	(43)
PANI/CNT	-	3-electrode	1266 F g^{-1}, 1 A g^{-1}	10,000 (83%)	Chemical grafting polymerization	(44)
PANI/MWCNT	1.0 M $LiClO_4$	3-electrode	174 F g^{-1}, 0.5 A g^{-1}	1,000 (100%)	Chemical synthesis	(45)
PANI/MWCNT	1.0 M H_2SO_4 PVA/H_2SO_4/ NQS	3-electrode 2-electrode	1100 F g^{-1}, 5 mVs^{-1} -	3,000 (93%)	Enzymatic synthesis	(46)
GNS/PANI	1.0 M H_2SO_4	3-electrode	532.3 F g^{-1}, 2 mVs^{-1}	1,000 (99%)	Hydrothermal synthesis	(20)
Graphene/MnO2/PANI	1.0 M Na_2SO_4	3-electrode	305 F g-1 , 1 A g^{-1}	1,000 (90%)	Hydrothermal synthesis	(47)
PC-Cs/CNTs/PANI	6.0 M KOH	3-electrode 2-electrode	767 F g^{-1} , 1 A g^{-1} 102.5 F g^{-1}, 0.5 A g^{-1}	5,000 (88%)	Chemical synthesis	(48)
PANI//MWCNTs/AY17-3	3.0 M KCl	3-electrode 2-electrode	814.1 F g^{-1}, 5 mVs^{-1} 127 F g^{-1}, 5 mVs^{-1}	2,500 (82%)	Hydrothermal synthesis	[This work]
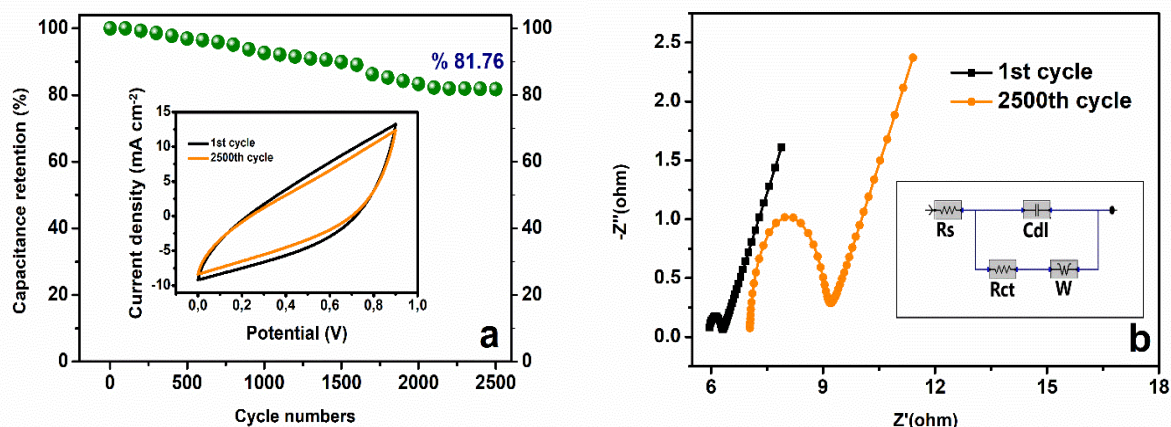
Figure 5: a) Long life cycling test of symmetric supercapacitor, b) Nyquist impedance curves of symmetric supercapacitor. The inset is equivalent circuit model.
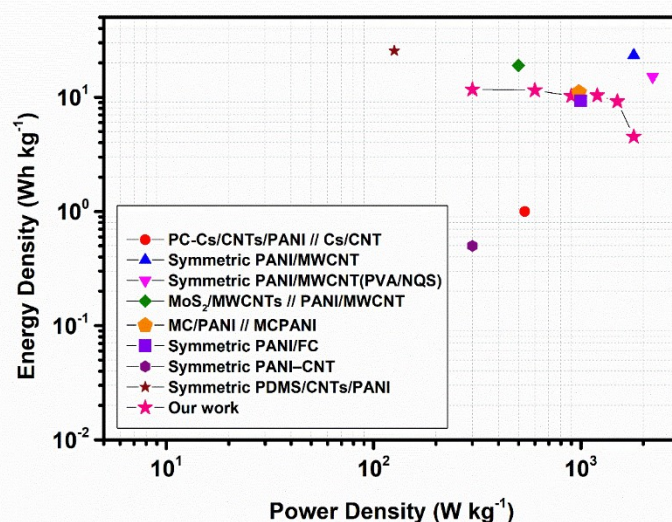
Figure 6: Energy density and power density for comparing our supercapacitor in Ragone plot.

According to Equations (3) and (4), the symmetric supercapacitor had a maximum energy density of 11.7 Wh/kg at 0.3 A g^{-1} and a maximum power density of 1800 W/kg at 2.0 A g^{-1} (4). Figure 5 shows that the built symmetrical supercapacitor had a good energy and power density range when compared to the literature. The device's Ragone plot is based on the GCD test. In the asymmetrical supercapacitor made utilizing PC-Cs/CNTs/PANI as the positive electrode and PC-Cs/CNT as the negative electrode, the device had an energy density of 56.9 Wh kg^{-1} at a power density of 537 W kg^{-1}, which was higher than some previously reported PANI-based supercapacitors (48). At a high power density of 2217.95 W/kg, the MoS$_2$|MWCNTs and PANI|MWCNTs composite electrodes had an energy density of 15.09 Wh/kg (49). At 0.5

kWkg^{-1}, the complete symmetric cell made of MC/PANI has a high energy density of 19 Whkg^{-1}. (50). For PANI/MWCNT, energy density and power density for the device were calculated as 11.1 Wh/kg and 0.98 kW/kg (51). The maximum specific energy of 0.5 Wh kg^{-1} and a maximum specific power of 0.3 kW kg^{-1}, were found for PANI–CNT flexible supercapacitors (52).

CONCLUSIONS

PANI//MWCNTs/AY17-3 composite electrode was successfully synthesized by hydrothermal synthesis, and its supercapacitor performance was investigated via electrochemical characterizations. By altering the dye content of AY17, the behavior of AY17 in modulating electrochemical

characteristics of PANI/CNT composite was investigated. At a scan rate of 5 mV s^{-1}, the PANI/MWCNTs/AY17 composite electrode with 3mM AY17 demonstrated a maximum specific capacitance of 814.1 F g^{-1}, which was much greater than PANI and PANI/MWCNTs composite electrodes. In a 3.0 M KCl aqueous electrolyte, a symmetric supercapacitor has a maximum energy density of 11.7 W h kg^{-1} and a maximum power density of 1800 W kg^{-1}. After 2000 cycles, the capacitance retention of the symmetric supercapacitor was determined to be greater than 80%. The influence of a textile dye on a multi-walled carbon nanotubes/polyaniline composite as a promising supercapacitor electrode material for next-generation textile-based flexible supercapacitors was supported by all of the findings.

REFERENCES

1. Chakraborty S, L. MN. Review{\textemdash}An Overview on Supercapacitors and Its Applications. J Electrochem Soc [Internet]. 2022;169(2):20552. Available from: <URL>.

2. Mohd Abdah MAA, Azman NHN, Kulandaivalu S, Sulaiman Y. Review of the use of transition-metal-oxide and conducting polymer-based fibres for high-performance supercapacitors. Mater Des. 2019;186:108199. <URL>.

3. Yazar S, Arvas MB, Sahin Y. An ultrahigh-energy density and wide potential window aqueous electrolyte supercapacitor built by polypyrrole/aniline 2-sulfonic acid modified carbon felt electrode. Int J Energy Res [Internet]. Available from: <URL>.

4. Uke SJ, Mardikar SP, Kumar A, Kumar Y, Gupta M, Kumar Y. A review of π-conjugated polymer-based nanocomposites for metal-ion batteries and supercapacitors. R Soc Open Sci. 2021;8(10). <URL>.

5. Arvas MB, Gencten M, Sahin Y. One-step synthesized N-doped graphene-based electrode materials for supercapacitor applications. Ionics (Kiel). 2021 May;27(5):2241–56. <URL>.

6. Arvas MB, Yazar S, Sahin Y. Electrochemical synthesis and characterization of self-doped aniline 2-sulfonic acid-modified flexible electrode with high areal capacitance and rate capability for supercapacitors. Synth Met [Internet]. 2022;285:117017. Available from: <URL>.

7. Liao G, Gong Y, Yi C, Xu Z. Soluble, Antibaterial, and Anticorrosion Studies of Sulfonated Polystyrene/Polyaniline/Silver Nanocomposites Prepared with the Sulfonated Polystyrene Template. Chinese J Chem [Internet]. 2017;35(7):1157–64. Available from: <URL>.

8. Beygisangchin M, Abdul Rashid S, Shafie S, Sadrolhosseini AR, Lim HN. Preparations, Properties, and Applications of Polyaniline and Polyaniline Thin Films-A Review. Polymers (Basel) [Internet]. 2021 Jun

18;13(12):2003. Available from: <URL>.

9. Thakur AK, Choudhary RB, Majumder M, Majhi M. Fairly improved pseudocapacitance of PTP/PANI/TiO2 nanohybrid composite electrode material for supercapacitor applications. Ionics (Kiel) [Internet]. 2018;24(1):257–68. Available from: <URL>.

10. Thakur AK, Deshmukh AB, Choudhary RB, Karbhal I, Majumder M, Shelke M V. Facile synthesis and electrochemical evaluation of PANI/CNT/MoS2 ternary composite as an electrode material for high performance supercapacitor. Mater Sci Eng B [Internet]. 2017;223:24–34. Available from: <URL>.

11. Dawouda HD, Altahtamounia TM, Zaghoa MM, Bensalahb N. A brief overview of flexible CNT/PANI super capacitors. Mater Sci Nanotechnol. 2017;01(02).

12. Li J, Qiu S, Liu B, Chen H, Xiao D, Li H. Strong interaction between polyaniline and carbon fibers for flexible supercapacitor electrode materials. J Power Sources [Internet]. 2021;483(August 2020):229219. Available from: <URL>.

13. Lü QF, Chen G, Lin TT, Yu Y. Dye-functionalized graphene/polyaniline nanocomposite as an electrode for efficient electrochemical supercapacitor. Compos Sci Technol [Internet]. 2015;115:80–6. Available from: <URL>.

14. Wang Q, Song H, Li W, Wang S, Liu L, Li T, et al. Facile synthesis of polypyrrole/graphene composite aerogel with Alizarin Red S as reactive dopant for high-performance flexible supercapacitor. J Power Sources [Internet]. 2022;517:230737. Available from: <URL>.

15. Xueying Y, Jijue L, Xinkun S, Yingzhao H, Xiaoxiao D, Yongjin Z, et al. Facile Synthesis of Polyaniline-Prussian Blue Composite for High-Performance Supercapacitors. Int J Nanoparticles Nanotechnol. 2017;3(1).

16. Arvas MB, Gürsu H, Gencten M, Sahin Y. Preparation of different heteroatom doped graphene oxide based electrodes by electrochemical method and their supercapacitor applications. J Energy Storage [Internet]. 2021 Mar;35:102328. Available from: <URL>.

17. Wang Q, Feng Y, Feng J, Li D. Enhanced thermal- and photo-stability of acid yellow 17 by incorporation into layered double hydroxides. J Solid State Chem [Internet]. 2011;184(6):1551–5. Available from: <URL>.

18. Jin L, Jiang Y, Zhang M, Li H, Xiao L, Li M, et al. Oriented Polyaniline Nanowire Arrays Grown on Dendrimer (PAMAM) Functionalized Multiwalled Carbon Nanotubes as Supercapacitor Electrode Materials. Sci Rep [Internet]. 2018;8(1):6268. Available from: <URL>.

19. Yasuda A, Shimidzu T. Chemical Oxidative Polymerization of Aniline with Ferric Chloride. 1993;25(4):329–38. <URL>.

20. Wang R, Han M, Zhao Q, Ren Z, Guo X, Xu C, et al. Hydrothermal synthesis of nanostructured graphene/polyaniline composites as high-capacitance electrode materials for supercapacitors. Sci Rep

[Internet]. 2017;7(1):44562. Available from: <URL>.

21. Pandey K, Yadav P, Mukhopadhyay I. Elucidating the effect of copper as a redox additive and dopant on the performance of a PANI based supercapacitor. Phys Chem Chem Phys. 2015;17(2):878–87. <URL>.

22. Lim SP, Huang NM, Lim HN. Solvothermal synthesis of SnO2/graphene nanocomposites for supercapacitor application. Ceram Int [Internet]. 2013;39(6):6647–55. Available from: <URL>.

23. Sajjad M, Chen X, Yu C, Guan L, Zhang S, Ren Y, et al. High Energy Density Asymmetric Supercapacitor Based on NiCo2S4/CNTs Hybrid and Carbon Nanotube Paper Electrodes. J Mol Eng Mater [Internet]. 2019;07(01n02):1950004. Available from: <URL>.

24. Qiu G, Zhu A, Zhang C. Hierarchically structured carbon nanotube-polyaniline nanobrushes for corrosion protection over a wide pH range. RSC Adv. 2017;7(56):35330–9. <URL>.

25. John A, Mahadeva SK, Kim J. The preparation, characterization and actuation behavior of polyaniline and cellulose blended electro-active paper. Smart Mater Struct. 2010;19(4). <URL>.

26. Padmapriya S, Haripriya S, Jaidev K, Sudha V, Kumar D, Pal S. Storage and evolution of hydrogen in acidic medium by polyaniline. Int J Energy Res. 2018;42(3):1196–209. <URL>.

27. Iqbal J, Ansari MO, Numan A, Wageh S, Al-Ghamdi A, Alam MG, et al. Hydrothermally Assisted Synthesis of Porous Polyaniline@Carbon Nanotubes–Manganese Dioxide Ternary Composite for Potential Application in Supercapattery. Polymers (Basel) [Internet]. 2020;12(12). Available from: <URL>.

28. Mitra M, Kulsi C, Chatterjee K, Kargupta K, Ganguly S, Banerjee D, et al. Reduced graphene oxide-polyaniline composites—synthesis{,} characterization and optimization for thermoelectric applications. RSC Adv [Internet]. 2015;5(39):31039–48. Available from: <URL>..

29. Tang L, Duan F, Chen M. Fabrication of ferric chloride doped polyaniline/multilayer super-short carbon nanotube nanocomposites for supercapacitor applications. J Solid State Electrochem. 2016;20. <URL>.

30. Rajagopalan B, Hur SH, Chung JS. Surfactant-treated graphene covered polyaniline nanowires for supercapacitor electrode. Nanoscale Res Lett [Internet]. 2015;10(1):1–9. Available from: <URL>.

31. Ali LIA, Ismail HK, Alesary HF, Aboul-Enein HY. A nanocomposite based on polyaniline, nickel and manganese oxides for dye removal from aqueous solutions. Int J Environ Sci Technol [Internet]. 2021;18(7):2031–50. Available from: <URL>.

32. Ahmad S, Sultan A, Raza W, Muneer M, Mohammad F. Boron nitride based polyaniline nanocomposite: Preparation, property, and application. J Appl Polym Sci. 2016;133(39). <URL>.

33. Bhat MA, Rather RA, Shalla AH. PEDOT and PEDOT:PSS conducting polymeric hydrogels: A report on their emerging applications. Synth Met [Internet]. 2021;273(January):116709. Available from: <URL>.

34. Hilário RB, de Moraes TH, da Rocha Pimentel Gonçalves JM, Gandara M, Gonçalves ES. Influence of heat treatment and electrochemical treatment on the properties of PANI electrodeposited on carbon fiber felt. Diam Relat Mater [Internet]. 2022;123:108867. Available from: <URL>.

35. Ibrahim NI, Wasfi AS. Electrochemical evaluation of polyaniline/multi-walled carbon nanotube composite synthesized by microwave plasma polymerization as a supercapacitor electrode. IOP Conf Ser Mater Sci Eng. 2020;757(1). <URL>.

36. Yazar S, Atun G. Electrochemical synthesis of tunable polypyrrole-based composites on carbon fabric for wide potential window aqueous supercapacitor. Int J Energy Res [Internet]. Available from: <URL>.

37. Rincón RA, Artyushkova K, Mojica M, Germain MN, Minteer SD, Atanassov P. Structure and Electrochemical Properties of Electrocatalysts for NADH Oxidation. Electroanalysis [Internet]. 2010;22(7–8):799–806. Available from: <URL>.

38. Jarjes ZA, Samian MR, Ab Ghani S. Conductive polymers: Their preparations and catalyses on NADH oxidation at carbon cloth electrodes. Arab J Chem [Internet]. 2015;8(5):726–31. Available from: <URL>.

39. Song E, Choi J-W. Conducting Polyaniline Nanowire and Its Applications in Chemiresistive Sensing. Nanomaterials. 2013;3:498–523. <URL>.

40. Li Y, Patrick BO, Dolphin D. Near-Infrared Absorbing Azo Dyes: Synthesis and X-ray Crystallographic and Spectral Characterization of Monoazopyrroles, Bisazopyrroles, and a Boron−Azopyrrole Complex. J Org Chem [Internet]. 2009 Aug 7;74(15):5237–43. Available from: <URL>.

41. Ates M, Serin MA, Calisskan S. Electrochemical supercapacitors of PANI/MWCNT, PEDOT/MWCNT and P(ANI-co-EDOT)/MWCNT nanocomposites. Polym Bull [Internet]. 2019 Jun 27;76(6):3207–31. Available from: <URL>.

42. Pal R, Goyal SL, Rawal I. High-performance solid state supercapacitors based on intrinsically conducting polyaniline/MWCNTs composite electrodes. J Polym Res [Internet]. 2020;27(7):179. Available from: <URL>.

43. Dong B, He B-L, Xu C-L, Li H-L. Preparation and electrochemical characterization of polyaniline/multi-walled carbon nanotubes composites for supercapacitor. Mater Sci Eng B [Internet]. 2007;143(1):7–13. Available from: <URL>.

44. Che B, Li H, Zhou D, Zhang Y, Zeng Z, Zhao C, et al. Porous polyaniline/carbon nanotube composite electrode for supercapacitors with outstanding rate capability and cyclic stability. Compos Part B Eng [Internet]. 2019;165:671–8. Available from: <URL>.

45. M. J, M. M, Jayalekshmi S, Jayaraj MK. PANI/MWCNT composite electrode for supercapacitor

applications. In: Kobayashi NP, Talin AA, Islam MS, Davydov A V, editors. Low-Dimensional Materials and Devices 2018 [Internet]. SPIE; 2018. p. 33–8. Available from: <URL>.

46.   Shumakovich GP, Morozova O V, Khlupova ME, Vasil'eva IS, Zaitseva EA, Yaropolov AI. Enhanced performance of a flexible supercapacitor due to a combination of the pseudocapacitances of both a PANI/MWCNT composite electrode and a gel polymer redox electrolyte. RSC Adv [Internet]. 2017;7(54):34192–6. Available from: <URL>.

47.   Chen W, Tao X, Li Y, Wang H, Wei D, Ban C. Hydrothermal synthesis of graphene-MnO2-polyaniline composite and its electrochemical performance. J Mater Sci Mater Electron. 2016;27(7):6816–22. <URL>.

48.   Hong X, Wang X, Li Y, Deng C, Liang B. Potassium citrate-derived carbon nanosheets/carbon nanotubes/polyaniline ternary composite for supercapacitor electrodes. Electrochim Acta [Internet]. 2022;403:139571. Available from: <URL>.

49.   Cheng B, Cheng R, Tan F, Liu X, Huo J, Yue G. Highly Efficient Quasi-Solid-State Asymmetric Supercapacitors Based on MoS2/MWCNT and PANI/MWCNT Composite Electrodes. Nanoscale Res Lett [Internet]. 2019;14(1):66. Available from: <URL>.

50.   Banerjee J, Dutta K, Kader MA, Nayak SK. An overview on the recent developments in polyaniline-based supercapacitors. Polym Adv Technol [Internet]. 2019;30(8):1902–21. Available from: <URL>.

51.   Malik R, Zhang L, McConnell C, Schott M, Hsieh Y-Y, Noga R, et al. Three-dimensional, free-standing polyaniline/carbon nanotube composite-based electrode for high-performance supercapacitors. Carbon N Y [Internet]. 2017;116:579–90. Available from: <URL>.

52.   Liu Q, Nayfeh MH, Yau S-T. Brushed-on flexible supercapacitor sheets using a nanocomposite of polyaniline and carbon nanotubes. J Power Sources [Internet]. 2010;195(21):7480–3. Available from: <URL>.

Osunniran WA et al. JOTCSA. 2022; 9(4): 1309-1322.

RESEARCH ARTICLE

Heteroleptic Transition Metal Complexes of Eflornithine Hydrochloride Monohydrate: Synthesis, Characterization, *in silico* and *in vitro B*iological Studies

Wahab A. Osunniran[1]* , Yusuf O. Ayipo[1,3] iD **, Abdullahi O. Rajee[2] , Adebayo T. Bale[1] , Mercy O. Bamigboye[4] , and Joshua A. Obaleye[2]**

[1]Mus Alparslan University, Department of Math, Mus, Turkey
[1]Kwara State University, Department of Chemistry and Industrial Chemistry, Malete, P.M.B 1530, Ilorin, Nigeria.
[2]University of Ilorin, Department of Chemistry, P.M.B 1515, Ilorin, Kwara State, Nigeria
[3]Universiti Sains Malaysia, Centre for Drug Research, Pulau, 11800 USM, Pinang, Malaysia.
[4]University of Ilorin, Department of Industrial Chemistry, Ilorin, Kwara State, P.M.B 1515, Nigeria

Abstract: Incessant development of resistance to drugs by microorganisms remains a major setback associated with the currently available antibiotics, thereby making imperative a continuous search for alternative candidates with improved efficacy. Previous studies have shown enhanced antimicrobial activity of some bioactive molecules upon coordination with metal ions. Thus, in this study, Cu(II), Co(II), and Ni(II) complexes of eflornithine hydrochloride monohydrate (EHM) were synthesized and probed for bactericidal activity via *in vitro* and *in silico*. The characterization results such as CHN analysis, FTIR, UV-visible magnetic susceptibility and Electrospray Ionization Mass Spectrometry (ESI-MS) reveal that EHM coordinates as a bidentate ligand to each central metal ion in the molar ratio 1:2 through O and N in the COO^- and NH_2 group respectively, and also suggest octahedral geometry in each complex. The physicochemical and pharmacokinetics parameters predicted *in silico* support the bio-applicability and safety of the complexes. From the *in vitro* antibacterial study, the complexes demonstrate improved activity against *Staphylococcus aureus*, *Escherichia coli,* and *Pseudomonas aeruginosa* with an average minimum inhibitory concentration (MIC) of 0.01 mg/L similar to ciprofloxacin, compared to EHM whose MIC >1.00 mg/L. Although, not all the complexes satisfy Lipinski's drugability rule of 5 due to their molecular weight, however, coordination with metal ions improves the biological activities of EHM and the complexes demonstrate potential for further transformation into antibiotic therapeutics.

INTRODUCTION

The significance of metal ions or metal ion binding components into biological systems for diagnosis and treatment of diseases is one of the focal segments in the field of bioinorganic chemistry (1).

A characteristic feature of metals is that they form positively charged ions by losing electrons to become soluble in biological fluids. In this cationic forms, metals play their important roles in biological functions. Metal ions are electron deficient and a good number of biological molecules such as

proteins and DNA are electron rich. Thus, the interaction of these opposing charges leads to strong affinity between metalloproteinase-inclined metal ions and the corresponding biological targets (2). Some important biological functions are strongly dependent on the coordinated metal ion within the structures of the relevant enzymes and cofactors. Examples of such metal-organic framework for biological processes include the hemoglobin in red blood cells which contains an iron porphyrin complex for oxygen transport and storage, the chlorophyll in green plants for photosynthetic process which contains magnesium porphyrin complex, cobalt complex in the coenzyme B_{12} is essential for the transfer of alkyl groups and Vitamin B_{12} (cobaloxime), a cobalt complex containing a glyoxime ligand, and is one of the examples of a naturally occurring organometallic complex (3).

The rapid occurrence of antibiotic resistance (AR) has become a global threat which oftentimes endanger the efficacy of the available therapeutics against emerging pathogenic diseases. In addition to the resistance features constantly developed by the microbes after a prolong treatment, AR is also attributed to the abuse or misuse of the antibiotic medications as well as inadequate pharmaceutical innovations to match the meteoric transmutations and translations of the microorganism genomes (4). Thus, a coordinated research development is continuously required to manage the crisis. Inorganic compounds especially metal complexes have performed an essential role in the advancement of new metal based drugs which were found not only to have good spectrum of activity, but having novel mechanistic potentials which are amenable for overcoming AR (5). Metals not only offer templates for synthesis, but they also introduce functionalities that improve drug delivery vectors and interact favorably with metalloproteinases to accomplish biological purposes. The pharmacological activity of metal complexes is greatly dependent on the type of the metal ions and the donor sequence of the ligands since separate ligands exhibit different biological properties (5,6). Moreso, the efficacy of various organic molecules with therapeutic potentials can be enhanced upon coordination to appropriate metal ions to form complexes (7,8). The pharmacodynamics and pharmacokinetics of these complexes usually increase, with the resultant tendency to penetrate the cell membrane of the microbes. Again, the decrease in the polarity of the metal ions by partial sharing of its positive charges with the donor group of ligands have been proposed as reasons for their better efficacy over their parent compound ligands while the structural modifications favor multitarget pharmacological mechanisms to overcome AR (5).

Eflornithine hydrochloride monohydrate with molecular formula of $C_6H_{12}F_2N_2O_2.HCl.H_2O.$, an antiprotozoal agent, is a specific, irreversible inhibitor of the enzyme ornithine decarboxylase.The drug was initially formulated for use in cancer and is in phase III clinical trials for its use in preventing recurrence of superficial bladder cancer. It has been used as antiprotozoal agent in the treatment of meningoencephalic stage of trypanosomiasis caused by(African trypanosomiasis). Eflornithine has been tested for its anti inflammatory activity. Eflornithine 13.9% cream is used to inhibit growth and reduce the amount of facial hair in women. (9,10,11). This article however focuses on the potential of eflornithine hydrochloride monohydrate as antibiotic agent.

Therefore, in continuation of our studies on coordination of metal with biologically important ligands (12-14), we aim to synthesize and characterize new set of transition divalent metals (Cu(II), Co(II) and Ni(II)) complexes containing Eflornithine hydrochloride monohydrate (EHM) (Fig. 1) as ligand with different donor atoms and probe their multi-mechanistic pharmacological potentials against some drug-resistant bacterial strains.
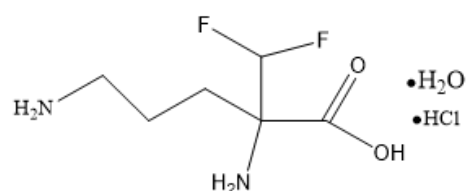
Figure 1: Molecular structure of eflornithine hydrochloride monohydrate. (11,15)

EXPERIMENTAL

Materials
The EHM, copper(II) nitrate trihydrate, nickel(II) acetate tetrahydrate and cobalt(II) acetate tetrahydrate, silver nitrate, ammonia, methanol, and acetone were commercially obtained from British Drug House Chemical Limited Co. Poole England. Isolates of S*taphylococcus aureus*, *Escherichia coli* and *Pseudomonas aeruginosa* were cultured and obtained from the University of Ilorin Teaching Hospital through Microbiology Department, University of Ilorin, Nigeria.

Synthesis of [Cu(EHM)₂(NO₃)(Cl)].2H₂O (Complex 1)
A 0.2416 g (1 mmol) of copper(II) nitrate trihydrate dissolved in 20 mL methanol with slow addition of 0.4734 g (2 mmol) of EHM in 10 mL concentrated ammonia while stirring resulted in blue colored solution. The solution was refluxed for 6 hours and left at room temperature for 8 hours after which blue precipitates were formed (Scheme 1). The progress of the reaction was monitored using TLC and melting point determination. The precipitates

(complex) formed were separated out by filtration, washed with cold methanol and dried over silica gel in a desiccator.
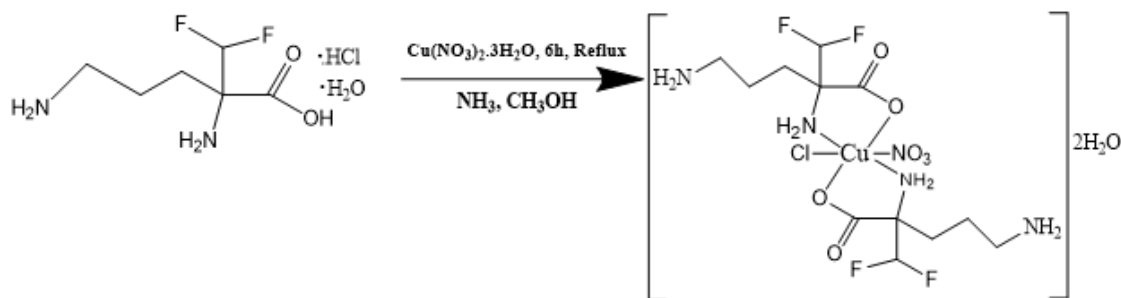
Scheme 1: Synthesis of complex 1.

Synthesis of [Ni(EHM)$_2$(CH$_3$COO)$_2$]Cl$_2$.2H$_2$O (Complex 2)

To the 10 mL aqueous solution containing 0.4734 g (2 mmol) EHM, 20 mL of methanolic solution containing 0.2489 g (1 mmol) nickel(II) acetate tetrahydrate was added under constant stirring. The resulting mixture was refluxed for 12 hours until stable green precipitates appeared (scheme 2). The progress of the reaction was monitored using TLC and melting point determination. The precipitate formed were separated out by filtration, washed thrice with cold acetone, recrystallized in water/acetone (3:1) solution and dried over silica gel in a desiccator.
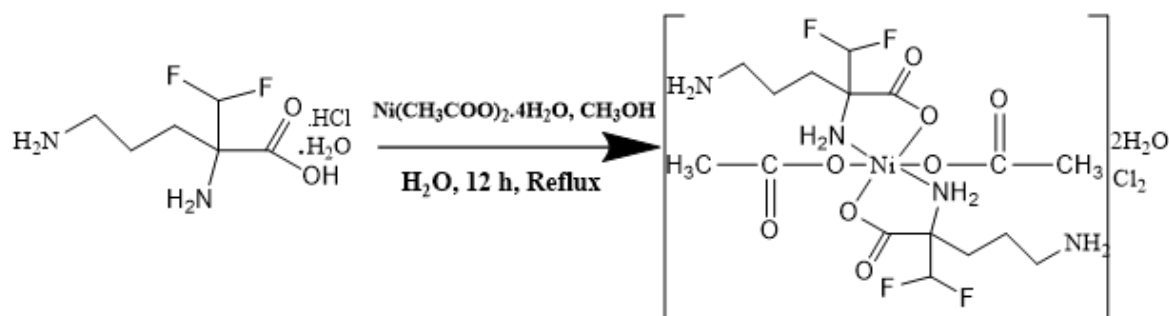
Scheme 2: Synthesis of complex 2.

Synthesis of [Co(EHM)$_2$(H$_2$O)$_2$]Cl$_2$ (Complex 3)

A 0.4734 g (2 mmol) of EHM was dissolved in 15 mL of distilled water followed by a slow addition of 0.2491 g (1 mmol) of cobalt(II) acetate tetrahydrate previously dissolved in 10 mL of methanol. The resulting pinkish solution was then refluxed for 4 h until stable precipitates were formed (Scheme 3). After cooling, the product was filtered, dried and redissolved in methanol for recrystallization. The progress of the reaction was monitored using TLC and melting point determination. The recovered solution was allowed to evaporate slowly at room temperature. The purple precipitate obtained was then dried over silica gel.
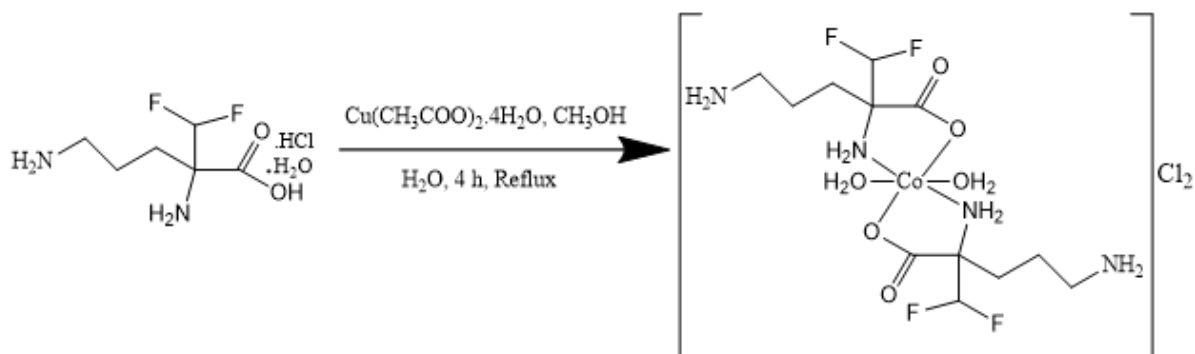
Scheme 3: Synthesis of complex 3.

Preliminary test for water molecule, chloride and nitrate ions
The presence of water of crystallization within or outside the coordination sphere of each complex was assessed using cobalt chloride paper. The color change of the paper from blue to pink indicates positive. For the chloride ion outside the coordination sphere, aqueous $AgNO_3$ and NH_4OH were used for confirmation on the solution of each complex. A white precipitate soluble in excess NH_4OH indicate the presence of uncoordinated Cl^- ion. The complexes were strongly heated to qualitatively observe the fumes produced due to the presence of suspected nitrate ion from the salts.

Instrumental analyses for characterization
The elemental (CHN) analyses were carried out using micro-analytical laboratory of Medac Limited United Kingdom on Thermo Flask 112 CHNSO while FTIR spectra were measured on FTIR -8501 Shimadzu spectrophotometer over 4000-400 cm^{-1} using KBR pellets. Melting points were determined on MPA100 OptiMelt Automated Melting Point system. Solution electronic absorption spectra of the ligand as well as complexes were run in the range of 180-400 nm and 180-1100 nm respectively on Jenway 6405uv/vis. The electrospray ionization mass spectra were recorded using Micromass Autoseptic Premier/Agilent HP6890GC at Medac Limited, UK. Magnetic susceptibility measurement of the chelates of metals were determined on a Gouy balance at room temperature using $Hg[Co(SCN)_4]$ with the corrections of diamagnetic on Pascal's constants.

In silico predictions of biological activity and ADMET properties
The broad spectrum of biological activities of the synthesized complexes were predicted using the cheminformatics and bioinformatics interface of Molinspiration server (https://molinspiration.com/cgi-bin/properties) by input of SMILES file in each case. The Java tools incorporated within the server supports computational analysis through the algorithm of active training sets generation from which the cumulative bioactivity of the target molecules are predicted through their probable fragments. Each complex molecule was scored for likeliness in activity through various inhibition mechanisms on G protein-coupled receptor (GPCR), kinase, nuclear receptor and enzyme as well as ability to modulate ion channel.

The physicochemical and pharmacokinetics profiles of the complexes were predicted in terms of adsorption, distribution, metabolism, excretion and toxicity (ADMET) using the web-based Swiss ADME computational tools by inputting the SMILE file of each complex (16,17). The properties further reveal the drug-likeness of the molecules under study.

Antimicrobial screening
The in vitro antibacterial activity of the Eflornithine hydrochloride monohydrate and its metal complexes was evaluated using agar diffusion technique (18). Three clinical gram negative and gram positive bacteria, *Escherichia coli* (*E. coli*), *Staphylococcus aureus* (*S. aureus*) and *Pseudomonas aeruginosa* (*P. aeruginosa*) isolates were challenged with varying degree metal complexes and ligand concentrations. Zones of inhibition were explained using standard recommendation of Clinical and Laboratory Standards Institute, 29th Edition (19).

RESULTS AND DISCUSSION

Complex 1: M.wt: 559.36 gmol^{-1}; Yield: 63.2%; Elemental analysis for $Cu(EHM)_2(NO_3)(Cl)].2H_2O$ ($C_{12}H_{26}F_4N_4O_5ClCu$) calculated (found)%: C 25.77 (26.11), H 4.69 (4.70), N 12.52 (12.56); IR data (KBr, cm^{-1}): 3311, 3214, 3104, 3018, 1671, 1452, 1278, 1185, 1156, 1069, 1020, 798, 556, 530, 425. UV−vis spectrum in water (λ_{max} nm (cm^{-1})): 256 (39,063), 650(15,384). Molar Conductivity (Λ, Scm^2 mol^{-1}): 155, Magnetic susceptibity (μ_{eff}(B.M)): 2.0

Complex 2: M.wt: 646.04 gmol^{-1}; Yield: 99.4%; Elemental analysis for $[Ni(EHM)_2(CH_3COO)_2]Cl_2.2H_2O$ ($C_{16}H_{32}F_4N_4O_{10}Cl_2Ni$) calculated (found)%: C 29.75 (29.99), H 4.99 (5.05), N 8.67 (8.46); IR data (KBr cm^{-1}): 3441, 3235, 3161, 1600, 1371, 1198, 1112, 1031, 771, 553, 435. UV−vis spectrum in water (λ_{max} nm (cm^{-1})): 278(35,971), 373 (26,810), 651(15,361), 991(10,091). Molar Conductivity (Λ, Scm^2 mol^{-1}): 387, Magnetic susceptibity (μ_{eff}(B.M)): 3.29

Complex 3: M.wt: 528.19 gmol^{-1}; Yield 83.26%; Elemental analysis for $[Co(EHM)_2(H_2O)_2]Cl_2$ ($C_{12}H_{26}F_4N_4O_6Cl_2Co$) calculated (found) (%) : C, 27.29 (27.21); H, 4.96 (4.78); N, 10.61 (10.04). IR data (KBr, cm^{-1}): 3404, 3269, 3165, 3073, 1601, 1398, 1198, 1172, 1030, 841, 793, 565, 549, 444. UV−vis spectrum in water (λ_{max} nm (cm^{-1})): 295 (33,898), 485 (20,619), 550 (18,182), 680 (14,706). Mass Spectrum [ESI]: $[M + H + Li]^+$ m/z 537.09 (calculated), 537.10 (found) ; $[2EHM + 2H]^{2+}$ 183.09 (calculated.), 183.10 (found). Molar Conductivity (Λ, Scm^2 mol^{-1}): 362, Magnetic susceptibity (μ_{eff}(B.M)): 4.07

From the result Table 1, the purity of the synthesized metal complexes is supported by sharp melting point ranges while the variations in comparison with the starting material (EHM) indicate changes in chemical characteristics possibly due to progress in the reaction which was confirmed using TLC. Color difference is also a contributing factor for the formation of new compounds. All the synthesized metal complexes are soluble in DMSO and water to form electrolytes but insoluble in usual organic solvents. The presence of water of crystallization outside the coordination sphere in

complexes 1 and 2 is indicated by the cobalt chloride paper. The droplets of colorless liquid stemmed out from gently heating of metal complexes (1 and 2) turned blue cobalt chloride paper pink, thus confirming the occurrence of water molecules outside the coordination sphere. The water molecules in complex 3 is complexed hence gave negative result with cobalt chloride paper. Similarly, when some drops of 0.1 M $AgNO_3$ was added to each of the metal complexes in test tube, complexes 2 and 3 gave white precipitate of AgCl soluble in excess NH_4OH confirming the presence of chloride anions outside the coordination sphere (Schemes 1 and 2), however, no precipitate was noticed in complex 1, indicating the possibility of its chloride ion in coordination to the metal ion (scheme 1). Upon strong heating, only complex 1 produced a dense reddish-brown fumes of NO_2, indicating the presence of nitrate ion in the complex (Scheme 1) while others test negative. These are supporting indications for the formation of new compounds.

Table 1: Analytical data of ligand and metal complexes.

	mp (°C)	Yield (%)	(Found) Calculated %			Color
			C	H	N	
EHM	236 – 237	--	(30.06) 30.45	(6.52) 6.39	(11.70) 11.84	White
Complex 1	202 – 204	63.2	(26.11) 25.77	(4.70) 4.69	(12.56) 12.52	Blue
Complex 2					(8.46)	
	211 – 213	99.4	(29.99) 29.75	(5.05) 4.99	8.67	Light green
Complex 3	138 – 140	83.3	(27.21) 27.29	(4.78) 4.96	(10.04) 10.61	Purple

Fourier Transform Infra-Red spectra
The characteristic FTIR bands of the metal complexes differed from the free ligand (EHM) and supplied important signals regarding the complexation and bonding sites of the ligand. Pertinent characteristic bands of the metal complexes are listed in Table 2. The principal bands attributed to asymmetric (u_{as}) and symmetric (u_s) stretching frequencies of OCO groups are reported in Table 3. The infrared spectrum of the ligand shows a medium intensity band at 3048 cm^{-1} assigned to u(OH) of carboxylic acid group. On complexation with transition metal ions, this band shifted significantly, indicating possible coordination through the carboxylate oxygen atoms through deprotonation. The disappearance of this band in the spectrum of complex 2 is another proof of coordination through the site (12,14,20). This is further supported by the shifts in u_{asy}(OCO) and u_{sym}(OCO) as contained in Table 3. Thus, the data in Table 3 can be explored to deduce that the carboxylate groups take part in coordination to metal atom because the observable difference, Δu = u_{asy}(OCO)−u_{sym}(OCO) in the range 148-229 characterizes the metal-carboxylate bond type. The differences between u_{asy}(OCO) and u_{sym}(OCO) stretching frequencies of all the metal complexes were found to be greater than that of the ligand and also greater than 200 cm^{-1} as reported in Table 3. This confirms the monodentate coordination of the carboxylate group to the central metal ion (13,21,22), in good conformity with earlier study on the same ligand where X-ray single crystal was obtained (13). The bands in the region 3254 and 3173 cm^{-1} attributable to the asymmetric and symmetric stretching frequencies of primary amine (NH_2) in the spectrum of the ligand undergo a red shift in the spectra of the complexes, indicating the involvement of NH_2 in the chelation (22,23). The observation was further strengthened by the sharp absorption band at 754 cm^{-1} in the spectrum of the ligand, due to NH_2 deformation (out-of-plane band) which moved to higher frequencies after coordination to metal ions through amino nitrogen atom. A strong band observed at 3393 cm^{-1} is assignable to stretching frequency of lattice water molecules (24–26) which shifts to higher wavenumber (3404–3441 cm^{-1}) on complexation. In the lower frequency region, new bands (non-ligand bands) with medium to weak intensities which provide direct evidence for the complexation (Metal – Ligand bond) were spotted in the spectra of the complexes in the range of 444 and 553 cm^{-1} assigned to u(M-O)/(M-N)/(M-Cl) stretching frequencies (25, 27), while the coordination of water molecule to the metal ion in complex 3 is indicated by the δ(H_2O) at 841 cm^{-1} while similar bands in others are attributable to the δ(NH_2) (28). The shifting, disappearance or appearance of bands from the spectra of EHM to those of the complexes (Fig. 2-5) further support the argument for the formation of new compounds.

Table 2: Characteristic FTIR absorption band (cm^{-1}) of ligand and its metal complexes.

Compound	υ(OH) carboxylic	υ(NH$_2$) asy/sym	υ(OCO) asy/sym	υ(C-N)	υ(H$_2$O)	υ(M-N)/ υ(M-O)/ υ(M-Cl)	δ(NH$_2$)/ δ(H$_2$O)	υ(NO$_3$)
EHM	3048	3254/3173	1647/ 1499	1138	3393	-	754	-
Complex 1	3018	3214/3104	1671/ 1452	1185	3311	530,425	798	1069, 899
Complex 2	-	3235/3161	1600/ 1371	1198	3441	553,435	771	-
Complex 3	3073	3269/3165	1601/ 1398	1198	3404	549,444	841	-

Table 3: Principal IR bands (cm^{-1}) for OCO groups in ligand and metal complexes[1].

Compound	Y$_{asy}$ (OCO)	Y$_{sym}$ (OCO)	$\Delta u = u_{asy} - u_{sym}$
EHM	1647	1499	148
Complex 1	1671	1452	219
Complex 2	1600	1371	229
Complex 3	1601	1398	203
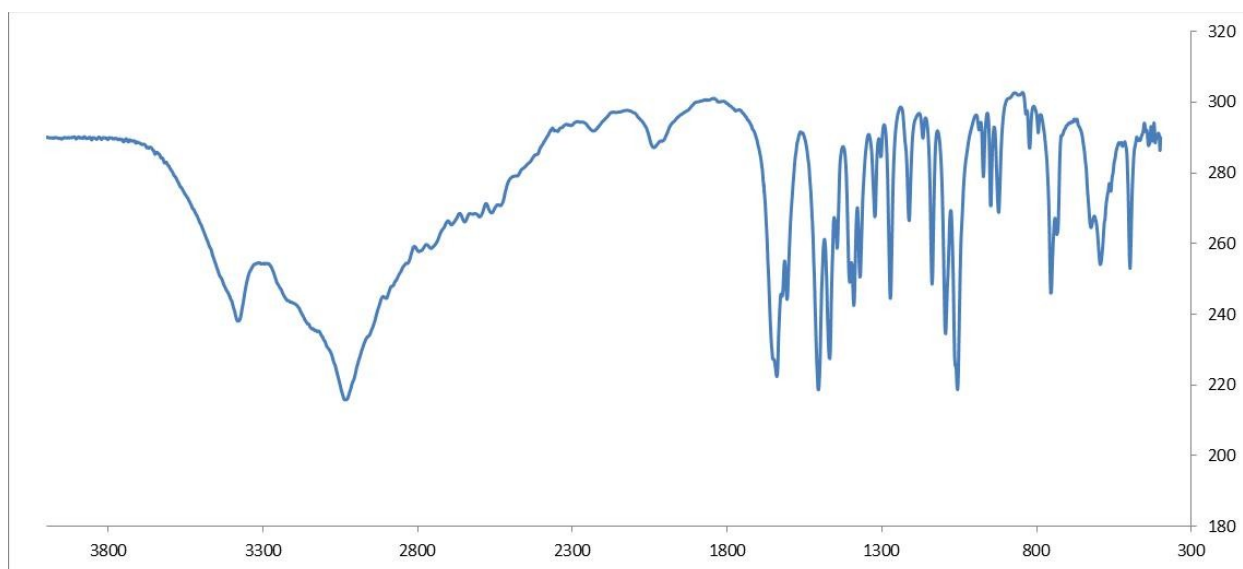
Figure 2: FTIR spectrum of the EHM (eflornithine ligand).

1　The coordination is monodentate.
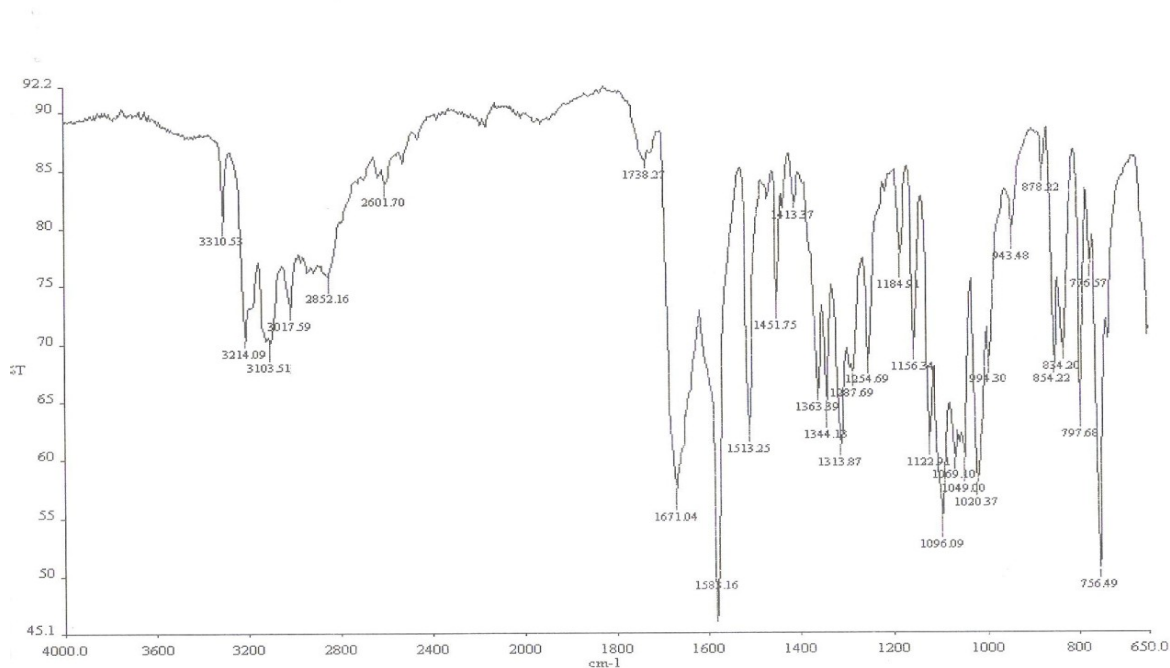
Figure 3: FTIR spectrum of the copper complex of EHM (eflornithine ligand).
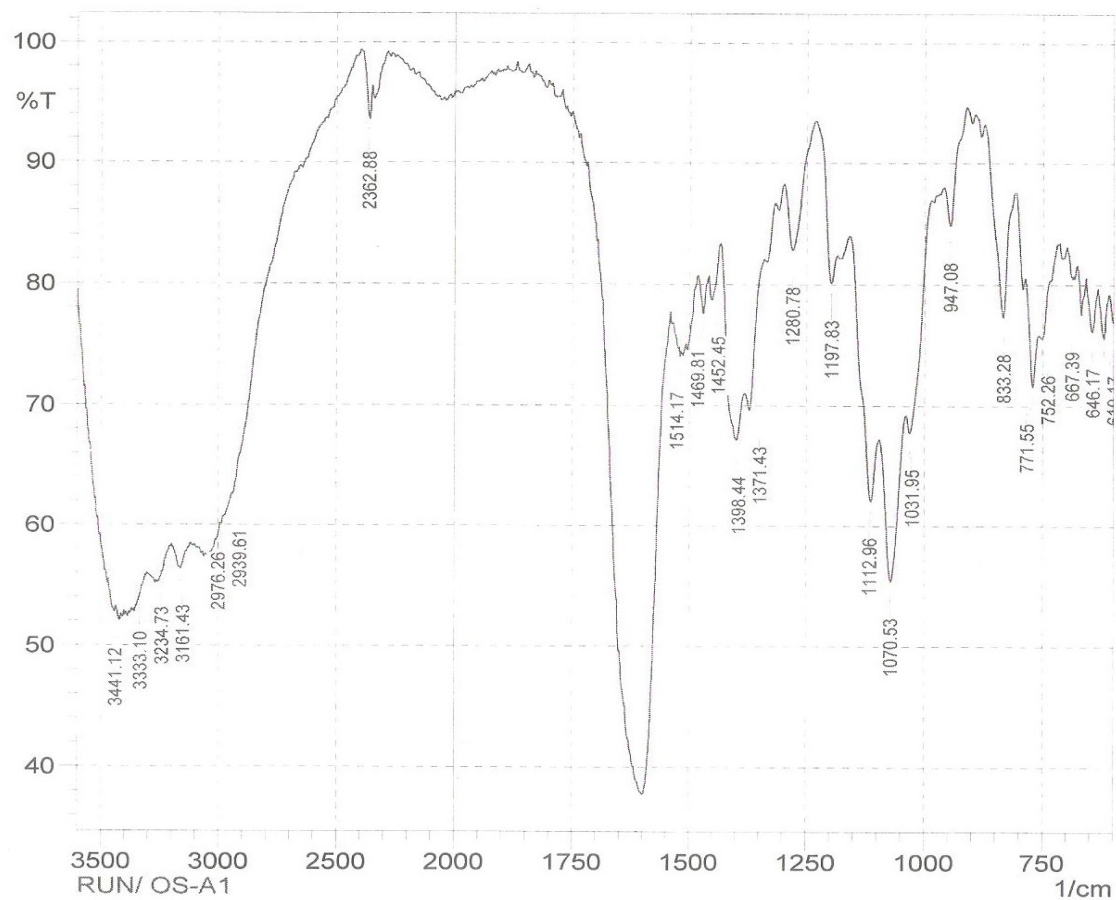
Figure 4: FTIR spectrum of the nickel complex of EHM (eflornithine ligand).
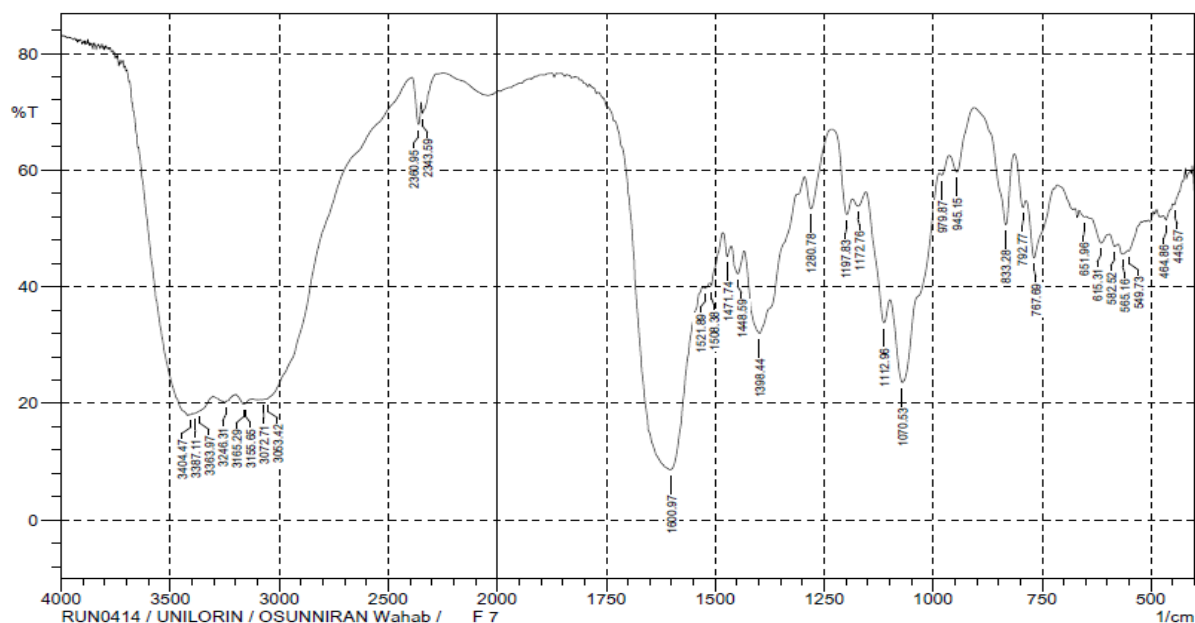
Figure 5: FTIR spectrum of the cobalt complex of EHM (Eflornithine ligand).

Electronic spectra and magnetic susceptibility

The electronic spectra data, their respective assignments/transitions and magnetic susceptibility of metal complexes were presented in Table 4. The electronic spectra of the complexes with EHM show bands in the region 256-299 nm which were assigned to n → π* transition due to non-bonding electrons present on the oxygen of (C=O) and nitrogen of amine group. The absorption spectra of Cu (ll) complex of EHM showed a single broad band in the visible region at 650 nm conforming to ^2E_g → $^2T_{2g}$ transition with an expected splitting due to the tetragonal distortion of the octahedral d^9 Cu(II) ion. For the Ni(II) complex, the absorption bands within the visible region of 651 and 991 nm corresponding to ^3A_2g → $^3T_1g(F)$ transition respectively. Similar absorption occurs at visible regions of 485 and 680 nm in the case of Co(II) complex which are attributable to ^4T_1g → $^4A_2g(P)$ and ^4T_1g → $^4A_2g(F)$ transition respectively. These strongly suggest the formation of perfect octahedral geometry in the complexes (17,29). The magnetic susceptibility measurement revealed that the copper-containing complex 1 has effective magnetic moments of 2.00 B.M., which further confirm its octahedral geometry. The effective magnetic moment of 3.29 B.M. was obtained for the Ni(II) complexes thus, strengthen the octahedral geometry suggested for Ni(II) complexes with two unpaired electrons. The electronic spectra of the aqueous solution of Co(II) complexes of EHM showed three bands corresponding to the electronic transition of d^7 high spin octahedral geometry. The magnetic moment of 4.07 B.M. established for Co(II) complexes of EHM are in agreement with high spin octahedral (with three unpaired electrons) Co(II) complexes (29,30). The magnetic moments in the range of 2.00 – 4.07 B.M. further buttress the argument for the formation of octahedral complexes between Cu(II), Ni(II) and Co(II) transition metal ions and the EHM ligand (17).

Table 4: Molar conductivity, electronic spectra and magnetic susceptibility of metal complexes.

Compound	Molar Conductivity (Λ) Scm^2mol^{-1}	$μ_{eff}$(B.M)	$λ_{max}$ (nm)	$\bar{υ}$ (cm^{-1})	Assignments
Complex 1	155	2.00	280	35,714	n → π*
			650	15,384	$^2Eg → {}^2T_{2g}$
Complex 2	387	3.29	280	35,714	n → π*
			373	26,810	$^3A_2g → {}^3T_1g(P)$
			651	15,361	$^3A_2g → {}^3T_1g(F)$
			991	10,091	$^3A_2g → {}^3T_1g(F)$
Complex 3	362	4.07	295	33,898	n → π*
			485	20,619	$^4T_1g → {}^4A_2g(P)$
			550	18,182	$^4T_1g → {}^4A_2g(F)$
			680	14,706	$^4T_1g → {}^4A_2g(F)$

Electrospray Ionization Mass Spectrometry (ESI-MS)

The major fragment ions, peaks assignment (theoretical and found), mass per charge ratio (m/z) and relative abundance of complex 3 is shown in Table 5. The fragment ions were formed by the addition of molecular adducts (mainly alkali metal and ammonium ions), formation of dimers and multiply charged ions which are characteristics nature of the technique. The m/z experimental values observed in each case compete satisfactorily well with the theoretical values; an evidence which further support molecular formulation of metal complexes (1:2 metal-ligand chelate). The quasimolecular ion were obtained in each case by the following fragment ions: $[M+NH_4+K]^+$, m/z = 588.10/586.06 (Fig. 3). Although, the ESI-MS analyses for complexes 1 and 2 could not be accomplished for a fair test due to the contaminations found in the samples possibly developed during the course of packaging for transportation, however, the presence of peak at m/z = 183.10 in all the spectra of complex 3 signify the involvement of EHM in the coordination sphere.

Table 5: ESI-MS data for $[Co(EHM)_2(H_2O)_2]Cl_2$.

Compound	Major Fragment Ions	Peak (m/z) Found	Assignment Theoretical	Relative intensity (%)
$[Co(EHM)_2(H_2O)_2]Cl_2$ $^m/_z = 529.05$	$[M + NH_4 + K]^+$	588.10	586.06	0.63
	$[M + H + Li]^+$	537.10	537.09	5.70
	$[M + Li + Na]^+$	559.10	559.07	16.46
	$[M - 2H_2O + Li]^+$	500.10	500.06	39.24
	$[Co(EHM)_2(H_2O)(Cl) + 2Na]^{2+}$	261.10	261.03	36.08
	$[Co(EHM)Cl + K + Na]^+$	338.00	337.94	100.00
	$[2EHM + 2H]^{2+}$	183.10	183.09	16.46
	$[2EHM + Co + Na + 2H]^{2+}$	224.50	224.06	6.33
	$[2EHM+Co + H_2O + H + 2Na]^{2+}$	244.50	244.05	7.59
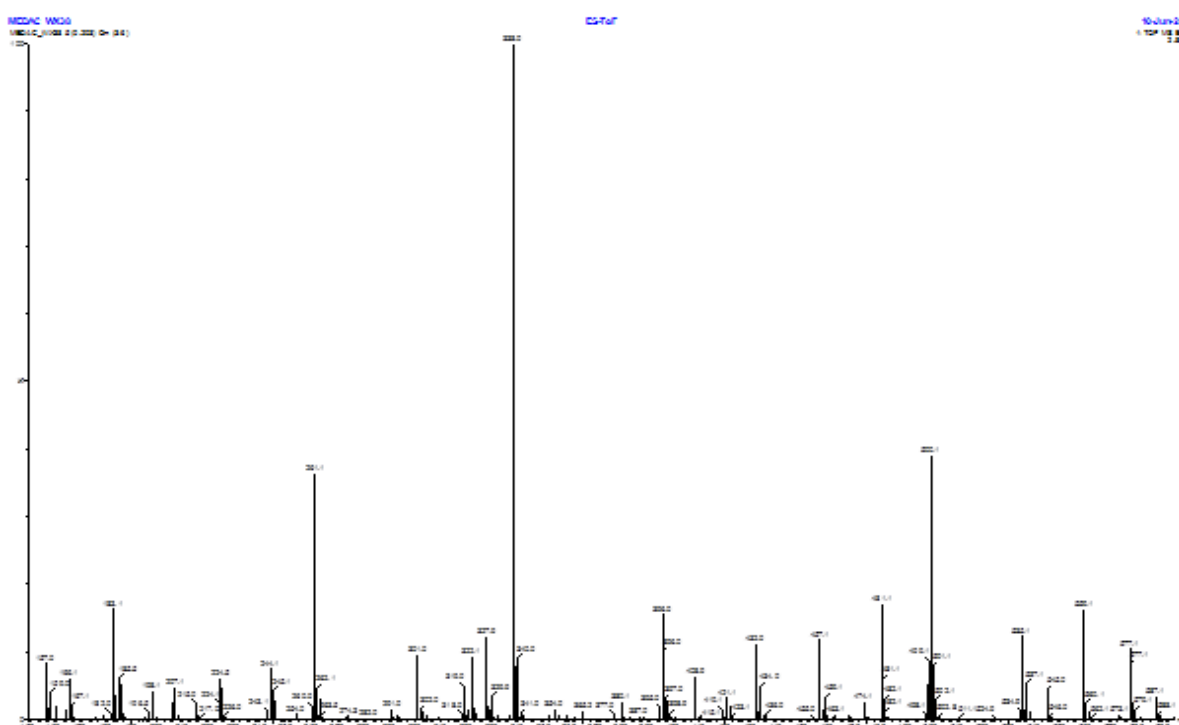
Figure 6: ESI-MS spectrum of complex 3.

The bioactivity profiles of the complexes are predicted *in silico* in comparison with the parent ligand, EHM in order to observe the possibility of enhanced pharmacology due to coordination (Table 6). The interaction with major targets for essential biofunctionalities such as the GPCR, ion channel, kinases, nuclear receptor, protease and enzymes are evaluated in terms of binding affinity. All the complexes virtually demonstrate competitive/higher binding affinity against the receptors than the parent EHM with exceptions to GPCR and protease where the ligand binds stronger. The theoretical interactions with these targets further support their applicability as bioactive agents (17).

Table 6: Predicted bioactivity profile of EHM and its complexes.

Compound	GPCR Ligand	Ion Channel Modulator	Kinase Inhibitor	Nuclear Receptor Ligand	Protease Inhibitor	Enzyme Inhibitor
EHM	0.01	0.19	-0.78	-0.72	0.14	-0.08
Complex 1	0.20	0.01	-0.07	0.00	0.20	0.09
Complex 2	0.16	0.08	0.02	0.10	0.28	0.04
Complex 3	0.22	0.11	0.05	0.12	0.36	0.05

The physicochemical parameters predicted for both the ligand, EHM and its metal complexes are presented (Table 7). Only the ligand EHM and complex 3 possess a Mol.wt <500, others are higher due to the nature of coordination with the metal ions and other ligands. They all soluble in water with fair molar refractivity, have hydrogen bond donor (HBD) groups ≤5 except complex 3 but higher number of hydrogen bond acceptors (HBA) than 10 except the ligand. They display topological polar surface area (TPSA) >60Å standard including the parent ligand possibly due to their structural morphology.

1318

Table 7: Physicochemical properties of EHM and its complexes.

Compound	Mol.wt	Fraction Csp3[a]	HBA[b]	HBD[c]	Molar Refractivity	Water Solubility	TPSA[d] (Å²)
EHM	236.64	0.83	7	4	48.30	Highly soluble	98.57
Complex 1	521.31	0.83	15	4	95.48	Soluble	183.75
Complex 2	537.09	0.75	16	4	103.29	Soluble	181.30
Complex 3	455.27	0.83	14	6	85.48	Very soluble	147.16

a: The ratio of sp^3 hydridized carbon over the total number of carbon atoms in a molecule; b: The number hydrogen bond acceptors; c: The number of hydrogen bond donors; d: Topological polar surface area

The predicted pharmacokinetic profiles of the ligand, EHM and its complexes (Table 8) indicate that all the complexes have low ability for gastrointestinal absorption compared to the ligand. None of them including the parent ligand can predictably penetrate the blood brain barrier (BBB), inhibit the cytochrome P450, indicating their insignificance for drug-drug interaction to induce adverse effects. They all possess low skin permeation indicated by Log Kp value of -9.58 to -8.33 cm/s and are P-G substrates except the ligand. Although, some of them show slight violations to the Lipinski's Rule of 5 (31) for drugability due to higher molecular weights than 500 g/mol commonly to coordination compounds (17,32), however they demonstrate good pharmacokinetics and bioavailability for further bioactivity probes.

Table 8: Pharmacokinetics properties of EHM and its complexes.

Compound	GI Abs.[a]	BBB Permeation[b]	P-G Substrate[c]	CYP1A2 Inhibitor[d]	LogKp[e] (cm/s)
EHM	High	No	No	No	-9.58
Complex 1	Low	No	Yes	No	-8.33
Complex 2	Low	No	Yes	No	-9.19
Complex 3	Low	No	Yes	No	-9.51

a: The ratio of sp3 hydridized carbon over the total number of carbon atoms in a molecule; b: The number hydrogen bond acceptors; c: The number of hydrogen bond donors; d: Topological polar surface area

The zones of inhibitions shown in Fig. 4 indicate that the metal complexes exhibit stronger inhibition effects on the test organisms than the parent ligand and in good competition with a renown antibiotic, ciprofloxacin *in vitro*. It has also been observed that antibacterial potency in each case appears to be concentration-dependent as the degree of inhibition increases with increase in concentration (30, 33). The complexes inhibit the bacterial growth at similar minimal bactericidal concentration and in strong competition with a renowned antibiotic for treating bacterial resistance, ciprofloxacin. The improved activity of the metal-drug chelates can be justified on the basis of chelation effect (34) and it indicates the worthiness of the complexes for therapeutic transformations against drug-resistant antibacterial upon further studies.
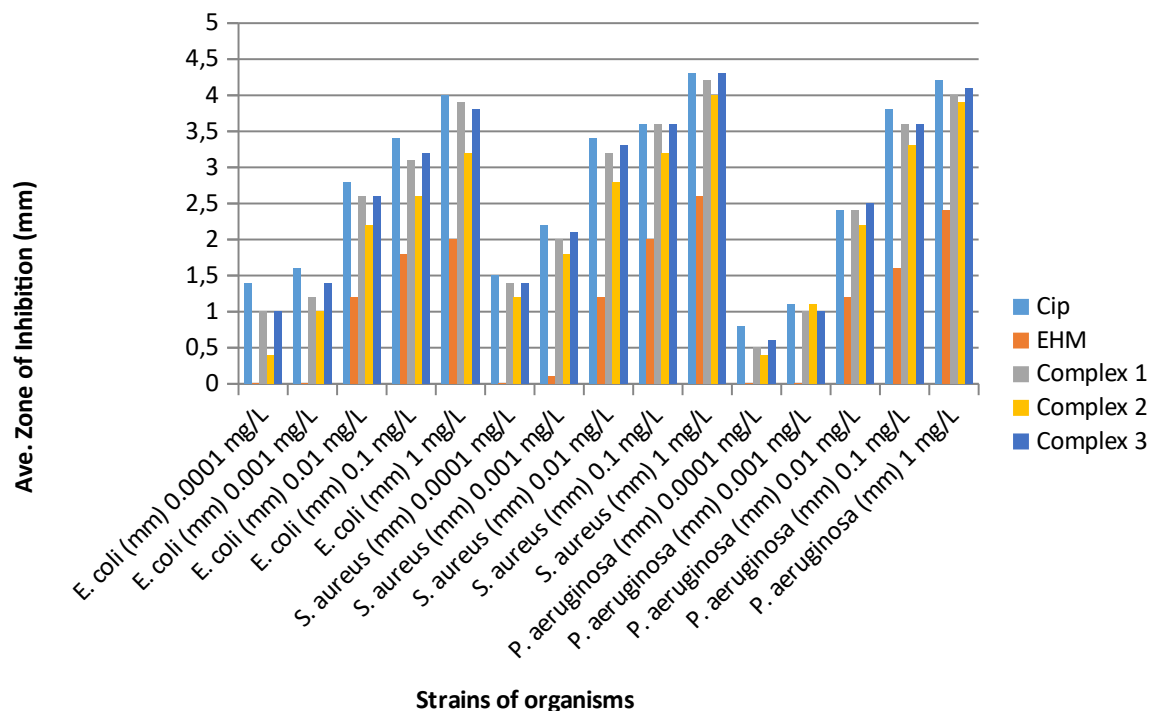
Figure 7: Comparative effect of inhibitory level of the ligand and metal complexes on *E. coli, S. aureus and P. aeroginosa* at different concentrations (mgL^{-1})

CONCLUSION

New eflornithine hydrochloride monohydrate-metal(II) complexes were synthesized with oxygen, nitrogen and chloride donor atoms by 1:2 molar condensation of metal ions and the ligand. The ligand and the metal complexes were characterized using elemental analysis, FT-IR, electronic spectra, magnetic susceptibility and ESI-MS. Eflornithine hydrochloride monohydrate acted as a bidentate ligand in each case, coordinating to the metal ion through the carboxylate oxygen atom and amine nitrogen atom and octahedral geometry is reasonably proposed for all the metal complexes based on the characterization results. Metal(II) complexes of the ligand showed enhanced antibacterial activity than the free ligand and compete favorably well with a renowned antibiotic, ciprofloxacin, indicating that the metal complexes are potentially good antibacterial agent. It has also been observed that degree of inhibition is concentration dependent as the activity increased with increased concentration. Although, the complexes could not be achieved in single crystal forms after several recrystallization attempt and more robust characterization and biological assays are required for more accurate elucidation, however, the study presents fundamentals amenable for therapeutic development in form of divalent metal complexes of EHM against drug-resistant bacteria.

REFERENCES

1.   Jing L, Dejuan S, Yueying Y, Mingxue L, Hua L, Lixia C. Discovery of metal-based complexes as promising antimicrobial agents. Discovery of metal-based complexes as promising antimicrobial agents. European Journal of Medicinal Chemistry. 2021; 224, 113696:1-14. <URL>.

2.   Raman N, Sobha S, Mitu L. Synthesis, structure elucidation, DNA interaction, biological evaluation, and molecular docking of an isatin-derived tyramine bidentate Schiff base and its metal complexes. Monatshefte Fur Chemie. 2012;143:1019–30. <URL>.

3.   Saddam Hossain Md, Zakaria CM, Kudrat-E-Zahan Md. Metal Complexes as Potential Antimicrobial Agent: A Review. American Journalof Heterocyclic Chemistry. 2018, 4(1):1-21.<URL>.

4.   Ayipo YO, Osunniran WA, Babamale HF, Ayinde MO, Mordi MN. Metalloenzyme mimicry and modulation strategies to conquer antimicrobial

resistance: Metal-ligand coordination perspectives. Coordination Chemistry Review 2022;453:214317. <URL>.

5. Frei A. Metal complexes, an untapped source of antibiotic potential. Antibiotics. 2020; 9(2) :1-25 <URL>.

6. Tella AC, Obaleye JA. Metal complexes as antibacterial agents : Synthesis , characterization and antibacterial activity of some 3d metal complexes of sulphadimidine. Electronic Journal of Chemistry. 2010;2(1):1–16.

7. Anacona JR, Ortega G. Metal-based antibacterial agents: Synthesis, characterization, and biological evaluation of ternary Mn(II) and Co(II) complexes containing sulfamethoxazole and cephalosporins. Synthesis and Reactivity in Inorganic, Metal-Organic, and Nano-Metal Chemistry. 2015;45(3):363– 69 <URL>.

8. Abdullahi OR, Halimah FB, Amudat L, Abdulbasit AA, Wahab AO, Ayinla, OS, Misitura L, Joshua AO. Mn(II), Co(II), Ni(II), And Cu(II) Complexes Of Amıno Acıd Derıved Schiff Base Lıgand: Synthesıs, Characterızatıon And *In-vıtro* Antıbacterıal Investıgatıons. Bull. Chem. Soc. Ethiop. 2021; 35(1): 97-106. <URL>.

9. Ikmeet K, Sukhbir S, Sandeep A, Neelam S. Application of Central Composite Design for Development and Optimization of Eflornithine Hydrochloride-loaded Sustained Release Solid Lipid Microparticles. Biointerface Research in Applied Chemistry. 2022; 12(1): 618-37 <URL>.

10. Amit K, Vijender S, Praveen K. Spectrophotometric Determination of Eflornithine Hydrochloride using Vanillin as Derivative Chromogenic Reagent. Tropical Journal of Pharmaceutical Research. 2014; 13 (11): 1917-23. <URL>.

11. Ikmeet KG, Sukhbir S, Sandeep A, Neelam S. Development And Valıdatıon Of Uv-Spectrophotometer Analytical Method Of Eflornithıne Hydrochlorıde. Plant Archives. 2020; 20(1), 3265-70

12. Osunniran WA, Obaleye JA, Tella AC, Amolegbe SA. Synthesis, characterization and in vitro antibacterial studies of novel transition metal(II) complexes of 2,5-diamino-2-(difluoromethyl)pentanoic acid hydrochloride hydrate. Orbital. 2018;10:367– 380. <URL>.

13. Obaleye JA, Tella AC, Osunniran WA, Simon N, Omojasola PF. Synthesis, Characterization, Crystal Structure and Antimicrobial Evaluation of a

Novel -M-X-M-X- Type Infinite Chain 1D Cu(II) Complex with Eflornithine Hydrochloride Hydrate as Ligand. *J Inorg Organomet Polym Mater.* 2014; 24:827–35. <URL>.

14. Osunniran WA, Obaleye JA, Ayipo YO. Six Coordinate Transition Metal(II) Complexes of Mixed Ligands of Eflornithine Hydrochloride Hydrate and 2,2-Bipyridine: Synthesis, Characterization and Antibacterial Study. Jordan Journal Chemistry. 2018;13:149–57.

15. Barman Balfour JA, McClellan K. Topical Eflornithine. American Journal of Clinical Dermatology. 2001; 2(3): 197-201

16. Daina A, Michielin O, Zoete V. SwissADME: A free web tool to evaluate pharmacokinetics, drug-likeness and medicinal chemistry friendliness of small molecules. *Sci Rep* 2017;7:1–13. <URL>.

17. Okasha RM, Al Shaikh NE, Aljohani FS, Naqvi A, Ismail EH. Design of novel oligomeric mixed ligand complexes: Preparation, biological applications and the first example of their nanosized scale. International Journal of Molecular Science. 2019; 20(3),743. <URL>.

18. Ayipo YO, Obaleye JA, Badeggi UM. Novel Metal Complexes of Mixed Piperaquine-Acetaminophen and Piperaquine-Acetylsalicylic acid : Synthesis, Characterization and Antimicrobial Activities. Journal of Turkish Chemical Society A. 2017;4:313–26. <URL>.

19. Limbago B. M100-S11, Performance standards for antimicrobial susceptibility testing. Clin Microbiol Newsl. 2019;23(6): 23-49. <URL>.

20. Osunniran WA, Obaleye JA , Tella AC , Ayipo YO, Bale AT, Rajee AO. Toxıcologıcal Assessment Of Synthesızed And Characterızed Transıtıon Metal(II) Complexes Of Eflornıthıne Hydrochlorıde Hydrate On Albıno Rats. Bull. Chem. Soc. Ethiop. 2020; 34(3), 489-50. <URL>.

21. Rajee AO, Aliyu AA , Babamale HF, Lawal A, Ayinla SO, Osunniran WA, Obaleye JA. Preparation, characterization and antibacterial activity of Mn(II), Cu(II) and Zn(II) complexes of methionine and 2,2-bipyridine co-ligands. Journal of the Kenya Chemical Society. 2020; 13(1): 16-21.

22. Modec B, Podjed N, Lah N. Beyond the simple copper(II) coordination chemistry with quinaldinate and secondary amines. Molecules. 2020; 25(7), 1573. <URL>.

23. Karthik P, Shaheer ARM, Vinu A, Neppolian B. Amine Functionalized Metal–Organic Framework

Coordinated with Transition Metal Ions: d–d Transition Enhanced Optical Absorption and Role of Transition Metal Sites on Solar Light Driven H2 Production. Small. 2020;16(12):1–10. <URL>.

24. Turan N, Buldurun K. Synthesis, characterization and antioxidant activity of Schiff base and its metal complexes with Fe(II), Mn(II), Zn(II), and Ru(II) ions: Catalytic activity of ruthenium(II) complex. European Journal of Chemistry. 2018; 9(1):22–9. <URL>.

25. Tadewos D, Digafie Z, Tegene D, Demissie TB, Eswaramoorthy R. Synthesis, Characterization, and Biological Activities of Novel Vanadium(IV) and Cobalt(II) Complexes, *ACS Omega* 2022;, 7(5) : 4389–404. <URL>.

26. Salazar-Medina AJ, Gámez-Corrales R, Ramírez JZ, González-Aguilar GA, Velázquez-Contreras EF. Characterization of metal-bound water in bioactive Fe(III)-cyclophane complexes. Journal of Molecular Structure. 2018;1154:225–31. <URL>.

27. Osunniran WA, Ayipo YO, Adeyemo MA, Bale AT, Obaleye, JA. Comparison of Solid and Solvent - Based Syntheses, Characterization and Antioxidant Property of Metal Complexes of Sodium Diclofenac, Fountain Journal of Natural and Applied Science. 2020; 9(1): 11-18. <URL>.

28. Wail AZ, Abbas A, Salih A, Susan DA, Young GK. Synthesis, characterization, and biological activity of Schiff bases metal complexes. Journal of Physical Organic Chemistry. 2017; 31(2) e3752:1-13. <URL>.

29. Srivastava VK. Synthesis, characterization, and biological studies of some biometal complexes. Future Journal of Pharmaceutical Sciences. 2021; 7(51):1-11. <URL>

30. Obaid SMH, Jarad AJ, Salih AA. Synthesis, Characterization and Biological Activity of Mixed Ligand Metal Salts Complexes with Various Ligands. Journal of Physics: Conference Series, 2020; 1660, 012028: 1-14. <URL>.

31. Lipinski CA. Lead- and drug-like compounds: The rule-of-five revolution. Drug Discov Today Technol. 2004;1(4):337– 41. <URL>.

32. Syed AFS, Paulpandiyan R, Nagarajan ER. Expatiating biological excellence of aminoantipyrine derived novel metal complexes: Combined DNA interaction, antimicrobial, free radical scavenging studies and molecular docking simulations. Journal of Molecular Structure. 2019;1178:179–91. <URL>

33. Kuti JL. Optimizing Antimicrobial Pharmacodynamics: a Guide for Your Stewardship Program. Rev Médica Clínica Las Condes. 2016; 27(5):615–24. <URL>.

34. Coraça-Huber D, Dichtl S, Steixner S, Nogler M, Weiss G. Iron chelation destabilizes bacterial biofilms and potentiates the antimicrobial activity of antibiotics against coagulase-negative Staphylococci. Pathogens and Disease. 2018; 76(5):1-8. <URL>.

Structural, Optical, and Morphological Characterization of Silica Nanoparticles Prepared by Sol-Gel Process

Most. Nilufa Yeasmin[1]* (iD) , **Munira Sultana**[1] (iD) , **Ayesha Siddika**[1] (iD) , **Samia Tabassum**[1] (iD) ,
Saeed Mahmud Ullah[2] (iD) , **Muhammad Shahriar Bashar**[1] (iD)

[1]Institute of Fuel Research and Development, Bangladesh Council of Scientific and Industrial Research, Dhaka, 1205, Bangladesh
[2]University of Dhaka, Department of Electrical and Electronic Engineering, Dhaka, 1000, Bangladesh

Abstract: In the current years, silica nanoparticles have become more favorable in various disciplines like medicine, nano-biotechnology, the food industry, and drug delivery due to their tunable physicochemical characteristics. In this paper, the silica nanoparticles were synthesized by hydrolysis and condensation of tetra-ethyl-ortho-silicate (TEOS) in an ethanolic medium using ammonia as a stimulator in the reaction. The chemical bond structures of silica nanoparticles were analyzed by Fourier Transform Infrared Spectroscopy (FT-IR) which confirmed the existence of the Si-O bonds according to the different absorption peaks of the samples. The amorphous structure of these nanoparticles was certified by finding the board peaks in the X-Ray Diffraction (XRD) patterns. The elemental chemical composition of silica nanoparticles was investigated by Energy Dispersive X-Ray Spectroscopy (EDX) where 61.48wt % of silicon and 23.48wt% of oxygen were found. Almost round-shaped spherical and uniform silica nanoparticles with smooth surfaces were investigated by Scanning Electron Microscopy (SEM) measurement. The different particle sizes of silica nanoparticles within the range of 95±5.59 to 280±7.8 nm were found by controlling the concentration of TEOS. The optical absorption spectra and band gap calculations were also analyzed by Ultraviolet-Visible (UV-Vis) spectrophotometry for the different concentrations of TEOS. The results revealed that with increasing the concentration of TEOS, the absorption spectra of silica nanoparticles increased and their optical bandgap decreased from 3.92 eV to 3.79 eV.

INTRODUCTION

Nowadays research on nano-materials has drawn great attention to the scientific community for their size-dependent appealing characteristics at the nano-scale (1–3). In recent years, colloidal silica nano-spheres have been caught up a prominent position across various scientific disciplines due to their huge industrial demands and different potential applications as biosensors, thin films, catalysis, nano-glass, nano-filler, ceramics, stabilizers, electronic substrates, photonic crystal, electrical/ thermal insulators, emulsifiers, binder, pigments, and semiconductor adsorbents (4–9). Due to their high surface area, non-toxicity, controlled particle size, and high functionality, they are also widely used in the DNA-conjugation, food industry, drug delivery, and as a doping material in various nanotech industries (1,10). To ensure the quality of these products, narrow particle size and

uniform distribution of silica nanoparticles are a great concern in this case (11).

There are mainly two distinct approaches to producing silica nanoparticles; one is the physical synthesis and another is the chemical synthesis approach. As these nanoparticles need more development due to their high purity and narrow size distribution so, the chemical synthesis method is more efficient than the physical synthesis method (10,12). However, this widely used chemical synthesis approach can be further classified as the fumed (pyrogenic) synthesis, the micro emulsion-gel synthesis, and the sol-gel synthesis process. Again, the sol-gel synthesis process can be categorized as precipitated synthesis, stöber method synthesis, and biomimetic sol-gel synthesis process (13,14).

Firstly, in the pyrogenic synthesis process, silicon tetrachloride ($SiCl_4$) is used to produce silica nanoparticles by combustion at a temperature of 100 °C. This process is however not industrially feasible for the difficulty to control their particle sizes and morphology (13–15). Then, in the micro-emulsion gel process, highly stabilized nanoparticles are yielded from the homogenous mixture of water, oil, and surfactant medium. Though this procedure is very efficient for producing ultrafine silica nanoparticles, it is not industrially cost-effective (16,17). Among those processes, the highly reactive, spherical, and industrially suitable nano-silica can be easily synthesized through the sol-gel process. Because, this process offers many benefits over other processes, due to its simplicity and flexibility by changing the different parameters during synthesis (18,19).

However, silica nanoparticles can be extracted from various natural sources such as rice husk, sugarcane bagasse, corn cob, wheat husk, coffee husk, and also other agricultural wastes. Since extracted silica nanoparticles from these biomass sources contain a large amount of metal and non-metal impurities, so they aren't favorable for advanced industrial applications (1,20). For example, Zaky et al. produced silica nanoparticles with an average size of 50-70 nm from rice straw. These produced particles are agglomerated which limits their usage for industrial applications (21). For this reason, tetra-ethyl-ortho-silicate (TEOS) or tetra-methyl-ortho-silicate (TMOS) is used as a precursor during synthesis for commercial applications. In addition, we also used tetraethyl-ortho-silicate (TEOS) as a silicon source to get spherical and uniform silica nanoparticles.

In 1968, Stöber et al. as a pioneer of this work, first synthesized silica nanoparticles through the sol-gel process where the hydrolysis and condensation of tetra-ethyl-ortho-silicate (TEOS) occurred under the catalytic influence of ammonia in an ethanolic medium. They obtained quasi-monodisperse silica nanoparticles with particle sizes of 0.5-2 μm by varying the concentration of precursor and using the different alcohol media as solvents (22). From the author's point of view, the morphology of particles and their size distribution with different degrees of dispersity can be strongly affected by the five key parameters such as the concentration of precursor (TEOS), catalyst, water, solvent (alcohols), and the reaction temperature (23–25). By controlling these variables, Rao et al. produced monodisperse and spherical silica nanoparticles with sizes ranging from 20 to 460 nm(26). Typical amorphous silica nanoparticles with different degrees of dispersity and particle size compared with other previous studies are summarized in Table 1.

Table 1: The comparison of average particle size, dispersity, and morphology of silica nanoparticles with the previous studies[1].

Synthesis process	Silicon source	Catalyst	Optimum Average particle size	Dispersity	Ref.
Sol-gel method	TEOS	NH_4OH	95 nm	Quasi-monodisperse	Present study
Sol-gel method	TEOS	NH_3	9 nm	Disperse	(27)
Sol-gel method	TEOS	PVP	25 nm	Monodisperse	(19)
Sol-gel method	TEOS	NH_3	7.1 nm	Disperse	(28)
Sol-gel Method	TEOS	$N(CH_2OH)_3$	42 nm	Aggregate	(29)
Microemulsion	TMOS	NH_3	11 nm	Aggregate	(16)

1 The morphology is spherical in all instances.

Yeasmin MN et al. JOTCSA. 2022; 9(4): 1323-1334.

RESEARCH ARTICLE

Furthermore, the size and shape morphology of silica nanoparticles can be controlled by adding different kinds of electrolytes such as sodium iodide (NaI), ammonium bromide (NH_4Br), and also various types of surfactants such as cetyltrimethylammonium bromide (CTAB), polyvinyl pyrrolidone (PVP), sodium dodecyl sulphate (SDS) respectively (27,30,31). For example, Kim et al. have reported spherical and very fine silica nanoparticles by adding a slight amount of different electrolytes during synthesis (32). Similarly, R. Stanley and his coworkers have also prepared silica nanoparticles with the use of various surfactants by wet chemical synthesis route (15). Moreover, Guo et al. found the dispersed spherical, and amorphous silica nanoparticles with average particle sizes ranging from 13 to 32 nm by the modified Stöber synthesis method with a slow hydrolysis catalyst in water (33).

In our present work, quasi-monodisperse, spherical, and amorphous silica nanoparticles were fabricated via the sol-gel synthesis process using TEOS as a precursor and ammonia as a catalyst. In the sol-gel process, the concentration of TEOS is one of the most important controlling tools to get desired particle size and dispersity of silica nanoparticles. So, the uniform nanoparticles within a range of 95±5.59 ~280±7.8 nm in diameter were also reported in this paper by conducting the reaction at various concentrations of TEOS. After successfully synthesizing the silica nanoparticles, they were characterized by Scanning Electron Microscopy (SEM), Energy Dispersive X-Ray Spectroscopy (EDX), X-Ray Diffraction Spectroscopy (XRD), Fourier transform infrared spectroscopy (FT-IR), and Ultraviolet-Visible (UV-Vis) spectroscopy techniques.

EXPERIMENTAL SECTION

Materials
For the synthesis of silica nanoparticles, the chemicals such as Tetraethyl Ortho-silicate (TEOS, 99% GC), absolute ethanol (C2H5OH, 99.9%), and ammonium hydroxide (NH_4OH, 30%) were received from Sigma Aldrich and Merck Company Ltd respectively. All reagents and laboratory-produced distilled water were used without further purification.

Synthesis of Silica Nanoparticles
The most generalized reaction to form silica nanoparticles through the hydrolysis and poly-condensation of silicon alkoxides $Si(OR)_4$ can be expressed as (19):

$$Si(OR)_4 + H_2O \Leftrightarrow Si(OH)_4 + 4ROH$$
$$Si-OH + OH-Si \rightarrow Si-O-Si + H_2O$$
$$Si-OR + OH-Si \rightarrow Si-O-Si + ROH$$
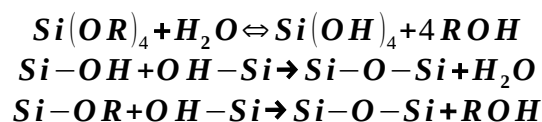
The quasi-mono-disperse and spherical silica nanoparticles were synthesized from the sol-gel process through the hydrolysis and condensation reaction of TEOS. The whole procedure is schematically described in Figure 1. The amounts of precursor, solvent, and catalyst used in this experiment are also summarized in Table 2. The reaction was carried out in a 150 mL beaker where 30 mL of ethanol and 5 mL of distilled water were taken at first. The mixture of both ethanol and water was then stirred vigorously at 460 rpm at 55 °C temperature using a magnetic stirrer. After 10 minutes, TEOS was added drop-wise using an adjustable micropipette into the solution and agitated for the next 2 hours. Subsequently, ammonium hydroxide as a catalyst was added to keep up the expected alkalinity of the solution. The pH of the solution was measured by pH meter and recorded at pH=11-12 level (34). This transparent solution was then constantly agitated for the next 5 hours. Here, the volume of TEOS was varied to control the particle size and dispersity of silica nanoparticles where the other chemicals were kept at a fixed level. However, after adding the catalyst, the solution was finally turned into bluish milky white color. Then, the sol was centrifuged at 5000 rpm for 10 minutes, and separated the silica nanoparticles by washing with ethanol for three times to remove unreacted chemicals.
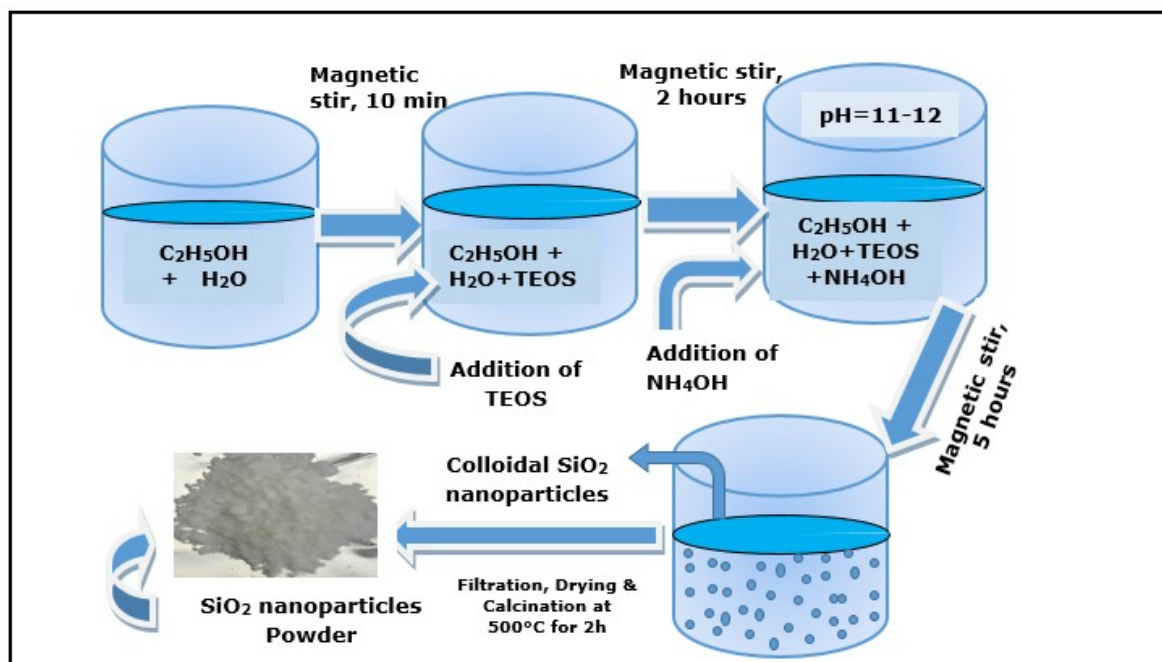
Figure 1: Schematic diagram of silica nanoparticles synthesis from the sol-gel process.

Table 2: Different amounts of chemicals used in this experiment[2].

Sample no.	Amount of TEOS (mL)	Average Particle Size, D(nm)
S1	1	95±5.6
S2	2	175±10.5
S3	3	280±7.8

The washed particles were then collected and dried at 70 °C for 24 hours. After oven-drying, the silica nanoparticles were calcined at 500 °C for 2 hours and finally kept in a desiccator for further preservation.

Characterizations

The surface morphology, particle size, and shape of the silica nanoparticles were inspected by Scanning Electron Microscope (SEM, EVO-18, Carl Zeiss, Germany). The XRD patterns of these particles were obtained from GBC Emma X-ray Diffraction Spectroscopy that was equipped with the monochromatic Cu kα X-ray detector (λ=1.5206 Å at 35.5 KV and 28 mA). As a great tool for chemical bond identification, Fourier-transform infrared (FT-IR) spectroscopy (IR Tracer-100, Shimadzu, Japan) was conducted at a frequency range of 400-4000 cm^{-1}. The chemical composition of silica nanoparticles was analyzed by Energy Dispersive X-ray Spectroscopy (EDX) equipped with a Scanning Electron Microscope (SEM, JEOL/EO, Japan). The UV-Vis absorbance spectra were also recorded within the wavelength range of 300 to 1100 nm by Ultraviolet-Visible (UV-Vis) spectrophotometry using a UH4150 (Hitachi, Japan) Spectrophotometer.

RESULTS AND DISCUSSION

Fourier-transform infrared spectroscopy (FT-IR) Analysis

To investigate the chemical bonds of the synthesized silica nanoparticles within the range 400-4000 cm^{-1}, FT-IR spectrum analysis was applied to the samples. The FTIR spectra for three different samples prepared using different amounts of TEOS and calcination at 500 °C for 2 hours are shown in Figure 2.

---

2 In the experiments, 2 mL of NH_4OH, 30 mL of C_2H_5OH, and 5 mL of distilled H_2O were used.
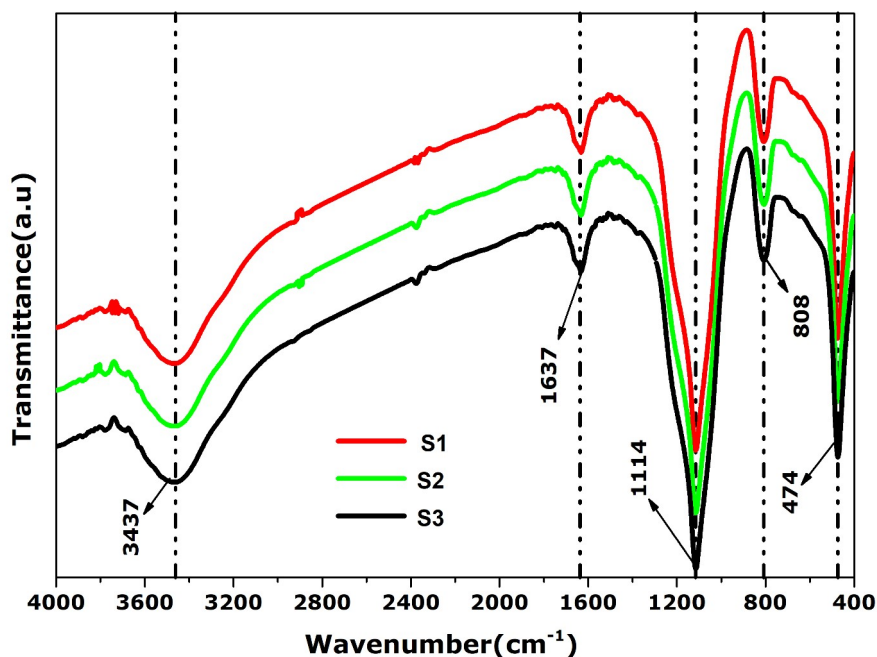
Figure 2: FT-IR spectra of silica nanoparticles prepared using different volume ratios of TEOS: water: Ammonia = **(S1)** 1:5:2 **(S2)** 1:2.5:1 **(S3)** 1.5:2.5:1 respectively.

The absorption peaks in FTIR spectra originated due to the different vibrations of chemical bonds of silica nanoparticles are described in **Table 3**. In FTIR spectra, the absorption peaks of the S1 sample indicate the silica nanoparticles which are produced from 1 mL of TEOS. For the S1 sample, the broad absorption peak at 3437 cm^{-1} is assigned to the stretching vibration of structural water -OH. A slightly intense absorption peak at 1637 cm^{-1} is attributed to the bending vibration of O-H due to the trapped water molecules inside the sample (27,35,36). This water was physically absorbed by the sample from the air after calcination. So, to prevent the absorption of water, the silica nanoparticles are recommended to keep in a moisture-free environment.

Table 3: Summary of common absorption peaks in FTIR analysis of the synthesized silica nanoparticles.

Serial No.	Absorption peak (cm^{-1})	Bond identification	References
1	474	-Si-O- bending vibration	(8,27,35,36)
2	808	-Si-O- symmetric stretching vibration	(8,27,35,36)
3	1114	-Si-O- asymmetric stretching vibration	(8,27,35,36)
4	1637	-O-H bending vibration due to trapped water molecules	(8,29,33,36)
5	3437	-O-H stretching vibration	(8,29,33,36)

However, the dominant absorption peaks in the S1 sample at 474, 808, and 1114 cm^{-1} are attributed to the stretching and bending vibrations of Si-O-Si (33,35,36). Furthermore, the sharp absorption peak at 1114 cm^{-1} is ascribed to the asymmetric stretching vibration of Si-O-Si while the absorption peak at 808 cm^{-1} and 474 cm^{-1} are expressed the relation to the symmetric stretching vibrations and bending vibrations of Si-O respectively (36,37). The FT-IR spectra in Figure 2 of S2 and S3 samples produced from the precursor using 2 mL and 3 mL of TEOS respectively show similar absorption peaks. Three dominant absorption peaks at 474, 808, and 1114 cm^{-1} related to the bending, symmetric and asymmetric vibrations of Si-O-Si respectively are found clearly in the three samples. Furthermore, the board absorption peak at 3437 cm^{-1} confirms the existence of the −OH group in all samples (8,29,33,36). Finally, The FT-IR spectra indicate that there are no significant differences in chemical structures among all the synthesized samples. However, these findings are consistent with the observations reported by Guo et al (33). He found almost similar absorption peaks in FT-IR spectra

using different types of catalysts to produce spherical silica nanoparticles with uniform size distribution.

X-Ray Diffraction (XRD) Analysis
Figure 3 shows the XRD patterns of all samples of the silica nanoparticles to check the crystalline structures which were synthesized using different amounts of TEOS. From Figure 3, it has been shown that the XRD patterns of all the samples exhibit only

broad diffused peaks around the region of $2\theta=24.58^0$ and there are no sharp diffraction peaks corresponding to any crystalline structures (19,33,36). However, these broad diffraction peaks correspond that all the samples are amorphous structures in nature. These peaks are confirmed according to the standard crystallographic database of silica nanoparticles with Card (no.47-0715) of the JCPDS (Joint Committee on Powder Diffraction Standards) (37,38).
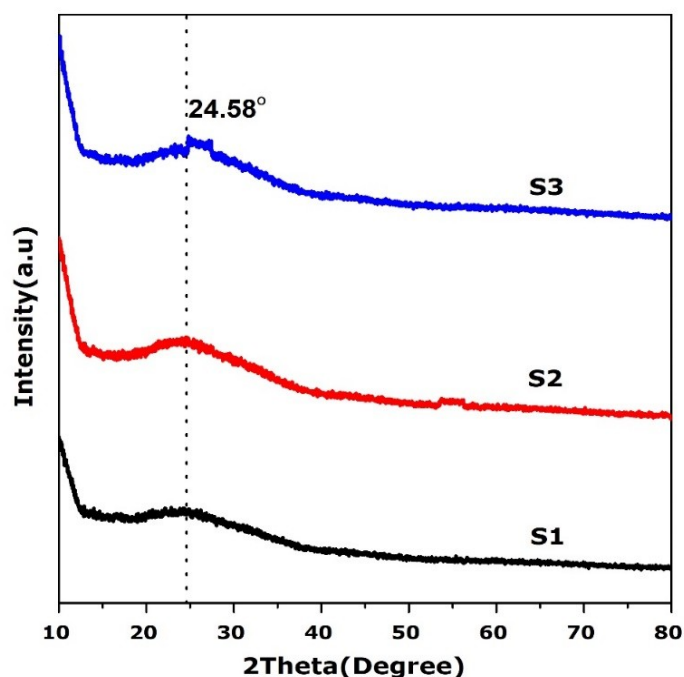
Figure 3: XRD patterns of the silica nanoparticles prepared using different volume ratios of TEOS: water: Ammonia = (S1) 1:5:2 (S2) 1:2.5:1 (S3) 1.5:2.5:1 respectively.

Scanning Electron Microscopy (SEM) and Energy Dispersive X-Ray Spectroscopy (EDX) Analysis
The surface morphology of silica nanoparticles was explored by Scanning Electron Microscopy (SEM) analysis. From the SEM images, as shown in Figure 4, it is clearly illustrated that almost monodisperse, spherical, and uniform size of silica nanoparticles have been successfully prepared from the sol-gel synthesis process. The influence of different concentrations of TEOS on the particle size and size distribution of silica can be also analyzed from the SEM images. From Figures 4(a, d), it can be seen that the silica nanoparticles with the particle size distribution of 60-140 nm and the average particle size of 95±5.59 nm are produced from 1 mL of TEOS. When the amount of TEOS is increased to 2 mL during synthesis, comparatively larger particle sizes are found. The particle size of these silica nanoparticles ranging from 120 to 240 nm with the

average particle size of 175±10.5 nm has been shown in Figures 4(b, e). From a group of researchers, it has been studied that the concentration of TEOS is one of the key factors which determines the size of silica nanoparticles by controlling the concentration of primary particles present in the solution (23). Because of being at the early stage of supersaturated solution in the sol-gel process, nucleation will first take place which will induce the formation of a large number of primary particles within a short time. After this induction period, they rapidly aggregated to produce stable particles. Highly monodisperse and spherical nanoparticles can be obtained by implying that the stable particles formed during the induction period are sufficient to consume all primary particles nucleated after the induction period. That's why the particle sizes are directly influenced by the concentration of TEOS (39)(40).
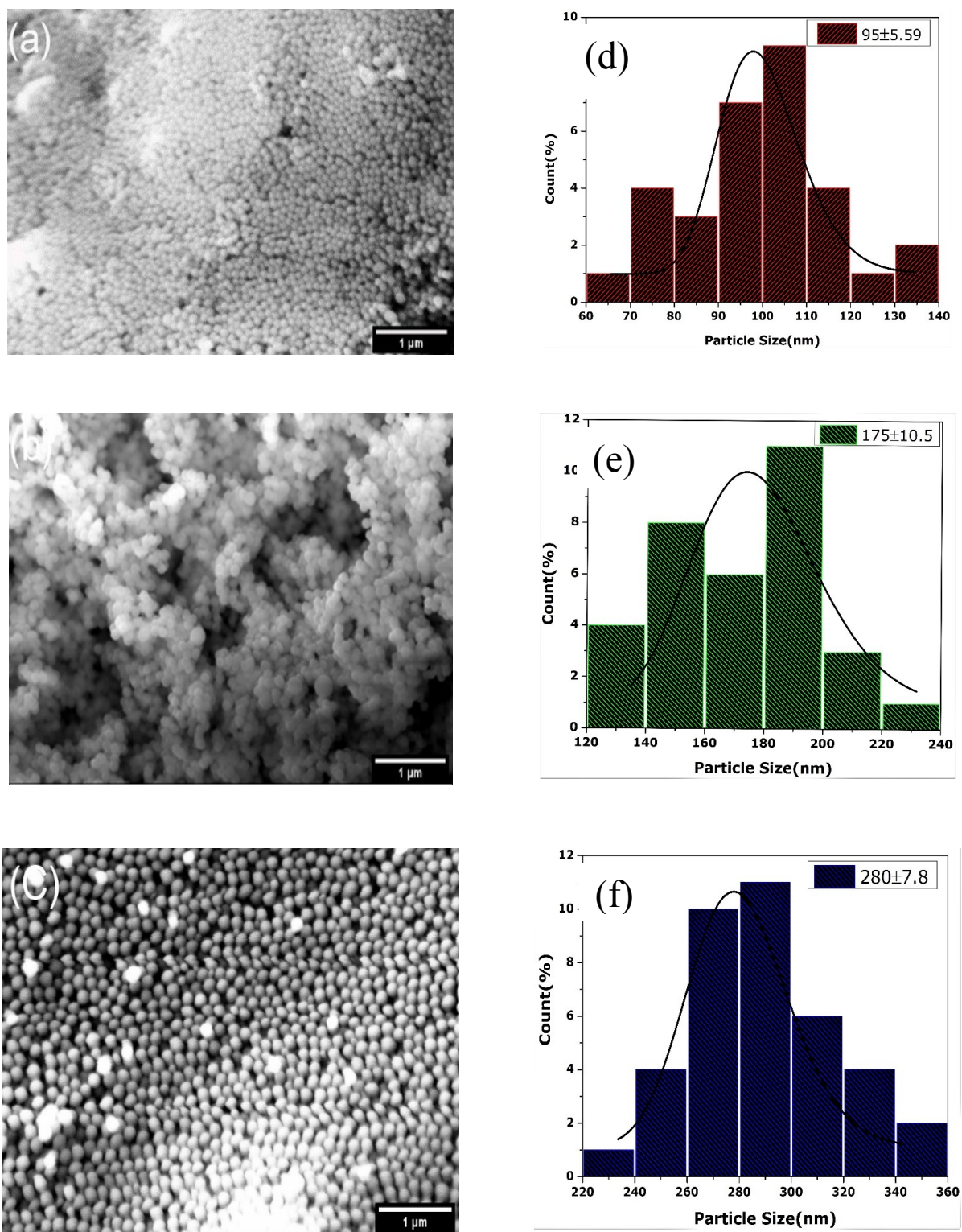
Figure 4: SEM images and size distribution histograms of silica nanoparticles synthesized from volume ratios of TEOS: water: Ammonia =**S1 (a, d)** 1:5:2; **S2 (b, e)** 1:2.5:1; **S3 (c, f)** 1.5:2.5:1 respectively.
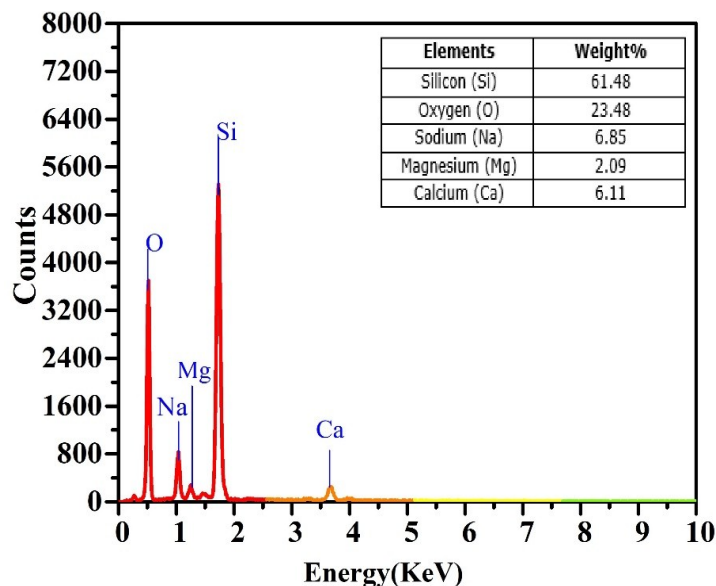
Figure 5: EDX spectrum of amorphous silica nanoparticles of S1 sample (average size of 95±5.59 nm and size distribution of 60-140 nm).

When the amount of TEOS is increased from 1 mL to 2 mL in the reaction vessel, the average size of silica particles is also increased from 95±5.59 nm to 175±10.5 nm. As the amount of TEOS is increased, both rate of hydrolysis and condensation reaction also increase predominantly. In consequence, due to the high hydrolysis reaction, a large number of the intermediates [Si(OR)$_{4-X}$(OH)$_X$] will be rapidly increased to generate a supersaturation solution.

After reaching that region, the consumption rate of intermediates through condensation reaction is also relatively fast. Thus, it probably shortens the nucleation period. Therefore, a fewer number of nuclei will be formed and we get a bigger particle size at the end (23,41). From Figures 4(c, f), it can be seen that the bigger silica nanoparticles are produced from 3 mL of TEOS with size distribution ranging from 220 to 360 nm and the average particle size of 280±7.8 nm. The SEM image in Figure 4(a) shows that the size distribution of silica nanoparticles is somewhat narrower than in Figures 4(b) and 4(c). At low concentrations of TEOS, relatively smaller particle sizes and narrower size distribution are formed due to slow hydrolysis and condensation reaction rate. At this time the electrostatic repulsive force impedes the uncontrollable growth and aggregation among the particles and stabilizes them(42). As a result, the particle size distribution of the S1 sample is relatively narrower than S2 and S3 samples. To check the elemental chemical composition of silica nanoparticles, Energy Dispersive X-Ray Spectroscopy (EDX) analysis was performed in SEM mode. The EDX spectrum of S1 sample due to smaller particle size and narrower size distribution is shown in Figure 5. The outcome from the EDX analysis indicates that the synthesized silica nanoparticles contain 61.48 wt% of silicon and

23.48 wt% of oxygen. Some contaminants such as Sodium (Na), Magnesium (Mg), and Calcium (Ca) are also detected with a little percentage in the EDX spectrum which could originate during the fabrication process. This data verifies that the EDX result of the synthesized silica nanoparticles is consistent with the FT-IR results.

Ultraviolet-Visible Spectrophotometry (UV-Vis) analysis
Ultraviolet-Visible analysis was used to characterize the optical properties of silica nanoparticles prepared from different concentrations of TEOS. The optical absorption spectra of silica nanoparticles were measured by introducing them into thin films which were coated on glass slides by the spin coating technique. The UV-Visible spectral analysis was performed using a UV-Visible spectrophotometer between the wavelength range of 300-1100 nm. The optical absorbance spectra of silica nanoparticles with different amounts of TEOS are shown in Figure 6. From the graph, it can be analyzed that with a higher concentration of TEOS, the absorbance value of silica nanoparticles increases. Because the high concentration of TEOS speeds up the rate of hydrolysis and condensation reaction and thereby it produces a larger particle size (43). When the average particle size of silica nanoparticles is 95±5.59 nm for the S1 sample, the absorption coefficient (α) is found to 5.24×10^5 cm^{-1}. The absoption coefficients are gradually increased to 7.47×10^5 cm^{-1} and 9.98×10^5 cm^{-1} for S2 and S3 samples respectively due to the formation of larger particle sizes. The optical band gap can be calculated from tauc's equation which gives the relationship between the absorption coefficient (α) and incident photon energy (hν) (44). The equation can be expressed as $(\alpha h\vartheta)^{1/n} = \beta(h\vartheta - E_g)$(1).
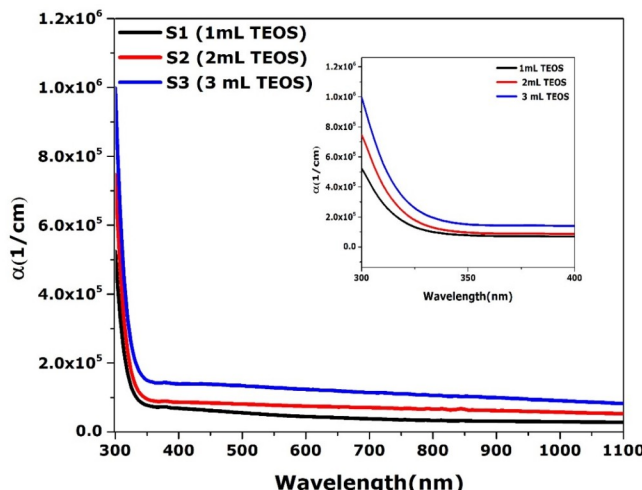
Figure 6: The absorbance spectra of silica nanoparticles prepared using different volume ratios of TEOS: water: Ammonia = **(S1)** 1:5:2 **(S2)** 1:2.5:1 **(S3)** 1.5:2.5:1 respectively.

Where, E_g is the band gap energy of the material, v is the photon's frequency, α is the absorption coefficient, h is planck's constant, β is the band tailing parameter which depends on the disorder of the materials and n is the power factor of the optical transition mode that depends on the material's property. The power number (n) reveals ½ for direct allowed, 3/2 for direct forbidden, 2 for indirect allowed, and ≥3 for indirect forbidden

transitions (45,46). Now the power factor n can be easily calculated from the equation

$$\frac{1}{n} ln\left(\alpha h\vartheta\right) = \ln \beta + ln\left(h\vartheta - E_g\right) \qquad (2)$$

The optical band gaps of the silica nanoparticles are obtained from the Tauc plot by plotting incident photon energy $h\nu$ in eV against $(\alpha h\nu)^2$.
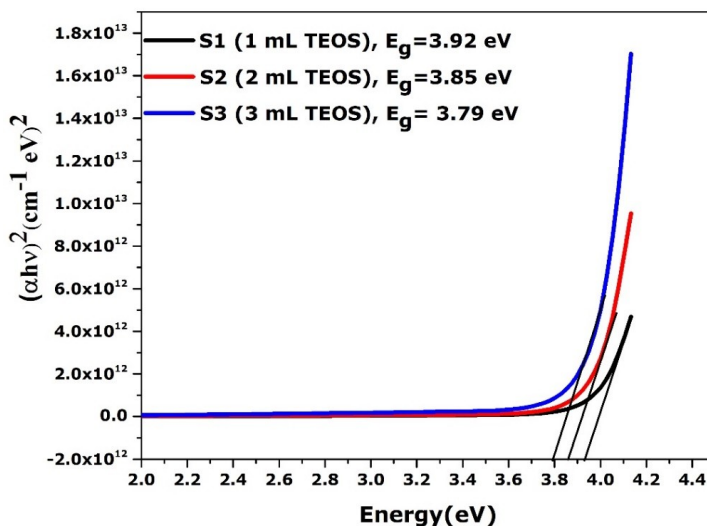
Figure 7: Determination of optical band gaps of Silica nanoparticles prepared from using different volume ratios of TEOS: water: ammonia = **(S1)** 1:5:2 **(S2)** 1:2.5:1 **(S3)** 1.5:2.5:1 respectively.

Figure 7 shows the optical band gaps of the samples S1, S2, and S3 are 3.92 eV, 3.85 eV, and 3.79 eV, respectively, which are found by extrapolating the intercept at $\alpha=0$ in the Tauc plot. It is observed that the optical band gaps of silica nanoparticles continuously decrease with increasing the

concentration of TEOS. This is because the particle sizes of silica are increased with increasing the concentration of TEOS whereas its dielectric function remains constant in the wavelength range of 300-1100 nm (43,46).

CONCLUSION

Silica nanoparticles were successfully synthesized from the hydrolysis and condensation reaction of TEOS in ethanol solution. During the fabrication process, TEOS was utilized as a precursor and ammonia as a catalyst. The chemical bonds in silica nanoparticles were noticed from FTIR analysis by confirming the different absorption peaks related to the Si-O-Si bonds. Furthermore, from the XRD spectrum, a broad diffused peak was discovered which asserted the amorphous structure of the silica nanoparticles. However, the spherical and uniform size of silica nanoparticles ranging from 95±5.59~280±7.8 nm were found from the different amounts of TEOS while keeping the other reaction parameters at a fixed condition. It was discovered that the size of nanoparticles became larger when the concentration of TEOS was gradually increased. So, when using 1 mL of TEOS, spherical and amorphous silica nanoparticles with the average particle size of 95±5.59 nm and particle size distribution of 60-140 nm were produced. The particle size and size distribution became wider when using the higher concentration of TEOS. Hence, the average particle sizes of 175±10.5 and 280±7.8 nm and particle size distributions of 120-240 nm and 220-360 nm were found from 2 mL and 3mL of TEOS respectively. The variation in TEOS concentration also affects the optical absorbance of silica nanoparticles. Therefore, the optical absorbance of silica nanoparticles was increased with increasing the concentration of TEOS. Consequently, the optical bandgap of silica nanoparticles was reduced from 3.92 eV to 3.79 eV.

ACKNOWLEDGMENTS

REFERENCES

1.   Jeelani PG, Mulay P, Venkat R, Ramalingam C. Multifaceted Application of Silica Nanoparticles. A Review. Silicon. 2020;12(6):1337–54. <URL>

2.   Karim AH, Ali A, Mezan S. Synthesis and Characterization of Silica Nanoparticle (Sio 2 Nps) Via Chemical Process. 2021;25(6):6211–8. <URL>

3.   Zhang W, Tu J, Long W, Lai W, Sheng Y, Guo T. Preparation of SiO2 anti-reflection coatings by sol-gel method. Energy Procedia [Internet]. 2017;130:72–6. Available from: <URL>

4.   Musigapong P, Briffa SM, Lynch I, Soontaranon S, Chanlek N, Valsami-Jones E. Silica nanoparticle synthesis and multi-method characterisation. Mater Sci Forum. 2019;947 MSF:82–90. <URL>

5.   Kim KIDO, Kim HEET. Formation of Silica Nanoparticles by Hydrolysis of TEOS Using a Mixed Semi-Batch / Batch Method. 2002;183–9.

6.   Zhao S, Xu D, Ma H, Sun Z, Guan J. Controllable preparation and formation mechanism of monodispersed silica particles with binary sizes. J Colloid Interface Sci [Internet]. 2012;388(1):40–6. Available from: <URL>

7.   Gleiter H, Schimmel T, Hahn H. Nanostructured solids - From nano-glasses to quantum transistors. Nano Today [Internet]. 2014;9(1):17–68. Available from: <URL>

8.   Wang XD, Shen ZX, Sang T, Cheng X Bin, Li MF, Chen LY, et al. Preparation of spherical silica particles by Stöber process with high concentration of tetra-ethyl-orthosilicate. J Colloid Interface Sci [Internet]. 2010;341(1):23–9. Available from: <URL>

9.   Xu J, Ren D, Chen N, Li X, Ye Z, Ma S, et al. A facile cooling strategy for the preparation of silica nanoparticles with rough surface utilizing a modified Stöber system. Colloids Surfaces A Physicochem Eng Asp [Internet]. 2021;625(January):126845. Available from: <URL>

10.   Rahman IA, Padavettan V. Synthesis of Silica Nanoparticles by Sol-Gel : Size-Dependent Properties , Surface Modification , and Applications in Silica-Polymer Nanocomposites — A Review. 2012;2012. <URL>

11.   Huang Y, Pemberton JE. Synthesis of uniform, spherical sub-100nm silica particles using a conceptual modification of the classic LaMer model. Colloids Surfaces A Physicochem Eng Asp [Internet]. 2010;360(1–3):175–83. Available from: <URL>

12.   Rahman IA, Vejayakumaran P, Sipaut CS, Ismail J, Chee CK. Size-dependent physicochemical and optical properties of silica nanoparticles. Mater Chem Phys. 2009;114(1):328–32.<URL>

13.   Pe J, Liz-marza LM. Recent Progress on Silica Coating of Nanoparticles and Related Nanomaterials. 2010;36310:1182–95. <URL>

14.   Hyde EDER, Seyfaee A, Neville F, Moreno-atanasio R. Colloidal Silica Particle Synthesis and Future Industrial Manufacturing Pathways : A Review. 2016; <URL>

15.   Stanley R, Nesaraj a S. Effect of Surfactants on the Wet Chemical Synthesis of Silica Nanoparticles. 2014; (October 2013):9–21.<URL>

16.   Finnie KS, Bartlett JR, Barbé CJA, Kong L. Formation of silica nanoparticles in microemulsions. Langmuir. 2007;23(6):3017–24. <URL>

17.   Ren D, Xu J, Chen N, Ye Z, Li X, Chen Q, et al. Controlled synthesis of mesoporous silica nanoparticles with tunable architectures via oil-water microemulsion assembly process. Colloids Surfaces A Physicochem Eng Asp [Internet]. 2021;611(August):125773. Available from: <URL>

18.   Deng TS, Zhang QF, Zhang JY, Shen X, Zhu KT, Wu JL. One-step synthesis of highly monodisperse hybrid silica spheres in aqueous solution. J Colloid Interface Sci [Internet]. 2009;329(2):292–9. Available from: <URL>

19.   Dubey RS, Rajesh YBRD, More MA. Synthesis and Characterization of SiO2 Nanoparticles via Sol-gel Method

for Industrial Applications. Mater Today Proc [Internet]. 2015;2(4–5):3575–9. Available from: <URL>

20. Prabha S, Durgalakshmi D, Rajendran S, Lichtfouse E. Plant-derived silica nanoparticles and composites for biosensors, bioimaging, drug delivery and supercapacitors: a review. Environ Chem Lett [Internet]. 2021;19(2):1667–91. Available from: <URL>

21. Zaky RR, Hessien MM, El-Midany AA, Khedr MH, Abdel-Aal EA, El-Barawy KA. Preparation of silica nanoparticles from semi-burned rice straw ash. Powder Technol. 2008;185(1):31–5. <URL>

22. Stober WERNER. Controlled Growth of Monodisperse Silica Spheres in the Micron Size Range 1. 1968;69:62–9.

23. Bogush GH, Zukoski IV CF. Studies of the kinetics of the precipitation of uniform silica particles through the hydrolysis and condensation of silicon alkoxides. J Colloid Interface Sci. 1991;142(1):1–18.

24. Qasim M, Ananthaiah J, Dhara S, Paik P, Das D. Synthesis and Characterization of Ultra-Fine Colloidal Silica Nanoparticles. Adv Sci Eng Med. 2014;6(9):965–73.<URL>

25. Meier M, Ungerer J, Klinge M, Nirschl H. Synthesis of nanometric silica particles via a modi fi ed Stöber synthesis route. Colloids Surfaces A [Internet]. 2018;538(September 2017):559–64. Available from: <URL>

26. Sreenivasa K, El-hami K, Kodaki T, Matsushige K. A novel method for synthesis of silica nanoparticles. 2005;289:125–31. <URL>

27. Guo Q, Huang D, Kou X, Cao W, Li L, Ge L, et al. Synthesis of disperse amorphous SiO2 nanoparticles via sol–gel process. Ceram Int. 2017;43(1):192–6. <URL>

28. Rahman IA, Vejayakumaran P, Sipaut CS, Ismail J, Bakar MA, Adnan R, et al. An optimized sol-gel synthesis of stable primary equivalent silica particles. Colloids Surfaces A Physicochem Eng Asp. 2007;294(1–3):102–10. <URL>

29. Sung JY, Lee BRD. Structure and transmittance behavior of sol – gel silica nanoparticles synthesized using pH-stable alkanolamines. 2017;1–9. <URL>

30. Gao GM, Zou HF, Liu DR, Miao LN, Ji GJ, Gan SC. Influence of surfactant surface coverage and aging time on physical properties of silica nanoparticles. Colloids Surfaces A Physicochem Eng Asp. 2009;350(1–3):33–7.<URL>

31. Devi P, Vishal, Singla ML. Effect of surfactant concentration, solvents and particle size on Π-A isotherm of silica nanoparticles. Mater Lett [Internet]. 2013;107:107–10. Available from: <URL>

32. Kim S, Kim H, Geon S, Kim W. Effect of electrolyte additives on sol-precipitated nano silica particles. 2004;30:171–5. <URL>

33. Guo Q, Yang G, Huang D, Cao W, Ge L, Li L. Synthesis and characterization of spherical silica nanoparticles by modified Stöber process assisted by slow-hydrolysis catalyst. Colloid Polym Sci. 2018;296(2):379–84. <URL>

34. Das S, Banerjee C, Kundu A, Dey P. Silica nanoparticles on front glass for efficiency enhancement in superstrate-type amorphous silicon solar cells. 415102.

35. Jiang X, Tang X, Tang L, Zhang B, Mao H. Synthesis and formation mechanism of amorphous silica particles via sol–gel process with tetraethylorthosilicate. Ceram Int [Internet]. 2019;45(6):7673–80. Available from: <URL>

36. Yang G, Guo Q, Yang D, Peng P, Li J. Disperse ultrafine amorphous SiO 2 nanoparticles synthesized via precipitation and calcination. Colloids Surfaces A Physicochem Eng Asp [Internet]. 2019;568:445–54. Available from: <URL>

37. Yang D, Yang G, Liang G, Guo Q, Li Y, Li J. High-surface-area disperse silica nanoparticles prepared via sol-gel method using L-lysine catalyst and methanol/water co-solvent. Colloids Surfaces A Physicochem Eng Asp [Internet]. 2021;610(July 2020):125700. Available from: <URL>

38. Kim TG, An GS, Han JS, Hur JU, Park BG, Choi SC. Synthesis of size controlled spherical silica nanoparticles via sol-gel process within hydrophilic solvent. J Korean Ceram Soc. 2017;54(1):49–54. <URL>

39. Ibrahim I a. M, Zikry a. a. F, Sharaf M a. Preparation of spherical silica nanoparticles: Stober silica. J Am Sci. 2010;6(11):985–9.

40. H GHB, Y MAT, IV CFZ. Preparation of Monodisperse Silica Particles: Control of Size and Mass Fraction. J Non Cryst Solids. 1988;104:95–106.

41. Chou K Sen, Chen CC. Preparation of monodispersed silica colloids using sol-gel method: COSOLVENT effect. Ceram Trans. 2005;166:57–67.

42. Giesche H. Synthesis of Monodispersed Silica Powders I . Particle Properties and Reaction Kinetics. 1994;14:189–204.

43. Jamali N. Effect of Tetraethyl-Orthosilicate , 3-Aminopropyltriethoxysilane and Polyvinylpyrrolidone for synthesis of SiO 2 @ Ag core-shell nanoparticles prepared by chemical reduction method. 2021;1:31–8. <URL>

44. Al-bataineh QM, Alsaad AM, Ahmad AA, Telfah A. Heliyon A novel optical model of the experimental transmission spectra of nanocomposite PVC-PS hybrid thin fi lms doped with silica nanoparticles. Heliyon [Internet]. 2020;6(June):e04177. Available from: <URL>

45. Gupta P, Kumar K, Kumar N, Bal P, Yadav C, Hasan S. Effect of annealing temperature on a highly sensitive nickel oxide - based LPG sensor operated at room temperature. Appl Phys A [Internet]. 2021;127(4):1–15. Available from: <URL>

46. Sankar S, Kaur N, Lee S, Kim Y.Rapid Sonochemical Synthesis of Spherical Silica Rapid Sonochemical Synthesis of Spherical Silica Nanoparticles Derived from Brown Rice Husk. Ceram Int [Internet]. 2018; Available from: <URL>.

REVIEW ARTICLE

Formation and Uses of Imidazo[1,2-*a*]pyrimidines and Related Compounds: A Review Comprising Years 2000-2021

Rabia Zeynep Uslu Kobak* (iD), **Barbaros Akkurt** (iD)

Istanbul Technical University, Faculty of Science and Letters, Department of Chemistry, Maslak, 34469 Sariyer-Istanbul, Türkiye

Abstract: This work covers the selected synthetic papers of imidazo[1,2-*a*]pyrimidine and its derivatives between the years 2000 and 2021. Synthesis of the heterocyclic moiety, application of this scaffold to biological activities, and secondary applications like corrosion inhibition are provided. The authors hope that readers will find the treatise useful.

INTRODUCTION

This review article has been designed in a way that the grand category, sub-categories, and examples are provided, starting from the least recent article to the most recent one.

SYNTHETIC WORKS ASSOCIATED WITH BIOLOGICAL ACTIVITY

Known Molecules

There are known drug candidates in the market with imidazopyrimidine skeleton. Here are some examples for them (See Figure 1):

Divaplon   Taniplon   Fasiplon

p38 kinase inhibitor   Aurora-A kinase inhibitor   Androgen receptor antagonist

for anxiety disorders   used in CK2 inhibition
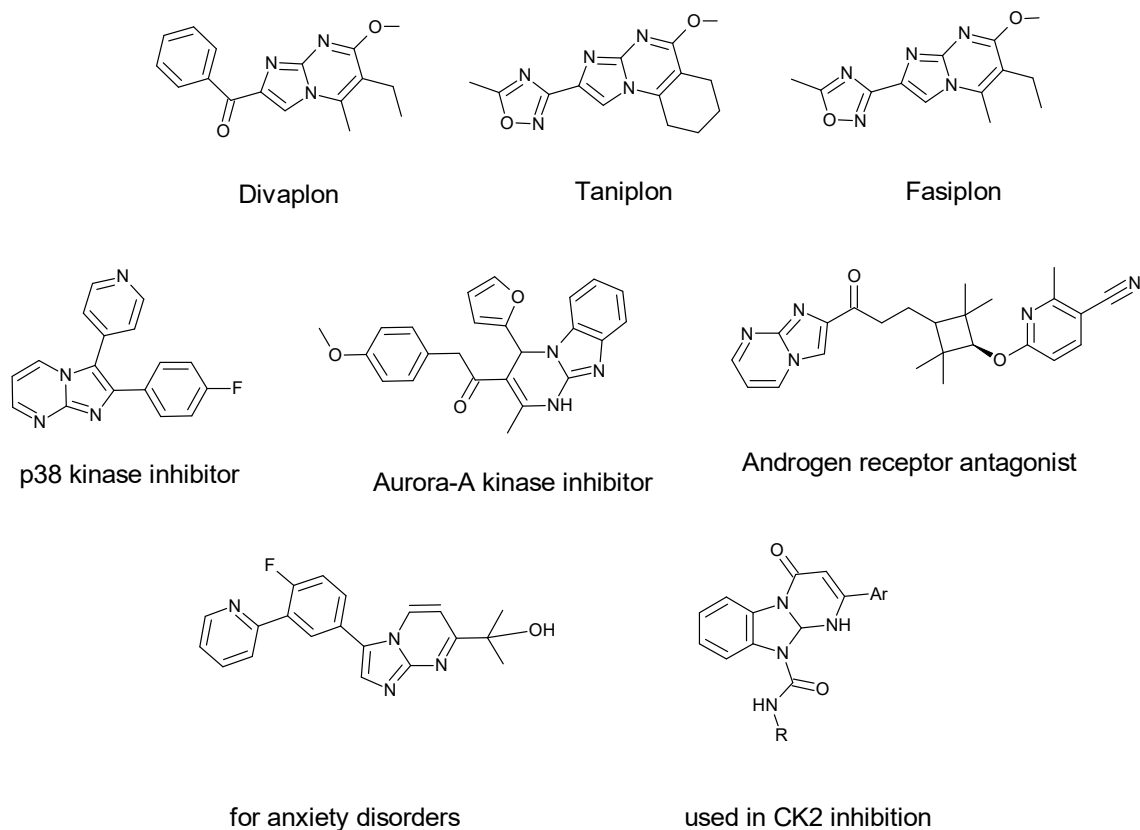
Figure 1: Some known examples of imidazopyrimidines in use.

GABA_A Ligands that are Functionally Selective
Jensen and coworkers reported that γ-Aminobutyric acid (GABA) is the major inhibiting neurotransmitter in the central nervous system. Imidazo[1,2-a]pyrimidines are GABA_A receptor benzodiazepine binding site ligands. They can show functional selectivity for the α3 subtype over the α1 one (1) (See Figure 2).
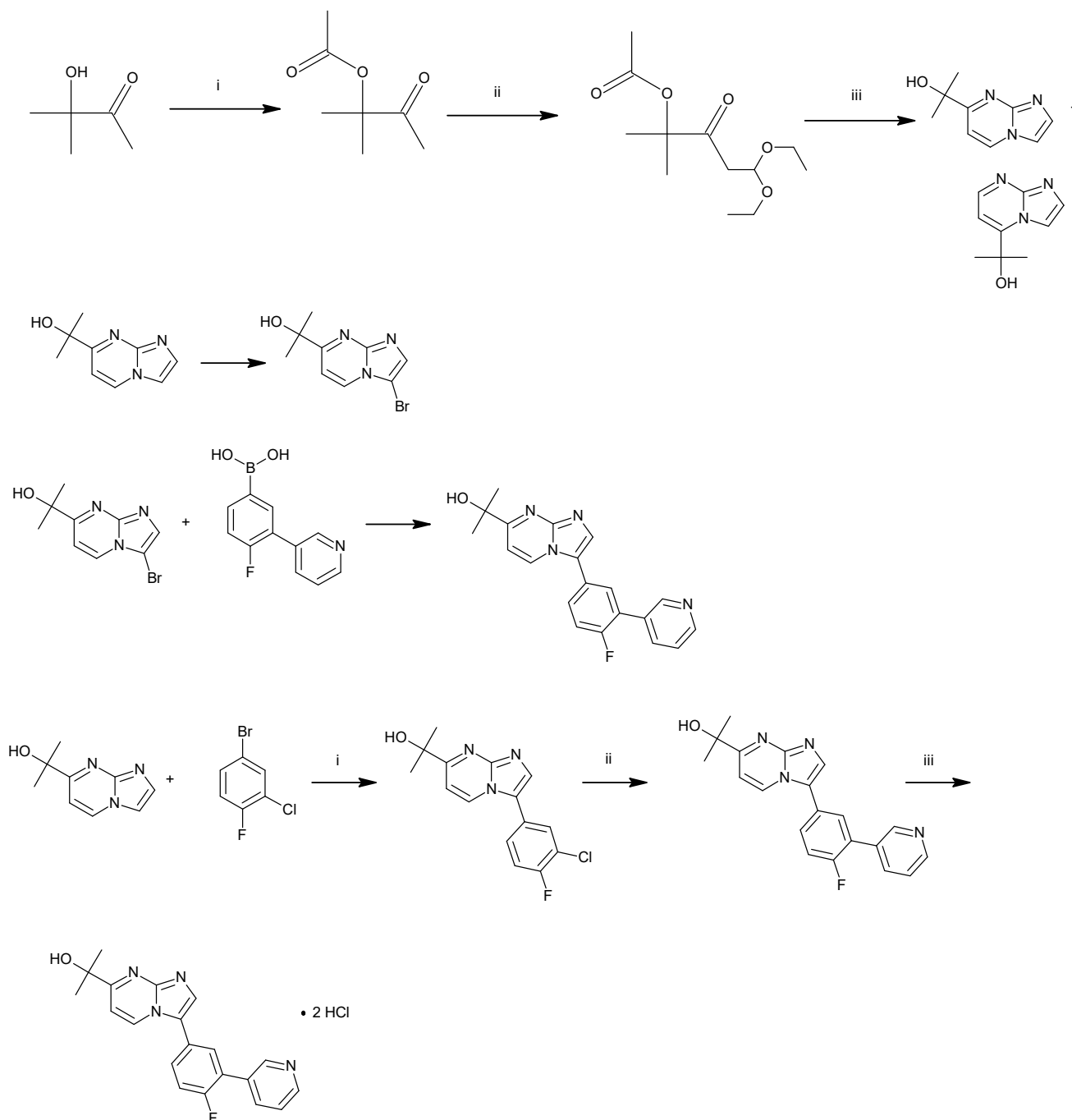
Figure 2: Preparation of pyridylphenylimidazo[1,2-*a*]pyrimidines as GABA$_A$ receptor benzodiazepine binding ligands.

Synthesis and Biological Activities of Some Imidazopyrimidines

An Armenian research group has studied the synthesis and biological activities of 4-substituted 6,7-dihydro-7,7-dimethyl-5-oxo-9H-pyrano-

[4′,3′:4,5]- thieno [3,2-e]imidazo [1,2-a] pyrimidines and their hydrochlorides and their anticonvulsant and tranquilizer properties (2) (See Figure 3).
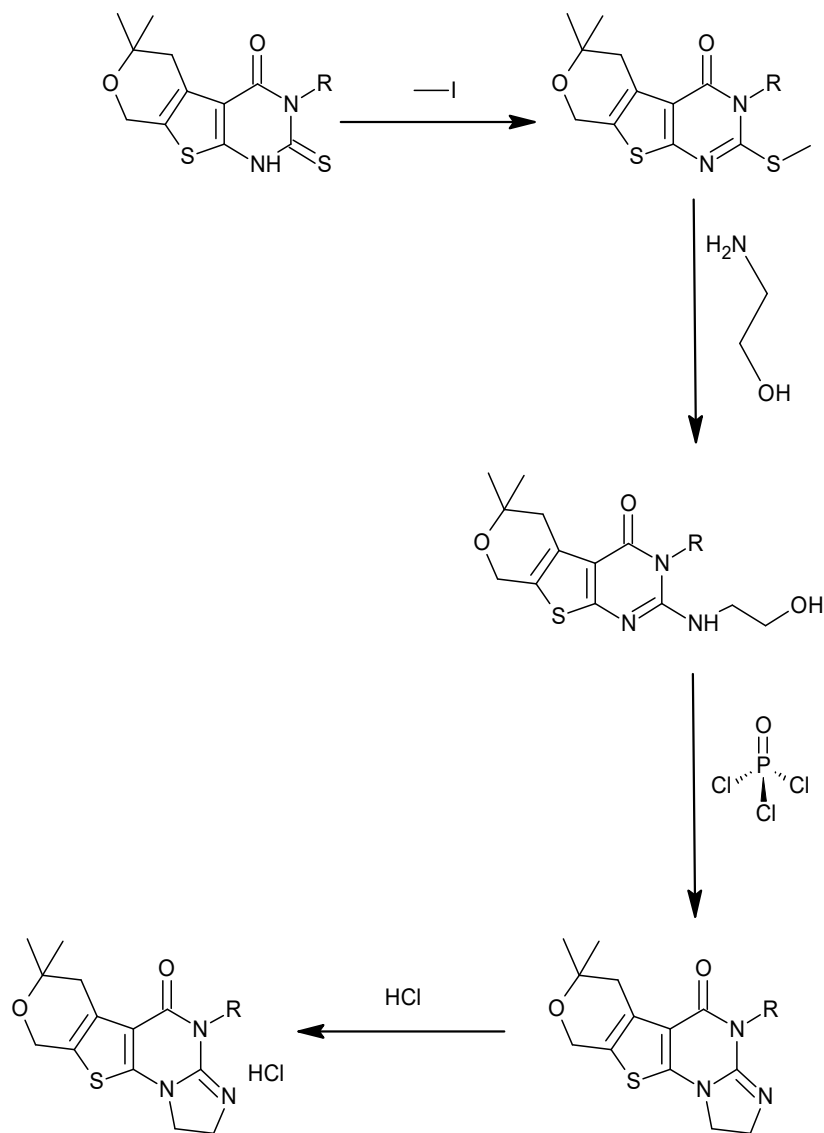
Figure 3: Synthesis of pyranothienoimidazo[1,2-*a*]pyrimidine compound.

**Antiinflammatory Response of
Imidazopyrimidine Derivatives**
Vidal and co-authors (2001) prepared six imidazo[1,2-a]pyrimidine (IP) derivatives and tested on leukocyte functions in vitro and inflammatory response was also tested, this response is induced by zymosan in the mouse air pouch. The authors reported that imidazo[1,2-a]pyrimidines possess antiinflammatory potential (3) (See Figure 4).
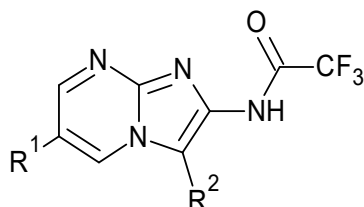
Figure 4: Imidazopyrimidine derivatives for researching the antiinflammatory activity.

Synthesis of GABA Agonists
A group from Merck, Inc with Blackaby as the first author has reported the preparation of GABA-selective agonists through a series of synthetic steps (4) (See Figure 5).
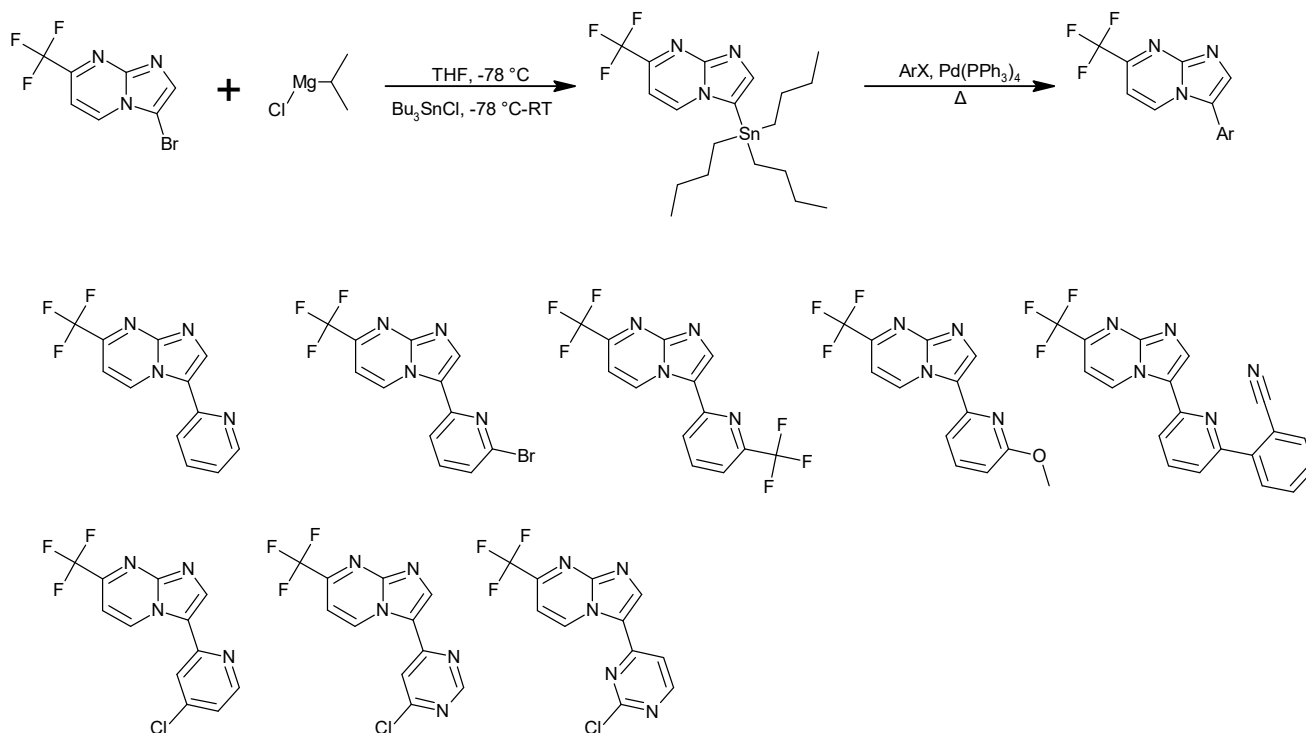
Figure 5: Preparation of tributyl Sn-C bond and reaction with aryl halide; eight instances were reported.

Preparation of GABAₐ Agonists Against Anxiety

Jennings et al. showed that imidazo[1,2-a]pyrimidines and triazines could function as GABAₐ agonists for the treatment of anxiety. The group has prepared seven compounds and investigated their affinity and efficacy at α1 and α3 subtype GABAₐ receptors, by varying the terminal pyridine ring. The route to synthesize the molecules has been shown in the figure below (5) (See Figure 6).
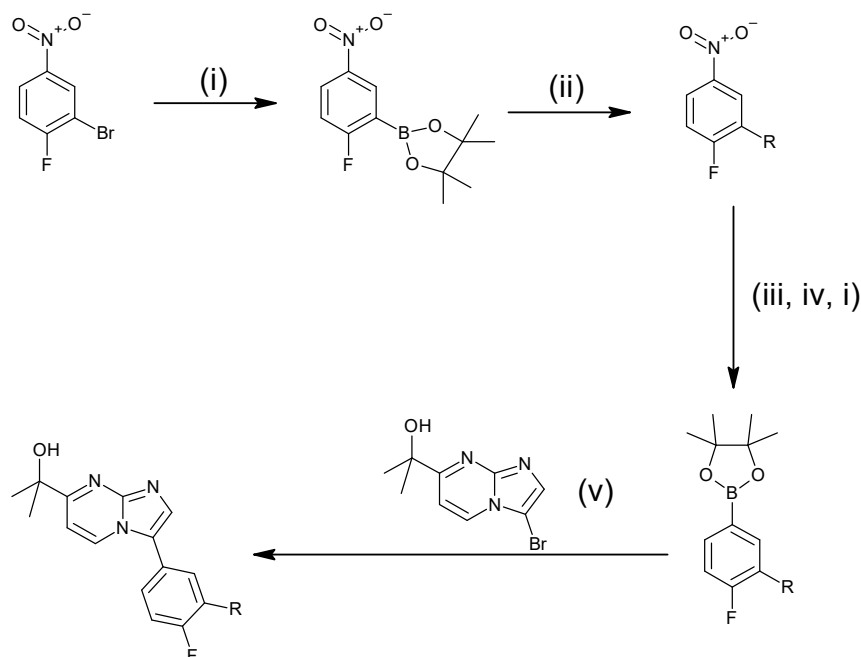
Figure 6: Preparation of 3-aryl-substituted imidazopyrimidine derivative.

Compounds Showing Anti-inflammatory Property and COX-2 selectivity
A Chinese research group (Zhou et al.) has investigated the synthesis and anti-inflammatory activity of imidazo[1,2-a]pyrimidine derivatives positioned adjacently with two aryl groups were designed and synthesized in order to improve their anti-inflammatory activities. The synthesized compounds presented anti-inflammatory activities with some COX-2 selectivity (6) (See Figure 7).
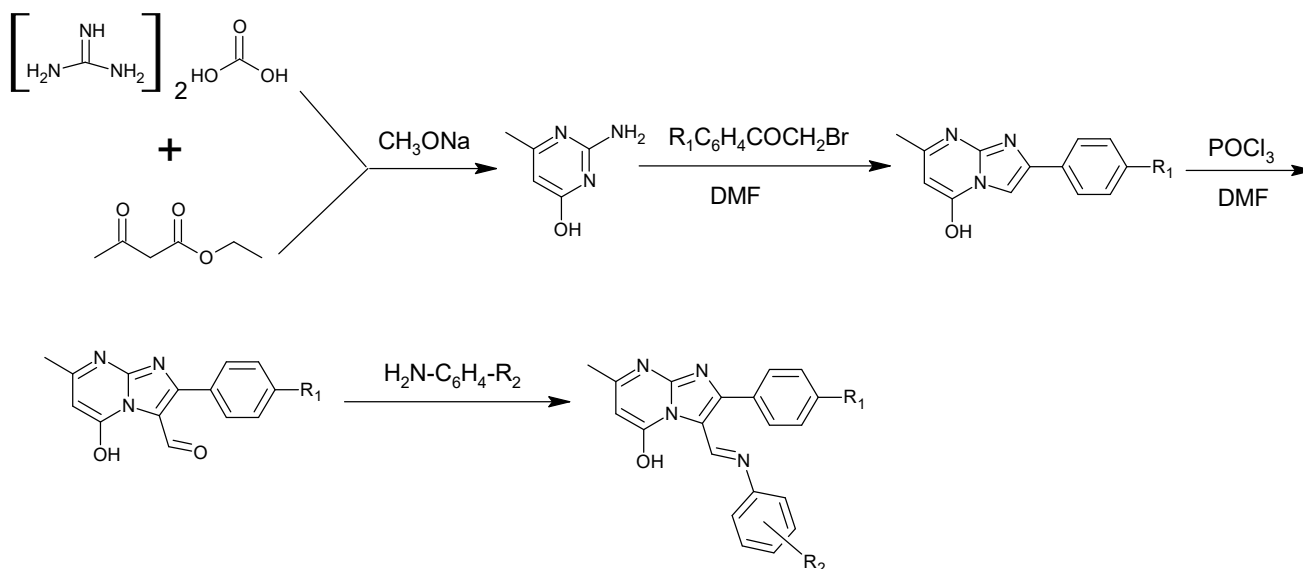
Figure 7: Synthesis of imidazopyrimidines for anti-inflammatory activity.

Preparation of New Antimicrobial Agents
New antimicrobial agents, containing imidazo[1,2-a]pyrimidine skeletons, have been synthesized by Al-Tel and Al-Qawasmeh in 2010. The antimicrobial activities were tested with Gram-positive and -negative bacteria. Some of the test compounds were efficient in the inhibition of Gram-positive and -negative strains. According to the results, the substituents on phenyl rings are the determining factor of biological activity. The antibacterial activity is dramatically lowered if the molar refractivity is increased (7)(See Figure 8).

Dual KSP and Aurora-A Kinase Inhibitors
Geng and coworkers reported that four series of dihydropyrazolo[3,4-b]pyridines and benzo[4,5]imidazo[1,2-a]pyrimidines were designed and synthesized as being KSP and Aurora-A kinase inhibitors, at the same time. This was achieved by adding some Aurora-A kinase inhibitory fragments into the KSP inhibitor body and it was named as CPUYL064. Two enzyme inhibition assays and a cytotoxicity assay in vitro were conducted with 19 target compounds. The results indicated that some target compounds could inhibit both enzymes and several compounds were significantly inhibitive against HCT116 cell line. Although they were moderate KSP and Aurora-A kinase inhibitors, two compounds displayed a remarkable cytotoxic activity in the micromolar range, especially against the HCT116 and HepG2 cell lines. Cancer treatment with dual-function inhibitors seems to be possible (8) (See Figure 3).

Figure 8: Synthesis of new antimicrobial agents containing imidazopyrimidine moiety.

Figure 9: Preparation of dual-function inhibitors. R^1 is furyl. R^2 is 4-methoxy, 4-nitro, 4-trifluoromethyl, 3-chloro-4-fluoro, and 4-fluoro.

Compounds Inhibiting Wnt/b-catenin signaling pathway

In the regulation of embryonic development and tumorigenesis, Wnt/b-catenin signaling possesses an important role. When it is deregulated, severe cases like cancer occur and Wnt signaling helps establish a good platform for the pharmacology-related targeting of cancer. A series of imidazopyrimidines were prepared by Cosimelli ant

coworkers, and they discovered that some compounds were able to inhibit the signaling pathway of Wnt/b-catenin with the help of a luciferase reporter assay. Also, cell proliferation was found in selected cancer lines and APC or b-catenin gene was mutated. The most successful compounds in the series could downregulate the expression of Wnt target genes (9) (See Figures 10 and 11).
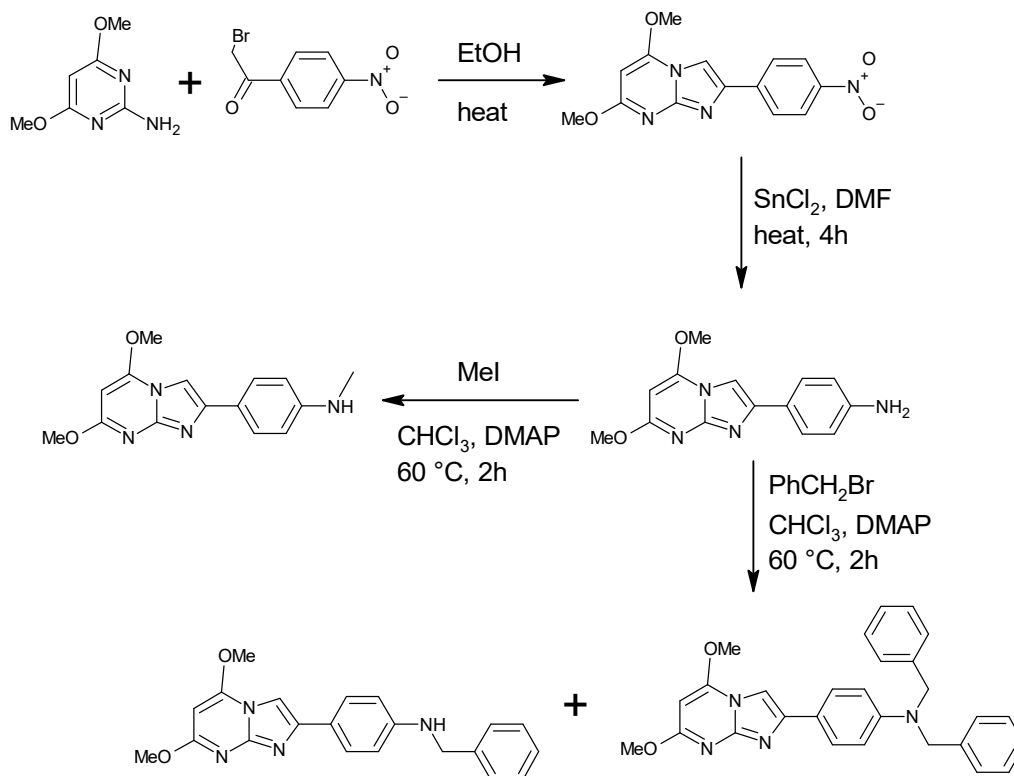
Figure 10: Preparation of mono- and di-benzyl-substituted imidazopyrimidine compounds.
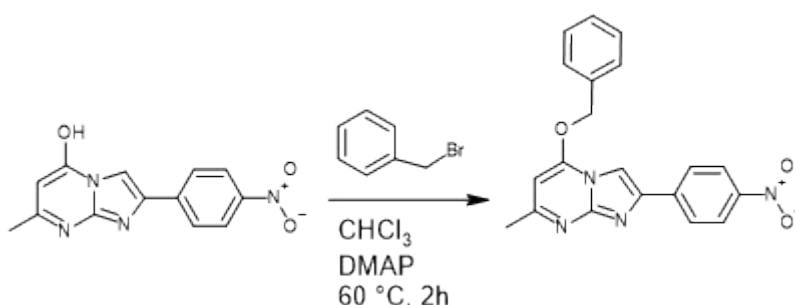
Figure 11: Benzylation of the 5-hydroxy group.

Synthesis of Some Mannich Bases Incorporating Imidazopyrimidine Core

Aeluri and co-workers prepared Mannich bases containing imidazo[1,2-*a*]pyrimidine skeleton. Imidazo[1,2-*a*]pyrimidine skeleton was prepared with a one-pot, three-component reaction, in which 2-aminopyrimidine, a secondary amine or

piperazine, and excess formaldehyde in methanol were used. The products were tested in vitro against three human cancer cell lines. Antiproliferative activity was found for most of the compounds. Three of them showed effective inhibition, with GI 50 values similar to the standard drug used (10) (See Figure 12).
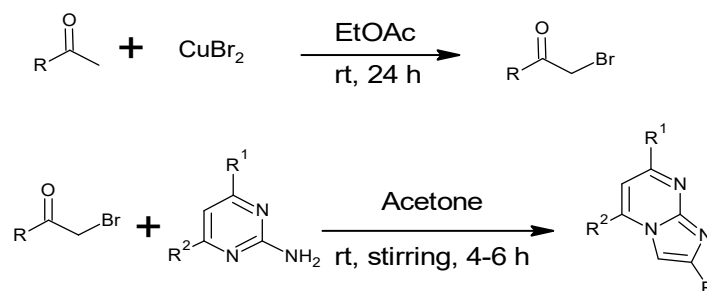
Figure 12: Formation of substituted imidazopyrimidine derivatives for screening cancer cell lines.

Synthesis of Tricyclic Dihydropyrimidines

Some tricyclic dihydropyrimidines were synthesized by Kaur et al. using a procedure which endows a one-pot, three-component Traube-Schwarz reaction, along with $Zn(ClO_4)_2.6H_2O$ as the catalytic entity. All the purified compounds were screened for their *in vitro* anticancer activity, against three cancer cell lines, namely prostate cancer cells (PC3), lung cancer cells (NCI-H1299), and colon cancer cells (HCT116). The authors investigated *in vitro* DNA-intercalation ability with UV-Vis spectrophotometry, and found that the compound was inserted into the DNA base pairs and interacted strongly with the DNA double helix (11) (See Figure 13).
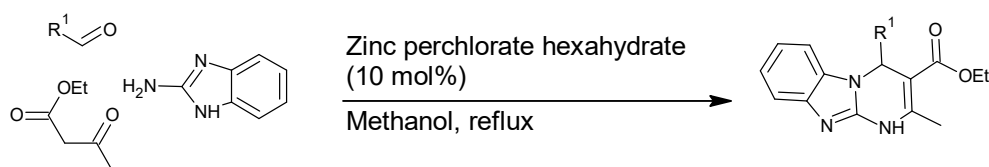
Figure 13: Synthesis of tricyclic dihydropyrimidines with a three-component reaction for the hopes of anticancer activity.

Antigiardial Response of Imidazopyrimidines

Velázquez-Olvera and co-workers investigated in vitro of the antigiardial response of a group of imidazopyrimidine compounds against *Giardia lamblia* WB's trophozoites and albendazole was employed as the reference drug. The synergism of albendazole with the most active imidazopyrimidine compound was also studied. The most potent compound had 3-hydroxymethyl-4-fluorophenyl substituents on the skeleton, and the parent compound to compare had p-tolyl substituent only. As a conclusion, researchers found that 2-aryl-3-hydroxymethyl substituents created a good synergism against the reference (12) (See Figure 14).
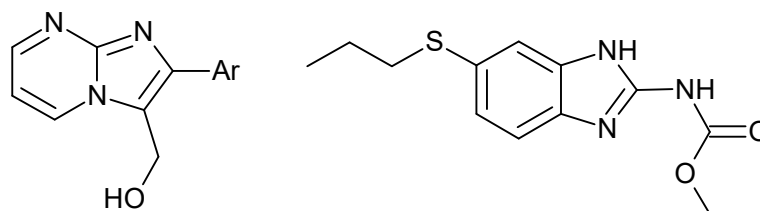
Figure 14: 2-Aryl-3-hydroxymethyl-substituted imidazopyrimidine compound and albendazole as a reference compound for antigiardial response.

Synthesis and Biological Activity of Biphenyl-Containing Imidazopyrimidines

Al-Lami and coworkers reported the four-step synthesis of fourteen compounds. In the first step, 2-aminopyrimidine and biphenyl phenacyl bromide were reacted to give the imidazopyrimidine skeleton. In the second step, Vilsmeier-Haack reaction was employed to introduce an aldehyde group at the 3-position. The aldehydes formed were reacted with various aromatic amines to form

Schiff's bases in the third reaction. Sodium borohydride was used to reduce the Schiff's bases to 3-aminomethyl-2-biphenylimidazo[1,2-

a]pyrimidines. Different bacteria were tested for antimicrobial effect of some of the synthesized compounds (13) (See Figure 15).
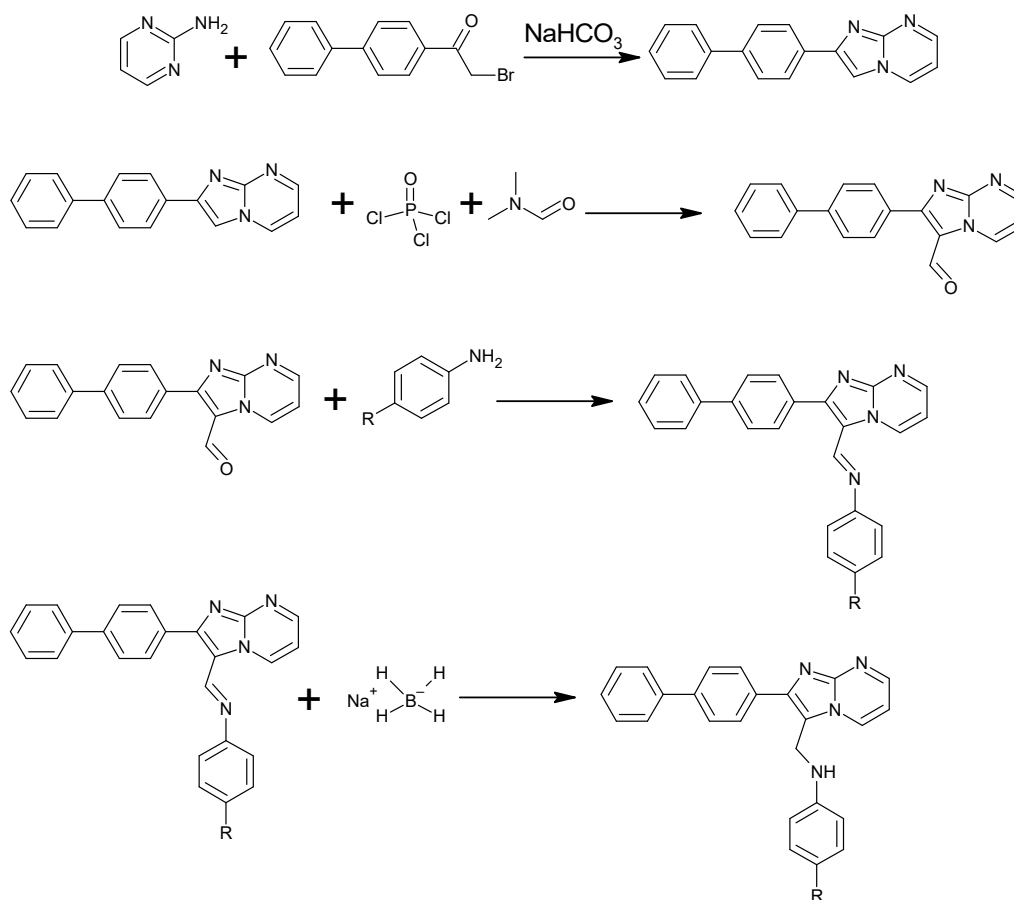
Figure 15: Four step synthesis of fourteen compounds for antimicrobial assay.

PDE10A enzyme inhibitors

Moszczyński-Pętkowski and coworkers synthesized new substances containing imidazo[1,2-*a*]pyrimidine skeleton for possible interaction with PDE10A. Some compounds displayed a very high activity and also presented a good metabolic stability (14) (See Figure 16).
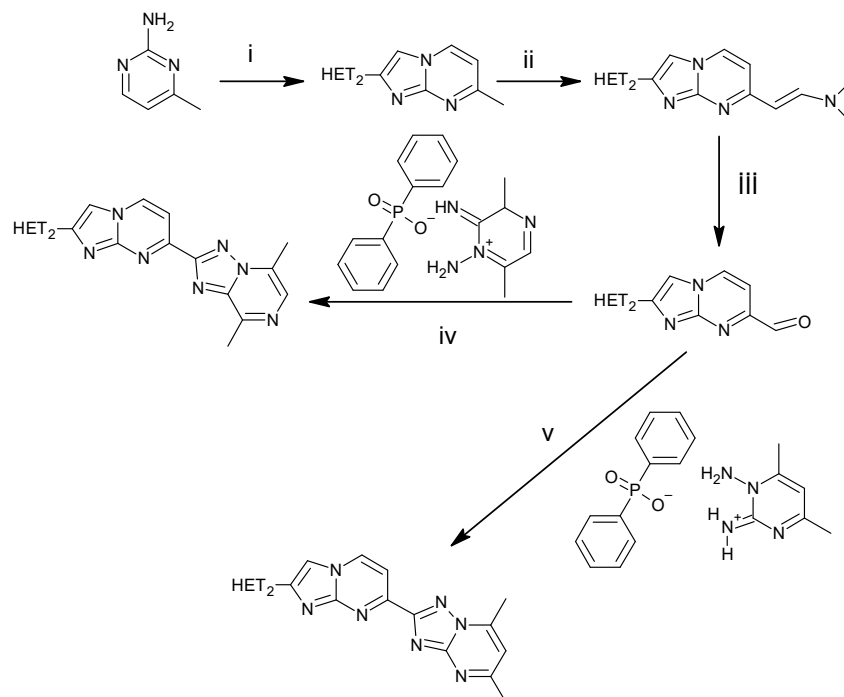
Figure 16: Synthesis of an imidazopyrimidine compound having a triazolopyrimidine substituent and another heterocycle at 2 position for PDE10A inhibition.

Antitumor Activity along with Antimicrobial and Antioxidant Effect of some Imidazopyrimidine Derivatives

Farag and coworkers investigated the potential utility of imidazo[1,2-*a*]pyrimidine derivatives. Many compounds synthesized in this study showed a very good *in vitro* antitumor activity against MCF-7 cell line. Their antimicrobial and antioxidant activities were also found to be high. Some computational studies like DFT and SAR were also reported (15) (See Figures 17).
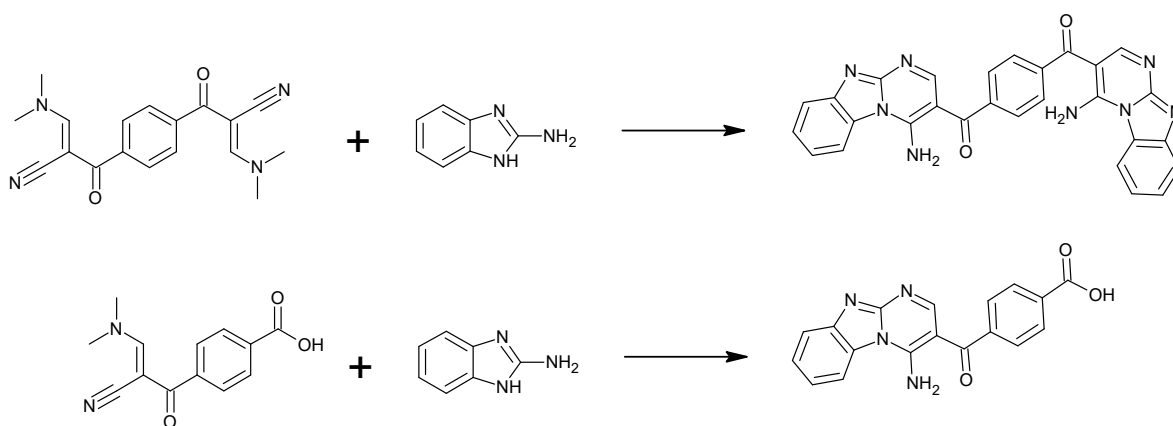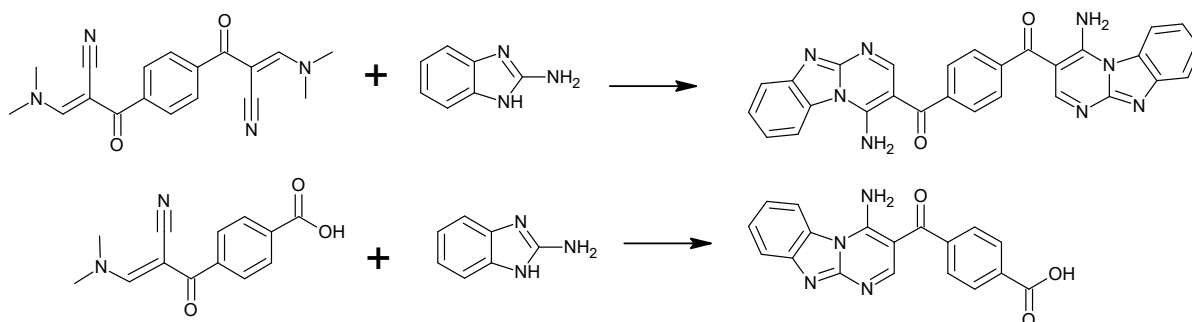
Figure 17: Synthesis of benzimidazopyrimidines from nitriles and aminobenzimidazoles.

Homopiperazine-Containing Imidazopyrimidine Derivatives

Homopiperazine-containing new imidazo[1,2-*a*]pyrimidine derivatives (3 in total) were prepared and screened by Mantipally and coworkers, in terms of *in vitro* cytotoxicity against HeLa and A549 by MTT technique (16) (See Figure 18).
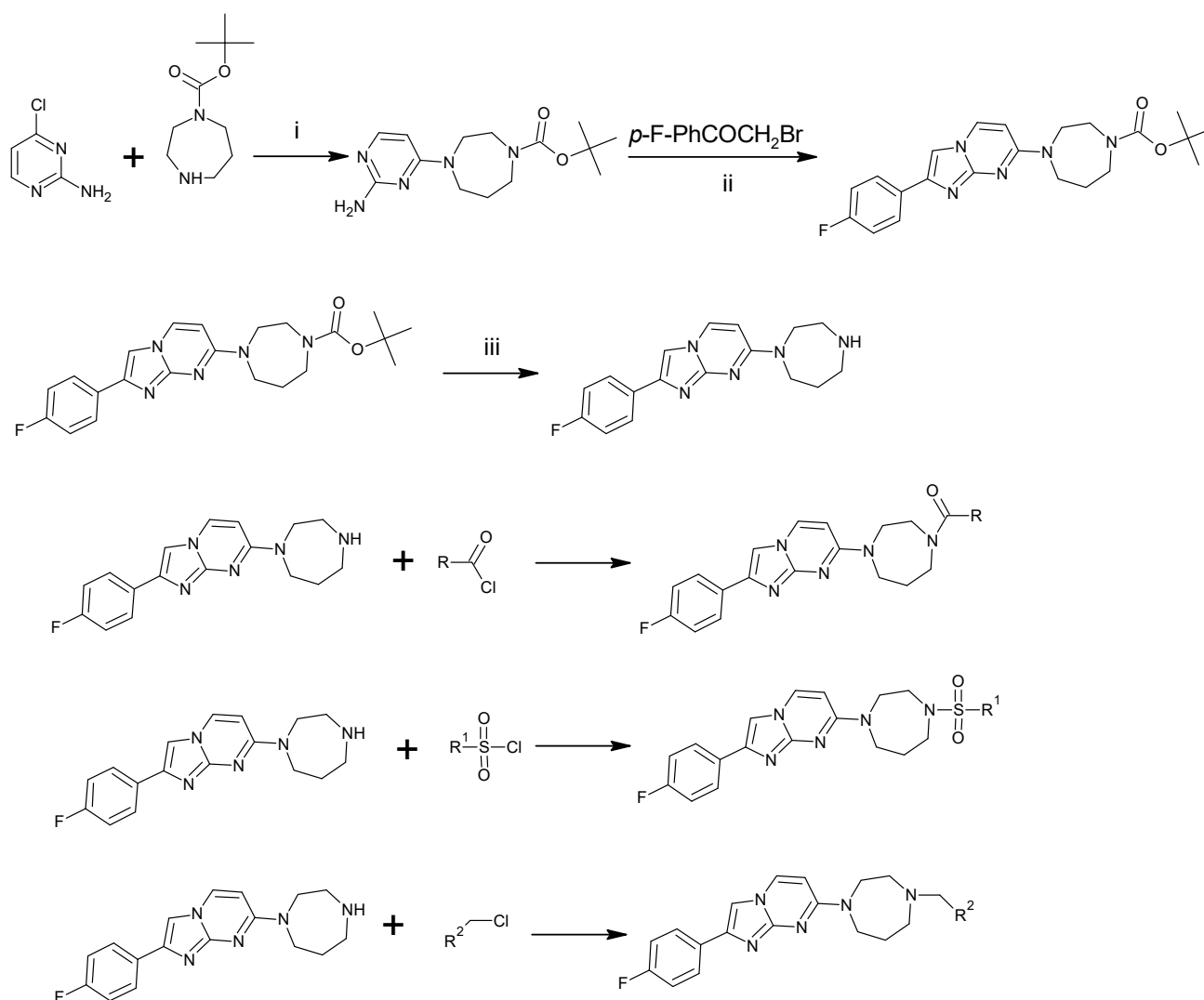
Figure 18: Preparation of imidazopyrimidine from aminoimidazole and substitution of the chloro group with homopiperazine and further functionalization of the homopiperazine side group.

Dihydropyrimidine as Monastrol Analogs
Tawfik and co-workers prepared twenty-one 3,4-dihydropyrimidine compounds, as monastrol analogs, having 1,3-benzodioxole moieties at position 4 and also having different substituents at positions 2, 3 and 5. These compounds were screened towards 60 cancer cell lines under NCI

(USA) protocol. The researchers also reported the assay of levels of active caspase-3 and caspase-9. They also studied molecular docking of some compounds to illustrate the interaction between inhibitors and the kinesin spindle protein allosteric binding site (17) (See Figure 19).
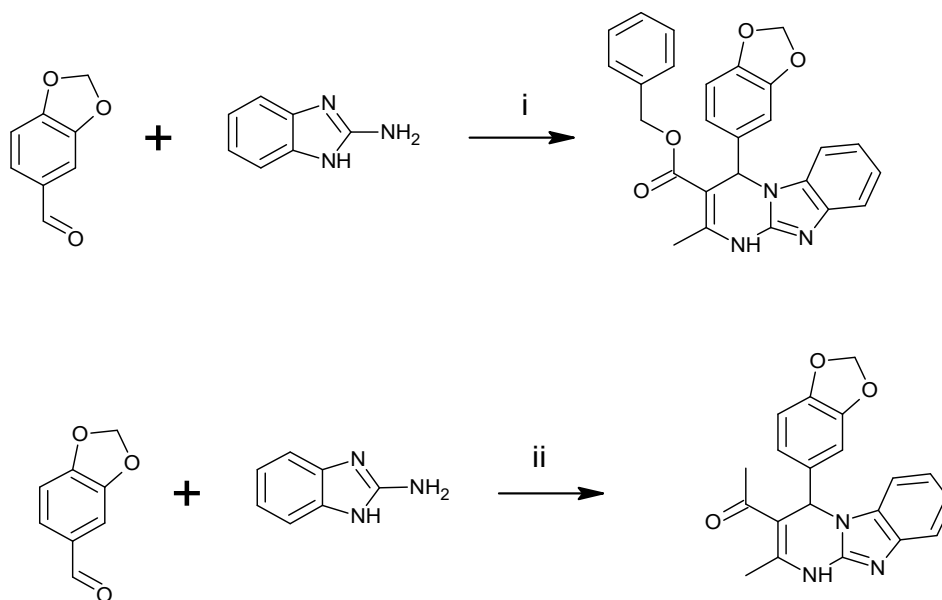
Figure 19: Synthesis of imidazopyrimidine derivatives as monastrol analogs.

Synthesis and Antimicrobial Activity of Quinoline-Containing Imidazopyrimidines
Quaternary salts from a quinoline compound were prapared by Elenich and coworkers, then imidazo[1,2-*a*]pyrimidine derivatives, along with

other heterocycles, were produced with the use of dinucleophilic reagents. A great deal of the synthesized compounds showed antimicrobial activity (18) (See Figure 20).
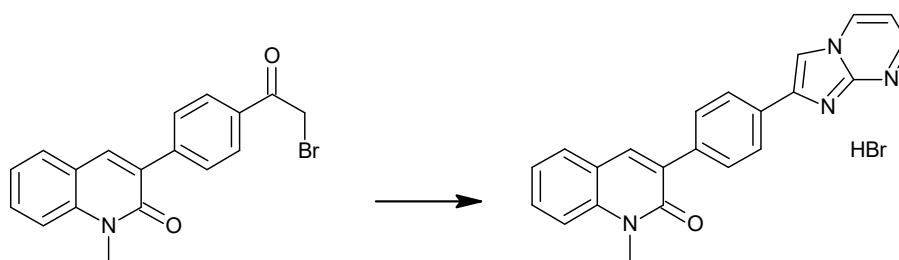
Figure 20: Imidazopyrimidine compounds for antimicrobial activity.

Fluoromethylated Imidazopyrimidines
Jismy and coworkers synthesized fluoromethylated derivatives of imidazo[1,2-*a*]pyrimidines and benzimidazo[1,2-*a*]pyrimidines with a Michael addition/intramolecular cyclization. In this reaction, 2-aminoimidazole derivatives were reacted with 4,4,4-trifluorobut-2-ynoate under C-O bond

activation. The formed compounds are examples of C-C, C-N, and C-S bond-forming synthons. Some derivatives possessed micromolar IC50 values against monoamine oxidase B and butyrylcholinesterase and as known well, these two enzymes are important targets considered by neurodegenerative disorders (19) (See Figure 21).
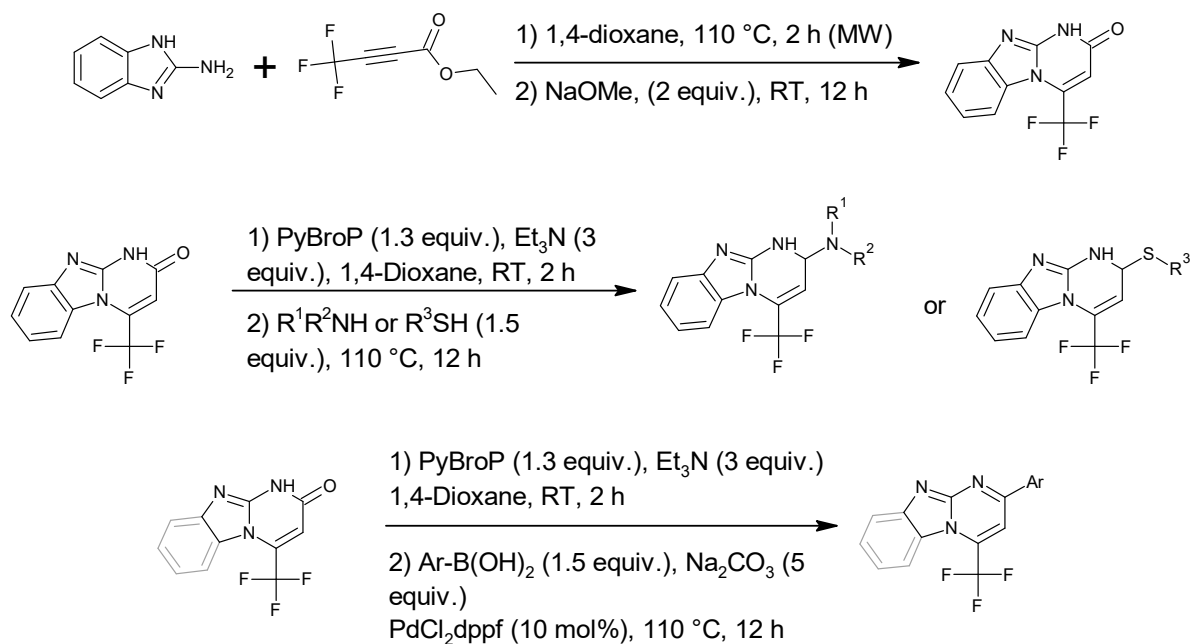
Figure 21: Fluoromethylated derivatives of imidazopyrimidines.

Stabilizing Effect for KRAS 24

Pancreatic, pulmonary, and colorectal cancers involve an oncogene named KRAS, so it constitutes an important target for the treatment of these cancers. A group of molecules were found by D'Aria and coworkers to perform a stabilizing effect on the NMR structure of 22-mer KRAS 24. Finally, compound 19 was found to be the best candidate and it may be considered that this compound is possibly a prototype of a new class of drugs which could be used for the treatment of tumors which express mutations of KRAS and which resist current therapies (20) (See Figure 22).
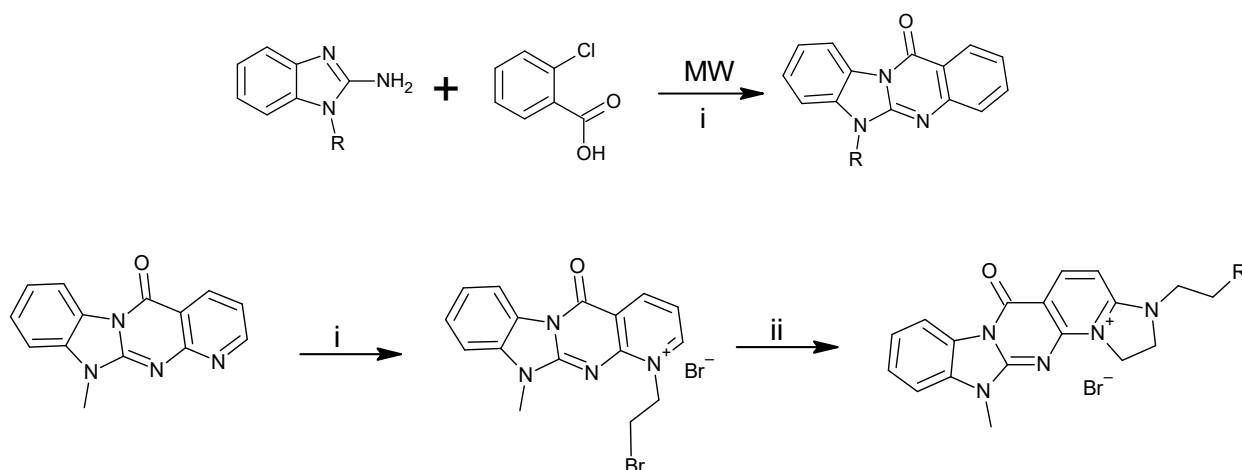
Figure 22: Quaternarization and ring formation from a benzimidazopyrimidine.

Ten Year Review of Therapeutic Potentials of Pyrimidines

Zhuang and coworkers described the 10-year review of therapeutic potentials of pyrimidine-based compounds and their antimicrobial activities (21) (See Figure 23).
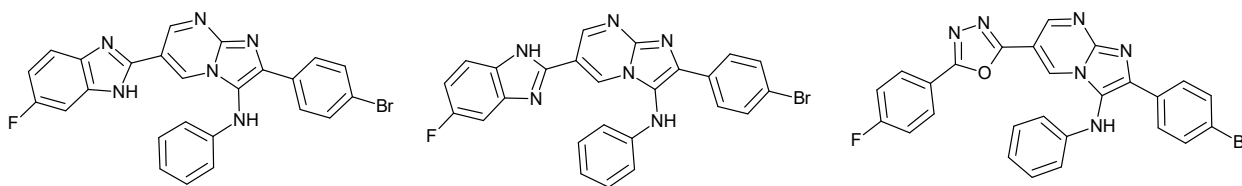
Figure 23: Antimicrobial imidazopyrimidines reviewed by Zhuang and coworkers.   .

HIV-1 Integrase Inhibitors

As known well, anti-human immunodeficiency virus 1 (anti-HIV-1) drugs make it a target for HIV-1 integrase (IN) enzyme. The researchers with Zadeh as the first author modified the structure of N-arylindole β-diketoacids (favorite inhibitors of IN) with 4-oxo-4,10-dihydrobenzo[4,5]imidazo[1,2-a]pyrimidine-3-carboxylic acid derivatives for the development of new anti-HIV-1 drugs (22) (See Figure 24).
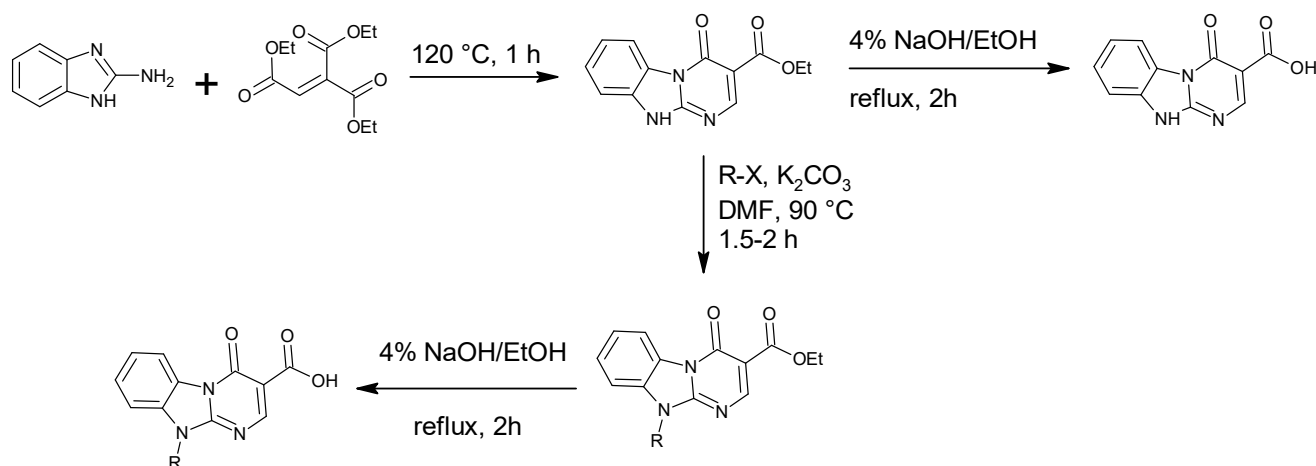
Figure 24: Synthesis of benzimidazopyrimidine compounds for HIV-1 integrase inhibitors.

Attempts to Use Imidazo[1,2-a]pyrimidines in Photodynamic Therapy

Some imidazo[1,2-a]pyrimidines were found by Lima and coworkers to generate singlet oxygen and thus, they could serve as intracellular photosensitizers. Photodynamic therapy of these compounds indicated that they absorbed and emitted within 400-500 nm, they showed low cytotoxicity when not in use (in the dark), they are taken inside cells efficiently, they fluoresce inside cells, they generate singlet oxygen with irradiation of the system, and cancer cells are killed in two hours and at a low concentration (23) (See Figure 25).

PURELY SYNTHETIC WORKS

Vilsmeier Formylation of Imidazo[1,2-a]pyrimidines

Vilsmeier reaction is largely employed to add formyl groups to a molecule. In this reaction, phosphorus oxytrichloride and N,N-dimethylformamide are used. A Latvian group with Saldabol was the first author has used this methodology to add formyl (-CH=O) groups to imidazo[1,2-a]pyrimidine at the 3

position. When the formylating reagent is taken as double, the side furyl group was also formylated (24) (See Figure 26).

Synthesis of 2-carbamoyl-3-arylimidazo[1,2-a]pyrimidines

Majcen-Le Marechal and coworkers have reported a series of 3-aryl-substituted imidazo[1,2-a]pyrimidine-2-carboxamide structures (25) (See Figure 27).

Synthesis of Dihydroimidazopyrimidine

Kochergin and coworkers used 2,3-dihydroimidazo[1,2-a]pyrimidine in the synthesis where 2-aminopyrimidine was used by two different routes. The first route involved reacting 2-aminopyrimidine with ethylene halohydrin (bromo or chloro) and further reacting with thionyl chloride, while the other method involved 1,2-dibromoethane reacting with 2-aminopyrimidine and when the intermediary product was treated with sodium hydroxide and then with hydrobromic acid, dihydroimidazopyrimidine was obtained (26) (See Figure 28).
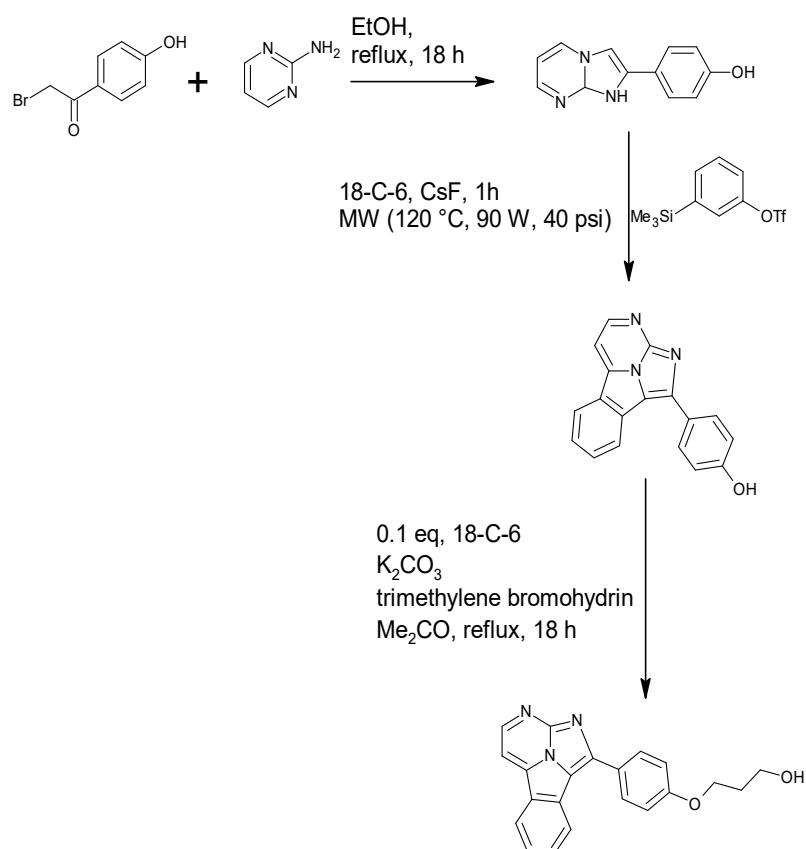
Figure 25: Synthesis of a tricyclic hetero compound for photodynamic therapy applications.
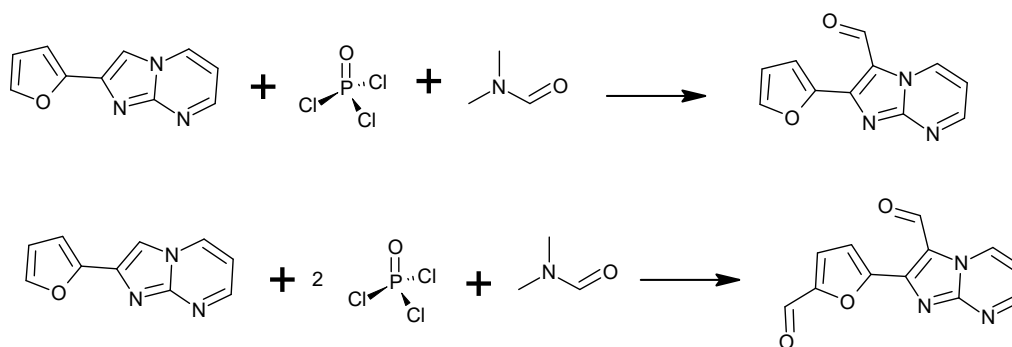
Figure 26: Formylation of 2-furyl-containing imidazopyrimidines.
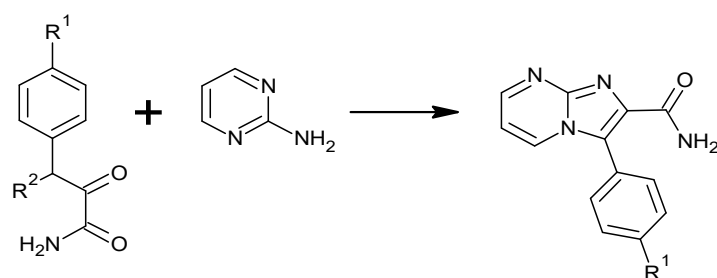
Figure 27: A series of 3-aryl-substituted imidazopyrimidine-2-carboxamides.
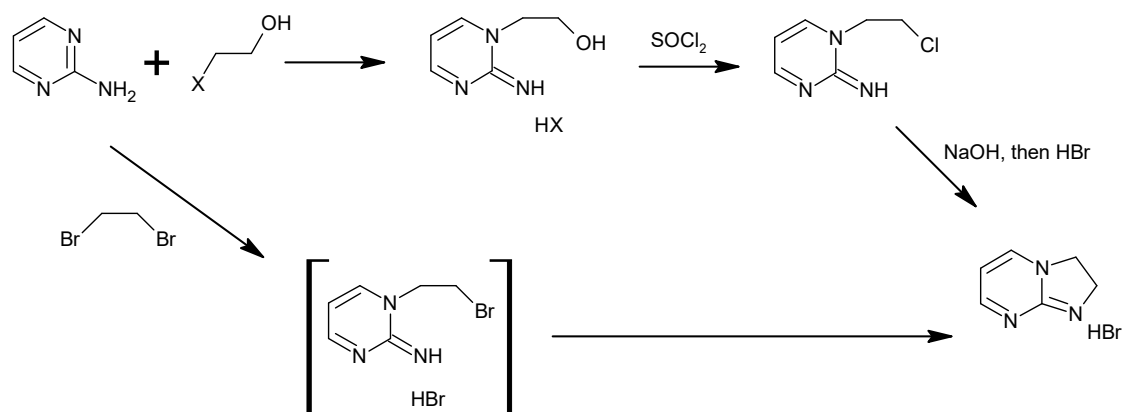
Figure 28: Synthesis of 2,3-dihydroimidazo[1,2-a]pyrimidine with two different routes.

Fusion to the imidazopyrimidine core
A double annelation reaction by Chowdhury and colleagues yielded a variety of tri- and tetracyclic heterocycles in a one-pot reaction (27) (See Figure 29).

Antipyrine-containing imidazopyrimidine heterocycle
Abu-Elmaati described the syntheses of many heterocycles, in which he reported an imidazo[1,2-a]pyrimidine that contains an antipyrine substituent (28) (See Figure 30).

One-pot synthesis of imidazo[1,2-a]pyrimidines
Late professor Alan Roy Katritzky is a legend in heterocyclic chemistry, and he has reported the one-pot synthesis of imidazo[1,2-a]pyrimidines. He and his colleagues used 2-aminopyrimidine and 1,2-bis(morpholinyl)-1,2-dibromoethane, with which two intermediates, namely A and B occurred with the sequential removal of benzotriazolyl (denoted as Bt here) moieties, then a rearrangement in the ring gives two imidazopyrimidine derivatives (29) (See Figure 31).
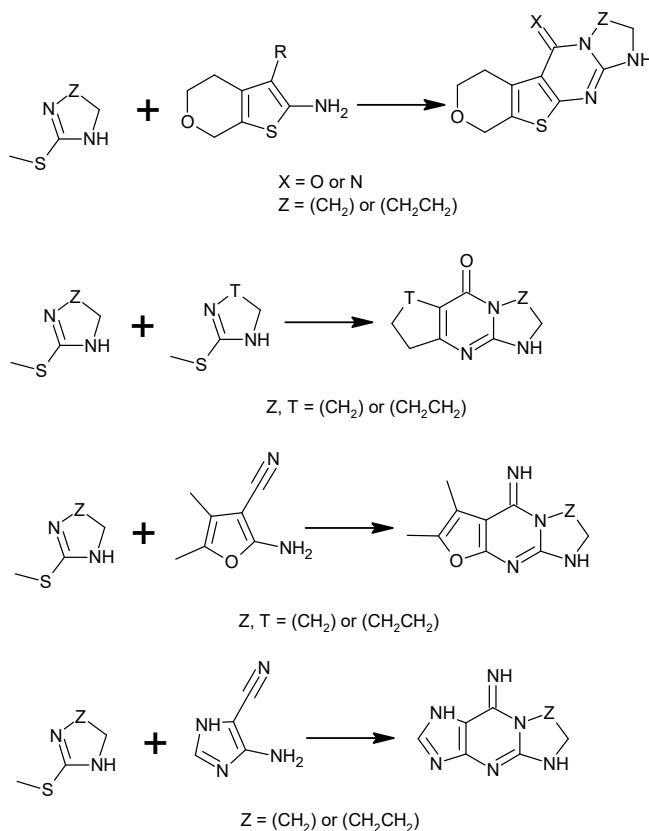
Figure 29: Tricyclic and tetracyclic imidazopyrimidine derivatives in one-pot reactions.
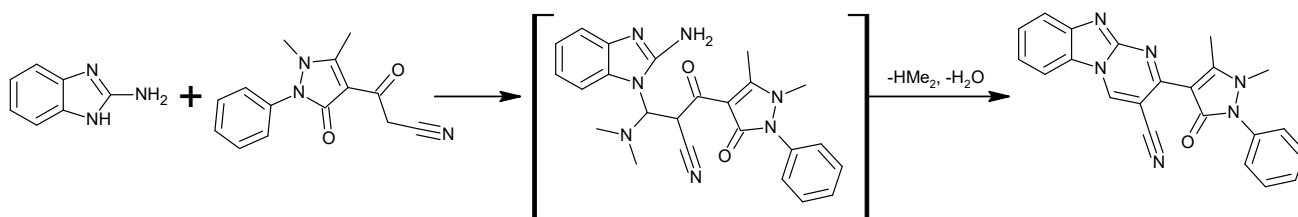
Figure 30: Synthesis of pyrazole-containing imidazopyrimidines.
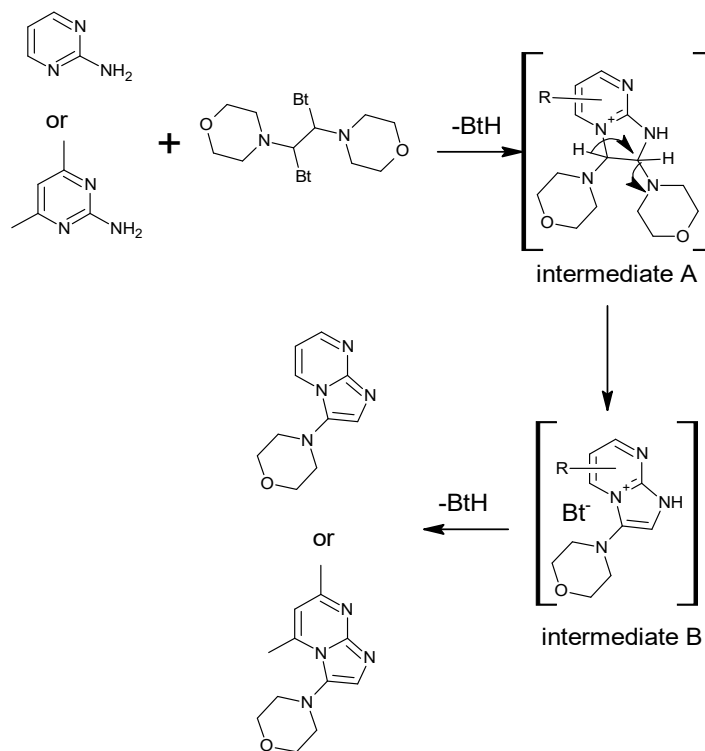
Figure 31: Syntheses of two imidazopyrimidines with the use of dibromo-dimorpholinylethane. Two compounds were reported.
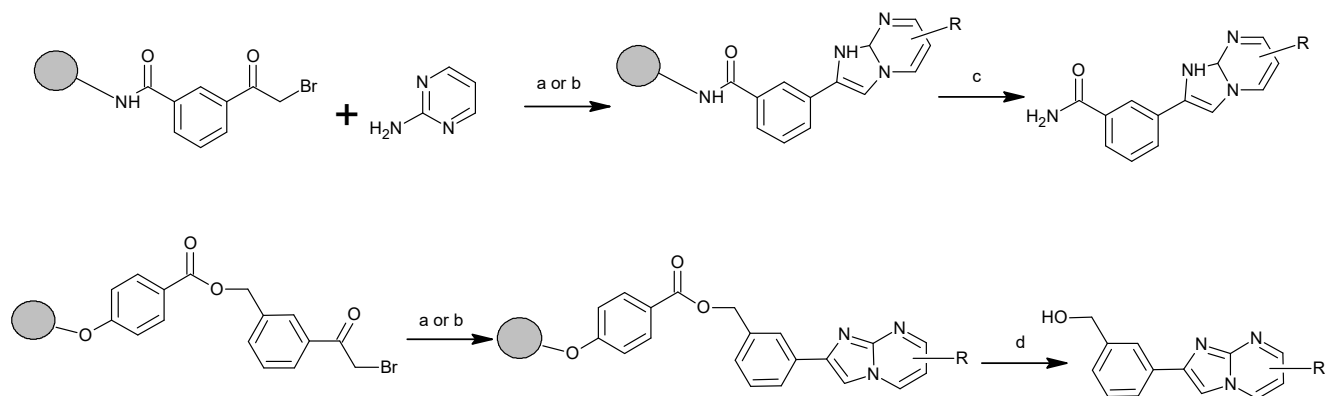
Figure 32: Synthesis of imidazopyrimidines on solid support.

Heterocycle formation on a solid support

El Kazzouli and his coworkers reported the formation of imidazo[1,2-*a*]pyrimidine by employing a solid-phase support (30) (See Figure 32).

Formylation on Monosaccharides
Bari et al. reported another formylation reaction applied on monosaccharides and the heterocycle was obtained with 2-aminobenzimidazole (31) (See Figure 33).
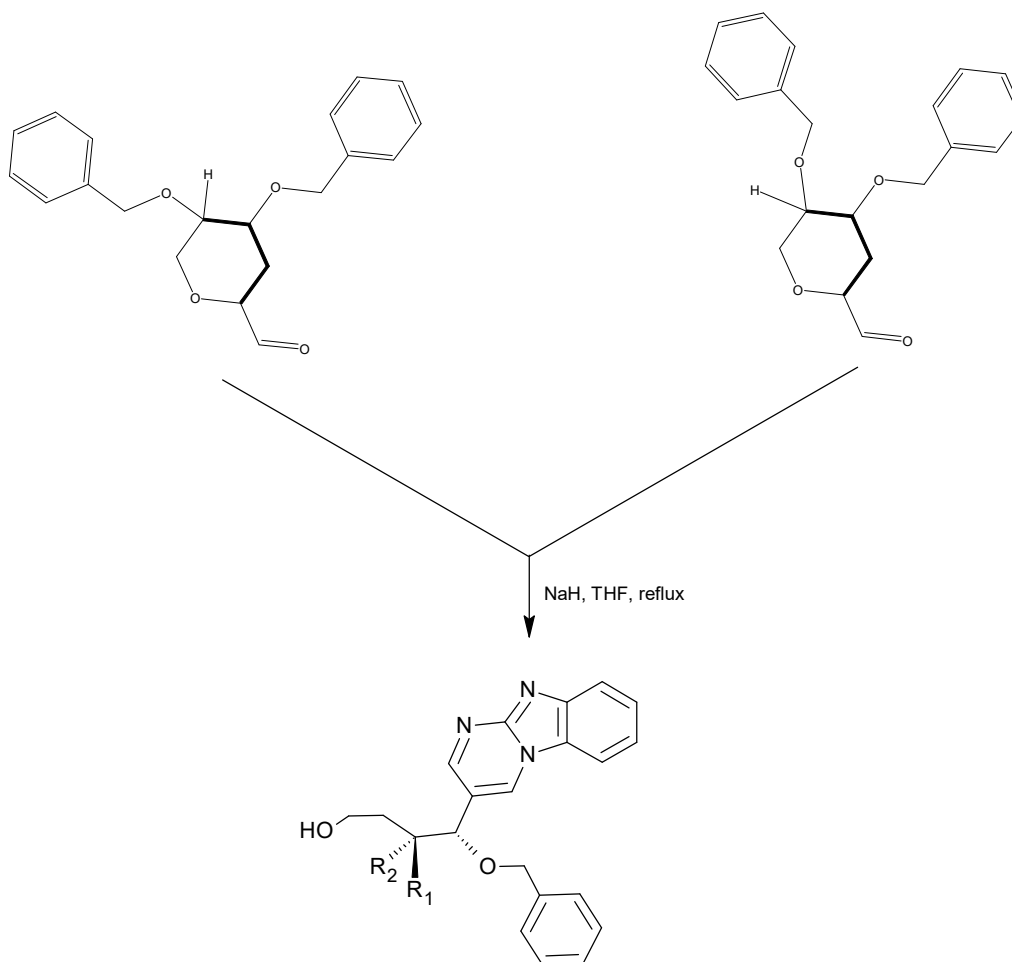
Figure 33: Imidazopyrimidine obtained with monosaccharides.

Imidazo[1,2-a]pyrimidin-5-ones
According to the publication by Sączewski et al., imidazolin-2-oxime ethers react with alkenes and imidazo[1,2-*a*]pyrimidin-5-ones. In addition, a retro-ene reaction takes place when ethyl prop-2-ynoate and 2,3-dihydroimidazo[1,2-a]pyrimidin-5(1H)-one is obtained (32) (See Figure 34).

Fluorescent Probes for the Localization and Function of Peripheral Benzodiazepine Receptor (PBR)
PBRr is mainly found in the mitochondria, and its overexpression is encountered, for example, in glioma, breast cancer, Alzheimer's disease, and activated microglia. Among the handful of compounds synthesized by Laquintana and

coworkers, an imidazopyridine-7-nitrofurazan conjugate showed the best result and could be considered as a new useful fluorescent probe for the visualization of activated microglia and PBR (33) (See Figure 35).

Reaction of an Imidazole and a Pyran to Give Imidazopyrimidine Derivatives
A new method was proposed by El Otmani and their co-workers used 4-hydroxy-6-methylpyran-2-one and 2-amino-4,5-dicyanoimidazole with an alcohol (methanol, ethanol, *n*-propanol, and *n*-butanol) to obtain dicyanoimidazopyrimidine acetic acid derivatives and their corresponding esters of the alcohol used (34) (See Figure 36).
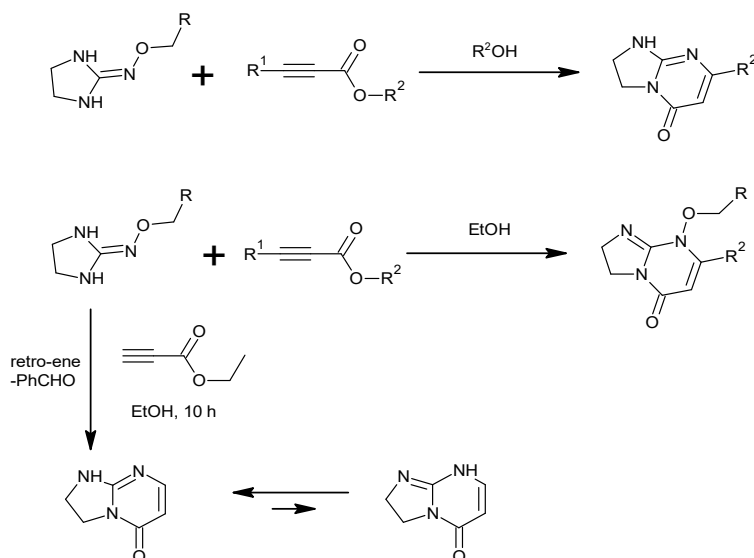
Figure 34: Use of imidazolin-2-oxime ethers in the construction of partly hydrogenated imidazopyrimidines.

Formation of Imidazopyrimidines via a Nucleophilic Attack on Styrenes

A new stereoselective nucleophilic attack on styrenes was described by Muzalevskiy and colleagues. First, the styrene is reacted with sodium methoxide and potassium tert-butoxide, then brominated to yield the trifluoromethyl ketones. These compounds were found to be good starting materials having a trifluoromethyl moiety. Imidazopyrimidine compounds were reported to be obtained in medium yields (35)(See Figure 37).

Hydrazinolysis of Imidazopyrimidines

Ermolat'ev and co-workers reported the microwave-assisted hydrazinolysis of imidazopyrimidines to yield mono- and di-substituted imidazoles. This protocol is advantageous due to the absence of the use of strong acids and is better than the classical reaction in which α-haloketones react with N-acetylguanidine (36)(See Figure 38).

Synthesis of Benzylimidazopyrimidines

Bakherad devised an efficient synthesis of 2-benzylimidazo[1,2-a]pyrimidines in water, incorporating Sonogashira coupling with various aryl iodides, and without copper co-catalyst, in the presence of K_2CO_3 as the base. (37) (See Figure 39).
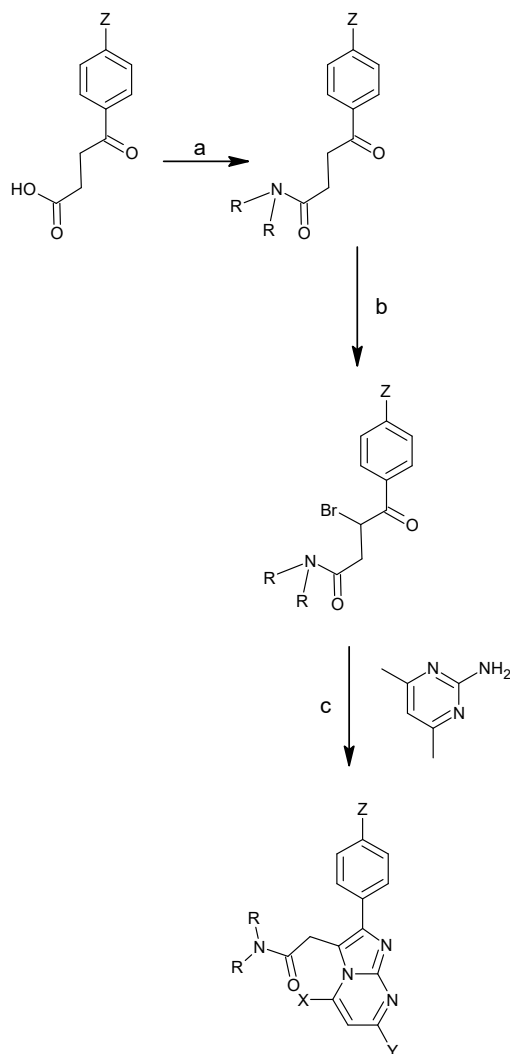
Figure 35: Synthesis of fluorescent probes for peripheral benzodiazepine receptor.
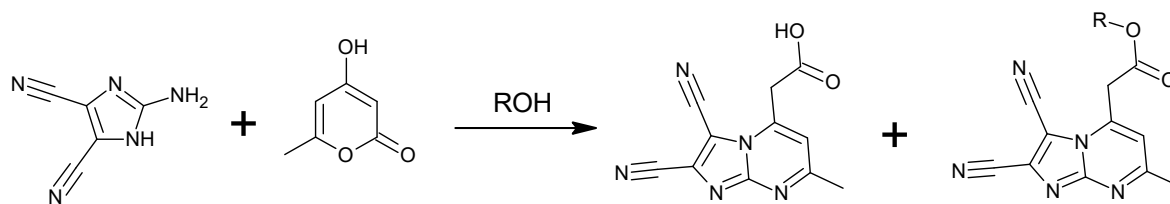
Figure 36: Formation of 7-methyl-2,3-dicyanoimidazo[1,2-a]pyrimidine-5-acetic acid and its ester.
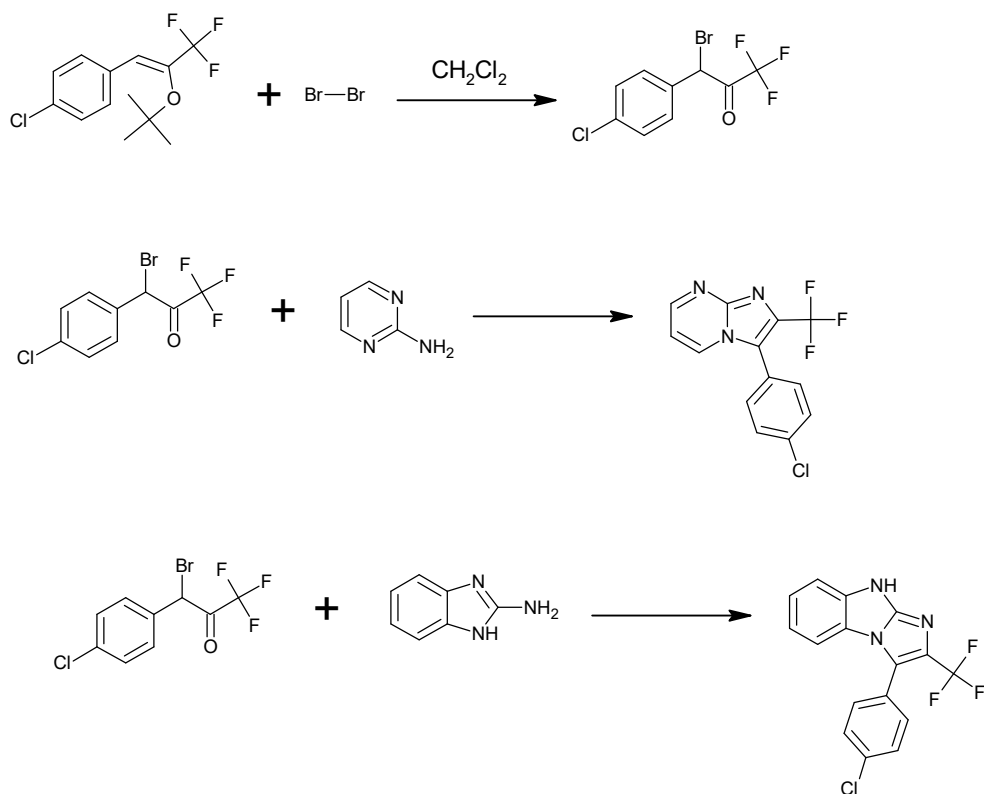
Figure 37: Use of styrene derivatives to yield imidazopyrimidines.
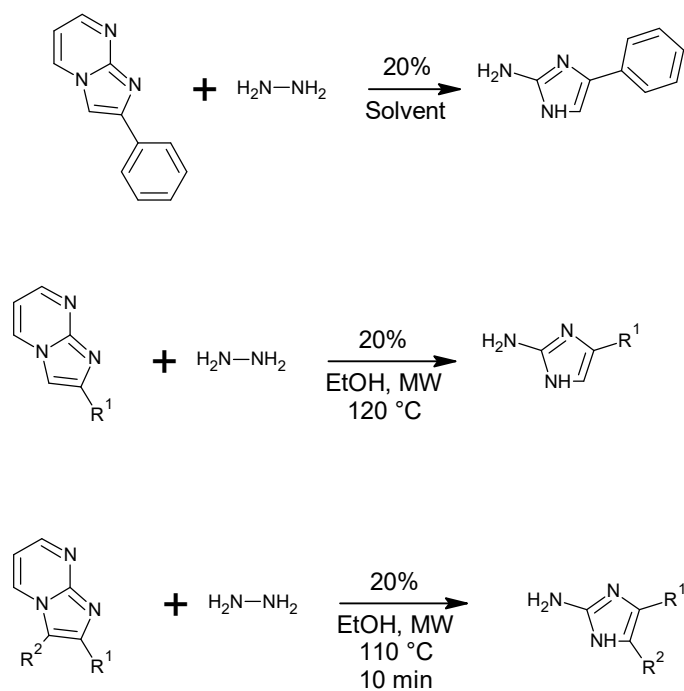
Figure 38: Hydrazinolysis of imidazopyrimidines.
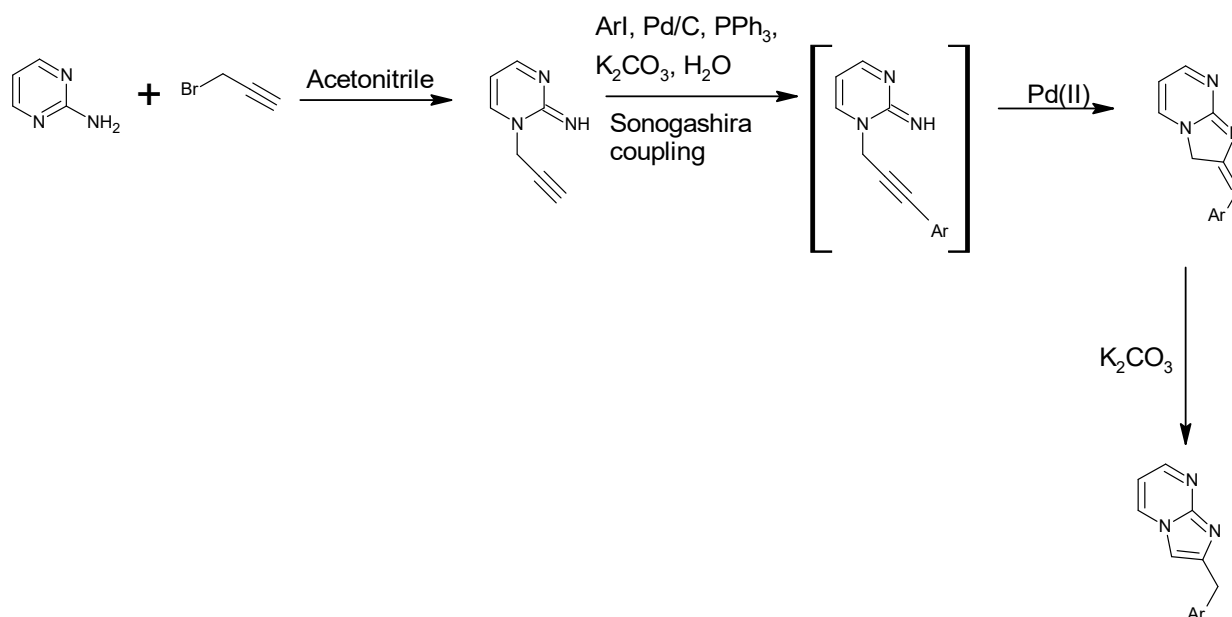
Figure 39: Sonogashira-powered cyclization of 2-aryl substituted imidazopyrimidines.

Catalytic Chalcogenation of Imidazopyrimidines

Li and coworkers reported a very potent and environmentally friendly catalytic chalcogenation of imidazopyrimidine compounds with dichalcogenides.

They used copper(I) iodide as catalyst and the reaction was conducted under air. Smooth reactions were observed and the yields were moderate to excellent and no other additive was required (38) (See Figure 40).
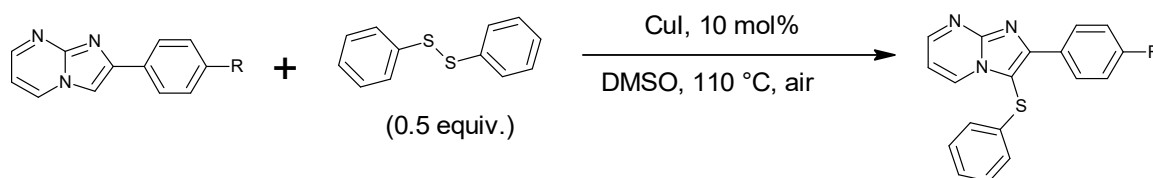
Figure 40: Chalcogenation at the 3-position by using diphenyldisulfide and copper iodide.

Synthesis of 4-Amino-1,2-dihydrobenzo[4,5]imidazo[1,2-*a*]pyrimidine-6-carbonitrile Derivatives

Hu and coworkers developed a fast and green method for the preparation of 4-amino-1,2-dihydrobenzo[4,5]imidazo[1,2-*a*]pyrimidine-6-carbonitrile derivatives. The reaction is

characterized by its one-pot condensation of 2-aminobenzimidazole, several aldehydes, and malononitrile and the catalyst employed was ammonium acetate in ethanol. The catalyst is very cheap and is readily available, and the workup is environmentally friendly (39) (See Figure 41).
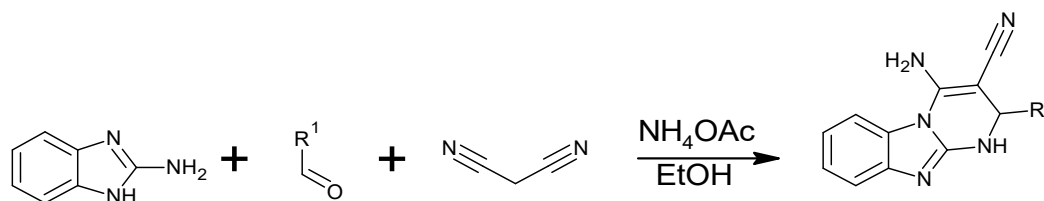
Figure 41: Three-component reaction of aminobenzimidazole, an aldehyde, and malononitrile in ammonium acetate medium. R^1 is phenyl, 4-methylphenyl, 4-methoxyphenyl, 4-chlorophenyl, 3-chlorophenyl, 2-chlorophenyl, 4-hydroxyphenyl, 4-cyanophenyl, and 4-pyridyl.

Synthesis of Some Imidazopyrimidines and Catalytic Hydrogenation of them

Some new derivatives of imidazo[1,2-*a*]pyrimidine have been studied by Borisov et al in 2013, and catalytic hydrogenation methods were developed for them. For the first time, partial reduction of the imidazole ring on imidazo[1,2-*a*]pyrimidine hydrogenation was reported (40) (See Figure 42).
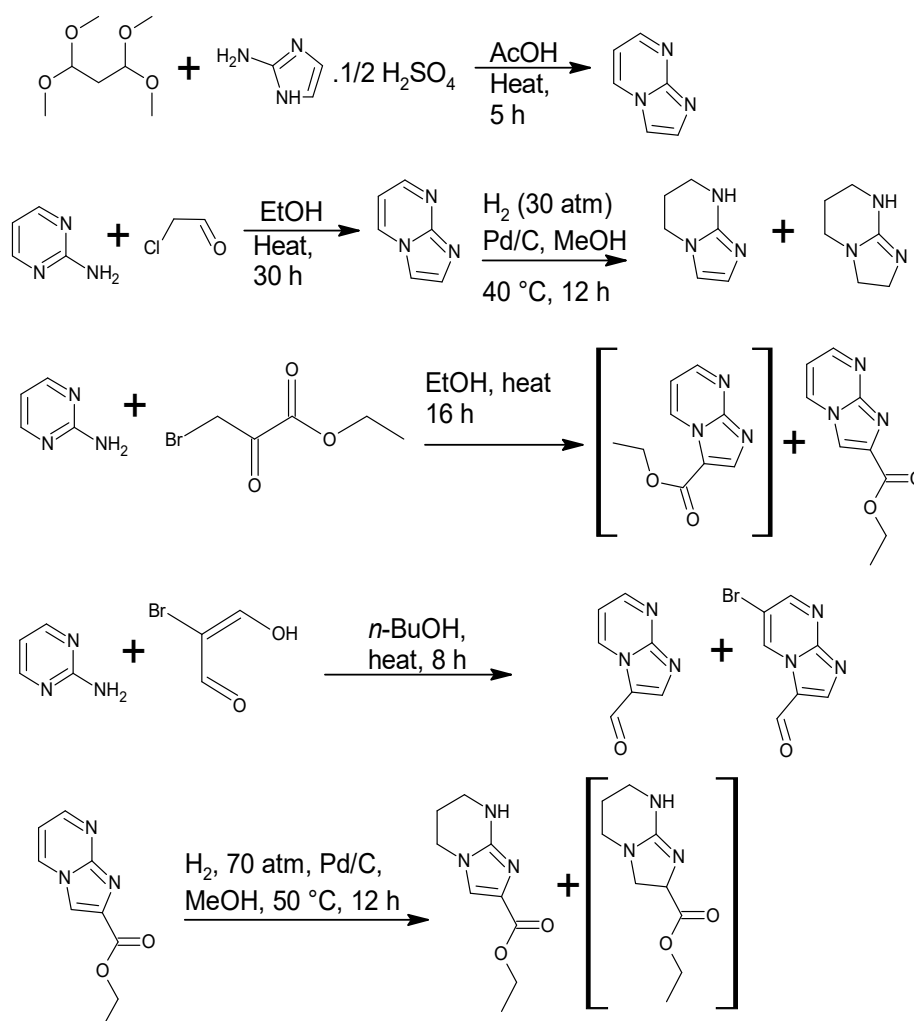
Figure 42: Formation of some imidazopyrimidine heterocycles and partial hydrogenation of some of them.

Synthesis of New Benzimidazole Derivatives

Novel benzimidazole derivatives were synthesized by Mehranpour and Zahiri with the reaction between 2-substituted 1,3-bis(dimethylamino)-trimethinium salts and 2-aminobenzimidazole in the presence of acetic acid or triethylamine in acetonitrile as solvent (41) (See Figure 43).
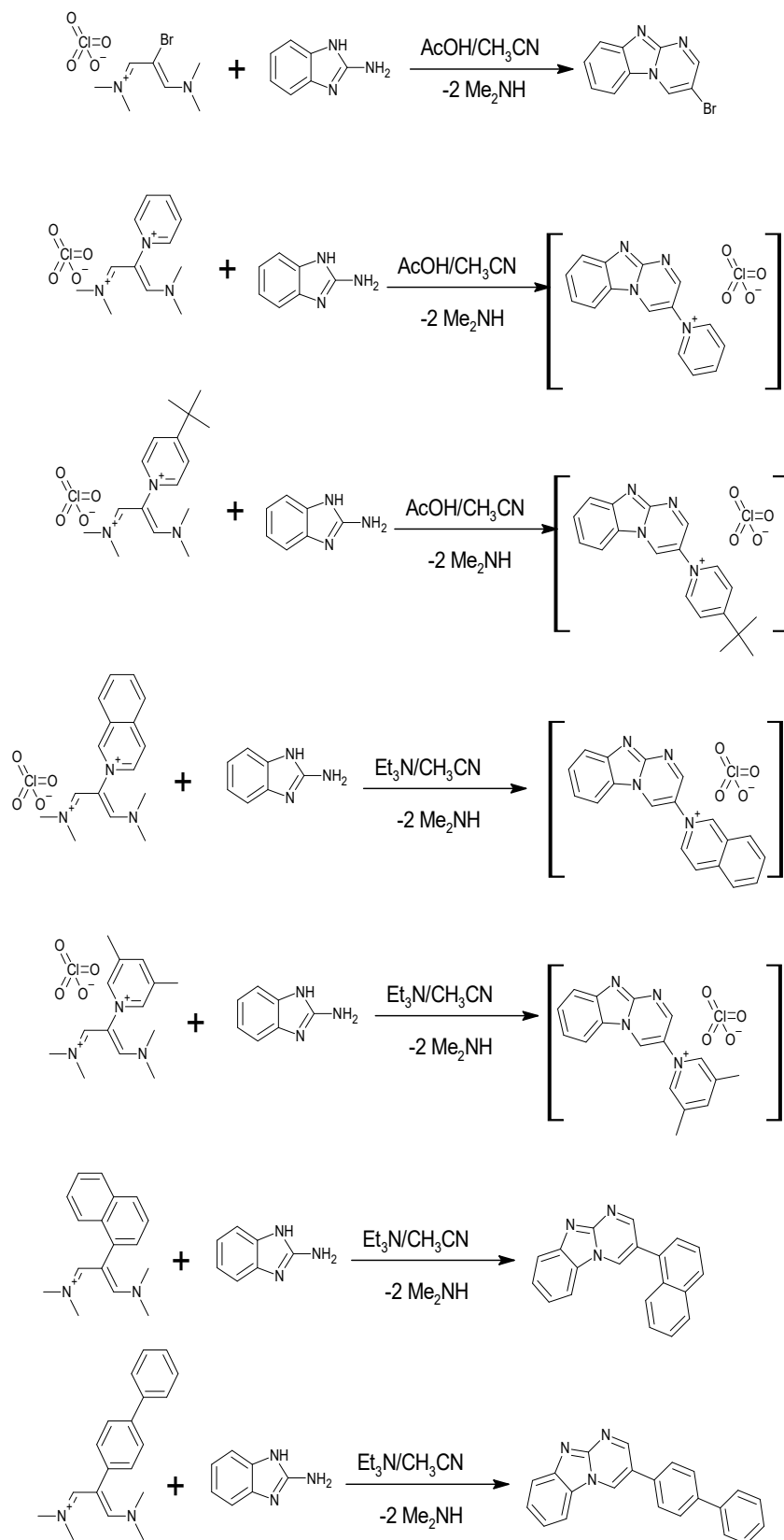
Figure 43: Formation of imidazopyrimidines via dimethylaminomethinium salts.

Thermal Cyclization of Thioxopyrimidines
Burbuliene et al. reported the reaction of methyl (2-methylsulfanyl-6-phenyl-4-thioxopyrimidin-3(4H)-yl)acetate with hydrazine hydrate, at room temperature, in 1-butanol as solvent to yield the hydrazide. They committed the same reaction at

reflux temperature by employing different solvents like methanol, acetonitrile, n-butanol or dimethylformamide and they found that 1-amino-7-phenyl-5-thioxo-1,5-dihydroimidazo[1,2-*a*]pyrimidin-2(3H)-one with a thermal cyclization pattern (42) (See Figure 44).
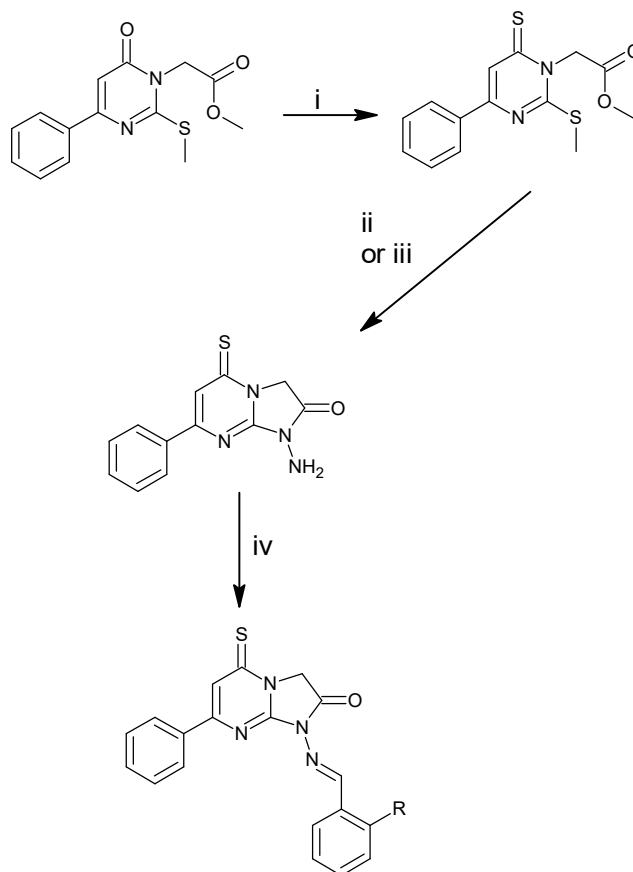
Figure 44: Synthesis of imidazopyrimidines with thermal cyclization of thioxopyrimidines.

Review about C-H Arylation
Aziz and Piguel, in their mini-review published in 2017, studied C-H arylations of heterocycles, in

which imidazo[1,2-*a*]pyrimidines played a major role. Some examples were provided (43). (See Figures 45-54).
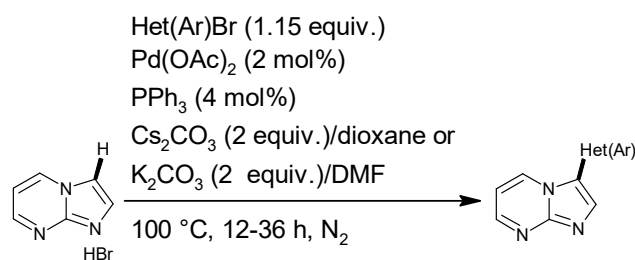
Figure 45: Arylation of imidazopyrimidine at 3-position.

ArBr (1.1 equiv.)
Pd(OH)$_2$/C (10 mol equiv.)
KOAc (2 equiv.)
DMA,
145 °C, 12-24 h
N$_2$
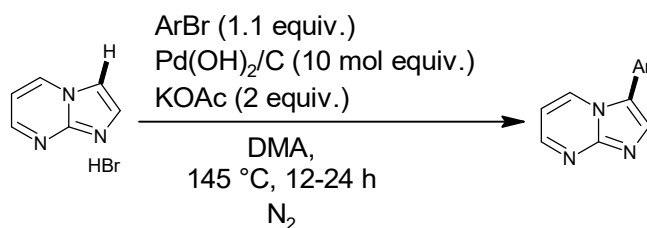
Figure 46: Arylation at 3-position.

4-methylphenyl bromide
(0.9 equiv.)
Pd(OAc)$_2$ (5 mol%)
PCy$_3$.HBF$_4$ (10 mol%)
PivOH (30 mol%)
K$_2$CO$_3$ (1.5 equiv.)
DMA (0.3 M),
100 °C, overnight
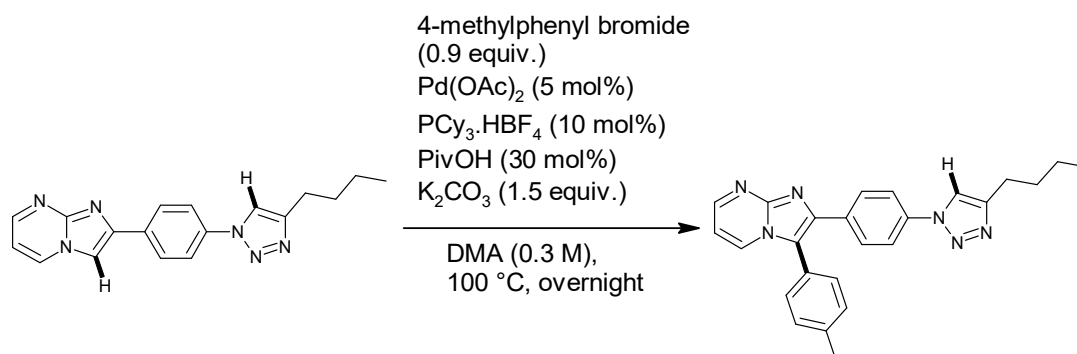
Figure 47: Arylation at 3-position while there is another group at 2-position.

1,2-dibromobenzene (1.5 equiv.)
Pd(OAc)$_2$ (10 mol%)
XPhos (20 mol%)
K$_2$CO$_3$ (3 equiv.)
DMF, 160 °C, 24 h
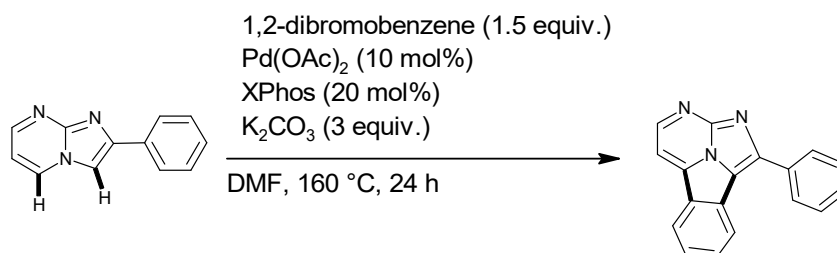
Figure 48: Heteroannulation at 3- and 5-positions.

3 steps

Br$_2$
first strategy,
problems

(1.1 equiv.)

Pd(OAc)$_2$ (2 mol%)
PPh$_3$ (4 mol%)
Cs$_2$CO$_3$ (1 equiv.)

first strategy,
problems

Pyridine-3-boronic
acid (1.05 equiv.)
Pddba$_2$ (5 mol%)
t-Bu$_3$P (5 mol%)
K$_2$HPO$_4$ (1.6 equiv.)

water, dioxane,
80 °C, 16 h
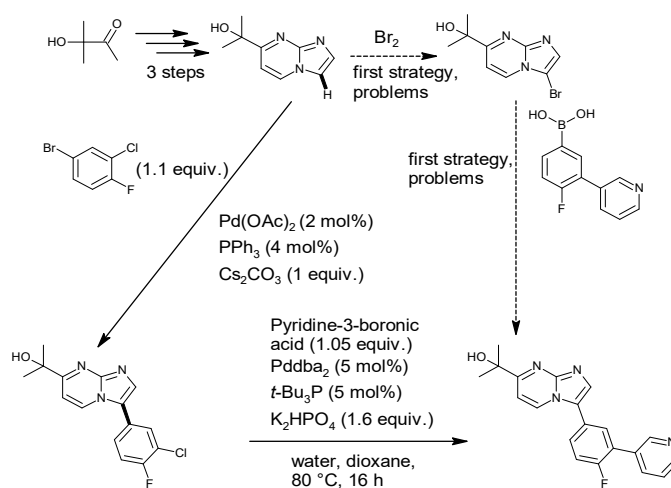
Figure 49: Development of a new strategy over the problematic,
previous one.
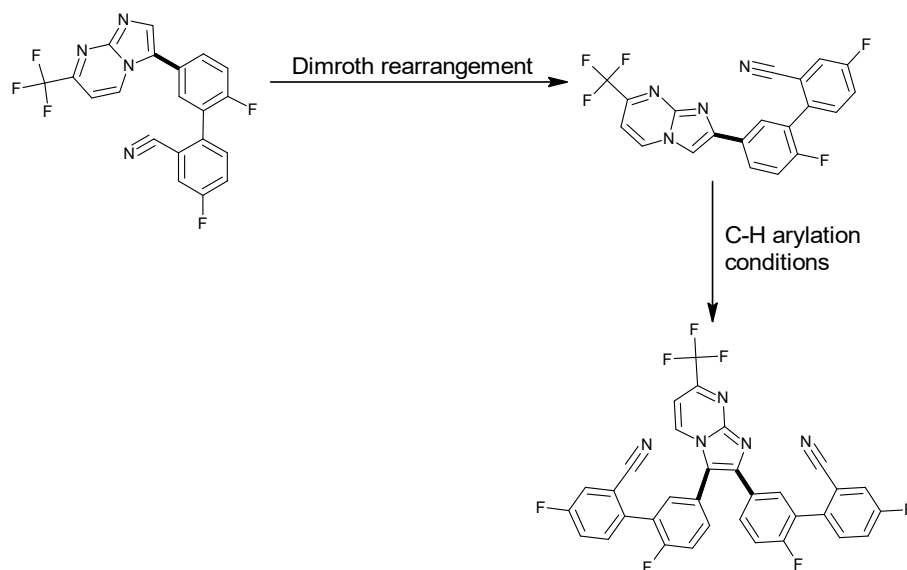
Figure 50: Dimroth rearrangement and subsequent C-H arylation of an imidazopyrimidine.
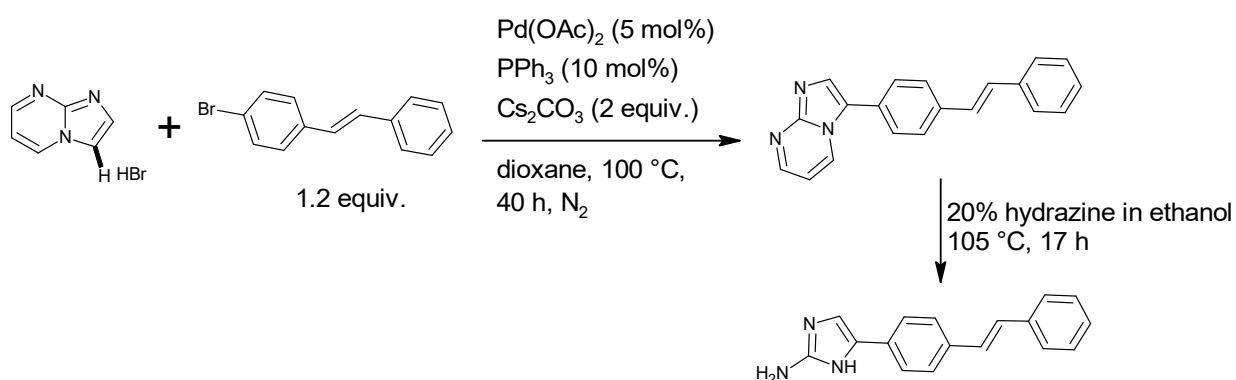
Figure 51: Arylation and subsequent hydrazinolysis of an imidazopyrimidine.
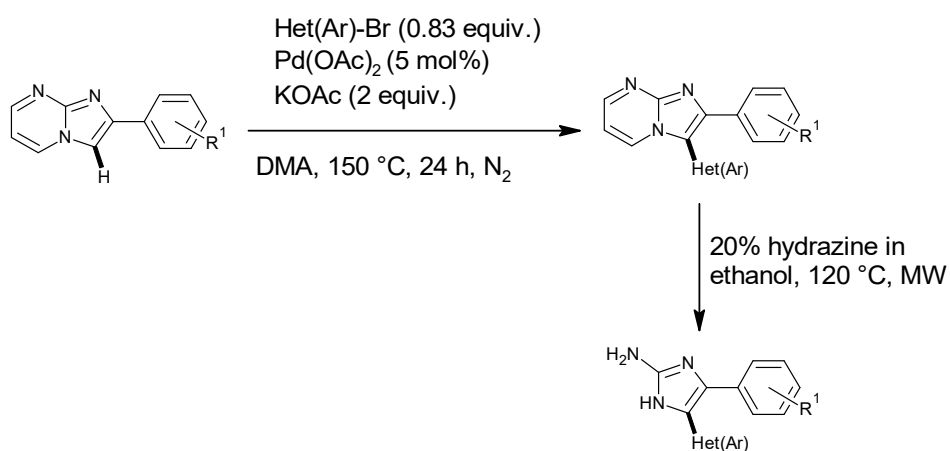
Figure 52: C-H (het)arylation and subsequent hydrazinolysis.
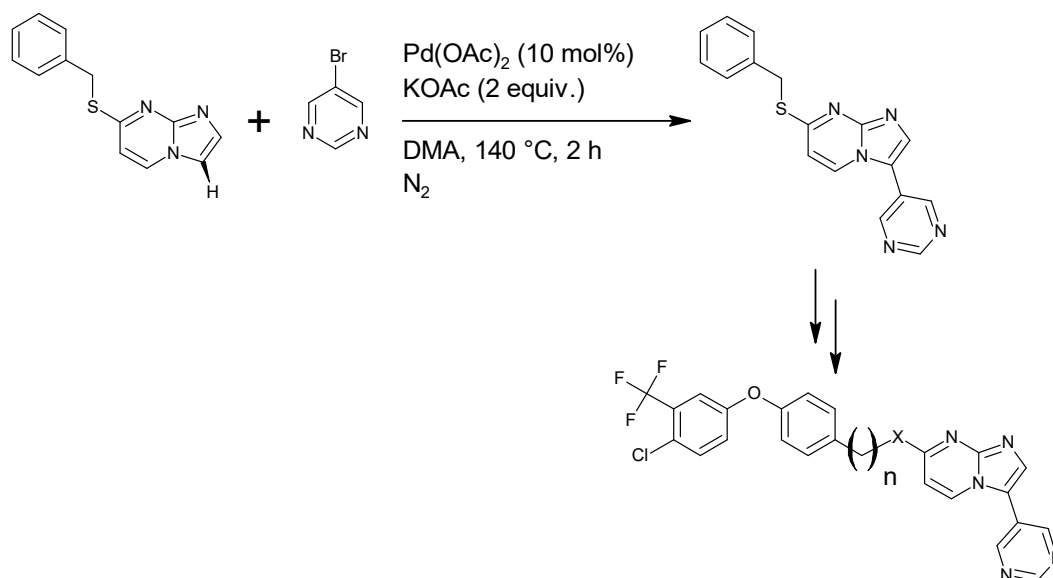
Figure 53: Arylation and functionalization of a pyrimidinyl imidazopyrimidine.
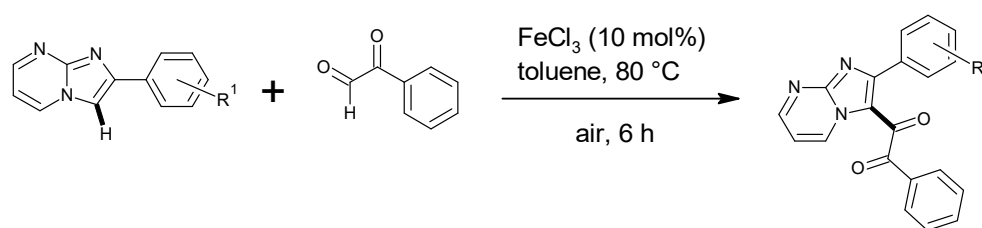
Figure 54: Addition of a carbonyl group at 3-position of imidazopyrimidine in the presence of iron(III) chloride and aerial oxygen.

Formation of Some Bridgehead Heterocycles
Reacting 2-aminopyrimidine and acetyl acetone, Bhagat and Telvekar reported the formation of

Imidazo[1,2-*a*]pyrimidines at around 70% reaction yield (44) (See Figure 55).
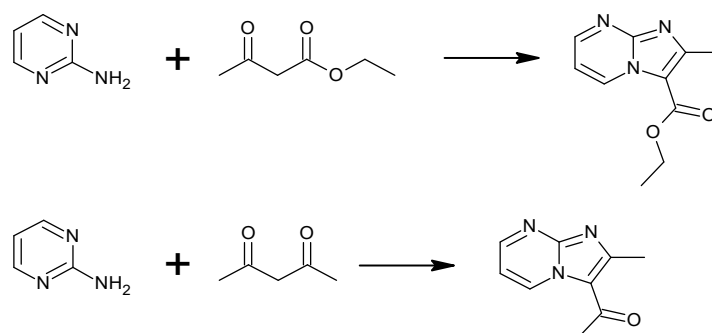
Figure 55: Acetyl acetone and ethyl acetoacetate were used to prepare imidazopyrimidines.

Use of Copper Oxide Nanoparticles in the Formation of Imidazopyrimidines
Rawat and Rawat studied the copper oxide nanoparticles-catalyzed reaction employed 2-aminobenzimidazole, several aldehydes, and several

terminal alkynes to give imidazo[1,2-*a*]pyrimidines. The reaction did not employ solvents, and 6-endo-dig cyclization occurs. Of the 20 compounds, 2,4-bis(4-methoxyphenyl)-substituted compound was found to sense zinc ion in a fluorescent manner.

WHO's maximum allowable zinc concentration in drinking water is much higher than the detection limit of this sensor (45) (See Figure 56).
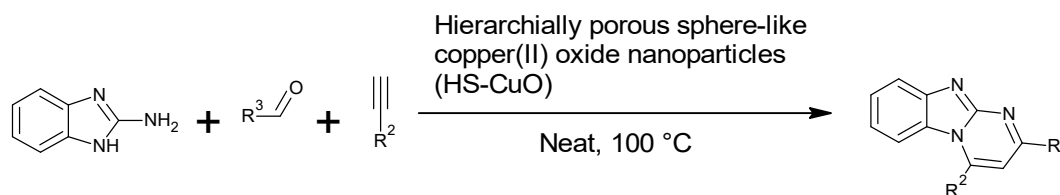
Figure 56: A three-component reaction catalyzed by HS-CuO to yield imidazopyrimidines.

C-H Bond Chalcogenation of Imidazopyrimidines

Bettanin and coworkers studied the C-H chalcogenation of N-heteroaryl compounds with ammonium iodide as the catalyst, in a minimal amount of dimethylsulfoxide, water, and acetic acid (2.5 M, 2.5 M, 1 M, respectively) and no metallic catalyst was used. This approach was also very efficient in the C-H bond chalcogenation of other 5-membered N-heteroaryl compounds (46) (See Figure 57).

Figure 57: C-H chalcogenation of imidazopyrimidines.

Chromen-2-one-Containing Imidazopyrimidine Derivatives

Yagodinets et al. Reported the reactions of 4-(4-bromoacetylphenyl)-3-hydroxy-2H-chromen-2-one with suitable heterocycles yielded quaternary salts, and the reactions of the same bromo derivative with pyrimidin-2-amine provided corresponding imidazo[1,2-*a*]pyrimidine derivatives (47) (See Figure 58).
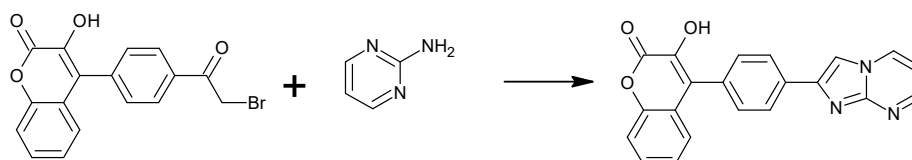
Figure 58: Formation of imidazopyrimidine from a chromen-containing compound.

IBX/NIS-Induced Intramolecular Oxidative Annulation without Metallic Catalyst

Imidazo-heterocycles were synthesized by Makra and coworkers, without a metallic catalyst, with an IBX/NIS-induced intramolecular oxidative annulation of Mannich substrates. The reaction includes iodination, NH-oxidation, formation of intramolecular C-N bonds, and retro-Claisen-Schmidt reaction with high reaction yields. A sequential one-pot reaction process has also been reported (48) (See Figure 59 and 60).
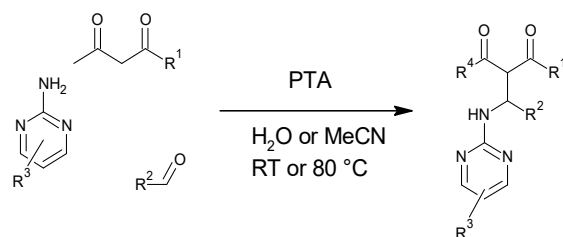
Figure 59: A three-component one-pot reaction involving the formation of an imidazopyrimidine.
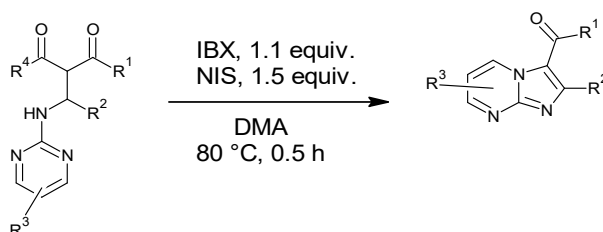
Figure 60: IBX- and NIS-mediated reaction yielding imidazopyrimidine derivatives.

A Review About Pyrimidine-Containing Five-Membered Heterocycles

Pyrimidine-containing five membered heterocyclic ring systems were reviewed for the last two decades by Maji in 2019 (49). (See Figures 61-65).
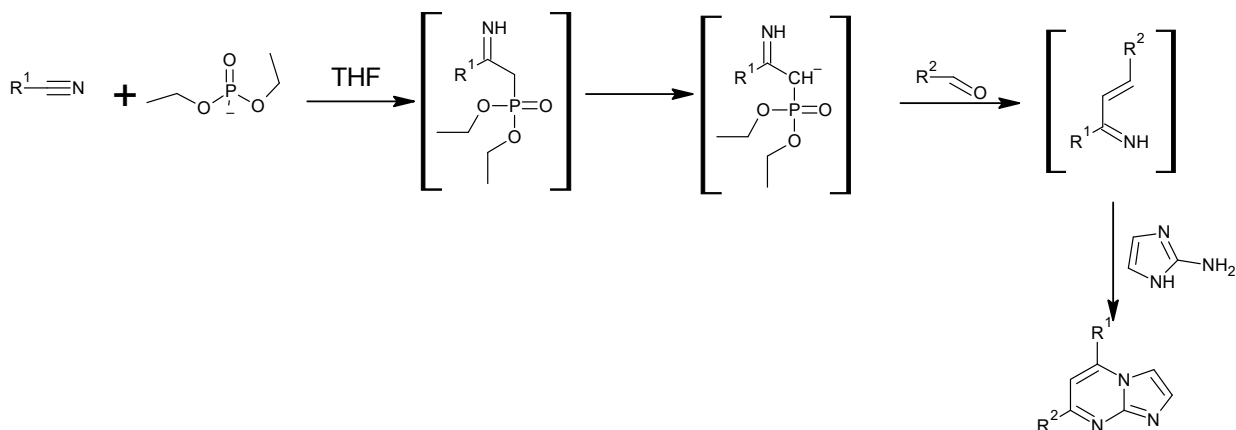
Figure 61: Formation of imidazopyrimidines via an iminoalkene.
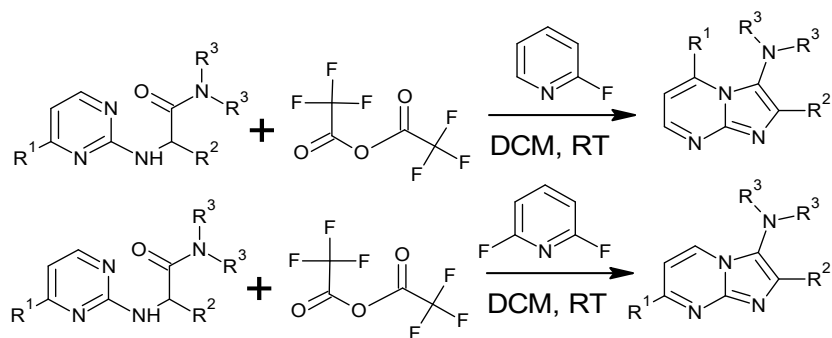
Figure 62: Using fluoro or difluoropyridine, the authors obtained imidazopyrimidines at room temperature.
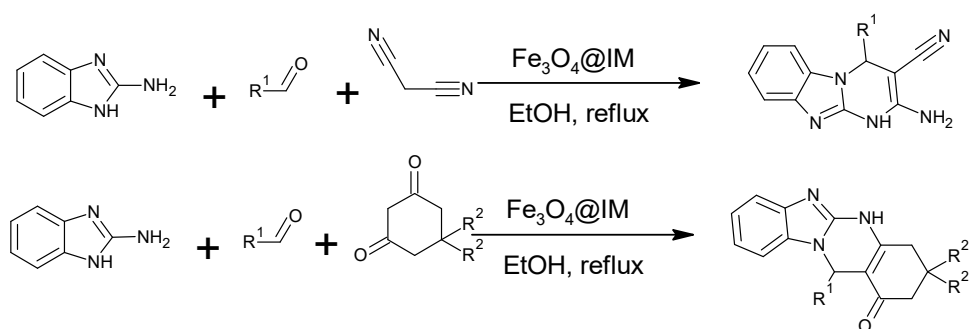
Figure 63: Three-component syntheses in which magnetite was used as a catalyst.
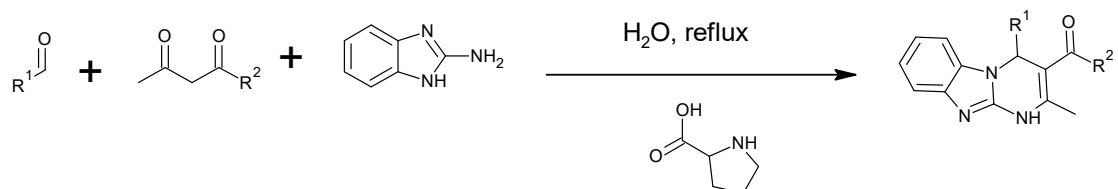
Figure 64: Three-component synthesis of a benzimidazopyrimidine ketone.
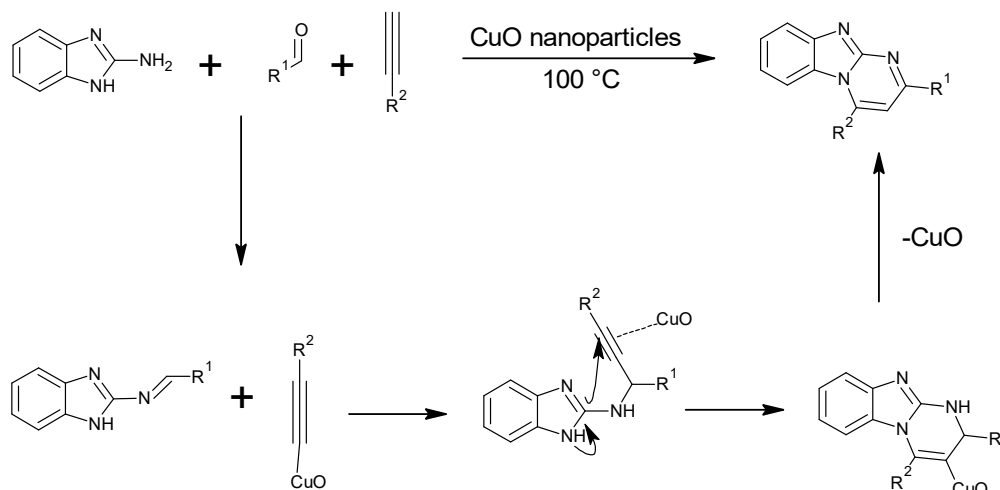
Figure 65: Synthesis of benzimidazopyrimidine derivatives from an aldehyde and an acetylene derivative, with CuO nanoparticles as the catalyst.

Improved Synthesis of 18F-GTP1
In the past, 18F-GTP1's synthesis was hard and yields were low, chromatographic separations were inefficient, and product quality was variable. This synthesis was referred to as the first-generation. White and coworkers devised a more successful, second-generation synthesis, which could be extended to the kilogram scale. Lithium aluminum deuteride caused the placement of geminal deuterium atoms on the structure, then an efficient amide-forming reaction led to the key acrylamide coupling partner compound. Tricyclic imidazo[1,2-a]pyrimidine compound was introduced with a highly successful annulation reaction. Unlike the first-generation synthesis, no chromatographic separations were required and the final step involved a successful and reproducible tosylation step (50) (See Figure 66).

Dichalcogenation of Imidazopyrimidines
Obah Kosso and coworkers treated imidazo[1,2-a]pyrimidine and similar heterocycles with dichalcogenation at C6 position and the oxidizing medium was iodine coupled with dimethylsulfoxide and the starting compound were diarylchalcogenides. This strategy was efficient, and the regioselectivity and yields were excellent (51) (See Figure 67).

Halogenation of Imidazole-Derived Heterocycles
Neto and coworkers reported trihaloisocyanuric acid as a practical and eco-friendly reagent for regioselectively halogenation of imidazole-derived heterocycles (52) (See Figures 68 and 69).

Review of Imidazopyrimidines for Direct C-H Bond Functionalization
Patel and coworkers prepared a review article in which direct C-H bond functionalization of imidazopyrimidines and other related compounds (53) (See Figures 70-77).
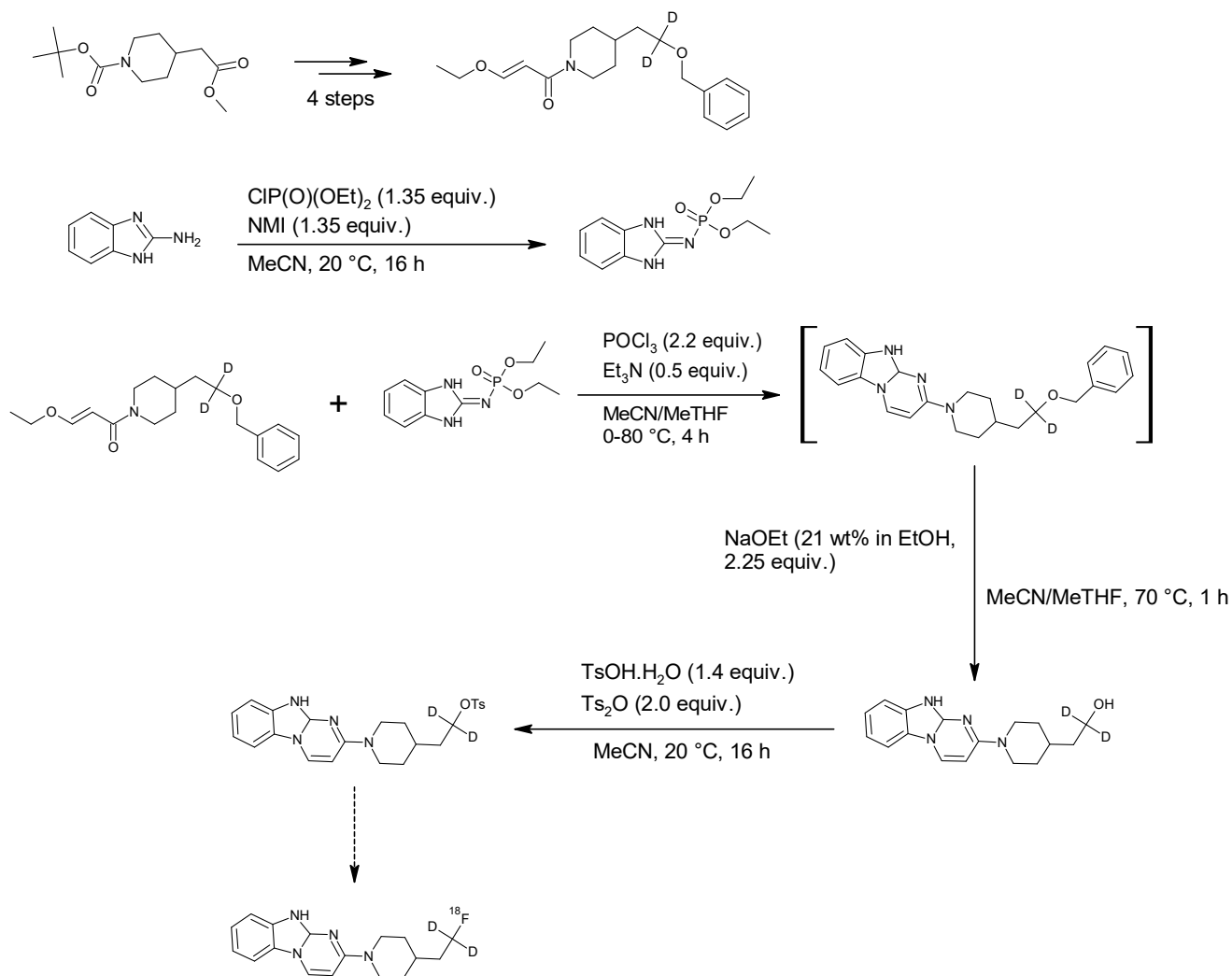
Figure 66: Improved synthesis of an imidazopyrimidine derivative.
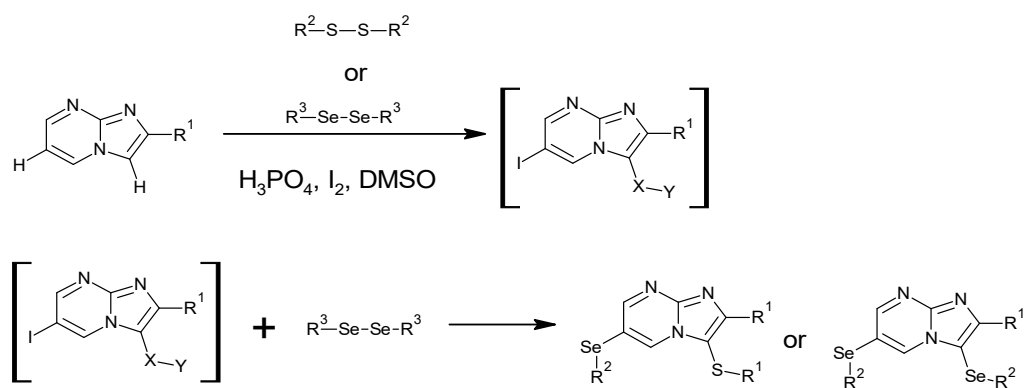
Figure 67: Dichalcogenation of imidazopyrimidine at 3-position and 6-position.
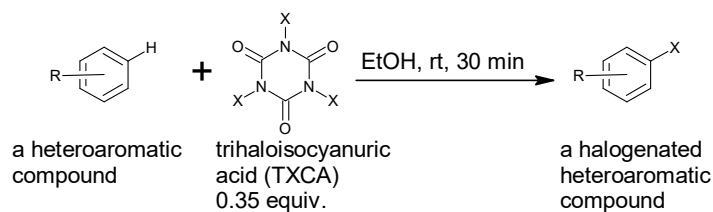
Figure 68: Use of trihaloisocyanuric acid with a heteroaromatic compound for imidazole-derived heterocycles.
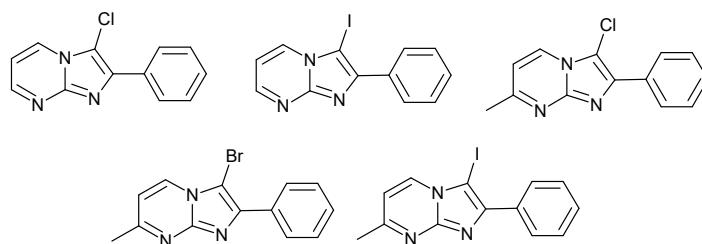
Figure 69: Synthesized imidazopyrimidine bases.
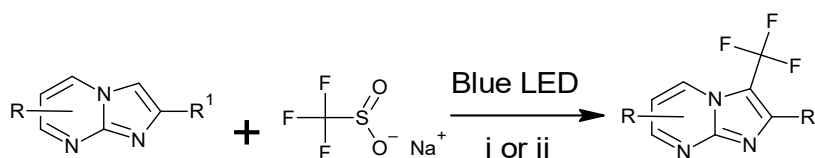
Figure 70: C-H bond functionalization of an imidazopyrimidine derivative.
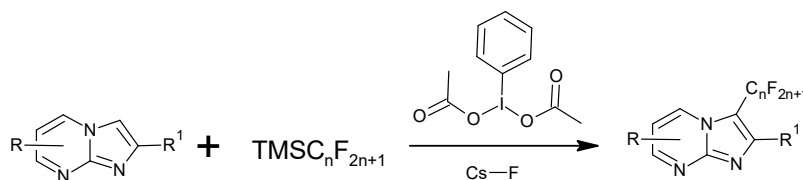
Figure 71: Substitution of 3-H with a hydrocarbon chain.
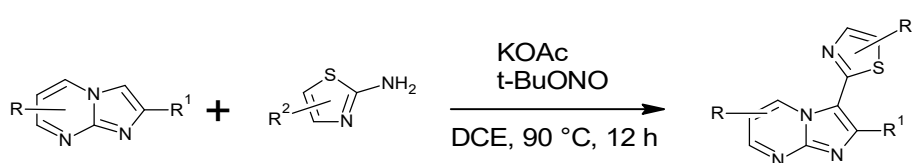
Figure 72: Functionalization of 3-H with an aminothiazole derivative.
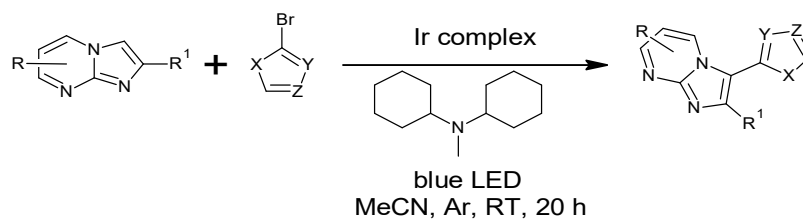
Figure 73: Functionalization of 3-H position with a photochemical route employing an iridium complex.
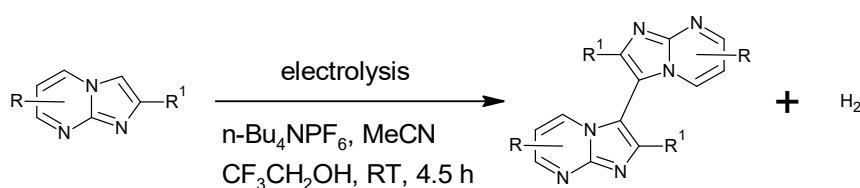
Figure 74: Electrolysis of an imidazopyrimidine derivative, yielding a 3,3'-dimer.
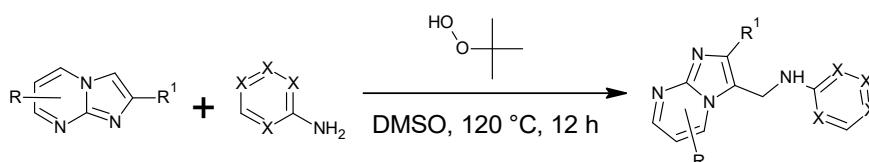
Figure 75: Addition of an aminoheterocycle at 3 position with tert-butylhydroperoxide.
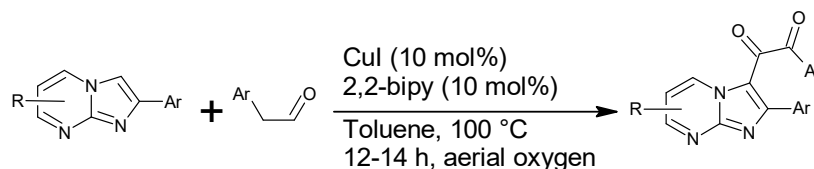
Figure 76: Addition of an aldehyde group to the 3-position.
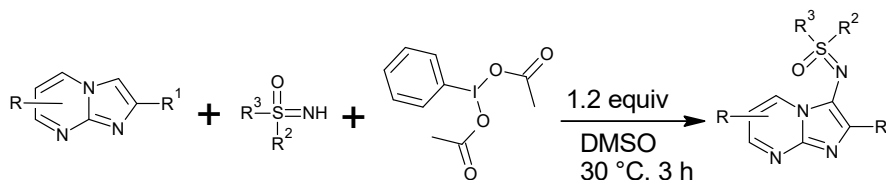
Figure 77: Functionalization of imidazopyrimidine 3-position with a sulfonimidoyl group.

Formation of Benzoimidazotriazolopyrimidines
Fedotov and coworkers described a new synthetic methodology to benzo[4,5]imidazo[1,2-*a*][1,2,3]triazolo[4,5-*e*]pyrimidines. The synthesis included the condensation of 3-(arylazo)benzo[4,5]imidazo[1,2-*a*]pyrimidine-4-amines from aminobenzimidazoles and 3-oxo-2-phenylazopropionitrile and, with copper(II) acetate as catalyst, the mentioned compounds formed with oxidative cyclization with around 75% yield. The compounds showed good quantum yields, maximal absorption within 380-400 nm, and maximal emission within 470-500 nm (54) (See Figure 51).
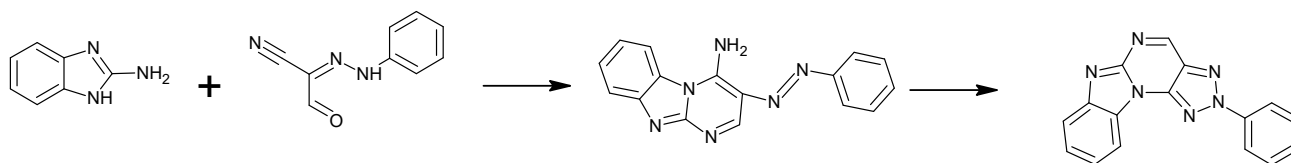
Figure 78: Synthesis of a benzoimidazotriazolopyrimidine compound.

ONE-POT, MULTICOMPONENT SYNTHETIC METHODS

Multicomponent Reaction Approach

A one-pot approach to substituted imidazo[1,2-a]pyrimidines is described by Kiselyov and Smith, II, with a convenient protocol. The reaction is general with nitrile, aldehyde, and aminoheterocycle components. The reaction yields are around 70% and isolation is easy (55) (See Figure 79).
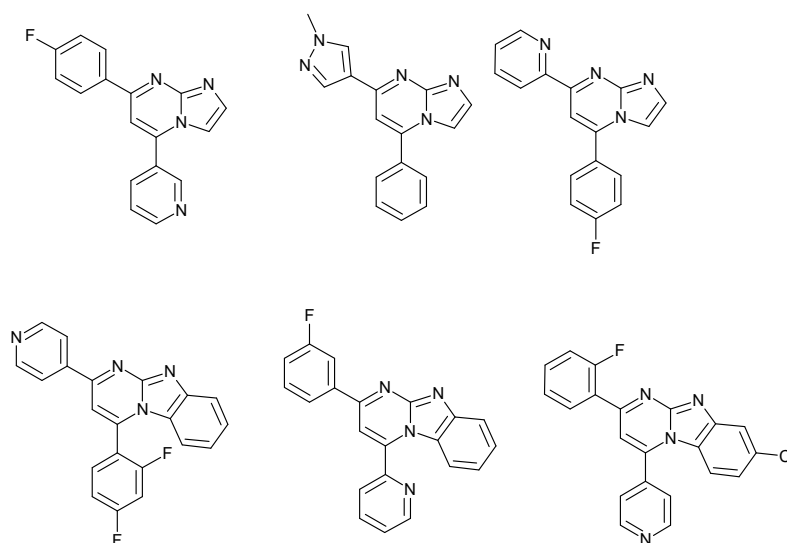
Figure 79: Structures of the formed compounds.

A Multicomponent Reaction with Isonitriles

2-Aminopyrimidine, aldehydes, and isonitriles undergo a multicomponent reaction to yield imidazopyrimidines. A Russian research group, with Parchinsky as the first author, published a paper in which they showed the very possibility of the formation of several isomeric compounds (56) (See Figure 80).

One-pot multicomponent synthesis of 3-amino-2-arylimidazo[1,2-a]pyrimidine derivatives

Adib and co-workers used 2-aminopyrimidine, a benzaldehyde (substituted or not), and imidazolin-2,4,5-trione in a one-pot, solvent-free and multicomponent reaction to obtain imidazopyrimidine derivatives (57) (See Figure 81).
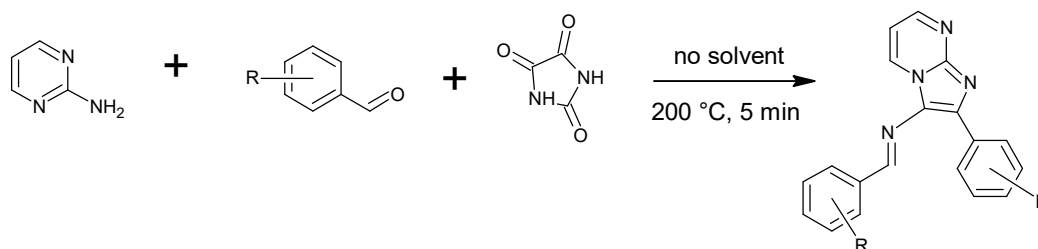
Figure 80: A multi-component reaction to give imidazopyrimidine derivatives.
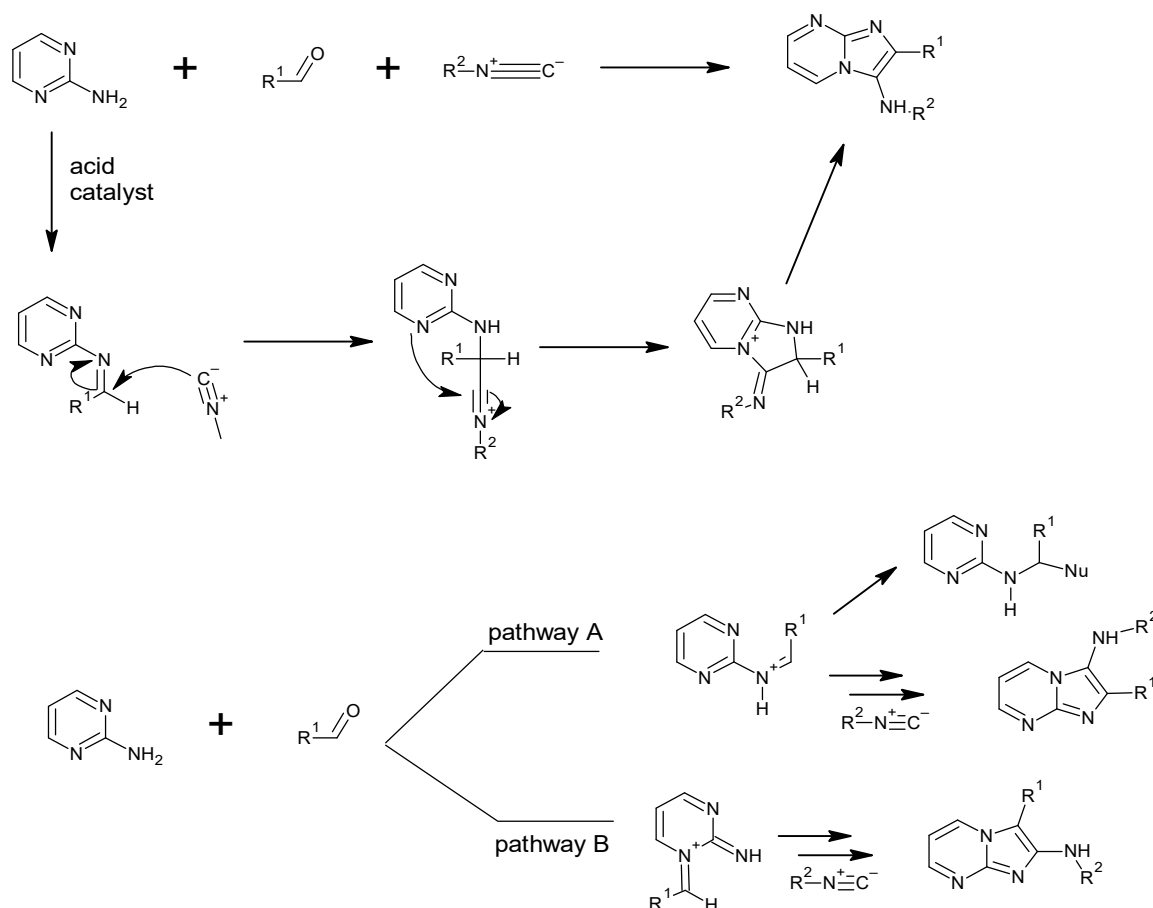
Figure 81: Formation of 2,3-disubstituted imidazopyrimidines via two different pathways.

Synthesis of aryl-benzo[4,5]imidazo[1,2-a]pyrimidine amines

Reddy et al. grafted tetraethylene glycol-bridged 1-vinylimidazolium mesylate onto the surface of cross-linked polyethylene glycol methacrylate. This structure served as an excellent catalyst for the synthesis of N-methyl-2-nitro-aryl-benzo[4,5]imidazo[1,2-a]pyrimidine amines in a multi-component reaction employing 1H-benzo[d]imidazol-2-amine and (E)-N-methyl-1-(methylthio)-2-nitroethenamine and several aldehydes under solvent-free conditions. The catalyst can be reused and its catalytic activity can maintain its superiority after seven cycles. The whole protocol is green, no waste side products, no solvent involved, and no column chromatography is needed (58) (See Figure 82).
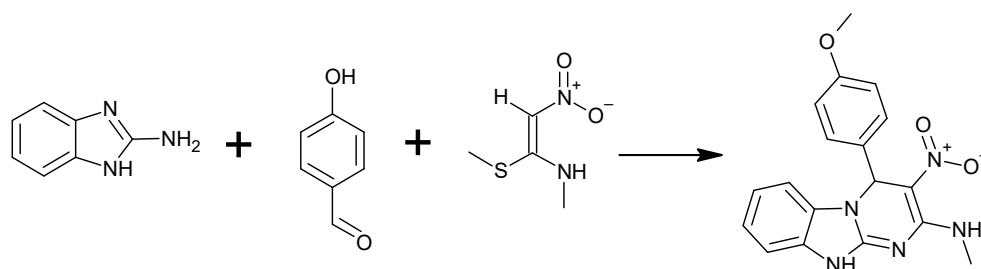
Figure 82: Synthesis of N-methyl-2-nitroarylbenzo[4,5]imidazo[1,2-a] pyrimidine amines.

Synthesis of Benzoimidazopyrimidine Derivatives with NiFe$_2$O$_4$ as the Catalytic Entity

Hamidinasab and coworkers prepared a modified NiFe$_2$O$_4$ nanoparticle for use in the multicomponent synthesis of benzo[4,5]imidazo[1,2-a]pyrimidine derivatives under green conditions. The reaction provided high reaction yields, reaction times were shorter, purification was simple, and reaction conditions were mild by environmental means (59) (See Figure 83).
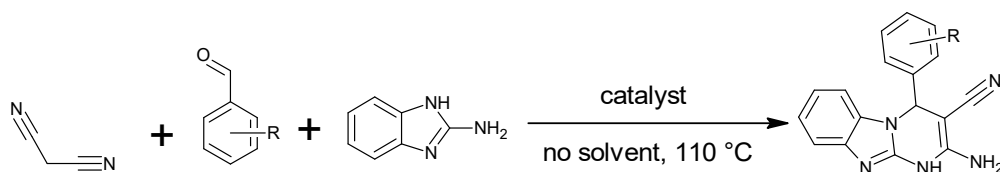
Figure 83: Synthesis of benzo[4,5]imidazo[1,2-a]pyrimidine derivatives.

Silica Sulfuric Acid as the Catalytic Entity
Basyouni and coworkers devised a simple and efficient, and eco-friendly synthetic method for synthesizing benzo[4,5]imidazo[1,2-*a*]pyrimidine-3-carbonitrile derivatives with excellent yields. They prepared the final compounds with a multicomponent reaction among 2-aminobenzimidazole, several aldehydes, malononitrile or ethyl cyanoacetate as active nitriles, and silica sulfuric acid/ethylene glycol as the catalytic system. The significant aspects of this synthetic methodology are very short reaction times in terms of minutes, high yields, and cost-effectiveness (60) (See Figure 84).
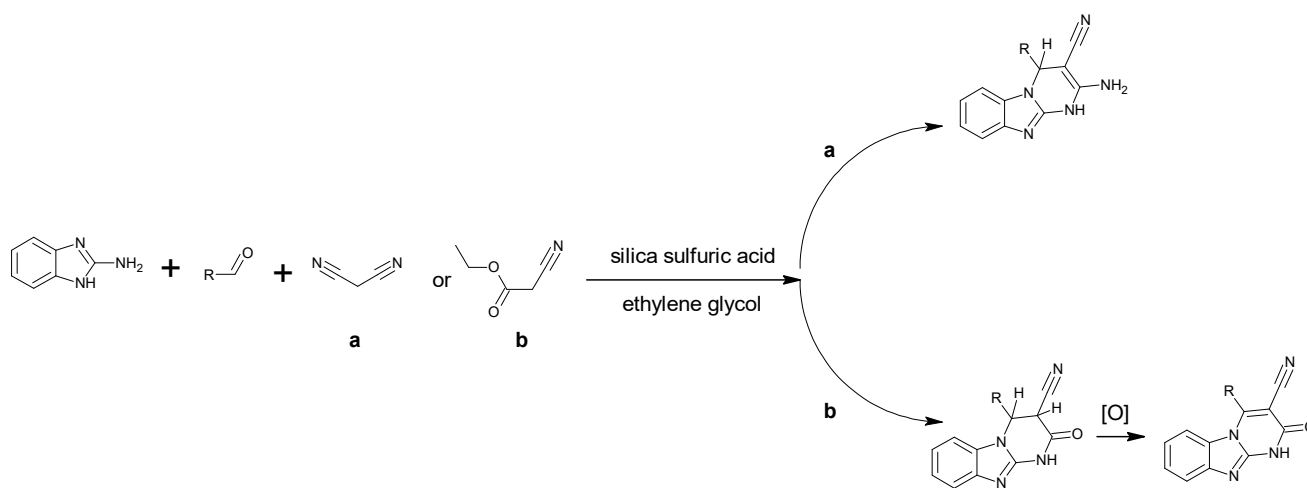
Figure 84: Synthesis of imidazopyrimidine carbonitrile derivatives in two different routes.

Fe₃O₄@C-SO₃H Nanoparticles as the Catalytic Entity
In order to synthesize a separable magnetic Fe₃O₄@C-SO₃H nanoparticle (MNPs) with high catalytic activity in organic transformation, three environmental-benign and low-cost sulfonic acid functionalized magnetic nanoparticles (Fe₃O₄@C-SO₃H) were successfully synthesized by Damghani et al. Benzo[4, 5] imidazo[1,2-*a*]-pyrimidine derivatives were synthesized under solvent-free conditions in excellent yields (61) (See Figure 85 and 86).
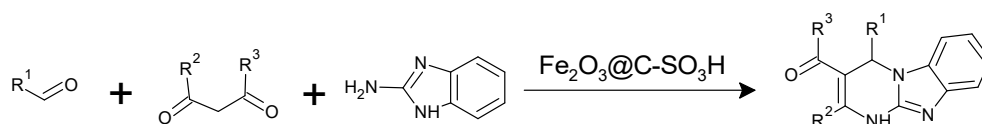
Figure 85: Magnetite-catalyzed synthesis of imidazopyrimidine compounds.
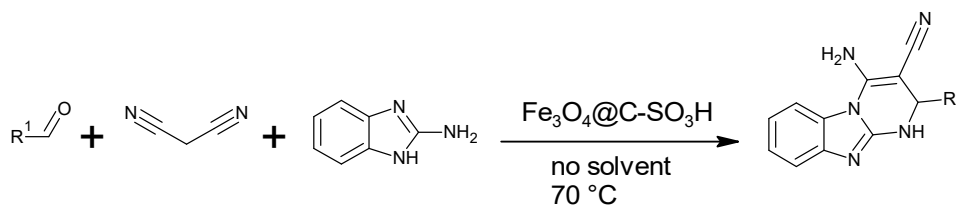
Figure 86: An examplary reaction involving the three-component synthesis.

Use of Starch-Functionalized Magnetite Nanoparticles as the Catalytic Entity

One-pot, multicomponent synthesis of imidazopyrimidine compounds was realized in an efficient and environmentally friendly fashion by Verma et al. The components were aromatic aldehydes, active methylene compounds, and 2-aminobenzimidazole and ultrasonic irradiation was employed. Starch-functionalized magnetite nanoparticles were used as the catalytic entity in the reaction. The developed reaction system used mild reaction conditions, isolation was easy, atom economy was high, products were obtained in good to excellent reaction yields, no column chromatography was involved, and the catalyst was magnetically separable and reusable. (62) (See Figure 87).
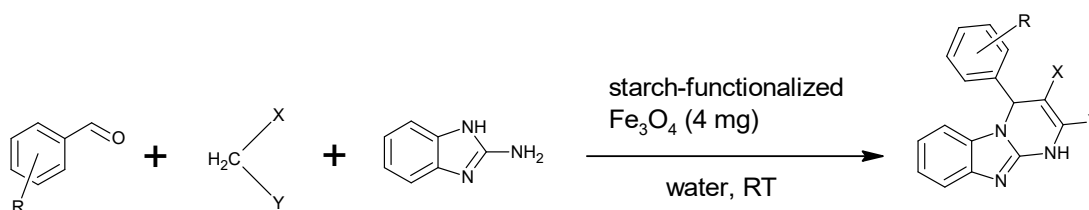
Figure 87: An aldehyde, an active methylene compound, and benzimidazole react to give a benzimidazolo[1.2-a]pyrimidine compound at room temperature, with silica-functionalized magnetite particles as the catalytic entity. 21 compounds were reported.

Synthesis of Imidazopyrimidine-Based Pyrans

Imidazo[1,2-a]pyrimidine-2-carbaldehyde, malononitrile, acids in which C-H activation is possible and sodium carbonate as base were reacted by Güngör in a one-pot fashion to yield new imidazo[1,2-a]pyrimidine-based pyrans at room temperature and similar to other compounds, a multicomponent reaction scheme was adopted. Mild reaction conditions, the absence of the need for column chromatographic separations, and the medium to good reaction yields are the main advantages for this multicomponent reaction (63) (Figure 88).
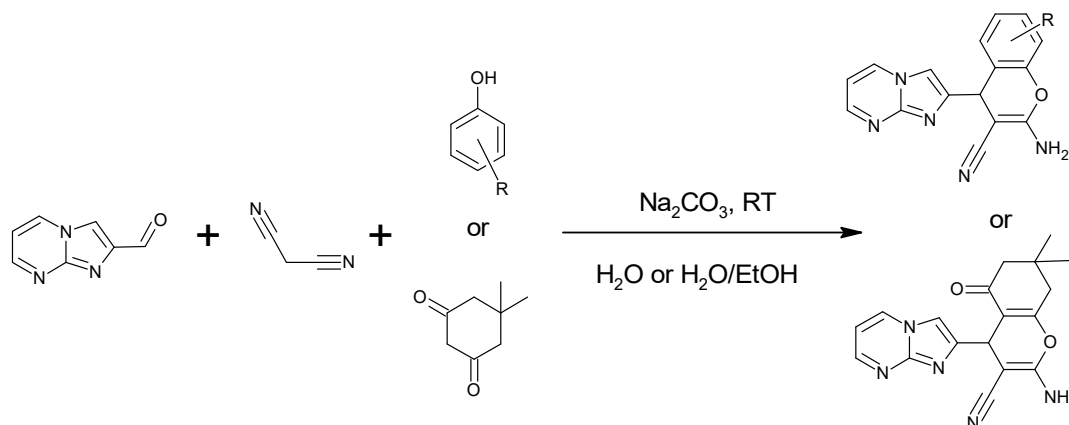
Figure 88: New imidazopyrimidine-based pyran compounds.

Heteroannulation of Imidazopyrimidines

Akbari and coworkers prepared a nanomaterial heterogeneous catalyst and used this in the

heteroannulation of imidazopyrimidines with a multicomponent reaction among 2-aminobenzimidazole, compounds having acidic C-H entities, and several aromatic aldehydes. The protocol was green and catalyst loading was low, yields were high to quantitative, reaction times were short, and the catalyst could be recycled at least four runs (64). (See Figure 89).

Dihydrobenzoimidazopyrimidine Synthesis with ZnFe₂O₄ as the Catalytic Entity

2-Amino-4-substituted 1,4-dihydrobenzo[4,5]imidazo[1,2-*a*]pyrimidine-3-carbonitriles were synthesized with a multicomponent reaction among benzimidazole, aldehydes, and malononitrile under ultrasonic irradiation and heterogeneous $ZnFe_2O_4$ as the nanocatalyst. The synthetic methodology is especially remarkable in that the reaction time is short, handling is easy, simple, efficient, and the reaction yield is high and the catalyst is recoverable (65) (See Figure 90).
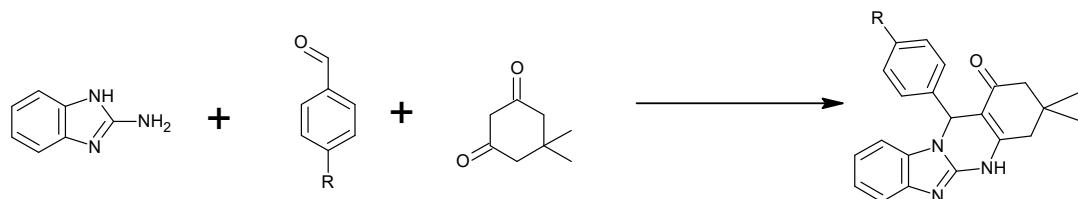
Figure 89: Three-component synthesis of heteroannulated imidazopyrimidines.
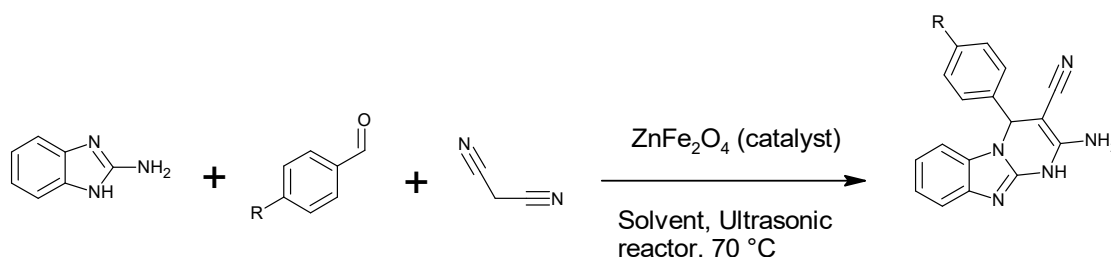
Figure 90: 2-Amino-4-substituted 1,4-dihydrobenzo[4,5]imidazo[1,2-a]pyrimidine-3-carbonitrile compounds.

Magnetite@Titanium Dioxide@Ionic Liquid Zeolitic Imidazolate Framework as the Catalytic Entity

One-pot synthesis of benzoimidazopyrimidine compounds was utilized with a magnetite@titanium dioxide@ionic liquid-zeolitic imidazolate framework, which showed high catalytic activities. The three-component reaction (various aldehydes, 2-aminobenzimidazole, and ethyl acetoacetate) was

conducted at room temperature. Similarly to other magnetic catalysts, the nanocatalyst was easily recovered with a magnet and the catalytic behavior of it remained the same for six catalytic runs. The advantages were that yields were excellent, procedures were simple, reaction times were short, workup was simple, and reaction conditions were mild (66) (See Figures 100 and 101).
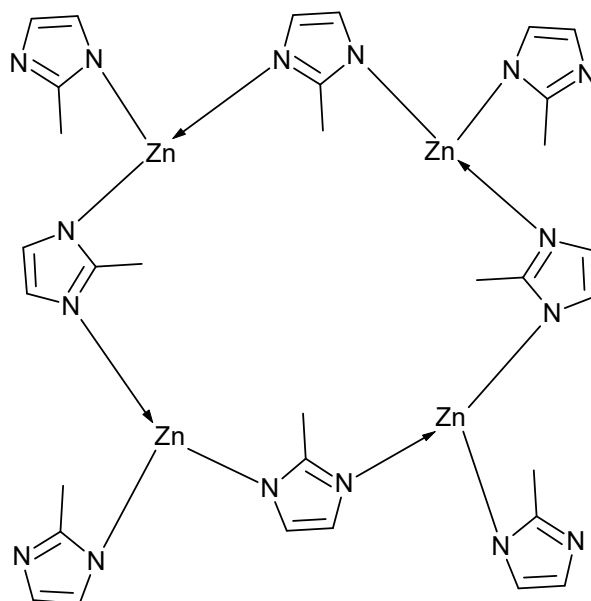
Figure 91: A part of the catalyst used visualized.
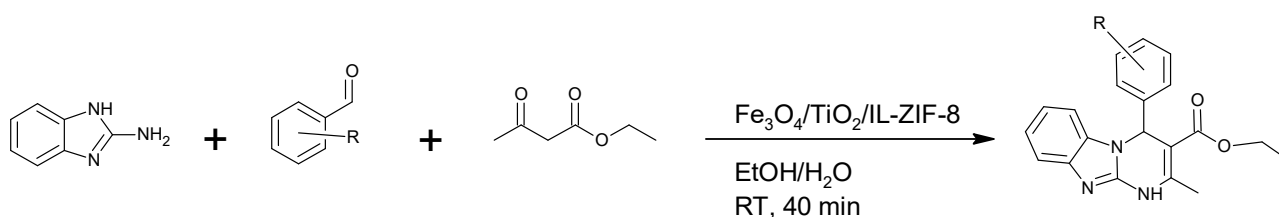
Figure 92: The three-component reaction and the product obtained.

Synthesis of Imidazopyrimidines with a Ferrocene-containing Zinc(II) Dithiocarbamate complex as heterogeneous bifunctional catalyst

Anamika and coworkers prepared a ferrocene-dithiocarbamate zinc(II) complex to serve as a heterogeneous bifunctional catalyst in the three-component synthesis of imidazopyrimidines (67) (See Figure 93).
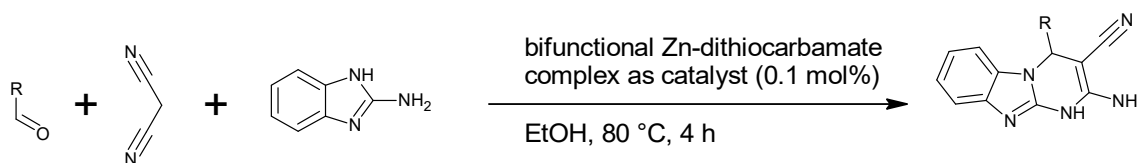
Figure 93: Three-component synthesis in the presence of a ferrocene-dithiocarbamate zinc(II) complex as the catalyst.

p-Toluenesulfonic Acid as the Catalytic Entity
Güngör prepared ten imidazo[1,2-*a*]pyrimidines with imidazole substituents in which imidazo[1,2-*a*]pyrimidine-2-carbaldehyde, benzil, a selection of primary amines, and ammonium acetate with p-toluenesulfonic acid as catalyst were reacted in a one-pot and multicomponent reaction, under microwave irradiation. The reaction yields are medium to good, carrying many different substituents on the skeleton and the reaction conditions are optimum. The solvent utilized was ethanol, which can be considered as a green solvent. (68) (See Figures 94 and 95).
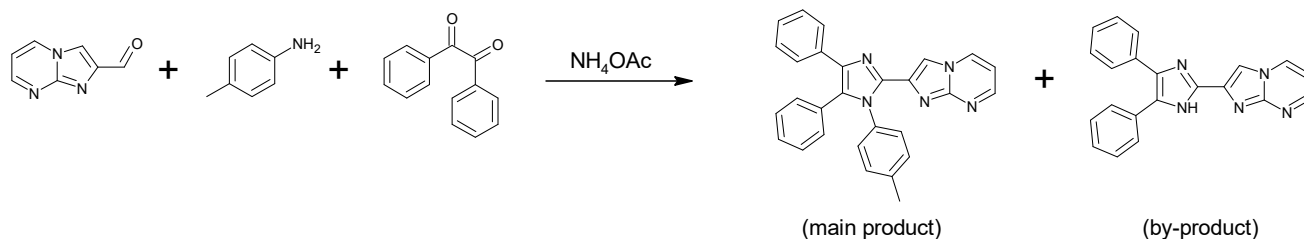
Figure 94: Three-component reaction yields a main product and a by-product.
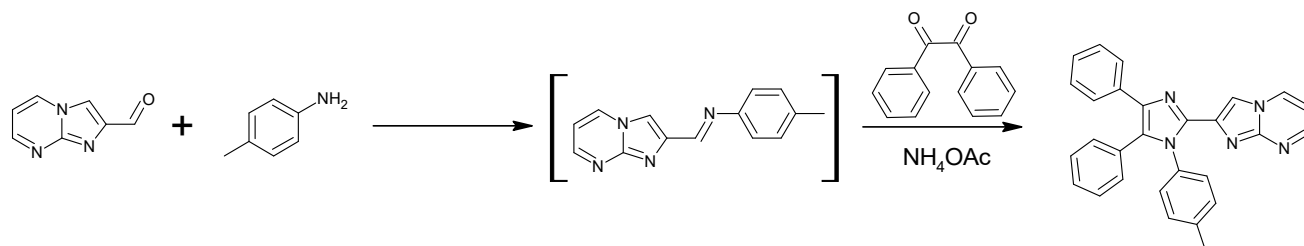
Figure 95: A second reaction used a two-component reaction, then the third molecule gets in.

MISCELLANEOUS USES

Proton Sensitive Organic Fluorescent Dyes

Aydıner and Seferoglu devised a series of proton sensitive functional organic fluorescent dyes based on coumarin and imidazo[1,2-*a*]pyrimidine. They reported the synthetic effort, photophysics in different solvents, and protonation study with trifluoroacetic acid as the titrant. 7-dialkylaminocoumarin-based compounds had the best fluorescent performance, and the compound having morpholine moiety was considered for its potential of colorimetric and luminescent pH sensor compound (69) (See Figures 96 and 97).
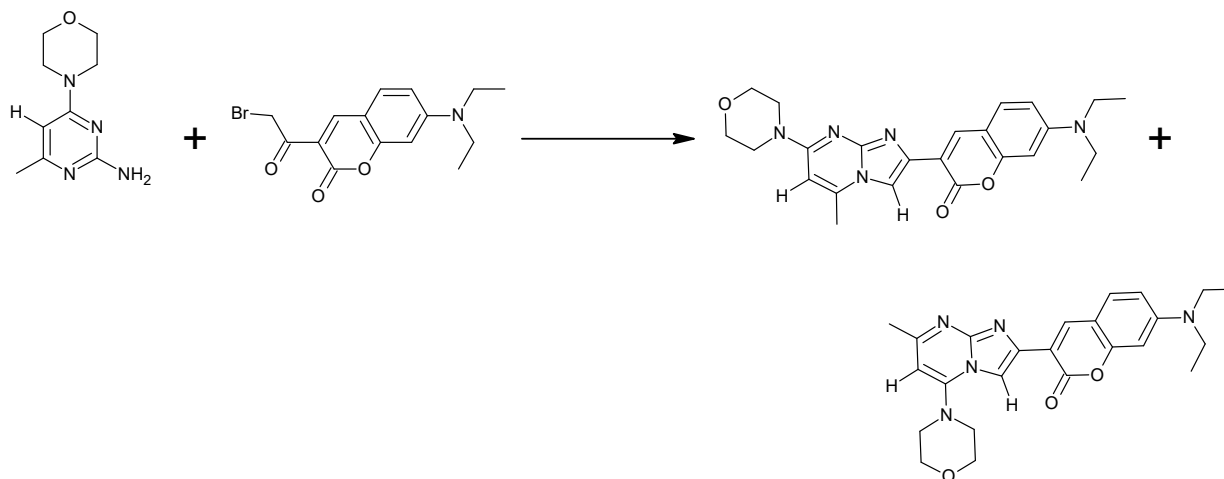
Figure 96: Formation of coumarin-based imidazopyrimidines with morpholine group.
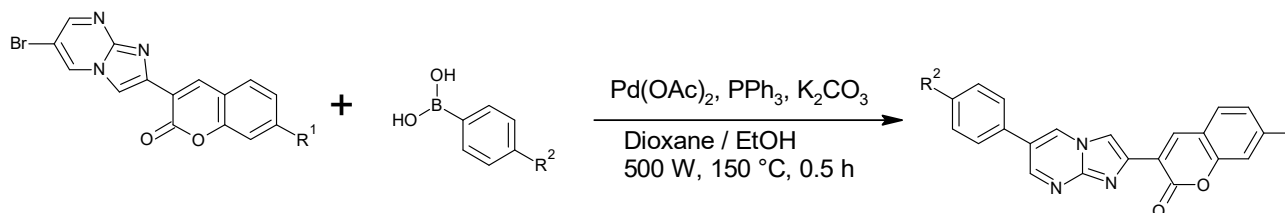
Figure 97: Incorporation of an aromatic group at the 6-position with Suzuki coupling. Six compounds were reported.

Use of Selenoester Derivatives in the Treatment of Mercury(II) Chloride

In situ-generated sodium selenocarboxylates reacted with 2-(chloromethyl)imidazo[1,2-a]pyrimidine in water and ethanol. Phenyl/4-tolyl selenoesters of imidazo[1,2-a]pyrimidine were obtained in water and 4-chlorophenyl/2-thienyl selenoesters of the same heterocyclic system were only obtained in ethanol. A model compound was used for studying the behavior of selenoesters with mercury(II) chloride. Reaction with HgCl₂ yielded a bis(imidazopyrimidinyl)selenide, bis(imidazopyrimidinyl)diselenide and the HgCl₂ compound. The selenoester derivatives could be considered in the treatment of mercury(II) chloride-induced toxicity (70) (See Figure 98-100).

Figure 98: Formation of chloromethylimidazo[1,2-a]pyrimidine scaffold.
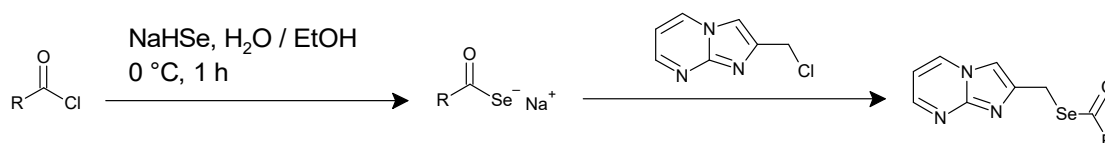
Figure 99: Synthesis of the selenoacetate derivative of imidazopyrimidine.
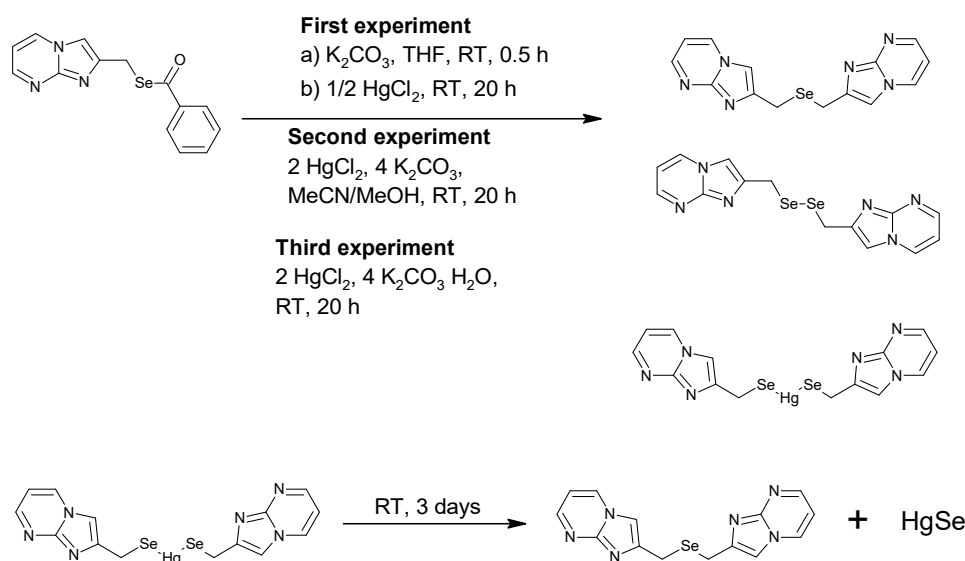
Figure 100 : Three separate experiments for the synthesis of mercury(II) selenide.

Heterocycles Having Long Fatty Chains
El-Sayed and coworkers reported condensed and non-condensed heterocycles having long fatty chains in the hope of obtaining surface active biological compounds. 2-Cyano-3-(dimethylamino)-N-octadecylacrylamide was the starting compound to obtain several pyrimidine, pyran, and similar heterocycles. Propylene oxide helped these compounds transform into nonionic surface active compounds. The high solubility of these compounds allowed them to be used in easy absorption. The authors report that they reduce the surface tension of liquids, and they have high wetting and emulsification property (71) (See Figure 101).
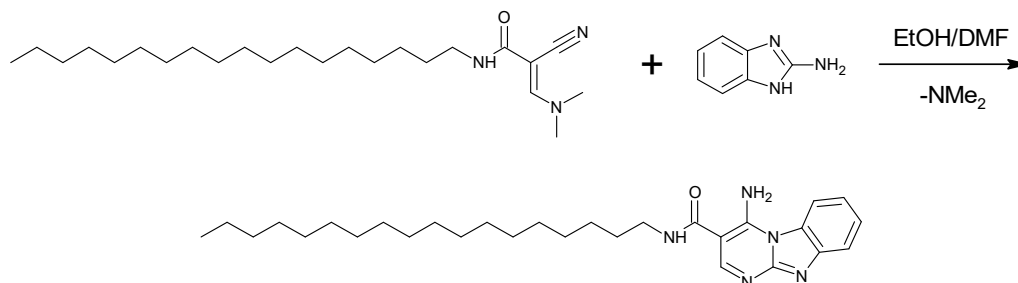
Figure 101: An enaminonitrile compound reacts with 2-aminobenzimidazole, with the elimination of dimethylamine, forms the long-chained benzimidazolopyrimidine compound.

CORROSION INHIBITION

Corrosion Inhibition of C38 Steel in 1 M HCl
2-(m-Methoxyphenyl)imidazo[1,2-*a*]pyrimidine was tested along with another compound, in the corrosion inhibition study by Ghazoui et al. According to potentiodynamic polarization studies, it was found that the inhibitors employed behaved as mixed-type. The inhibitors were found to be adsorbed on the steel surface according to Langmuir isotherm. Corrosion rate decreased with the use of these two inhibitive compounds, and when the concentrations increased, the effect was remarkable. Inhibitory concentration of the compound was 1 millimolar and EI% was 95.7% (72) (See Figure 102).
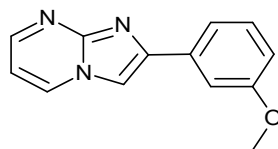
Figure 102: 2-(3-methoxyphenyl)imidazo[1,2-a]pyrimidine, used as a corrosion inhibitor.

Inhibitive Effect of 2-phenylimidazo[1,2-*a*]pyrimidine-3-carbaldehyde
In hydrochloric acid solution, corrosive inhibition of the synthesized compound, 2-phenylimidazo[1,2-*a*]pyrimidine-3-carbaldehyde, was tested on carbon steel. It is an expected consequence that increasing concentration of the inhibitor will lead to a decreased rate of corrosion. A mixed-type inhibition was discovered with the polarization studies. Langmuir's isotherm model was used to describe the adsorption behavior of the inhibitory entity. B3LYP/6-31+G(d,p) level of DFT was used to explain the inhibitive effects of the synthesized compound. Molecular dynamics simulation showed that the molecule could adsorb on alpha-iron(III) oxide (111) surface in hydrochloric acid through the oxygen and nitrogen atoms and pi-electrons. Experimental and theoretical results are quite harmonious with each other (73) (See Figure 103).
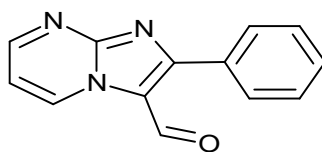
Figure 103: 2-Phenylimidazo[1,2-a]pyrimidine-3-carbaldehyde.

Anodic Dissolution of Copper in Sodium Chloride Medium

The mechanism of anodic dissolution of copper in sodium chloride medium has not been discovered until now. 4-Amino-3-(phenyldiazenyl)benzo[4,5]imidazo[1,2-a]pyrimidin-2(1H)-one was tested for its efficiency as a corrosion inhibitor for copper, in sodium chloride solution at a concentration of 3.5% by weight. Aerated NaCl solution simulates a marine environment and adding the inhibitor or not adding it serves as a solution to uncovering the mechanistic part. According to potentiodynamic polarization (PDP), the inhibitor is effective at a low concentration in the 3.5% NaCl solution. The inhibition efficiency was about 93% owing to adsorption and to electrochemical investigation. Electrochemical impedance spectroscopy (EIS) showed that the inhibitor acted with both diffusive and kinetically controlled processes. The adsorptive isotherm model fit with Langmuir's. The inhibitor can be used in marine environments like water coolers, desalination plants, power plants, and oil production. DFT and MD studies supported experimental part and explain more about the mode of adsorption on Cu surface (74) (See Figure 104).
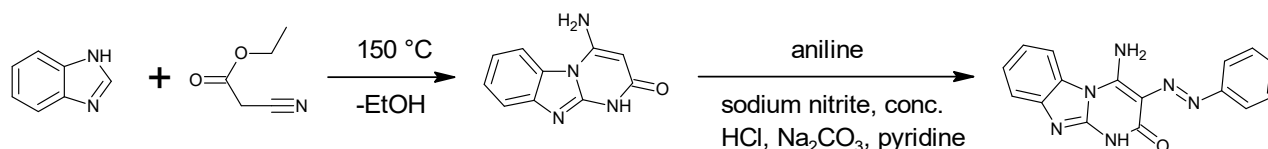
Figure 104: Preparation of the imidazopyrimidin-2(1H)-one compound and subsequent diazotization to obtain a representative corrosion inhibitor.

THEORY-POWERED EXPERIMENTAL STUDIES

Non-planarity of Imidazopyrimidines

2,4-Diphenyl-1,4-dihydrobenzo[4,5]imidazo[1,2-a]pyrimidine and some other derivatives of it were researched both theoretically and experimentally, in the solvents, namely 1,4-dioxane and dimethylformamide. All of the compounds are non-planar, which is indicative of great electronic and structural properties. One of the compounds are reactive at the highest owing to its lowest E(HOMO), E(LUMO) and DE. The electronic spectra of the compounds were studied in terms of the number of bands. In addition, TD-B3LYP/6-311G (d, p) in gas phase, 1,4-dioxane, and dimethylformamide showed a nice agreement with the spectra recorded (75) (See Figure 105).
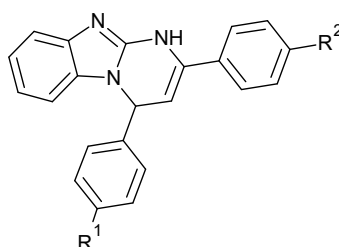
Figure 105: Structures synthesized in this study. R^1 is hydrogen, fluorine, bromine, methyl, nitro, or methoxy, and R^2 is hydrogen, fluorine, or methoxy.

Studying the Tautomerism of Six Imidazopyrimide Compounds by IR, NMR, and DFT

A combination of spectral analyses like FTIR and NMR and theoretical calculations were performed for six imidazopyrimidine compounds. The compounds were synthesized with the 1-aryl-4,5-dihydro-1H-imidazol-2-amine hydrobromide and diethyl phenylmalonate, and sodium methoxide was used as a base. Tautomeric transitions in the structures were investigated in the gas, solution, and crystalline states. NMR and FTIR analyses did not help much about identification of the tautomeric forms present in the solution and also in the solid state. X-ray analysis, however, identified that all compounds were present in the keto-keto tautomeric form in the crystalline state. Theoretical studies at DFT/B3LYP/6-311++G(d,p) level was successful to indicate that, in the gas phase and in the solution, two tautomeric forms coexist. Theoretical studies and FTIR-NMR spectra allowed for the calculation of all tautomeric forms and, to a limited extent, the identification is possible (76) (See Figure 106).
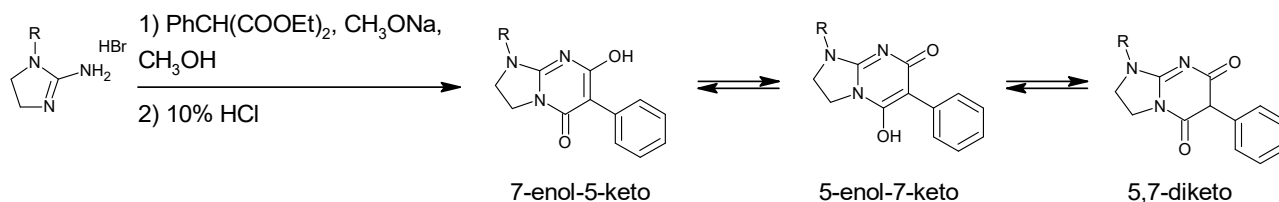
Figure 106: Synthesis of a reduced form of an imidazopyrimidine and illustration of existing tautomeric forms. Six compounds with differing R radicals were reported.

Single-Crystal and Theoretical Study of an Imidazopyrimidine and its Thiazole Analog

Dylong and coworkers prepared imidazo[1,2-*a*]pyrimidin-2-ylacetic acid and its thiazole analog, and structurally characterized with single-crystal X-ray diffraction and computational studies in the form of Hirshfeld surfaces, which helped understand the intermolecular interactions of the crystals. FTIR and Raman spectra of both crystals were obtained and interpretations were made with DFT calculations and potential energy distribution (PED) analyses of computed normal vibrations. When the researchers recrystallized the compounds from deuterium oxide, they observed that the carboxylic OH groups were completely deuteriated (77) (See Figure 107).

1,4-Dimethyl–2-oxopyrimido[1,2-a]benzimidazole Hydrate and Some Properties of it

El-Bakri and colleagues synthesized a new compound, 1,4-dimethyl-2-oxopyrimido[1,2-a]benzimidazole hydrate and used NMR and FTIR, and also used single-crystal X-ray diffraction to characterize the compound. The tricyclic core was found to be almost planar with X-ray studies. The molecules stack along the a-axis direction in head-to-tail fashion through p-stacking interactions involving all three rings. DFT calculations at B3LYP/6-311 G(d,p) in gas phase helped find a very good correlation between experimental and theoretical data (78) (See Figure 108).
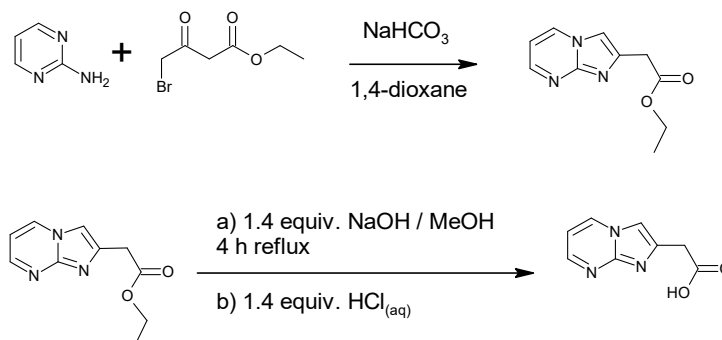
Figure 107: Synthesis of imidazopyrimidine ester in low yield and basic/acidic hydrolysis of the compound to obtain a carboxylic acid.
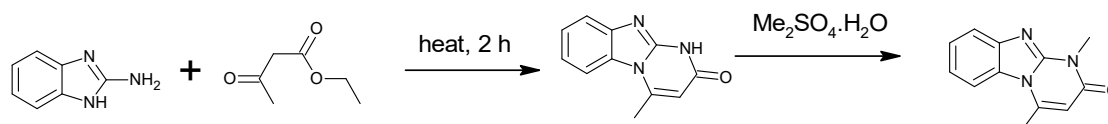
Figure 108: Formation of the benzimidazolopyrimidine and subsequent methylation of the compound.

REFERENCES

1.   Jensen MS, Hoerrner RS, Li W, Nelson DP, Javadi GJ, Dormer PG, et al. Efficient Synthesis of a GABA A α 2,3 -Selective Allosteric Modulator via a Sequential Pd-Catalyzed Cross-Coupling Approach. J Org Chem. 2005 Jul 1;70(15):6034–9. <URL>.

2.   Oganisyan AS, Noravyan A, Dzhagatspanyan I, Nazaryan I, Akopyan A. Derivatives of condensed thienopyrimidines: Synthesis and anticonvulsant and tranquilizer activity of hydrochlorides of pyrano [4′, 3′: 4, 5] thieno [3, 2-e] imidazo [1, 2-a] pyrimidines. Pharm Chem J. 2007;41(11):588–90.

3.   Vidal A, Ferrándiz ML, Ubeda A, Acero-Alarcón A, Sepulveda-Arques J, Alcaraz MJ. Effect of imidazo[1,2-

a]pyrimidine derivatives on leukocyte function. Inflamm Res. 2001 Jun;50(6):317–20. <URL>.

4.   Blackaby WP, Atack JR, Bromidge F, Castro JL, Goodacre SC, Hallett DJ, et al. Imidazo[1,2-a]pyrimidines as functionally selective GABAA ligands. Bioorg Med Chem Lett. 2006 Mar;16(5):1175–9. <URL>.

5.   Jennings ASR, Lewis RT, Russell MGN, Hallett DJ, Street LJ, Castro JL, et al. Imidazo[1,2-b][1,2,4]triazines as α2/α3 subtype selective GABAA agonists for the treatment of anxiety. Bioorg Med Chem Lett. 2006 Mar;16(6):1477–80. <URL>.

6.   Zhou JP, Ding YW, Zhang HB, Xu L, Dai Y. Synthesis and anti-inflammatory activity of imidazo[1,2-a]pyrimidine derivatives. Chin Chem Lett. 2008 Jun;19(6):669–72. <URL>.

7.   Al-Tel TH, Al-Qawasmeh RA. Post Groebke–Blackburn multicomponent protocol: Synthesis of new polyfunctional imidazo[1,2-a]pyridine and imidazo[1,2-a]pyrimidine derivatives as potential antimicrobial agents. Eur J Med Chem. 2010 Dec;45(12):5848–55. <URL>.

8.   Fu R geng, You Q dong, Yang L, Wu W tong, Jiang C, Xu X li. Design, synthesis and bioevaluation of dihydropyrazolo[3,4-b]pyridine and benzo[4,5]imidazo[1,2-a]pyrimidine compounds as dual KSP and Aurora-A kinase inhibitors for anti-cancer agents. Bioorg Med Chem. 2010 Nov 15;18(22):8035–43. <URL>.

9.   Cosimelli B, Laneri S, Ostacolo C, Sacchi A, Severi E, Porcù E, et al. Synthesis and biological evaluation of imidazo[1,2-a]pyrimidines and imidazo[1,2-a]pyridines as new inhibitors of the Wnt/β-catenin signaling. Eur J Med Chem. 2014 Aug;83:45–56. <URL>.

10.   Aeluri R, Alla M, Polepalli S, Jain N. Synthesis and antiproliferative activity of imidazo[1,2-a]pyrimidine Mannich bases. Eur J Med Chem. 2015 Jul;100:18–23. <URL>.

11.   Kaur N, Kaur K, Raj T, Kaur G, Singh A, Aree T, et al. One-pot synthesis of tricyclic dihydropyrimidine derivatives and their biological evaluation. Tetrahedron. 2015 Jan;71(2):332–7. <URL>.

12.   Velázquez-Olvera S, Salgado-Zamora H, Jiménez-Cardoso E, Campos-Aldrete ME, Pérez-González C, Ben Hadda T. In vitro anti-Giardia lamblia activity of 2-aryl-3-hydroxymethyl imidazo[1,2-a]pyridines and -pyrimidines, individually and in combination with albendazole. Acta Trop. 2016 Mar;155:6–10. <URL>.

13.   Al-Lami N, Amer Z, Ali RA. Pryparation, Characterization And Biological Activity of New Derivatives of 2-Biphenyl-3-Aminomethylimidazo (1, 2-a) Pyrimidine. J Pharm Sci Res. 2018;10(12):3344–50.

14.   Moszczyński-Pętkowski R, Majer J, Borkowska M, Bojarski Ł, Janowska S, Matłoka M, et al. Synthesis and characterization of novel classes of PDE10A inhibitors - 1H-1,3-benzodiazoles and imidazo[1,2-a]pyrimidines. Eur J Med Chem. 2018 Jul;155:96–116. <URL>.

15.   Farag AM, Fahim AM. Synthesis, biological evaluation and DFT calculation of novel pyrazole and pyrimidine derivatives. J Mol Struct. 2019 Mar;1179:304–14. <URL>.

16.   Mantipally M, Gangireddy MR, Gundla R, Badavath VN, Mandha SR, Maddipati VC. Rational design, molecular docking and synthesis of novel homopiperazine linked imidazo[1,2-a]pyrimidine derivatives as potent cytotoxic and antimicrobial agents. Bioorg Med Chem Lett. 2019 Aug;29(16):2248–53. <URL>.

17.   Tawfik HO, El-Moselhy TF, El-Din NS, El-Hamamsy MH. Design, synthesis, and bioactivity of dihydropyrimidine derivatives as kinesin spindle protein inhibitors. Bioorg Med Chem. 2019 Dec;27(23):115126. <URL>.

18.   Elenich OV, Lytvyn RZ, Blinder OV, Skripskaya OV, Lyavinets OS, Pitkovych KhE, et al. Synthesis and Antimicrobial Activity of 3-Phenyl-1-Methylquinolin-2-One Derivatives. Pharm Chem J. 2019 Mar 15;52(12):969–74. <URL>.

19.   Jismy B, Akssira M, Knez D, Guillaumet G, Gobec S, Abarbri M. Efficient synthesis and preliminary biological evaluations of trifluoromethylated imidazo[1,2-a]pyrimidines and benzimidazo[1,2-a]pyrimidines. New J Chem. 2019;43(25):9961–8. <URL>.

20.   D'Aria F, D'Amore VM, Di Leva FS, Amato J, Caterino M, Russomanno P, et al. Targeting the KRAS oncogene: Synthesis, physicochemical and biological evaluation of novel G-Quadruplex DNA binders. Eur J Pharm Sci. 2020 Jun;149:105337. <URL>.

21.   Zhuang J, Ma S. Recent Development of Pyrimidine-Containing Antimicrobial Agents. ChemMedChem. 2020 Oct 19;15(20):1875–86. <URL>.

22.   Zadeh EE, Vahabpour R, Beirami AD, Hajimahdi Z, Zarghi A. Novel 4-Oxo-4,10-dihydrobenzo[4,5]imidazo[1,2-a]pyrimidine-3-carboxylic Acid Derivatives as HIV-1 Integrase Inhibitors: Synthesis, Docking Studies, Molecular Dynamics Simulation and Biological Activities. Med Chem. 2021 Nov;17(9):1060–71. <URL>.

23.   Lima MLSO, Braga CB, Becher TB, Odriozola-Gimeno M, Torrent-Sucarrat M, Rivilla I, et al. Fluorescent Imidazo[1,2-a]pyrimidine Compounds as Biocompatible Organic Photosensitizers that Generate Singlet Oxygen: A Potential Tool for Phototheranostics. Chem – Eur J. 2021 Apr 7;27(20):6213–22. <URL>.

24.   Saldabol NO, Popelis J, Slavinskaya VA. Formylation of furyl-substituted imidazo[1,2-a]pyridine, imidazo[1,2-a]pyrimidine and imidazo[2,1-b]thiazole. Chem Heterocycl Compd. 2001;37(8):1021–4. <URL>.

25.   Majcen-Le Marechal A, Le Grel P, Robert A, Biškup J, Ferk V, Toplak R. Reactivity of 3-halo-2-oxopropanamides and 3-halo-2-cyano-2-hydroxypropanoates: synthesis of S and N containing heterocycles. ARKIVOC. 2001;119:132.

26.   Kochergin PM, Mazur IA, Rogul'chenko GK, Aleksandrova EV, Mandrichenko BE. Investigations of Imidazoles. 101. Synthesis of 2,3-Dihydroimidazo[1,2-a]pyrimidine from 2-Aminopyrimidine. Chem Heterocycl Compd. 2001;37(2):224–6. <URL>.

27.   Chowdhury AZMS, Shibata Y. Synthesis of fused pyrimidines with N -, S -heterocyclic moieties by double-annelation reaction. J Heterocycl Chem. 2001 May;38(3):743–7. <URL>.

28.   Elmaati TMA. Reactions with Heterocyclic Amidines: New Routes for the Benzo [4, 5] imidazo [1, 2-a] pyrimidine, Some Pyridine, Pyran and Pyrazole Derivatives Containing the Antipyrine Moiety. Acta Chim Slov. 2002;49:721–32.

29.   Katritzky AR, Xu YJ, Tu H. Regiospecific Synthesis of 3-Substituted Imidazo[1,2-a]pyridines, Imidazo[1,2-a]pyrimidines, and Imidazo[1,2-c]pyrimidine. J Org Chem. 2003 Jun 1;68(12):4935–7. <URL>.

30.   El Kazzouli S, Berteina-Raboin S, Mouaddib A, Guillaumet G. Solid-phase synthesis of imidazo[1,2-a]pyridines and imidazo[1,2-a]pyrimidines. Tetrahedron Lett. 2003 Aug;44(33):6265–7. <URL>.

31.   Bari A, Feist H, Michalik D, Michalik M, Peseke K. Synthesis of Heterocyclic Compounds by Ring Transformations of 2-Formyl Pentose Glycals. Synthesis. 2004 Oct 7;2004(17):2863–8. <URL>.

32.   Sączewski J, Brzozowski Z, Gdaniec M. Synthesis of 2,3-dihydroimidazo[1,2-a]pyrimidin-5(1H)-ones by the domino Michael addition retro-ene reaction of 2-alkoxyiminoimidazolidines and acetylene carboxylates. Tetrahedron. 2005 May;61(22):5303–9. <URL>.

33.   Laquintana V, Denora N, Lopedota A, Suzuki H, Sawada M, Serra M, et al. N-Benzyl-2-(6,8-dichloro-2-(4-chlorophenyl)imidazo[1,2-a]pyridin-3-yl)-N-(6-(7-nitrobenzo[c][1,2,5]oxadiazol-4-ylamino)hexyl)acetamide as a New Fluorescent Probe for Peripheral Benzodiazepine Receptor and Microglial Cell Visualization. Bioconjug Chem. 2007 Sep 1;18(5):1397–407. <URL>.

34.   El Otmani B, El Mahi M, Bouhfid R, Essassi EM, Rohand T, Dehaen W, et al. Synthesis of new derivatives of 2, 3-dicyano-imidazo [1, 2-a] pyrimidine from 4-hydroxy-6-methylpyran-2-ones. Arkivoc. 2008;2:59–70.

35.   Muzalevskiy V, Nenajdenko V, Shastin A, Balenkova E, Haufe G. Synthetic Approach to Alkoxy-β-(trifluoromethyl)styrenes and Their Application in the Synthesis of New Trifluoromethylated Heterocycles. Synthesis. 2009 Jul;2009(13):2249–59. <URL>.

36.   Ermolat'ev DS, Svidritsky EP, Babaev EV, Van der Eycken E. Microwave-assisted synthesis of substituted 2-amino-1H-imidazoles from imidazo[1,2-a]pyrimidines. Tetrahedron Lett. 2009 Sep;50(37):5218–20. <URL>.

37.   Bakherad M, Keivanloo A, Kalantar Z, Jajarmi S. Pd/C-catalyzed heterocyclization during copper-free Sonogashira coupling: synthesis of 2-benzylimidazo[1,2-a]pyrimidines in water. Tetrahedron Lett. 2011 Jan;52(2):228–30. <URL>.

38.   Li Z, Hong J, Zhou X. An efficient and clean CuI-catalyzed chalcogenylation of aromatic azaheterocycles with dichalcogenides. Tetrahedron. 2011 May;67(20):3690–7. <URL>.

39.   Hu L, Zhan Z, Lei M, Hu L. Facile and Green Method for the Synthesis of 4-Amino-1,2-Dihydrobenzo[4,5]Imidazo[1,2-a]Pyrimidine-3-Carbonitriles Catalysed by Ammonium Acetate. J Chem Res. 2012 Dec;36(12):738–9. <URL>.

40.   Borisov A, Tolmachev A, Zavada O, Kovalenko S. Synthesis of imidazo [1, 2-a] pyrazine and imidazo [1, 2-a] pyrimidine derivatives. Chem Heterocycl Compd. 2013;49(5):704–11.

41.   Mehranpour AM, Zahiri M. Synthesis and characterization of new benzimidazole derivatives using 2-substituted 1,3-bis(dimethylamino)-trimethinium salts. Tetrahedron Lett. 2014 Jul;55(29):3969–71. <URL>.

42.   Burbulienė MM, Dargytė J, Vainilavičius P. Interaction of methyl (2-methylsulfanyl-6-phenyl-4-thioxopyrimidin-3 (4H)-yl) acetate with hydrazine hydrate. Chemija. 2014;25(1).

43.   Aziz J, Piguel S. An Update on Direct C–H Bond Functionalization of Nitrogen-Containing Fused Heterocycles. Synthesis. 2017 Oct;49(20):4562–85. <URL>.

44.   Bhagat SB, Telvekar VN. NBS mediated protocol for the synthesis of N-bridged fused heterocycles in water. Tetrahedron Lett. 2017 Sep;58(37):3662–6. <URL>.

45.   Rawat M, Rawat DS. Copper oxide nanoparticle catalysed synthesis of imidazo[1,2-a]pyrimidine derivatives, their optical properties and selective fluorescent sensor towards zinc ion. Tetrahedron Lett. 2018 Jun;59(24):2341–6. <URL>.

46.   Bettanin L, Saba S, Doerner CV, Franco MS, Godoi M, Rafique J, et al. NH4I-catalyzed chalcogen(S/Se)-functionalization of 5-membered N-heteroaryls under metal-free conditions. Tetrahedron. 2018 Jul;74(29):3971–80. <URL>.

47.   Yagodinets PI, Rusnak OV, Lytvyn RZ, Skrypska OV, Pitkovych KhYe, Obushak MD. 4-(4-Acethylphenyl)-3-hydroxycoumarin in the Synthesis of Nitrogen-containing Heterocycles with a Neoflavonoid Moiety. Russ J Org Chem. 2019 Aug;55(8):1145–52. <URL>.

48.   Makra Z, Puskás LG, Kanizsai I. A convenient approach for the preparation of imidazo[1,2-a]-fused bicyclic frameworks via IBX/NIS promoted oxidative annulation. Org Biomol Chem. 2019;17(40):9001–7. <URL>.

49.   Maji PK. Synthesis of Pyrimidine-Annulated Five-Membered Heterocycles: An Overview. Curr Org Chem. 2019 Dec 24;23(20):2204–69. <URL>.

50.   White NA, Clagg K, Sirois LE, Lim NK, Nack WA, O'Shea PD, et al. Practical Synthesis of a Stable Precursor for Positron Emission Tomography Imaging Agent 18 F-GTP1. Org Process Res Dev. 2020 Sep 18;24(9):1690–9. <URL>.

51.   Obah Kosso AR, Kabri Y, Broggi J, Redon S, Vanelle P. Sequential Regioselective Diorganochalcogenations of Imidazo[1,2-a]pyrimidines Using I 2 /H 3 PO 4 in Dimethylsulfoxide. J Org Chem. 2020 Mar 6;85(5):3071–81. <URL>.

52.   Neto JSS, Balaguez RA, Franco MS, de Sá Machado VC, Saba S, Rafique J, et al. Trihaloisocyanuric acids in ethanol: an eco-friendly system for the regioselective halogenation of imidazo-heteroarenes. Green Chem. 2020;22(11):3410–5. <URL>.

53.   Patel OPS, Nandwana NK, Legoabe LJ, Das BC, Kumar A. Recent Advances in Radical C−H Bond Functionalization of Imidazoheterocycles. Adv Synth Catal. 2020 Oct 21;362(20):4226–55. <URL>.

54.   Fedotov VV, Ulomsky EN, Belskaya NP, Eltyshev AK, Savateev KV, Voinkov EK, et al. Benzimidazoazapurines: Design, Synthesis, and Photophysical Study. J Org Chem. 2021 Jun 18;86(12):8319–32. <URL>.

55.   Kiselyov AS, Smith L. Novel one pot synthesis of polysubstituted pyrazolo[1,5-a]- and imidazo[1,2-a]pyrimidines. Tetrahedron Lett. 2006 Apr;47(15):2611–4. <URL>.

56.   Parchinsky VZ, Shuvalova O, Ushakova O, Kravchenko DV, Krasavin M. Multi-component reactions between 2-aminopyrimidine, aldehydes and isonitriles: the use of a nonpolar solvent suppresses formation of multiple products. Tetrahedron Lett. 2006 Feb;47(6):947–51. <URL>.

57.   Adib M, Sheibani E, Bijanzadeh HR, Zhu LG. A new, one-pot, multi-component synthesis of imines of 3-amino-2-arylimidazo[1,2-a]pyridines, 3-amino-2-arylimidazo[1,2-a]pyrazines, and 3-amino-2-arylimidazo[1,2-a]pyrimidines. Tetrahedron. 2008 Nov;64(47):10681–6. <URL>.

58.   Reddy MV, Byeon KR, Park SH, Kim DW. Polyethylene glycol methacrylate-grafted dicationic imidazolium-based ionic liquid: Heterogeneous catalyst for the synthesis of aryl-benzo[4,5]imidazo[1,2-a]pyrimidine amines under solvent-free conditions. Tetrahedron. 2017 Aug;73(35):5289–96. <URL>.

59.   Hamidinasab M, Mobinikhaledi A. Organoacid-Decorated NiFe 2 O 4 Nanoparticles: An Efficient Catalyst for Green Synthesis of 2 H -Indazolo[2, 1-b]phthalazine-Triones and Pyrimido[1,2-a]benzimidazoles. ChemistrySelect. 2019 Jan 10;4(1):17–23. <URL>.

60.   Basyouni WM, Abbas SY, Abdelazeem NM, El-Bayouki KAM, El-Kady MY. Silica sulfuric acid/ethylene glycol as an efficient catalyst for the synthesis of benzo[4,5]imidazo[1,2-a]pyrimidine-3-carbonitrile derivatives. Synth Commun. 2019 Nov 17;49(22):3112–20. <URL>.

61.   Damghani FK, Pourmousavi SA, Kiyani H. Sulfonic Acid-Functionalized Magnetic Nanoparticles as an Efficient Catalyst for the Synthesis of Benzo[4, 5]imidazo[1, 2-a]pyrimidine Derivatives, 2-Aminobenzothia Zolomethylnaphthols and 1-Amidoalkyl-2-naphthols. Curr Org Synth. 2019 Dec 26;16(7):1040–54. <URL>.

62.   Verma P, Pal S, Chauhan S, Mishra A, Sinha I, Singh S, et al. Starch functionalized magnetite nanoparticles: A green, biocatalyst for one-pot multicomponent synthesis of imidazopyrimidine derivatives in aqueous medium under ultrasound irradiation. J Mol Struct. 2020 Mar;1203:127410. <URL>.

63.   Güngör T. One pot, multicomponent protocol for the synthesis of novel imidazo[1,2-a]pyrimidine-based pyran analogs: a potential biological scaffold. Monatshefte Für Chem - Chem Mon. 2020 May;151(5):781–9. <URL>.

64.   Akbari A, Dekamin MG, Yaghoubi A, Naimi-Jamal MR. Novel magnetic propylsulfonic acid-anchored isocyanurate-based periodic mesoporous organosilica (Iron oxide@PMO-ICS-PrSO3H) as a highly efficient and reusable nanoreactor for the sustainable synthesis of imidazopyrimidine derivatives. Sci Rep. 2020 Dec;10(1):10646. <URL>.

65.   Chavan P, Bangale S, Pansare D, Shelke R, Jadhav S, Tupare S, et al. Synthesis of substituted pyrimidine using ZnFe 2 O 4 nanocatalyst via one pot multi-component reaction ultrasonic irradiation. J Heterocycl Chem. 2020 Jul 11;jhet.4048. <URL>.

66.   Bakhshali-Dehkordi R, Ghasemzadeh MA. Fe3O4@TiO2@ILs-ZIF-8 Nanocomposite: A Robust Catalyst for the Synthesis of Benzo[4,5]imidazo[1,2-a]pyrimidines. J Mol Struct. 2021 Jul;1236:130298. <URL>.

67.   Anamika, Yadav CL, Drew MGB, Kumar K, Singh N. Ferrocene-Functionalized Dithiocarbamate Zinc(II) Complexes as Efficient Bifunctional Catalysts for the One-Pot Synthesis of Chromene and Imidazopyrimidine Derivatives via Knoevenagel Condensation Reaction. Inorg Chem. 2021 May 3;60(9):6446–62. <URL>.

68.   Güngör T. Microwave assisted, sequential two-step, one-pot synthesis of novel imidazo [1, 2-a] pyrimidine containing tri/tetrasubstituted imidazole derivatives. Turk J Chem. 2021;45(1):219–30. <URL>.

69.   Aydıner B, Seferoğlu Z. Proton Sensitive Functional Organic Fluorescent Dyes Based on Coumarin-imidazo[1,2- a]pyrimidine; Syntheses, Photophysical Properties, and Investigation of Protonation Ability: Proton Sensitive Functional Organic Fluorescent Dyes Based on Coumarin-imidazo[1,2-a]pyrimidine; Syntheses, Photophysical Properties, and Investigatio. Eur J Org Chem. 2018 Nov 25;2018(43):5921–34. <URL>.

70.   Sharma N, Kumar S, Kumar S, Mehta SK, Bhasin KK. Synthesis and characterization of fused imidazole heterocyclic selenoesters and their application for chemical detoxification of HgCl 2. New J Chem. 2018;42(4):2702–10. <URL>.

71.   El-Sayed R, Katouah HA. Synthesis of Pyrimidine and Pyran Derivatives with the Related Systems and the Study of Their Behavior in the Liquid Solutions. J Heterocycl Chem. 2019 Aug;56(8):2134–43. <URL>.

72.   Ghazoui A, Saddik R, Benchat N, Guenbour M, Hammouti B, Al-Deyab S, et al. Comparative study of pyridine and pyrimidine derivatives as corrosion inhibitors of C38 steel in molar HCl. Int J Electrochem Sci. 2012;7:7080–97. <URL>.

73.   Ech-chihbi E, Belghiti ME, Salim R, Oudda H, Taleb M, Benchat N, et al. Experimental and computational studies on the inhibition performance of the organic compound "2-phenylimidazo [1,2-a]pyrimidine-3-carbaldehyde" against the corrosion of carbon steel in 1.0 M HCl solution. Surf Interfaces. 2017 Dec;9:206–17. <URL>.

74.   Pareek S, Jain D, Hussain S, Biswas A, Shrivastava R, Parida SK, et al. A new insight into corrosion inhibition mechanism of copper in aerated 3.5 wt.% NaCl solution by eco-friendly Imidazopyrimidine Dye:

experimental and theoretical approach. Chem Eng J. 2019 Feb;358:725–42. <URL>.

75.   Elshakre ME, Moustafa H, Hassaneen HuwaidaME, Moussa AbdelrahimZ. Electronic spectra and DFT calculations of some pyrimido[1,2-a]benzimidazole derivatives. Spectrochim Acta A Mol Biomol Spectrosc. 2015 Jun;145:1–14. <URL>.

76.   Wysocki W, Karczmarzyk Z, Rządkowska M, Szacoń E, Matosiuk D, Urbańczyk-Lipkowska Z, et al. Structural investigations of a series of 1,6-aryl-7-hydroxy-2,3-dihydroimidazo[1,2-a]pyrimidin-5(1H)-ones with potential antinociceptive activity. J Mol Struct. 2015 Aug;1094:137–47. <URL>.

77.   Dylong A, Goldeman W, Sowa M, Ślepokura K, Drożdżewski P, Matczak-Jon E. Synthesis, crystal structures and spectral characterization of imidazo[1,2-a]pyrimidin-2-yl-acetic acid and related analog with imidazo[2,1-b]thiazole ring. J Mol Struct. 2016 Aug;1117:153–63. <URL>.

78.   El Bakri Y, Anouar EH, Ramli Y, Essassi EM, Mague JT. Synthesis, crystal structure, spectroscopic characterization, Hirshfeld surface analysis, and DFT calculations of 1,4-dimethyl-2-oxo-pyrimido[1,2-a]benzimidazole hydrate. J Mol Struct. 2018 Jan;1152:154–62. <URL>.